THE DYNAMICS OF THE AMERY ICE SHELF FROM A COMBINATION OF TERRESTRIAL AND SPACE GEODETIC DATA

by

Matthew A King (Matthew Alistair)

B.Surv Hons. (University of Tasmania)

A thesis submitted in fulfillment of the requirements for the degree of

Doctor of Philosophy (Ph.D.)

Centre for Spatial Information Science, University of Tasmania

May, 2002

DECLARATION

I received assistance from others for some of the work presented in this thesis. The processing of the 1990-91 GPS data (chapter 5) was performed in collaboration with Rachael Manson. The processing of the 1995-96 kinematic data (chapter 5) was performed by Chris Watson. The design of the GPS system (chapter 7) was done in partnership with Anthony Sprent and Chris Watson.

Tidal data and constituents for Beaver Lake were supplied by the National Tidal Facility, The Flinders University of South Australia, Copyright reserved.

Other than those cases already mentioned, this thesis contains no material that has been accepted for a degree or diploma by the University or any other institution, except by way of background information and duly acknowledged in this thesis. To the best of my knowledge and belief, no material previously published or written by another person, except where due acknowledgment is included in the text of this thesis.

.....

Matthew A King

AUTHORITY OF ACCESS

This thesis may be made available for loan and limited copying in accordance with the *Copyright Act 1968*.

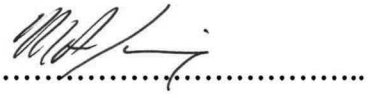

.....

Matthew A King

SUPPORTING PUBLICATIONS

Some of the work presented in this thesis appears in published papers. Where substantial parts of these papers are reproduced in this thesis, it is in all cases my own original contribution to those papers that is transposed.

The papers directly related to this thesis are:

Chapter 4 (section 4.3.3)

King M., Nguyen L. N., Coleman R., and Morgan P. (2000). "Strategies for High Precision Processing of GPS Measurements with Application to the Amery Ice Shelf, East Antarctica." *GPS Solutions*, 4(1), 2-12.

Chapter 4 (section 4.4)

King M., Coleman R., and Morgan P. (2000). "Treatment of horizontal and vertical tidal signals in GPS data: A case study on a floating ice shelf." *Earth Planets Space*, 52(11), 1043-1047.

Chapter 5 (section 5.12)

Manson R., **King M.**, and Coleman R. (1998)."GPS: Putting it on ice." *Proceedings of the 39th Australian Surveyors Congress*, Launceston, Tasmania, 8-13 November 1998, 31-42.

The most exciting phrase to hear in science, the one that heralds the most discoveries, is not "Eureka!", but "That's funny..."

Isaac Asimov

...man will occasionally stumble over the truth, but usually manages to pick himself up, walk over or around it, and carry on.

Winston S. Churchill

The fear of the LORD *is the beginning of wisdom; all who follow his precepts have good understanding.*

Psalm 111:10

ABSTRACT

Understanding and monitoring the changes occurring in the Earth's climate are of increasing interest to scientists, legislators and policy makers, environmentalists and to the wider-population. The Antarctic continent is particularly suitable for studies into climate change, as it is the major geographical region where the climate signature influences the production and storage of water and ice. The outlet glaciers and ice shelves are the most dynamic regions of Antarctica and as such can be expected to respond to variations in the climate signal sooner than the other regions. Unlike the glaciers, which may have response lags of hundreds or thousands of years, the ocean-ice interface of the ice shelves are sensitive to changes in sea level or ocean temperature, resulting in a much faster response times. If an accurate determination of change is to be made, it is of critical importance that baseline (and future) measurements of change and rate of change are of the highest accuracy and precision.

The Lambert Glacier-Amery Ice Shelf system is a major feature of East Antarctica. This study uses a combination of historical-terrestrial and modern-space geodetic measurements to increase our understanding of the dynamics of the Amery Ice Shelf (AIS). Parameters of interest are horizontal and vertical velocity and strain. Vertical ice shelf motion induced by the tides is also of significant interest. The available data spans approximately 30 years, providing an opportunity to test for change in the state of the ice shelf.

Continuous Global Positioning System (GPS) measurements that are longer than one day were processed using a segmentation technique for use in tidal studies. Tidal signals are evident as far south as 73°S, confirming that the southern-most part of the grounding zone is more than 200km to the south of the previously adopted position. Upon analysis, significant north-south amplification is revealed in each of the tidal constituents caused by a reduction in the depth of the water column close to the

grounding zone. First-estimates of the height of the water column are made for the southern-most sites based on an analysis of the GPS-derived tidal constituents. Higher order and non-linear tides are evident in the residuals and thus need to be modelled for high accuracy applications. Comparisons were made with three different numerical tidal models with a view to addressing fundamental corrections for future satellite missions, such as ICESat and CryoSat. These missions will require high resolution, accurate tidal models to remove the tidal signals from ice shelf measurements. Significant amounts of *in situ* tidal measurements (>2 months and up to 1 year) are required for input into the tidal models if these missions are to reach their promised accuracy. To provide sufficient ice shelf tidal measurements, an inexpensive autonomous GPS system was designed to run for periods greater than 8 weeks during the Antarctic summer, yet can be easily modified to make longer term measurements of up to one year.

The terrestrial ice shelf surveys of 1968-69 and 1969-70 provide the backbone to the current glaciological understanding of the AIS. This investigation shows that the widely circulated coordinate and velocity results from this survey had significant error. The data are reanalysed using modern least-squares methods and new results provided in a modern, stationary (tide-free), highly precise and accessible International Terrestrial Reference Frame (ITRF96). Coordinate uncertainties (95% confidence level) of the new ITRF solution are generally less than 5m, while the velocity uncertainties are better than 3.7myr^{-1} in magnitude and 0.6° in flow direction.

More recent GPS data, collected from 1988 onwards, were analysed using modern least squares processing techniques in which the results of each field season were held as quasi-observations and then combined in the ITRF97. Velocity uncertainties (95%) are generally less than 3.9myr^{-1} in magnitude and 0.8° in flow direction. The final velocities (both terrestrial and GPS) were compared to an independent set of velocities derived from sequential Radarsat images, revealing systematic biases in the remote sensing velocity magnitude of ±20-40myr^{-1} and 1-4° in direction. The combined terrestrial and

GPS velocities represent the most comprehensive, consistent and accurate set of velocities from *in situ* data presently available for the AIS.

A congruency test is performed to test the hypothesis that the ice shelf velocity profile is unchanged during the period 1968-1999. This approach provides an overview of both change and rate of change occurring on the Amery Ice Shelf for the first time and hence provides an important contribution with new information on the ice shelf dynamics. The test is shown to fail at the 95% confidence interval for velocity directions and velocity magnitude. While the sample size is small (9 station pairs), the sign of the differences are essentially uniform, with the GPS velocities being less. Consequently, we suggest that the ice shelf may have slowed by 1-5myr^{-1} during the thirty-year period 1968-70 to 1998-99 where velocity comparisons are available. Such a slowing may be a result of changes in one of the other balance forces acting on the Amery Ice Shelf (temperature of the ocean, snow accumulation, ice discharge rate).

Strain rate estimates can be deduced through the combination of the terrestrial data and the quasi-observations from the GPS analysis using four dimensional integrated geodesy. Strain rates are determined using both the individual terrestrial and GPS velocities along with an analysis combining the two data sets. This combined strain solution represents the most precise and spatially dense set of strain grids available for the AIS from *in situ* data. Further strain information is gathered from computing forward and transverse strain rates in the direction of the terrestrial traverse. These results agree with those strain rates computed from Radarsat images.

Using a combination of the derived velocities (horizontal and vertical) and strain rates, combined with snow accumulation, surface slope, ice thickness and water and ice density information, melt rates were determined at four GPS locations. The results generally agree with estimates from two numerical ocean circulation models and measurements using velocities and strains derived from Radarsat images, although the

precision of the available accumulation measurements limits the precision of the derived melt rates.

Accurate ground data plays a vital part in the calibration and validation of remote sensing measurements, especially for radar altimeters (ERS-1/2), laser altimeters (ICESat), synthetic aperture radar (SAR) measurements and the new generation of satellite gravity missions (GOCE/GRACE). What is needed for this to occur is GPS data collected and processed to the highest precision in a consistent reference frame, while longer GPS time series are required to measure and hence correct biases introduced by ice shelf tidal motion. This thesis provides methods and recommendations to achieve these goals. Such calibration/validation activities will undoubtedly play an essential role in the integration of future data and measurements for ice sheet mass balance studies.

TABLE OF CONTENTS

ACKNOWLEDGMENTS

A PhD is not undertaken in isolation – there are many people to thank for the many and varied contributions they have made on both professional and personal terms.

Firstly, thanks to those who supplied data that enabled this project to be performed. Ian Allison provided the early GPS data, while Mike 'Duk' Craven and Andrew Ruddell provided the 1995-96 and 1997-98 data sets respectively. They answered numerous questions about these data sets – sometimes several times over! AUSLIG Geodesy Section provided GPS data and answered numerous requests for information on Antarctic survey marks and methods. Paul Tregoning (ANU) supplied the BVLK and LDBF data.

Max Corry was continually enthusiastic about the project even when asked to remember technical information from thirty years prior! The terrestrial data analysis would not have occurred without his meticulous survey methods and notes from the 1968-69 and 1969-70 surveys.

Helen Amanda Fricker was a great encouragement and provided data. Neal Young supplied data and helped me understand more about ice shelf glaciology, as did Roland Warner and Bill Budd. The GAMITeers at MIT (Bob King, Tom Herring and Simon McClusky) provided many patient answers to questions about the software. Danan Dong also helped in understanding the FONDA software. John Hunter provided the tidal analysis software. The GMT software – used for creating some figures in chapter 2 – is made freely available by Paul Wessel and Walter H. F. Smith. I am most thankful for all of this assistance.

I would also like to thank my roommates during the last four years, particularly those in the geodesy program here in CenSIS: Rachael Hurd, Lau Nguyen, Chris 'quick question' Watson and Paul 'Diggers' Digney. They have been a fantastic group of

friends and have made a big contribution to this being such an enjoyable time of my life. Rach and I travelled to Antarctica together – and her previous Antarctic experience was of great help and comfort as we enjoyed the visual splendour that is Antarctica. Thanks for putting up with me and making the trip such an amazing one! A big thank you to the remainder of the Amery Ice Shelf team from 1998-99: Andrew Ruddell, Barbara Smith, Ben Galbraith and John Tomms.

My thesis supervisors, Richard Coleman and Peter Morgan, have been simply fantastic. I have tremendously enjoyed working with them, and have appreciated them regarding me as an equal. They have shown themselves incredibly thoughtful and patient and, in the end, great friends. Their knowledge across a broad range of fields continues to amaze me and they never failed to operate on an 'open door' policy. I must also apologise to their wives, Virginia and Carol – I am sorry that they have spent so much time after hours reading this thesis! In addition, a big thank you to Elisabeth Wilson who carefully scrutinised this document.

My parents, Graham and Estelle, and two brothers, Simon and Jason, have provided me with a great start to life, for which I am tremendously thankful. Thanks mum and dad for giving me a free hand to pursue my field of interest and for supporting and loving me all the way!

Near the beginning of 1997 – at the start of my PhD – I travelled to Cyprus for an archaeological excavation carried out by the University of Sydney. I wasn't to know I would meet an amazing woman from Sydney who, in January 2000, became my wife! Julia, thank you for being such an amazing friend and for being so patient, caring and loving especially in these last months. I look forward to spending these extra hours with you.

Finally, I give thanks for the grace and mercy shown to me by God in providing me with the eternal hope found in Jesus Christ and for giving me such an opportunity to investigate and explore his world.

Chapter 1

INTRODUCTION

1.1 Overview

This study is concerned with the application of terrestrial and space geodetic data to the Amery Ice Shelf, East Antarctica. In particular, high precision positions are determined spanning a period of over thirty years, leading to the derivation of climatically valuable information on ice shelf and ocean variables. If accurate measurements of climate change are to be made, what is required are accurate baseline measurements against which further measurements can be compared. In regard to ice shelves, the parameters of interest are grounding zone location, the amount of basal melt and re-freezing under the ice shelf and three-dimensional velocity and strain. Affecting the basal melt and freezing is the ocean circulation and tidal motion beneath the ice shelves. For the effects of climate change to be seen in these parameters, rigorous processing methodologies must be applied to the collected data.

The Amery Ice Shelf forms the coastal outlet of one of Antarctica's major drainage basins, the Lambert Glacier-Amery Ice Shelf system. The immediate response of the ice shelves to climate change is increased basal melt and a southerly shift in the position of the ice shelf grounding zone. Longer-term changes may include increased iceberg calving and even total ice shelf disintegration. This thesis shows that historical-terrestrial and early GPS measurements benefit from a re-examination using modern processing and least squares techniques. Furthermore, a combination of historical-terrestrial and modern-space geodetic observations provides the most precise determination of changes (velocity and strain) in the condition of the ice shelves currently available. Modern GPS data are also analysed, showing that this measurement tool is extremely valuable for precise determination of ice shelf tidal motion and grounding zone location.

Tidal range is a determining factor in the ability of an ice shelf to remain connected to the continental ice. Precise determination of tidal motion is also required for accurate modelling of the sub-ice shelf ocean circulation and for correction of remote sensing signals designed to measure ice shelf topography such as from ERS, ICESat and CryoSat. Each of these applications contributes to the understanding of the response of Antarctica's ice shelves to variations in climate, and hence the ability to detect climate change and its rate of change.

1.2 Climate change and Antarctica

1.2.1 Climate change

In May 2001, the Intergovernmental Panel on Climate Change (IPCC) in the Third Assessment Report concluded that global average surface temperature has increased by 0.6±0.2°C in the 20th Century, about 0.15°C greater than the figure reported in 1994 (IPCC, 2001b). Furthermore, it is "very likely" that the 1990s were the warmest decade and 1998 the warmest year on record. There has been a marked increase in global temperatures since the industrial revolution. Snow cover has also reduced by 10% since the 1960s, non-polar glaciers have retreated *en masse* and Northern Hemisphere sea ice has decreased by 10-15% since the 1950s. In regard to sea level, tide gauge data show that global average sea level rose between 0.1 and 0.2m during the 20th Century (IPCC, 2001b). On the other hand, some areas appear to be unchanged at present, such as the Antarctic sea ice extent (Jacka and Budd, 1998).

The IPCC has concluded that "there is new and stronger evidence that most of the warming observed over the last 50 years is attributable to human activities" (IPCC, 2001b). The consequence of such climate change is also likely to be felt by humans. For example, changes in extremes of weather and climate are expected, such as higher temperatures, increased drought and more intense tropical cyclones are all likely results of a warming climate (IPCC, 2001a). Furthermore, the currently observed changes are expected to continue, with sea level, for example, expected to rise by between 0.09 and 0.88m before 2100.

In regard to the Antarctic ice sheet, regional warming is known to have occurred on the Antarctic Peninsula (Vaughan and Doake, 1996). Many other Antarctic sites also suggest a similar warming, although this result is not consistent across the entire continent (Jacka and Budd, 1998).

With impacts upon the human population almost certain, legislators, policy makers, scientists and the general public have an increasing interest in climate change research. Many of the predictions of climate change will have dramatic consequences on the human population, agriculture and industry. For accurate planning to take place, the precisions of both the measurements and models need to be increased from those presently available. It is therefore vital that new technologies and methods are implemented quickly and both old and new data used efficiently, to determine best estimates of climate change and its effects around the world.

1.2.2 Antarctica's role in the global climate system

The Antarctic continent cannot be studied in isolation from the rest of the Earth, since the Earth is an open system. The ocean-ice and ice-atmosphere interfaces are examples of this. Any change in the state of balance of the Antarctic continent will have a consequent impact on the ocean and atmosphere, which in turn have an impact on the Antarctic continent. Figure 1-1 illustrates the interaction of the major Earth systems: the atmosphere; cryosphere (ice sheets, glaciers, snow, permafrost and sea ice); lithosphere (solid surface of the Earth); hydrosphere (rivers, oceans); biosphere (regions where life exists).

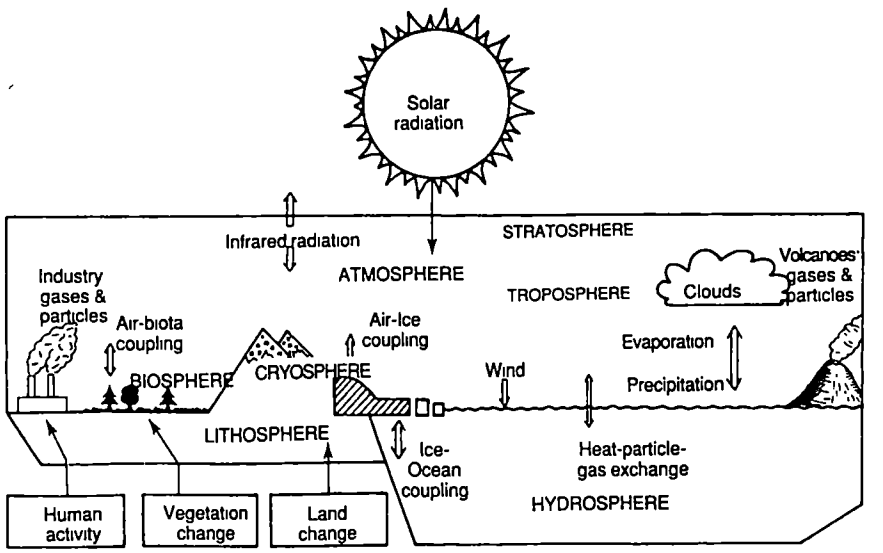

Figure 1-1· Interaction of the major Earth systems as shown in (Ellis, 1991)

While Antarctica has a wide range of *effects* on the Earth's climate systems, by far the most important Antarctic *response* to climate change is that of the release or storage of water as ice. This response occurs both rapidly (sea ice and snow) and slowly (continental ice) (Meier, 1983). The polar regions store as much as 88% of the world's fresh water as ice. While this is only 2.1% of the total volume of water on the Earth, if it were to entirely melt, the resulting sea level rise would be approximately 66m. This value comprises 60m and 6m of sea level rise from the East and West Antarctic ice sheets, respectively (Oerlemans and van der Veen, 1984). Of the two regions of Antarctica (see Figure 1-2), the West Antarctic ice sheet is more vulnerable to climate change since much of the bedrock in this region is below sea level. Consequently, if the ice shelves in this region disintegrate, the oceans will immediately influence the grounded ice (Oppenheimer, 1998).

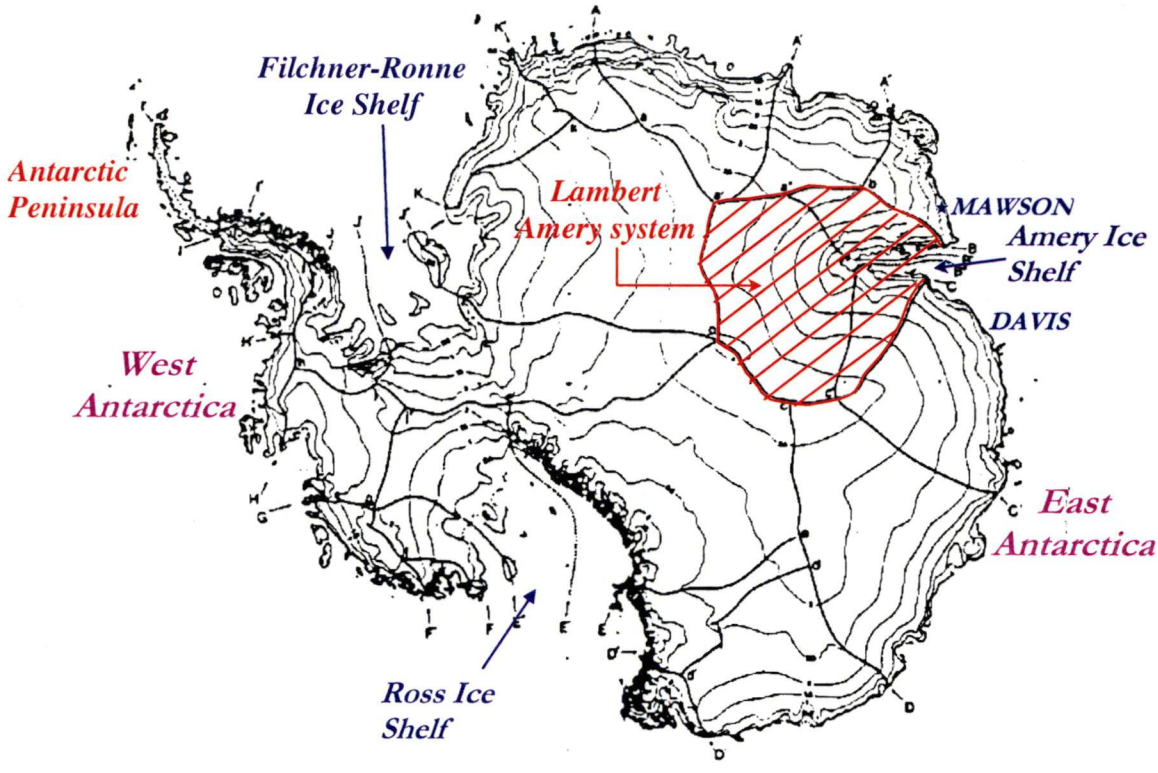

Figure 1-2: Map of Antarctica showing the major features and the Lambert-Amery System. Adapted from Phillips (1999), itself adapted from Giovinetto and Bentley (1985).

When compared to most other regions of the Earth, Antarctica is still largely a scientific unknown. This is even true of the most accessible coastal Antarctic locations. Further understanding of this vast continent is limited by the hostile weather conditions during all but a few months in summer, and the large amounts of infrastructure involved in mounting any campaign in Antarctica. The fields of glaciology and geodesy are no different in this regard. Antarctica's major ice shelves – physical continuations of the Antarctic continent onto the oceans – have perhaps received more attention than other areas due to their relative ease of access from the oceans. However, even here the lack of adequate data limits scientific understanding. For example, it is not presently known if the mass balance of Antarctica is positive or negative (Meier, 1993), fifty years after the beginning of research in the International Geophysical Year. It is therefore important to use the available data in an efficient manner, deriving as much accurate information as possible from the data resources that are available and identifying the key limitations for future measurement campaigns.

1.2.3 Ice shelves

> *"A glacier which primarily occurs in a floating state is called an ice shelf. Such a glacier is recharged by the influx of continental ice, accumulation of atmospheric precipitation, freezing of seawater into ice and the attachment of icebergs. It also possesses a characteristically flat shape owing to the peculiar ice flow in the absence of any significant friction from below." (Barkov, 1985)*

To this definition one may add that ice is lost from an ice shelf by the reverse of the above means of addition: namely, discharge/calving in the form of icebergs, melting of the ice shelf along its lower boundary by seawater, and surface ablation, although by far the most dominant processes are calving and melt.

Floating ice shelves occupy 44% of the Antarctic coastline (Drewry, 1983), 10.8% of the area and 2-3% of the volume of the entire Antarctic ice mass (Barkov, 1985). They are characteristically composed of 0-2%, 5-20% and 80-95% snow, firn and ice in terms of thickness, respectively (Barkov, 1985). They receive a relatively high amount of accumulation with ~25% of net Antarctic ice sheet precipitation occurring on only 10.8% of its area (Jacobs *et al.*, 1992). Most of the mass loss from the Antarctic continent occurs through the ice shelves, via icebergs or basal melt – a total loss of approximately 2560Gtyr^{-1} (Jacobs *et al.*, 1992).

The ocean-ice interface of ice shelves makes them particularly susceptible to changes in the Earth's climate (Williams *et al.*, 1998). Figure 1-3 shows a typical scenario. Warming of the oceans may cause an increase in ice shelf basal melt, with resultant ice shelf thinning. Increased loss of ice through increased iceberg calving may occur as a result. An increase in basal melt will change the salinity and temperature of the ocean, with wider effects caused by consequent changes in ocean circulation (Barkov, 1985; Jacobs *et al.*, 1992). Furthermore, ocean warming along with associated sea level rise will result in a shift in the position where the grounded continental ice becomes afloat[1] (Vaughan, 1995). Conversely, Nicholls (1997) has suggested that ice shelf thickening may occur in a warming climate due

1. This location is known as the ice shelf grounding zone.

to a lower level of winter sea ice production causing a reduction in High Salinity Shelf Water, especially near the grounding zones. An increase in the air temperature will result in increased surface melting during the summer time, further thinning the ice shelves (Phillips, 1998). Melt pooling is thought to be a significant contributor to ice shelf disintegration (Scambos *et al.*, 2000).

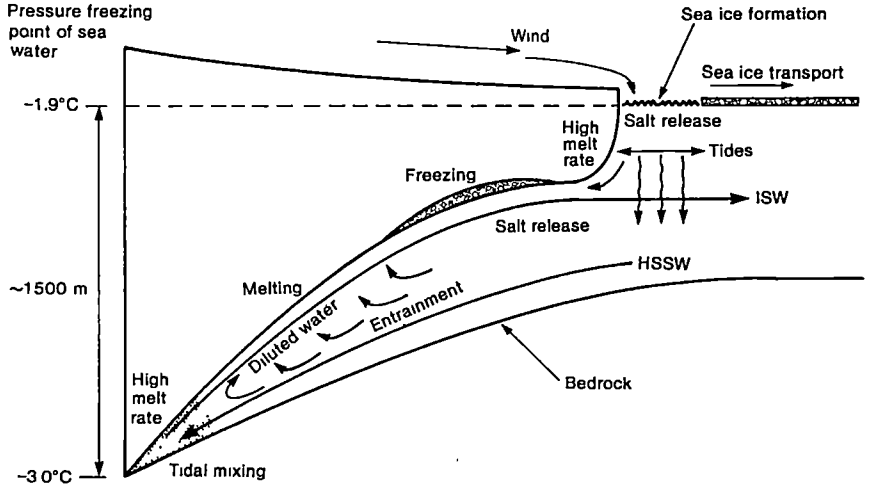

Figure 1-3 Schematic representing the ocean circulation beneath the Ross Ice Shelf (Morris, 1991). The circulation beneath the Amery Ice Shelf is similar (see Wong, 1994). Dense High Salinity Shelf Water (HSSW) flows beneath the ice shelf where it interacts with the ice shelf ice. Due to the addition of fresh water from ice shelf basal melting it re-emerges in the form of relatively fresh Ice Shelf Water (ISW).

An increase in basal melt rates does not affect sea level since the ice shelf is already afloat. However, it is thought that the ice shelves may act as buffers, preventing the grounded continental ice from moving more rapidly onto the ocean surface, and thus affecting sea level (Hughes, 1992). The break-up of an ice shelf may, therefore, result in a surge of previously grounded ice.

Actual ice shelf breakup along the Antarctic Peninsula has been reported on numerous occasions during the last decade (Doake and Vaughan, 1991; Skvarca, 1993; Rott *et al.*, 1996; Vaughan and Doake, 1996). Such events were predicted by Mercer (1978), who recommended that the ice shelves be monitored regularly for change. Bouin and Vigny (2000) have suggested ice shelf break-up in the Antarctic Peninsula may be a cause of measured anomalous crustal motion in this region. Ocean and atmospheric warming, tidal

motion and wave action from storms are all thought to be contributors to such rapid ice shelf break-up. Changes in the ice shelf dynamics (particularly ice shelf velocity, strain and thickness) are hence important to monitor. Knowledge of tidal motion, ocean circulation and grounding zone location are also vital parameters for modelling the effects of potential climate change on ice shelves (Williams *et al.*, 1998).

1.2.4 Lambert Glacier-Amery Ice Shelf system

The Lambert Glacier-Amery Ice Shelf system is located in East Antarctica, between latitudes 67°S and 75°S and longitudes 68°E and 75°E[2]. It is the most prominent feature of East Antarctica and is the largest glacier-ice shelf system located entirely within East Antarctica (see Figure 1-2). The Lambert-Amery system is extremely dynamic, draining approximately 16% of the grounded Antarctic continent (Phillips, 1999) through only approximately 1.7% of the total Antarctic coastline (Giovinetto and Bentley, 1985). Consequently, it is an important drainage system in terms of the total Antarctic mass balance.

Until recently, the southern grounding zone of the Amery Ice Shelf (AIS) was widely thought to be located around latitude 71.5°S (Budd *et al.*, 1982), although Robin (1979) argued for a more southern location due to high levels of frozen marine ice in an ice core taken near the ice shelf front. Phillips and (1999) and Fricker *et al.* (2001a) showed that the grounding zone was located around 73.0°S, approximately 250km to the south of the previously stated position.

Significant regions of basal melt and freeze have also been identified (Fricker *et al.*, 2001b), consistent with the results from a three-dimensional ocean circulation model (Williams *et al.*, 1998). Marine ice thicknesses of up to 200m may be found on the western side of the AIS. The net result is super-cooled, relatively fresh Ice Shelf Water exiting from under the AIS on the western side (Wong, 1994). These results have been confirmed during a recent

2. A visual flyover of the Lambert-Amery system may be downloaded from http://svs.gsfc.nasa.gov/imagewall/Antarctica.html

hydrographic cruise across the front of the AIS (personal communication, N. Bindoff, 2001).

The AIS is at a latitude similar to the Antarctic Peninsula ice shelves, and so may be at risk of similarly rapid break-up. However, the AIS is confined on three sides and therefore receives more protection from the potentially destructive action of the ocean. Furthermore, as with most of the East Antarctic ice sheet, the grounded continental ice surrounding the AIS is above sea level, so any sudden disintegration of the ice shelves is unlikely to allow significant melting of this ice.

1.3 Thesis aims and structure

The aim of this thesis is to establish a more thorough and precise understanding of the dynamics of the Amery Ice Shelf using a combination of terrestrial and Global Positioning System (GPS) measurements. This chapter has outlined the importance of this work in terms of climate change research.

Chapter 2 provides a background to the GPS system as applied to the Antarctic environment. Background is also provided on reference frames in the context of the need for measurement results to be held in consistent and accessible reference frames.

Chapter 3 describes the types of ice movement experiments conducted in Antarctica using both terrestrial and space-geodetic methods. The Amery Ice Shelf measurement campaigns are also described in some detail, particularly the 1968-70 terrestrial surveys, noting significant results and any difficulties encountered.

Chapter 4 contains the analysis of GPS data collected on the Amery Ice Shelf for the purpose of determining ice shelf tidal motion. Tidal constituents are determined at each of the GPS ice shelf sites and compared against other sites, numerical ocean tide models and *in situ* data.

Chapter 5 contains the analysis of both the 1968-70 terrestrial and all GPS data for the purpose of deriving ice shelf velocity fields. Derived velocities are compared between the methods and with satellite-derived estimates.

Chapter 6 describes the relevant strain theory and the computation of strain values from each of the results given in Chapter 5. The terrestrial and GPS data are combined using the theory of integrated geodesy resulting in the best estimates of long-term strain for the Amery Ice Shelf. The strain rates are then combined with the velocities and other ice shelf parameters to determine basal melt rates at distinct geographical locations.

Chapter 7 provides a series of recommendations for GPS measurements in Antarctica, with a particular focus on ice movement measurements. An autonomous GPS ice movement system is described in full, providing an inexpensive means of collecting medium term (>12 weeks) of Antarctic ice movement measurements.

Chapter 8 brings together the conclusions of the thesis. The Chapter summarises the contributions of this thesis to the knowledge of the dynamics of the Amery Ice Shelf.

Chapter 2

REFERENCE FRAMES AND THE GLOBAL POSITIONING SYSTEM

2.1 Introduction

The measurements dealt with in this thesis, like most measurements made across different epochs, require a consistent frame of reference if they are to be compared or combined (Seeber, 1993). This may require some effort on the part of the researcher, but it is necessary if the alternative – an *ad hoc* series of measurements in an equally *ad hoc* series of reference frames – is to be avoided. For the data analysed in this thesis, this is borne out by the need to compare and combine measurements made over a period of thirty years, across nine measurement epochs and using two quite different measurement techniques.

Global reference frames, rather than local frames, are focussed on here. Global reference frames are particularly important in the context of this thesis since they are required to compare the results presented here with those derived using remote sensing techniques. Remote sensing measurements are held in global reference frames and to allow for inter-comparison the results presented here also need to be considered in such a frame.

An outline of the second of these techniques, the Global Positioning System (GPS), occupies the later part of this Chapter, providing a background on the system, and in particular any difficulties in making measurements in Antarctica. Firstly, however, reference systems and frames are dealt with, providing an explanation of modern global reference system and frames. The initial GPS connection of the Antarctic continent to the global reference frame is explained in some detail.

2.2 Reference systems and frames

2.2.1 Overview

Observations made at a given epoch may be converted to positions by means of a geodetic reference system. The coordinates of a point will differ according to which reference system and epoch they refer. Reference systems are normally divided into two classes: *space-fixed (celestial)* and *Earth-fixed (terrestrial)*. Celestial reference systems are required for the description of satellite motion. Terrestrial reference systems are required for the positions of the observation stations and for the description of results from satellite geodesy (Seeber, 1993). Most users also find it easiest to consider position in terms of a terrestrial reference system.

A realisation of a reference system, known as a *reference frame*, is based on a set of adopted or estimated coordinates. In the case of the celestial reference frames, these are the coordinates of a set of stars or quasars (e.g., Ma *et al.*, 1998). In the case of terrestrial reference frames, they are the coordinates and velocities of a set of observing stations on the Earth's surface (e.g., Boucher *et al.*, 1996; Sillard *et al.*, 1998). By definition, there may be an infinite number of realisations of a reference system since reference frames depend on the chosen set of quasars/stations.

2.2.2 Inertial reference systems and frames

An inertial reference (coordinate) system is one that is at rest or is in a state of uniform rectilinear motion, without any acceleration. That is, it conforms to Newton's first law of motion (Seeber, 1993). The origin of one such system (known as the IERS[1] Celestial Reference System, ICRS) is defined as having its origin at the barycentre of the solar system and the directions of the axes are fixed with respect to the quasars (McCarthy, 1996). See Arias (1995) for more details. Such a system is important for determination of satellite motion, including GPS satellites, and for observations of stars and quasars for Very Long Baseline Interferometry (VLBI).

Of particular importance is the realisation of the ICRS, the IERS Celestial Reference Frame (ICRF) described in McCarthy (1996). This frame is defined by VLBI observations of extra-galactic radio sources (quasars) (Ma *et al.*, 1998). The directions of

1. International Earth Rotation Service

the ICRF are also consistent with those of the fundamental star catalogue FK5 at J2000.0. As of January 1, 1998 the ICRF replaced the stellar FK5 catalogue as the fundamental celestial reference frame (Ma *et al.*, 1998). While direct access to the quasars is limited to VLBI observations, indirect access may be gained through ties to appropriate terrestrial reference frames.

2.2.3 Terrestrial reference systems and frames

The most commonly used terrestrial reference system is the IERS Terrestrial Reference System (ITRS) and its various realisations, known as International Terrestrial Reference Frames (ITRF) (Boucher and Altamimi, 1989). The ITRS is defined as being geocentric, with the z-axis coinciding with the mean rotation axis of the Earth defined by the IERS Reference pole. The x-axis is in the plane of the 0° IERS Reference Meridian, defined by the adopted longitudes of the reference stations (McCarthy, 1996), with the y-axis at right angles to the x-z plane.

These ITRFs are based on combinations of data from a variety of space based techniques, such as GPS, Doppler Orbit Determination and Radio-positioning System (DORIS), VLBI, Satellite Laser Ranging (SLR), Lunar Laser Ranging (LLR), etc. The individual solutions of station positions and velocities provided by each of these methods may be seen as a realisation of a particular reference frame. These solutions are combined using two (position and velocity) 7-parameter similarity transformations to form the ITRF (Sillard *et al.*, 1998). The position of a point located on the surface of the solid Earth at particular epoch (t), is expressed by (McCarthy, 1996):

$$\vec{X}(t) = \vec{X}_0 + \vec{V}_0(t - t_0) + \sum_i \Delta\vec{X}_i(t) \qquad (2.1)$$

where $\Delta\vec{X}_i(t)$ are coordinate corrections due to various time variable effects, and $\vec{X}_0$ and $\vec{V}_0$ are site position and velocity at the reference epoch t_0. The corrections to be considered include solid Earth tide displacement, ocean loading, post glacial rebound, and atmospheric loading.

Since the late 1980s, updated realisations of the ITRS have been released approximately every one to two years as significant amounts of new data are assimilated, with details published in IERS Technical Notes (e.g., Boucher *et al.*, 1996).

The realisation consists of a set of station cartesian coordinates and velocities and the full variance-covariance matrix (VCV matrix) of these parameters. Prior to the 1996 realisation of the ITRF (denoted as ITRF96), the VCV matrix was only provided for the station coordinates (Sillard *et al.*, 1998). The current frame realisation is ITRF97, although ITRF2000 is currently being computed. Each realisation brings an increased number of station coordinates and velocities, along with improved standard deviations for these parameters. These improvements in precision are a result of both extra observations and improved local survey ties for collocated sites. In ITRF96, station coordinate accuracy was sub-centimetre for 50% of stations, whereas in ITRF94 no stations achieved this accuracy level.

For GPS users, the World Geodetic System 1984 (WGS84) is an important reference system (Malys and Slater, 1994; NIMA, 1997). The coordinates uploaded to the GPS satellites are in WGS84, and consequently so are the user-received satellite coordinates via the broadcast ephemerides. The WGS84 system has been updated at least twice to date. These updates are known as G730 (Malys and Slater, 1994) and G873 (Cunningham *et al.*, 1998), with the update names referring to the GPS week of implementation. WGS84 is now equivalent to the ITRF (ITRF94 onwards) at the 100mm level (NIMA, 1997).

2.2.4 Transformations between systems and frames

The transition from the terrestrial reference system (TRS) to the celestial reference system (CRS) at the date t is achieved through a series of transformations:

$$[CRS] = PN(t)\,R(t)\,W(t)[TRS] \tag{2.2}$$

where the transformation matrices $PN(t)$, $R(t)$ and $W(t)$ account for motion (precession, nutation) of the Celestial Ephemeris Pole (CEP) in the CRS, the rotation of the Earth around the axis of the CEP and Polar motion respectively. The IERS Earth Orientation Parameters provide the permanent tie of the ICRF to the ITRF. The details of the three matrices are found in McCarthy (1996) and Mueller (1969).

A set of cartesian coordinates (x_1, y_1, z_1) may be converted to another cartesian system (x_2, y_2, z_2) by means of a 7-parameter similarity transformation (McCarthy, 1996):

$$\begin{pmatrix} x_2 \\ y_2 \\ z_2 \end{pmatrix} = \begin{pmatrix} x_1 \\ y_1 \\ z_1 \end{pmatrix} + \begin{pmatrix} T_x \\ T_y \\ T_z \end{pmatrix} + \begin{pmatrix} D & -R_3 & R_2 \\ R_3 & D & -R_1 \\ -R_2 & R_1 & D \end{pmatrix} \begin{pmatrix} x_1 \\ y_1 \\ z_1 \end{pmatrix} \tag{2.3}$$

where T_x, T_y, T_z are the coordinates of the origin of frame 1 in frame 2; R_1, R_2, R_3 are the differential rotations (expressed in radians) around the axes of (x_2, y_2, z_2) to establish parallelism with the (x_1, y_1, z_1) frame; and ($1+D$) is the differential scale change. Positive rotations are counterclockwise rotations as viewed looking toward the origin of the right-handed coordinate system (McCarthy, 1992).

Cartesian coordinates may also be converted into other coordinate systems, such as local terrestrial systems, local or global ellipsoidal or spherical. Seeber (1993) provides a good overview of these coordinate systems and the means of transformation from one system to another.

2.2.5 Reference frames in change detection

The importance of reference systems to deformation measurements has been emphasised by Lambeck (1988), amongst others. Both the instantaneous geocentre and Earth axes at the epoch of measurement must be referred back to defined reference values, such as the IERS Reference Pole and Reference Meridian. Consistency in the use of reference frames is also vital. Since movement and deformation studies require observations at two epochs, it is imperative that each of the coordinates determined by the observations has the same frame of reference. If this is not the case then any difference in reference frames between epochs will introduce a systematic error that may be erroneously interpreted as motion. Since the latest ITRFs (ITRF94 and onwards) are largely independent of tectonic plate models, they are a useful choice of reference frame for deformation studies (Sillard *et al.*, 1998).

2.2.6 Tying Antarctica to the global frame

Prior to the introduction of global reference frames, regional reference frames were used. Most countries would have their own regional reference frame, based on a reference system optimised for that region. For example, in Australia the non-geocentric Australian Geodetic Datum was adopted in 1966, and then updated in 1984. In Antarctica, the remoteness of the various regions meant that reference frames were

developed on a regional basis, rather than on a continental scale. Also, since more than one country may be working in a similar area several different reference frames may cover the same region. Initially, datum definitions tended to be arbitrarily adopted; by choosing a reference ellipsoid (e.g., the Hayford International 1924 ellipsoid) after the adoption of a datum point with coordinates determined from an 'astrofix'.

The Antarctic continent was first connected to a global reference frame by means of space geodesy techniques following the launch of the Passive Geodetic Earth Orbiting Satellite (PAGEOS) project in 1966. PAGEOS observations were conducted at McMurdo, Mawson, Palmer and Casey stations in 1969 (Schmid, 1977). Whilst producing satisfactory results, this method was time consuming and was quickly overtaken by the all-weather Doppler satellite technology (Dunnell *et al.*, 1977; Murphy *et al.*, 1990). More extensive Doppler observations were made during the 1970s, further strengthening and expanding the connections with global reference frames. Widespread connections did not occur, however, until a series of GPS campaigns occurred in the early 1990s. The first of these campaigns were organised by the Scientific Committee on Antarctic Research (SCAR).

2.2.6.1 SCAR90

The SCAR 1990 (SCAR90) program was the first major experiment in Antarctica with GPS. In all, four Antarctic sites were observed during this seven-day pilot campaign. Further Southern Hemisphere sites operated at three sites in Australia and one in New Zealand (Figure 2-1). While the McMurdo and Mawson sites experienced L2 tracking problems with Magnavox WM102 receivers, the others were positioned with a precision of approximately 0.3m (Morgan and Tiesler, 1991).

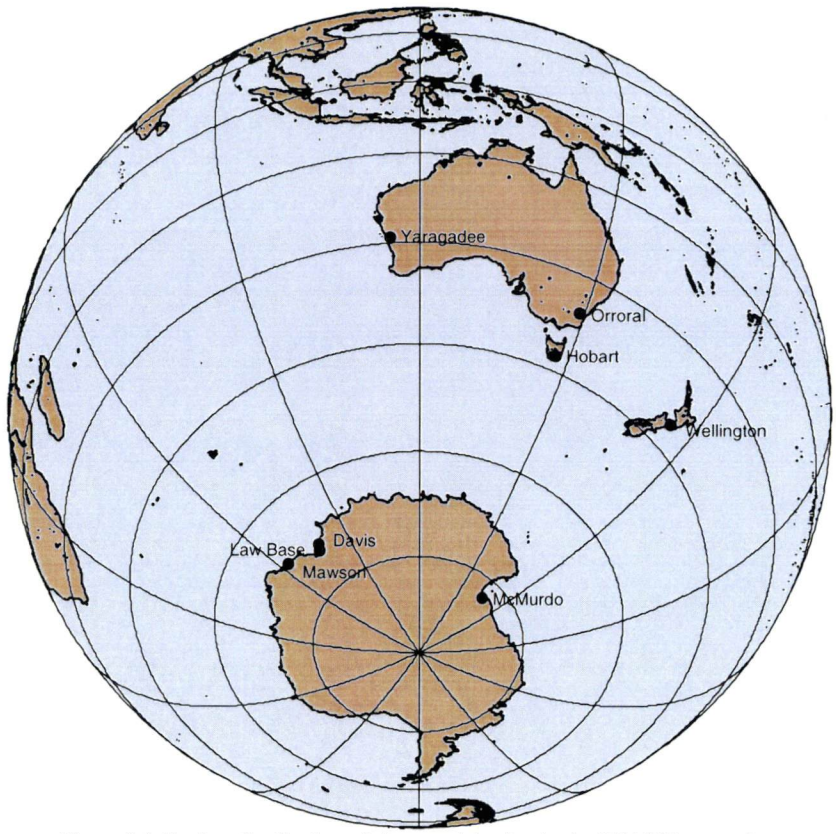

Figure 2-1: Station distribution of sites participating in the SCAR90 campaign.

2.2.6.2 GIG91

During January and February 1991, the largest global GPS experiment (at the time) was conducted - the first GPS IERS and Geodynamics experiment 1991 (GIG91) campaign (Melbourne *et al.*, 1991). In all, approximately 120 GPS receivers were used in the experiment, with about eighty co-located with other existing or planned space geodetic techniques. Data from a sub-network of twenty-one P-code Rogue receivers were collated for quick dissemination to analysis centres. The GIG91 data set allowed Antarctic data to be processed with an unprecedented number of globally distributed sites (Figure 2-2). The most important effect of this large data set on the Antarctic sites was improvements in the precision of station coordinates due to the improved satellite orbit determination and additional double-differences available. Additionally, this campaign produced significant results for the wider geodetic community (Herring *et al.*, 1991; Heflin *et al.*, 1992; Lichten *et al.*, 1992; Andersen *et al.*, 1993), encouraging the later evolution of the International GPS Service (IGS).

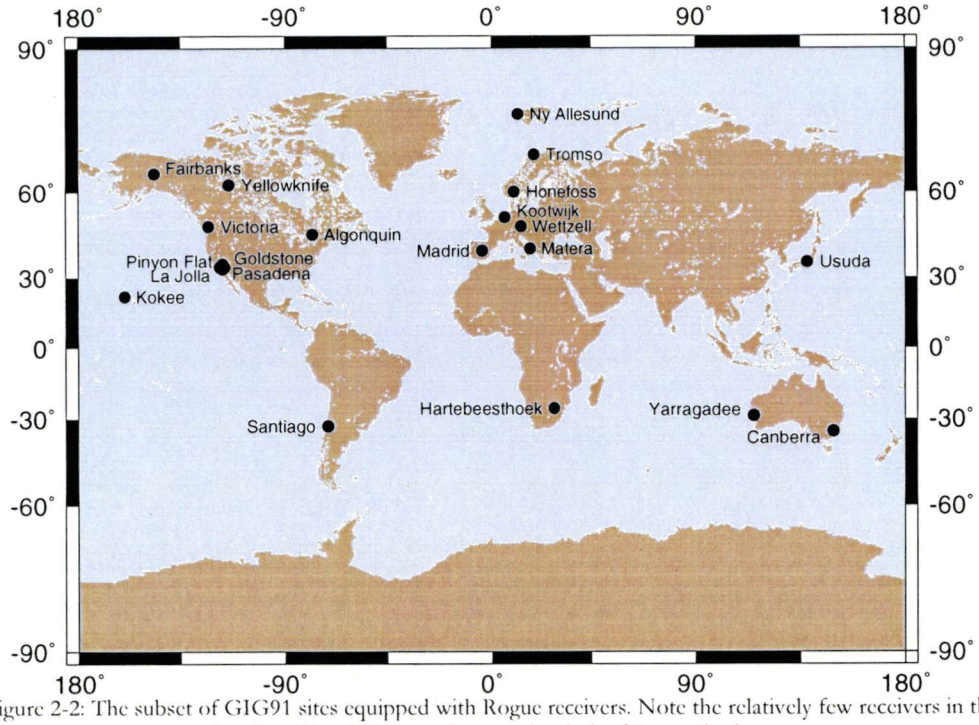

Figure 2-2: The subset of GIG91 sites equipped with Rogue receivers. Note the relatively few receivers in the Southern Hemisphere and a complete lack of Antarctic sites.

2.2.6.3 SCAR91

The SCAR91 campaign, a follow-up to the SCAR90 campaign, overlapped with a subset of the GIG91 data. Running from January 23-28 in 1991, the SCAR91 project formed phase two of the Antarctic pilot campaign. As shown in Figure 2-3, data was recorded at six Antarctic sites, with a significantly greater number of other Southern Hemisphere sites observed as well (Morgan *et al.*, 1992). These six sites were included in the full release of the combined GIG91/SCAR91 data set. Of the six Antarctic sites, two were located on ice, with the Dovers GPS station on relatively stable fast-ice and the Georg Neumayer GPS station located on a moving ice shelf (Morgan, 1994). Unfortunately, observations made at Tahiti and Tristan de Cunha were unusable due to problems tracking L2. Other sites also had difficulties tracking L2. Daily repeatabilities of results from this experiment have only been reported for data during the overlap with the GIG91 campaign, being better than 100mm (Morgan *et al.*, 1992). Repeatabilities outside the overlap with GIG91 are expected to be twice this value (personal communication, P. Morgan, 2001).

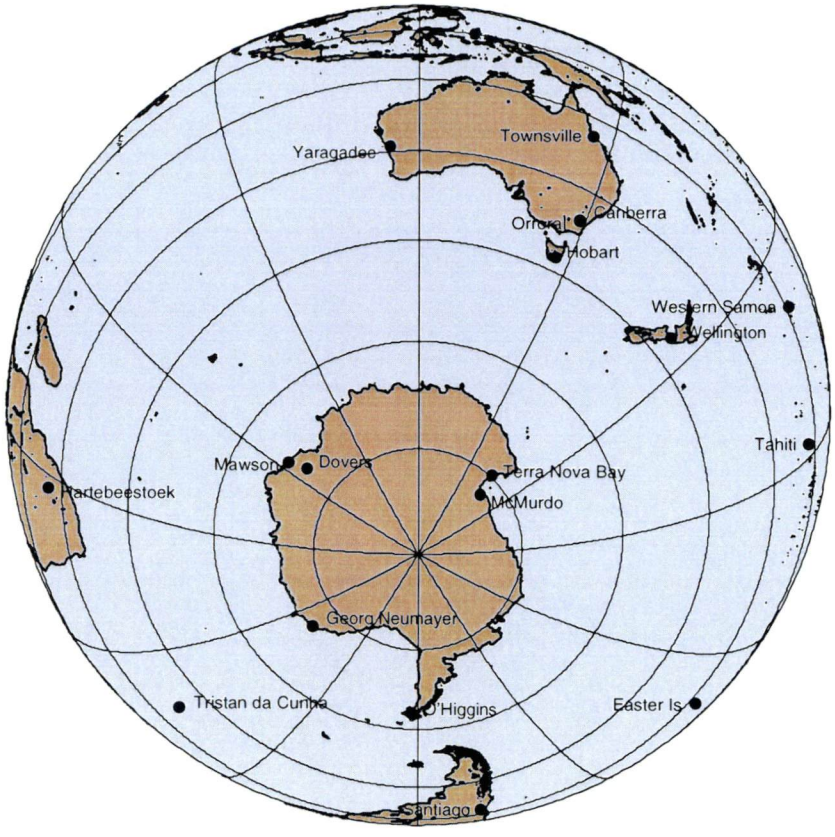

Figure 2-3: Station distribution of sites participating in the SCAR91 campaign.

2.2.6.4 Recent advances

Further SCAR campaigns have occurred since these early attempts at connecting Antarctica to the other continents, and to global reference frames (e.g., Dietrich *et al.*, 1996). Perhaps the most significant advance has been the introduction of several permanently installed GPS receivers at bases in the Antarctic and sub-Antarctic regions through the organisation of the IGS. These data are now routinely accessible on a daily basis via the Internet and are included in modern definitions of the global reference frame, such as the International Terrestrial Reference Frames. SCAR have proposed that the forthcoming ITRF2000 become the standard reference frame for all future Antarctic measurements (SCAR WG-GGI, 2000).

The permanent SCAR Antarctic GPS sites are shown in Figure 2-4, with the current subset of IGS sites listed in Table 2-1. Additional stations are also operating, although most do not include real time data transfer. Antarctic GPS sites, in this case, are defined as those south of the Antarctic Convergence. The most significant challenge remaining is to penetrate beyond the coastal regions of this vast continent, by installing

permanent, autonomous GPS receivers in remote regions. Work is currently being conducted by institutions such as the Jet Propulsion Lab (Donnellan and Luyendyk, 2000) and the Australian National University (Tregoning *et al.*, 2000) to install remote autonomous systems in Antarctica.

Figure 2-4: Permanent Antarctic GPS sites obtained from the SCAR Geodesy and Geographic Information web site http://www.scar-ggi.org.au/geodesy/perm_ob/gps/gps.htm . Data from sites in red are transmitted back from Antarctica via satellite communications, while data from sites shown in blue are delivered via ship or air transport at certain times, mainly during the Austral summer. Note that almost all of the sites are located around the perimeter of the continent.

IGS station code	Location	Latitude (°S)	Longitude (°E)	Ellipsoidal Height (m)
syog	Syowa	69.0070	39.5837	50.1
maw1	Mawson	67.6048	62.8707	59.2
dav1	Davis	68.5773	77.9726	44.5
cas1	Casey	66.2834	110.5197	22.6
mcm4	Ross Island	77.8383	166.6693	97.9
ohig	O'Higgins	63.3207	302.0997	30.6
vesl	Sanae IV	71.6738	357.1583	862.4

Table 2-1: Current IGS sites on the Antarctic continent.

2.3 GPS Overview

The Navigation System with Timing and Ranging (NAVSTAR) Global Positioning System (GPS) came into being with the launch of the first satellite in February 1978. Developed by the United States Department of Defense, the system involves Earth-orbiting satellites transmitting microwave signals that are received by receivers near the Earth's surface or in low Earth orbiting satellites. It is an all-weather system capable of providing, at its most basic level, the position of a receiver when observation of four or more satellites is possible. The measurement of three-dimensional baselines with precisions of several millimetres is possible with measurement of the transmitted carrier phase on two frequencies, knowledge of the receiver clock to one microsecond and of the motion of the satellite to 5-100 parts-per-billion.

The system became operational in 1994 when the full constellation of satellites was in orbit. The GPS consists of three segments: the space segment, the control segment, and the user-segment, each of which are described below. A general overview of the GPS system is provided in Herring (1996) with details found in Wells *et al.* (1986), Leick (1995) and Kaplan (1996). Descriptions of the methods involved in applying GPS to surveying and geological applications are found in King (1985) and ++(Dixon, 1991 #227), while Segall and Davis (1997) and Herring (1999) provide excellent overviews of the method in regard to geodynamics and geodesy.

2.3.1 Space segment

2.3.1.1 Satellite Configuration

The space segment of the GPS involves twenty-eight satellites orbiting the Earth at 20200km about the surface of the Earth, resulting in a period of about twelve sidereal hours. Four of the satellites are in orbit to act as spares in the case of a satellite failure. The system provides global coverage, although 'holes' exist in Polar regions where satellites do not pass overhead. The function of the satellites is to broadcast time and satellite position information that may be received by a GPS receiver. The types of satellites used and the signals they broadcast are discussed below. Currently, groups of four satellites are positioned in six separate orbital planes, equally spaced in longitude by 60° and each plane is inclined at 55° to the equatorial plane. Previously the constellation had been arranged differently. Initially, this was to provide adequate coverage of the western United States during system testing. Later, further constellation changes occurred as the budgeted active constellation design varied between eighteen, twenty-one and twenty-four satellites at different orbital inclinations and satellite spacing (Mazur, 1982). Additionally, spare satellites are also kept in orbit to replace other satellites as they are decommissioned.

Prior to the GPS becoming operational, observation periods were limited to certain times in the day when four or more satellites were visible. Even when a consistent global coverage of four satellites became available, results were adversely affected by a lack of redundancy. Today, observations from five to twelve satellites are possible at all times, even in Polar regions.

2.3.1.2 Satellite Categories

Each of the GPS satellites used to date falls into one of three categories: Block I, Block II/IIA and Block IIR, divided by the manufacturing contract. Each Block model number denotes a different design and features. A thorough guide to each of these is given in Wiederholt and Kaplan (1996), with only a brief overview of the major differences provided here. Each satellite contains precise clocks, computers and signal transmitters, although the types and features of these items vary between the categories:

- *Block I*: These satellites were the first to be placed into orbit, and were developed by Rockwell International. They contained four atomic clocks – two rubidium and two caesium, and had an expected life-span of less than five years, although they proved to last much longer. Frequent ground contact was required with these satellites since they contained no onboard momentum management. The final Block I satellite was decommissioned in 1995.

- *Block II/IIA (upgraded)*: The most important difference from the previous Block I satellites involved the restriction of access to civilians of the signals (see below for a description of this). Military users still had access to the full range of signals. The Block II satellites first went into orbit in 1989. Block IIA satellites included onboard momentum management, meaning they could survive without ground contact for six months. The Block IIA satellites went into orbit for the first time in late 1990. These satellites were developed by Rockwell International.

- *Block IIR (Replenish)*: Most changes to the satellite design of the Block IIR from the Block IIA do not greatly affect the user, with the major changes involving the navigation of the satellite. These satellites were equipped with three atomic clocks – two rubidium and one caesium. Block IIR satellites first went into orbit in 1997. These satellites were developed by Martin Marietta. Block IIF (follow-on) satellites are the next generation of satellites to follow the Block IIR satellites, with potential changes in the area of accuracy of position and timing amongst others.

2.3.1.3 Signals

Using the clocks present in the satellite, the satellites produce a highly precise fundamental frequency of 10.23MHz. Two other signals are derived by multiplying the fundamental frequency by 154 and 120 to produce two signals within the L-band, the L1 and L2 carrier signals respectively. This produces:

$$L1 = 154 \times 10.23 = 1575.42\text{MHz}$$

L2 = 120 x 10.23 = 1227.60MHz

Further signals are modulated on each of these carriers. The C/A code (Coarse /Acquisition code) is modulated on the L1 frequency only. The P-code (Precision code) is modulated onto both the L1 and L2 frequencies. These modulated signals are known as pseudo-random noise (PRN) codes. Additionally, a navigation message containing satellite ephemerides, ionospheric modelling coefficients, satellite health, system time and satellite clock bias and drift information, is also modulated onto the carrier signals (Wells *et al.*, 1986). Wavelengths of each of the different signals are shown in Table 2-2.

Signal	Wavelength (m)
L1	~0.190
L2	~0.244
C/A	~300
P1	~30
P2	~30

Table 2-2: Wavelengths of transmitted GPS signals.

Each of these signals is affected by the atmosphere, resulting in either a delay or advance of the signal. Both the troposphere and ionosphere have such an impact on the signals. As shall be seen in Section 2.4.4, the observation of two frequencies allows the first order term of the ionospheric delay of the signal to be calculated and removed. Other methods are required to handle the tropospheric delay, and these are discussed in more detail in Section 2.3.3.4.2.

A modernisation of the GPS space segment is planned for the first decade of the third millennium, with new satellite designs planned to go into orbit, incorporating additional civilian frequencies (Hatch, 1996).

2.3.1.4 Civilian Operational Restrictions

Since the system was developed for military applications, certain restrictions have been placed on signal availability and positional accuracy to the general civilian community. These are known as *anti-spoofing* and *selective availability*. This degraded system is known

as the Standard Positioning Service (SPS), while the un-degraded version is known as the Precise Positioning Service (PPS).

Anti-spoofing (A-S). Block II and later satellites have the ability to encrypt the P-code. This is done by combining an encrypted code (known as the W-code) with the P-code in order to produce the Y-code. P-code may then only be accessed in real time by users who have the correct deciphering software or hardware, generally only the United States military and their allies. Anti-spoofing was switched on in early 1994 following intermittent testing during 1993.

Selective Availability (SA). The accuracy of the position gained from a single GPS receiver can be degraded by "dithering" the satellite clock and broadcast satellite positions. The majority of the influence is believed to come from the satellite clocks (Langley, 1996). This effectively produced anomalous ranges between the satellite and the receiver. While the error is different for every satellite the total positional error introduced is approximately 100 metres horizontally and 156 metres vertically at the 95% confidence level. SA was switched on and operated consistently from July 4 1991, although at varying levels. It had previously been tested as each Block II satellite was launched, but was turned off for the duration of the Gulf War in August 1990. SA was switched off permanently on May 1 2000 at approximately UT 04:00. Consequently, uncorrected positions from GPS receivers are now accurate to 10-20m in real time.

2.3.2 Control segment

The control segment consists of Monitor Stations, a Master Control Station and Ground Antennas. The Monitor Stations, located at Hawaii, Kwajalein, Ascension Island, Diego Garcia and Colorado Springs, passively track each of the satellites, accumulating ranging data. The Master Control Station, located at Schriever Air Force Base in Colorado, processes this information to provide satellite ephemerides. One of three Ground Antennas, located at Ascension Island, Diego Garcia, Kwajalein, then uploads this information to the satellite. Under the DoD's GPS Accuracy Improvement Initiative, seven new Monitor Stations are scheduled to go online in the

near future (Hay, 2000). This should improve the quality of the uploaded predicted orbit among other things.

2.3.3 User segment

The user segment consists of receivers capable of tracking and processing the GPS signals. There has been a variety of receiver types developed, using quite different tracking methodologies. Antenna design has also varied significantly in an attempt to provide multipath resistance and high signal-to-noise ratios (SNRs). An overview of both of these is provided below (Yunck, 1995).

2.3.3.1 Multipath

Signal multipath is of significant concern to the GPS community since its presence can bias carrier phase processing results at the few centimetre level and reduce the likelihood of ambiguity resolution. Multipath occurs when a signal arrives by a route that is not directly from the satellite antenna to the receiver antenna. A single transmitted signal may arrive via several different paths, although a multipathed signal will always arrive later than line-of-sight signals due to the increased path length. Pseudo-range multipath may amount to an extra 1-4m of path length, although the number is more like 0.4-0.5m in typical conditions using modern receivers. Carrier phase multipath has a maximum value of 0.05m (Langley, 1996).

Since the GPS orbits repeat exactly every year, multipath will have an annual cycle. Orbits also repeat every sidereal day, so multipath will also be nearly identical between consecutive days. This allows multipath to be examined using consecutive days' data. Other methods have also been developed to determine the size of pseudo-range multipath using less than one day's data (Estey and Meertens, 1999).

2.3.3.2 Receivers

When compared with the current generation of receivers, the first models were both primitive and expensive - often more than $US100,000! Typically, receivers could only track four or five satellites at one time, and only on a single frequency. This was especially the case for field units that are required to be transportable. Storage was on magnetic tape, further complicating the process and increasing power requirements in

the field. Among these early receivers were (King *et al.*, 1985; Hofmann-Wellenhof *et al.*, 1992):

Macrometer V-1000: Developed at the Massachusetts Institute of Technology. This codeless single frequency receiver could track up to six satellites simultaneously using six channels. This instrument required a satellite ephemeris to be uploaded prior to data collection, and required clock synchronisation with every receiver before and after the survey.

Texas Instruments TI-4100: Using technology developed by the Defense Mapping Agency (DMA) and the U.S. National Geodetic Survey (NGS) and the U.S. Geological Survey (USGS). This dual-frequency receiver was one of the few that observed the P-code, tracking a maximum of four satellites using a single 'multiplexing' channel[2]. Unlike the Macrometer, satellite ephemerides and timing information were downloaded from the satellites. Recordings were made to magnetic tape.

Trimble 4000S: This receiver, produced in 1985, logged data to an external computer.

Wild Magnovax WM101: A five-channel single frequency receiver logging carrier data to a magnetic tape. Using multiplexing technology, this receiver could track nine satellites at one time. This receiver was later superseded by the dual-frequency WM102 receiver that also implemented the multiplexing technology, tracking all the L2 signals using a single channel.

Significant problems were encountered with the use of these early receivers. They tracked only a small number of satellites, they often required external data storage, and consumed large amounts of power – a problem in field use. Single frequency (L1) instruments were insufficient for measuring precise baselines over medium to long distances due to ionospheric effects (Rizos *et al.*, 1990). The performance of the dual-frequency WM102 was particularly poor in the presence of high ionospheric activity,

2. Multiplexing involves a process of tracking each satellite for a short time then rapidly switching to the remainder of tracked satellites in succession.

since it could not keep track of the L2 signal and continually lost lock (Morgan and Tiesler, 1991). Despite these limitations, surveyors and geodesists continued to widely use the system and pushed the development of receiver technology.

Modern receivers, in contrast, allow the simultaneous tracking of up to twelve satellites on both frequencies. Often many days of data are stored on internal solid state memory or removable 'flash' cards. Baseline precisions now exceed 1 part-per-billion, something that was never envisaged in the early years of the system. A modern receiver can determine phase to approximately 1% of the signal wavelength, that is, about 2mm for L1 or L2 carrier signals.

Further advancement has come in the form of multipath mitigation techniques and receiver satellite tracking technology, with an outline of these developments below.

2.3.3.2.1 *Receiver-based multipath mitigation*

Many different schemes have been devised for the mitigation of multipath signals. These may be divided into antenna-based and receiver-based methods. The receiver-based methods include narrow correlator and strobe correlator technology (Weill, 1997), although these are not yet in wide use. Antenna-based methods are mentioned briefly in Section 2.3.3.3. Early GPS receivers, however, did not have such complicated mitigation methods, and as a result, higher levels of multipath found their way into the GPS data.

2.3.3.2.2 *Tracking technology*

GPS receivers acquire and track a satellite signal by replicating the PRN code that is transmitted and then shifting in phase the replica until it matches the received PRN. That is, when the correlation between the incoming and replicated signals reaches a maximum the signal is 'code-locked'. A satellite is *tracked* while the receiver continuously has the signal locked. This is relatively simple to achieve using the C/A code since the code is predictable and repetitive. However, since the P code is encrypted by the AS process this code cannot be tracked as readily and other more sophisticated methods must be used. Broadly, there are two methods by which the carrier wave can be recovered from the incoming signal. The first of these is to square the incoming signal, while the other method involves reconstructing the carrier wave

by removing the AS-affected ranging code and broadcast message modulations (Rizos, 1995). Different implementations of these are discussed below (Ashjaee and Lorenz, 1992; Leick, 1995).

Squaring

Squaring an incoming signal results in three occurrences, two of which are undesirable and one desirable. The desirable feature of this method is that squaring a signal causes any modulation to disappear. This then allows a squared carrier signal to be generated within the receiver to correlate with it. The first undesirable feature is the resultant halving of the wavelength of the carrier signal. This usually occurs only on the L2 signal, since the C/A pseudo-range is unencrypted on L1. This makes ambiguity resolution difficult since the standard 'wide-lane' combination can no longer be formed. Additionally, the noise is also increased upon squaring, reducing the SNR by 30dB compared to direct correlation with the P-code. As can be seen in the comparison with other methods in Table 2-3, the squaring method is up to 13dB noisier than other methods.

A low SNR will cause tracking problems where high ionospheric variability is present, such as in the equatorial and Polar regions. This will be emphasised further during ionospheric maxima. The Macrometer and Trimble 4000S and 4000SST receivers used this method to observe the L1 carrier, although it is not used in modern receivers.

Code Correlation/Carrier Squaring

Taking advantage of the similarities of the known structure of the P-code and the unknown structure of the Y-code, an improvement to the squaring technique was developed. The 'code-aided squaring' technique involves the receiver generation of a P-code which is then correlated with a filtered version of the incoming carrier signal. The result of the correlation is a narrow bandwidth signal that is then squared to remove the code from the carrier signal. Squaring this narrow bandwidth signal results in a much lower noise level than the standard squaring technique, although the carrier signal remains half-wavelength. This method has been used in the WM102 and Series 200 Leica receivers (i.e., SR299) to obtain L2 P(Y)-code ranges in addition to the C/A code.

Cross-correlation

Since both the L1 and L2 carrier are modulated with the same P(Y)-code, the carrier signals may be cross-correlated. This produces the difference in the pseudo-ranges $P_{L1}(Y)$-$P_{L2}(Y)$ and the phase differences between the carrier signals. The differenced pseudo-ranges are combined with the C/A-code pseudo-range, and the carrier signal phase differences combined with the L1 carrier phase. As seen in Table 2-3, the SNR of this method is better than the squaring method, although the low SNR may cause the receiver to experience tracking problems in a highly dynamic ionospheric environment. This is especially true at low elevations. This method has been used extensively, from the early TI-4100 receivers to the more modern TurboRogue SNR 8000 and Trimble 4000 SSE receivers. Recently, these receivers have experienced severe data dropouts and cycle-slips while tracking low elevations satellites in equatorial and Polar regions (Springer, 1998). Many of these receivers have been replaced by newer models using Z-tracking technology.

Z-tracking

The Z-tracking method is too complex to be described other than briefly here. The interested reader is referred to Ashjaee and Lorenz (1992) for a complete description. In brief, the Y-code on both carriers is matched against two different receiver-generated P-codes. Low-pass filtering the results of the correlations yields the encryption code on each frequency. The encryption code is then removed from the received signals to allow locally generated replicas of the code to be locked against the P-code signals on the carriers. The Z-tracking technique provides full-wavelength carrier phases on L1 and L2 along with Y-code pseudo-ranges on L1 and L2. In addition, Z-tracking provides the best SNR of all the methods. This is the method used in the Ashtech Z12, for example.

Tracking Method Parameters	Squaring	Code-aided squaring	Cross-correlation	Z-tracking
C/A-code	No	Yes	Yes	Yes
Pseudo-range (Y)	No	Y1	Y2-Y1	Y1,Y2
Carrier wavelength	Half	Half	Full	Full
Signal-to-noise	-16dB	-3dB	-13dB	0dB

Table 2-3: Comparison of AS technologies (Ashjaee and Lorenz, 1992). To compare these SNR values to pure Y-code measurements, subtract 14dB.

2.3.3.3 Antennas

The role of the GPS antenna is to filter, amplify and convert the energy of the arriving electromagnetic waves into electric current that can be processed by the GPS receiver (Rizos, 1995). The filtering of the GPS signals involves the rejection of signal interference, such as reflected signals (multipath). The measured signals are amplified using an amplifier located inside the antenna. Since they are the physical collecting point of the GPS signals, GPS antenna design has been an important focus of development. It is important to know the exact measurement location or locations, as it is this point that is referred to a fixed ground mark. The GPS antenna also plays an important part in the physical mitigation of multipath. Langley (1998) provides a good overview of the characteristics of GPS antennas.

2.3.3.3.1 Antenna design

Early GPS antennae were generally one of five designs: cross-dipole, monopole, quadrifilar helix, microstrip or spiral helices (Wells *et al.*, 1986). Each design has its advantages and disadvantages in regard to its ability to receive both frequencies, the need for a ground-plane, level of gain, physical size, stability of the phase centre and its multipath resistance. Due to its rugged construction and low profile, the microstrip antenna became the most popular of the five. This style of antenna is still widely used today for low precision navigation and surveying work, both with, although more often without a multipath resisting ground-plane. For precise geodetic applications, the choke-ring antenna has now become the standard due to its increased multipath resistance. The choke-ring antenna is a microstrip antenna with several concentric rings mounted on the upper surface of a standard ground-plane. This antenna is now the accepted antenna for use in the International GPS Service (IGS) global network.

Multipathing of GPS signals may occur via reflection from the ground or buildings near the receiver or from reflection off the satellite itself. Multipath resistance normally happens on two levels, at the physical level through the antenna design, and at the electrical level using signal-processing techniques in the receiver. By taking advantage of the polarisation of the GPS signal, a GPS antenna may reject a significant number of multipathed signals. GPS signals are right-hand polarised, while signals reflected on a highly reflective surface have their polarisation reversed. This allows antennas to be

manufactured in such a way that they attenuate any signal with a left-handed polarisation. Ground-planes attached to antennas were initially thought to help in attenuating multipath signals. This was not always the case, however, since a surface wave could be set up on the ground-plane's surface countering the ground-plane's usefulness. The more modern choke ring antenna design has been useful in attenuating multipathed signals, especially from underneath the antenna. Several other methods have also been suggested including multiple antennas, antenna location strategies and daily differencing techniques (Weill, 1997). Unfortunately, these methods do not eliminate all multipathed signals, and further efforts need to be made to improve antenna design and mitigation at the receiver and software levels.

2.3.3.3.2 Phase centre

GPS measurements are not made relative to a single point on the GPS antenna element – known as the *physical phase centre* – but instead to the *electrical phase centre* which varies depending on satellite azimuth and zenith-angle. So that a single reference point exists, corrections may be made to measurements of the GPS signals so that they refer to a single electrical phase centre. This is performed using *antenna phase centre models* (Rothacher and Springer, 1997; Mader, 1999). These are normally determined relative to the Dorne Margolin choke ring antenna since the determination of absolute phase patterns are expensive and difficult to obtain. Most phase centre models currently only correct for zenith dependant differences, choosing to ignore any potential azimuthal differences. Any confusion about the location of the electrical phase centre will introduce systematic errors into the GPS results, although the inclusion of appropriate models is now routine in most scientific geodetic GPS processing software.

2.3.3.4 Signal-propagation effects

The Earth's atmosphere affects the GPS signals in one of three ways. The signal is delayed, advanced or unchanged depending on the region of the atmosphere it is passing through. With the GPS microwave signals, the ionosphere and troposphere are the two atmospheric regions that influence the signal.

2.3.3.4.1 Ionosphere

The ionosphere is the region between approximately 50-1500 kilometres above the surface of the Earth, although the most active region is normally in a much smaller

band than this. This region is characterised by a significant number of ionised particles - free electrons (negatively charged) and positively charged atoms and molecules. This ionisation process is triggered by ultraviolet radiation from the Sun. The Total Electron Content (TEC) of the ionosphere is often measured in TEC units, with one TEC unit equal to 10^{16} electrons per 1-square metre. The TEC will normally be in the range of 10^{16} and 10^{18} electrons/m^2 (1-100 TEC units). The number of free electrons in the ionosphere will vary with the relative solar activity of the Sun, both in the short term (solar flares) and in the long term (the eleven-year solar cycle). A plot of the eleven-year solar cycle is shown in Figure 2-5. Generally, the ionospheric activity is at its highest around 14:00 local time. Geographically, the greatest activity is adjacent to the magnetic equator and beneath the Polar auroral zones (Heroux and Kluesberg, 1989). The Polar auroral zones can experience significant spatial and temporal variation due to auroral activity and magnetic storms (Leick, 1995).

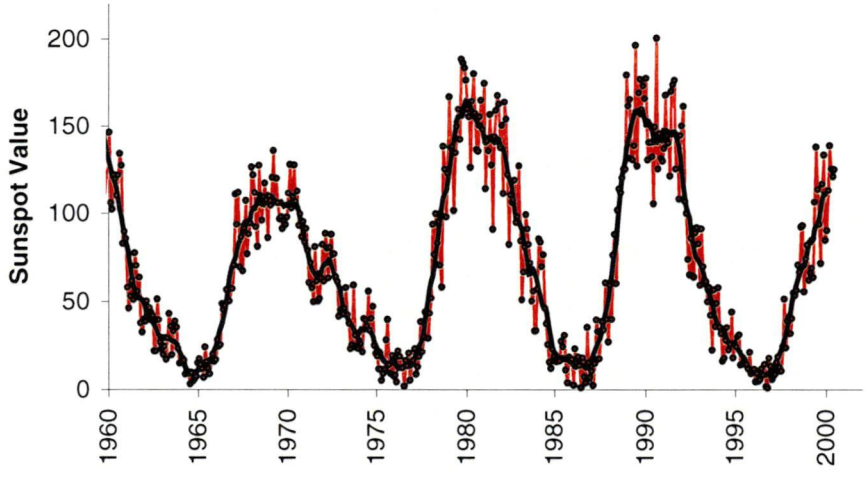

Figure 2-5: Sunspot Cycles 1960-present. Plotted data is monthly values, with smoothed values shown in bold. The data was obtained from the Sunspot Index Data Center (http://www.oma.be/KSB-ORB/SIDC/).

The free electrons in the ionosphere affect the propagation of radio waves, and hence the GPS signal. The ionosphere is a dispersive medium, and as such affects different frequencies differently. In terms of the GPS signal, the pseudo-ranges and carrier phases are both affected by the same amount, but with different signs due to the difference between group and phase delays. The pseudo-ranges are delayed, while the carrier phases are advanced. Additionally, the L1 and L2 carriers are affected differently. The different delays of the carrier phase can be used in an advantageous

way; by using linear combinations of observations equations shown in Section 2.4.4.1, the first-order delay caused by the ionosphere may be either removed or calculated. The ionospheric delay may cause as little as 1m error in a range at a quiet mid-latitude site, or as much as 100m at an equatorial site (Klobuchar, 1991).

The higher order (second and third) ionospheric group delays are not dealt with, however, by the dual frequency combination. Second-order ionospheric group delays may cause residual range errors of the order of -0.11mm per TEC. The phase advance is approximately half this value. Bassiri and Hajj (1993) show theoretical examples of residual range errors of up to 40mm at low elevation angles. Third-order delays are sub-millimetre, even at ionospheric maxima. Although the effects of the second-order delay may be modelled, these corrections are normally not included in current GPS processing software. This may result in errors as large as several millimetres in the coordinate estimates, and these will be largest when observation spans are short and the ionospheric activity is high.

Unfortunately, not all of the effect of the ionosphere is found in phase delay or advance. Some of the phase variations are converted to amplitude variations by means of diffraction. This results in rapid variation in both amplitude and phase. Although not regular, these variations (known as *scintillations*) have a significant impact on GPS observations. Loss of lock may occur due to fading of the signal strength, with only a 0.2% change in the ionosphere in a time interval equal to the inverse of the receiver bandwidth (Langley, 1996). Cycle slips may also occur, particularly if the receiver is not designed or programmed to accommodate such rapid shifts in the signal. In equatorial zones, scintillations normally last several hours in the evenings. In the Polar regions these scintillations, while not usually as strong as near the magnetic equator, may persist for several days and are not limited to the late evenings (Klobuchar, 1991). Menge (1996) show large scintillations (up to 1 TEC unit/min $\cong$ 0.2m/min) occurring in Antarctic GPS data, particularly in the auroral regions, although this varies significantly from day to day.

Modern GPS receivers are significantly better than previous models at maintaining lock on satellite signals through ionospheric scintillation. Receivers using L2 squaring were particularly poor at maintaining lock on that signal. However, even the most modern

receivers are likely to have problems with scintillations, particularly during the Sunspot cycle maxima.

2.3.3.4.2 Troposphere

The neutral atmosphere consists of the troposphere, tropopause and stratosphere, although these are generally grouped together under the name troposphere. The troposphere consists of the atmosphere from the Earth's surface to approximately 40km above the surface. In contrast to the ionosphere, the troposphere is a non-dispersive medium, so each of the signal frequencies is affected in the same way and by the same amount. Signals passing through this layer are affected by what is referred to as the tropospheric delay.

The tropospheric delay consists of hydrostatic ('dry') and 'wet' components. The signal delay caused by the hydrostatic component can be modelled to a few millimetres using accurate barometers. However, the wet delay, although only 10% of the total path delay, is more spatially and temporally varying and is thus more difficult to model accurately (Tralli and Lichten, 1990).

The actual delay of the satellite signals will vary depending mostly on the water vapour content of the troposphere and the satellite's elevation angle. For a satellite with a low elevation angle, the signal is required to pass through a thicker section of troposphere than if the satellites were overhead. The magnitude of the delay is 2.0-2.5m for a satellite at zenith and 20-28m for a satellite at five degrees (Leick, 1995).

The tropospheric delay may be accounted for in one of two ways. The first method involves using a model of the troposphere. These models often are altitude, latitude, temperature or surface pressure dependant, or a mixture of all four. (Normally standard temperature and pressure values are used if required.) The Saastamoinen model is the most widely used tropospheric model in GPS applications (Saastamoinen, 1972; Saastamoinen, 1973). This model has also been shown to be superior to other models when compared with ray trace values, especially at high latitudes (Janes *et al.*, 1991). Models are 'mapped' to the elevation angle of the satellite by using an appropriate mapping function. The Niell mapping function is currently regarded as the most precise for use in high precision GPS processing (Niell, 1996).

The second method involves estimation of the total zenith delay (TZD) using the GPS data. The hydrostatic delay is well estimated by tropospheric models and may be removed from the TZD to produce the zenith wet delay. Using a tropospheric model and mapping function as *a priori* information, the TZD is estimated either using a stochastic process (Lichten, 1990) or a piecewise linear function. For the random walk method, a typical process noise rate is 10-20mm/hr^2, while for the piecewise linear method, thirteen estimates (i.e., 2 hourly) per site per day are typical. The piecewise linear approach is adopted in the GAMIT[3] GPS processing software (King and Bock, 1999).

2.3.3.5 Earth-body deformations

Positions determined by GPS measurements are influenced by several other non-GPS error sources. Earth-body deformations caused by solid-Earth, ocean or pole tides or atmospheric loading will each influence the GPS estimates. Terrestrial observations will also be biased by these effects. Detailed explanation on the determination of the size of these deformations is given in (McCarthy, 1996). Each of these is discussed below in the context of how they are commonly dealt with.

2.3.3.5.1 Solid-Earth tide

The solid-Earth tide (or Earth body tide) is a response of the Earth's crust to the gravitational attraction of the Sun and Moon. Its magnitude may be as large as 0.4m in the vertical component in approximately six hours at low latitudes (Baker, 1984). Horizontal motion is approximately one order of magnitude smaller than the vertical motion. It is possible to model the solid-Earth tide at any given time to an accuracy of about 2mm (Chang, 1999).

2.3.3.5.2 Ocean tide

The weight of the ocean tide also causes a periodic deformation of the Earth's body, although not as large as the solid-Earth tide. Magnitudes of over 100mm vertical motion have been detected in some regions, with horizontal motions once again an order of magnitude smaller than the vertical motion. The size of Earth deformation due to the ocean tide decreases the further a site is from the coast, although the effects

3 GPS At MIT, developed at the Massachusetts Institute of Technology.

of ocean tide loading are still experienced hundreds of kilometres from the coast. Modelling of ocean tide loading is normally based on global ocean tide models such as the Le Provost *et al.* (1994) model. While some regions are well defined in these models, other areas may be in error by 10-20 percent (Baker *et al.*, 1995). This is particularly important in regions with large tidal variations (Stewart, 1988). The scatter of vertical coordinate estimates at some sites have been reduced by 15-20mm after applying an ocean tide loading model (Chang, 1999).

2.3.3.5.3 Pole tide

Earth body deformation caused by the wobble in the rotation of the Earth is a further geophysical signal that needs to be accounted for. The pole tide, as it is known, has a maximum magnitude of 25mm, with maximum horizontal displacements of 7mm (McCarthy, 1996). Models are also available that reduce the effect of the pole tide to almost zero (Wahr, 1985).

2.3.3.5.4 Atmospheric loading

Atmospheric loading occurs as a response to the time-varying regional atmospheric pressure. The Earth's surface is compressed in the presence of a high-pressure system relative to a standard pressure. Likewise, a low-pressure system allows the surface to relax. Earth-body changes due to atmospheric loading may be as large as 0.5mm per 1hPa difference between a local and a standard pressure (1013.25hPa). Vertical displacements of up to 25mm are possible with horizontal effects of one-third this amount. Atmospheric loading is correlated over distances of 1000-2000km and time-scales of two weeks (McCarthy, 1996). Atmospheric loading has been shown to exist in both VLBI and GPS data, although only at about 60% of the modelled amount (van Dam *et al.*, 1994; van Dam and Herring, 1994).

2.3.3.5.5 Post-glacial rebound

Post-glacial rebound is a slow 'bouncing back' of the Earth's surface following the retreat of the ice sheets since the last glacial maximum. Regions affected mostly by post-glacial rebound are typically rising at a rate of a 0-5mm/yr (Scherneck *et al.*, 1998), several orders of magnitude more slowly than the short period Earth deformations mentioned in the above sections. Models of post-glacial rebound (e.g., Peltier, 1994) suggest that the AIS region is rebounding at a rate of 0-14mm/yr, although there is

significant inter-model variability (Zwartz *et al.*, 1999). Over the period of the present study, this range equates to 0-420mm. An on-going GPS study is currently being conducted into the post-glacial rebound that is occurring in the AIS region, although the time series is presently too short to determine uplift rates (Tregoning *et al.*, 2000). Since precise knowledge of post-glacial rebound is not yet available and the station height component does not concern us in the present study, we do not consider it further.

2.4 GPS Theory

Background notation and theory on the GPS observables and mathematical combinations is given here. For a more complete description, the reader is referred to Leick (1995). In this Chapter and afterwards, the notation used by Teunissen and Kluesberg (1996) is adopted. This notation adopts the standard way of referring to particular satellites (superscript characters) and receivers (subscript characters).

2.4.1 Pseudo-ranges

The range between a GPS satellite k and a GPS receiver i as measured by the receiver is known as a pseudo-range P_i^k. It is equal to the difference between the receiver time t_i at signal reception and the satellite time at signal transmission t^k, scaled by the speed of light c. Mathematically, this is:

$$P_i^k(t) = c\left(t_i(t) - t^k\left(t - \tau_i^k\right)\right) + e_i^k \tag{2.4}$$

where τ_i^k is the signal travel time from the signal generator in the satellite to the signal correlator in the receiver and e_i^k is the pseudo-range measurement error. True time is represented by t.

This pseudo-range is not equal to the geometric distance between the satellite and receiver since various errors are unaccounted for – these errors being receiver and satellite clock errors, propagation effects and receiver noise. The complete expression for a pseudo-range is:

$$\begin{aligned} P_i^k(t) = {} & \rho_i^k\left(t, t - \tau_i^k\right) + I_i^k + T_i^k + dm_i^k \\ & + c\left[dt_i(t) - dt^k\left(t - \tau_i^k\right)\right] + c\left[d_i(t) + d^k\left(t - \tau_i^k\right)\right] + e_i^k \end{aligned} \tag{2.5}$$

where $\rho_i^k\left(t, t-\tau_i^k\right)$ is the geometric distance between the satellite antenna at signal transmission time, and the receiver antenna at signal reception time; I_i^k is the ionospheric refraction effect; T_i^k is the tropospheric refraction effect; dm_i^k is the multipath error; d_i is the delay between the signal being received at the antenna and being received at the signal correlator; d^k is the delay between signal generation and transmission from the antenna of the satellite; dt_i and dt^k are the receiver and satellite clock errors, respectively, so that:

$$t_i(t) = t + dt_i(t) \text{ and } t^k\left(t-\tau_i^k\right) = t - \tau_i^k + dt_i^k\left(t-\tau_i^k\right)$$

2.4.2 Carrier phases

The carrier phase observable $\phi_i^k(t)$ is equal to the difference between the phase of the receiver generated carrier signal at signal reception time ϕ_i, and the phase of the satellite generated carrier signal at signal transmission time ϕ^k. GPS receivers know nothing of the number of full carrier cycles that exist between the receiver and the satellite. Since only the fractional carrier phase can be measured, an integer number of full cycles is unknown – the so-called ambiguity *N*. The mathematical expression for the carrier phase observable (in units of metres) is:

$$\begin{aligned}\Phi_i^k(t) = \lambda\phi_i^k(t) &= \lambda\left[\phi_i(t) - \phi^k\left(t-\tau_i^k\right)\right] \\ &= \rho_i^k\left(t, t-\tau_i^k\right) - I_i^k + T_i^k + \delta m_i^k + c\left[dt_i(t) - dt^k\left(t-\tau_i^k\right)\right] \\ &+ c\left[\delta_i(t) - \delta^k\left(t-\tau_i^k\right)\right] + \lambda\left[\phi_i\left(t_0\right) - \phi^k\left(t_0\right)\right] + \lambda N_i^k + \varepsilon_i^k\end{aligned} \quad (2.6)$$

where λ is the wavelength of the particular carrier signal; δm_i^k is the carrier phase multipath; δ_i is the carrier phase signal delay between the signal being received at the antenna and being received at the signal correlator of the receiver; δ^k is the carrier phase signal delay between the signal generation and signal transmission from the antenna of the satellite; $\phi_i\left(t_0\right)$ and $\phi^k\left(t_0\right)$ are the constant, non-zero initial phases of the satellite and receiver generated signals, respectively; and ε_i^k is the carrier phase measurement error. Note the different sign of I_i^k when compared to the pseudo-range in equation (2.5) due to the different response to the ionosphere by the different signals.

2.4.3 Differences

2.4.3.1 Single differences

If two receivers i and j observed the same satellite k at some nominal epoch, the between-receiver single difference phase observable may be formed. This is more commonly referred to as the single difference. By differencing equation (2.6) and making the approximation that satellite clock and equipment delay errors are equal at both receivers:

$$\begin{aligned}\Phi_{ij}^{k} &= \Phi_{j}^{k} - \Phi_{i}^{k} \\ &\approx \rho_{j}^{k}\left(t, t-\tau_{j}^{k}\right) - \rho_{i}^{k}\left(t, t-\tau_{i}^{k}\right) - I_{ij}^{k} + T_{ij}^{k} \\ &\quad +\delta m_{ij}^{k} + cdt_{ij} + c\delta_{ij} + \lambda\phi_{ij}^{k}\left(t_0\right) + \lambda N_{ij}^{k} + \varepsilon_{ij}^{k}\end{aligned} \tag{2.7}$$

where a double subscript refers to the difference between the two receivers.

Likewise, the pseudo-range difference may also be performed, so that:

$$\begin{aligned}P_{ij}^{k} &= P_{j}^{k} - P_{i}^{k} \\ &\approx \rho_{i}^{k}\left(t, t-\tau_{i}^{k}\right) - \rho_{j}^{k}\left(t, t-\tau_{j}^{k}\right) \\ &\quad +I_{ij}^{k} + T_{ij}^{k} + dm_{ij}^{k} + cdt_{ij} + cd_{ij} + e_{ij}^{k}\end{aligned} \tag{2.8}$$

Equations (2.7) and (2.8) are known as the between-receiver difference. Their value rests in the cancellation of the satellite clock errors and the reduction of the remaining biases.

In the same way, a between-satellite combination may also be formed. Differencing carrier phase observations from one receiver i to two satellites k and l yields:

$$\begin{aligned}\Phi_{i}^{kl} &= \Phi_{i}^{l} - \Phi_{i}^{k} \\ &\approx \rho_{i}^{l}\left(t, t-\tau_{i}^{l}\right) - \rho_{i}^{k}\left(t, t-\tau_{i}^{k}\right) - I_{i}^{kl} + T_{i}^{kl} \\ &\quad +\delta m_{i}^{kl} + cdt^{kl} + c\delta^{kl} + \lambda\phi_{i}^{kl}\left(t_0\right) + \lambda N_{i}^{kl} + \varepsilon_{i}^{kl}\end{aligned} \tag{2.9}$$

The corresponding pseudo-range equation is:

$$
\begin{aligned}
P_i^{kl} &= P_i^l - P_i^k \\
&\approx \rho_i^l\left(t, t-\tau_i^l\right) - \rho_i^k\left(t, t-\tau_i^k\right) \\
&\quad + I_i^{kl} + T_i^{kl} + dm_i^{kl} + cdt^{kl} + cd^{kl} + e_i^{kl}
\end{aligned} \tag{2.10}
$$

Equations (2.9) and (2.10) show that the receiver clock errors have cancelled and the other biases are reduced.

2.4.3.2 Double differences

If two receivers i and j observe the same two satellites k and l at the same time, the double-difference phase observable is found by differencing equation (2.9):

$$
\begin{aligned}
\Phi_{ij}^{kl} &= \Phi_j^{kl} - \Phi_i^{kl} \\
&\approx \rho_j^l\left(t, t-\tau_j^l\right) - \rho_j^k\left(t, t-\tau_j^k\right) - \rho_i^l\left(t, t-\tau_i^l\right) + \rho_i^k\left(t, t-\tau_i^k\right) \\
&\quad - I_{ij}^{kl} + T_{ij}^{kl} + \delta m_{ij}^{kl} + \lambda N_{ij}^{kl} + \varepsilon_{ij}^{kl}
\end{aligned} \tag{2.11}
$$

Likewise, the double-difference pseudo-range observable is found by differencing equation (2.10):

$$
\begin{aligned}
P_{ij}^{kl} &= P_j^{kl} - P_i^{kl} \\
&\approx \rho_j^l\left(t, t-\tau_j^l\right) - \rho_j^k\left(t, t-\tau_j^k\right) - \rho_i^l\left(t, t-\tau_i^l\right) + \rho_i^k\left(t, t-\tau_i^k\right) \\
&\quad + I_{ij}^{kl} + T_{ij}^{kl} + dm_{ij}^{kl} + e_{ij}^{kl}
\end{aligned} \tag{2.12}
$$

Both the receiver and satellite clock errors are removed in the double-difference, while the other biases are reduced, except for the lumped integer cycle ambiguities in equation (2.11).

2.4.3.3 Triple differences

A further difference may be formed by differencing double-differences at two adjacent measurement epochs of the form shown in equation (2.11). This is known as the triple-difference, and the carrier signal version is defined as:

$$
\begin{aligned}
\Delta\Phi_{ij}^{kl} &= \Phi_{ij}^{kl}(t+\Delta t) - \Phi_{ij}^{kl}(t) \\
&\approx \rho_j^i\left(t+\Delta t, t+\Delta t-\tau_j^i\right) - \rho_j^k\left(t+\Delta t, t+\Delta t-\tau_j^k\right) \\
&\quad -\rho_i^l\left(t+\Delta t, t+\Delta t-\tau_i^l\right) - \rho_i^k\left(t+\Delta t, t+\Delta t-\tau_i^k\right) \\
&\quad -\rho_j^l\left(t, t-\tau_j^i\right) - \rho_j^k\left(t, t-\tau_j^k\right) + \rho_i^l\left(t, t-\tau_i^l\right) - \rho_i^k\left(t, t-\tau_i^k\right) \\
&\quad -\Delta I_{ij}^{kl} + \Delta T_{ij}^{kl} + \Delta\delta m_{ij}^{kl} + \Delta\varepsilon_{ij}^{kl}
\end{aligned}
\tag{2.13}
$$

where the meaning of the abbreviation denoted by Δ is the difference between parameters at adjacent epochs.

As in the case for the double-difference (2.11), no clock terms are present in the triple-difference combination. Additionally, equation (2.13) shows the absence of the integer ambiguity term. The remaining errors and biases are also further reduced. The pseudo-range triple-difference is not usually formed since there is no ambiguity term to remove when using pseudo-ranges.

2.4.3.4 Outline on the use of differences

Each of these differences has some value in the processing of GPS data. The GIPSY processing software (Lichten and Border, 1987) uses undifferenced observations, stochastically modelling the receiver and satellite clock errors. With high precision GPS orbits and satellite clock values now readily available through the IGS, the single-difference approach allows a precise position to be obtained using a single receiver. This is known as Precise Point Positioning (Zumberge *et al.*, 1997).

The majority of GPS data processing is performed using the double-difference operator. This is mainly due to improved computational efficiency when using double-differences. Integer ambiguity resolution is also more natural with double differences. This is the approach taken in the GAMIT (King and Bock, 1999) and Bernese (Rothacher and Mervart, 1996) software, for example.

The triple-difference operator is used most frequently to repair cycle slips in the data, since cycle slips appear as spikes in the triple difference time-series. Since the ambiguities cannot be fixed using this difference the potential accuracy is reduced, so one of the other approaches is normally used for the GPS processing once cycle slips have been identified.

2.4.4 Linear combinations of dual-frequency observations

Using a combination of dual-frequency pseudo-range and carrier phase signals, a range of useful linear combinations may be formed, based on equations (2.5) and (2.6). There are many of these combinations, although only the most common are shown below. A more complete description, including their development, may be found in Leick (1995).

2.4.4.1 Ionospheric-free combination

The mathematical model for the ionospheric-free combination (referred to in different software as the L_C combination (e.g., GAMIT) and L_3 (e.g., Bernese)) of the carrier phase is:

$$\Phi^k_{i,3}(t) = \alpha_1 \Phi^k_{i,1}(t) - \alpha_2 \Phi^k_{i,2}(t) \tag{2.14}$$

where

$$\alpha_1 = \frac{f^2_{L_1}}{f^2_{L_1} - f^2_{L_2}}, \text{ and } \alpha_2 = \frac{f^2_{L_2}}{f^2_{L_1} - f^2_{L_2}}$$

By inserting equation (2.6) into equation (2.14) and neglecting second-order ionospheric terms, the ionospheric-free model becomes:

$$\begin{aligned} \Phi^k_{i,3}(t) \approx{}& \rho^k_i\left(t, t - \tau^k_i\right) + T^k_i + \delta m^k_{i,3} \\ &+ c\left[dt_i(t) - dt^k(t)\right] + \lambda_1 b^k_{i,3} + \varepsilon^k_{i,3} \end{aligned} \tag{2.15}$$

where

$$\delta m^k_{i,3} = \alpha_1 \delta m^k_{i,1} - \alpha_2 \delta m^k_{i,2}$$

$$b^k_{i,3} = \alpha_1 N^k_{i,1} - \alpha_2 \frac{\lambda_2}{\lambda_1} N^k_{i,2}$$

$$\varepsilon^k_{i,3} = \alpha_1 \varepsilon^k_{i,1} - \alpha_2 \varepsilon^k_{i,2}$$

Since $b^k_{i,3}$ is important for ambiguity resolution it is often written in the form:

$$b_{r,3}^{k} = \frac{f_{L_1}}{f_{L_1} + f_{L_2}} N_{r,1}^{k} + \frac{f_{L_1} f_{L_2}}{f_{L_1}^2 - f_{L_2}^2}\left(N_{r,1}^{k} - N_{r,2}^{k}\right)$$

where the $\left(N_{r,1}^{k} - N_{r,2}^{k}\right)$ term is called the *wide-lane ambiguity*, while the $N_{r,1}^{k}$ term is the *narrow-lane ambiguity*. Ambiguity resolution is not possible in the ionospheric-free combination since the ambiguities are no longer integers. Furthermore, the noise of the observables is increased by a factor of $\sqrt{2}$. Despite this, the ionospheric-free combination is used in almost every GPS processing package available since it effectively removes the ionospheric delay.

2.4.4.2 Geometry-free combination

The geometry-free combination is also known as the ionospheric combination, or the L_4 combination. The mathematical model is:

$$\Phi_{r,4}^{k}(t) = \Phi_{r,1}^{k}(t) - \Phi_{r,}^{k}(t) \tag{2.16}$$

By inserting equation (2.6) into equation (2.16), and neglecting small differences:

$$\Phi_{r,4}^{k}(t) \approx -I_{r,4}^{k} + \delta m_{r,4}^{k} + \lambda_1 b_{r,4}^{k} + \varepsilon_{r,4}^{k} \tag{2.17}$$

where $b_{r,4}^{k} = N_{r,1}^{k} - \frac{f_{L_1}}{f_{L_2}} N_{r,2}^{k}$

The equations for the mathematical model of the L_4 pseudo-range combination may be generated in a similar way:

$$P_{r,4}^{k}(t) \approx I_{r,4}^{k} + dm_{r,4}^{k} + e_{r,4}^{k} \tag{2.18}$$

This combination is referred to as geometry-free as it is free from the effects of orbits or station coordinates. In particular, equations (2.17) and (2.18) do not contain either satellite or receiver clock corrections, with the dominant factor being the ionospheric delay.

2.4.4.3 Wide-lane combination

This linear combination is also referred to as the L_5 combination. Its mathematical model for the carrier phase is:

$$\Phi^k_{i,5}(t) = \frac{f_{L_1}\Phi^k_{i,1}(t) - f_{L_2}\Phi^k_{i,2}(t)}{f_{L_1} - f_{L_2}} \tag{2.19}$$

By inserting equation (2.6) into equation (2.19):

$$\Phi^k_{i,5}(t) \approx \rho^k_i\left(t, t-\tau^k_i\right) - I^k_{i,5} + \delta m^k_{i,5} + \lambda_5\left(N^k_{i,1} - N^k_{i,2}\right) + \varepsilon^k_{i,5} \tag{2.20}$$

where

$$\lambda_5 = \frac{c}{f_{L_1} - f_{L_2}}$$

$I^k_{i,5}$, $\delta m^k_{i,5}$ and $\varepsilon^k_{i,5}$ are determined in a similar way to equation (2.19).

This combination results in an 0.86m wavelength observable, although this is reduced to 0.43m if the data is half wavelength. Using this combination, the wide-lane ambiguity may be solved provided the *a priori* coordinates of the satellite and station are good and the ionospheric delay is known, as is the case with dual frequency measurements.

2.4.4.4 Melbourne-Wubbena combination

Unlike the models explained thus far, the Melbourne-Wubbena combination is a linear combination of both carrier phase and P-code pseudo-range observables. A full description is given in Melbourne (1985) and Wubbena (1985). The mathematical model of this combination is:

$$b^k_{i,5}(t) = \Phi^k_{i,5}(t) - \frac{f_{L_1}P^k_{i,1}(t) + f_{L_2}P^k_{i,2}(t)}{f_{L_1} + f_{L_2}} \tag{2.21}$$

Inserting equations (2.5) and (2.20) into equation (2.21) provides:

$$b^k_{i,5}(t) = \lambda_5\left(N^k_{i,1} - N^k_{i,2}\right) + dm^k_{i,5} + e^k_{i,5} \tag{2.22}$$

where $dm^k_{i,5}$ and $e^k_{i,5}$ are determined in a similar way to equation (2.21).

This combination eliminates the effect of the ionosphere, troposphere, geometry and the receiver and satellite clock errors. In low multipath environments, and with good

quality P-code measurements, this combination is very helpful in resolving the wide-lane ambiguities.

2.4.5 Arbitrary linear combinations

Further useful linear combinations of the L1 and L2 carrier signals may be formed with integer coefficients n and m (Seeber, 1993):

$$\Phi_{n,m}(t) = n\Phi_1(t) + m\Phi_2(t)$$

There are, of course, an unlimited number of combinations, with only the most useful of them listed in Seeber (1993). When processing GPS data in the presence of a highly active ionosphere, the (4, -3) and (5, -4) combinations are particularly useful. This is because the wavelengths are longer than the ionosphere free combination, while maintaining integer ambiguities. While still being affected by the ionosphere, the effect on these two combinations is less than 7% of the wide-lane combination. The two combinations are also known as the L_{43} and L_{54} combinations, respectively.

2.4.6 Single-frequency solutions

Without a second frequency to enable to removal of the ionospheric delay, data collected using single frequency receivers are significantly degraded by the ionospheric delay. As has been mentioned previously, this is especially so in equatorial and Polar regions. Fortunately for millimetre-level positioning, much of the ionospheric delay will be cancelled when using standard differencing techniques for receivers separated by less than 1-2km, although some cancellation will normally occur at distances up to 70km. However, as between-receiver distances increase the residual ionospheric delay grows, degrading the derived positions. Several ionospheric models have been proposed in order to overcome this distance barrier. Firstly, however, a difference equation may be formed between equations (2.5) and (2.6):

$$\begin{aligned} P_i^k - \Phi_i^k = {} & 2I_i^k + dm_i^k - \delta m_i^k + c\left[d_i(t) + d^k\left(t - \tau_i^k\right)\right] \\ & -c\left[\delta_i(t) - \delta^k\left(t - \tau_i^k\right)\right] + \lambda\left[\phi_i\left(t_0\right) - \phi^k\left(t_0\right)\right] \\ & -\lambda N_i^k + e_i^k - \varepsilon_i^k \end{aligned} \qquad (2.23)$$

Equation (2.23) demonstrates the difficulty of removing the ionospheric term algebraically, since so many terms remain. Even if all the delay and multipath terms are

ignored, the group delay and the ambiguity cannot be estimated separately, since the ionosphere changes every epoch. The size of pseudo-range measurement errors on current, and more so on early, GPS receivers also prevent this method from being widely used. Qiu *et al.* (1995) used this method to remove 90% of the ionospheric contribution to single frequency observations recorded on narrow-correlator receivers, by making the assumption that multipath had little effect on the data and there was a relatively constant ionospheric delay at the time of data collection.

Various ionospheric models have been developed as a result of the inability to remove the ionospheric delay by differencing. These fall into one of three categories: theoretical, empirical and regional. Theoretical models are the most common, since one of the models is included in the broadcast message of the GPS signals (Klobuchar, 1987). This model corrects for approximately 50-60% of the signal delay. The advantages of these types of model are their simplicity, with estimated delays possible using only a few calculations. A second type of ionospheric model is the global empirical model, such as the International Reference Ionosphere (Rawer *et al.*, 1978). These models rely on actual measurements of the ionosphere, and thereby provide realistic values for the TEC. They are however limited spatially and historically, especially in the Southern Hemisphere and Polar regions. At present, these models are not generally used in the correction of GPS signals since they do not appear significantly better than the broadcast model (Langley, 1996). Recent advancements in ionospheric modelling come in the form of regional models (e.g., Wilson *et al.*, 1995). These are based on dual-frequency GPS observations used to determine the ionospheric delay at certain locations in the region of single-frequency operation. Observations are then used to build a model of the regional ionospheric conditions (see e.g., Juan *et al.*, 1997), which may in turn be used to correct the single-frequency observations (Hansen, 1998). This method is now also being applied globally, constructing highly precise Global Ionospheric Maps (Schaer *et al.*, 1995; Ho *et al.*, 1997), although there is not complete coverage in Antarctica and other regions.

2.5 GPS Data Processing Approaches

The processing of GPS data is normally divided into two different approaches – *static* and *kinematic* processing. These are discussed below along with further hybrid

approaches. Further information may be found in ++(Leick, 1995 #92; Hofmann-Wellenhof, 1992 #97).

2.5.1 Static

Static processing assumes the GPS antenna to be stationary relative to the reference frame origin during the processed segment. One coordinate estimate is generated for each data segment. For global geodesy, the segment length is typically chosen to be 24 hours although other lengths may also be chosen to suit the experiment. This segment length is particularly convenient since many potential biases average or nearly average to zero over this period, including multipath and diurnal ocean loading effects. The large number of observations during a data segment allow for a high precision coordinate solution to be made and helps in the resolution of carrier phase ambiguities.

2.5.2 Kinematic

Kinematic processing, on the other hand, assumes the GPS antenna to be non-stationary during the survey and provides a position estimate at every measurement epoch. The coordinate precisions of a kinematic solution will normally be lower than those from a static solution for several reasons: 1) coordinates are estimated using fewer observations, 2) carrier phase ambiguities are more difficult to resolve and, 3) biases, such as multipath, do not average in the case of a moving antenna.

Until recently, to resolve ambiguities the antenna was required to be held stationary for a period of time, perhaps up to thirty minutes, at the beginning of a survey and at any subsequent cycle-slips or data drop-out. Recently methods have been developed to allow ambiguities to be resolved On-The-Fly (OTF; as the antenna is moving) under certain conditions, such as in locations where low multipath exists and greater than five satellites are visible.

2.5.3 Hybrid approaches

Hybrid approaches include stop-and-go and rapid-static processing. The stop-and-go method requires the continuous tracking of satellites following a period of static ambiguity initialisation. Once the ambiguities are resolved, the antenna may be relocated to another site, where only a few epochs of data are required to achieve high

precision results. This method is no longer widely used due to the wide use of kinematic OTF techniques.

2.6 Summary

Since the late 1980s and throughout the 1990s, GPS has been increasingly used as a tool for deformation measurements (Hager *et al.*, 1991; Larson *et al.*, 1991b; Larson *et al.*, 1991a). The GPS system has been reviewed in this Chapter, with the different error sources described along with means of overcoming them, where possible. Furthermore, consistent reference frames based on appropriate reference systems is vital if systematic errors are not to be introduced into data sets. Global reference frames are required if GPS measurements are to be compared with remote sensing missions such as ICESat.

With regard to the use of GPS in Antarctica, interesting challenges are presented with poorer satellite geometry (satellites generally lower than 70° above the horizon and a significant hole in the Southern sky) and higher ionospheric variability (in magnitude and scintillation levels) than many other places on Earth. Large distances from GPS base stations and inhospitable conditions further add to challenges. In particular, the use of single-frequency GPS receivers result in data significantly affected by the ionosphere over distances greater than just a few kilometres from the base station. A summary of the performance issues for GPS use in Polar regions compared with mid-latitude and equatorial operation is shown in Table 2-4. Despite these limitations, GPS has been used successfully in Antarctica for a wide range of applications, most notably mapping, satellite ground-truthing (Phillips *et al.*, 1998), ice thickness change (Hulbe and Whillans, 1994), velocity and strain determination (Whillans *et al.*, 1990; Chen *et al.*, 1998) and floating glacier and ice shelf movement studies (Capra *et al.*, 1997).

Effect	Polar	Mid-latitude	Equatorial
Satellite Orbits	No satellites at high elevations; Shorter satellite arcs	Hole in the Northern/Southern sky	Even distribution of satellites
Troposphere	Little water vapour; satellites at lower elevation pass through thicker portion of troposphere	Relatively stable	Relatively variable
Ionosphere	Variable at all times of the day; satellites at lower elevation pass through thicker portion of ionosphere	Mostly stable	Highly variable, particularly during the day
Solid earth tides	Well known	Well known	Well known
Ocean tides	Not well known in the vicinity of coastlines, and especially near ice shelves, due to difficulty in modelling sub-ice shelf tides	Generally well known	Generally well known
Station density	Sparse	Mostly good	Mostly good
Satellite orbit precision	Lower than average due to station sparseness	Average	Average
Reference frame precision	Lower than average due to permanent station sparseness	Average	Average

Table 2-4: Summary of performance issues for GPS use in Polar regions compared with mid-latitude and equatorial locations

Chapter 3

ANTARCTIC ICE MOVEMENT MEASUREMENTS

From the beginnings of polar research, scientists have endeavoured to understand the glacial/ice shelf systems and the processes driving those systems. Of particular importance to this understanding were answers to the questions:

- What forces are acting on and within the glacier/ice shelf?
- How fast is it moving?
- Where is its 'grounding line'?
- What is the interaction of the ice shelf and the ocean beneath it?
- What is the relationship between ice shelves and climate change?

Early researchers (e.g., Zumberge, 1964) found that measurement equipment was heavy, bulky, difficult to operate in polar conditions, and often did not achieve high levels of precision or accuracy. However, one distinct advantage existed over other geophysical studies of the Earth's surface – in general, flowing ice moves between 10^1 and 10^6 times faster than the Earth's crust. Measurement noise is therefore small compared to the signal, meaning glacial deformation studies could occur over a relatively short period of time – often within weeks or months, rather than years or decades.

This Chapter reviews the evolution of such (Antarctic and otherwise) ice deformation studies, from the early terrestrial measurements of the 1950s and 1960s through to the satellite-based measurements from the 1970s to the present. Ice deformation surveys in the Amery Ice Shelf / Lambert Glacier System are then summarised, describing observation methods, practical and technical difficulties encountered, and the significant results from each of the programs.

3.1 Ice Movement and Deformation Studies

3.1.1 Terrestrial Measurements

The International Geophysical Year (1957-58) marked the beginning of widespread interest in polar geophysical research, and in particular, glaciological studies. At that time, there existed very little data about Antarctic glaciers or ice shelves although their importance was well known (Sharp, 1956). Geophysicists were particularly interested in the dynamics of large bodies of ice, especially how they moved and deformed. Experiments were originally focused on either very small areas, in order to determine localised deformation, or very large areas, to study large-scale ice sheet dynamics or map and determine the extent of the ice.

Initially, only very simplistic tape measurements of elongation were made to determine the longitudinal component of ice deformation over relatively small areas. Nye (1959) was the first to investigate glacial deformation in a more comprehensive manner. Using repeat measurements of a 50 metre 'braced-quad' of stakes on the surface of a glacier in Norway, the three independent components of the horizontal strain rate tensor were determined using a least-squares method. A central stake was also placed to measure its 'absolute' velocity in relation to nearby bedrock. Shortly afterwards, a less rigorous 3 stake method was used to study deformation on the Antarctic Ross Ice Shelf over an area of several kilometres square (Kehle, 1960).

At the same time, plans were being made for extremely ambitious traverses, spanning hundreds of kilometres on ice shelves in Antarctica. The first of these traverses were conducted by the University of Michigan on the massive Ross Ice Shelf for the purpose of determining glaciological parameters – ice deformation, movement and snow accumulation (Hofmann *et al.*, 1964). Taking advantage of a previous tractor-trail stretching from "Little America V" to near McMurdo station that was marked regularly with bamboo canes and empty fuel-drum cairns, a repeat traverse was performed in 1959-60. Known as the Ross Ice Shelf Traverse (RIST) the traverse included the measurement of the heights of some 1800 bamboo poles for accumulation measurements, and the set out and measurement of strain networks every 32 kilometres along the traverse. Theodolite Sun-fixes were used to determine horizontal position at each of the 32 kilometre stations. Positioning errors were estimated to be

up to 1850 metres (~60 arc-seconds) in latitude and 1100 metres (~100 arc-seconds) in longitude, although 500 metres appeared to be a more realistic figure after comparison with later surveys (Zumberge, 1964). The resulting velocity errors are almost equivalent to the measured velocity at some locations on the ice shelf.

During the 1962-63 season, the traverse (now known as the Ross Ice Shelf Survey, RISS) was again repeated. However a conventional theodolite and Tellurometer method was used to determine the station positions, and hence the velocity of the ice shelf at these locations. Since the traverse was terminated at a stable rock site only at one end, estimates of the survey precision can only be based on repeated measurements of angles and distances. The precision of these measurements was calculated to be ±0.8″ and ±34mm respectively (Hofmann *et al.*, 1964). Propagating these values over the 910km traverse gives a maximum error of less than 10m at the end of the traverse, well within the allowable error margins of the survey (Hofmann *et al.*, 1964). To attain the best possible estimates of ice movement, the traverse was repeated again in 1965-66 (RISS-II). The precision of the angle measurements from this survey were calculated to be slightly better than the previous traverse - now at ±0.6″, while the distance precision was unchanged from the previous traverse (Dorrer *et al.*, 1969). When combined with the results from the previous season, these precisions led to a potential maximum velocity error of less than one metre per year, although external systematic errors might increase this number significantly.

Following on from this work, the British Antarctic Survey conducted a deformation survey on the Brunt Ice Shelf during 1966 and 1967 (Thomas, 1970). The network consisted of 64 markers making up a series of triangulated braced quadrilaterals with side lengths of 3-4 kilometres. Scale was controlled by a 5 kilometre taped baseline, and Tellurometer distances were used to check for gross errors within the network. The least precise velocities had precisions of $\pm 3.5 myr^{-1}$ and ±3° (of arc) for the magnitude and direction of ice flow, respectively. Computed strain rates were precise to $\pm 3.3 \times 10^{-5} yr^{-1}$, about 33 μstrain/yr.

The Australian Antarctic Division conducted several traverses on the AIS during the early and late 1960s. The detail of these traverses is included in Section 3.2, although in

terms of survey design, they were conducted using similar methods to that used on the Ross Ice Shelf.

During 1957-1962, the Argentinean Antarctic Institute measured the movement of the front of the Filchner Ice Shelf using a triangulation network (Lisignoli, 1964). This network, spanning 70km, was established in 1957 and remeasured in 1958 and 1962 and in part in 1961. Astronomic determinations were made as checks on the triangulation work. Unfortunately, details of estimated precision are not provided in Lisignoli (1964).

3.1.2 GPS Measurements

Given the size of Antarctica and the desire to reduce or eliminate the time spent in traversing from known locations, satellite surveying methods were introduced quickly into glaciological and geodetic field campaigns. Satellite-based systems also had the advantage of being inherently three dimensional in nature - latitude, longitude and height could all be measured using the one technique, and without any line-of-sight restrictions. In the 1970s and 1980s the TRANSIT Doppler system was used with some success for geodetic positioning, although this system was somewhat limited in precision (to about 1-5 metres). Several ice movement surveys were also conducted using the system (e.g., Young, 1979; Bindschadler *et al.*, 1987), with coordinate precisions around 3-10 metres, although this figure depended greatly on the observation and processing strategies employed and the ionospheric conditions prevalent at the time of observation (Young, 1979; Medhurst, 1985).

Antarctic scientists were quick to make use of the increased precision of the GPS system during the late 1980s. Moller and Ritter (1988) were the first to use GPS in Antarctica in 1985-86 when they established control for ice movement surveys on the Ekstrom Ice Shelf. Later in the season, Hinze and Seeber (1988) also used GPS in conjunction with TRANSIT measurements for ice movement studies on the Filchner-Ronne Ice Shelf. Neither author provides details on data quality or processing results.

In these early campaigns, the usefulness of GPS was somewhat limited by, among other things, the small size of the satellite constellation at this time, with as few as only seven satellites available. Additionally, a significant hole exists over the southern sky,

further weakening the solutions in the North-South component. Improvement in the constellation continued until 1994 when the system, consisting of twenty-four satellites in active use, was declared operational.

Gubellini and Postpischl (1991) used GPS in the 1988-89 season in the Mt. Melbourne area, albeit for solid-Earth deformation studies. They encountered significant problems while using Trimble SL single-frequency receivers. The Australian Antarctic Division used single frequency WM101 receivers during the same season, experiencing significant problems caused by the ionospheric activity (see Section 3.2.2). Tseng *et al.* (1989) found that during the same season the high variability of the ionosphere above Antarctica was causing their TI-4100 GPS receivers to experience frequent cycle slips. Curiously, Japanese investigators performing a traverse during the previous season between Syowa station and Mizuho Plateau, close to the southern auroral zone where ionospheric scintillation is known to occur at high levels, experienced little difficulty and obtained excellent results using their Sony GTT-3000 single-frequency receivers (Toh and Shibuya, 1992). This difference may be explained by the multiplexing channel on the TI-4100 receiver, while the Sony receiver had parallel channels.

As dual-frequency instruments became available, greater precision over longer baselines became possible. At the same time, computational methods were improving, further increasing the accuracy of results. During the 1989-90 season, baselines were observed between three sites in Australia, one in New Zealand, and four in Antarctica. Although significant data drop-outs occurred on L2 on some receivers, results of the processing were at a precision of 1 part in 100 million, similar to regional studies elsewhere (Morgan and Tiesler, 1991).

The use of GPS in Antarctica became increasingly widespread as the number of satellites increased and GPS receiver technology improved to allow more satellites to be tracked concurrently. Scientists began to see the value of GPS for a wide range of activities, such as precise control of photogrammetric photos, strain grids, geodetic networks or navigation (Whillans *et al.*, 1990).

Since this early period, GPS has been used to calculate geoid heights, study the tidal flexure of an ice shelf, determine ice thickness change or measure strain, amongst

others (e.g., Shibuya *et al.*, 1991; Hulbe and Whillans, 1993; Hulbe and Whillans, 1994; Vaughan, 1994). It is also now widely used in the calibration of a variety of satellite measurements, including satellite altimetry (Robin, 1966; Brooks *et al.*, 1978; Phillips, 1999) and satellite radar interferometry (Bindschadler, 1998; Massonnet and Feigl, 1998), providing wide-ranging information on the behaviour of the Antarctic ice sheet, over both short and long time scales. GPS will also be an essential part of the validation of several new satellite missions, including the forthcoming Geoscience Laser Altimeter System (GLAS) mission (Schutz, 1998; Wahr *et al.*, 2000). These satellite-based techniques provide measurements of surface height or three-dimensional motion with spatial resolutions far beyond previous techniques. Consequently, GPS measurements will continue to play an important role in Antarctic measurement for the foreseeable future.

3.1.3 Summary

As is the case in other places in the world, GPS has become an efficient and precise method for performing many medium to large-scale Antarctic surveys. However, the value of older terrestrial measurements should not be understated. They have significant value since they provide a significantly longer time-history of measurements than is available from GPS measurements alone. Terrestrial measurements, even relatively imprecise ones, are of increasing value as the time between them and modern measurements increase. In the case of ice movement surveys they provide an opportunity to asses if the ice velocities and strain have changed during the intervening period, something that is not yet possible using GPS measurements alone.

Having looked at the broad picture of the development of ice movement and deformation measurements on several ice shelves in Antarctica, we now look more closely at the Amery Ice Shelf. The measurements that have been made in the Lambert Glacier / Amery Ice Shelf System will be reviewed with a view to determining as much information relating to the region as is possible from the data that currently exists. It is hoped, as is often the case, that more information can be gleaned from the combination and re-examination of data sets than was previously possible using a fragmented approach.

3.2 The Amery Ice Shelf

Since it was first sighted and named in 1931, the Amery Ice Shelf has been of significant interest to the international Antarctic scientific community. Australian scientists led the way in the investigation of this massive system with the first of several major field campaigns beginning in the summer of 1963. At the same time, survey networks were being extended from Mawson station toward this region, providing much needed geodetic control on the surrounding rocky outcrops. Only the glaciological measurements will be dealt with in this section, since the geodetic measurements made at that time do not affect the results of this thesis.

3.2.1 Terrestrial Observations

3.2.1.1 1963-65

During 1963-65, field parties placed and measured a network of three metre long bamboo canes with the aim of measuring snow accumulation, forward movement and deformation of the Amery Ice Shelf. This network stretched longitudinally (approximately north-south) for a distance of over 200 kilometres down the centre of the ice shelf. Two perpendicular lines (approximately east-west) were also placed near the front and back of the main line, reaching some 100 kilometres and 60 kilometres respectively (Figure 3-1). In all, more than two hundred poles were placed (approximately every 3.2km) with additional square strain grids at stations G1, G2 and G3 on the central flow line (Budd, 1966a). Five metre long black bamboo canes were used to mark the strain grids, consisting of a square with approximately 1600 metre diagonals. Astronomical observations of the Sun were taken at one of the grid locations to determine position and hence velocities and rotations with respect to surrounding rocky outcrops, while distances between the strain grid stakes were taped. All other distances were measured using a sledge-wheel, directions measured by compass, and heights measured by precise barometer (Corry, 1987a; Corry, 1996). Other than the Sun observations, no connection was made to the surrounding geodetic network for this experiment.

During the following season (1964-65) the traverse was repeated with strain grids remeasured, new astro-fixes performed and the northern end of the main traverse line extended to the point T5, where a new strain grid was also established (Budd, 1966a).

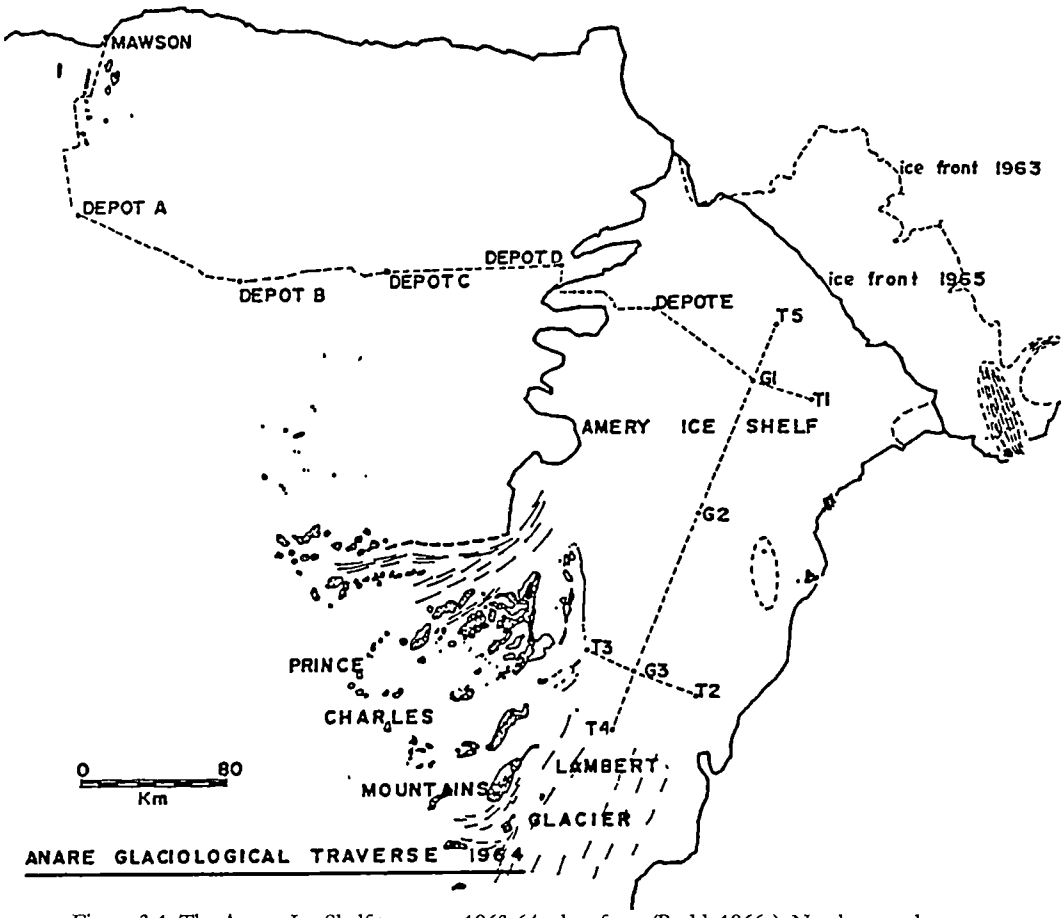

Figure 3-1: The Amery Ice Shelf traverses 1963-64 taken from (Budd, 1966a). North is up the page.

Several conclusions were made from the first two seasons of study on the ice shelf of which the following are of importance here (Budd, 1966a; Budd, 1966b):

- The forward speed of the ice shelf ranges from 300myr^{-1} at the Lambert Glacier entry point[1], to 1500myr^{-1} at the front of the ice shelf.
- The high increase in velocity at the front of the ice shelf is caused by internal deformation (creep) as the ice expands and thins under its own weight.
- The velocity across the ice sheet is not uniform due to the ice shelf being held at its sides and thus has a parabolic shape.
- The rapid longitudinal stretching is accompanied by high lateral-tension crevasses.

1. The point where the Lambert Glacier was believed to have started floating and become the Amery Ice Shelf was until recently believed to be between G3 and T4. Recent investigations have concluded that the grounding zone is some 200 kilometres further south, in the proximity of the 'crease line' adjacent to Mount Stinear (Phillips, 1999).

- Basal melt-rates of up to $1myr^{-1}$ may have been occurring at station G1.
- The accumulation in the Amery/Lambert basin area was calculated to be about three times higher than that required for a balanced system. This was based on very little accumulation data, and hence the errors in the estimate were large. Even with these large errors taken into account, the system appeared to be in significant positive mass balance.

The astronomical positions were initially thought to be accurate to ±100m, thereby providing horizontal velocities accurate to $\sim 150myr^{-1}$, although the agreement with the measured strain rates was better than this and hence the position accuracies were revised upward (Budd, 1966a). The estimates of the potential error in the results were $25\text{-}100myr^{-1}$ in velocity and $0.5 \times 10^{-3}yr^{-1}$ (500μstrain/yr) in both longitudinal and transverse components of strain. The strain rate error was greater than the estimated longitudinal and transverse strain rates at G3 and the transverse component at G2.

3.2.1.2 1968-70

Following the success of this initial work, a far more ambitious project (known as the Amery Ice Shelf Project) was proposed by scientists at the Australian Antarctic Division. A team spent the Austral winter of 1968 on the AIS to study "the relationship between stress, crystallographic orientation and thermal gradient in the ice and to measure ice thickness, surface profile, accumulation, and strain and flow rates over the Shelf" (Corry, 1987b). The results from the earlier seasons had shown that a more detailed and accurate survey was required, and so the Tellurometer, theodolite and optical level replaced the sledge-wheel, compass and barometer for this new work. A Wild T3 theodolite and MRA3 Tellurometer were used, capable of measuring angles and distances at a precision of 0.8″ and 5mm + 3 parts-per-million (ppm), respectively[2]. In Antarctic conditions 4″ and 50mm + 5ppm, have been used as *a priori* standard deviations by AUSLIG[3] in their network adjustments based on repeatabilities of measurements in Antarctica (personal communication, G. Johnston, 1999; Kirkby, 1965). Budd (1966a) suggested that the resurvey of some of the 1963-65 survey marks

2 These values are taken from the manufacturer's specifications.

3. Australian Surveying and Land Information Group.

using this more accurate equipment would help in reducing the errors within the velocities, velocity gradients and elevation profiles of the original survey.

The 1968 season camp was to be located at the G1 strain grid site established in 1963. However, this site was not immediately located and their camp (known as A1) was later found to be some 10km to the West of G1. Unfortunately the weather was not in the team's favour and very little geodetic work could be done until an improvement came in the spring of 1968.

The first fieldwork that could be conducted away from the camp was the optical levelling, due to the short sighting distance required. While previous campaigns had given an approximate value for the surface profile of the Amery, both the increased precision of the optical level and the advantage of tying the heights to mean sea level were significant. The levelling began at G1 and commenced in a SSW direction with sighting distances of 120 metres. As the weather improved, sighting distances were increased to 150 metres, then to 200 metres. None of the canes from the 1963-65 campaigns were encountered until the survey party reached G2. When sufficient canes were visible, the levelling route was brought into line with the original traverse two-thirds of the way between G2 and G3 (Figure 3-2). On reaching G3, the levelling run was extended to T4 in the south, T2 in the east, and Jetty Peninsular in the west. Barometric levelling conducted at Jetty Peninsula allowed the conclusion to be made that tidal Beaver Lake was at sea level, to which the levelling agreed to within one metre. At the conclusion of the season, the route from G1 to Sandefjord Bay route was levelled, and measurements were made through the sea ice to the water's surface, linking somewhat approximately the levelling to sea level at Nickols Island. See Appendix A for a further discussion of the levelling connections to sea level.

The procedure for marking the traverse route involved the removal of the original canes as the rear levelling party went past them, and placing steel poles at the local high-points to which the later Tellurometer survey would be referenced. These steel poles consisted of three metre lengths, with each length flanged at one end to allow another section to be added. For the majority of the traverse, three sections were used to produce a nine metre steel pole, with more than six metres protruding above the snow. Due to a shortage of lengths, only six metre poles were placed in the southern

end of the survey where snow accumulation is nearly zero, or ablation occurs. However, these poles still protruded more than four metres above the surface of the ice shelf (Corry, 1996).

As the weather had improved significantly by the time the levelling party reached Beaver Lake, the traversing was completed quite quickly using a Tellurometer to measure distances and a T3 theodolite to measure angles. Angles were read eccentric to the measurement pole, and a distance and direction measured from the eccentric station to the measurement pole. As had become standard practice, the Tellurometer was elevated to prevent the emitted signal bouncing off the ground (hence reducing multipath, or ground swing), thereby preventing erroneous measurements (Tellurometer Limited, 1963; Yaskowich, 1964). Problems, however, were encountered with atmospheric disturbance when observing at twilight. The survey party commenced the distance and direction observations where the levelling had concluded, proceeding back to G3 then north to G1. From G1, the traverse proceeded in a WNW direction towards Depot E, although the survey party later discovered they were several kilometres to the north of this site. Just before Christmas 1968 the traverse proceeded from G1 north to T5. However, it was not until a fresh field party arrived in January 1969 that the final stages of the traverse were completed. The Landing Bluff to G1 strain grid connection and the extension of the survey north, beyond the T5 strain grid towards the front of the ice sheet, were conducted at this time. Observations to rock sites from A119 (to Landing Bluff), T2 (A207) (to New Year Nunatak) and T4 (A406) (to Blustery Bluff) completed the season's traversing - the network finally extending some 500 kilometres using 88 steel markers.

Due to the inclement autumn and winter weather, only one traverse had been conducted in 1968-69 and so a follow-up season was quickly planned for the 1969-70 summer. The season's work included the re-measurement of the entire network using theodolite and Tellurometer, and the extension of the southern end of the levelling network from T4 south for 30-50 kilometres, into what was believed to be the Lambert Glacier. Ties were again made to rock sites from G1, T2 and T4, allowing a comparison to the previous survey.

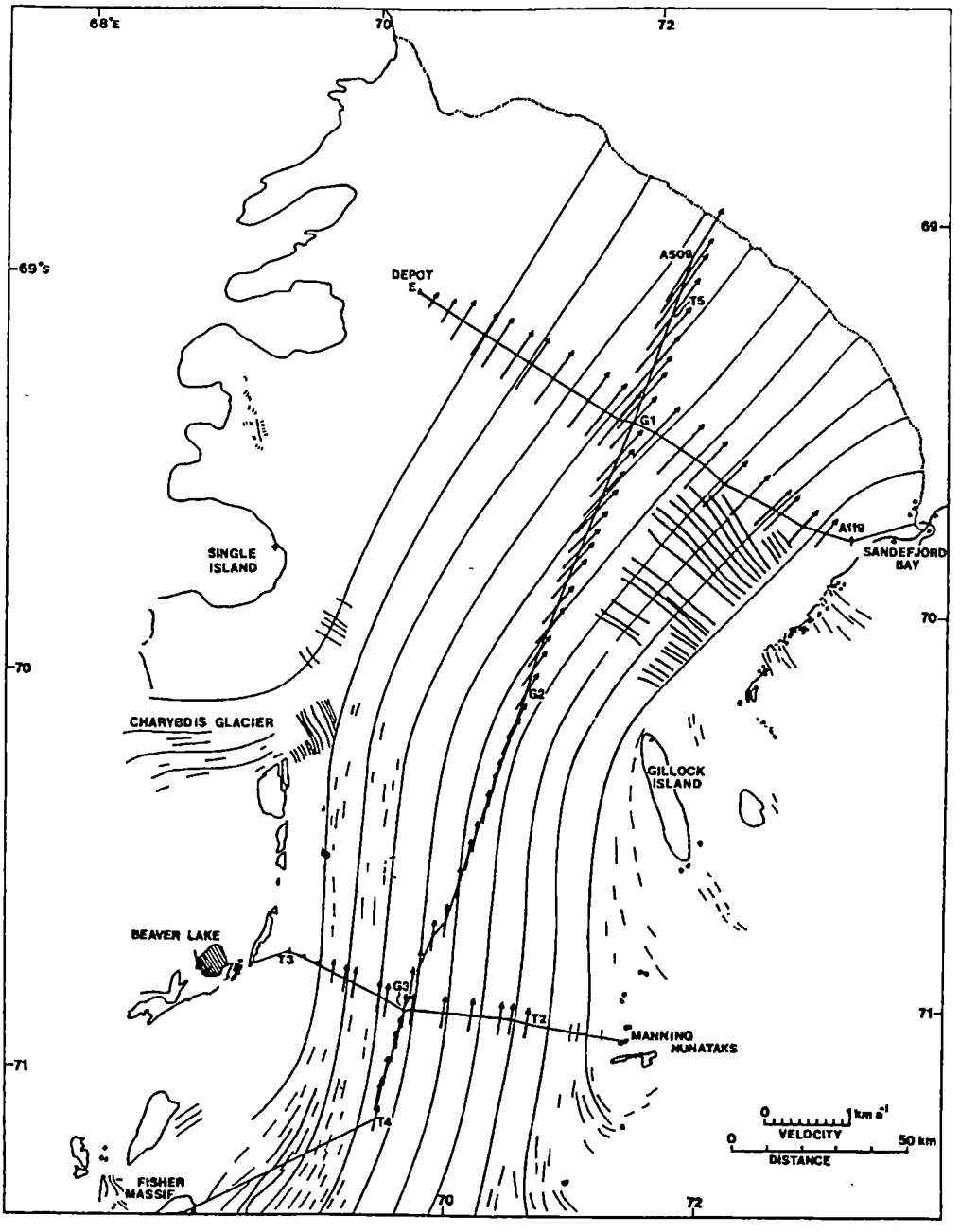

Figure 3-2: The Amery Ice Shelf traverses 1968-70 taken from (Budd *et al.*, 1982) using the Hayford 1924 ellipsoid. Velocity vectors derived from the traverse data are shown, along with flowlines inferred from satellite imagery. Sandefjord Bay is referred to as Landing Bluff in the text, while Fisher Massif is Blustery Bluff and Manning Nunataks is New Year Nunatak.

The angles and distances were reduced to the measurement pole and sea level, respectively, and coordinates and velocities were computed using a computer program written specifically for the project (personal communication, M. Corry, 2000). This program implemented the reduction to epoch method used on the Ross Ice Shelf survey (Hofmann *et al.*, 1964; Dorrer *et al.*, 1969). Strain was calculated by differencing the velocity between adjacent sites. This provided the extension (or compression)

between the two sites in the line of, and perpendicular to, the flow direction. At the completion of the Amery Ice Shelf Project, the following conclusions were reached (Budd *et al.*, 1982; Corry, 1987c):

- The profile of the ice shelf is generally flat in the transverse direction, with a substantial slope in the longitudinal component.
- The surface slope provides the primary driving force for a high centre-line velocity that varies from 350myr^{-1} at T4 to 1200myr^{-1} near the ice front.
- The computed velocities appear to match flow-lines that appear in Landsat satellite imagery.
- The thinning of the shelf due to high strain rates (reaching 16x10^{-3}strain/yr at the shelf front) is more influential than basal melting. The thinning combined with tidal/wave action then causes periodic calving of large icebergs from the front of the ice shelf.

During the compilation and analysis of this traverse as undertaken in the present study, several issues have arisen. Firstly, errors were not propagated through the traverses, and thus coordinate and velocity precisions are available. Secondly, an error in the National Mapping (now AUSLIG) control traverse on the eastern side of the AIS has been identified by AUSLIG. Thirdly, the traverse appears to have been reduced onto a different ellipsoid from that of the control coordinates. Finally, and most concerning, the computer output from the traverse reduction that has been in wide use reveals a very large misclose. The misclose is >2km in terms of coordinates, or ~44 arc-minutes in terms of angular misclose. Consequently, the 1968-70 traverses are re-analysed in Chapter 5.

3.2.1.3 1971-74

With useful information now known about the dynamics of the Amery Ice Shelf, glaciologists turned to the basin of the Lambert Glacier to determine the mass budget of the entire Lambert Glacier – Amery Ice Shelf System. In the 1971-72 season, eleven ice movement stations were placed between the 1500 and 2000 metre contours around the southern end of the basin. The theodolite and Tellurometer traverse involved placing ice movement stations at least 30 kilometres from the nearest exposed rock so

as to be representative of the entire system. At each of the stations, strain grids were measured, each grid comprising the central station and four other stations of 100 metres from the centre. The vertical coordinate was found by reciprocal vertical angles to mountaintop stations. The end of the traverse was closed at a station on the southern end of the Mawson Escarpment. The survey was repeated two years later in the summer of 1973/74 and velocities were calculated for the period with an estimated precision of 0.4myr^{-1} (Allison, 1979).

After combining the data from the Amery Ice Shelf surveys with ice-thickness data (Morgan and Budd, 1975), Allison (1979) estimated that the Lambert Glacier system was in overall mass excess by 12 Gtyr^{-1}.

3.2.2 GPS surveys

3.2.2.1 Amery Ice Shelf Surveys

3.2.2.1.1 1988-91

The advent of the Global Positioning System and the need for further study into the behaviour of the ice shelf led to an air-supported campaign beginning in the 1988-89 season (Murphy *et al.*, 1990). Twenty-nine ice movement stations were established[4] using single-frequency measurements from Wild Magnavox 101 GPS receivers (WM101). Ten stations were established near the expected grounding zone location, thirteen near where the Charybdis Glacier joins the Amery Ice Shelf, and six stations upstream on the Charybdis and Scylla Glaciers (Figures 3-3 and 3-4) (Allison, 1991). Rizos *et al.* (1990) have described the performance of the WM101 receiver in Antarctic conditions, with repeatabilities as poor as 10-40 parts per million. Significant problems were encountered in the original processing[5] of the data collected during the 1988-89 season due to the high ionospheric disturbance that exists commonly in Polar conditions (see e.g., Medhurst, 1985; Tseng *et al.*, 1989). This effect was heightened by the occurrence of a Sunspot maximum during the period 1989-1991. With just seven satellites available, the satellite constellation was also somewhat limited at the time.

4. All of the AIS GPS measurements made during 1988-1996 were conducted by the Australian Antarctic Division.

5. The data were originally processed using Wild Magnovox's proprietary software – the PoPS post processing software version 3. Significant amounts of manual cleaning and editing of the data were required for the data to be processed successfully (personal communication, I. Allison, 1998). (Piechocinska and Sjoberg, 1989) have reported that preliminary tests revealed that this version of the software had some major problems, although no details were provided in the paper as to whether these would result in numerical problems with the baseline solutions.

Further data drop-outs occurred due to channel switching (multiplexing), used by the WM101 receivers when more than five satellites are being tracked by the receiver simultaneously. Normally much of the data that was collected would have been discarded because of its low precision. However, due to the high velocity of the ice shelf, these data were still useful when reobservations occurred after one or more years (Craven *et al.*, 1995).

Unfortunately during the following season (1989-90) bad weather limited the number of reoccupations possible with the superior dual-frequency instruments (WM102). However, fifteen sites were occupied as shown in Figures 3-3 and 3-4. Problems were again experienced with multiplexing when using the new WM102 receivers, as only a single channel was assigned to track the L2 frequencies of up to six satellites, frequently resulting in data drop-outs (Craven *et al.*, 1995).

The 1990-91 season commenced with the aim of completing measurements from previous seasons as well as collecting enough measurements to conclude the study. Dual-frequency measurements were again made using the WM102 receivers. With the satellite constellation having now grown to sixteen satellites, significantly better results were expected from the season's observations.

All ice movement stations occupied in the original season were resurveyed along with eight new stations established to the south and east of the existing grounding line network (Figures 3-3 and 3-4). These new sites were measured twice during the season. Site GA31 was reoccupied during the first few days of 1991, and then subsequently melted out due to the appearance of a large melt lake in the region. A new site was established approximately 200 metres away and measured twice before the end of the season.

Further to these stations, two of the Amery Ice Shelf Project markers (A37 and A308[6]) were located and resurveyed. This allowed a comparison of the long term average velocity between the previous (1968-70) and current surveys, with differences less than 0.5% (Allison, 1991).

6. Station A308 was occupied, however the data was unable to be recovered from the WM102 tape.

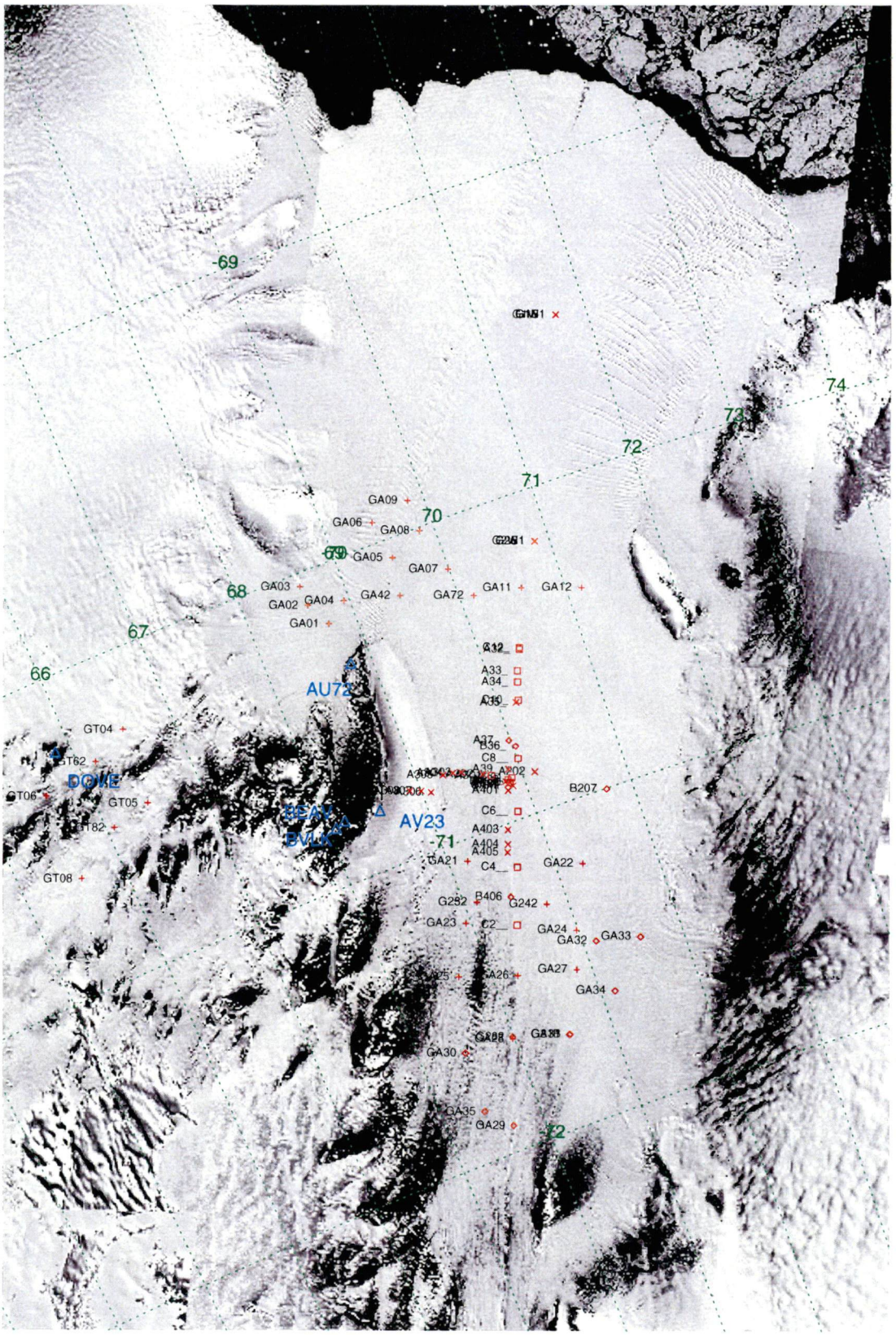

Figure 3-3: Sites occupied by GPS from 1988-1999. The season in which each of the marks were first observed using GPS are denoted by symbol; plus (1988-89); diamond (1990-91); square (1995-96); cross (1998-99).

Occupation times at the ice movement stations during the first season were normally less than one hour, and often less than thirty minutes. During the following two seasons, occupation times increased to one to two hours, at either 30 or 60 second epochs, although logistics and local conditions resulted in some sites being recorded for less than half an hour.

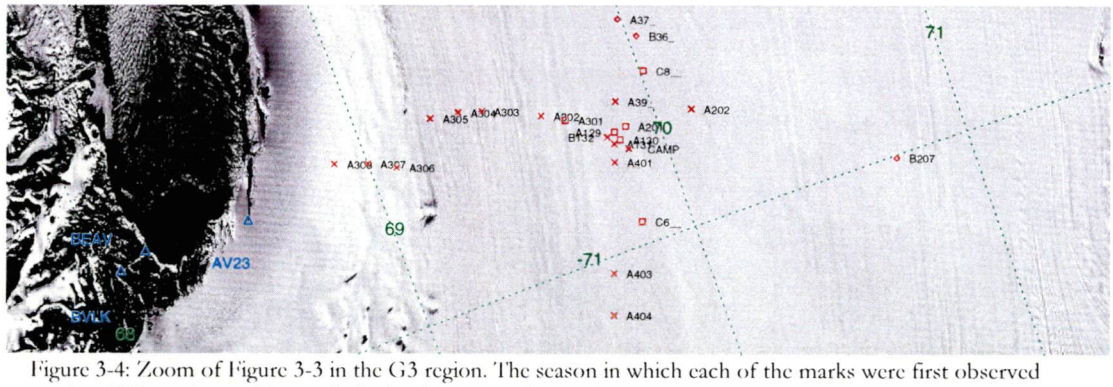

Figure 3-4: Zoom of Figure 3-3 in the G3 region. The season in which each of the marks were first observed using GPS are denoted by symbol; plus (1988-89); diamond (1990-91); square (1995-96); cross (1998-99).

3.2.2.1.2 1995-96

In the 1995-96 season the Amery Ice Shelf was again visited, this time with a ground-based program designed to validate heights from an altimeter-derived digital elevation model (Phillips *et al.*, 1997). Using Leica SR299 GPS receivers mounted on skidoos, twenty-four squares with sides of 10 kilometres were surveyed using kinematic methods. Tripod-based GPS observations were also made at six nearby ice shelf campsites (C2, C4, C6, C8, C10 and C12; see Figure 3-3 and Figure 3-4). Additionally the traverse team hoped to find markers from the 1968-70 traverse located in the same area. In all, eight of the steel poles were located[7]. Unfortunately, only a few minutes of kinematic observations were made at each by backing the skidoos as close to the poles as practical. Initial results suggested no change in velocity at these poles from the original survey within the expected errors of the surveys (Craven, 1996).

An unexpected outcome of the mission was the resolution of the ice shelf tidal signal at each of the GPS base camps. Dividing the static observations into two-hour sections, Phillips *et al.* (1997) computed twelve heights per day for each site. A clear tidal signal was evident and provided excellent agreement with a Beaver Lake tidal

7. The stations located were A129, A130, A201, A301, A35, A34, A33 and A32.

prediction produced by the National Tidal Facility (NTF) (Nielsen, 1999). The constituents used in the prediction were obtained from nearly one month of *in situ* tide gauge observations at Beaver Lake in 1990-91.

3.2.2.1.3 1997-98

Observations made at six sites during 1997-98 were conducted approximately 150-200km further south of the previous southern-most observations. While four of the sites[8] were occupied for only a period of a few hours, observations at two of the sites[9] spanned more than 4 days. Observations were made using Leica SR9500 dual-frequency full wavelength receivers. Initial processing of these two sites revealed a tidal signal, suggesting that the AIS extended significantly further south than previously believed (personal communication, A. Ruddell, 1999).

3.2.2.1.4 1998-99

During January-February 1999, a field campaign was conducted to relocate and re-measure the 'Corry poles' that had not been covered by snow during the intervening years. In all, twenty-two of these poles were relocated in the G3 region (Figure 3-4), with observation of 2-4 hours. Three of the four G3 strain grid poles were relocated, with twenty-four hour observations made at these sites. An additional pole was placed near G3[10], with a continuous record of measurements made spanning approximately eleven days. Observations were made using both Leica SR9500 and Ashtech Z12 receivers.

3.2.2.1.5 1999-2000

The longest continuous AIS GPS record to-date was acquired during January-February 2000. This observation period and location coincided with the test campaign of the Amery Ice Shelf Oceanographic Research (AMISOR) Hot Water Drill program (Craven *et al.*, 2000a; Craven *et al.*, 2000b). Thirty-one days of data were acquired at this location[11] using a Leica CRS1000 receiver, with only brief outages due to power failures. Furthermore, the five sites placed in the southern region of the AIS during the

8. V1, V2 and V4.

9. V3 and V5

10. This site was named CAMP.

11. Known as HWDT.

1997-98 season were re-occupied for a period of 2-4 hours each, allowing the computation of velocities for each of these sites.

3.2.2.1.6 2000-01

Six autonomous receivers were placed onto the AIS during December 2000 and January 2001 for the purpose of tidal studies. The design of this system is described in Chapter 4. The system includes a CRS1000 receiver. Three of these receivers were retrieved during March 2001. However, the remaining three sites could not be retrieved and an attempt will be made to retrieve them during December 2001.

3.2.2.2 Lambert Glacier Basin Survey

Following the intense work on the Amery Ice Shelf, one of the remaining and important unknowns of the Amery/Lambert system was information on the upper basin area. During the 1989-90 season, an ambitious project to traverse the entire basin from Mawson in the west to Law Base in the east began, with the aim to collect ice movement, accumulation, ice core and atmospheric data. Ice movement stations placed every 30 kilometres were measured using WM102 GPS receivers, with automatic weather stations placed at strategic locations (AWS; personal communication, I. Allison, 1998).

Further traverses were conducted in 1990-91, 1992-93, 1993-94 and 1994-95, each providing valuable information on the upper basin area. The 1992-93 traverse included a section parallel to the original traverse, but offset by approximately 50 kilometres, providing information on the terrain slope in this area of the upper basin. The final two traverses (1993-95) were complete traverses of the entire basin, with the direction of travel from Mawson to Law Base in 1993-94 and the reverse direction in 1994-95. Leica SR299 dual-frequency receivers were used for these final traverses with significant improvements in maintaining lock on L2, and consequently better quality solutions.

Results from the traverses are presented in Higham and Craven (1997) and Manson *et al.* (2000) and the reader is referred to Manson (2001, in preparation) for more information and detailed results.

3.3 Summary

The 20th Century began with almost a total lack of scientific understanding of the Antarctic continent. Looking back from the beginning of the 21st Century, things are quite different. Early Antarctic explorers paved the way for a surge of scientific interest, from the International Geophysical Year to the present. In the case of our understanding of ice movement, this chapter has outlined the process and results of the evolution from early ground-based surveys through to modern satellite positioning systems, such as the Global Positioning System. Remote sensing techniques are now furthering our knowledge by increasing the spatial resolution of ice movement information.

Comparing the results of early terrestrial surveys of large Antarctic ice shelves with those using GPS shows the advantage of using GPS over long baselines. Early surveys used either astronomical techniques or traversing for position determination. Results of astronomical observations in Antarctica are poor, perhaps ±100m at best, but more often ±500m. Long traverses are hampered by the need to account for ice movement during the time of the traverse. This is not the case with GPS. Regardless of distance from land, position (and hence velocity) is always measured relative to stationary sites using GPS. Typical baseline precisions are ±0.1-0.5m even with short observation periods. Long distances may be measured, even in poor weather, resulting in a significant time saving. This improved precision allows more frequent reoccupation times, potentially a significant cost saving (Manson *et al.*, 2000).

In the case of the Amery Ice Shelf, the most significant information pertaining to ice movement currently comes from the surveys of 1968-70, led by Max Corry. This information combined with associated measurements of snow accumulation and the borehole at site A1 has provided the foundation for our present understanding of the dynamics of the AIS. Recent GPS surveys have managed to re-observe many of the 'Corry' poles in the G3 region, while providing a recent estimate of ice shelf movement. Unfortunately, there appears to be large miscloses in both 1968-70 traverses, perhaps caused by a systematic error. An investigation into these miscloses is reported in Chapter 5 as part of a comprehensive reanalysis of the AIS terrestrial and GPS data.

Chapter 4

TIDAL MOTION OF THE AMERY ICE SHELF

4.1 Introduction

4.1.1 Tides under ice shelves

The study of the sub ice shelf tides is of significant value to our understanding of the motion and the changing nature of ice shelves. Antarctic tides are generally mixed in nature, with the majority of West Antarctica affected by mainly diurnal tides, while the majority of East Antarctica experiences mainly semi-diurnal tides (Holdsworth, 1977). The tidal range varies in magnitude from 1-3m, with the largest values in the Filchner-Ronne ice shelf region. Larger tidal ranges than these occur in sub ice shelf cavities, especially near the grounding zone (Robertson *et al.*, 1998). Tidal magnitudes in East Antarctica are generally in the 1-2m range.

Tidal motion is the source of the largest short-term vertical motion an ice shelf experiences, and hence has a significant impact on ice shelves, particularly near the grounding zone, at the ice shelf front and in the shear margins. The tidal range at the hinge zone has a determining influence on whether glacier ice will succeed in becoming afloat without being detached from the continental ice (Holdsworth, 1977).

Tides have a significant impact on ice shelf crevassing, iceberg calving and ice shelf disintegration. For ice shelves with a thickness of 200-400m at the hinge line, tidal ranges greater than ~1-2m are likely to produce hinge line bending stresses that might trigger hinge line calving when the length of the ice shelf reaches ~1km. For ice shelves that are much thicker at their hinge-line, such as the AIS, the tides are only sufficient to produce relatively shallow surface tide cracks (Holdsworth, 1977). However, repeated straining in grounding zones caused by tidal motion can result in the development of ice fabrics, potentially influencing ice shelf flow (Vaughan, 1995).

The tides also have a significant impact on sub ice shelf cavities where they contribute to melting and marine ice accretion, and hence mass balance calculations. Water 'pumped' into the sub ice shelf cavity by the tides is brought into contact with the ice shelf base and hence melting and freezing can occur.

Doake (1978) suggested that a large proportion of the total tidal energy budget may be accounted for in ice shelf grounding zones. While this view is no longer held (Vaughan, 1995; Ray and Egbert, 1997), these regions are still of significant interest (Potter *et al.*, 1985).

Beyond this, understanding of tides provides important information for research on ocean currents and sea ice formation (Padman and Kottmeier, 2000). Bos *et al.* (2000) showed that current ocean models are not of sufficient precision to accurately determine the long-period ocean loading tides at the South Pole. Accurate ocean loading parameters, derived from tide models, are required for geodynamic, post-glacial rebound and water vapour studies (e.g., Dach and Dietrich, 2000; Tregoning *et al.*, 2000). GPS measurements of tides can contribute useful *in situ* data to numerical tide models, especially in the sub ice shelf regions where modelling is difficult and tide measurements are sparse.

Perhaps the most widespread use of information on tidal motion of ice shelves is for remote sensing measurements, such as Synthetic Aperture Radar (SAR) and altimetry. Since the tidal motion is time-dependent, and not in phase with the satellite orbits, systematic biases exist in the vertical component between satellite passes. With remote sensing providing height information with precisions at the tens-of-centimetre level, differential tidal motion is a significant contributor to the error budget of such experiments. In the wider terms of the Antarctic continent, accurate ocean tide models are vital if accurate ocean loading parameters are to be determined. Although the effects of ocean loading are greatest at the coast (Yi *et al.*, 2000), they are still significant at the South Pole (Agnew, 1995). Interestingly, modelled long-period ocean tides at the South Pole appear to be worse when ocean tide models consider sub ice shelf regions (Bos *et al.*, 2000). This may be caused by the poor performance of ocean tide models in these regions. Future satellite missions, such as the Ice, Cloud, and land Elevation

Satellite (ICESat), promise to improve resolution and measurement accuracy further, and so detailed understanding of the sub ice shelf tides is required.

This Chapter investigates the tidal motion of the AIS using GPS, following a brief review of current methods of determining ice shelf tidal motion. Since ice shelves are freely floating more than 9km from their grounding zone (Rignot *et al.*, 2000), a GPS station situated outside this area will act like a tide gauge. For the AIS region, the resulting heights can be compared with tidal predictions based on a harmonic analysis of data recorded at the nearby Beaver Lake. We estimate tidal constituents from the GPS data using both the harmonic and response methods. These constituents are then compared with recent ocean tide models, providing an assessment of the accuracy of these models.

4.1.2 Tides

4.1.2.1 Gravitational attraction

The periodic variation of the ocean surface, known as ocean tides, has its theoretical foundation in Newton's law of gravitation (Pugh, 1987):

$$F = G\frac{m_1 m_2}{r^2} \tag{4.1}$$

where F is the force generated, G is the universal gravitational constant[1], m_1 and m_2 are the masses of two particles and r is the distance between them. In the case of very large bodies, such as the Earth, Moon and Sun, the total gravitational attraction is the sum of a vast number of such particles. Fortunately, the total forces can be calculated by treating each body as a single point at its centre. For example, the net gravitational force between the Moon and the Earth is:

$$F = G\frac{m_e m_m}{R_1^2} \tag{4.2}$$

where R_1 is the distance between the two centres, m_e and m_m are the masses of the Earth and Moon respectively. The Sun and Moon are the only bodies to produce significant tidal variations of the ocean surface. The Moon has a greater influence than

1. $G=6.67\times10^{-11}Nm^2kg^{-2}$

the Sun, due to its proximity to the Earth being more significant than the Sun's great mass. The tidal variation due to the Sun is ≈0.46 of that caused by the Moon.

By considering the Earth-Moon relationship, the cause of the tidal motion is described as follows (Pugh, 1987). (The influence of the Sun can be determined similarly.) The Earth and Moon rotate around their joint centre of mass. Consider a particle of mass m located at P_1 in Figure 4-1 on the Earth's surface in such a system. From Equation (4.2) the force towards the Moon is:

$$G\frac{mm_m}{(R_1 - a)^2} \tag{4.3}$$

The force required for its rotation is the same as for a particle at O in Figure 4-1:

$$G\frac{mm_m}{R_1^2} \tag{4.4}$$

The difference between equations (4.3) and (4.4) is the tide producing force at P_1:

$$Gmm_m\left(\frac{1}{(R_1 - a)^2} - \frac{1}{R_1^2}\right) \tag{4.5}$$

By expanding and making some approximations, the net force toward the Moon at P_1 is:

$$F_{P_1} = \frac{2Gmm_m a}{R_1^3} \tag{4.6}$$

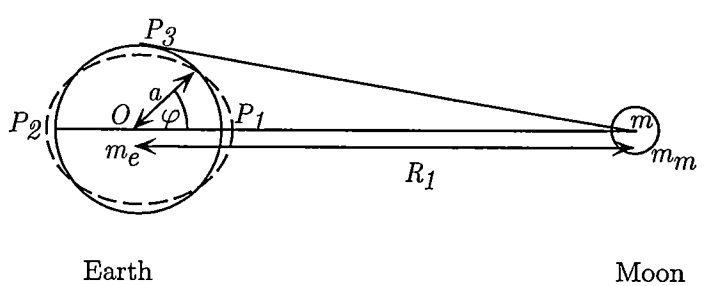

Figure 4-1: The Earth-Moon system used to derive the tidal forces (Pugh, 1987).

By similar calculations, the net force at P_2 is the negative of this term. That is, there is a net force away from the Moon. The net force at P_3 is directed toward the Earth's centre. Consequently, the net effect is for particles at P_1 and P_2 to be displaced away from the centre of the Earth, while a particle at P_3 moves toward the centre of the Earth. This point is further illustrated in Figure 4-2.

By considering the rotation of the Earth on its own axis, it can be seen from Figure 4-1 that each point on the surface of the Earth will have two maxima and two minima per day – the semidiurnal tides. The diurnal tides are generated since these maxima and minima are not equal in amplitude.

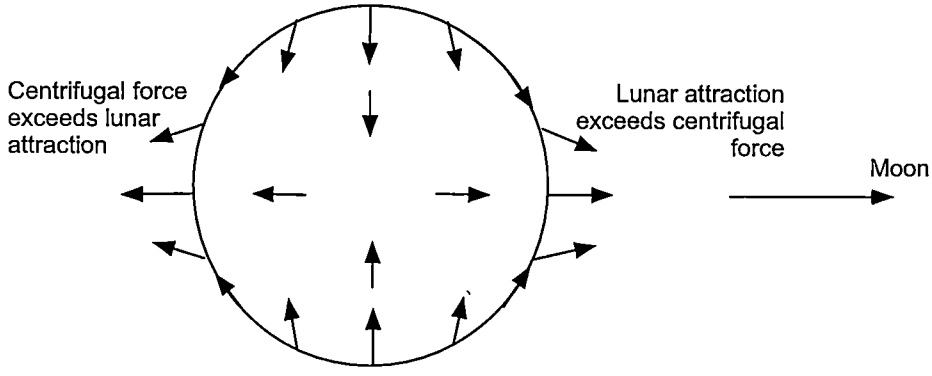

Figure 4-2: Net gravitational forces on different locations on the Earth.

4.1.2.2 The equilibrium tide

The equilibrium tide is defined as the elevation of the sea surface that would be in equilibrium with the tidal forces if the Earth were covered with water to such a depth that it responded instantly to the tidal forces. While not bearing any physical resemblance to the real observed tide, the equilibrium tide serves as an important reference system for tidal analysis. While the equilibrium tides are normally small when compared to the observed ocean tides, the observed tides have their energy at the same frequencies as the equilibrium tide. The equilibrium tide is important in tidal prediction since observed phases and amplitudes of harmonic tidal constituents can be related to it.

The equilibrium tide is defined for a point P as (Pugh, 1987):

$$\bar{\zeta} = a\left(\frac{m_m}{m_e}\right)\left(C_0(t)\left(\frac{3}{2}\sin^2\varphi_p - \frac{1}{2}\right) + C_1(t)\sin 2\varphi_p + C_2(t)\cos^2\varphi_p\right) \quad (4.7)$$

where the time dependant coefficients are:

$$C_0(t) = \left(\frac{a}{R_1}\right)^3 \left(\frac{3}{2}\sin^2 d_1 - \frac{1}{2}\right)$$
$$C_1(t) = \left(\frac{a}{R_1}\right)^3 \left(\frac{3}{4}\sin^2 2d_1 \cos C_p\right) \qquad (4.8)$$
$$C_2(t) = \left(\frac{a}{R_1}\right)^3 \left(\frac{3}{4}\cos^2 d_1 \cos 2C_p\right)$$

and a and R_1 are defined in Figure 4-1, φ_p is the latitude of point P, d_1 is the lunar declination and C_p is the hour angle of P. The equilibrium tide due to the Sun is expressed in a similar form to equation (4.7).

The three coefficients in (4.8) describe the three main 'species' of tides: the long-period species $C_0(t)$, the diurnal species $C_1(t)$ and the semidiurnal species $C_2(t)$. The long-period tidal species have maximum amplitude at the poles and zero amplitudes at 35°16′ north and south of the equator. The diurnal species has a maximum at 45° latitude and zero amplitude at the equator and poles. The semidiurnal species has maximum amplitude at the equator and zero amplitude at the poles (Pugh, 1987).

For further information on the background of tides, the reader is referred to Pugh (1987) and Cartwright (1993).

4.2 Tidal data and models

4.2.1 Methods of measuring tidal motion on ice shelves

The vertical motion of an ice shelf induced by tides has been measured in a variety of ways: levelling, tilt meters, gravity meters, bottom-mounted tide gauges, Electronic Distance Measurement (EDM), GPS and recently Interferometric Synthetic Aperture Radar (InSAR) have all been used with varying degrees of success (e.g., Stephenson *et al.*, 1979; MacAyeal, 1984; Pedley *et al.*, 1986; Doake, 1992; Bondesan *et al.*, 1994; Vaughan, 1995; Aoki *et al.*, 2000; Rignot *et al.*, 2000). Typical measurement precisions, spatial resolutions and restrictions are shown in Table 4-1.

Method	Precision (mm)	Spatial Resolution	Maximum distance from grounded ice or rock	Other restrictions
Tilt meters	~10-50	Point	N/A	Difficult to monument; most useful in grounding zone
Gravity meters	~10-50	Point	N/A	Need water salinity measurements
Bottom-mounted Tide gauges	~5-10	Point	N/A	Difficult to install and download in ice shelf regions; Need salinity/temperature measurements
Levelling	~5-15	Point	~1Km	Line-of-sight
EDM	~5-200	Point	~40Km	Line-of-sight
GPS	~10-50	Point	N/A	Reliance on batteries as power source
InSAR	~5-100	Large areas	N/A	Current satellite orbital periods are in phase with semi-diurnal tides; Calibration required

Table 4-1 : Details and restrictions of ice shelf tidal motion measurements.

Each method has certain limitations. While levelling, tilt meters, gravity meters and bottom-mounted tide gauges only provide measurements of vertical movement, EDM, GPS and InSAR also provide the potential for measuring horizontal motion. Both levelling and EDM rely on measurement areas being close to non-tidal regions (so as to establish a datum) and good visibility, a restriction that limits the effectiveness of these methods on large Antarctic ice shelves, such as the AIS. Tilt meters work well in ice shelf grounding zones, where tilt is larger, but are less effective further afield (Doake, 1992). Solid monumentation of the tilt meter in the ice is the main difficulty of this technique. Gravity meters provide measurements of the gravity changes as water moves under the ice shelf. They have been shown to work effectively, with results agreeing well with independent tide models (Thiel *et al.*, 1960). Bottom-mounted tide gauges have been used successfully on the George VI ice shelf (Pedley *et al.*, 1986), although they are both difficult and expensive to install and retrieve, making them impractical in many situations.

The InSAR technique has been used to accurately identify the grounding zone of large regions of ice shelves, and more recently to identify constituents of tidal motion. This method is presently somewhat limited since the orbital periods of the current

generation of satellites capable of high latitude measurements (namely ERS1/2) are in phase with semi-diurnal tidal motion. Consequently, long periods are required to resolve the majority of constituents as seen in Table 4-2 (Rignot *et al.*, 2000). There may be several months between satellite passes, and since basal melt/freeze or surface melt/accumulation/ablation will cause an ice shelf to adjust vertically, potential systematic errors exist if these parameters are not known. Furthermore, the phase coherency between SAR images decreases with time. Future SAR satellites may have lower orbital periods and hence not face this limitation, although such orbits would results in decreased spatial coverage.

Constituent	M_2	S_2	N_2	K_1	O_1	P_1
Alias Period (days)	94.49	∞	97.39	365.25	75.05	365.25

Table 4-2: Alias periods for the 35-day repeat orbit of the ERS satellites (Chelton *et al.*, 2001).

GPS data have been used to detect and determine ice shelf grounding zone locations using kinematic and stop-and-go processing. These data have also been used for vertical measurements of ice motion away from grounding zones using both kinematic and static processing techniques. In our experience, kinematic data processing is problematic over baselines longer than 20km in Antarctica especially in the AIS region. This is normally due to a combination of a high numbers of cycle slips and low data rates in the data we have. Processing GPS data on an ice shelf using a static methodology also poses difficulties, as discussed in Section 4.2.3.

4.2.2 Tidal models

Tidal information in the region of Antarctic ice shelves may also be obtained from ocean tide models (e.g., Egbert *et al.*, 1994; Le Provost *et al.*, 1994; Robertson *et al.*, 1998; Padman *et al.*, 2001). The advantage of these models is that they are spatially dense, providing coverage of an ice shelf while not having the current technical limitation of InSAR. These models may be computed for the entire globe (Shum *et al.*, 1997) or for a particular region and are often computed at a higher grid resolution using more regional data. Their current disadvantage is a lack of data in the Antarctic region. For example, most models rely heavily on assimilated TOPEX/POSEIDON data which has a southern limit of 66°S, well to the north of all but a few of Antarctica's ice shelves. Furthermore, these models are particularly sensitive to the

input bathymetry, which is often poorly known in Antarctica and especially in the sub ice shelf regions. Energy losses through ice shelf friction are also largely unknown and hence estimates are required. Consequently, the accuracy of the models often rest on spatially sparse tide gauge measurements.

4.2.2.1 Global

Prior to the advent of the TOPEX/POSEIDON system in 1994, the classic global ocean tide model was that of (Schwiderski, 1980a; 1980b; 1983). This model was calculated using an integration of data from more than 2000 global tide gauges into the hydrodynamic model (Schwiderski, 1980b) and was considered to be accurate at the 70-80mm level in the open ocean. Cartwright and Ray (1990) were amongst the first to use altimeter data to determine tidal constituents using the Geosat Exact Repeat Mission. For the first time, a large spatial density of tidal measurements could be made away from the coast. Cartwright and Ray (1990) compared the model with 66 ground-truth locations and the results suggested that the values obtained were of a similar precision to that of (Schwiderski, 1980c) although differences of 100-150mm were found in some areas.

The large spatial and temporal density of the TOPEX/POSEIDON altimeter along with advances in numerical techniques, allowed the production of a series of global tide models – more than twenty since 1994 (Shum *et al.*, 1997). These models are comparable at the 20-30mm level in the deep ocean (Andersen *et al.*, 1995; Shum *et al.*, 1997). Examples of such global models are the TPXO (Egbert *et al.*, 1994) and FES (Le Provost *et al.*, 1994) models. These models do differ significantly, however, in continental shelf regions. This is due mainly to a poor understanding of tidal energy dissipation and lack of bathymetric data. Antarctica is even worse off, in this case. It is common for bathymetric data to be non-existent in ice shelf regions. For example, Le Provost *et al.* (1995) and Lefevre *et al.* (2000) were forced to use an estimate of the water column thickness under the AIS, introducing significant error into their model for this region. Additionally, the tidal energy dissipation through ice shelves is poorly understood.

4.2.2.2 Regional

Since global models often do not contain the coastal data required for the production of accurate models in these regions, regional models are often computed. Since these models do not need to include the vast amounts of data required for a global model, they can focus on incorporating more precise and spatially dense regional data where available. Robertson *et al.* (1998) produced such a regional model for the Weddell Sea, West Antarctica, including the ocean cavity under the Filchner-Ronne Ice Shelf. Most of the modern tide models have TOPEX/POSEIDON altimeter data assimilated into them, although no such data exists south of 66°S. An alternative method is to use global models to provide the boundary conditions for the model. Consequently, they rely heavily on *in situ* data such as that obtained from tide gauges. Unfortunately, such data is often sparsely distributed, particularly away from the densely populated Antarctic Peninsula (see Lutjeharms and Stavropoulos, 1985). Also, current models do not incorporate the new definition of the AIS grounding zone, and so are in error in our study region.

In an attempt to produce a high quality ocean model for the Antarctic region, Padman *et al.* (2001) have produced a high resolution (1/4° x 1/12°) regional model known as the Circum-Antarctic Data Assimilation Model (CADA). This model covers the region south of 58°S and includes the sub ice shelf cavities. The model assimilates Antarctic tide gauge, bottom pressure, gravity and static GPS ice shelf data into a finite element model. The inclusion of these additional data results in a significant improvement of the CADA model compared with previous models that lack the additional information.

4.2.3 Tidal measurements using GPS

While regional tide models are making advances in terms of accuracy, there still may be significant departures between modelled values and those measured by GPS or other methods (Riedel *et al.*, 1999). Consequently, GPS is currently the most convenient and precise method available for the measurement of sub ice shelf tidal signals on a point-by-point basis. As discussed in Chapter 2, however, the collection of GPS data in Antarctic is affected by environmental and logistical factors.

These problems are compounded when it comes to the processing of the GPS observations. In particular, significant problems are encountered when attempting to

process GPS data collected on fast moving, floating ice shelves, since this situation does not conform to a typical static processing scenario. On the AIS, GPS receivers may experience movement of up to 150mm in horizontal and 300mm in vertical position in just one hour of observations.

To date, the typical method of handling this problem has been to collect GPS data in kinematic mode, and to process these data relative to nearby stationary base station(s). For example, Vaughan (1995) has used kinematic GPS to measure tidal flexing around the Rutford Ice Stream grounding zone, while Capra *et al.* (1999) and Vittuari (1994) have used kinematic GPS to measure the motion of floating glacier tongues. Capra *et al.* (1999) report agreements between heights from kinematic GPS observations and a local tidal model at the 50-70mm level over 5-100km baselines. However the presence of high frequency noise in the GPS data, caused largely by the rapid variation of the ionosphere, meant that they needed to smooth their 15 second data over 15 minute intervals.

The repeat period of the GPS constellation (23.93hrs) is essentially the same as the period of the K1 luni-solar diurnal tide. Consequently, any satellite constellation related influences, such as low numbers of satellites or multipath, will either weaken or bias the solution and hence the estimate of this constituent.

4.3 Amery Ice Shelf tidal motion

For the AIS work, processing GPS data in kinematic mode is not appropriate for several reasons. Firstly, using kinematic processing techniques destroys the benefits inherent in static observations; that is, increased precision by using longer occupation times. Additionally, much of our data appears to be affected by a higher number of cycle slips than that reported by Capra *et al.* (1997). Baseline lengths between ice and stable rock sites, which are mostly greater than 50km and typically 100-500km, further amplify these issues.

4.3.1 Present understanding of Amery Ice Shelf tides

Our present understanding of the sub-AIS ocean circulation and tides is somewhat limited, illustrated by the fact that it was only recently that the commonly-held grounding zone definition was discovered to be incorrect by approximately 200km

(Fricker *et al.*, 2001a)! Despite this, important information is known about the movement of water underneath the AIS as described in the following sections.

4.3.1.1 Salinity/density/temperature measurements

By studying the salinity/density/temperature of the water in Prydz Bay, to the north of the AIS, (Wong *et al.*, 1998) has shown that there exists a net production of melt water under the AIS of 11-22Gtyr^{-1}. This is evidenced by the presence of much cooler and fresher water exiting the AIS cavity on the north-western corner compared with the temperature of the water entering on the north-eastern corner. Preliminary results from a more recent, detailed oceanographic cruise along the front of the AIS show that the mean circulation is as shown in Figure 4-3 (personal communication, N. Bindoff, 2001). Mean currents are about 10mm/s (personal communication, J. Hunter, 2001). No data is available south of the ice shelf front, and so little is known about the actual ocean circulation in this region.

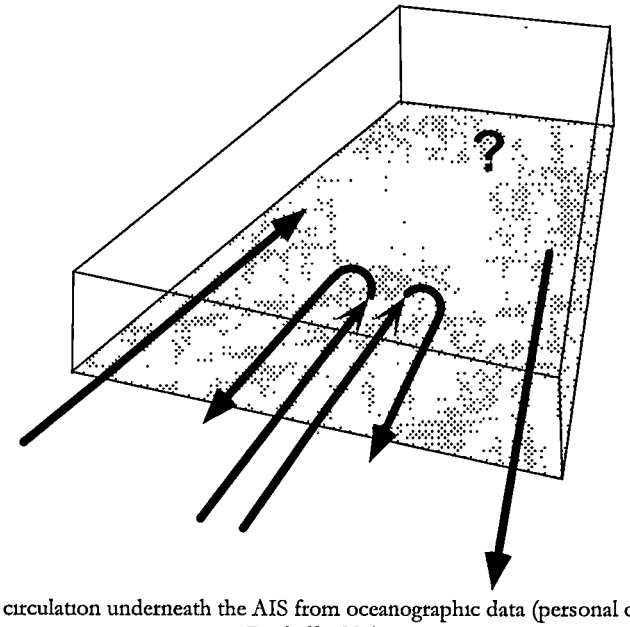

Figure 4-3: Ocean circulation underneath the AIS from oceanographic data (personal communication, N. Bindoff, 2001).

4.3.1.2 AIS ocean circulation model

The understanding of the ocean water circulation under the AIS was further advanced by Williams *et al.* (1998) when they produced a three-dimensional ocean model for the cavity under the AIS. This model suggests basal freezing/melting levels are in the range of $\pm 1 ma^{-1}$. The largest area of freezing was shown to be in the north-western corner of the ice shelf. The majority of the melting occurs around the perimeter of the ice shelf,

particularly the southern end of the ice shelf (although the old grounding zone definition was in use at the time of the study). These freezing and melting regions correspond to the areas where the ice shelf is thinnest and thickest, respectively. Ocean circulation was found generally vertically coherent throughout the water column, although where inflow occurred it was stronger near the seabed, while where outflow occurred it was stronger near the ice shelf base.

4.3.1.3 Hydrostatic anomaly

The hydrostatic assumption was used by Phillips (1999) to assess the areas of the ice shelf that were subject to melt/freeze. Since a floating ice shelf is in hydrostatic equilibrium, the relationship between the orthometric surface height (H) and ice thickness (Z) is known, i.e.:

$$H = \frac{Z(\rho_w - \rho_i)}{\rho_w} \tag{4.9}$$

where ρ_w and ρ_i are the column-averaged densities of the sea-water and the ice respectively. Equation (4.9) can be used to define a hydrostatic height anomaly term, given by:

$$\Delta h' = \overline{H} - \frac{Z(\rho_w - \rho_i)}{\rho_w} \tag{4.10}$$

where $\overline{H}$ is the measured height. $\Delta h'$ can be used to define the extent of the floating ice over an ice mass, if the surface height, ice thickness and densities are known.

Using ERS altimeter measurements Phillips (1999) produced a Digital Elevation Model (DEM) of the AIS. By applying geoid-ellipsoid separation values from the EGM96 geopotential model (Lemoine *et al.*, 1996), $\overline{H}$ was produced. Since the ice thickness data does not include the marine ice layer[2], a positive hydrostatic anomaly is largely due to the presence of marine ice. An estimate of the thickness of marine ice on the base of the AIS has been obtained (Fricker *et al.*, 2001b) and reveals significant freezing of seawater in the north-west corner of the AIS. Up to 190m of marine ice exists in the north-western corner of the AIS. The spatial pattern of marine ice distribution agrees

2. The Radar measurements at the frequency used in the RES instrument do not penetrate the marine ice layer.

with that of Williams *et al.* (1998), and its presence is consistent with the circulation of water under the AIS. It is thought that water is super-cooled at depth as it travels along the eastern side of the AIS (see Figure 4-3). As it travels north, it then rises with the sea floor until the point where its freezing point becomes less than its physical temperature, when it freezes onto the base of the AIS.

4.3.1.4 Tide gauge measurements

Little work has been done to understand the tidal motion of the AIS. Tide gauge observations made at Beaver Lake in 1991 and 1998 represent the closest tide gauge observations to the Amery Ice Shelf. The next nearest records are for stations Davis and Mawson, several hundred kilometres away. The Beaver Lake measurements were taken using a bottom-mounted pressure gauge. Two different locations were used for the two campaigns, with a distance between them of less than one kilometre. There is no precise link between the two tide gauge zeros, although timed-water level measurements were conducted during each campaign and related to separate benchmarks.

Details of the observations are shown in Table 4-3. Two independent tidal models have been computed from these data sets, known as Beaver Lake Tide Model 1991 (BLTM91) and BLTM98 (Nielsen, 1999). No attempt has been made to relate these models to the same height datum, and so there is a bias between the two models (see Z_0 in Table 4-3). The difference equates to 0.690m. Since for our data we only require relative differences, and we use only the BLTM98 (due to the longer time series), this does not affect us.

Year	Dates of Observations	Days Observed	No. of Constituents	Std. Dev. of Residuals (m)	Z_0 (m)
1990-91	26/12/90-18/01/91	23	41	0.027	0.446
1998	1/1/98-9/2/98	39	40	0.053	1.136

Table 4-3: Details of pressure gauge operation at Beaver Lake.

It is known from Phillips *et al.* (1998) that the BLTM91 agrees well with the vertical component of GPS data collected on the AIS at approximately the same latitude as Beaver Lake. The BLTM91 was used to remove the AIS tidal signal from their altimeter-derived DEM. The RMS of the difference between two predictions for

January 1999 using each of BLTM91 and BLTM98 is 58mm. Table 4-4 shows the four major constituents for both models. The BLTM98 model is consistently 8-15mm lower in amplitude and slightly lower in the phase values. This difference may most likely be explained by the shorter duration of observations used to determine the BLTM91 constituents.

Constituents Model	O1 (m, °)	K1 (m, °)	M2 (m, °)	S2 (m, °)
BLTM91	0.297, 288.6	0.285, 295.4	0.249, 252.3	0.262, 357.6
BLTM98	0.287, 285.8	0.277, 294.7	0.240, 250.7	0.247, 354.2

Table 4-4: The major constituents for BLTM91 and BLTM98.

4.3.1.5 Regional/ice shelf ocean tide models

A further level of understanding of the currents and tides under the AIS comes from ocean models. In this regard, the CADA model (Padman *et al.*, 2001) currently offers the most detailed modelling of the Antarctic region. Four diurnal (O_1, K_1, P_1, Q_1), four semi-diurnal (M_2, S_2, K_2, N_2) and two long-period (Mm, Mf) constituents are modelled. Particular attention has been paid to the AIS region, with tide gauge data from Davis, Mawson and Beaver Lake assimilated into the model. Later versions of the model also incorporate results from ice shelf GPS tidal measurements of the AIS as presented in this thesis (Padman *et al.*, 2001). The CADA model is based on the CATS forward model (Padman *et al.*, 2001) which is driven by the TPXO model (Egbert *et al.*, 1994) at the northern boundary of the model and the astronomical tide-generating potential within the model domain.

The CADA model shows firstly that the tides in the region of the AIS are mixed diurnal/semi-diurnal. The tidal range is normally in the range of 1-2m. Tidal currents are typically <50mm/s. Furthermore, it shows an increase in phase from east to west for the major constituents (Figure 4-4). The phase of the M2 constituent in this region is significantly affected by the location of a tidal node (no amplitude) to the west of Mawson. Amplitudes along the AIS increase from north to south, by approximately 150mm for the semi-diurnal and 50-100mm for the diurnal constituents.

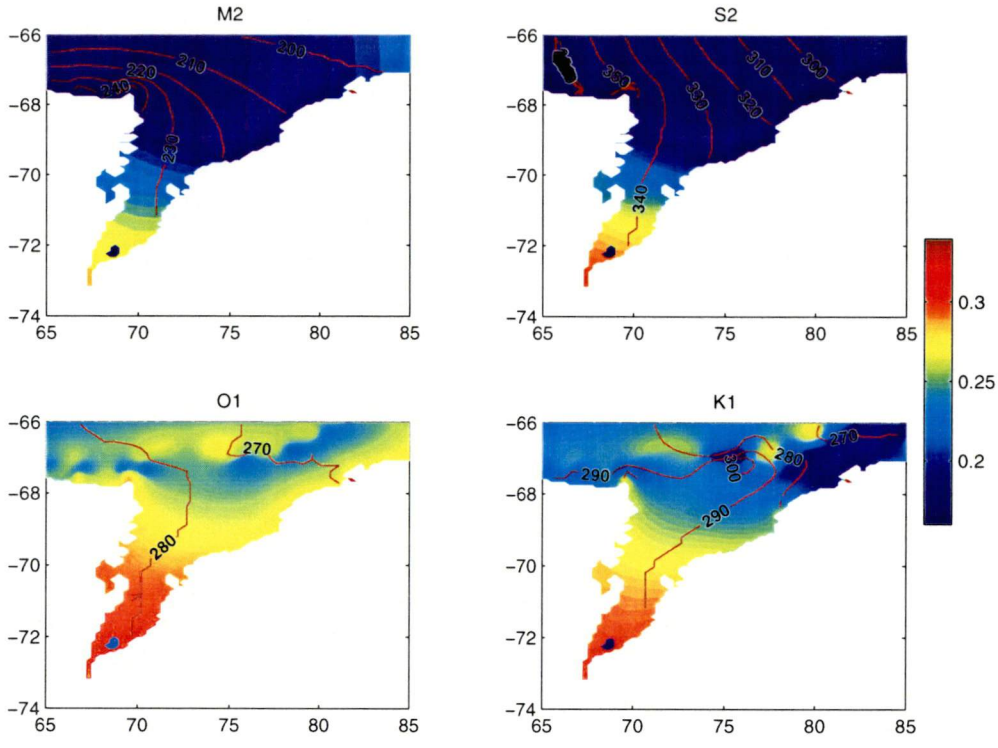

Figure 4-4: The amplitude and phase of the four major constituents in the AIS region, derived from the CADA00.10 model described in Section 4.3.8.2. Contours are the phase lags from Greenwich in degrees, while the amplitudes are in metres.

4.3.2 Available GPS data

GPS data has been collected on the AIS since the late 1980s, although it is only since 1995 that data has been of sufficient quality and duration to be used in tidal analysis. Sites where data exists with a duration of 24 hours or greater are listed in Table 4-5 and their locations are shown in Figure 4-5. The data are not continuous since a number of gaps exist within the data sets (mainly due to battery problems). Consequently, the number of hours shown in Table 4-5 refer to the total number of hours of useful data, rather than the length of the observation span. In general, the duration of observations has increased from 1-2 days in 1995, to 4-5 days in 1997-98, 13 days for CAMP in 1998-99 and 31 days for HWDT in 1999-2000. During the 2000-01 season 6-10 weeks of data were collected at six sites, but these data are not included in the current study.

GPS sites G1 and G2 are not measurements at the same G1 and G2 poles observed in the terrestrial surveys mentioned in Chapter 3. Accumulation in the region of G1 and G2 is ~0.5-1.5m of snow per annum, so the 1968-70 poles would now be ~9-40m

below the present snow surface. These sites are only approximately relocated at the geographic coordinates (epoch 1969.0) of the terrestrial sites.

Site	Year	Site Location		Data Span (hrs)	IGS[3] Receiver Code	IGS Antenna Code	Mount Type	Atm. Press.
		Lat. (°)	Long. (°)					
G1	1999	-69.50129	71.72224	20	LC9500	LC202G	Pole	Daily
HWDT	2000	-69.71359	73.58440	617	LC_CRS	LC_504	Tripod	Daily
G2	1999	-70.16912	70.86381	44	LC9500	LC202G	Pole	Daily
C12	1995	-70.47726	70.38851	27	LC299E	LC202G	Tripod	None
C10	1995	-70.64386	70.20278	29	LC299E	LC202G	Tripod	None
C8	1995	-70.81415	70.01086	23	LC299E	LC202G	Tripod	None
CAMP	1999	-70.89179	69.87335	253	ASHZ12	ASHDMG	Pole	Daily
C6	1995	-70.98117	69.82644	24	LC299E	LC202G	Tripod	None
C4	1995	-71.14900	69.63137	39	LC299E	LC202G	Tripod	None
C2	1995	-71.31602	69.43473	27	LC299E	LC202G	Tripod	None
V3	1998	-72.60915	67.56807	83	LC9500	LC202G	Pole	None
V5	1998	-72.97624	67.48241	91	LC9500	LC202G	Pole	None

Table 4-5. AIS tidal GPS sites where data exists for approximately 24 hours or greater. Sites are listed in order of latitude, north to south. Hours are the number of hourly solutions obtained from the data set (i.e., data are not necessarily continuous).

The Leica SR299 (LC299E) receiver used during 1995 was a squaring-type receiver, and hence the data is not as good quality as the data from the other seasons where full wavelength receivers were used. In the 1997-98 and 1998-1999 seasons, the antenna was mounted on aluminium or fibreglass poles drilled into the snow to a depth of approximately one metre. It is thought that the poles would be substantially more stable than a tripod. Pressure values, required to correct for the inverse barometer effect (see Section 4.3.5.1), are only available for sites observed in the later two seasons. Unfortunately, these pressure measurements were only taken once per day.

3. International GPS Service. (Beutler and Kouba, 1998).

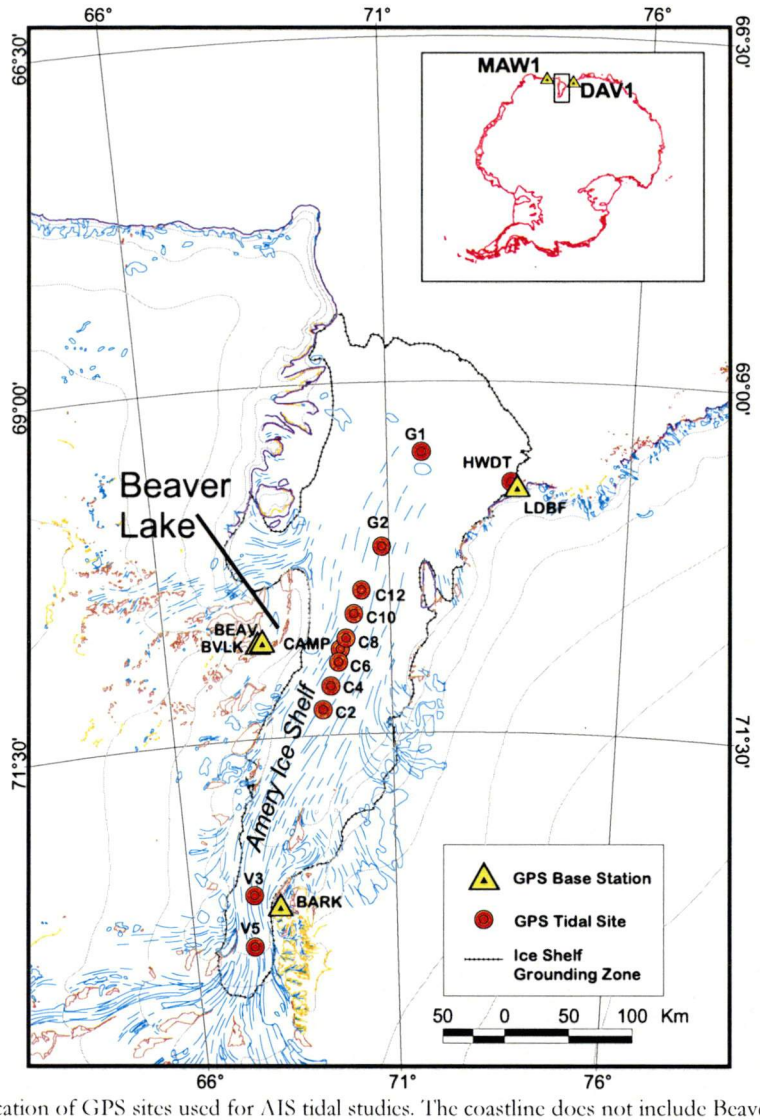

Figure 4-5: Location of GPS sites used for AIS tidal studies. The coastline does not include Beaver Lake since its definition is currently uncertain.

4.3.3 GPS Processing details

When processing GPS data, only two broad processing methodologies exist; data may be processed using either a static or a kinematic technique. Since, as has been mentioned earlier, high numbers of cycle slips caused by ionospheric disturbance and long baselines adversely affect much of our data, a kinematic approach is not entirely suitable. Additionally, since the ice shelf is moving significant distances over short time periods, the data do not conform to a standard static scenario either.

Instead we process our data using a static processing methodology by firstly choosing a data segment length of one hour rather than the usual twenty-four hour period (King *et al.*, 2000). These files are then processed independently in the solution. Naturally,

horizontal positions (and hence velocity) are also determined at the same time as the vertical motion. A similar method has previously been adopted by Bondesan *et al.* (1994) who used data collected during 30-minute sessions every two hours to measure the tidal motion of a small ice shelf in Antarctica. Their result, over generally shorter baseline lengths than those present in our AIS data, agreed at the few centimetre level with a local tide model. Phillips *et al.* (1997) and Phillips *et al.* (1998) used a two-hour segmentation interval to process data on the AIS (at sites C2, C4, C6, C8, C10 and C12, see Figure 4-5) using a similar network to what we use. Their results compared well (within 10 to 50mm) to the independent BLTM91 tide model, after a mean bias removal (i.e., datum issues).

The choice of segmentation interval is a balance between two opposing requirements. On the one hand, there is a requirement for enough data to provide a precise solution, given the baseline length and accounting for any other environmental influences. While on the other hand, the data segment needs to be short enough so as to prevent the solution from being adversely affected by too much tidal or horizontal motion.

The level of vertical motion observed during a certain period depends on the specific tidal cycle at the time of the GPS observations. If observations are made at a time in the tidal cycle where tidal constituents tend to cancel, then little motion will occur. In this case, the horizontal motion will be much larger than the vertical motion, even over a short period. Conversely, if the GPS observations are made during a rapid rate of change in the tide, the vertical motion will be significant even over quite short time periods. Table 4-6 highlights the varying vertical tidal motion that may occur over a two-hour period at Beaver Lake during January 1999 estimated by the BLTM98. Two-hourly height changes may be as little as 5mm, and as great as 726mm. One-hourly height changes are approximately half the values displayed in Table 4-6. In regard to the GPS processing of data containing such motions, we assumed that the motion predominantly ends up in the residuals, although some may contaminate the tropospheric zenith delay or horizontal coordinate estimates.

	Height change in any two hour period (m)
Min	0.010
Max	0.724
Median	0.219
Mean	0.244
Standard Deviation	0.153

Table 4-6: Predictions of vertical movement of the water height at Beaver Lake during any two-hour period in January 1999. Predictions are based on the BLTM98 constituents.

In order to investigate the effect of averaging GPS data over a one hour period, we performed a simulation using a section of the BLTM98 predicted for January 1999 as shown in Figure 4-6. Also shown are values obtained by applying a one hour moving average (no overlap) along the BLTM98 time series. In general, the one hour average is representative of the actual curve, although at the nodes there is some variation. However, the variation is less than 5mm and cannot be seen at the scale of the figure (see also Capra *et al.*, 1997). This variation will always be in the form of an underestimation of the true tidal range. Figure 4-6 highlights that any one point can not be assumed to be located at a node (maxima in this case), and hence exactly represent the extremes of the tidal cycle. In the case of the node near day 26.6, the nearest data point has amplitude of 20-30mm less than actually occurs. Despite these small variations, we can have confidence that the segmentation of the GPS data into batches of one hour will result in height coordinates that accurately represent the actual motion of the ice shelf. A maximum error of only a few millimetres in the GPS heights will occur, with the GPS heights underestimating the true tidal range.

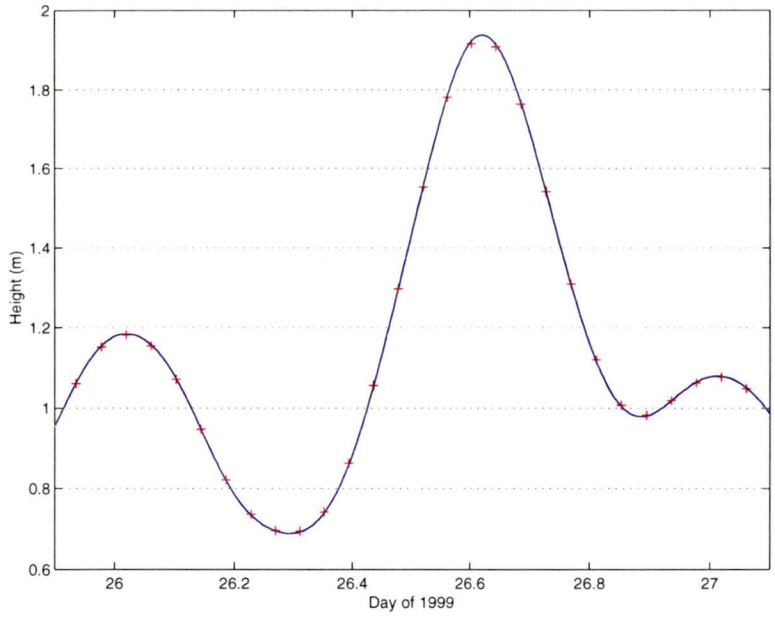

Figure 4-6: The effect of averaging over one hour intervals. The blue line is a prediction from the BLTM98, while the red crosses are centered one hour averages of the BLTM98.

For our processing, we choose a one-hour processing interval, since this presents a good compromise between precision from longer segments and increased noise from tidal motion. Other than segmenting the data files, data are processed using standard processing options. Using GAMIT software (King and Bock, 1999), we processed the tidal data in a regional network consisting of 3-5 continuous rock sites (see Figure 4-5, Table 4-7 and Table 4-8 for site locations, details and availability). Details of the ice shelf receivers have been discussed in Chapter 3. IGS precise satellite ephemerides were fixed. The two sites located near Beaver Lake, BEAV and BVLK are located approximately 2km apart. The BVLK site was established during 1997-98 and has been operated permanently for geophysical studies during the summer periods since that time (Tregoning *et al.*, 2000). BEAV was established during 1995-96 and has been operated intermittently for glaciological studies since that time. A satellite elevation cut-off angle of 15° was adopted. Thirteen tropospheric parameters are estimated per-site per-day (i.e., one parameter every two hours at every site). Solid-Earth tides are modelled using standard models. Antenna phase centre models are applied to correct for zenith dependent phase centre variations between antennas.

Site	Location	Lat.	Long.	Receiver Details	Antenna Details
DAV1	Davis Station	-68.57732	77.97261	Turbo Rogue 8100	Dorne Margolin Choke Ring
MAW1	Mawson Station	-67.60476	62.87071	Turbo Rogue 8100	Dorne Margolin Choke Ring
BEAV	Beaver Lake	-70.80308	68.17917	Leica 299	Leica AT202 with Groundplane
BVLK	Beaver/Radok Lake	-70.81396	68.07451	Ashtech Z12	Ashtech Choke Ring
BARK	Barkell Platform	-72.69064	68.18577	Leice SR9500	Leica AT202 with Groundplane
LDBF	Landing Bluff	-69.74229	73.71038	Ashtech UZ12	Ashtech Choke Ring

Table 4-7: Regional GPS base station information at the time of measurement. There have been a number of changes of receiver at the permanent DAV1 and MAW1 sites over the timeframe dealt with here. The receiver types shown for DAV1 and MAW1 are representative only. The BEAV site had an ASHZ12/ASHDMG combination in 1999.

Base Year	DAV1	MAW1	BEAV	BVLK	BARK	LDBF
1995	✔	✔	✔			
1998	✔	✔		✔*	✔	
1999	✔	✔	✔*	✔		
2000	✔	✔		✔		✔*

Table 4-8: Availability of regional GPS base station data for the AIS tidal measurements. An asterix denotes that the site was available for only part of the observation period.

4.3.4 Inter-site comparison

Figures 4-7 through 4-10 show the measured tidal heights of each of the sites listed in Table 4-5 and shown in Figure 4-5. Raw *in situ* measurements of instantaneous sea level are contaminated by regional atmospheric and oceanic effects, such as wind, atmospheric pressure or salinity and temperature variations. For the GPS data shown in these figures, no corrections for atmospheric effects, such as the inverse barometer effect (IBE) have been made. The IBE is discussed in a later section of this Chapter. For the other effects, such as those caused by swell, the ice shelf acts as a low pass filter, largely removing the impacts of high frequency variations. The segmentation technique will further average out these effects. The GPS heights are plotted against predicted data for nearby Beaver Lake from the BLTM98. Since the 1998 pressure

gauge data set at Beaver Lake is significantly longer than the 1991 data set, we use the BLTM98 in this thesis.

GPS height error bars shown in this chapter are for relative comparison only and are not meant as an absolute measure of the precision of the estimate. They are the GAMIT formal errors based on an arbitrary carrier phase precision of 10mm.

The GPS data for 1995 has been processed in one hour segments and is shown in blue in Figure 4-7. These data have previously been processed by Phillips *et al.* (1998), but with approximately two hour data windows – the two hourly results are shown in red. The differences between the two GPS results are due to the choice of segment length. Phillips *et al.* (1998) chose to split the data only approximately, rather than exactly, every two hours in an attempt to maximise the continuous observations of particular satellites. The longer segmentation length gave smaller formal errors; however the one hour solutions still maintained a similar level of agreement with the BLTM98.

Since the data span for the 1995 GPS campaign is only 1-3 days at each of the sites, there are many breaks in the measurements, and the tidal range for sites C4 and C6 is small, these data are not ideal for tidal studies. However, they do provide some valuable information with the sites other than C4 and C6 revealing a shift in phase between the BLTM98 and the GPS data of about one hour (with the ice shelf leading). While this phase shift is apparent at these sites, it is not obvious if the phase change is uniform across the sites, or varies from site to site, as may be expected.

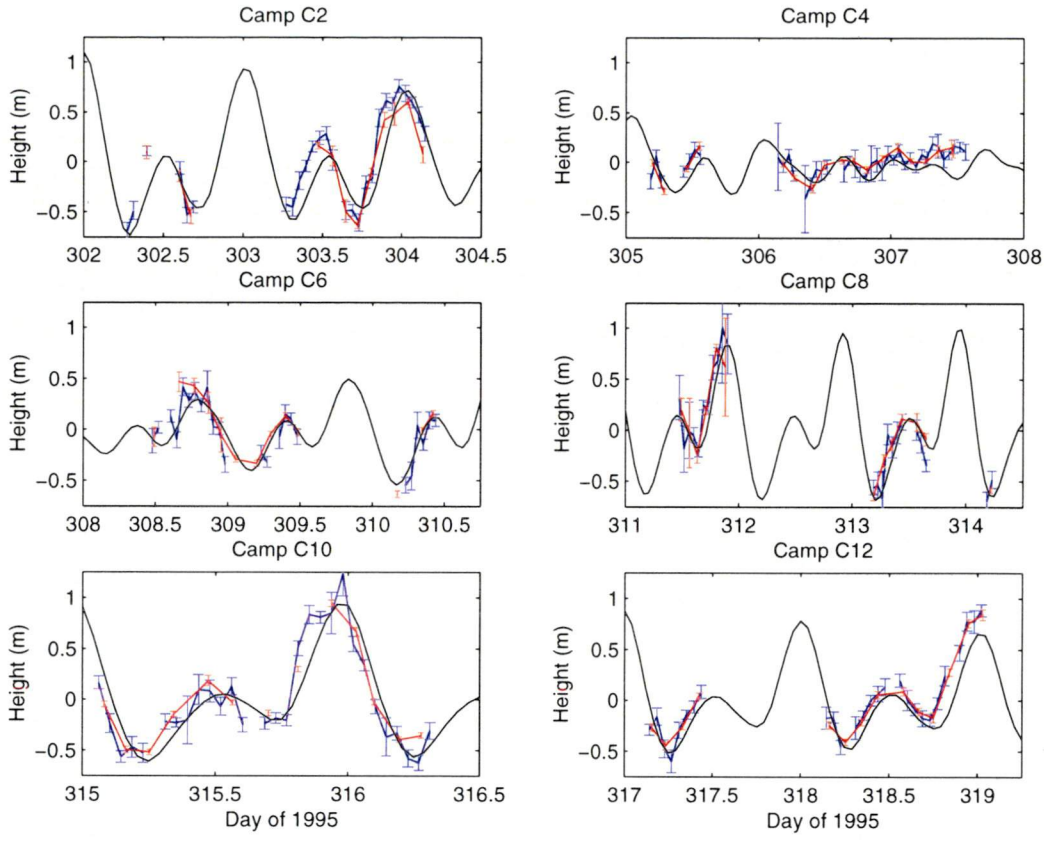

Figure 4-7: Tidal motion as recorded by GPS at sites measured in 1995, splitting files approximately every two hours (red) and exactly one hour (blue). Error bars are a only a relative measure of the precision of the GPS estimates. The solid line is the BLTM98. A mean height has been removed from each of the data sets.

Figure 4-8 shows results from processing GPS data collected in 1998 at sites V3 and V5 located at the southern end of the AIS. The tidal signal at the time of measurement is dominated by a diurnal cycle. Again very good agreement exists between the GPS heights and the BLTM98. As is the case for the 1995 data, a phase shift exists between the measured heights and the tide model for Beaver Lake. The value of the phase shift is again approximately one hour. No differential shift in phase between the sites is obvious from the figure. Furthermore, the GPS heights appear to suggest higher amplitude at these sites than the model values. This is despite the expectation that the GPS segmentation scheme results in GPS heights that have slightly lower amplitude than actually occurs because of the 'averaging' effect of the hourly solutions. There is approximately 100mm difference between the amplitude of V3 and V5 and the BLTM98. Such a large amplitude difference is not apparent in the 1995 data. A similar amplitude increase occurs near the grounding zone of the Filchner-Ronne Ice Shelf and Larsen Ice Shelves (Robertson *et al.*, 1998).

These sites confirm that the AIS is indeed floating at approximately 72.98° (Fricker *et al.*, 2001a), approximately 230km further south than the commonly-held definition (Budd *et al.*, 1982), and in line with the location proposed by (Robin, 1979).

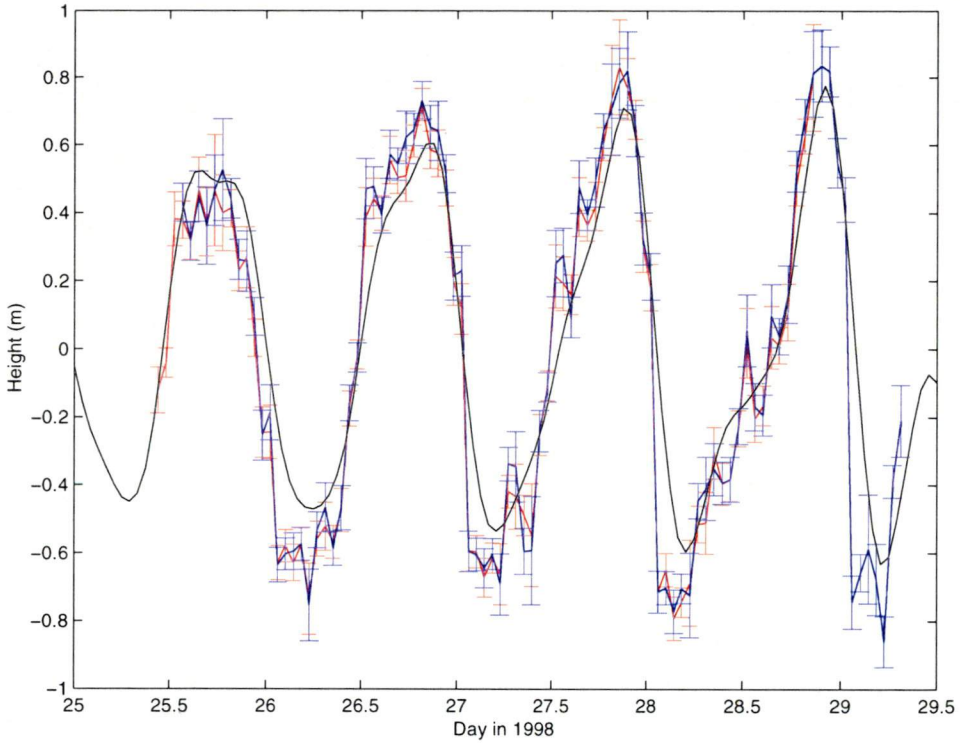

Figure 4-8: Tidal motion as recorded by GPS at V3 (red) and V5 (blue) in 1998. Error bars are a only a relative measure of the precision of the GPS estimates. The solid line is the BLTM98. A mean height has been removed from the data sets.

Results from the analysis of the GPS data collected at sites G1, G2 and CAMP in January-February 1999 are shown in Figure 4-9. Some breaks occur in the CAMP data due to battery failure. Again, the phase shift is evident at all sites when compared to the BLTM98. The phase differences are approximately one hour with the ice shelf sites leading the BLTM98. No significant amplitude difference is evident at either G1 or G2, although these are short data sets. As with the southern sites of V3 and V5, an amplitude difference of approximately 100mm is evident in the CAMP data when compared with the BLTM98. No such amplitude difference is evident at the nearby C6 site (Figure 4-7), but this may be due to the shorter time series.

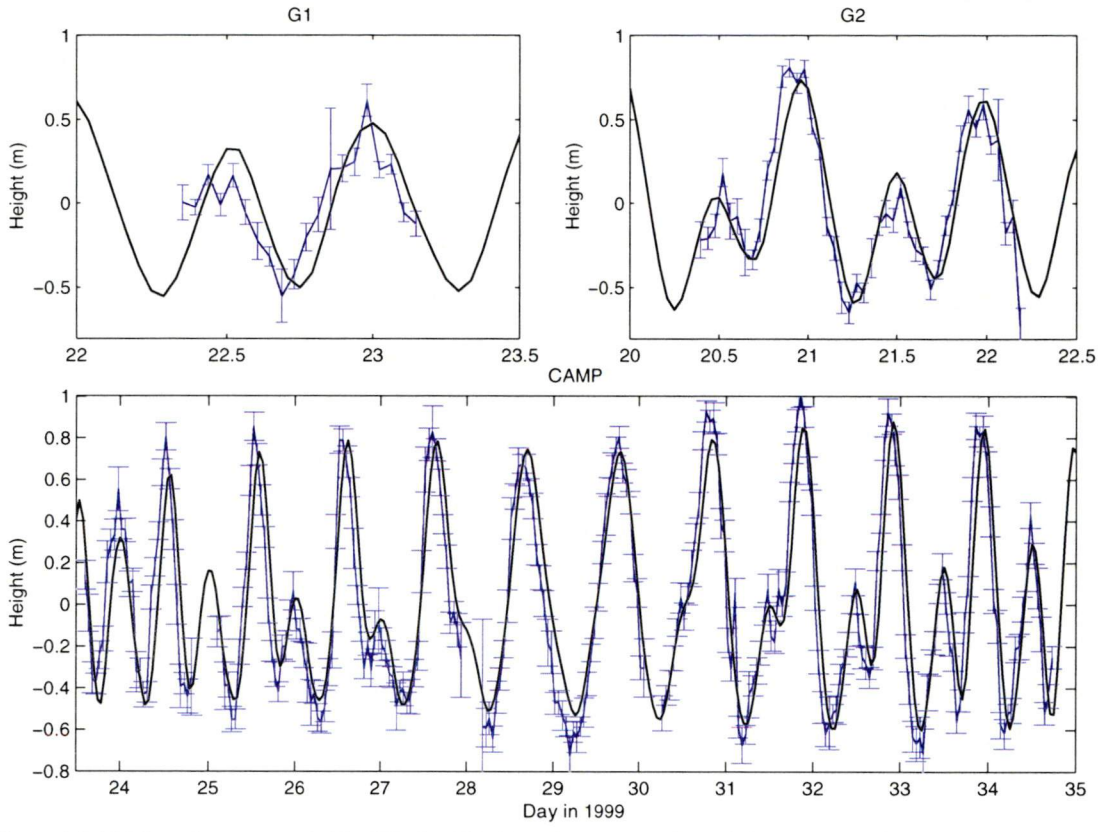

Figure 4-9: Tidal motion as recorded by GPS in 1999. Error bars are a only a relative measure of the precision of the GPS estimates. A mean height has been removed from the data sets.

With thirty-two days of data collected at HWDT in January-February 2000, this site represents the longest AIS tidal data set currently available. Some breaks in the data exist due to battery problems. The GPS antenna was shifted after day 20 due to a buildup of snow around the tripod, so the data set is split into two sessions. A mean offset has been removed from each of the two data sessions. The location of this site is approximately six kilometres from the lateral ice shelf grounding line, and so is within the 9km transition zone in which ice may or may not be totally freely floating (Rignot *et al.*, 2000). Despite this, the GPS derived heights from this site generally agree with the BLTM98, although there are some significant departures (RMS of differences is 0.25m). The phase is again shifted by approximately one hour, while the amplitude of the GPS derived heights are at times quite different to BLTM98. The tidal constituents of this site are further examined in Section 4.3.5.

In addition to the static GAMIT processing at this site, we have had success processing a section of this data using a kinematic methodology. This corresponds with the availability of data from the nearby LDBF site from day 035 onwards (shown in red in

Figure 4-10). The processing was performed using Track (Chen, 1998; personal communication, T. Herring, 2001) version 1.04, with site coordinates and one tropospheric zenith delay parameter determined for every data epoch (every thirty seconds). For the Track processing, the coordinates of LDBF were fixed while the ice site motion was constrained at the 10mm/epoch level, and ambiguities were not fixed to integer values. The mean one sigma error for each coordinate solution is approximately 50mm. Comparing the kinematic and the static results shows a good level of agreement (Figure 4-10). Phase is nearly identical in both solution types, whilst some departures (e.g., days 041-044) are seen in amplitude of up to 200-300mm. The major source of this disagreement is most likely caused by the static solution, given the lengths of the segments used in the analysis, although there may be some uncorrected cycle slips in the kinematic solutions.

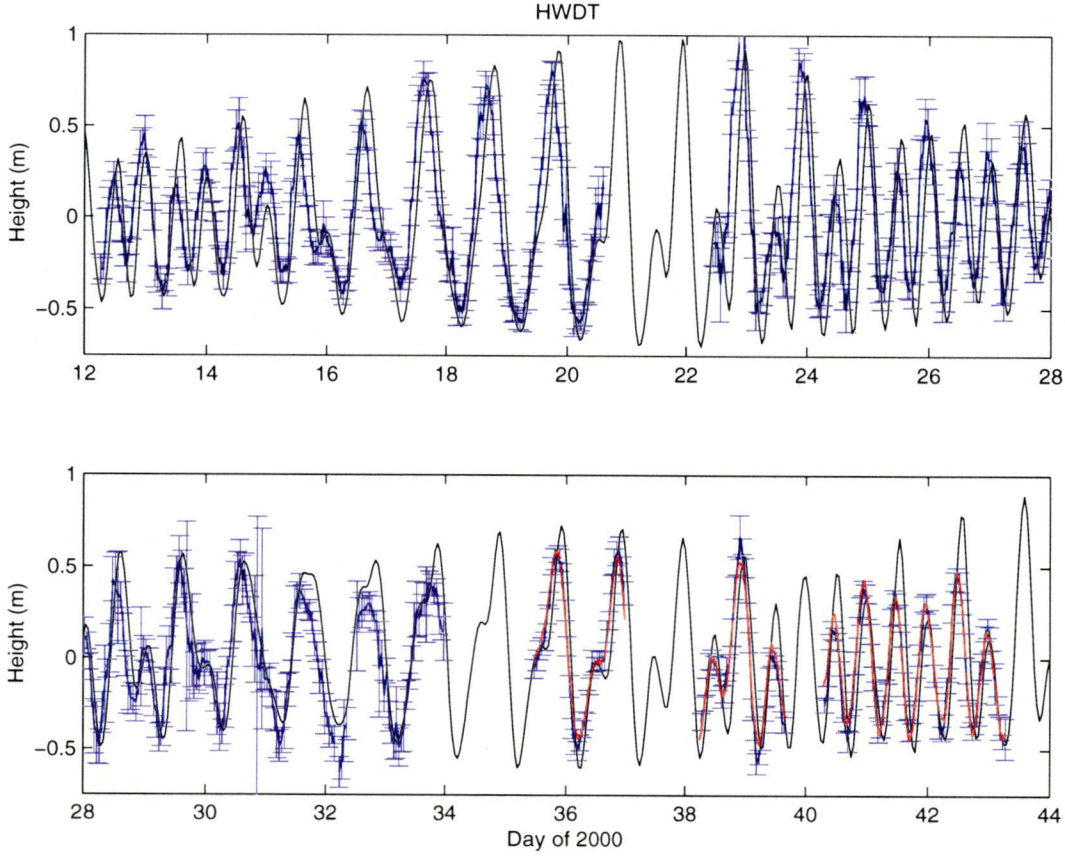

Figure 4-10: Tidal motion as recorded by GPS at HWDT in 2000. The blue line and error bars refer to the hourly solution. Error bars are a only a relative measure of the precision of the GPS estimates. The red line is the result from kinematic processing of day 035 onwards using Track. The solid black line is a prediction from the BLTM98. A mean height has been removed from each of the data sets.

4.3.5 Determination of constituents

To provide a more thorough analysis of the tidal signal at each of the twelve sites, we solve for their tidal constituents (Doodson, 1921). To do this, we apply the standard method, that is, a multivariate least squares fit of sine and cosine waves at known frequencies (Pugh, 1987). We also analyse the data using the response method (Munk and Cartwright, 1966) since this method does not require a strict minimum length data set, at least in theory (Cartwright, 1993). The two methods have been compared several times (e.g., Zetler *et al.*, 1979; Smith *et al.*, 1997) with differences only at the millimetre level, although these comparisons have been performed on data sets much longer than that presented here. These comparisons have also shown the response method to be slightly more accurate than the harmonic method using fewer tidal constituents.

Prior to the analysis of our GPS data we need to remove the effects of changes in atmospheric pressure during the measurement period. This is known as the inverse barometer effect. Over long periods (such as observed by permanent tide gauges) these effects average out, although these corrections are still made. Over our relatively short measurement periods it is particularly important to remove these systematic biases.

4.3.5.1 Inverse Barometer Effect

Response of the sea surface to variations in atmospheric pressure is known as the inverse barometer effect (IBE), since an increase in pressure will cause a reduction in sea surface height, and vice versa. The variation is approximately -10mm per 1hPa increase in pressure, and is defined by (Smith, 1979):

$$\frac{\partial \eta}{\partial x} = -\left(\frac{100}{\rho g}\right).\frac{\partial p}{\partial x} \tag{4.11}$$

where η is the water level, g is gravity, ρ is water density, p is the atmospheric pressure and x is the distance from some reference point. Since the IBE is not simply a localised effect, but regional, the measured pressure is normally related to an average regional or standard pressure, such as 1013.3hPa, as (in units of metres):

$$\Delta\eta = -\left(\frac{100}{\rho g}\right)(p - \overline{p}) \tag{4.12}$$

where $\overline{p}$ is a reference pressure. The value for gravity is usually adopted as constant, with corrections to measured water level varying using Equation (4.12) according to changes in atmospheric pressure or local water density. Slight water density changes are known to occur across the front of the AIS (Wong, 1994). The density of seawater can vary between 1000 and 1028 kgm^{-3}, although the variation in the AIS region is much less, so even an extreme variation in density will affect the water level correction by only 0.2mm/hPa. The IBE begins to break down in very shallow water, as is the case near ice shelf grounding zones, and so the response will be much less than given by Equation (4.12) (Born, 1997).

In practice, significant departures from the theoretical value for IBE have been reported (Hamon, 1966). Although it is possible to solve for this value using real data, to do so this requires longer time series than we have here. Consequently, we adopt an IBE value of -10.0mm/hPa for correcting the measured AIS GPS heights. On annual time-scales, surface pressure in the region of the AIS may vary by 70-80hPa[4], although more commonly 30-50hPa due to the passing of polar low pressure systems. Consequently, the IBE in this region may be as much as 300-500mm in water level.

Unfortunately, pressure data is not available at all sites where GPS tidal measurements on the AIS have been made (see Table 4-5). Even where pressure data exists, measurements were made only once a day. To correct the hourly GPS results for the IBE, these daily pressure values need to be interpolated to hourly values. Consequently, any (small) semi-diurnal terms will not be accounted for and will map into the derived constituents.

The precision of the IBE corrected GPS values may be computed from propagation of errors,

$$\begin{aligned}\sigma_h^2 &= \sigma_{GPS}^2 + \sigma_{\Delta\eta}^2 \\ &= \sigma_{GPS}^2 + \left(\frac{100}{\rho g}\right)^2 \sigma_p^2\end{aligned}$$

4. Based on annual values for Davis and Mawson during 1998 and 1999.

We estimate pressure readings to have one sigma errors of 2hPa, although there may be a further unknown systematic bias. The GPS height estimates have one sigma error of approximately 50mm for most points. Therefore, typical heights adjusted for IBE have a precision of 54mm (one sigma). This shows that the errors introduced by correcting for the IBE is negligible.

4.3.5.2 Harmonic method

The harmonic analysis of observed tidal data is based on the assumption that tidal variations correspond to a finite number N of harmonic terms of the form:

$$H_n \cos(\omega_n t - g_n) \tag{4.13}$$

where H_n is an amplitude, g_n is the phase lag on the equilibrium tide at Greenwich and ω_n is an angular speed. Given tidal measurements for a particular location, a set of constituents may be estimated using a least squares methodology. The functional model is (Pugh, 1987):

$$T(t) = Z_0 + \sum_N H_n f_n \cos\left[\omega_n t - g_n + (V_n + u_n)\right] \tag{4.14}$$

with the unknown parameters being Z_0 (the constant offset between the mean of the data and the measurement datum), H_n and g_n. The f_n and u_n terms are the nodal adjustments and the terms $\omega_n t$ and V_n determine the phase angle of the equilibrium constant. The nodal adjustment terms apply only for the lunar constituents since they are a function of the longitude of the lunar ascending node and sometimes the longitude of lunar perigee. These values are evaluated and used as constants in equation (4.14). See (Pugh, 1987, pp. 98-108) for further details.

Observations of sea level are normally equally weighted in this solution, since tide gauges have a high level of repeatability. On the other hand, heights derived from GPS data are not always of equal weight due to various influences listed previously. A typical high-low ratio of the GPS precisions in one twenty-four hour period is ~2.5. The estimates of the constituents shown below are from solutions where the observations are equally weighted due to software constraints. Consequently, the constituents

derived from the short data time series dealt with in this thesis may be adversely affected by inadequate techniques and unknown uncertainties.

The number of constituents that can be solved depends on the available number of days of GPS data, since many of the constituents are similar in period. The constituents with the most energy are the diurnal O1 and K1, and the semi-diurnal M2 and S2 terms (see Table 4-9). A minimum of fifteen days of data is required to separate each of these constituents, although in practice this may need to be significantly longer due to various environmental factors and time series noise. While it may not be possible to explicitly resolve each of these components using short data sets, they may be able to be inferred from those that can be resolved (Pugh, 1987).

Tidal Component	Period (solar hours)	Description
O1	~25.82	Principal lunar diurnal
K1	~23.93	Luni-solar diurnal
M2	~12.42	Principal lunar
S2	~12.00	Principal solar

Table 4-9: The most significant of the tidal components

The data sets for each of the AIS GPS sites have been analysed using the harmonic method, with astronomical arguments supplied by Proudman Oceanographic Laboratory, UK. The results for the four major constituents are shown in Table 4-10. The number of constituents estimated varies between data sets, although for sites other than HWDT only M2, K1 and M4 are estimated independently. Other constituents are inferred from those resolved constituents. For the data sets other than HWDT, the inferred constituents are Q1, O1, P1, 2N2, N2, NU2, L2, T2, S2 and K2. Approximately 26 constituents are independently solved using the longer data set at HWDT, although P1, 2N2, NU2 and K2 can not be estimated explicitly. King *et al.* (1983) and Merriman (1985) have shown that inferring constituents in harmonic analyses of short data sets may lead to poor results. However, it is preferable to infer these constituents rather than omit them altogether from the analysis.

An estimate of the goodness of fit of the solution may be defined using the variance of the observed data and the residuals:

$$\frac{\sigma^2_{postfit}}{\sigma^2_{prefit}} \tag{4.15}$$

A high value of this ratio suggests that the derived constituents do not fit the data well. The estimates for sites C4 and C6 in 1995 are poor since the tidal amplitude was low at the time of measurement. Site G1 also does not perform as well as the other sites with only 89% of the variance of the motion modelled. This may also be because of the shortness of this data set. Given the lengths of their data sets, sites V3 and V5 have higher than expected residuals. This may be caused by shallow water effects as these sites are near the grounding zone. Additionally, the pressure variation during the time of observation may have been larger than at the other sites. The residuals at these sites will be analysed in a later section.

The results of the harmonic analyses are shown in Figure 4-11 in the form of a phasor plot. The figure shows sites C4 and C6 as consistent outliers in amplitude, although their phase is relatively satisfactory. Site G1 has significantly lower amplitude in constituent S2 than the other sites, perhaps due to the lack of data there. The similarity of the amplitude of the constituents other than S2 for G1 and HWDT suggests that the inference of S2 may be resulting in a lower than actual amplitude. (Alternatively, this may be a result of amplification of S2 at the HWDT site, significantly closer to grounded ice.)

4.3.5.3 Response method

The response method does away with the assumption that tidal motion is precisely defined by a set of astronomical arguments. Rather it works on the principle that a system, such as the ocean, given an impulse will provide a response. By representing the gravitational potential V as a series of complex spherical harmonics, Munk and Cartwright (1966) represent the tidal variations, $\zeta(t)$, as the weighted sum of past values of each input spherical harmonic:

$$\hat{\zeta}(t) = \sum_s w(s) V(t - \tau_s) \tag{4.16}$$

where the weights w are determined so that the prediction error $\zeta(t) - \hat{\zeta}(t)$ is a minimum in the least-squares sense. τ is a time lag, normally chosen to be 48 hours.

The weights may be simply interpreted as representing the sea level response to a unit impulse $V(t)=\delta(t)$ at the location. Hence the name 'response method'.

The method proposed by Munk and Cartwright (1966) is not easily reduced to a universally applicable procedure, however, since the solution becomes ill conditioned in some instances. Consequently, Groves and Reynolds (1975) proposed a modification of the method in which the tidal input functions and observed tide are represented as linear combinations of a set of special orthogonal tidal functions, known as orthotides.

The number of terms required to describe tidal motion is significantly less using the response method in comparison to the harmonic method. Additionally, the resolution of the weights is in principle independent of the criterion for minimum duration of data. Non-gravitational components are also much easier to incorporate into the solution. These may include atmospheric or non-linear shallow water affects. See Pugh (1987, pp. 118-124 and Appendix 2) for further information on this method.

An analysis of the data from each of the sites was attempted using software implementing the methods of Munk and Cartwright (1966) and Groves and Reynolds (1975). Eight constituents were estimated in the software, four diurnal (K1, O1, P1, Q1) and four semi-diurnal (M2, S2, N2, K2). Prior to the analysis, the effects of the varying atmospheric pressure were removed from the time series (where pressure data was available). Unfortunately, only the solutions for HWDT and CAMP proved realistic. This is most likely due to the extremely short data sets at the other sites. With very short data spans, it is difficult to separate the various diurnal constituents since their frequencies are so similar. The same can be said for the semi-diurnal constituents.

The results for HWDT and CAMP are shown in Table 4-10. In the case of HWDT, the harmonic analysis residuals have 30% less variance than the response method residuals. This is most likely due to the presence of unmodelled higher order and non-linear terms in the response analysis. The determined constituents compare well, except for S2, with this constituent having more than 10mm and about 8° difference in amplitude and phase respectively. Given that we estimated only eight tidal constituents using the response method, thirty were estimated (at HWDT) using the harmonic

analysis and hence the response method compares well. The two CAMP analyses are much closer, in terms of the ratio of variances. Fewer high order and non-linear terms have been modelled in the harmonic solution of CAMP, and so the comparison at this site is more representative of the difference between the two methods. The similarity in the variance ratio does not result from a similarity in the determined constituents, however. Differences of more than 30mm and 8° occur in amplitude and phase respectively, although the largest differences are for S2 and O1, both of which have been inferred in the harmonic solution. This suggests that the inference of S2 is too low and O1 is too high in the harmonic analysis. This agrees with the earlier assertion that the inference of S2 at G1 is too low.

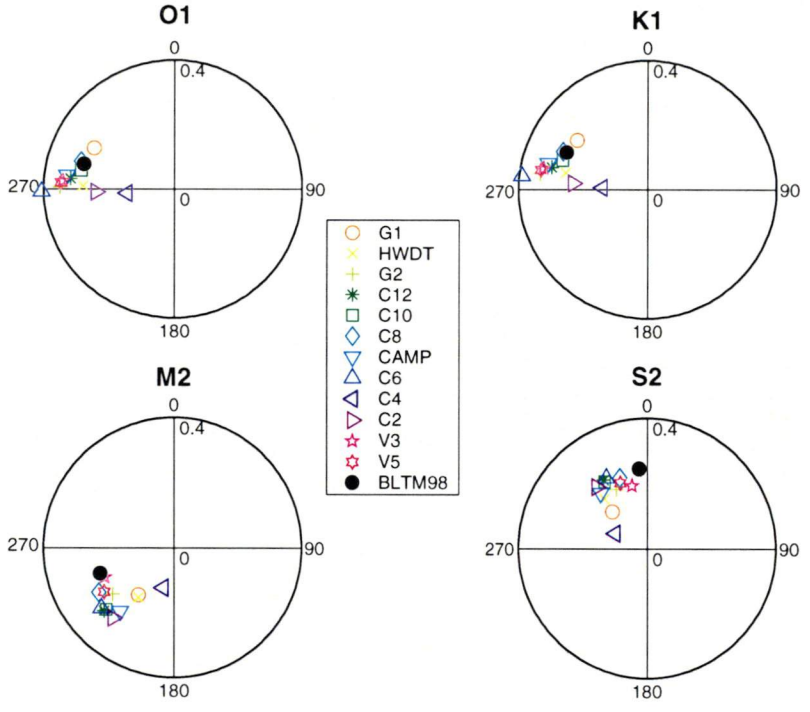

Figure 4-11: Phasor plot of the four major constituents from the GPS data using the harmonic method. The radius of the circle (shown at zero degrees phase) is the amplitude in metres.

Site	Data Length (hrs)	Harmonic Method M2 (m) (°)	S2 (m) (°)	O1 (m) (°)	K1 (m) (°)	# Solved	# Inferred	$\frac{\sigma^2_{postfit}}{\sigma^2_{prefit}}$	Response Method M2 (m) (°)	S2 (m) (°)	O1 (m) (°)	K1 (m) (°)	# Solved	$\frac{\sigma^2_{postfit}}{\sigma^2_{prefit}}$
G1[∝]	20	0 181 *216.9*	0 158* *316.4*	0 277* *297.7*	0 268 *305.0*	3	10	0 115	–	–	–	–	–	–
HWDT	617	0.188 *215.3*	0 203 *319.3*	0 281 *271.5*	0.262 *281.4*	26	4	0 052	0 189 *216.8*	0 190 *311.4*	0 276 *272 9*	0 262 *280.7*	8	0 076
G2[∝]	44	0.236 *232.7*	0 206* *332.2*	0 350* *271.2*	0 338 *278.5*	3	10	0 067	–	–	–	–	–	–
C12[∝]	27	0 289 *227.7*	0 251* *327.2*	0 319* *275 8*	0 307 *283 1*	3	10	0 050	–	–	–	–	–	–
C10[∝]	29	0 281 *227.4*	0 245* *326.9*	0.291* *281.7*	0.280 *289 0*	3	10	0 083	–	–	–	–	–	–
C8[∝]	23	0.269 *239 1*	0.234* *338 6*	0.298* *287.0*	0 288 *294.3*	3	10	0.069	–	–	–	–	–	–
CAMP	253	0 257 *220.0*	0 224* *319 5*	0 331* *277 6*	0 320 *284.9*	3	10	0 071	0.245 *226 4*	0 255 *320.8*	0 309 *269 7*	0 322 *286 2*	8	0 069
C6[∝]	24	0 290 *230.2*	0 253* *329.7*	0 406* *269.1*	0 392 *276 4*	3	10	0 192	–	–	–	–	–	–
C4[∝]	39	0 127 *195.5*	0 111* *295.0*	0.146* *265.2*	0 141 *272 5*	3	10	0.793	–	–	–	–	–	–
C2[∝]	27	0 285 *221.0*	0 248* *320.5*	0.240* *267.9*	0.232 *275 2*	3	10	0.057	–	–	–	–	–	–
V3[∝]	82	0 231 *247.1*	0 201* *346 6*	0 342* *274.4*	0 330 *281.7*	3	10	0 079	–	–	–	–	–	–
V5[∝]	91	0 253 *238.0*	0 220* *337 5*	0 349* *273.5*	0.337 *280.8*	3	10	0 103	–	–	–	–	–	–
BLTM98	–	0.240 *250.7*	0 247 *354.2*	0 287 *285.8*	0 277 *294.7*	–	–	–	–	–	–	–	–	–

Table 4-10: Amplitude and phase of the constituents derived from GPS data using the Harmonic and Response methods (listed in order from north to south). The number of parameters independently estimated (harmonic and response method) and inferred (harmonic method) are also shown. An asterix denotes that constituents were inferred from others in the analysis. [∝] denotes the sites where no pressure data exists.

4.3.6 Analysis of constituents

4.3.6.1 North-to-south amplification

Referring back to the harmonic solutions, a progression in phase from the northern sites to the southern sites is seen in each of the constituents. A linear increase in amplitude is also seen in the diurnal constituents from the north to the south. Such a linear increase may be caused by the reduction in the water column thickness under the AIS, as sites approach the grounding zone. This is caused by either an increase of ice thickness closer to the grounding zone or by a slope in the ocean bottom, or both.

An assumption can be made that the ice shelf behaves like a shallow canal of slowly varying depth (Williams and Robinson, 1979). Since conservation of energy must occur, in the theoretical case of no ocean bottom friction, reflection or energy dissipation through the ice shelf grounding zone, the amplitude (A) of the tide is related to water column thickness (h) by (Williams and Robinson, 1979):

$$Ah^{\frac{1}{4}} = b \tag{4.17}$$

where b is constant for a given constituent.

While the above assumptions are unlikely, they do allow us to determine first order estimates of water column thickness at the GPS sites. Given the above assumptions, the value for b is unity, although in reality the relationship may depart significantly from this value, due to the presence of friction, reflection and dissipation. This makes it difficult to apply Equation (4.17). If the water column thickness is well known, the value of b may be solved for (e.g., Williams and Robinson, 1979). Unfortunately, the water thickness under the AIS is poorly known, particularly in the southernmost part where very little detail exists. However, if friction, reflection and dissipation are similar at two different locations (likely in regions not affected by grounding line dynamics), the relationship may apply relatively:

$$\frac{A_1 h_1^{\frac{1}{4}}}{A_2 h_2^{\frac{1}{4}}} = 1 \tag{4.18}$$

where A_1, A_2 and h_1, h_2 are the tidal amplitudes and the water thickness at two sites respectively.

If the water thickness at one site is known well, Equation (4.18) may tell us valuable information about the water column thickness at other locations. Water column thicknesses are available for the AIS region based on seismic and radar echo sounding (RES) measurements. The values used here are similar to those used in Williams *et al.* (1998), although the data we use has been reanalysed, gridded and new RES data added (personal communication, J. Hunter, 2001). Using a water column thickness of 380 metres at G1, water column thicknesses at the other sites have been determined using both the GPS and CADA-derived constituents described in Section 4.3.8.2. The results are shown in Figure 4-12 with the CADA results plotted as stars and the GPS results plotted as circles. The CADA model is not totally independent of the water column thickness information, since the model uses the bathymetry data from Williams *et al.* (1998). Sites C4 and C6 have been omitted since their GPS-derived constituents are of poor quality.

The estimation has been done using both the M2 and K1 constituents (represented by blue and green colours respectively in Figure 4-12). The agreement between the diurnal and semidiurnal approaches is poor, suggesting that energy is being dissipated differently across the frequencies or some other non-linear interaction is occurring. This difference between frequencies agrees with the results of Williams and Robinson (1979) who found that there was no simple relationship between tidal amplitude and water column thickness for the M2 constituent on the Ross Ice Shelf. Overall, on the AIS the K1 estimates are more realistic than M2, since they agree better with the water column thicknesses as shown by a solid line in Figure 4-12. Williams *et al.* (1998) do not provide precision estimates for these water column thickness values, although they did represent them with 100m contour intervals and so we show them with 100m error bars in the figure. Greater errors may be present if the topography of the bottom or ice shelf base is highly varying, due to the gridding of the water column thickness information.

The estimates from the GPS-derived constituents are in best agreement at the sites with the longest time-series (HWDT, CAMP, V3 and V5). The value for HWDT was

taken from the raw measurements rather than interpolated from the grid, due to its proximity to the coast and the sparseness of the RES and seismic data in this region. The estimates at C2 give the poorest agreement with each other and with the value interpolated from the grid. An earlier version of the gridded data with less filtering applied had greater agreement with the GPS K1 estimate at C2, but this earlier grid was considered sub-optimal, especially near the grounding zones. Of the remaining sites, the GPS K1 estimate is in the best overall agreement, suggesting that this method is satisfactory in determining water column thickness using the GPS-derived constituents. The CADA model, while in general agreement, is not yet capable of estimating the fine features present in the water column thickness grid.

No information exists on the water column thickness at V3 and V5[5], and hence the values shown here for the GPS K1 thicknesses (190m and 150m, respectively) represent best estimates at these locations with an estimated uncertainty of 100m. These estimates are an important first step in determining the water column thickness in these regions. In turn, they can be used in tidal models to improve the estimates of the tidal motion in these regions.

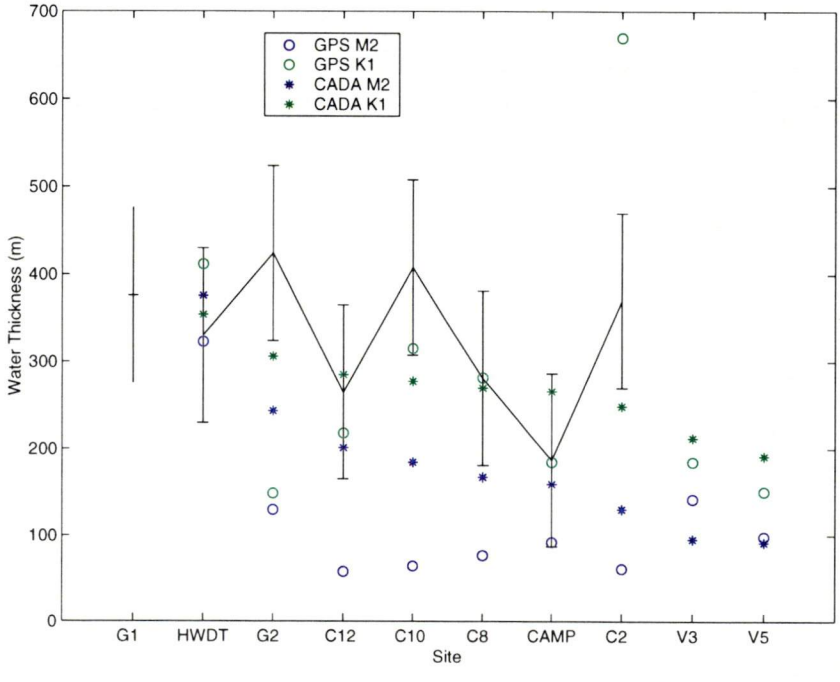

Figure 4-12: Water thickness derived from Equation (4.18) using G1 as the reference site. Circles and stars represent thicknesses derived using the M2 and K1 amplitudes, respectively from each of the GPS results (blue)

5. No data exists south of approximately 72°S.

and CADA model (green). Thicknesses determined from seismic and RES measurements are shown as a solid line with 100m error bars where data is available.

4.3.6.2 Tidal energy dissipation

Ice shelf grounding zones have previously been suggested as being the most significant source of global tidal energy dissipation, dissipating as much as 2×10^{12} W (Doake, 1978). While this is now regarded as a significant overestimation (Webb, 1982; Ray and Egbert, 1997), these regions still play an important role in energy dissipation (Webb, 1982; Pedley *et al.*, 1986). One of the most common ways of gauging the amount of energy dissipated in a region is by examining the age of the tide. This is the delay of the tidal response behind the tidal forcing and is defined as (Pugh, 1987):

$$\text{Age} = \frac{g_{S_2} - g_{M_2}}{2\left(\omega_{S_2} - \omega_{M_2}\right)} \tag{4.19}$$

where g is the phase lag on the equilibrium tide at Greenwich and ω is the angular speed of the constituent.

Using values from the HWDT harmonic analysis, the age of the tide for the AIS region is 51h, just less than the figure of 60h normally associated with strong tidal dissipation. The age of tides at other ice shelves varies from 17h near the Filchner Ice Shelf to 165h at the George VI Ice Shelf. Doake (1978) has reported that the majority of tides near Antarctica's ice shelves have ages greater than 60h. Thus, the AIS region experiences below average ice energy dissipation when compared to other ice shelf regions.

4.3.7 Analysis of residuals

By analysing the residuals left in the GPS data after the removal of the determined tidal constituents, we hope to detect any unmodelled or non-gravitational components in the data. Since we had the most success with the harmonic method, we analyse the residuals from this method. Analysing time series less than a few days in length is impractical, and so this analysis is limited to the three longest time series, HWDT, CAMP and V5.

4.3.7.1 HWDT residuals

Figure 4-13 shows the residuals from site HWDT in blue in the top frame. The RMS of the residuals is 0.074m. The measured pressure is over-plotted to determine if all the IBE has been removed appropriately. The correlation between the residuals and the pressure is 0.08, and so they are effectively uncorrelated. While visual inspection may suggest a phase shift existing between the pressure and residuals, the results of performing a cross-correlation on the two signals does not support this. Solving for the best-fit slope over the length of the time-series results in a 1mm/day (±0.3mm/day) decrease in height of the GPS antenna. This change may be attributed to the sinking/settling of the tripod into the snow, although it is more likely it is a part of unresolved long-term tidal motion. Vertical motion of the GPS antenna due to the surface slope of the ice shelf is negligible over such a short time period.

A curious signal exists in the residuals before day 20. By computing the power spectral density (PSD) of the full residual time series (Figure 4-13, middle frame) it may be seen that no significant power peaks exist over the entire time series. The cyclical signal prior to day 20 is the cause of the rise in power at low frequency. It is uncertain what the cause of the signal prior to day 20 may be, although ice shelf grounding zone dynamics may account for it.

Any high frequency motions of the ice shelf at this location may be studied by using the results of the kinematic processing. Thiel *et al.* (1960) and Williams and Robinson (1981) have identified high frequency oscillations on the Ross Ice Shelf with periods between 100s (0.01Hz) and 1200s (8.3×10^{-4} Hz), with the motion being propagated via flexure in the ice. This is caused by ocean swell interacting with the front of the ice shelf, and the motions were identified more than 600km from the open sea. By applying a high pass filter (passing signals with periods shorter than 4500 seconds) to the results of the kinematic processing (shown in Figure 4-10), this data may be examined for high frequency oscillations. Since the sampling rate for this data is thirty seconds, the highest frequency oscillation that is detectable has a period of 60s (0.016Hz). The bottom frame of Figure 4-13 shows a PSD of the filtered data. The cyclic nature of the peaks in the PSD is most likely caused by filter aliasing, as the power is negligible. It is therefore concluded that no high frequency oscillations occur

in this region of the AIS during the time of these observations. This is not to exclude the possibility of such oscillations occurring elsewhere on the AIS, since the ice shelf front near HWDT may be protected from high swell due to its proximity to the coast.

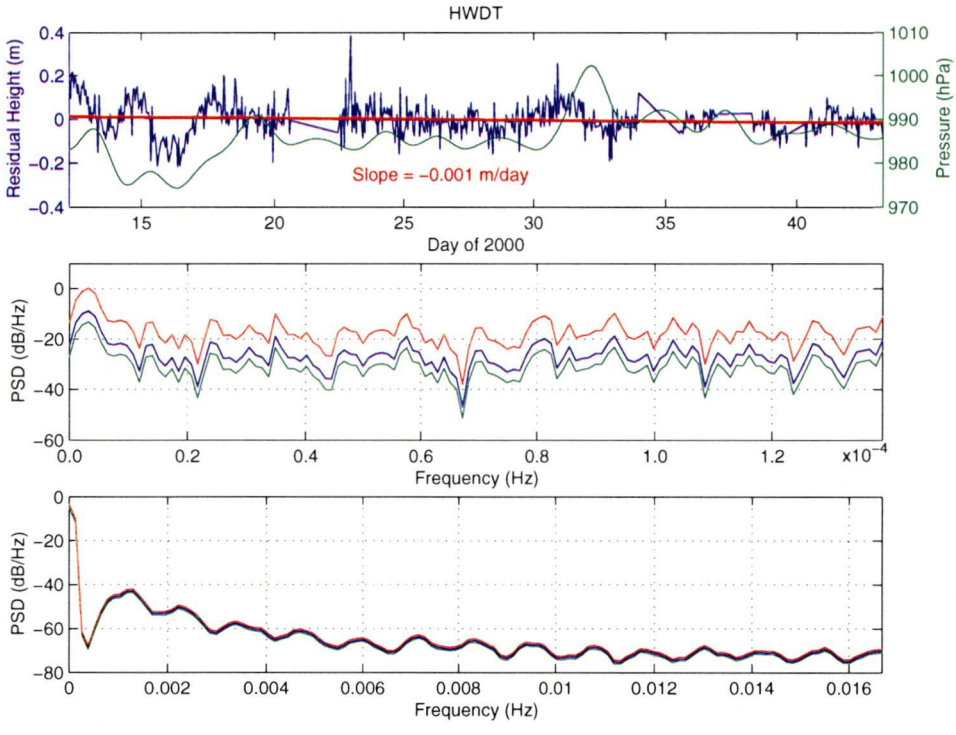

Figure 4-13: The top frame shows the residuals from the harmonic analysis at HWDT (blue), along with the best fit line (red) and the daily atmospheric pressure measurements interpolated to hourly values (green). The middle frame is a PSD plot of the residuals showing the 95% confidence intervals. The lower frame is a PSD plot of the GPS results (a high pass filter was applied to the Track results) showing the 95% confidence interval.

4.3.7.2 CAMP residuals

The residuals from the analysis of CAMP are shown in blue in the top frame of Figure 4-14. The most striking feature of this time series is the dramatic downward motion of the residuals prior to day 25. By linear regression, the best-fit line has a slope of -272mm/day (±54mm/day) prior to day 25 and +4mm/day (±2.5mm/day) thereafter. This first slope seems quite large. It is likely that it is caused by the antenna pole sinking into the snow, with the period corresponding with maximum daily temperatures of +1-2°C. The maximum daily temperatures are below zero for the majority of the remainder of the data set. The slope after day 25 may be explained by a unresolved long term tidal motion – snow densification and melting-in of the pole

cannot be the major source due to the positive sign of the slope. The RMS of the residuals from day 25 onwards is 0.109m.

The correlation between pressure and the tidal residuals is interesting. Using data corrected for IBE, the correlation is +0.262, while using data not corrected for IBE the correlation is -0.152. Therefore, correcting for the IBE actually increases the correlation while changing the sign. This may of course be simply due to the shortness of the data set.

The lower panel in Figure 4-14 shows a PSD of the CAMP residuals. It is clear that some non-linear periodic terms still exist in the residuals, including diurnal and semidiurnal signals and the third harmonic. While not statistically significant at the 95% confidence interval, some power exists at the sixth and eighth harmonics also. These non-linear terms are synonymous with shallow water effects (Pugh, 1987). Non-linear tides have also been measured on the Ross and Ronne Ice Shelves (Pedley *et al.*, 1986), where grounding zone effects were suggested as the cause. They are not apparent in the HWDT residual time series since non-linear terms up to and including the sixth harmonic are solved for in the HWDT data set.

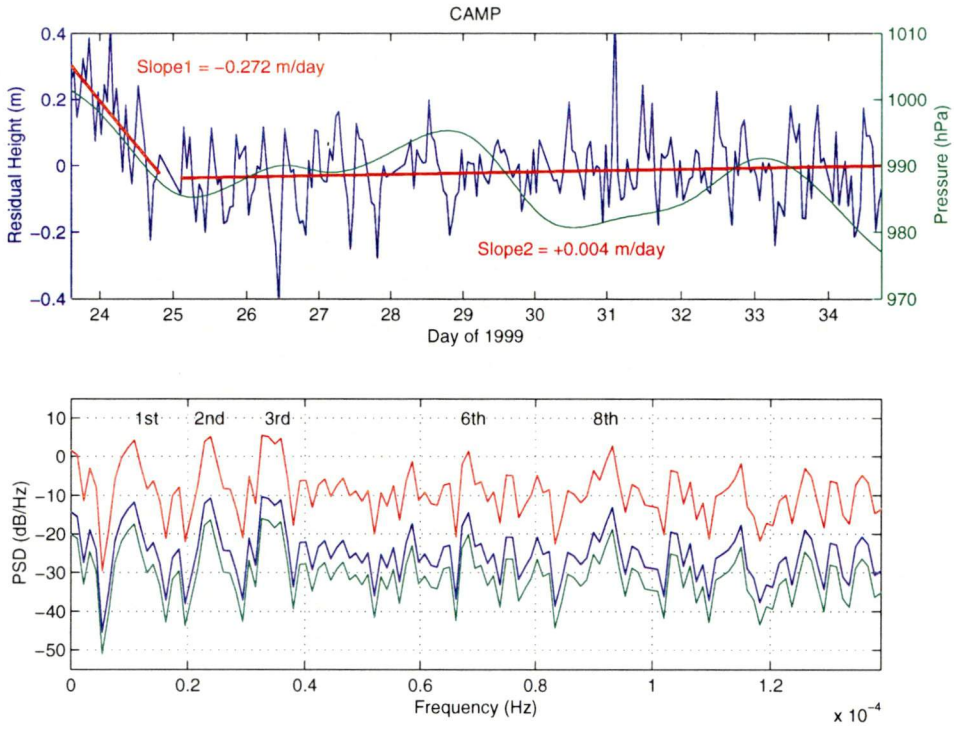

Figure 4-14: The top frame shows the residuals from the harmonic analysis at CAMP (blue), along with the best fit lines (red) and the daily atmospheric pressure measurements interpolated to hourly values (green). The bottom frame is a PSD plot of the residuals showing the 95% confidence intervals.

4.3.7.3 V5 residuals

The time series of residuals from the harmonic analysis of V5 is shown in Figure 4-15. This site differs from the other two, as local pressure was not observed and hence these residuals include the effects of changing barometric pressure. The residuals are flat with a best-fit slope of +3mm/day (±16mm/day). Their RMS is 0.167m, significantly higher than HWDT. The output from a low-pass filter applied to the residuals is shown in blue in the middle panel of Figure 4-15. The GPS data was padded at both ends with the mean value to avoid filter edge effects. Also shown in the middle panel is the IBE computed using measured pressure at Davis and Mawson. While these sites are close to 1000km away from the measurement area, their correlation with the low-pass filter output is significant, particularly at Davis where it is +0.74. This suggests that the majority of the low frequency signal remaining in the residuals is due to IBE. Furthermore, there does not appear to be any systematic effects caused by sinking or settling of the pole at this site.

The PSD of the residuals is shown in the bottom panel of Figure 4-15. No residual power exists in the data set at the 95% confidence interval. This is probably due to the shortness of the data sets, since the frequency of the peaks that do appear in the plot are in close agreement with the frequencies for the third, fourth, sixth and eight harmonics.

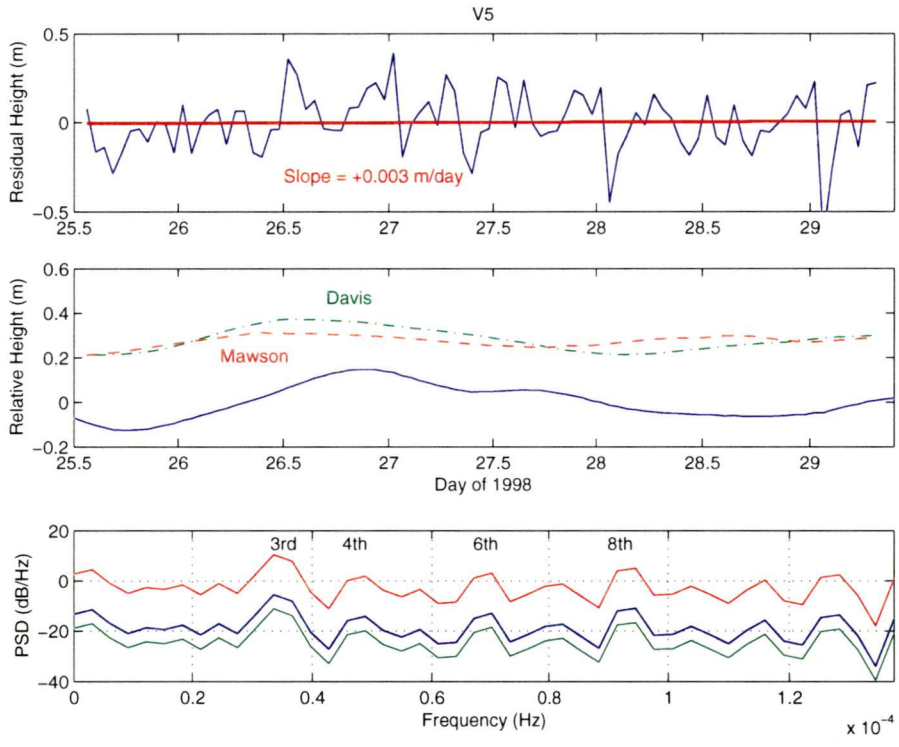

Figure 4-15: The top frame shows the residuals from the harmonic analysis. This data set has not had the IBE removed since no pressure measurements are available. The middle frame shows the results of applying a low pass filter to the residuals (blue), along with the computed IBE values for pressure measurements made at Mawson (red dashed line) and Davis (green dot-dashed line). The bottom frame is a PSD plot of the residuals showing the 95% confidence intervals.

4.3.8 Comparison against independent models

In order to assess the performance of a subset of the recent ocean tide models for the AIS region, we have compared the constituents from our harmonic analysis of the GPS data with three tidal models. These are the global FES99 model (Lefevre *et al.*, 2001) and the CADA00.10 and CATS00.10 models (Padman *et al.*, 2001), developed for the Antarctic region.

4.3.8.1 FES99

As the name suggests, the Finite Element Simulation model (FES) is based on a finite element computation technique. This technique allows for the improvement of the modelling of rapid changes in ocean depth, the refinement of the grid resolution in shallow waters and the description of coastline irregularities (Le Provost *et al.*, 1994; Le Provost *et al.*, 1995). The three parameters of such a model are the surface elevation and the two components of the barotropic velocity field. In all, eight constituents are modelled, four diurnal (O_1, K_1, P_1, Q_1) and four semi-diurnal (M_2, S_2, K_2, N_2).

Early versions of the model were purely hydrodynamic, that is, they contain no external tide gauge or satellite data, but are based solely on the barotropic[6] nonlinear shallow water equations (Le Provost *et al.*, 1994). Later versions of the model have assimilated satellite altimeter data and tide gauge data (Lefevre *et al.*, 2000). Including altimeter data in tide models provides significant accuracy improvements in the open oceans, while tide gauge data are particularly valuable for coastal regions. The 1999 version of FES (FES99) assimilates data from both the TOPEX/Poseidon altimeter and a set of global tide gauges (Lefevre *et al.*, 2001), including Davis but not Mawson or Beaver Lake. The model has been made available by the authors in the form of a 0.25° x 0.25° gridded version of the full finite element solution.

Unfortunately, FES99 contains only the old definition of the AIS grounding zone, and so its evaluation is not possible south of site C6. Furthermore, an estimate of the height of the water column underneath the AIS was made (100m everywhere), introducing significant error into the model in this region.

4.3.8.2 CADA/CATS

The Circum Antarctic Tidal Simulation model (CATS) is a high-resolution (grid node spacing of 1/4° x 1/12°, or about 10km near the Antarctic coast) tidal model around the Antarctic continent (Padman and Kottmeier, 2000; Rignot *et al.*, 2000). CATS covers the entire southern ocean south of ~58°S, with open boundary conditions along 58°S provided by the TPXO5.1 model (see Egbert *et al.*, 1994). The model constituents are computed using the depth-integrated shallow water equations

6 The strict meaning of the term "barotropic" is that the pressure is constant on surfaces of constant density, and hence is constant on their interface. (Gill, 1982).

(Robertson *et al.*, 1998). Four diurnal (O_1, K_1, P_1, Q_1), four semi-diurnal (M_2, S_2, K_2, N_2) and two long-period (Mm, Mf) constituents are modelled. Unlike other existing models, CATS version 00.10 also includes the new definition of the AIS grounding zone.

Pure hydrodynamic models, such as the earlier FES models and CATS, rely heavily on an accurate understanding of bathymetry. Unfortunately, bathymetric information in the Antarctic region is often poor, even non-existent in large areas. For example, no information exists on the bathymetry under the AIS south of ~72°S. Furthermore, little is currently known about the level of tidal energy dissipation under ice shelves. The forward models tend to suffer accordingly.

In order to overcome this, inverse models may be computed that assimilate tidal or current data. Based on CATS, the Circum-Antarctic Data Assimilation model (CADA) is such a model. CADA assimilates TOPEX/POSEIDON altimetry, tide gauge, ice shelf gravity and GPS observations into the model (Padman *et al.*, 2001). CADA00.10 includes tide gauge data from Mawson, Davis and Beaver Lake along with the GPS observations made at HWDT in 2000.

4.3.8.3 Comparison

The three models (FES99, CATS00.10 and CADA00.10) have been evaluated at CAMP to coincide with a subset of the GPS data (Figure 4-16). FES99 performs very poorly at this site during this time, while both the CATS and CADA models agree well with the GPS data, although there is still some difference at the 100mm level. In order to examine these differences more closely, the four major constituents of each of the models are shown in Table 4-11 and in the form of a phasor plot in Figure 4-17. BLTM98 is shown in the table and figure as a reference. In general, bicubic interpolation was used to determine the constituents, although several sites were too close to the grounding zone in FES99 and bilinear interpolation was used instead.

The Table and Figure show that FES99 is very different to both CADA00.10 and CATS00.10 away from the ice shelf front (G1), particularly in the semidiurnal components. This is a result of the poor bathymetry used in FES99 and the incorrect definition of the grounding zone. Both of these may result in an increase in the

amplitude of the constituents, although the errors in the bathymetry might result in a decrease in the constituent amplitudes. The phase of FES99 semi diurnal terms becomes very poor away from the ice shelf front, perhaps for the same reasons, although the reason for this poor agreement is not well understood. On the other hand, the FES99 semidiurnal terms are in closer agreement with CADA00.10 than CATS00.10 at G1, perhaps due to the assimilation of tide gauge / altimetry data in these models.

As would be expected, the agreement between CADA and CATS is much better, although again the differences become amplified away from the ice shelf front. The semidiurnal constituents display the greatest variation. The assimilation of the local tide gauge and GPS data has clearly provided an improvement in the agreement of the CADA model with the GPS shown in Figure 4-17. This shows that assimilating GPS data into tide models is important if such models are to be improved in ice shelf regions. What is required is long term ($\geq$ 1 year) GPS measurements so that the annual constituents can be determined.

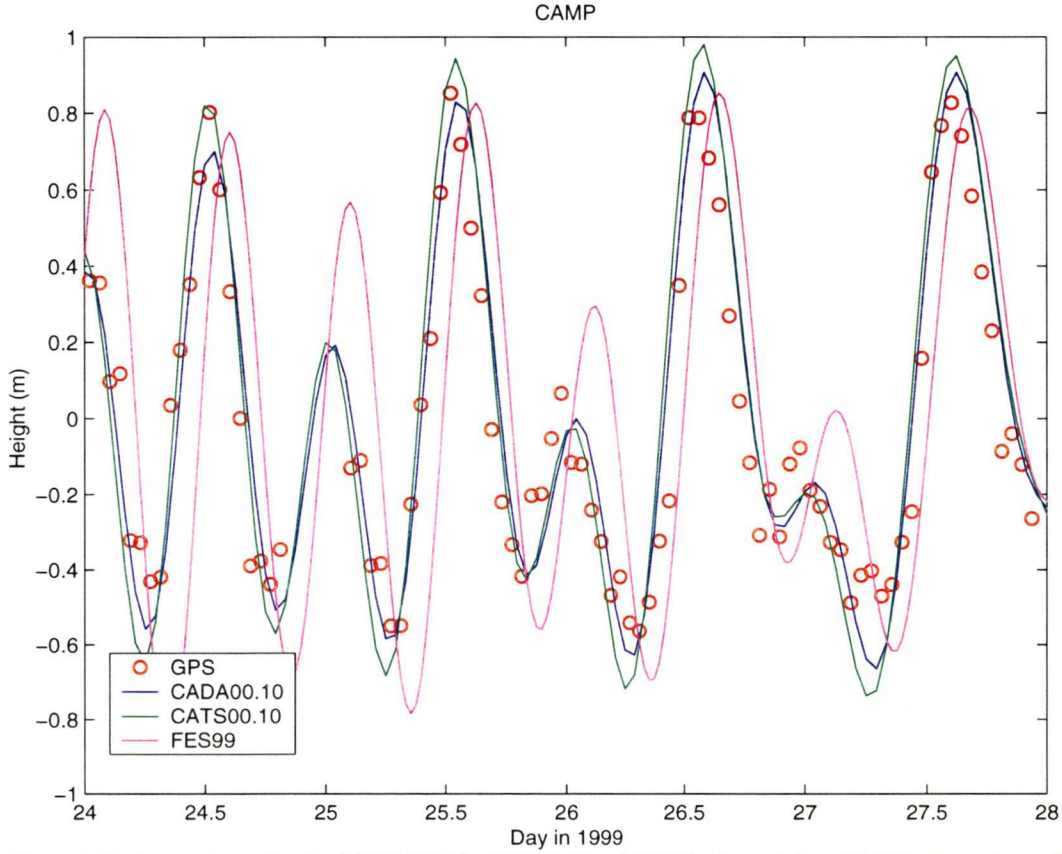

Figure 4-16: Comparison of each of CADA00.10, CATS00.10 and FES99 tide models at CAMP with a subset of the GPS data at that site.

	FES99				CATS00.10				CADA00.10			
	M2	S2	O1	K1	M2	S2	O1	K1	M2	S2	O1	K1
	(m)	(m)	(m)	(m)	(m)	(m)	(m)	(m)	(m)	(m)	(m)	(m)
Site	(°)	(°)	(°)	(°)	(°)	(°)	(°)	(°)	(°)	(°)	(°)	(°)
G1	0.205	0.212	0.309	0.297	0.243	0.253	0.315	0.299	0.201	0.201	0.279	0.267
	227.5	333.1	268 4	283.4	222.0	322.1	281.0	288.0	229.1	338.1	280.0	290.1
HWDT	0.207	0.213	0.304	0.293	0.240	0.249	0.304	0.320	0.201	0.198	0.283	0.271
	219.4	323.9	267.4	281.7	216.0	316.0	285.0	278.0	223.0	331.0	277.0	288.0
G2	0.254	0.284	0.305	0.296	0.270	0.286	0.328	0.313	0.224	0.227	0.291	0.281
	266.8	27.4	279.0	298.3	222.0	322.5	280.5	287.6	230.5	339.0	279.6	290.0
C12	0.325	0.365	0.312	0.306	0.283	0.302	0.333	0.319	0.235	0.240	0.295	0.286
	286.5	23.8	286.2	309.3	223.1	323.5	281.1	288.1	231.5	339.5	280.1	289.9
C10	0.356	0.405	0.317	0.311	0.289	0.311	0.336	0.322	0.240	0.247	0.297	0.288
	289.6	26.9	287.6	311.6	223.2	323.1	281.0	288.0	232.2	340.2	280.0	290.1
C8	0.381	0.439	0.324	0.318	0.297	0.320	0.337	0.324	0.246	0.254	0.299	0.290
	290.8	28.3	288.0	312.5	224.0	324.0	281.0	288.0	233.0	341.0	280.0	291.0
CAMP	0.392	0.453	0.328	0.321	0.300	0.324	0.338	0.325	0.249	0.257	0.300	0.291
	291.3	28.9	288.2	312.7	224 0	324.1	280.9	288.0	233.0	341.0	280.0	290.6
C6	0.403	0.468	0.331	0.325	0.303	0.328	0.339	0.326	0.252	0.260	0.301	0.292
	291.2	28.7	288.0	312.6	223.7	323.9	281.0	288.0	232.7	340.7	280.0	290.8
C4	-	-	-	-	0.310	0.336	0.341	0.328	0.257	0.267	0.303	0.294
					224.0	324.6	281.0	288.0	233.0	341.1	280.0	290.5
C2	-	-	-	-	0.316	0.344	0.330	0.343	0.262	0.273	0.304	0.296
					224.0	324.2	281.0	288.0	233.1	341.0	280.0	290.0
V3	-	-	-	-	0.341	0.377	0.354	0.343	0.283	0.300	0.314	0.308
					224.0	324.0	281.0	288.0	233.0	341.0	280.0	290.0
V5	-	-	-	-	0.345	0.382	0.356	0.346	0.286	0 304	0.310	0.316
					224.0	324.0	281.0	288.0	233.0	341.0	290.0	280.0
	BLTM91				BLTM98							
Beaver	0.249	0.262	0.297	0.285	0.240	0.247	0.287	0 277				
Lake	252.3	357.6	288.6	295.4	250.7	354.2	285.8	294.7				

Table 4-11. Comparison of constituents from the FES99 and CADA models for M2, S2, O1 and K1. Constituents for Beaver Lake from the BLTM91 and the BLTM98 are shown for purposes of comparison.

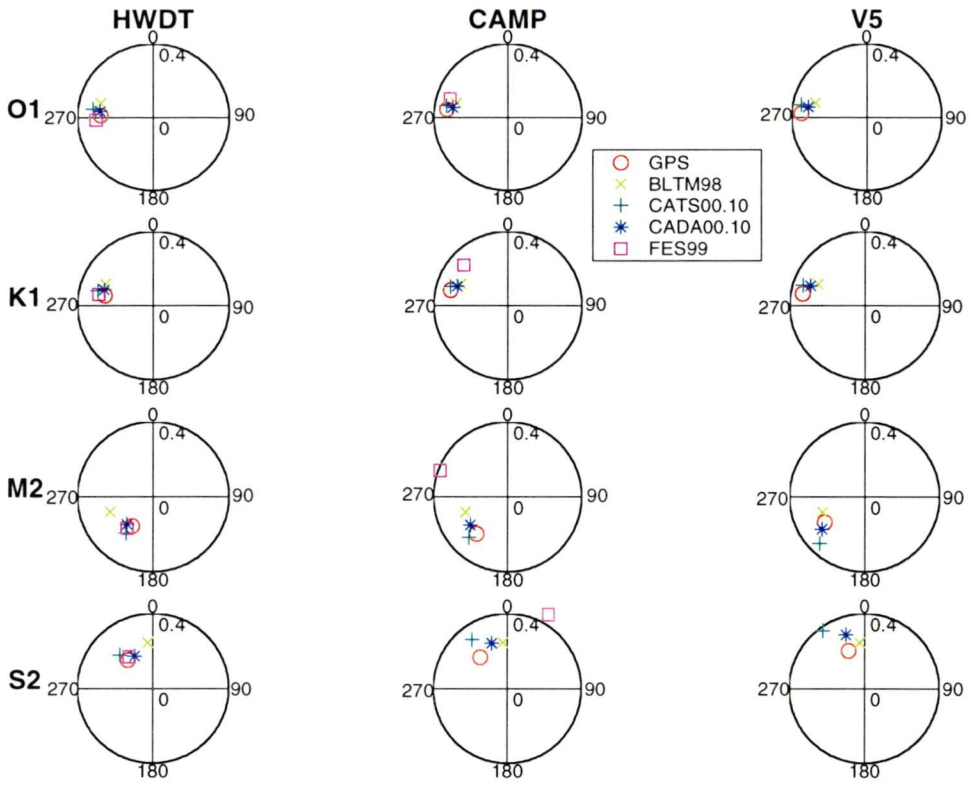

Figure 4-17: Phasor plot of the four major constituents at the three AIS sites with the longest time-history of GPS observations. Data is from the harmonic analysis of the GPS data along with the CATS00.10, CADA00.10 and FES99 models. Data is not available in the FES99 model at V5. The BLTM98 is shown as a reference.

4.4 Removal of vertical (tidal) and horizontal signals

4.4.1 Introduction

While the ice shelf motion can be measured by GPS, what is needed for integration of such measurements for long term monitoring of the ice shelf is a static reference system. The advantage of such a static reference system is that it allows the integration or comparison of long-term horizontal or vertical positions or velocities in a consistent reference frame. Chapter 5 outlines the combination of several epochs of GPS data to derive an accurate velocity model for the AIS. Terrestrial observations are also combined with the GPS data, emphasising even further the need for well-defined reference systems.

For the vertical component, this is best provided by a tide-free surface, such as a specified datum level. (The treatment of the other geophysical corrections, such as solid Earth tides, is also required and is dealt with during the standard GPS processing.) For the horizontal components, we need to correct all data to a specific

epoch during the measurement period. Implicit in the above is the assumption that the motion of the ice shelf over some time period can be exactly described by some chosen model, such as a tide model or a horizontal velocity field. Any imperfections in the models used or differences between this model and the GPS data will directly cause biased results. With these stated assumptions, we describe below procedures for removing ice shelf motion from raw GPS observations.

4.4.2 Removal of vertical motion

Since the BLTM98 provides a good comparison to the GPS data in this region, we use this model as representative of the true ice shelf response to the tides. Any difference between it and the GPS results is regarded as measurement error. In regions where tide gauge observations have not been made, or are not possible, predictions based on long-term (preferably more than 1-3 months) GPS observations or a regional tidal model (Robertson *et al.*, 1998; Padman *et al.*, 2001) could be used. As regional tidal models improve in accuracy, they will become the preferred option. This is because they are capable of modelling the tidal motion at all locations on an ice shelf, without need to account for variations such as a phase shift as is required for the BLTM98.

In order to remove the tidal signal from the GPS data, we use a five-step process:

1. Solve for a best-fit phase shift of the tide model to the GPS data, using a cross correlation technique. Computed shifts for the AIS are presented in King *et al.* (2000) and are approximately 45 minutes, with the GPS sites on the ice shelf leading (i.e., motions occurring before) the BLTM98.
2. Apply this shift to the tide model and compute the modelled tidal value at each GPS epoch of measurement.
3. Read in raw GPS data from a RINEX observation file and convert the carrier phase ranges to units of metres.
4. Read in a RINEX navigation file for calculating the position (and hence elevation) of satellites at the measurement epochs. Earth rotation during signal travel time is also accounted for at this stage.
5. Correct the observed ranges as shown below and write out a new RINEX file.

The geometry of the problem is two-dimensional and is presented in Figure 4-18.

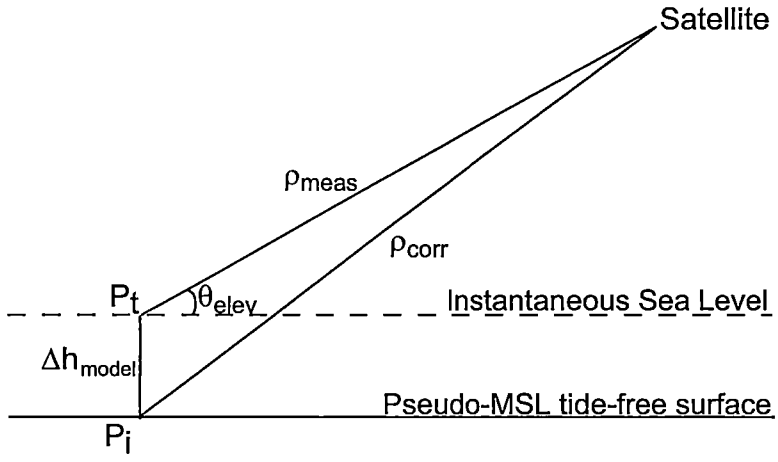

Figure 4-18: Geometry of removing tidal signal from GPS data.

Using the cosine rule, the tide-free corrected range for a particular satellite is (in metres):

$$\rho(t)_{corr} = \left[\rho(t)^2_{meas} + \Delta h^2_{model} - 2\rho(t)_{meas}\,\Delta h(t-\delta)_{model} \cdot \cos\left(90° + \theta(t)\right)\right]^{\frac{1}{2}} \tag{4.20}$$

where:

ρ is the corrected and measured carrier phases (converted to metres) and pseudoranges.

Δh is the instantaneous modelled height of the tide above a pseudo-MSL tide-free surface.

θ is the angle of elevation of the satellite above the horizon.

t is the time at some measurement epoch

δ is the computed phase shift required to fit the tide model to the GPS data.

The corrected ranges may then be converted back into carrier phase cycles where necessary, and written back into a RINEX file. Note that this correction is azimuth independent, and only relies on the elevation angle of the satellite.

4.4.3 Removal of horizontal motion

In order to remove the horizontal motion of a GPS antenna during an observation session, an estimate of the horizontal velocity of the antenna is required. In practice these could be obtained via long-term GPS observations, satellite techniques or, as we

do here, short-term GPS observations such as from the method described in Section 4.3.3.

The correction of receiver-satellite ranges for horizontal motion of the GPS antenna is more complicated than the correction for the vertical since the correction is dependant on the azimuth, as well as the zenith, of the satellite. The geometry of the problem is three-dimensional and is shown in Figure 4-19.

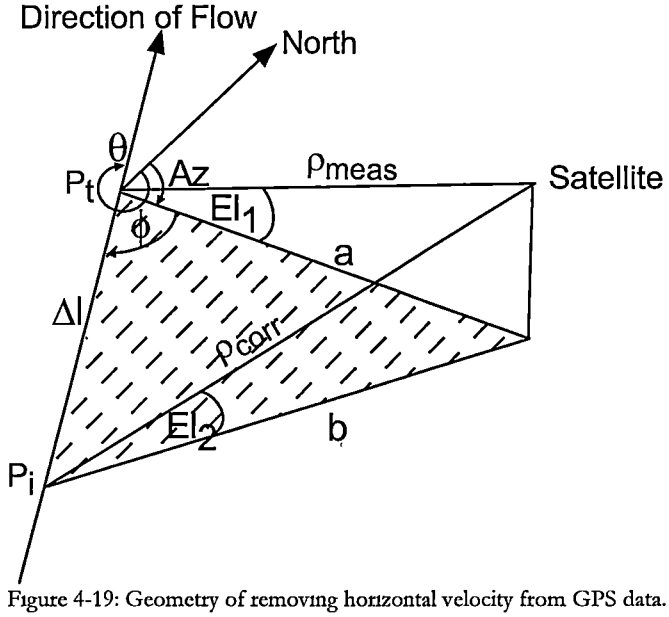

Figure 4-19: Geometry of removing horizontal velocity from GPS data.

Using two applications of the cosine rule and taking advantage of similar triangles, the horizontal velocity-free corrected range for a particular satellite is (in metres):

$$\rho(t)_{corr} = \left[\rho(t)^2_{meas} + (b(t) - a(t))^2 - 2\rho(t)_{meas}(a(t) - b(t))\cos\left(El_1(t)\right)\right]^{\frac{1}{2}} \quad (4.21)$$

where:

$a(t) = \rho(t)_{meas}\cos\left(El_1(t)\right)$

$b(t)^2 = a(t)^2 + \Delta l(t)^2 - 2a(t)\Delta l(t)\cos\phi(t)$

$\phi(t) = \left(Az(t) - \theta + 180°\right)$, if $t > i$ (measurement occurs after the reference epoch), or otherwise, $\phi(t) = \left(Az(t) - \theta\right)$

$Az(t)$ is the observed azimuth of the satellite

$El_1(t)$ is the observed elevation of the satellite

θ is the azimuth of the ice flow

$\Delta l(t)$ is the horizontal distance the ice travels along azimuth θ during time t-i

i is the time of the chosen reference epoch

Using this approach, the GPS signal can be corrected to any given reference epoch. However, since it is convenient we corrected the measurements to a midday epoch (i = 43200s).

It is noted that Equations (4.20) and (4.21) are analogous to the corrections applied when correcting GPS observations for the phase-centre variations of a GPS antenna.

4.4.4 Analysis of results

4.4.4.1 Segmented analysis

Both of the corrections outlined above (i.e., both the horizontal and vertical corrections) were applied to a 34 hour subset of data from site G2 described in Section 4.3.2. The BLTM98 was used for the vertical corrections and the short-term velocities given in King *et al.* (2000) used for the horizontal corrections. A 50 minute phase shift was applied to the BLTM98 to best fit the GPS data. For the purpose of comparison with the original segmented data results, the corrected data was processed in hourly segments. Both the uncorrected and corrected-segmented data were processed according to the method described in Section 4.3.3. Results from the GAMIT solutions were transformed into a local North-East-Up system and are shown in Figure 4-20. The error bars are one sigma formal errors from GAMIT, and are approximately 50mm. The periodic motions in the East-West component of the uncorrected data will not be discussed here as they are the subject of a more detailed explanation to be published elsewhere (personal communication, L. Nguyen, 2001). In brief, these horizontal motions are caused by a failure to resolve the carrier phase ambiguities. The corrected data contains no such signal. These apparent motions disappear upon the successful resolution of the ambiguities, even with the tidal motion present in the data. The jumps at day 21 in the North and East components of the corrected data sets are due to the choice of the reference epoch of midday on the day of observation (i.e., data on day 20 is centred on midday on day 20, while data on day 21 is centred on midday on day 21).

With regard to the vertical correction, it can be seen that the tidal signal is largely removed. The standard deviations of the corrected solution are 90mm for day 20 and 70mm for day 21 in the vertical component. In terms of the horizontal correction, the results are even better, with standard deviations being 27mm (days 20 and 21) in the north component, and 66mm (day 21) and 29mm (day 21) in the east component. After removing the first point from the data set the standard deviation for the east component on day 20 became 28mm. No other significant signs of misfit are evident, showing that the motion of the antenna was constant throughout the day.

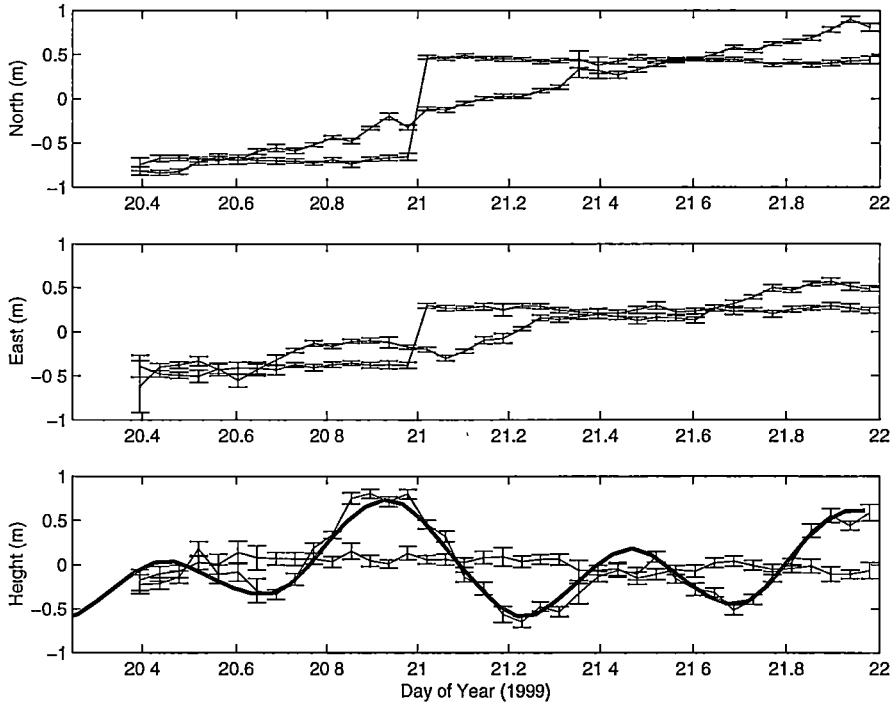

Figure 4-20. Site G2 showing North, East and Up components of motion for both the uncorrected and corrected velocity and tide free data. The BLTM98 is shown in bold in the lower panel. The jumps in the East and North components at day 21 are due to these measurements being relative to noon on the day of observation. Error bars are a only a relative measure of the precision of the GPS estimates

4.4.4.2 Static analysis

In order to test the performance of the 'static' ice site we have processed 10 days of corrected data from site CAMP, this time without segmenting the data (i.e., CAMP has one 24 hour segment per day). The GPS processing was performed as described in Section 4.3.3, although a larger (~20 site) regional network was used. We compare the formal errors of CAMP (from the GAMIT solution) with the formal errors from the same solution of nearby rock site BVLK (see Figure 4-5). Identical receivers were

present at both sites, and therefore receiver noise should be similar at both sites. Since formal errors presented in GPS processing software are a measure of the internal measurement noise, this test should reveal the quality of the corrected 'static' data. Both antennas are clear of multipath surfaces and are mounted on poles at similar heights above the rock/snow. Differences between the multipath environment at the two sites may remain, however, and this might result in some difference in noise between the sites. The 10 day time series of formal errors at both sites are presented in Figure 4-21 in the form of a Box-and-Whisker plot.

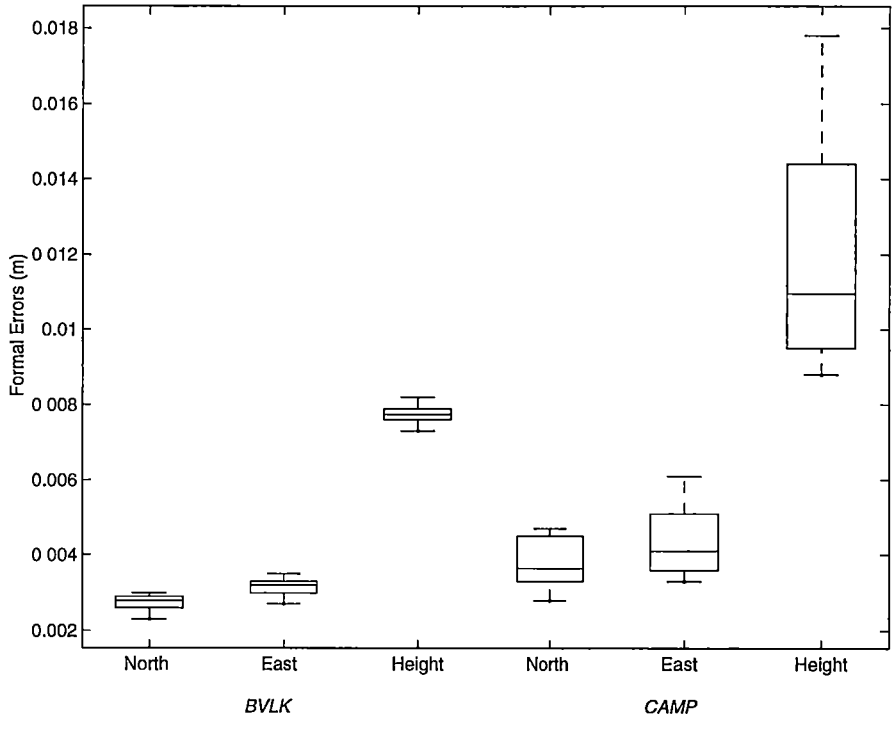

Figure 4-21: Box-and-whisker plot of the GAMIT formal errors from ten daily solutions of BVLK and CAMP data. The CAMP data has been corrected for both vertical and horizontal motion, and so can be regarded as static.

Over the length of the campaign, the mean formal error for BVLK (rock site) was better than that of CAMP (the ice shelf site) in all three North-East-Up components; by 1.1mm in north, 1.3mm in east and 4.6mm in height. The formal errors of the CAMP site were also more variable than the BVLK site. This difference is caused mostly by the misfit of the tide model to the GPS data. Further (although much less) error is introduced by differences between the modelled and measured horizontal velocities. Overall, the agreement between the two sites shows that while there is some

residual noise present in the CAMP data, the velocity and tide-free GPS data does conform to a static GPS processing model.

4.5 Summary

The scientific understanding of sub ice shelf tides is currently somewhat uncertain due to a dearth of *in situ* measurements. Significant advances have been made in our understanding of the tidal dynamics of the cavity below the Amery Ice Shelf as presented in this Chapter, using GPS data collected at sites mainly along the longitudinal axis of the ice shelf. The presence of a tidal signal at V5 (~73°S) confirms that the ice shelf is floating well to the south of the previously common-held position of the grounding line. This position is in line with that predicted by Robin (1979) and shown in Fricker *et al.* (2001a). This data also reveals that an amplitude increase exists in the diurnal constituents from the front to the back of the ice shelf, mainly due to a reduction of the water column thickness as the site gets close to the ice shelf grounding zone.

Several days of HWDT data were processed using both a kinematic and static methodology. A comparison revealed a close agreement between the heights determined using the two techniques. The results from the kinematic processing showed no sign of high frequency oscillations caused by ocean swell interaction with the ice shelf front, as found on the Ross Ice Shelf, although this may be a result of the proximity of the sites to the coast.

Comparing our results for sites C2-C12 in 1995 against those shown in Phillips *et al.* (1998) show a similar level of agreement with the Beaver Lake tide model, although with twice as many data points. This is due to the choice of a one hour processing interval. The identification of a ~1 hour phase shift on the AIS compared with Beaver Lake may have an impact on the validation of the ERS-derived DEM of Phillips (1999). Median one hour tide changes during the time of this campaign are ~0.1m, with maximum changes of ~0.4m.

Furthermore, comparisons with ocean tide models show a good level of agreement with the constituents derived from the GPS data using the harmonic method. The response method did not work effectively on our short data sets, although provided

good agreement with the harmonic method for the longer time series at CAMP and especially HWDT. The GPS data at HWDT has been integrated into the CADA model, contributing to a better understanding of regional Antarctic tides.

If results from ice shelf GPS observations over multiple epochs are to be compared or combined they must be referred to the same reference system. A method has been presented that allows the removal of horizontal and vertical tidal motions from raw GPS measurements. This allows the processing of the data as if collected on a static surface, with only a small reduction in precision when compared to a nearby GPS site located on rock.

Improved understanding of sub ice shelf tides is vital if the current and forthcoming generations of remote sensing satellites (e.g., ICESat, CryoSAT, etc) are to be used to their highest potential. Improved sub ice shelf tides are vital if accurate ocean loading corrections are to be made to these measurements. For example, this is not presently possible for the long-period tides at the South Pole (Bos *et al.*, 2000). Given the large coastal area occupied by ice shelves, improvements in the modelling of sub ice shelf tides will significantly increase the precision of these models. The work outlined in this Chapter is of significant value in advancing our knowledge of Antarctic tides, and hence to future satellite measurements.

Chapter 5

THE VELOCITY OF THE AMERY ICE SHELF FROM GPS AND TERRESTRIAL DATA

The aim of this Chapter is to present the entire set of AIS velocities, determined from space geodetic and terrestrial data collected over a period exceeding three decades, in a consistent reference frame. While velocity results from a subset of these measurements have been presented previously (Budd *et al.*, 1982; Phillips, 1999), they have not all been analysed in a rigorous manner. An example is the traverse misclose identified in Chapter 3. Rigorous estimates of precision were also not presented alongside the estimates of the position and velocity from this traverse. Furthermore, the processing of the GPS data has largely been inferior to the method we describe. We also present results within a modern global terrestrial reference frame, in contrast to the previous *ad hoc* adoption of reference frames.

Firstly, the terrestrial traverses observed during 1968-70 are re-analysed. The source of the large misclose reported in Chapter 3 is investigated. Position and velocity estimates are then presented, along with first estimates of their respective precisions. Secondly, all of the tripod-based GPS data[1] collected to date on the AIS is analysed within the context of a global terrestrial reference frame. Velocities determined using both techniques are then compared to determine if any change has occurred in the surface velocity of the ice shelf during the period between the terrestrial and GPS measurements. Furthermore, we compare these velocity results with velocity estimates obtained from a remote sensing method. We also perform a statistical test to determine if the surface velocity profile of the ice shelf has changed during the period of observations (1968-1999). Such a change would be an indicator for ice shelf response to climate change.

1. That is, the GPS data where the GPS antenna was stationary relative to the ice shelf surface at that location.

5.1 Velocity determination

5.1.1 Terrestrial data (1968-70)

5.1.1.1 Traverse analysis

The traverse and rock reference stations are shown in Figure 5-1. Only a part of the traverse information survives in the form of raw field measurements. Most of the remainder of the original survey data are in the form of reduced angles and distances, although some of this information is also missing. All of the observations required for the traverses are in the computer output derived from the original reductions. These reductions were performed using the 'reduction-to-epoch' method, described by Dorrer *et al.* (1969), as implemented in software written at the Australian Antarctic Division (personal communication, M. Corry, 2000).

Traverse surveys were performed using standard National Mapping Antarctic practice - six rounds of horizontal directions with a rejection criterion of eight arcsecs variation from the first observation. The star azimuth measurements were conducted using three observations on each face to both the star and reference object. Due to the difficulty in obtaining good star observations, no rejection criteria were specified for this observation type. For distances, two coarse readings and eight fine readings were taken on the MRA3 Tellurometer in one direction only. The rejection criterion for the distance measurements is unknown. With regard to the precision of the observations or coordinates derived from the traverse, little information exists. Coordinate precisions are not listed in the publications relating to the survey, nor is there any mention of expected precisions for angles, distances or astronomical observations. AUSLIG, in their recent Antarctic network adjustments, have used four arcsecs standard deviations for directions and 50mm + 5ppm for distances (personal communication, G. Johnston, 1999). Adopting these values for the 1968-70 surveys, fixing one end of the traverse and propagating throughout the network suggests that up to 20 metres error may exist in the coordinates of the network stations at the other end of the traverse.

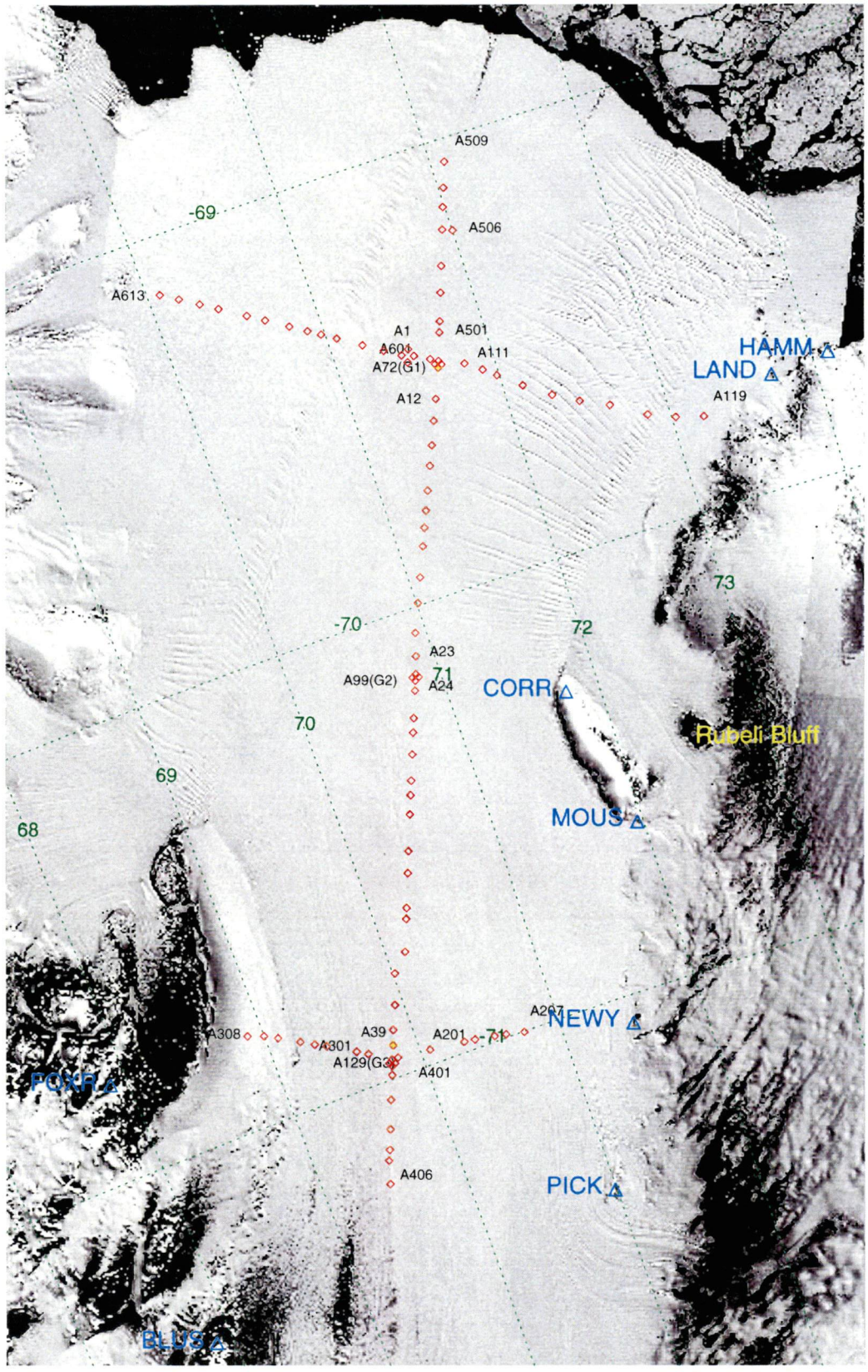

Figure 5-1: The Amery Ice Shelf traverses 1968-70. The ice shelf sites are marked in red. The sites where large angular miscloses were located are shown with a yellow plus sign. Shown in cyan are the traverse reference sites – LAND (Landing Bluff), HAMM (Hamm Peak), CORR (Corry Rocks), MOUS (Mousinho Rock), NEWY (New Year Nunatak), PICK (Pickering Nunatak), BLUS (Blustery Bluff/Cliffs) and FOXR (Fox Ridge). The ice shelf front shown in the satellite image mosaic (produced from separate images collected between 1988 and 1992) is significantly further north than was the case during the 1968-70 survey; station A509 was only 15-20km south of the ice shelf front at this time.

Since three ice sites at the south-western extent of the traverse are located on grounded ice (A306, A307 and A308; see Figure 5-1), a lower bound of the internal precision of the traverse survey may be gained by examining their velocities. The results from the traverse computer output show velocities for these sites of less than 15myr^{-1}. These values appear realistic, given that the velocities in this grounded region are expected to be relatively low (0-20myr^{-1}). This suggests that the traverse is accurate to approximately 5-15myr^{-1} in this region. Since both of the traverses were terminated on known rock sites, the miscloses will further give us an idea of the quality of the surveys.

Unfortunately, these miscloses do not appear to have been investigated at the time of the survey, since a very large misclose exists in the results of both campaigns. Portions of the computer output pertaining to the misclose at Landing Bluff are shown in Figures 5-2 through 5-4. It is somewhat uncertain if this output is the final version, as it was believed that the traverse had closed well when originally reduced (personal communication, M. Corry, 2000). There is no date on the computer output, although software development was conducted over a period of several years after the survey. Regardless, the coordinates and velocities contained in this output are the ones that have been widely used in the Australian Antarctic Division and elsewhere as the final and true record of the traverse survey.

JCT	STATION	HEIGHT DISTANCE	ANGLE DELTA	AZIMUTH	LATITUDE FWD AZIMUTH		LONGITUDE REV AZIMUTH
RO	HAMM PEAK						84 11 42.77
1	LANDING BLUF	119.00	179 1	17.20	S 69 44 35.536	E	73 42 50.152
		20253.69	180 26	27.03	254 12 59.96		74 41 26.99
2	A119	43.88	209 37	11.43	S 69 47 30.728	E	73 12 30.862
		7251.85	180 10	15.02	284 18 30.41		104 28 53.43

Figure 5-2: Output from the computer program that was used to reduce the Amery Ice Shelf traverses. The coordinates shown for Landing Bluff and the azimuth to Hamm Peak were taken from the National Mapping traverse results.

10	A118	44.29	172 50	54.43	S 69 47 36.142	E	5 12 31.933
		7251.85	179 49	46.37	105 11 22.17		285 1 8.54
11	A119	43.88	153 22	55.47	S 69 48 37.121	E	5 23 25.769
		20253.69	179 31	25.41	75 24 4.01		254 55 29.42
12	LANDING BLUF	119.00	189 59	15.50	S 69 45 49.756	E	5 53 52.874
					84 54 44.92	TO	HAMM PEAK

Figure 5-3: Output from the computer program showing the closing coordinate for Landing Bluff in 1969 along with the azimuth to Hamm Peak The longitudes in this output are not relative to Greenwich, in contrast to Figure 5-2. The latitude value, however, can be compared to that shown in Figure 5-2.

10	A118	44.29	174	30	12.17	S	69	47	26.320	E	5 12 56.533
		7089.32	179	50	6.91		107	24	45.06		287 14 46.98
11	A119	43.88	148	33	34.75	S	69	48	34.461	E	5 23 28.486
		28114.70	179	31	34.02		75	48	21.73		255 19 55.75
12	LANDING BLUF	119.50	189	39	18.51	S	69	45	52.697	E	5 53 46.417
							84	59	14.25	TO	HAMM PEAK

Figure 5-4· Output from the computer program showing the closing coordinate for Landing Bluff in 1970, along with the azimuth to Hamm Peak. The longitudes in this output are not relative to Greenwich, in contrast to Figure 5-2. The latitude value, however, can be compared to that shown in Figure 5-2.

For the purposes of determining the traverse miscloses, we use rock site coordinates determined by AUSLIG from a combination of terrestrial and GPS data. The data used to determine these coordinates are independent of the data presented in this thesis.

Figure 5-2 shows the correct coordinates for Landing Bluff as provided by the Division of National Mapping (now AUSLIG) at the time of the survey. Figure 5-3 (1969) and Figure 5-4 (1970) show the closing coordinates for Landing Bluff in these seasons. The longitudes shown in Figures 5-3 and 5-4 are not relative to Greenwich but to some local datum. The reason for this is unknown. Consequently, a comparison cannot be made to the Landing Bluff longitude shown in Figure 5-2. A summary of the miscloses at Landing Bluff and New Year Nunatak (1969 only) are shown in Table 5-1. To allow a comparison of the longitude, we recomputed the traverse using the same values as used in the original reduction although using a different reduction strategy (FONDA software; see Section 6.3.2 for a description). These misclose terms are affected by ice motion during the surveys, since using only one season's data, any motion of the ice shelf cannot be taken into account. The motion of the ice at the traverse station locations would be around 60-90m during the surveys, based on our current knowledge. Notice the very large values for misclose at Landing Bluff, while the misclose at New Year Nunatak is two orders of magnitude less.

The angular miscloses at Landing Bluff and New Year Nunatak to their respective reference sites[2] are shown in Table 5-2. Again, the miscloses are large, although in relative agreement at Landing Bluff between the two seasons. The New Year Nunatak misclose is significantly less, although this may be an indicator of a systematic angular

2. At the final survey mark occupied by the theodolite, angles are turned to another coordinated mark to allow the determination of the traverse's angular misclose.

error in the traverse. Such a systematic error would propagate with distance from Blustery Bluff.

Year	1968-69		1969-70	
Site	Latitude (m)	Longitude (m)	Latitude (m)	Longitude (m)
Landing Bluff	-1923.7	2857.8	-655.3	1752.8
New Year Nunatak	-31.3	-6.8	N/A	N/A

Table 5-1: Miscloses of the Amery Ice Shelf Survey traverse, using Blustery Bluff as the datum and reference site.

Year	1968-69	1969-70
Site		
Landing Bluff (Hamm Peak)	0° 43' 02".15	0° 47' 31".48
New Year Nunatak (Mousinho Rock)	0° 01' 34".59	N/A

Table 5-2: Angular miscloses at Landing Bluff and New Year Nunatak, with their respective reference sites shown in brackets. Blustery Bluff was used as the datum and reference site.

Since the misclose is in the same direction and of a similar magnitude in both campaigns, the most likely scenario is that a systematic error exists in both of the surveys – either at the observation or reduction stage. Some seasonal dependent errors must also exist.

A small part of these miscloses was recently identified in the control traverse conducted by National Mapping along the eastern side of the Amery Ice Shelf in 1969-70. Following recent GPS observations along the traverse route, a one minute angular error measured at Rubeli Bluff (Figure 5-1) in the original traverse was identified (personal communication, G. Johnston, 1999). This error resulted in 55 and 21 metre differences in Blustery Bluff and New Year Nunatak respectively, when compared to those used in the original surveys. Since Rubeli Bluff is to the north of both New Year Nunatak and Blustery Bluff, the angular error at these sites was the same, so the angular misclose at these sites is not altered. The remaining observations from the National Mapping traverse agree to within 0.05-0.1m with GPS observations, where available.

Additionally, the computations of the traverse were conducted on a different ellipsoid to that which the datum coordinates referred. At the time of the data reductions, the National Mapping supplied coordinates for the six reference sites[3] were on the International (Hayford) 1924 ellipsoid. On the other hand, the Amery Ice Shelf Survey distances and bearings were reduced to the International Astronomical Union 1964 ellipsoid[4]. The parameters for these ellipsoids are shown in Table 5-3 (Heiskanen and Moritz, 1967). Since this difference has only a small influence on angles, the difference will largely be seen in the form of a scale-factor. Modifying the Gauss Mid-latitude formulae (Allan *et al.*, 1968) to provide the indirect solution of an ellipsoidal distance, s_{12}, gives:

$$s_{12} = \sqrt{\left(\nu_m \cos\phi_m \Delta\lambda\right)^2 + \left(\rho_m \Delta\phi\right)^2} \tag{5.1}$$

where,

$$\rho_m = \frac{a\left(1-e^2\right)}{\left(1-e^2\sin^2\phi_m\right)^{\frac{3}{2}}}$$

$$\nu_m = \frac{a}{\left(1-e^2\sin^2\phi_m\right)^{\frac{1}{2}}}$$

$$\phi_m = \frac{\phi_1+\phi_2}{2}$$

$$e^2 = 2f - f^2$$

a, f are the relevant ellipsoidal semi-major axis and flattening terms respectively.

This assumes that the origins of the two ellipsoids are the same. The ratio of the distance on the incorrect ellipsoid, $\overline{s}_{12}$, to the distance on the correct ellipsoid, s_{12}, is:

$$error = \frac{\overline{s}_{12}}{s_{12}}$$

3. The six reference sites used in the traverse were, Blustery Bluff (NMS147), Pickering Nunatak (NMS146), Fox Ridge (NMS148), New Year Nunatak (NMS145), Mousinho Rock (NMS 144), Landing Bluff (NMS 138) and Hamm Peak (NMS 137). Direction observations were also taken to Corry Rocks (NMS 142) and a Russian Cairn located near NEWY, although they were not included in the original adjustment.

4. This ellipsoid was adopted as the Australian National Spheroid in 1966.

which is at a maximum along an East-West line, and a minimum along an North-South line. This error equates to approximately 48.25ppm at its maximum and 45.25ppm at its minimum in the region of the AIS. Because of this, an error of approximately eleven metres exists in the Amery Ice Shelf Survey. This error needs to be accounted for since a scale factor in the traverse effectively scales the derived strain parameters.

Ellipsoid	Semi-major axis (a) (m)	Inverse flattening ($1/f$)	Year of adoption
International (Hayford) Ellipsoid	6378388.0	297.0	1924
International Astronomical Union Ellipsoid	6378160.0	298.25	1964

Table 5-3: Ellipsoidal parameters of the reference surfaces used in the Amery Ice Shelf Survey reductions.

These two error sources suggest a total coordinate error of 50-60 metres in the traverse. While this error is large it is to be noted that it is approximately two orders of magnitude smaller than the total misclose error! The consequences of this unidentified large error are significant, given that much of the Amery Ice Shelf modelling and mass balance calculations rest on the derived velocity and strain parameters, which were derived from the position estimates. In an attempt to locate and correct the source of the error, a number of avenues were investigated. These included checking the reduction of directions and distances; eccentric corrections, possible site misidentification and typographic errors. The search was made all the more difficult since not all measurements were available in raw form in the field books (see Appendix D).

The source of the misclose (as shown on the computer output) was identified in the form of two large angular errors, plus other smaller errors. The first of the two large errors was a $1°01'$ error in the directions at A39 (see Figure 5-1) in both traverses. The difference between the original field books and the computer output was clear for the 1968-69 traverse. However, the reduced directions in the 1969-70 field books agree with the computer output to within a few minutes. It is not apparent why this disagreement occurs. No other information for these directions exists. Consequently, the 1968-69 value was adopted for the 1969-70 traverse. By comparing inter-season

angle changes, a one arc-minute standard deviation was chosen as a loose constraint on this angle.

The second of the two large angular errors was an 18′ error at A74 (see Figure 5-1) in both traverses. This error was a result of a reversal of forward and backward direction observations. The sum of these two errors was 43′ since the two errors were in opposite directions. One further error of ~5′ was found at A406 in the 1969-70 traverse. Other smaller 1′ differences were also found in the traverses, particularly between A129 (G3) and A99 (G2) due to errors at the data reduction stage.

Following these identifications, the angular misclose at each of the end sites was less than 5′ in both traverses, significantly less than the previous ~43′ shown in Table 5-2. This error is still large, but the adjustment that follows reveals its source.

Further errors have been located in the entry of the time of observation. Most of these are of the order of less than one day and so their effect is small. However, one significant error occurred for the measurements at A508 (directions to A507, A509, and a distance to A509) in 1969. An error in the date of ten months (19/11/69 instead of 19/1/69) resulted in a significantly different direction and lower velocity for A509.

The horizontal directions at A72 to A501 and A601 listed in the field notes are ambiguous, since there is no corresponding observation to the remainder of the traverse (A74). The problem is shown in Figure 5-5. These directions are not listed in the computer output. Rather, what are listed are the directions at A72 to A74 and A501 and the directions at A72 to A74 and A501. These were most likely computed from other direction measurements actually made in the field. Computing the angle between A501 and A601 at A72 from the computer output reveals a conflict with the field notes by several minutes. Thus, one of the directions in the computer output is in error, although the actual angle cannot be immediately identified since we do not have all of the information. Comparing the directions measured in 1969-70 sheds little light, since the differential motion of the stations is so large. The result of the correction will result in either a clockwise swing in the northern leg of the traverse or an anti-clockwise swing in the western leg. This will have a significant effect on the magnitude

(for the western leg) or direction (for the northern leg) of the traverse. This issue will be revisited in Section 5.1.1.3 when the traverse velocities can be further analysed.

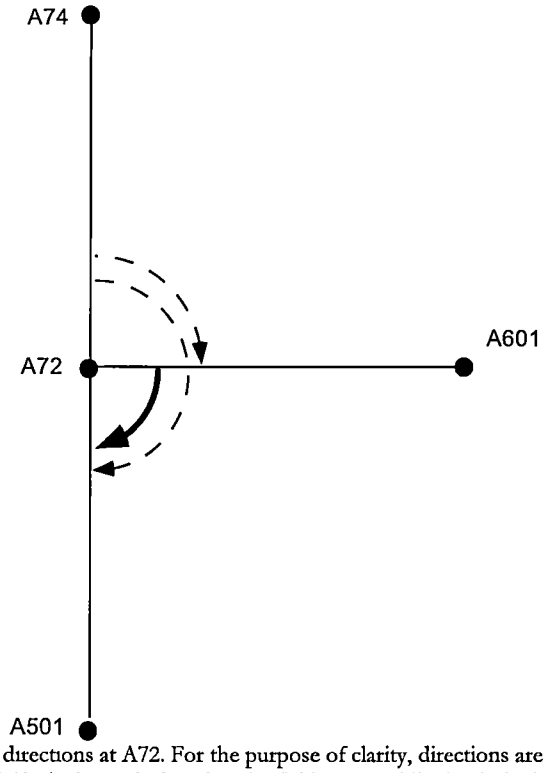

Figure 5-5: The ambiguous directions at A72. For the purpose of clarity, directions are shown as angles. The bold angle between A601 and A501 is the angle found in the field notes, while the dashed angles are those shown in the computer output.

5.1.1.2 Data preparation

5.1.1.2.1 Distance observations

The precision of the Tellurometer MRA3 is 5mm+3ppm as defined by the manufacturers. This appears to be a significant underestimate when used in Antarctica, since AUSLIG have adopted values of 50mm+5ppm. This later length-dependant term agrees with repeatability tests performed in Antarctica (Kirkby, 1965). The difference between the manufacturer's specifications and the values adopted by AUSLIG may be at least partly explained by the poor performance of the Tellurometer over ice (Yaskowich, 1964). Unfortunately, we have no lines where the distances have been measured twice in close succession in this study. We do however have redundant measurements when combined with the directions measured at the strain grids. These suggest that the Tellurometer is performing significantly better than the values used by AUSLIG. However, since there are so few of these measurements, we adopted the AUSLIG observational uncertainties, that is 50mm+5ppm for the AIS measurements.

For the eccentric corrections, we have adopted an uncertainty of 20mm. Angular observations were taken directly to the pole at the remote site, and consequently angular eccentric corrections need to only be applied at the master stations.

For distance measurements, both the Tellurometer master and the remote were usually eccentric to the ground mark. Corrections were applied to these distances as required. The Tellurometers were erected some three metres above the snow surface, with a measurement made to the nearest pole joint at both ends. Since the height of the first joint above the snow and the length of the pole sections were known, the height of the instrument above the snow was then deduced. Unfortunately, these heights are not amongst the field notes found to date, but this does not introduce significant errors. If the heights of instrument of the master and remote stations are within one metre of each other (a likely scenario), and both instruments are approximately three metres above the surface, only negligible errors are introduced into the mark-to-mark distances. Since our adjustment is a true three-dimensional adjustment, we use the mark-to-mark distances, rather than reducing them to the ellipsoid surface, which was the previous practice.

Taped distances were measured at each of the strain grids. These measurements would have provided an excellent check on the performance of the Tellurometer. Unfortunately, these measurements have not been located in the field notes or the computer output. See Chapter 6 for more details of the strain fields of the AIS.

5.1.1.2.2 Angular observations

As mentioned above, AUSLIG have adopted an observation standard deviation of four arcsecs for reduced directions observed in Antarctica. It is not expected that the AIS surveys would achieve this precision since observation conditions were not always favourable, with frequent near whiteout conditions, poor footing for the instruments and much colder conditions than on the rock sites. With rejection criteria of eight arcsecs used for the AIS surveys, the internal precision for one set of directions is obviously less than the AUSLIG value. However, by comparing reduced angles from different observing sets, a more realistic estimate of observation precision may be obtained. Finding a suitable set of observations to compare is somewhat complicated by the motion of the ice. Observations need to be made within a few days to prevent

any systematic bias entering the comparison. One such set of observations occurs at G3 within a few days of each other. The agreement is better than 0.5″. The internal reliability of the angles may also be assessed by examining the sum of the internal angles of the strain grids at G3, G2, G1, and A1. For the 1968-69 strain grids, the value of the term (sum-360°) are 4.8″ (G3), 10.3″ (G2), -2.9″ (G1) and 13″ (A1), suggesting the individual reduced directions are accurate to ~1-3″. These results for G1 are from a second measurement of this strain grid, since the first measurement yielded a ~6′ misclose. Only the G3 strain grid had all the internal angles measured in 1969-70, with a result of -26.6″, or ~7″ per angle. Since the eccentric measurements were made only to the nearest centimetre, and often several degrees in direction, there may be as much as 3″ additional error in many measurements. We thus choose 4″ as the precision of the reduced directions. In some cases, where less than six sets of directions were measured, we reduced this direction precision value to 12″. Further cases are down-weighted due to uncertainties in their eccentric measurements or poor visibility (when recorded in the field notes) at the time of the measurements. The latter problem is particularly the case during early 1968.

Each of the directions was observed at eccentric sites, normally within one metre of the ground mark. The reduced angles were corrected for this eccentricity using the standard methods (Clark, 1963). Other corrections, such as the deflection of the vertical, skew normal and geodesic corrections (Bomford, 1962) are small (typically 1″, 0.001″ and <<0.001″, respectively, in this region and over these distances), and are ignored since their magnitudes are well below the precision of the survey.

5.1.1.2.3 Astronomical observations

A variety of astronomical observations were made:

- Sun observations for latitude and longitude determination
- Sun observations for azimuth determination
- Star observations for latitude determination
- Star observations for azimuth determination

Star observations for azimuth determination make up by far the majority of measurements. The star observations for latitude determination were made when the

stars were near the local meridian. Typical precisions for this method are 4-5″ of latitude (~120-150m; Clark, 1963). Sun observations for latitude and longitude are imprecise, and hence are approximate only. It was decided to use only the star observations for azimuth, although the knowledge of the station latitude is required for the computation of azimuth. This choice was made since the other observations are difficult to decipher in the field notes, and the determinations of latitude and longitude are poor in terms of precision when compared to the angle and distances.

Some justification for the use of the astronomical azimuths is required since the astronomical azimuths are significantly less precise than the direction measurements (see below). These astronomic observations served two purposes in our analysis. Firstly, they provide an independent check on the direction measurements. Without these measurements, there would be almost no angular redundancy in the traverse. By propagating the direction errors along the traverse to G1, G3 and especially G2, it can be seen that the astronomic azimuth observations are of similar precision to the direction control at these locations. Secondly, and because of this, these astronomical azimuths helped identify the angular errors present in the initial reduction of the traverse. These angular errors are discussed further below.

The azimuths are determined from timed azimuth observations of stars. This method involves recording the horizontal circle reading at a reference object (RO) and a star. The time of observation to a star is read off a clock. The error in the clock can be deduced from the station's latitude and radio time signals. The azimuth A of the star is computed from the known latitude ϕ, the known star's declination δ and the hour angle t deduced from the observed clock time (Bennett and Freislich, 1979), as shown in equation (5.2).

$$\tan A = \frac{-\sin t}{\tan \delta \cos \phi - \sin \phi \cos t} \tag{5.2}$$

The declination is determined from a suitable star catalogue, such as the Star Almanac for Land Surveyors or the FK4/5 catalogues. By differentiating, the relationship between errors in the above quantities dA, $d\phi$, $d\delta$, dt, the star altitude h and the parallactic angle w is:

$$dA = \sec h \cos\omega \cos\delta dt + \tan h \sin A\, d\phi + \sec h \sin\omega d\delta \tag{5.3}$$

However, the declinations may be regarded as error free for our work, and so the effect on the azimuth of errors in the observations is:

$$dA = \sec h \cos\omega \cos\delta dt + \tan h \sin A\, d\phi \tag{5.4}$$

Using Equation (5.2) we can determine the astronomic azimuth for each of the stars observed in turn, and hence the astronomic azimuth of the RO. For our purposes, however, a geodetic azimuth is required. This may be derived using the standard Laplace equation (Bomford, 1962):

$$\begin{aligned} A_G &= A_A - \eta \tan\phi \\ &= A_A - \left(\lambda_A - \lambda_G\right)\sin\phi \end{aligned} \tag{5.5}$$

where λ denotes longitude, η the deflection of the vertical in the prime vertical and subscripts G and A refer to geodetic and astronomic azimuth, respectively. The conversion between astronomic and geodetic azimuth thus relies on a knowledge of η or both λ_A and λ_G. A value for η may be derived from an appropriate global geopotential model, such as EGM96 (Lemoine *et al.*, 1996), although such models have significant errors in Antarctica. Alternatively, values for λ_G can be derived from the traverse data, while λ_A is available from the sun observations. The initial observations by Max Corry were reduced using the later method since no geopotential model was available at the time. The method implemented was the 'Ney method' for geodetic azimuth. Unfortunately, a reference for this method has not been found. However, it is believed that the Ney method is a simple variation of the well-known Black method for geodetic azimuth determination in high latitudes described, for example, in (Bomford, 1962). This method is described briefly below.

Black's method involves the simultaneous computation of the two deflection terms and the Laplacian correction term when three or more stars are observed (Black, 1951). Robbins (1969) extended this method to use weighted (by star altitude h) observation equations:

$$\left(A_i - \overline{A}\right)\cos h_i = \alpha \cos h_i - \sin h_i \left(\xi \sin A_* + \eta \cos A_*\right)_i + \left(\cos h_i \tan h_R \left(\xi \sin \overline{A} + \eta \cos \overline{A}\right)\right) \quad (5.6)$$

where suffix i refers to the ith star

suffix R refers to the RO

A_* is the azimuth of the star computed using Equation (5.2)

A_i is the azimuth of the RO as computed from the ith star

$\overline{A}$ is the arithmetic mean of all A_i

A is the geodetic azimuth of the RO $= \overline{A} + \alpha$ where $\alpha = A_G - A_A$.

A least squares solution is then made to find α, ξ (the deflection of the vertical component in a direction perpendicular to the prime meridian) and η. Unless the RO is at a considerable elevation, the last term of the left-hand side will be very small and may be neglected. Following this reduction, the azimuths were corrected for the differences due to the measurement station being eccentric to the ground mark.

Thus, we have two independent methods of determining geodetic azimuth from astronomic azimuth. A comparison of the deflection terms (ξ, η) and corrections (α) obtained from each of the methods (Table 5-4) for the 1968-69 star observations reveals a poor level of agreement. The α values derived from the EGM96 deflection terms vary more dramatically than the values for Black's method, due to the high variability of η in the EGM96 model. This suggests that the Black values may be more reasonable, although the accuracy of the EGM96 model in this region is unknown. The difference between Black values for G1 and A1 is too large, given that the sites are separated by just 10km.

Site	RO	EGM96			Black		
		ξ (")	η (")	α (")	ξ (")	η (")	α (")
A129 (G3)	A131	-36.6	50.6	146.7	3.5	-13.3	7.9
A99 (G2)	A98	-15.7	0.1	0.3	75.8	-29.2	37.7
A72 (G1)	A74	-11.3	18.9	50.6	6.3	-8.3	27.4
A1	A11	-14.3	22.9	61.0	-34.4	21.5	6.1

Table 5-4. Comparison of geodetic-astronomic corrections for 1968-69 star observations determined using each of the EGM96 geopotential model and Black's method. Units for corrections are arc-seconds.

An estimate of the precision of the mean of the azimuths to the reference objects are obtained by the propagation of direction and timing errors (5.0 arc seconds and 0.5s respectively) (Bennett and Freislich, 1979). Further errors are introduced by the uncertainty in the geodetic position (5m for latitude and 10m for longitude), resulting in mean reference object azimuth precisions of 5-11″. These figures seem low, although they do not include the error due to the lack of plate bubble corrections. Given the unrealistic fluctuations in the figures from Black's method, 20″ was adopted as the precision of these corrections. Eccentric corrections may be in error by as much as 3.0 arc seconds, except for A1 where the eccentric correction is unknown. The eccentric error at this site is set to 30 arc seconds since this is a typical direction correction due to station eccentricity.

For the purposes of the adjustment, we adopted the geodetic azimuths computed using Black's method with a precision obtained from propagating the above errors of ~22″ for G3, G2 and G1, while 37″ was used for A1. These values are for the 1968-69 star observations for azimuth. Unfortunately, records for the 1969-70 star observations are either missing or the ones that have been located only list observations to 2-3 stars and are difficult to decipher and hence are not used.

5.1.1.3 Traverse adjustment

The FONDA software (see Chapter 6; Dong, 1993; Dong *et al.*, 1998), which allows for the time-dependant motion of stations, was used to adjust the traverse observations to produce station coordinates and velocities. The final coordinates are computed at a reference epoch of 1969.5. The parameters were estimated using the observation data and precisions, tightly constraining the positions (20mm in latitude and longitude and 50mm in height) and velocities (1mm/yr) of the surrounding rock sites. The positions of the sites were held in ITRF96, following an adjustment by AUSLIG of the Australian Antarctic Geodetic Network[5]. The AUSLIG adjustment included a combination of GPS and terrestrial solutions held in the AUSLIG database. For the remaining ice sites, horizontal position and velocity components were loosely constrained to their *a priori* solution (1000m and 2000myr^{-1}). Tighter constraints were applied to the vertical components of position and velocity (2m and 0.1myr^{-1}) since

5. The listing and coordinates of these sites may be found at http://geodesy.auslig.gov.au/ngdb/aagn.htm

they cannot be determined from the measurements we have. No further constraints were made at this stage, since the tight constraints on the surrounding rock sites overcomes the network rank defect.

An analysis of the residuals for this over-constrained solution suggested that there was an error of approximately 5′ in the angle entered for A406 in 1969-70. In the analysis of distances and angles discussed in Section 5.1.1.1, this value had been changed to correct a disagreement with the field notes and the computer output. It had been assumed that the computer output was in error. This appears to not be the case, with the adjusted angle being within a few seconds of the angle shown on the computer output. The computed angle for the case of incorrectly observing A404 rather than A405 did not match the value on the computer output. Therefore, there is no existing evidence for the computer output value for this angle. Despite this, we adopt the angle shown in the computer output due to the excellent agreement with the adjusted value, assuming the evidence for this value has been lost.

The 1969-70 angle at A39 that was loosely constrained to the 1968-69 value was adjusted by approximately -50″, well within the bounds of a reasonable adjustment, given that the actual angle is unknown.

The G1 strain grid contained large residuals for both direction and distances when initially adjusted. By analysing the sum of the internal angles, the directions observed at A73 during early 1968 were found to be in error. The error does not appear to have been caused by mis-pointing as the error varies between direction observations, suggesting a possible mis-levelling of the instrument, or other instrumental problems. Consequently, we removed the set of observations at A73 from the data set.

An error in the distance between A72 and A74 was also identified. Unfortunately, the only recording of this distance is on the computer output. According to the computer output, the distance is 1708.7m, with the post-fit residual being 1.1413m. Hence, the adjusted distance is 1707.5587, close to 1707.6m, suggesting a potential gross error in copying the final two digits of the distance from the field books to the punch cards. Given the other errors contained in the computer input, this is particularly plausible. The case for the adjusted value is strengthened by the redundancy in the network at

this point, since the measurement is part of a braced-quad of angle and distance observations. Since its influence on the final coordinates and velocities is not great, we include the corrected observation (1707.6000m) although with its *a priori* standard deviation increased.

The derived velocities shed some light on the ambiguous angle between A501 and A601 at A72 described in Section 5.1.1.1. Adjusting the direction to A501 results in unlikely velocity directions in the western leg. For example, A613 is moving south. Adjusting the direction to A601 results in reasonable estimates of all station velocities. Thus, we adopt this solution.

The value of χ^2 for the final solution was 66.06 with 69 degrees of freedom, so the χ^2 per degree of freedom is approximately unity (0.97). Thus, the different data types fit together well and there are no detectable observation blunders. The histogram of the ratio of residuals (v) to the a priori standard deviations (s) is shown in Figure 5-6 and shows that the residuals are approximately normally distributed in the case of horizontal directions and astronomical azimuths, but not for the distances. Except for a few distances, the residuals on these measurements are close to zero due to the weakness of the network. For the residuals to be normally distributed, the input distance errors need to be better than 1mm+0.1ppm, which is unrealistically tight!

The internal reliability of the network may be assessed by examining the redundancy number (Caspary, 1987) for each of the observations. Briefly, the redundancy number provides a relative measure of the influence of each observation in the network. As with traverses of this type, the values for the AIS traverse are typically less than 0.1. For the horizontal distances, the total of the redundancy number is 0.27, showing that this component of the network has a low level of internal reliability. The total of the redundancy numbers for the horizontal directions and azimuths are only slightly higher at ~6 and ~2, respectively. Consequently, errors in the traverse will not easily be identified and therefore systematic or gross errors may remain undetected.

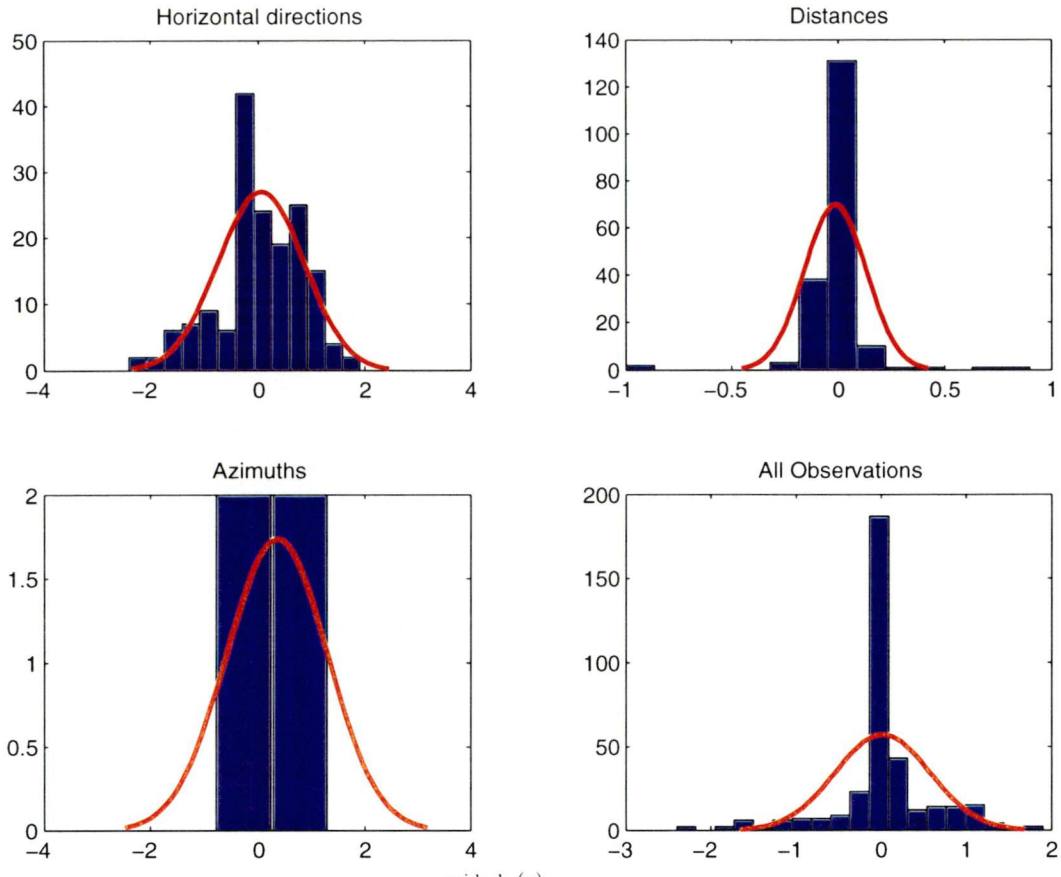

Figure 5-6: Histogram of $\frac{\text{residuals } (v)}{\text{a priori standard deviations } (s)}$ for the different observation types.

Following the over-constrained solution, another solution was computed holding only three rock sites fixed (BLUS, FOXR and PICK). This solution is essentially a minimum constraint solution since both FOXR and PICK were observed in different seasons and the azimuth observations, which are only in the first season, are only weakly constrained in the solution. This allowed a check on the coordinate (Table 5-5) and angular misclose (Table 5-6) of the traverse. As is seen in the tables, the misclose is now small. The results are even more impressive when it is considered that the traverse covers approximately 500km, was on a surface of snow and was performed in extreme conditions.

Site	Latitude (m)	Longitude (m)
Landing Bluff	2.6	2.1
New Year Nunatak	1.5	-0.9

Table 5-5: The coordinate miscloses of the Amery Ice Shelf Survey (combined 1968-69 and 1969-70) traverse from FONDA, using Blustery Bluff as the datum.

Site	Misclose
Landing Bluff (Hamm Peak)	11".5
New Year Nunatak (Mousinho Rock)	5".3

Table 5-6: Angular miscloses from the FONDA solution at Landing Bluff and New Year Nunatak, with their respective reference sites shown, using Blustery Bluff as the datum.

As mentioned above, traverses such as those dealt with here are inherently weak in terms of redundancy. To test the sensitivity of the network to gross errors, angular and distance errors were introduced into the traverse. Firstly, we introduced a 1′ error at the most remote point (A23) in the 1968-69 traverse. Secondly, we introduced a 1m error between A23 and A22, again in the 1968-69 traverse. In both cases, the 1969-70 traverse was unchanged. We introduced both of these errors one-by-one in the context of an over-constrained network. Since the redundancy numbers at these locations are <0.1, it is expected that these errors will go largely undetected.

For the angular error, the residual at A23 increased by only 5″, while the coordinates of A23 moved by approximately 4m. For the distance error, the residual for the length between A23 and A22 increased by 0.11m, while the coordinates of A23 moved by 0.06m. These tests suggest that undiagnosed gross errors may remain in the network, although the small angular miscloses suggest that angular errors are either small or have cancelled. Distance errors of some metres may remain in the network. However, the sizes of the coordinate changes are not significant, even at the weakest point in the network, since a large angular error will induce only small position and velocity biases. For the traverse legs west of G3 and west and north of G1, there is no redundancy and errors cannot be detected. Furthermore, if identical errors were to occur in both traverses, only the positions would be in error; no errors would result in the velocity and strain estimates.

5.1.1.4 Traverse results

By adjusting the traverse using an over-constrained solution described above, site coordinates and velocities and their respective precisions have been derived. The computed velocities are shown in Figure 5-7 in red. For the purposes of comparison, the Corry results are also shown (in yellow) where available. The coordinate and velocities are detailed in Table 5-7 with a reference epoch of 1969.5. Alongside the

results from FONDA are the differences from the results shown in the original Corry computer output. These differences should be interpreted as shifts from the Corry solution to the FONDA solution; if a shift occurs to the North (South) and West (East), the values are positive (negative). Some results are not present in the Corry output, as the measurements for some of the strain grid sites were not included in the version of the computer output we have.

The one sigma coordinate precisions of the network sites have a mean of 0.94m and 0.98m for latitude and longitude respectively. The slightly higher term for the longitude reflects the weakness in the network due to the long North-South section. Similarly, on the East-West lines the precisions of the latitudes are lower than for the longitudes. The weakest solution is for A613 since the traverse west of G1 is a radiation with no redundancy. Even here, the coordinate precision (3.5m and 2.4m for latitude and longitude, respectively) is still very good. The differences between the two sets of results are minimal south of A39 – note that the large angular error was found at A39. North of this site the differences increase rapidly to a maximum of ~4km at the northern-most point (A509). The shift in the position of the A1 campsite is perhaps the most significant as it was the location of the 1968 borehole. The shift is just over 1km to the North and just over 3km to the West.

As can be seen from Figure 5-7, the velocity gradient is smooth, tapering off gradually towards the lateral grounding zones, with a rapid change if the grounding zone is crossed (e.g., between A305 and A306). The velocities of the grounded sites to the West of G3 (A306, A307 and A308) reveal that the velocities are realistic in this region, being effectively equal to zero at the two sigma level. The velocities gradually increase to a maximum of 1075myr^{-1} at the ice shelf front (A509), significantly less than the values in the Corry output, and also the value of >1200myr^{-1} published in Budd *et al.* (1982). It is not known if the Budd *et al.* (1982) results were derived from the same version of the computer output as used here. It is important to emphasise that these results do not represent a change in the state of the ice shelf, but rather a re-analysis of the same data. A strain analysis of these data is presented in Chapter 6.

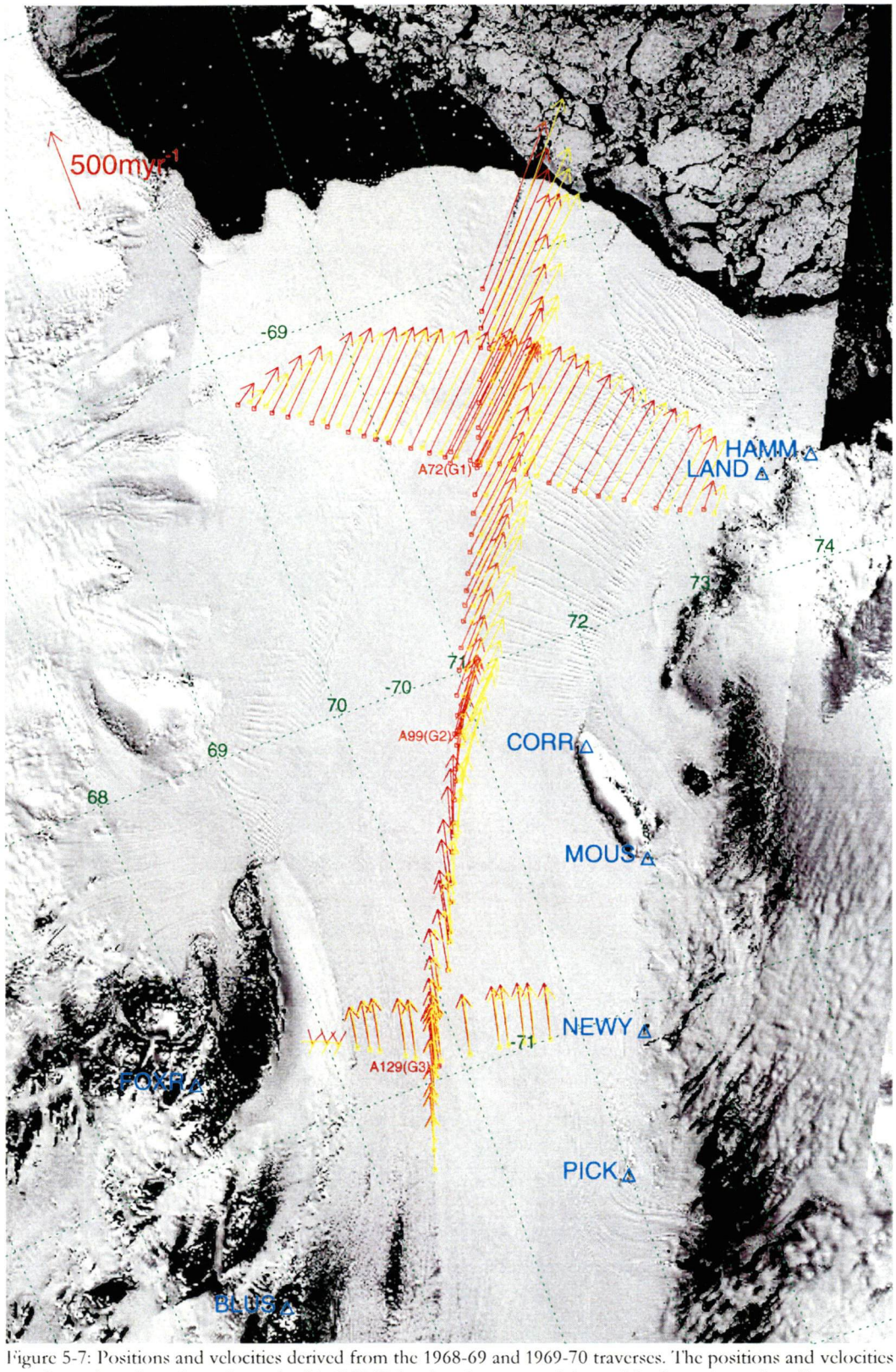

Figure 5-7: Positions and velocities derived from the 1968-69 and 1969-70 traverses. The positions and velocities shown in red are those determined in FONDA using the corrected data, while those shown in yellow are equivalent to those that have been widely circulated.

Figure 5-8 shows the centre-line velocity of the traverse (blue crosses and line) plotted against the distance from the geographical coordinates of A406, the southern-most

point. Error bars are not shown since at this scale they are almost indistinguishable. Again, the velocity gradient appears smooth, with the only deviation to the south of G2 (100km) where a rapid acceleration is followed by a levelling-off of the acceleration. This is perhaps caused by the influx of ice from the west due to flow of the Charybdis Glacier. The values of Budd *et al.* (1982, Figure 4a) have been digitised and are reproduced in the figure in red. The figure highlights the significantly lower velocity north of G1 and a systematically greater velocity in the remainder in the FONDA solution.

Figure 5-9 shows profiles at G1 and G3 as a function of distance from the ice shelf centreline. As mentioned by Budd *et al.* (1982), the profile across G3 conforms to a typical high power-law flow regime of the form:

$$V_y \propto y^{n+1} \tag{5.7}$$

where V_y is the velocity difference from the centreline velocity, y is the distance from the centre line and $n \approx 3$ is the index of the power law for ice flow. The profile across G1, however, does not conform to this regime. Instead, as seen in the figure, it conforms more to a parabolic shape ($n \approx 1$) near the centre, while approaching a $n \approx 3$ power law near the edges. Budd *et al.* (1982) suggests that this is caused by the dominance of the longitudinal strain rate near the centreline at G1, resulting in a higher velocity due to the "addition of the longitudinal stress to the octahedral stress". Our velocity results, although different from those used in Budd *et al.* (1982), support his analysis.

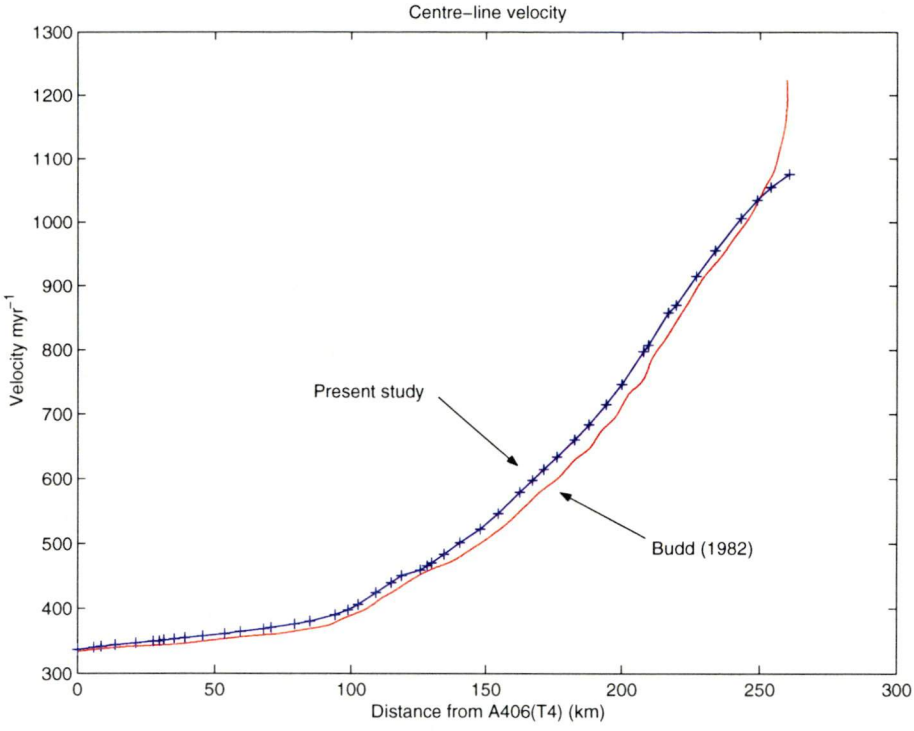

Figure 5-8: Traverse centre-line velocities from FONDA (blue crosses and line) and Budd *et al.* (1982) (red line) plotted against distance from A406.

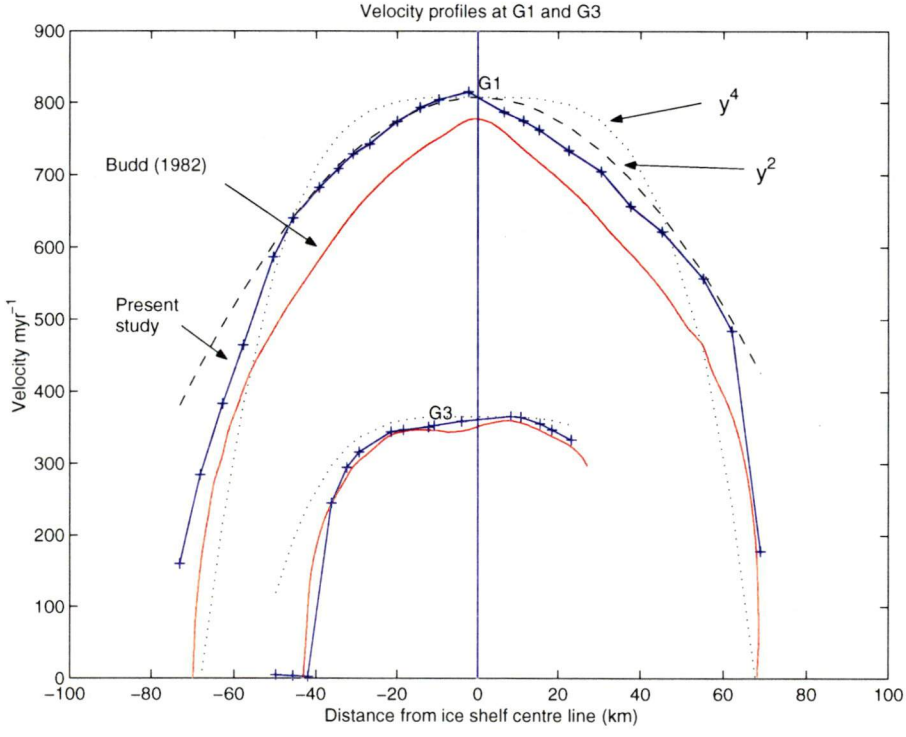

Figure 5-9: Traverse across-ice-shelf velocity profiles through G1 and G3 from FONDA (blue crosses and line) and Budd *et al.* (1982) (red line) plotted against distance from ice shelf centre line. The dotted lines are best-fit estimates of the velocity using $n \approx 3$ in Equation (5.7), while the dashed line shown for the G1 profile is $n \approx 1$.

Table 5-7: The geodetic positions (relative to the GRS80 ellipsoid) and velocities (and their precisions) of the 1968-70 AIS traverse stations derived from FONDA and differences with the Corry computer output as replicated in FONDA. The coordinates are computed at the reference epoch (1969.5). Differences in latitude and longitude should be interpreted as a shift to the North and West in the FONDA solution if the values are positive Some data is not available (N/A) since not all the sites are present in the computer output.

Site	Location	FONDA		Corry-FONDA		Precision		FONDA		Corry-FONDA		Precision	
		Latitude (ϕ)	Longitude (λ)	$d\phi$ (m)	$d\lambda$ (m)	$1\sigma_\phi$ (m)	$1\sigma_\lambda$ (m)	$V_{Magnitude}$ (myr^{-1})	$V_{Direction}$ (°)	$\Delta V_{Magnitude}$ (myr^{-1})	$\Delta V_{Direction}$ (°)	$1\sigma_{Mag}$ (myr^{-1})	$1\sigma_{Dirn}$ (°)
A406	South of G3	S 71 13 26.14237	E 69 28 10.44639	-1	-1	0.7	0.4	336.27	17.30	3.3	-0.4	1.36	0.14
A405	South of G3	S 71 10 21.37845	E 69 31 8.88787	-1	-1	0.7	0.4	339.83	16.24	3.8	-0.4	1.38	0.15
A404	South of G3	S 71 8 59.03726	E 69 33 5.76142	-1	-1	0.7	0.4	341.49	15.73	3.5	-0.4	1.39	0 15
A403	South of G3	S 71 6 22.31406	E 69 36 23.20245	-1	-1	0.7	0.5	343.90	14 83	3.9	-0.5	1.40	0.17
A402	South of G3	S 71 2 35.30715	E 69 40 56.80103	-1	-2	0.7	0.5	346.87	13.72	3.9	-0.4	1.42	0.20
A401	South of G3	S 70 59 26.72532	E 69 45 4.30868	-2	-2	0 7	0.6	349.68	12.83	3.9	-0.4	1.44	0.23
A129	G3 (A129)	S 70 57 26.92611	E 69 47 22.43326	-2	-2	0.7	0.7	351.24	12.27	4.2	-0.3	1 45	0.24
A130	G3 strain grid	S 70 58 4.62995	E 69 48 0.19323	-	-	0.7	0.7	351.36	12.41	-	-	1.45	0.24
A131	G3 strain grid	S 70 58 17.18730	E 69 46 24.62209	-2	-2	0.7	0.7	350.35	12.50	4.4	-0.4	1.45	0.24
A132	G3 strain grid	S 70 57 47.50925	E 69 45 38.35657	-	-	0.7	0.7	349.99	12.42	-	-	1.46	0.24
A201	East of G3	S 70 57 28.26905	E 69 49 57.68631	-2	-2	0.7	0.7	352.53	12.19	4 5	-0.4	1.44	0.24
A202	East of G3	S 70 58 0.13638	E 70 4 3.46357	-3	-2	0.7	0.7	358.84	11.93	4.8	-0.4	1.42	0.24
A203	East of G3	S 70 58 33.86941	E 70 18 49.47089	-3	-2	0.7	0.7	365 72	11.66	4.7	-0.4	1.43	0.23
A204	East of G3	S 70 58 45.29281	E 70 23 19.24727	-4	-2	0.7	0.7	364 59	11.63	4.6	-0.4	1.43	0.24
A205	East of G3	S 70 59 12.96586	E 70 31 38.04778	-4	-2	0.7	0.7	356 12	11.77	5.1	-0.4	1.40	0.24
A206	East of G3	S 70 59 33.20022	E 70 36 41.67722	-4	-2	0.7	0.7	347.20	12 19	5.2	-0.4	1.36	0.25
A207	East of G3	S 71 0 6 42183	E 70 44 40.10636	-5	-2	0.6	0.7	333.31	12 71	6.3	-0.4	1.26	0.26

Site	Location	FONDA		Corry-FONDA		Precision		FONDA		Corry-FONDA		Precision	
		Latitude (ϕ)	Longitude (λ)	$d\phi$ (m)	$d\lambda$ (m)	$1\sigma_\phi$ (m)	$1\sigma_\lambda$ (m)	$V_{Magnitude}$ (myr^{-1})	$V_{Direction}$ (°)	$\Delta V_{Magnitude}$ (myr^{-1})	$\Delta V_{Direction}$ (°)	$1\sigma_{Mag}$ (myr^{-1})	$1\sigma_{Dirn}$ (°)
A301	West of G3	S 70 55 35.27819	E 69 38 38.81516	-1	-2	0.8	0.7	346 76	12.07	1.8	-0.5	1.49	0.26
A302	West of G3	S 70 54 42.78209	E 69 34 19.6036	-1	-3	0.8	0.8	343.98	11.83	0.0	-0.7	1.53	0.27
A303	West of G3	S 70 52 34.62091	E 69 23 13.24539	-1	-3	0.9	0.9	315.74	11.05	-4 3	-1.0	1.73	0.33
A304	West of G3	S 70 51 47 22513	E 69 18 50.79847	-1	-3	1.0	0.9	294 37	10.13	-5.6	-1.1	1.85	0.36
A305	West of G3	S 70 50 43.96114	E 69 13 25.25913	0	-3	1.1	1.0	245 03	8.41	-7.0	-1.6	2 01	0.46
A306	West of G3	S 70 49 7.68005	E 69 5 13.48028	0	-3	1.3	1.1	1.51	197.07	-10.5	146.6	2.31	82.18
A307	West of G3	S 70 48 11.23324	E 68 59 56.10895	0	-3	1.5	1.1	2 81	207.18	-10.2	159 4	2.49	47.27
A308	West of G3	S 70 47 22.86417	E 68 53 24.89868	0	-4	1.6	1.2	4.39	213.52	-9.6	170.8	2.72	32.96
A39	G3-G2	S 70 55 39.59867	E 69 49 49.30568	-2	-2	0.7	0.7	353.05	11.79	4.1	-0.4	1.46	0.26
A38	G3-G2	S 70 53 40.97372	E 69 52 4.63246	24	74	0.7	0 7	354.69	11.42	4.0	-0.4	1.44	0.25
A37	G3-G2	S 70 50 32.48939	E 69 56 24.56032	74	194	0.7	0.8	357.39	10.88	3.9	-0.4	1.44	0.26
A36	G3-G2	S 70 46 28.84639	E 70 0 52.81942	126	349	0.7	0.9	361.28	10.39	3.8	-0.4	1.46	0.28
A35	G3-G2	S 70 44 12.28208	E 70 7 58.16447	207	435	0.8	1.0	364.15	10.29	3.2	-0.3	1.51	0.30
A34	G3-G2	S 70 39 59.89798	E 70 13 6.71995	266	594	0.8	1.1	368.67	10.46	3.7	-0.3	1.57	0.33
A33	G3-G2	S 70 38 36.19895	E 70 14 48.55152	286	647	0 8	1.2	370.33	10.64	3.3	-0 4	1.59	0 34
A32	G3-G2	S 70 34 12.11887	E 70 20 8.32678	347	812	0.9	1.3	376.02	11.56	4.0	-0.2	1.65	0.36
A31	G3-G2	S 70 31 24.82089	E 70 23 29.62377	386	916	0.9	1.4	380.33	12.59	4.3	-0.4	1.70	0.37
A30	G3-G2	S 70 26 45.46060	E 70 29 3.82563	451	1089	0.9	1 6	390.22	15.39	4.2	-0.4	1.78	0.39
A29	G3-G2	S 70 24 19.16397	E 70 31 58.02611	484	1179	1.0	1.6	397.82	17.40	4.3	-0.4	1.84	0.39

Site	Location	FONDA		Corry-FONDA		Precision		FONDA		Corry-FONDA		Precision	
		Latitude (ϕ)	Longitude (λ)	$d\phi$ (m)	$d\lambda$ (m)	$1\sigma_\phi$ (m)	$1\sigma_\lambda$ (m)	$V_{Magnitude}$ (myr^{-1})	$V_{Direction}$ (°)	$\Delta V_{Magnitude}$ (myr^{-1})	$\Delta V_{Direction}$ (°)	$1\sigma_{Mag}$ (myr^{-1})	$1\sigma_{Dirn}$ (°)
A28	G3-G2	S 70 22 27.88982	E 70 34 10 40243	510	1247	1.0	1.6	406.24	19.19	4.2	-0.4	1.88	0.39
A27	G3-G2	S 70 19 5.56802	E 70 38 10.46064	556	1371	1.0	1.7	424.62	23.02	4 6	-0.6	1.96	0.37
A26	G3-G2	S 70 16 17.29673	E 70 41 29.28212	594	1471	1.0	1.7	439.88	26.45	4 6	-1.3	2.04	0.36
A25	G3-G2	S 70 14 26.07736	E 70 43 40.13295	619	1538	1.0	1.7	451.20	28 42	4 2	-1.6	2 08	0.35
A24	G3-G2	S 70 10 54.72182	E 70 47 47.59204	666	1664	1.0	1.7	459.11	31 98	3.6	-1.8	2 14	0.33
A99	G2 (A99)	S 70 9 37.64724	E 70 49 17 45947	684	1711	1.0	1.7	465 62	33.04	3.3	-2 0	2.16	0.33
A98	G2 strain grid	S 70 8 48.49274	E 70 50 20 53631	696	1740	1.0	1.7	469.74	33.74	3.1	-2 0	2.16	0.32
A100	G2 strain grid	S 70 9 6.74034	E 70 48 38.21086	-	-	1 0	1.7	468.69	33.39	-	-	2.17	0.32
A101	G2 strain grid	S 70 9 18.51767	E 70 51 7.35742	-	-	1.0	1.7	467.28	33.42	-	-	2.16	0.32
A23	G2-G1	S 70 6 27.53267	E 70 52 45.83247	723	1822	1.0	1.7	483.87	35.55	3.9	-1.6	2.15	0.30
A22	G2-G1	S 70 3 23.32915	E 70 55 37.42016	755	1927	0.9	1.6	501.48	37.57	5.2	-1.2	2.11	0.27
A21	G2-G1	S 69 59 38.52059	E 71 0 32 19111	809	2056	0.9	1.5	522.72	39 93	6.7	-0.6	2.03	0.24
A20	G2-G1	S 69 56 24.69715	E 71 4 44.80064	856	2167	0.9	1.4	546.63	41.67	8.6	-0.1	1.94	0 21
A19	G2-G1	S 69 52 30.88449	E 71 9 47.07276	912	2299	0.8	1.2	578.77	42.98	10.8	0.5	1.80	0.18
A18	G2-G1	S 69 50 11 45028	E 71 12 46 51401	945	2378	0.8	1.1	597.61	43.83	11.6	0.7	1.71	0.17
A17	G2-G1	S 69 48 2.25536	E 71 15 32.06751	976	2451	0 8	1.0	614 54	44.33	12.5	0.9	1.61	0.15
A16	G2-G1	S 69 45 30.75477	E 71 18 45.50219	1012	2536	0.7	0.9	633.36	44 88	14.2	1.1	1 49	0.13
A15	G2-G1	S 69 42 23.46232	E 71 22 43.38524	1056	2641	0.7	0.8	659.87	45 44	15.9	1.4	1 33	0.12
A14	G2-G1	S 69 39 49 64818	E 71 25 57.95893	1092	2727	0.7	0.7	683.22	45 75	17.2	1.6	1.21	0.10

Site	Location	FONDA		Corry-FONDA		Precision		FONDA		Corry-FONDA		Precision	
		Latitude (ϕ)	Longitude (λ)	$d\phi$ (m)	$d\lambda$ (m)	$1\sigma_\phi$ (m)	$1\sigma_\lambda$ (m)	$V_{Magnitude}$ (myr^{-1})	$V_{Direction}$ (°)	$\Delta V_{Magnitude}$ (myr^{-1})	$\Delta V_{Direction}$ (°)	$1\sigma_{Mag}$ (myr^{-1})	$1\sigma_{Dirn}$ (°)
A13	G2-G1	S 69 36 45.47649	E 71 29 49.6569	1135	2829	0.6	0 5	714.52	45.84	19.5	1.8	1.08	0.09
A12	G2-G1	S 69 33 59.13708	E 71 33 17.22800	1174	2921	0.6	0.5	745.93	45.71	19.9	1.9	1.00	0.08
A72	G1 (A72)	S 69 29 10 9791	E 71 39 0.23661	1235	3073	0.6	0.4	807.47	45.13	20.0	1.8	0.98	0.07
A73	G1 strain grid	S 69 29 26 97366	E 71 37 18.11442	-	-	0.6	0 4	804.20	45.08	-	-	0.98	0 07
A74	G1 strain grid	S 69 30 1.97167	E 71 37 59.35531	1226	3051	0.6	0.4	796.92	45.19	21.2	2 0	0.97	0 07
A75	G1 strain grid	S 69 29 45 0291	E 71 39 37.57689	-	-	0.6	0.4	800.34	45.25	-	-	0.97	0.07
A501	North of G1	S 69 25 31.09819	E 71 42 47.45086	1267	3164	0.6	0.6	857.71	44.66	17.7	4 7	1.07	0.07
A502	North of G1	S 69 24 3.71917	E 71 44 17.17319	1280	3200	0.6	0.6	869.86	44.50	16.9	4.4	1.13	0.07
A503	North of G1	S 69 20 20.34341	E 71 48 5.63737	1312	3293	0.6	0.9	915.08	43.76	14.5	4.0	1.37	0 09
A504	North of G1	S 69 16 50.58938	E 71 51 38.72909	1342	3380	0.7	1.1	954 78	42 99	12.2	3.5	1 65	0.10
A505	North of G1	S 69 12 7.10717	E 71 56 24.36828	1384	3498	0.7	1.5	1006 24	41.72	8.2	2.7	2.10	0.13
A506	North of G1	S 69 12 38.09877	E 72 0 4.83620	1415	3487	0.8	1.5	1016.45	42.16	11.4	2.8	2.12	0.13
A507	North of G1	S 69 9 9.11791	E 71 59 20.87972	1409	3572	0.8	1.8	1034.14	40.76	5.1	2.5	2.40	0.15
A508	North of G1	S 69 6 37.04586	E 72 1 55 20776	1431	3635	0.9	2.0	1054.28	39.78	3.3	2.2	2.67	0.16
A509	North of G1	S 69 3 13.19680	E 72 5 22.78698	1532	3714	1 0	2.4	1075.06	38 12	-152 9	6.5	3.02	0.19
A110	G1-Landing Bluff	S 69 32 11.38757	E 71 54 13.09526	1363	3002	0.6	0.4	774.84	46.21	34.8	1.6	0.95	0.07
A111	G1-Landing Bluff	S 69 30 36.79563	E 71 48 15.11590	1313	3040	0 6	0.4	787.00	45 99	29.0	1.7	0.95	0.07
A112	G1-Landing Bluff	S 69 33 33.16131	E 71 59 3.49637	1404	2969	0.6	0 4	762.78	46 39	40.8	1 6	0.94	0.07
A113	G1-Landing Bluff	S 69 36 0.91680	E 72 7 56.82209	1479	2909	0.6	0.3	733.66	46.64	51.7	1.6	0.93	0.07

Site	Location	FONDA		Corry-FONDA		Precision		FONDA		Corry-FONDA		Precision	
		Latitude (ϕ)	Longitude (λ)	$d\phi$ (m)	$d\lambda$ (m)	$1\sigma_\phi$ (m)	$1\sigma_\lambda$ (m)	$V_{Magnitude}$ (myr^{-1})	$V_{Direction}$ (°)	$\Delta V_{Magnitude}$ (myr^{-1})	$\Delta V_{Direction}$ (°)	$1\sigma_{Mag}$ (myr^{-1})	$1\sigma_{Dirn}$ (°)
A114	G1-Landing Bluff	S 69 38 28.80599	E 72 17 48.58287	1561	2850	0.6	0.3	705.10	46.76	62 1	1.5	0.91	0.08
A115	G1-Landing Bluff	S 69 40 24.34756	E 72 27 25.69161	1642	2805	0.6	0.3	656.75	47.47	71.8	1.4	0.86	0.08
A116	G1-Landing Bluff	S 69 42 10.11757	E 72 38 18.11597	1733	2764	0.6	0 2	622.29	46.63	81.3	1.2	0.80	0.08
A117	G1-Landing Bluff	S 69 44 57.99349	E 72 51 20.95728	1843	2698	0.5	0.2	556.98	44.79	94.0	1.5	0 69	0.07
A118	G1-Landing Bluff	S 69 46 23 81232	E 73 1 36.65297	1930	2666	0 4	0.1	484 80	42 52	102 8	1.8	0.61	0 07
A119	G1-Landing Bluff	S 69 47 25.16936	E 73 12 22.21592	2020	2645	0.3	0.1	177.94	35.07	104.9	20.3	0.53	0.13
A601	West of G1	S 69 28 34.65207	E 71 36 5.64653	1208	3087	0.6	0.5	815.27	44.85	22.3	6.3	0.99	0.07
A1	1968 campsite	S 69 26 50 18625	E 71 25 47.8766	1115	3132	0.7	0.5	803.94	44.21	29.9	5.1	1.13	0.08
A2	A1 strain grid	S 69 26 19.54381	E 71 29 2.56659	-	-	0.8	0.6	814.81	44.29	-	-	1.26	0.09
A3	A1 strain grid	S 69 27 26.55293	E 71 30 22.58502	-	-	0.9	0.5	808.58	44.55	-	-	1.34	0 09
A11	A1 strain grid	S 69 28 0.75144	E 71 27 13.10713	-	-	0.7	0.6	798.08	44.44	-	-	1.25	0.09
A602	West of G1	S 69 25 26.22840	E 71 19 41.86138	1060	3168	0.8	0.6	793.40	43.83	35.4	5.1	1.28	0.09
A603	West of G1	S 69 23 46.36386	E 71 12 27.19122	995	3211	1.0	0.7	774 04	43.52	42.0	5.3	1.51	0 11
A604	West of G1	S 69 21 46.15405	E 71 3 47.20525	917	3263	1.2	0.9	742.59	43.48	50.6	5.4	1.83	0.14
A605	West of G1	S 69 20 32.51894	E 70 58 29.12468	869	3294	1.4	1.0	728.44	43.40	54.4	5 5	2.04	0.16
A606	West of G1	S 69 19 29.04121	E 70 53 55.80802	828	3322	1.5	1.1	708.71	43.22	58.7	5.7	2.25	0 18
A607	West of G1	S 69 18 3.44533	E 70 47 49.40475	773	3359	1.7	1.2	682.00	43.04	65.0	6.0	2 53	0.21
A608	West of G1	S 69 16 8.77807	E 70 39 39.60690	699	3408	2.0	1.4	640.22	42.82	72 2	6.3	2.95	0.26
A609	West of G1	S 69 14 42.81584	E 70 33 29.14814	643	3446	2.3	1.5	586.60	42.80	77.6	7.0	3.28	0 31

Site	Location	FONDA		Corry-FONDA		Precision		FONDA		Corry-FONDA		Precision	
		Latitude (ϕ)	Longitude (λ)	$d\phi$ (m)	$d\lambda$ (m)	$1\sigma_\phi$ (m)	$1\sigma_\lambda$ (m)	$V_{Magnitude}$ (myr^{-1})	$V_{Direction}$ (°)	$\Delta V_{Magnitude}$ (myr^{-1})	$\Delta V_{Direction}$ (°)	$1\sigma_{Mag}$ (myr^{-1})	$1\sigma_{Dirn}$ (°)
A610	West of G1	S 69 12 31.35260	E 70 24 5 58649	558	3503	2.6	1.8	464 12	44.49	88.1	8.9	3.78	0.46
A611	West of G1	S 69 11 3.22001	E 70 17 49.83871	502	3541	2.9	2.0	382.84	46.48	95.8	10.7	4.10	0.62
A612	West of G1	S 69 9 27.06118	E 70 11 0.89444	440	3583	3.2	2.2	284.04	49.63	105.0	14.9	4.42	0.95
A613	West of G1	S 69 7 59.63156	E 70 4 49.01164	384	3621	3 5	2.4	160.20	56.24	111 4	38.5	4.60	1.89

5.1.2 GPS data

5.1.2.1 Processing methodology overview

GPS data spanning more than a decade (1988-1999) are now available on the AIS (see Chapter 3 for individual measurement campaign details). The GAMIT software package (King and Bock, 1999) was used to process the data, producing individual daily solutions of the AIS data. The only exception was the kinematic observations of six 'Corry poles' observed during the 1995-96 field season. These data were processed in the Track kinematic processing package (Chen, 1998). For the GAMIT processing, standard methods were adopted as outlined in Feigl *et al.* (1993) and Bock *et al.* (1997), except where described below. For the older data, the AIS data were analysed within the context of a global network of stations and the satellite orbital motions were estimated. In some cases, however, insufficient global data were available and so the satellite orbits were held fixed at their broadcast values. For the more recent measurements, the AIS data were analysed within the context of a regional Antarctic network and IGS satellite ephemerides were held fixed.

Once individual daily solutions had been obtained, in the form of quasi-observations , they were combined together on a seasonal basis using the GLOBK Kalman Filter software (Herring, 1997). Quasi-observations and the theoretical aspects of GLOBK are described in detail in the following Chapter (see Section 6.3.2.1). In the cases where only regional daily solutions were made, the daily solutions were augmented with quasi-observations from the global IGS network derived at Scripps Institute of Orbitography (http://sopac.ucsd.edu).

Each of these loosely constrained seasonal solutions were then combined together in GLOBK and then transformed into ITRF97 (Boucher *et al.*, 1999) using 7-parameter similarity transformations for each of position and velocity. The occupation details of the AIS sites are shown in Appendix B while details of the GAMIT/GLOBK processing are shown in Table 5-8. The processing is described in detail below, on a season by season basis.

Year	1988-89	1989-90	1990-91	1995-96	1998-99
Global / Regional data source	CIGNET	CIGNET	CIGNET GIG91 SCAR91	IGS	IGS
Number of global sites	8	9	14-28	~60	~100
% of global sites in the Southern Hemisphere	0	0	30-40	~30	~34
Satellites in orbit	7	11	16	25	26
Network extent	Global / Regional	Global / Regional	Global	Regional	Regional
Number of network sites	8/2-6	9/2-7	20-40	~20	~22
Orbit	Adjusted broadcast orbit	Adjusted broadcast orbit	Adjusted broadcast orbit	Fixed IGS ephemeris	Fixed IGS ephemeris
Observable	L3/L1	L3	L3	L3	L3
Tropospheric parameters (per site per day)	1/0	13	13	13	13
Antenna phase centre corrections	None	None	None	IGS elevation model	IGS elevation model
Elevation cut-off	15°/10°	15°	15°	15°	15°
Cleaning	Manual	Automatic	Automatic / Manual	Automatic	Automatic
Ambiguities	Free	Free	Free	Free	Free
Earth tides	Solid Earth	Solid Earth	Solid Earth	Solid Earth	Solid Earth
Typical AIS session length (hrs.)	0.5-1.0	1.5-2.0	1.5-2.0	24-72, 0.1	2-3; 24+
AIS sampling interval (s)	60	60/15	30	30	30
Local rock sites	AU72, DOVE, AV23	AU72, DOVE, AV23	AU72, DOVE, AV23, WOMB	BEAV	BVLK
Tidal Correction	Point correction	Point correction	Point correction	RINEX correction	RINEX correction
Daily solutions combined with	N/A	N/A	N/A	IGS global solution	IGS global solution
Pole Tide	Modelled	Modelled	Modelled	Modelled	Modelled
Estimation of AIS velocities	No	Yes	Yes	Yes	Yes

Table 5-8. Global network and orbit information (section 1), processing details for GAMIT (section 2), observation session information (section 3) and GLOBK (section 4). Correction to a tide-free datum (section 3) for the ice shelf sites was performed either in GLOBK (for observations shorter than 2 hours) or in the RINEX files prior to processing in GAMIT (as described in Chapter 4).

5.1.2.2 1988-91

5.1.2.2.1 Daily Solutions (GAMIT)

The details of AIS observations for 1988-89 are shown in Appendix B, with processing parameters and options shown in Table 5-8. Single-frequency L1 data were collected using a WM 101 receiver (Brunner *et al.*, 1986) with observation lengths no longer than one hour and some as short as 20-30 minutes. Baseline lengths were between 2 and 110km, and consequently with only the C/A pseudo-range and L1 carrier phase observables available, the data were highly affected by the ionosphere. The data therefore required manual cleaning in GAMIT, introducing some subjective influence on the cleaning process. The use of proprietary software, tuned to process single frequency data using an automatic and repeatable algorithm, may have overcome the need for manual cleaning. However, significant difficulties and complexities are introduced when using automatic cleaning techniques. These include:

- Limited control over the cleaning algorithm,
- Enforced use of broadcast ephemeris for pre-IGS (1994) data,
- Over-optimistic variance-covariance matrices (Han and Rizos, 1995),
- The need to construct a more appropriate variance-covariance matrix,
- Transformation of the variance-covariance matrix into a free-network for combination in GLOBK, using S-Transformations (Baarda, 1973), for example.

The advantages of the GAMIT software include advanced automatic and manual editing capabilities, orbit relaxation techniques and a network processing strategy.

The daily solutions were thus processed using two steps. Firstly, the available CIGNET sites were processed together, adjusting both the station and satellite positions. As the CIGNET sites were dual-frequency receivers, the effect of the ionosphere could be removed from these observations. Only eight CIGNET sites were operating during 1988-89, all located in the Northern Hemisphere. Still, it is expected that some increase in orbit precision over the broadcast orbits will be experienced in the Southern Hemisphere, even as far south as Antarctica.

For the global solution, both station and satellite positions were adjusted. Station coordinates were only loosely constrained so as not to rigidly define a particular datum, while still allowing the inversion of the variance-covariance matrix. The Saastamoinen (Saastamoinen, 1972; Saastamoinen, 1973) tropospheric model was implemented, with corrections to *a priori* model values computed at two-hourly intervals. A satellite elevation cut-off angle of 15° was adopted. Ambiguities were not fixed to integer values, that is, a free solution was computed. The effects of solid-earth and frequency dependant tides were accounted for at this stage.

A different approach was taken for the data in the AIS region. The adjusted satellite orbits from the global solution were tightly constrained. A satellite elevation cut-off angle of 10° was chosen to maximise the number of double differences included in the processing. Only 4-5 satellites, of the seven satellite constellation, at most were in view, and each satellite pass was shorter than one hour every day. Tropospheric zenith delay parameters were not estimates due to the low number of redundancies and the residual tropospheric delay was minimal compared to the ionospheric effects. Due to the presence of ionospheric noise, the nrms values of the daily solutions were significantly increased over a typical ionosphere-free (L3) solution. The L1 solutions for these above data had nrms values of ~2-10 L1 cycles. Based on the *a priori* assumption of the precision of carrier phase observations (10mm), the precision of the L1 observations are therefore ~0.4-2.0m. However, it is difficult to compare nrms values from networks using different observation combinations and sampling intervals, since due to the effect of the ionosphere, L1 observations are correlated over longer time periods than L3 observations.

In contrast to the previous season, the 1989-90 AIS data were collected using dual frequency WM102 receivers. Dual frequency observations theoretically allow the removal of the first order ionospheric effects via the ionosphere-free linear combination. As shown in Table 5-8, the number of satellites had increased from seven to eleven since the 1988-89 season, providing greater redundancy in the solution. The available data for 1989-90 are shown in Appendix B.

Approximately two weeks of data were lost from the CIGNET archive beginning day 035, 1990. Unfortunately, this period coincides with the observations of the AIS sites.

In addition, the SCAR90 data set does not coincide with the AIS data. Consequently, the network is unable to sustain a complete orbit relaxation adjustment, and moderate constraints were required on the broadcast satellite orbits. To strengthen the links to the global network, several weeks of global data prior to the AIS campaign have also been included in the combination solution. This data set includes the observations in the Lambert Glacier Basin Survey (Manson *et al.*, 2000), including the DOVE base station used in the AIS survey.

The dual frequency observations allowed the formation and use of the L3 ionosphere-free observable, thereby removing the most significant error source in the 1988-89 L1 data. After 'tuning' the automatic cleaning algorithm to retain shorter data lengths and allow greater ionospheric variability, little manual cleaning intervention was required, except for four days where L1-only solutions were required to achieve satisfactory solutions. Elevation-dependent phase centre models were not used for two reasons. Firstly, there was no model available for the WM102 antenna. Secondly, corrections for the other antennas were not well defined at the time the data was processed.

The AIS observations were again made using WM102 receivers in 1990-91, with some additional measurements made with a dual frequency Trimble 4000SST. The number of global network sites again increased, with a significant boost in sites during part or all of the campaign from GIG91 and SCAR91 observations (Table 5-8). For the first time, a truly global network of sites was available in which to process the AIS data and determine the satellite orbits. A 50% increase in available satellites also served to increase the number of double differences formed.

The data required significant manual cleaning, mainly due to the inability of the WM102 receiver to maintain tracking over long periods. The result was a highly fragmented data set, particularly on L2. This is almost certainly due to an active ionosphere, since the observations from the previous season were not as badly disturbed. The process of manual editing involved restoring data that had been edited out by the automatic cleaner, and fixing cycle slips. This was frequently an iterative process. Even after the manual editing, a maximum of as few as ten continuous epochs per segment was common. Regardless, all of the days could be processed using the L3 observable, except for January 2, 1991, which was processed as L1-only.

5.1.2.2.2 Daily Combinations (GLOBK)

Individual daily solutions were then combined using GLOBK on a seasonal basis (1988-89, 1989-90 and 1990-91). Stations, satellite and earth orientation parameters were adjusted, with only 'light' constraints applied to the solution to prevent the imposition of a reference frame at this stage. L1-only solutions were combined separately from the LC solutions due to the different ways in which the orbital parameters needed to be treated at this stage. The heights of the ice shelf sites were reduced to the pseudo-MSL (tide-free) datum defined by the BLTM98 measurements. Station eccentricities were not recorded for all sites in 1988-89, and so random noise of 1m (north and east) and 1.5m (up) was added where appropriate. Further random noise was added to the height component of the AIS sites due to misfit of the BLTM98 model (100mm).

Since the observation spans were so short, the data were regarded as occurring at a single epoch in time, the mid-point of the data set, rather than treated as continuously moving as described in Chapter 4. Periodic horizontal signals exist in sub-daily estimates of position where linear or periodic motions exist in the data. The presence of periodic vertical signals in the data results in periodic artifacts in the east coordinate component, a bias equivalent to the gradient of the vertical signal. For the AIS tides, this is equivalent to a maximum bias of ~0.3m in the east component for 1hr data segment lengths. Further artifacts of 0.05m exist due to the horizontal motion of the ice. Consequently, we add 0.3m and 0.05m of random noise to the east and north components, respectively. Pole tide corrections (Wahr, 1985) were applied at this stage.

Since some ice sites were occupied twice during the same season, it was possible to estimate horizontal velocities for these sites at this stage. The solution from GLOBK was then stored in the form of quasi-observations and their respective variance-covariance matrices. These results are then combined with the other seasonal solutions as described in Section 5.1.2.4.

The scale of the variance covariance information from GAMIT is dependent on the *a priori* carrier phase precision estimates and the level of the applied constraints (although loose constraints are carried forward). For our solutions, this was standardly set at 10mm. To obtain realistic uncertainties for the final velocities, the GAMIT variance

covariance matrices must be scaled as appropriate for each data set. One way of assessing the true uncertainty is to examine the repeatability of the coordinate determinations for individual sites. For the AIS sites, this is not possible since most sites were occupied only on 2-3 occasions, with the maximum number of occupations being five during the 1988-91 campaigns. Instead, we attempt to mimic the performance of an AIS site by segmenting the rock site DOVE into 1hr segment lengths during the 1990-91 season. Such a simulation is suitable since both the AIS and DOVE data were collected on WM102 receivers in similar geographical locations. Data from only the 1990-91 season were selected since there were few days available in the earlier season where a second nearby base station was in operation. When such a base station was not available, the 1hr solutions were poorly determined or not possible. Other than the segmentation of DOVE, the processing options were the same as described above. In all, 38 1hr DOVE solutions were computed using data spanning nine different days (1990 days 360-364 and 1991 days 10,14 and 25). A weighted-best-fit velocity was removed from the solutions and the wrms and nrms statistics were computed (Table 5-9) from the residuals (Figure 5-10). To mimic the L1-only AIS data, identical solutions were performed except the AIS region data were solved using a L1-only strategy.

	LC		L1	
	wrms (m)	nrms	wrms (m)	nrms
North	0.32	0.70	0.65	1.98
East	0.21	0.58	1.13	3.88
Up	0.27	0.42	1.92	3.99

Table 5-9: Statistics of the LC and L1-only 1hr DOVE solutions.

The nrms values shown in Table 5-9 suggest that the uncertainties from the GAMIT/GLOBK solutions are slightly conservative while the L1-only solutions need to have their uncertainties scaled by a factor of approximately 4 to reflect their actual uncertainty. The DOVE data is not real ice shelf data and therefore there may be some difference in receiver performance on the ice shelf due to multipath and tripod stability. For the L1-only data, there will be differences in our ability to correctly remove outlier data and repair cycle slips (the L1-only data in these tests were derived from the cleaned LC data). Consequently, we deliberately chose conservative values for

the actual scale we apply to the uncertainties. For the LC AIS solutions, we left the uncertainties scaled by a unit weight within the context of the 1990-91 season. For the L1-only solutions, we scaled the variance covariance matrix by 50, equivalent to scaling the uncertainties by approximately 7.

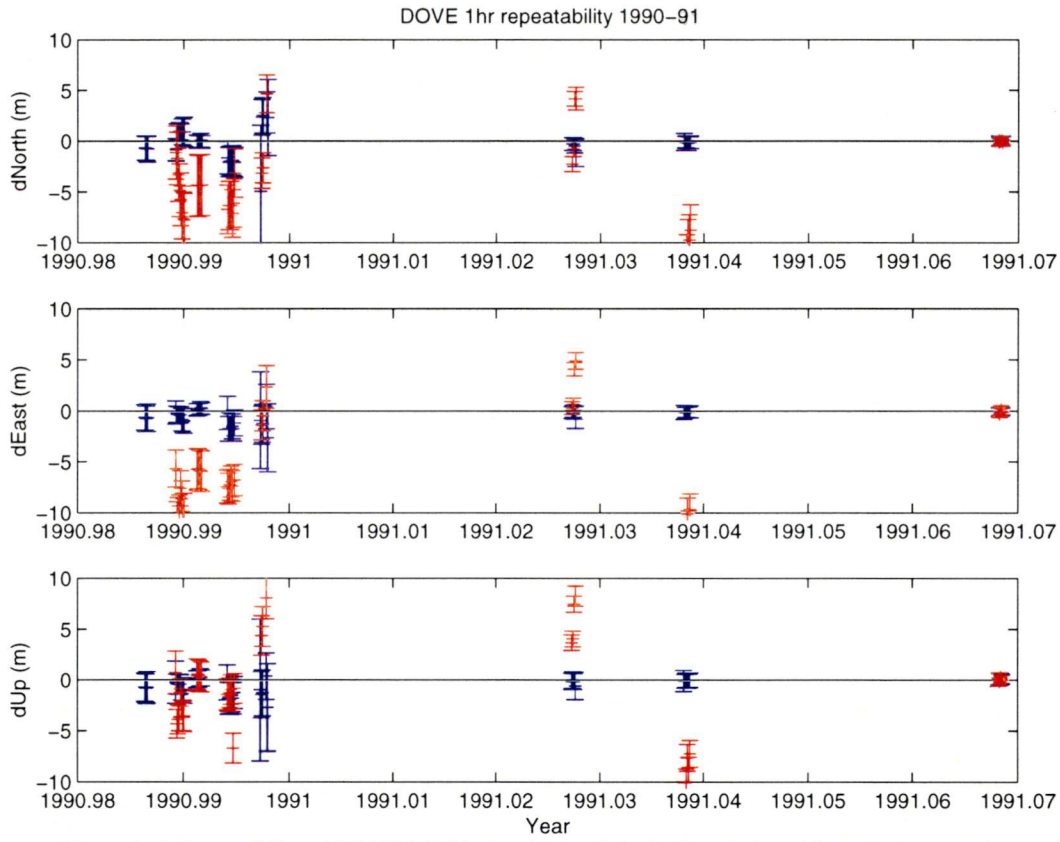

Figure 5-10: Repeatability of DOVE LC (blue) and L1-only (red) 1hr solutions. The error bars are the GAMIT/GLOBK 1σ uncertainties based on 10mm carrier phase uncertainty.

The presence of the GIG91 data in the 1990-91 season meant that two different sampling intervals had been used in the data analysis: GIG91 was sampled at 120s, while the remainder of the solutions were sampled at 30s. Due to the fewer observations in the GIG91 data, the GIG91 uncertainties will be approximately 4 times greater than the non-GIG91 data. To test this, we compared the repeatability of the global sites during GIG91 to the non-GIG91 data (Figure 5-11 and Figure 5-12, respectively). Nrms values are close to unity during GIG91, suggesting that uncertainties are realistic while the non-GIG91 is over-optimistic by a factor of approximately two. Consequently, we scaled the VCV matrices on the non-GIG91 days by four, with the GIG91 data scaled by unity.

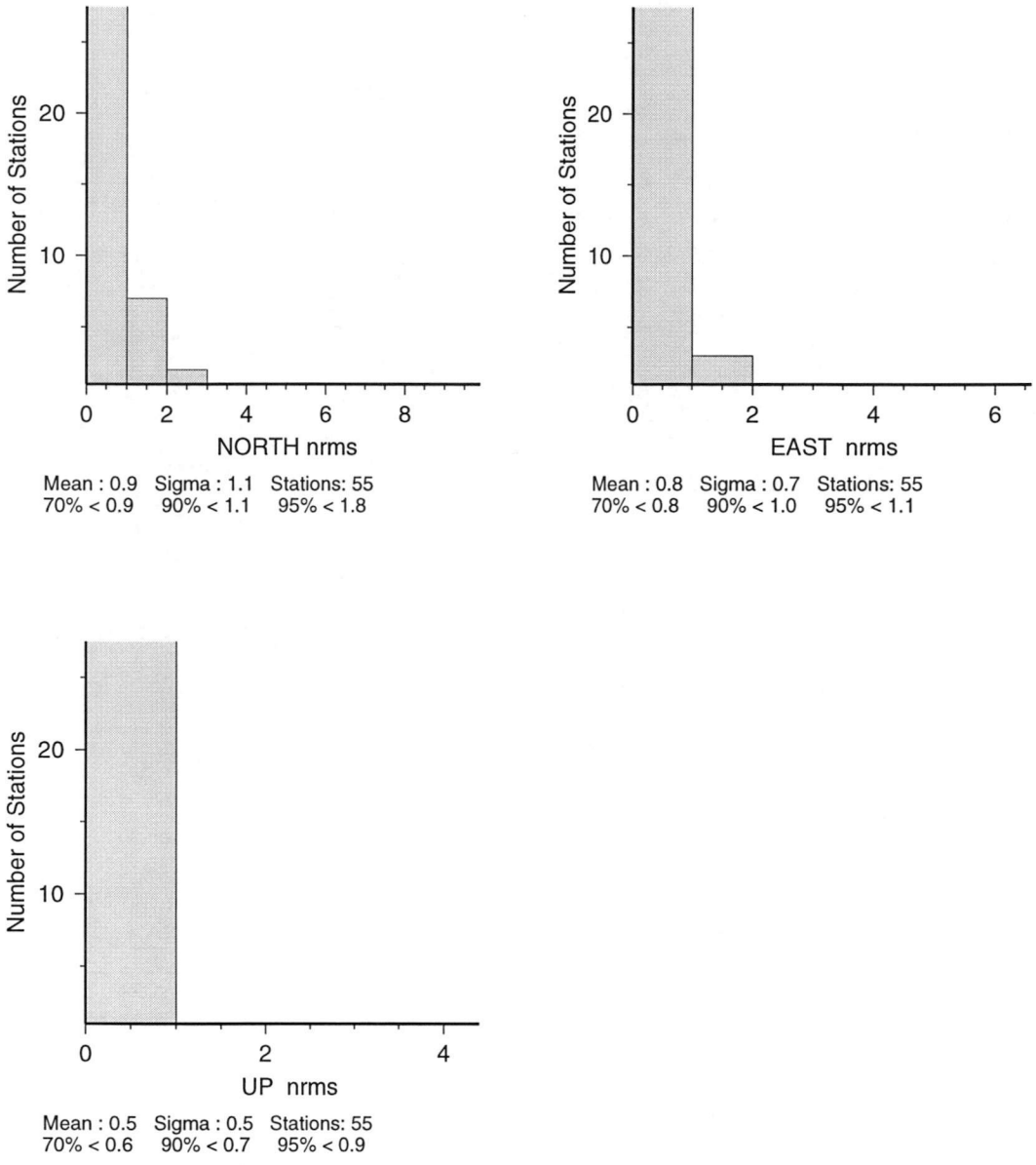

Figure 5-11: Histograms of local north-east-up coordinate nrms for stations during GIG91.

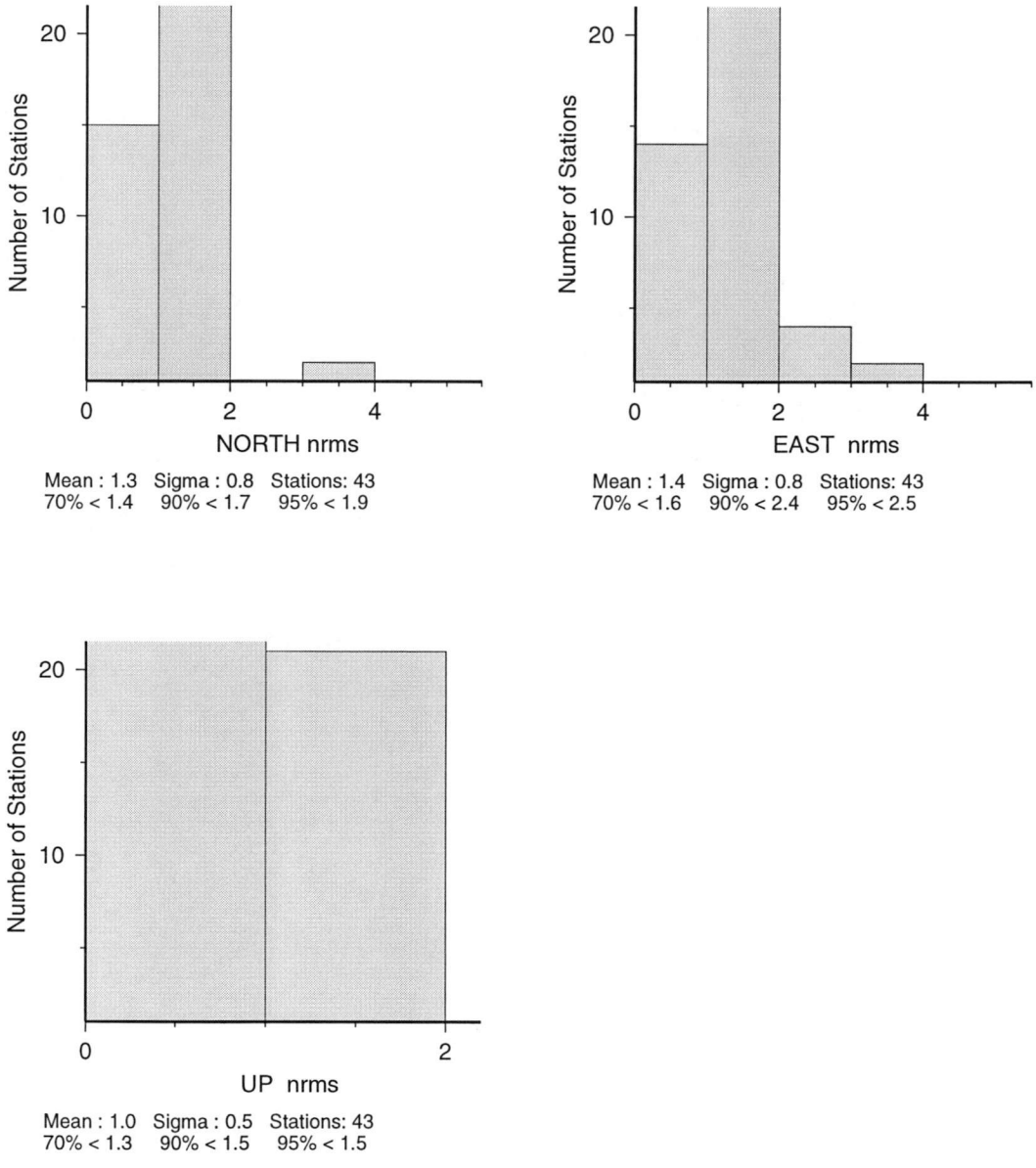

Figure 5-12: Histograms of local north-east-up coordinate nrms for stations during non-GIG91days.

5.1.2.3 1995-1999

5.1.2.3.1 Daily Solutions (GAMIT)

The data collected on the AIS during 1995 were the first AIS data set to span more than 1-2 hours (Phillips *et al.*, 1998). Furthermore, it was the first time that non-multiplexing dual-frequency receivers had been used, thus increasing significantly the resulting coordinate precisions. However, these longer session lengths present data processing problems since the ice shelf motion is significant over periods of greater

than one hour. Observations were made at six ice shelf sites (C2, C4, C6, C8, C10 and C12; Figure 5-13).

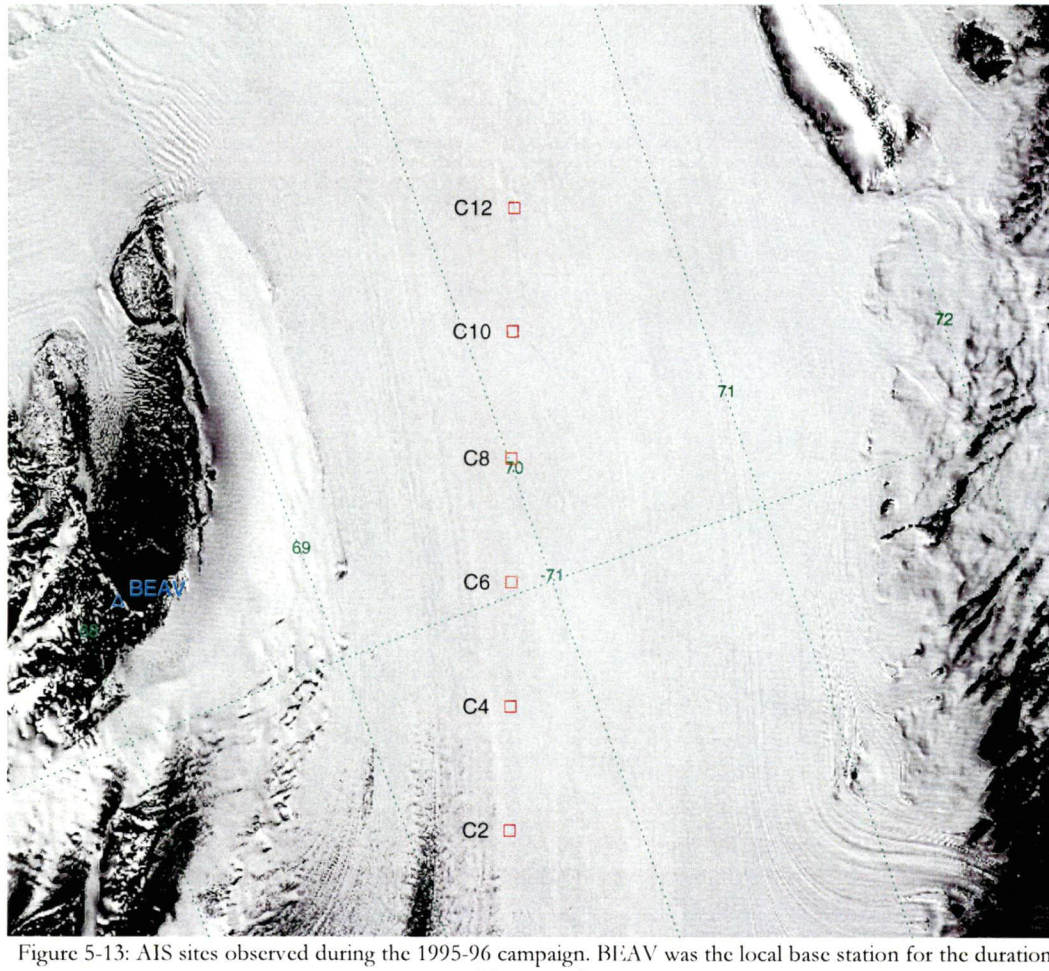

Figure 5-13: AIS sites observed during the 1995-96 campaign. BEAV was the local base station for the duration of the campaign.

We have been unable to process the campsite data satisfactorily using a kinematic methodology due to the long distances (>50km) between the rover and base station and also due to the squared L2 data observed on the Leica SR299 receivers for satellites with AS on. This prevents the forming of the wide-lane linear combination for all satellites. Additionally, we have found that kinematic processing software packages have trouble in satisfactorily correcting the carrier phase cycle slips in these data. Consequently, we process these data using two different static methodologies.

We firstly adopt the segmented approach described in Chapter 4. The data were again processed in the GAMIT software. In contrast to the earlier solutions, we did not use the broadcast orbits, preferring to use and then hold fixed the available daily IGS

precise ephemerides. Each set of daily AIS data were processed in a regional network of sites (DAV1, MAW1 and BEAV). By linear regression, a velocity was estimated for each of the ice shelf sites using the hourly solutions. An example is shown in Figure 5-14. The results for all the sites are shown in Table 5-10. Site C8 was moved when the tripod fell over on day 311 and hence the short-term velocities are from only the first section of the data. Phillips (1999) produced velocity magnitude estimates from her analysis of the same data using two hour data segments. Her results are reproduced in Table 5-10. Any difference between our analysis and Phillips (1999) is due to the different segment lengths and the segmentation methodology, the different station network used and the fact that orbit relaxation was used in the earlier GPS processing.

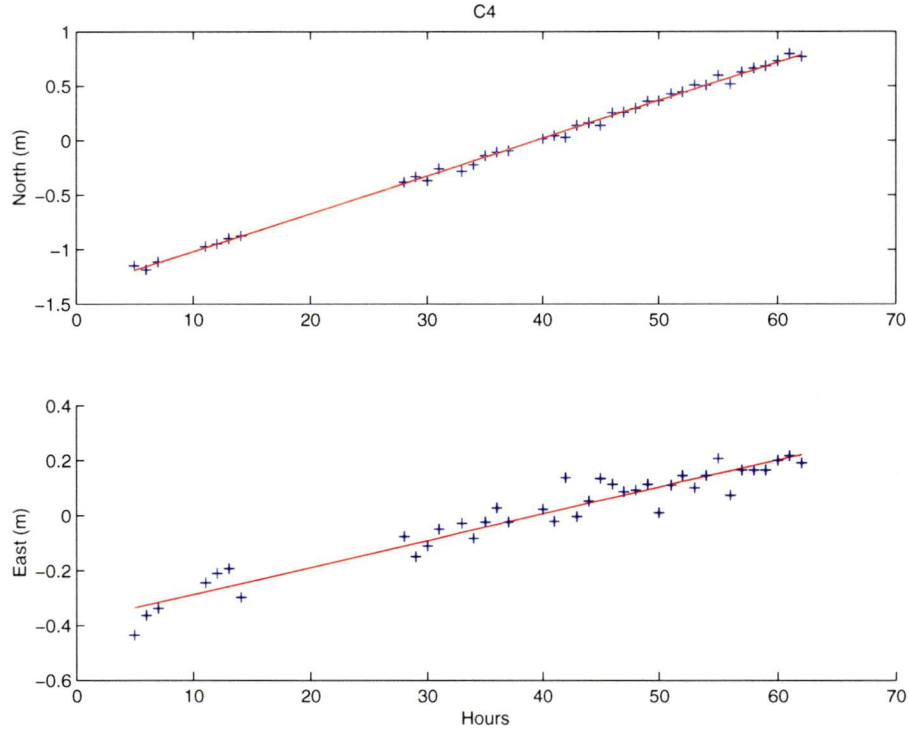

Figure 5-14: An example of a linear regression performed to find the best-fit velocity from the segmented data.

The second method applies the velocity and tide-free corrections to the RINEX data as described in Chapter 4. The *a priori* velocity corrections come from the segmented approach mentioned above. The tidal motions are accounted for with the BLTM98, shifted by 50 minutes to account for the phase difference between Beaver Lake and the AIS stations in this region. These corrections to the RINEX files result in pseudo-static site behaviour over a twenty-four hour period. The GPS data were then

processed in the same way as a standard rock location. For the processing, a 22-site Southern Hemisphere network was processed in GAMIT. The other processing options remained unchanged. To provide a check on this method, the site velocities were determined and compared against the velocities from the segmented approach (Table 5-10). The difference between the results is due to the longer segments available in the second approach, and to misfit in the models used to correct for the velocity and tidal motions. In the case of site C8, the improvement comes from the use of extra data. Notice that the up components over this timeframe are statistically zero. Additional noise has been added in the horizontal and vertical components (1m north and east and 0.5m up) of site C8 on day 311 to prevent a bias entering the solution. Following the down-weighting of the data, the C8 velocity appears realistic when compared against the other site velocities.

Site	V_{Mag} (myr^{-1})	σV_{Mag} (myr^{-1})	V_{Mag} (myr^{-1}) (Phillips, 1999)	RMS V_{Mag} (myr^{-1}) (Phillips, 1999)	V_{Dir} (°)	σV_{Dir} (°)	V_{Up} (myr^{-1})	σV_{Up} (myr^{-1})
C12	374.9	4.0	373.6	4.6	12.5	1.2	-	-
	386.2	*13.3*	-	-	*12.1*	*0.4*	*1.3*	*8.6*
C10	377.8	12.2	365.5	9.2	8.0	0.8	-	-
	370.3	*17.5*	-	-	*8.37*	*0.5*	*-0.6*	*8.9*
C8	349.6	27.8	360.7	19.8	14.6	2.9	-	-
	376.3	*23.6*	-	-	*9.9*	*0.7*	*-1.7*	*8.8*
C6	352.0	5.5	348.0	4.2	14.8	0.8	-	-
	348.4	*8.6*	-	-	*11.7*	*0.3*	*-6.1*	*8.6*
C4	316.4	2.7	322.8	3.2	15.7	0.8	-	-
	326.6	*4.7*	-	-	*14.9*	*0.3*	*0.4*	*8.5*
C2	341.4	7.9	326.9	0.4	17.6	0.7	-	-
	327.9	*0.7*	-	-	*19.9*	*0.1*	*0.5*	*2.8*

Table 5-10. Short-term AIS site velocities computed from one hour segments of the 1995 observations. The values shown in italics are those obtained using the velocity and tide corrected data from 1995 only. Vertical velocities are not shown for the segmented data since they are affected by the tidal signals.

Measurements were also made at several 'Corry poles' during the 1995 campaign. These data were collected using a kinematic methodology, whereby a skidoo would be driven as close to the pole as possible. The skidoo then remained stationary at this location for ~3-10 minutes. Vertical offsets to the top of the pole were measured,

although horizontal offsets were not. The result is that insufficient GPS data were collected for a static processing methodology to be applied. Consequently, these data have been processed using the Track processing software (Chen, 1998)[6]. This kinematic approach was not taken with the other data since the segmented approach provided a more precise and stable solution.

The processing strategy used is as follows (personal communication, Chris Watson, 2001). The coordinates of the Beaver Lake site BEAV and the IGS precise ephemerides were held fixed. The motions of the AIS campsites were loosely constrained at the 10mm/epoch level. This constraint was still considered quite loose considering the ice velocity in both horizontal and vertical tidal directions. The constraint helped correct large cycle slips in the data, while not biasing the rover position solutions. Three-dimensional coordinates and one tropospheric correction term per rover site were determined at each measurement epoch. The squaring-type Leica receivers used in the survey created some problems at this processing stage, since the software was designed for full-wavelength data only. Consequently, cycle slip detection and correction is problematic. Fortunately, the influence of coordinate errors caused by the failure to correctly fix cycle slips on the derived velocities is greatly reduced due to the long time spans between observations at the rover sites.

Since no time stamp for the measurement at the 'Corry poles' was made during the 1995 survey, the actual measurement epochs for each pole are not immediately evident. To determine the relevant epochs, the velocity of the skidoo was computed to identify those epochs with a velocity close to zero. To allow for measurement error, a velocity of less than 30mm/epoch was regarded as zero since the skidoos were generally moving at $10kmh^{-1}$ (13.9m/epoch for 5 second data) during other parts of the survey. The set of points with 'zero-velocity' consisted of the measured 'Corry poles' and other places where the skidoos were stopped (Phillips *et al.*, 1998). In order to distinguish between another stationary point and a 'Corry pole', coordinates of the poles were estimated at the epoch of measurement using the 1968-70 velocities. Those epochs relating to the 'Corry poles' were then obvious. Coordinates for each 'zero-velocity'

6. The kinematic processing using the Track software was done by Chris Watson at the Centre for Spatial Information Science, University of Tasmania.

location were averaged. We regard the coordinate precisions from the software to be over-optimistic given that the GPS L2 data were squared. Consequently, we estimate ice shelf coordinate precisions as 0.15m and 0.30 in the horizontal and vertical components, respectively. These coordinates and precisions were then entered into SINEX format for inclusion in GLOBK.

Data were observed at WOMB during five different days during January 1997 and these data were processed in the context of a regional network as described above.

The data collected during the 1998-99 season have been processed using the same two-step process as described above. Most of the sites have been observed for 2-4 hours, although some sites were observed for longer than twenty-four hours Firstly the raw RINEX data are corrected for ice movement during the measurement period. The horizontal motions are accounted for by first processing the data in one hour segments from which a horizontal velocity can be determined. The tidal movement is modelled using the BLTM98, as outlined above. This method allows the collected data to be processed as a single static site, even though movements of greater than one metre occur during a twenty-four hour period. Secondly, these data are then processed in the GAMIT/GLOBK software as described below.

Data observed in 1998-99, at sites labelled G1 and G2, were not made on the original 'Corry poles'. Over the 30 year period since their installation, these poles have been covered by several metres of snow and therefore could not be practically located. Rather, new measurements were made on newly placed poles at a similar geographic location as the original 1968 locations for these marks.

5.1.2.3.2 Daily Combinations (GLOBK)

The data from GAMIT and Track were combined together in GLOBK as described above, although we also introduced daily global network solutions from SOPAC[7]. This allows our regional solutions to be linked to the rest of the IGS network and hence the ITRF. Random noise of 500mm was added to the horizontal components of the 'Corry poles' since the GPS antenna on the skidoo was next to the pole, rather than above it, and the measurement between the two poles was not made. While the

7. Scripps Orbit and Permanent Array Center http://sopac.ucsd.edu/

measurements were referenced to the top of the pole, they were made by firstly measuring to the snow surface and then from the base of the pole to the top of the pole. Consequently, some uncertainty exists at the snow surface and a noise level of 100mm was added to the vertical component.

Random noise was also added to the tide- and velocity-free sites due to model misfit at the level of 0.03m (horizontal) and 0.1m (vertical). To allow for the movement of site C8 when the tripod blew over, we added 2m (horizontal) and 0.5m (vertical) random noise to this site.

The χ^2 per-degree-freedom value for each of the 1995-96, 1996-97 and 1998-99 combinations are shown in Table 5-11 as was determined using unit weighting of the daily GAMIT variance covariance matrices. Each of these 'goodness-of-fit' values suggest that the data for each season fits together well. The results were stored in the form of quasi-observations for later combination with other data sets.

Season	χ^2 per-degree-freedom
1995-96	1.30
1996-97	0.50
1998-99	1.90

Table 5-11: χ^2 per-degree-freedom for the 1995-99 solutions.

5.1.2.4 Combined 1988-1999 GPS results

The individual season solutions in the form of quasi-observations have been combined using the GLOBK software. The method is the same as described for the combination of daily solutions, although satellite parameters are not considered at this stage. Due to the small size of the global network in the early data sets, the solution is run backwards in time (most recent solutions first) to stabilise the solution. Our VCV weighting strategy described above does not take into account any long-term effects such as reference frame and tropospheric modelling errors.

Zhang *et al.* (1997) and Mao *et al.* (1999) have shown that when combining GPS time series, velocity uncertainties are underestimated by factors of up to 5-11 if a pure white noise model is used. This is because of unmodelled cm-level systematic effects that are

significant for the velocities of sites used in geophysical studies. However, these results do not necessarily hold for our ice data since they were determined using GPS receivers permanently mounted on rock and the size of the systematic errors are negligible when considering ice velocities. Instead, we assume that the long-term error model of the ice movement sites conforms to a white noise model. Consequently, we applied a uniform VCV scale to each of the seasonal solutions such that the χ^2 per-degree-freedom for the combination was statistically unity.

The size of the uniform scale was determined by analysing the repeatability of the rock sites and, where more than two occupations existed, the ice sites during the entire survey period 1988-1999 were added. By examining the nrms value computed for each site, we found a uniform scale of four was appropriate for each of the daily files, except for the GIG91 campaign (factor=unity) and the L1-only solutions (factor=200) for reasons described in Section 5.1.2.2.2.

Figures 5-15 through 5-20 show examples of site repeatabilities following the application of the above VCV scale factors. The first two (Figures 5-15 and 5-16) are examples of 1988-91 AIS sites at GA01 and GT6/2. Their nrms values indicate that their uncertainties are correctly, although conservatively, scaled. Figure 5-17 shows the repeatability of CAMP over consecutive 12 days. A residual tidal motion is evident in the vertical component due to the misfit of the BLTM98. The scaling and random noise applied to these sites has resulted in slightly conservative (nrms < 1) uncertainties at this site also. Three global sites are shown in Figures 5-18 through 5-20 – KOKE, ONSA and TROM. KOKE covers the period 1988-91, while ONSA and TROM cover part of the early (1988-91) and late (1995-1999) periods of the combination. Each of these sites suggests that they their uncertainties are well scaled. We consequently conclude that our chosen VCV scale factors provide slightly conservative estimates of the coordinate, and hence velocity, uncertainties.

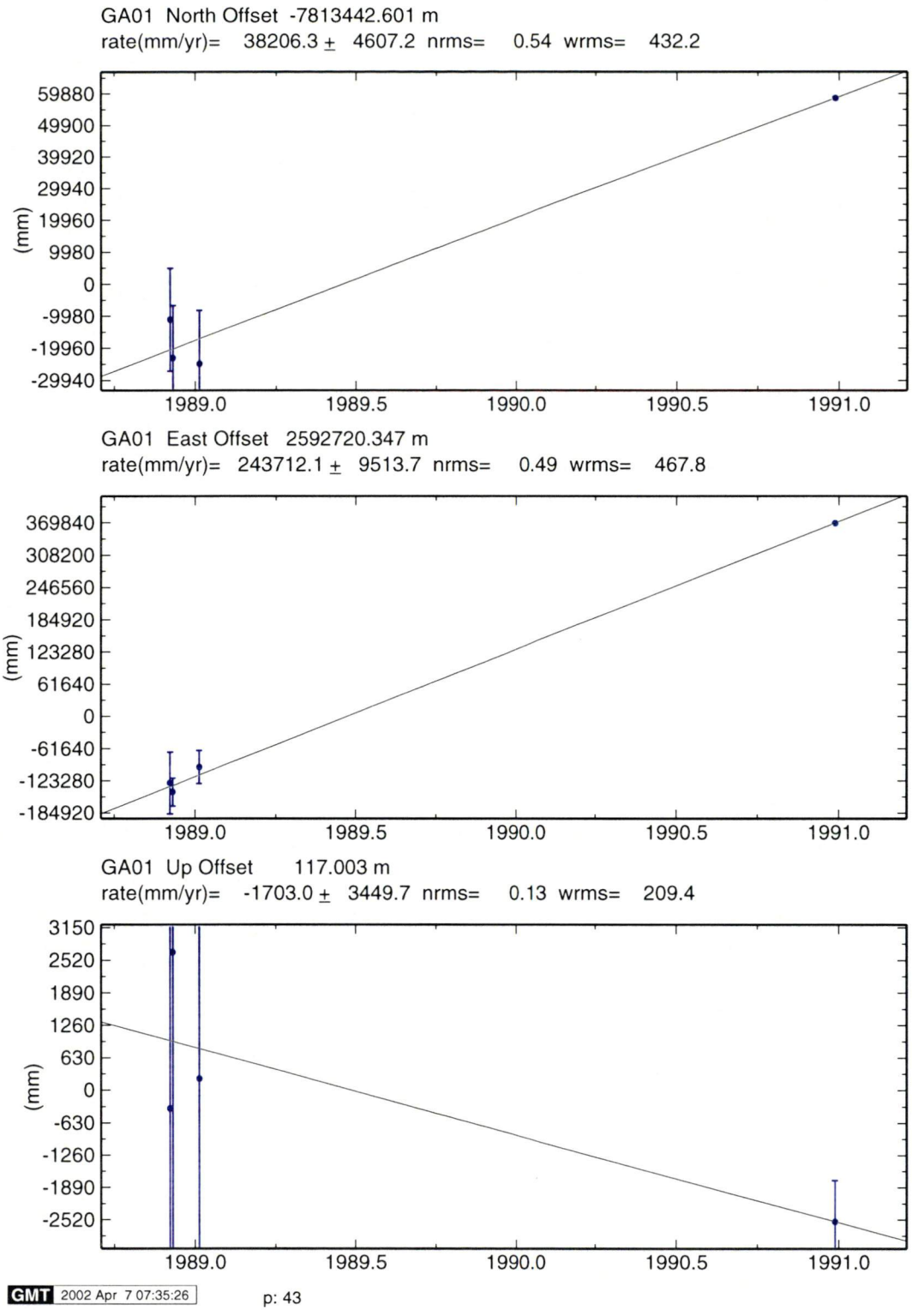

Figure 5-15: Repeatability of GA01. Error bars are the 1σ errors following the scaling of the VCV matrices.

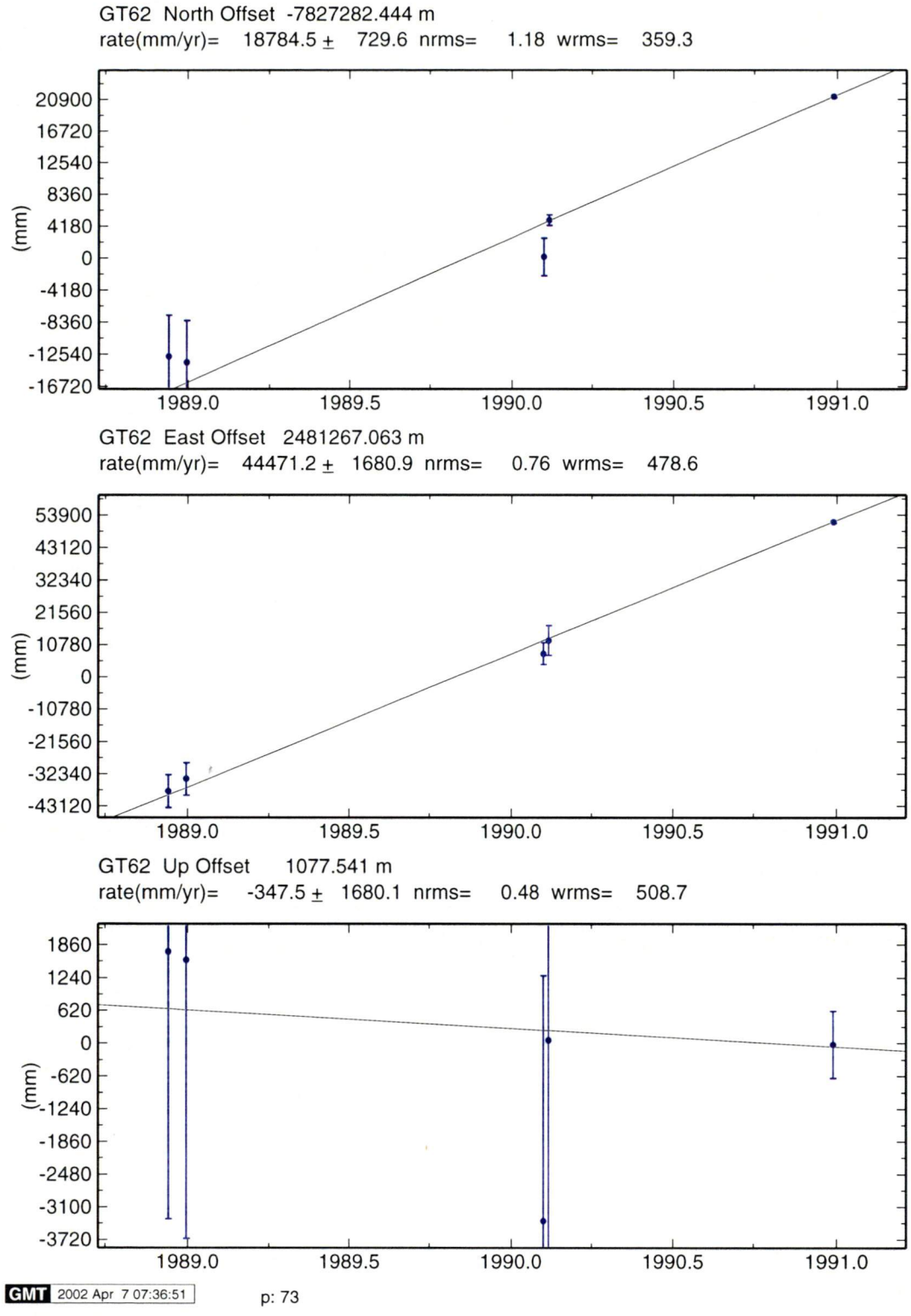

Figure 5-16: Repeatability of GT62. Error bars are the 1σ errors following the scaling of the VCV matrices.

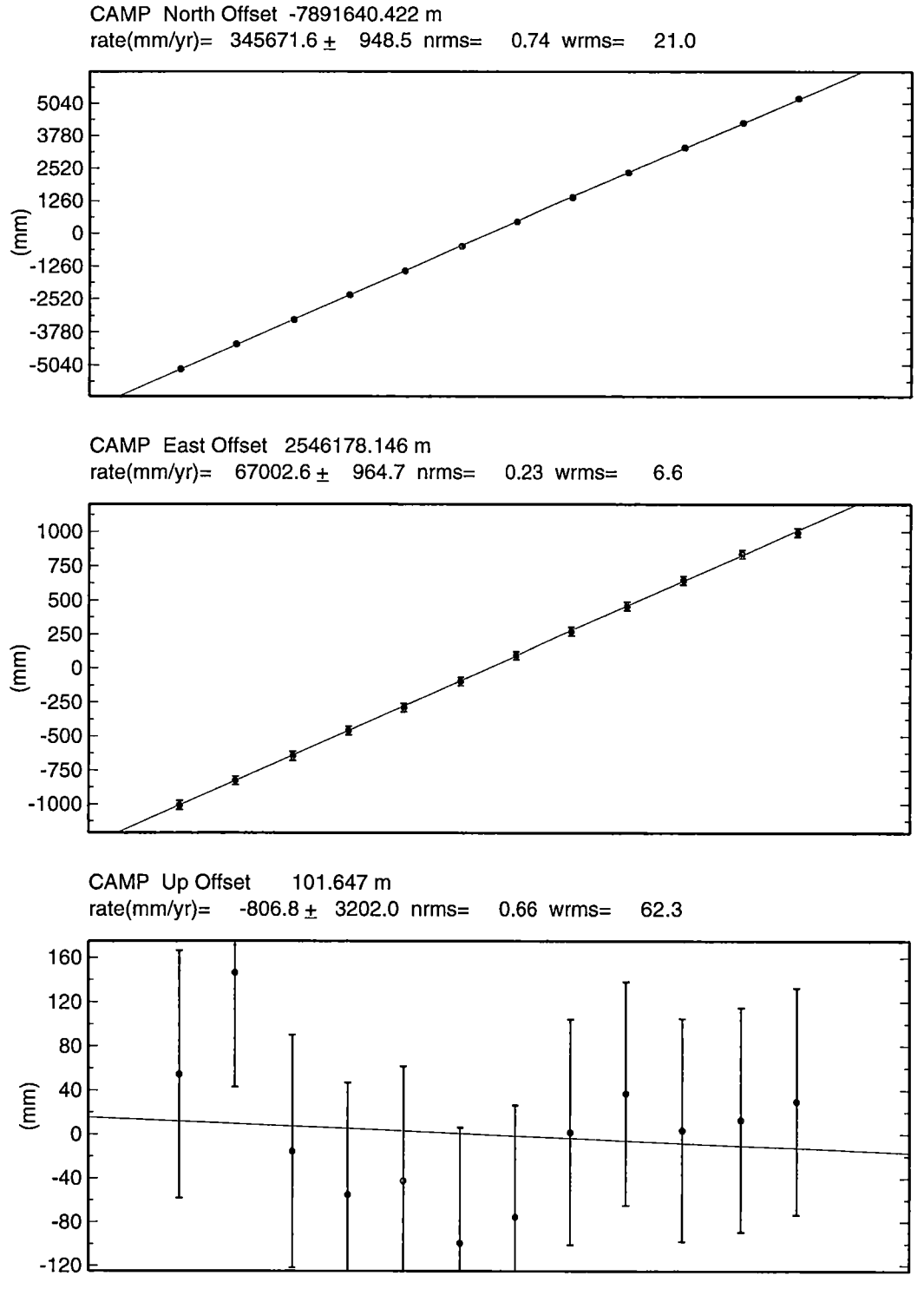

Figure 5-17: Repeatability of CAMP. Error bars are the 1σ errors following the scaling of the VCV matrices.

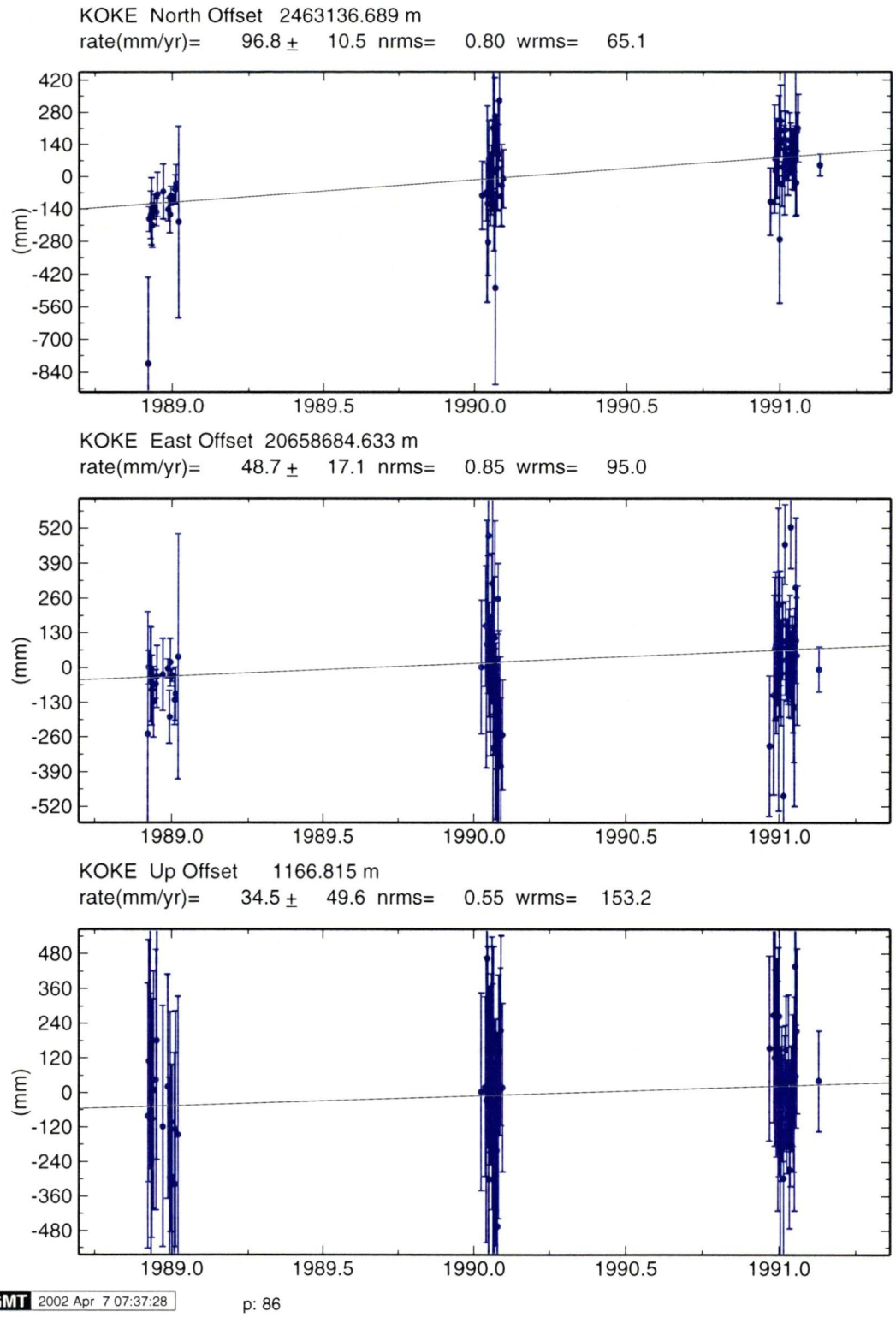

Figure 5-18: Repeatability of KOKE. Error bars are the 1σ errors following the scaling of the VCV matrices.

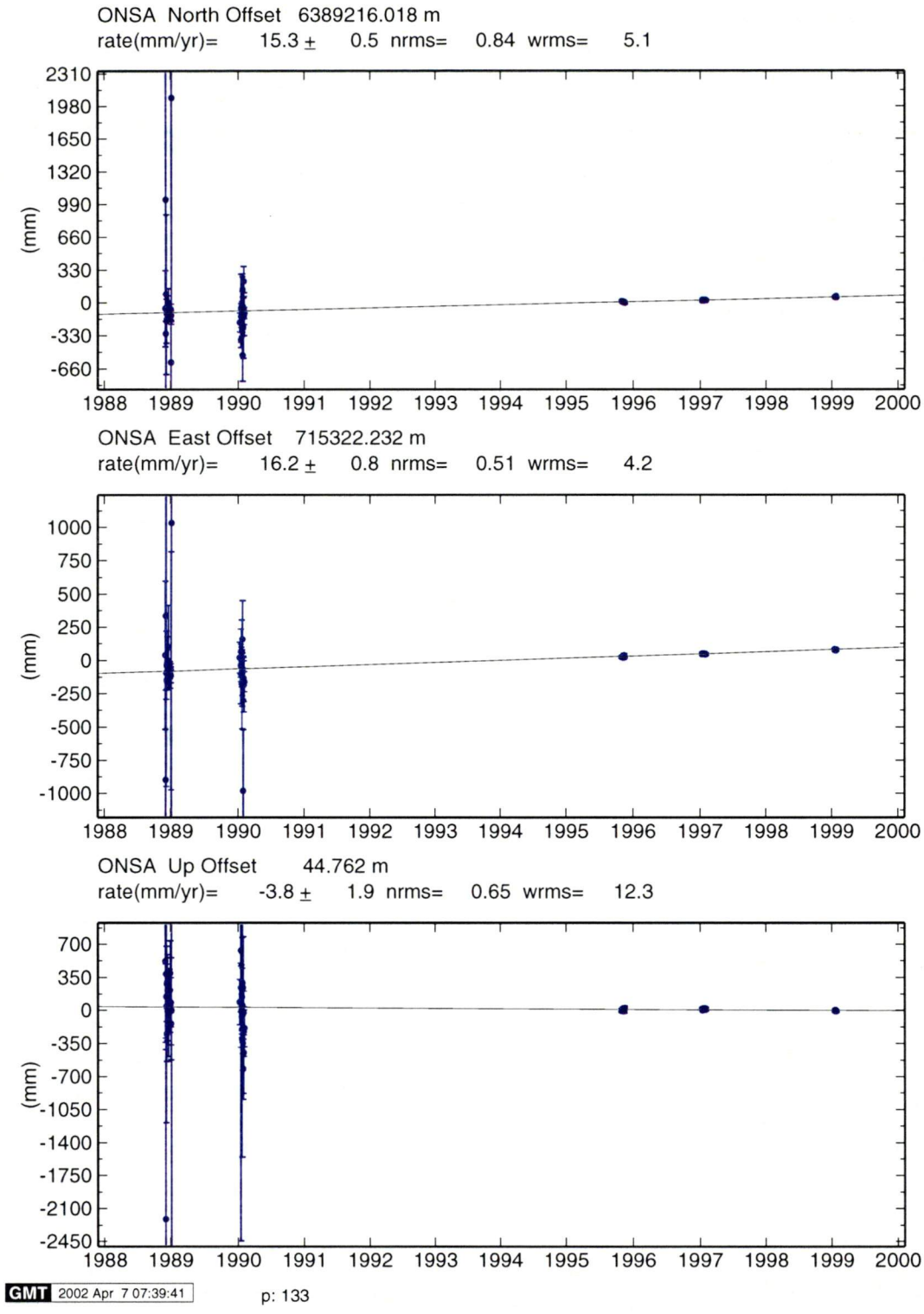

Figure 5-19: Repeatability of ONSA. Error bars are the 1σ errors following the scaling of the VCV matrices.

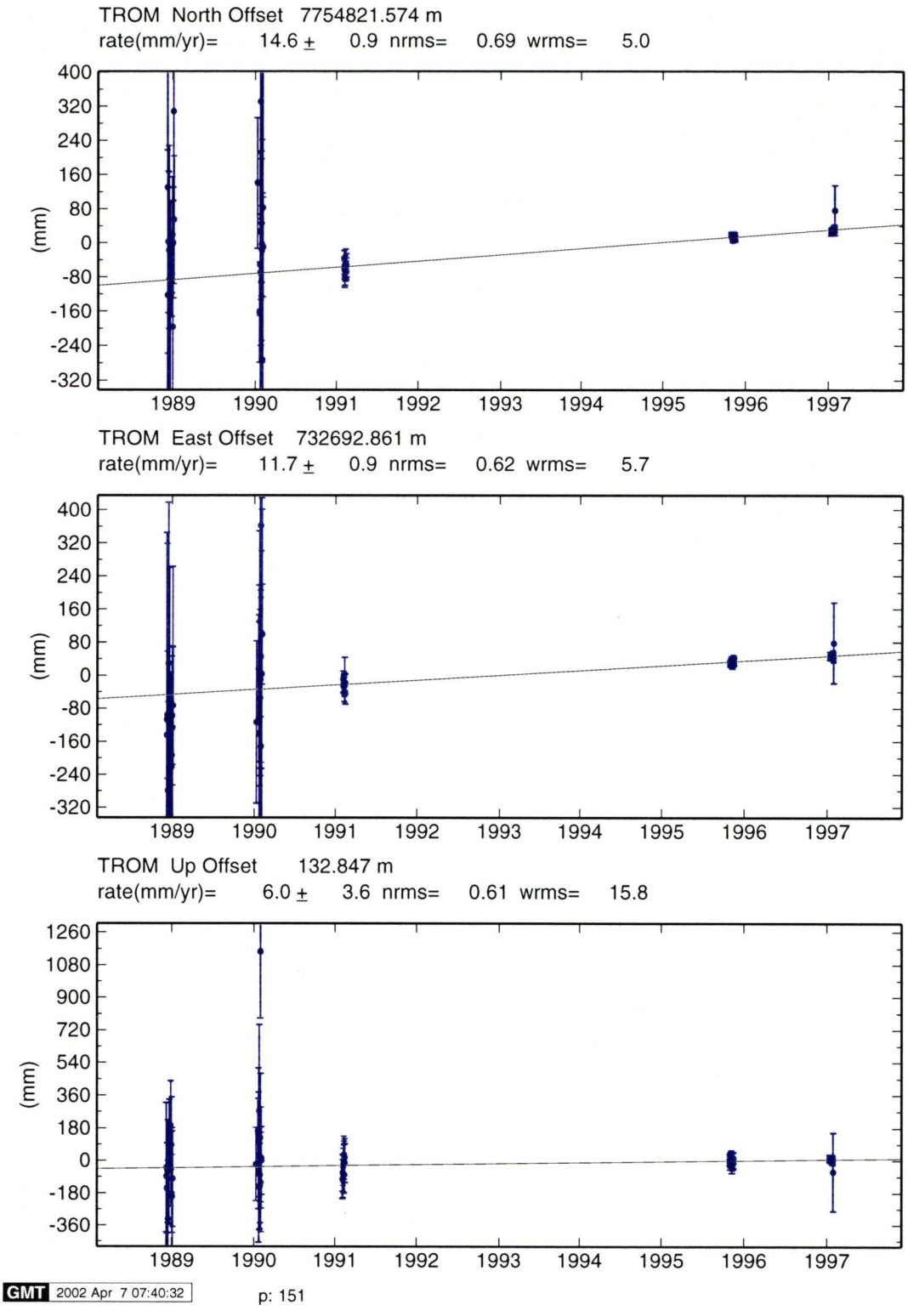

Figure 5-20: Repeatability of TROM. Error bars are the 1σ errors following the scaling of the VCV matrices.

The χ^2 per-degree-freedom value for the combination was 1.3, showing that the data fitted together well. The loosely constrained GLOBK solution was then transformed into ITRF97 by means of two seven parameter transformations, one for each of

position and velocity. To do this, 35 global sites were constrained at their ITRF97 values. Velocities at some collocated Southern Hemisphere sites were constrained to be the same at this stage. The resulting AIS positions and velocities are shown in Table 5-12 and plotted in Figure 5-21. The vertical velocities are not shown in Table 5-12 since they are treated separately in Section 5.1.2.6.

The AIS coordinate precisions (1σ) have median values of 0.15m, 0.17m and 0.17m for latitude, longitude and height, respectively. Grouping the coordinate precisions in terms of their reference epoch shows a distinct difference between the quality of the pre-1991 data and the post-1995 data. The median (1σ) precisions for the 1988-91 data are 0.29m, 0.29m and 0.32m in latitude, longitude and height. The 1995-1999 data have median (1σ) precisions of 0.05m, 0.03m and 0.09m for latitude, longitude and height – approximately an order of magnitude more precise than the results from the earlier data. This increase in precision is due to improvements in receiver technology, longer observing periods, more satellites, better orbits from a greater distribution of global sites and improvements in modelling the movement (horizontal and tidal) of the ice sites during the measurements.

In terms of horizontal velocity, the median (1σ) precisions of velocities and direction for the 1988-91 data are 2.2myr^{-1} and 0.44°, while for the 1995-1999 data they are 0.9myr^{-1} and 0.16° – again, approximately an order of magnitude more precise. Many of the velocities from the latter seasons are determined using data from one season only. Using all the data, the median precisions of the horizontal velocities are 2.0myr^{-1} and 0.41°, since the majority of the velocities are from the earlier data set.

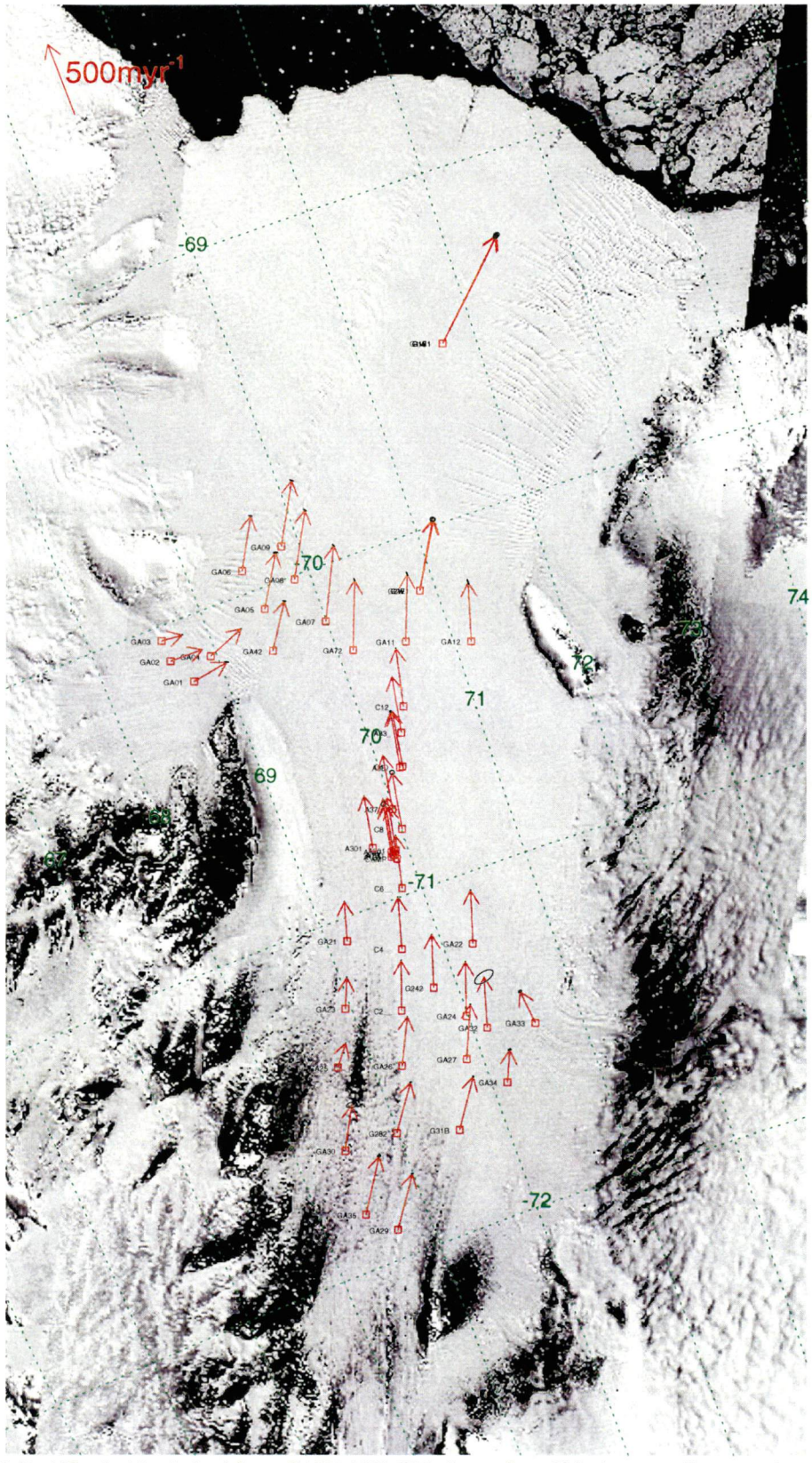

Figure 5-21: AIS velocities derived from all 1988-1999 GPS observations. Velocity error ellipses are shown at the 95% confidence interval.

Table 5-12 AIS station positions and velocities (and their precisions) determined from a combination of the 1988-1999 data sets GRS80 is the reference ellipsoid

Site	Latitude (°)	Longitude (°)	Height (m)	Epoch	$1\sigma_{Lat}$ (m)	$1\sigma_{Long}$ (m)	$1\sigma_{Height}$ (m)	V_{Mag} (myr^{-1})	V_{Dir} (°)	1σ V_{Mag} (myr^{-1})	1σ V_{Dir} (°)
G1N1	-69.500763	71.721614	77.26	1999.0950	0.02	0.01	0.04	-	-	-	-
G1W1	-69.500995	71.720028	77.37	1999.0600	0.04	0.03	0.07	796.10	44.28	7.91	0.57
G1E1	-69.501294	71 722251	77.16	1999.0600	0.04	0.03	0.07	784.75	44.23	7.88	0.58
G1S1	-69.501527	71.720604	77.18	1999.0600	0.04	0.03	0.07	806.08	44.58	8.05	0.57
GA09	-69.907689	69.848138	87.98	1991.1270	0.37	0.27	0.34	435.99	28.91	5.58	0.66
GA06	-69.935007	69 457831	94.23	1991.0130	0.98	1.11	1.44	363.81	29.16	4.96	0.60
GA08	-70.012229	69.859566	92.51	1991.1280	0.32	0.25	0.31	457.48	28.48	4.59	0.59
GA03	-70.043133	68.601115	138.96	1991.0380	0.44	0.54	0.57	140.16	95.17	1.69	0.51
GA05	-70.063130	69.528554	93.10	1991.0300	1 41	1.73	1.14	375 45	31.31	6.91	0.72
GA02	-70.108197	68.608479	128.09	1990.5320	0.40	0.32	0.54	221.21	90.97	0.57	0.18
GA04	-70.136797	68.946197	106.76	1990.6990	0.23	0.31	0.25	268.13	68.85	0.37	0.12
GA07	-70.159890	69.992725	92.05	1991.1000	0.83	0.72	0.84	498.01	25.60	3.22	0.56
G2W1	-70 168738	70.861426	91.19	1999.0550	0.04	0.02	0.07	472.18	29.02	7.84	0.95
G2E1	-70.169125	70.863815	90.88	1999.0560	0.03	0.02	0.05	473.61	29.79	6.10	0.74
G2S1	-70.169351	70.862061	90.99	1999.0950	0.02	0.02	0.04	-	-	-	-
GA42	-70.187222	69.470054	88.59	1990.7030	1.67	2.91	1.79	333.84	33 19	4.87	0.66
GA01	-70.188936	68.733201	114.96	1991.0970	0.28	0.41	0.32	247.22	80.44	3.57	1.74
GT04	-70.252320	66.526992	866.41	1990.9230	0.35	0.29	0.32	63.72	89.41	1.05	0.38
GA72	-70.267880	70.133648	95.69	1991.1280	0.26	0.12	0.38	459.60	20.76	2.34	0.68

Site	Latitude (°)	Longitude (°)	Height (m)	Epoch	$1\sigma_{Lat}$ (m)	$1\sigma_{Long}$ (m)	$1\sigma_{Height}$ (m)	V_{Mag} (myr^{-1})	V_{Dir} (°)	1σ V_{Mag} (myr^{-1})	1σ V_{Dir} (°)
GA11	-70.297290	70.597627	92.58	1991.1180	0.55	0.37	0.85	442.51	20.40	2.91	0.95
GT62	-70.313604	66.167038	1077.65	1990.5410	0.21	0.21	0.24	50.69	64.94	0.32	0.42
GT06	-70.349617	65.597664	1309.36	1990.6450	0.29	0.24	0.24	76.50	80.96	0.39	0.30
GA12	-70.359900	71.145512	94.55	1991.1290	0.32	0.30	0.49	388.28	15.45	2.96	1.44
C12_	-70.475279	70.389749	103.42	1996.4600	0.03	0.02	0.05	385.10	11.71	0.02	0.01
A32_	-70.481907	70.383746	102.74	1995.8730	0.59	0.59	0.61	-	-	-	-
GT05	-70.502393	66.462394	1004.95	1990.8160	0.23	0.27	0.25	111.00	68.12	0.52	0.27
GT82	-70.532043	66.074354	1186.13	1990.4440	0.17	0.22	0.18	65.52	73.36	0.21	0.41
A33_	-70.545957	70.294456	101.04	1999.0520	0.06	0.04	0.10	374.96	9.65	0.18	0.03
A34_	-70.580161	70.259708	103.70	1995.8730	0.59	0.59	0.61	-	-	-	-
GT08	-70.638574	65.586755	1442.83	1990.4110	0.21	0.28	0.24	76.61	60.75	0.35	0.40
C10_	-70.640749	70.204232	103.99	1996.8170	0.03	0.02	0.06	368.49	8.76	0.01	0.01
A35_	-70.640958	70.177928	102.17	1999.0810	0.03	0.02	0.06	372.04	9.67	3.00	0.50
A37_	-70.749067	69.988388	103.62	1999.0760	0.05	0.03	0.08	359.07	9.20	0.22	0.02
B36_	-70.774167	70.030099	102.18	1991.1330	0.23	0.30	0.31	-	-	-	-
A305	-70.780324	69.256556	91.50	1999.0950	0.06	0.04	0.12	-	-	-	-
A304	-70.785360	69.354940	96.45	1999.0950	0.05	0.04	0.10	-	-	-	-
A308	-70.789780	68.890536	300.17	1999.0380	0.04	0.02	0.07	4.83	11.09	7.79	92.43
A303	-70.793586	69.433331	97.27	1999.0950	0.06	0.04	0.11	-	-	-	-
A307	-70.803240	68.999729	179.26	1999.0950	0.06	0.04	0.10	-	-	-	-

Site	Latitude (°)	Longitude (°)	Height (m)	Epoch	$1\sigma_{Lat}$ (m)	$1\sigma_{Long}$ (m)	$1\sigma_{Height}$ (m)	V_{Mag} (myr^{-1})	V_{Dir} (°)	1σ V_{Mag} (myr^{-1})	1σ V_{Dir} (°)
C8__	-70.814161	70.010866	101.14	1995.8570	0.04	0.03	0.07	377.36	9.38	7.72	1.17
A306	-70.818843	69 088159	114.60	1999.0950	0.05	0.04	0.10	-	-	-	-
A302	-70.822511	69.624752	105.09	1999.0950	0.05	0.04	0.10	-	-	-	-
A39_	-70.836198	69.884213	101.50	1999.0950	0.03	0.02	0.05	-	-	-	-
A301	-70.836683	69.698544	103.87	1999.0560	0.05	0.04	0.10	347.90	10.39	0.18	0.03
A201	-70.866792	69.888695	103.80	1999.0540	0.05	0.04	0 10	352.39	10.59	0.18	0.03
A129	-70.866808	69.845618	100.44	1999.0300	0.05	0.03	0.09	355.17	10.70	0.18	0.03
B132	-70.870915	69.815489	97.11	1999.0950	0.01	0.01	0.02	-	-	-	-
A202	-70.873687	70.123585	102.37	1999.0950	0.06	0.04	0.12	-	-	-	-
A130	-70.877289	69.856893	100.54	1999.0300	0.05	0.03	0.09	355.46	10.79	0.18	0.03
A131	-70.880943	69.830779	97.11	1999.0660	0.05	0.03	0.09	350.29	11.20	7.87	1.28
CAMP	-70.891811	69.873347	101.62	1999.0770	0.02	0.01	0.03	353.26	10.95	0.95	0.15
A401	-70.900617	69.810158	96.88	1999.0950	0.06	0.04	0.10	-	-	-	-
C6__	-70.978848	69.828012	101.22	1996.6070	0.03	0.02	0.05	348.53	12.39	0.01	0.01
B207	-71.003442	70.738180	97.06	1991.1330	0.48	0.42	0.80	-	-	-	-
A403	-71.018492	69.675781	97.61	1999.0950	0.06	0.04	0.11	-	-	-	-
A404	-71.062968	69.625009	97.74	1999.0950	0.06	0.04	0.11	-	-	-	-
GA21	-71.067522	69.183771	100.24	1990.9470	0.39	0.37	0.52	259.10	16.58	0.72	0.24
A405	-71.086428	69.594808	98.52	1999.0950	0.06	0.04	0.10	-	-	-	-
C4__	-71.146868	69.633240	98.47	1996.5660	0.03	0.02	0.05	340.46	15.75	0.01	0.01

Site	Latitude (°)	Longitude (°)	Height (m)	Epoch	$1\sigma_{Lat}$ (m)	$1\sigma_{Long}$ (m)	$1\sigma_{Height}$ (m)	V_{Mag} (myr^{-1})	V_{Dir} (°)	1σ V_{Mag} (myr^{-1})	1σ V_{Dir} (°)
G232	-71.200447	69.125013	98.65	1988.9830	1.98	3.04	2.04	-	-	-	-
GA22	-71.204289	70.266257	102.65	1991.1200	0.18	0.28	0.20	350.31	17.06	1.83	0.25
B406	-71.224804	69.472696	107.51	1991.1330	0.52	0.43	0.88	-	-	-	-
GA23	-71.251558	68.947772	102.23	1990.3380	0.63	0.91	0.53	205.66	23.72	1.24	0.40
G242	-71.286721	69.788823	102.23	1991.1040	0.18	0.27	0.20	347.29	17.79	0.94	0.16
C2__	-71.316118	69.434633	97.34	1995.8380	0.03	0.02	0.05	327.29	19.98	0.89	0.16
GA24	-71.398008	69.983253	101.50	1990.3920	0.65	0 49	0.50	355.45	18.75	1.29	0.16
GA25	-71.404332	68.687613	108.44	1991.0610	0.19	0.27	0.23	167.87	39.50	0.86	0.31
GA32	-71.452297	70.134764	102.88	1991.0670	0.16	0.27	0.17	333.45	15.77	35.29	3.42
GA26	-71.469552	69.259621	96.43	1990.7280	0.34	0.31	0.38	324.73	26.72	0.58	0.12
GA33	-71.487210	70.573381	104.62	1991.0490	0.15	0.19	0.18	229.86	-6 59	5.99	0.94
GA27	-71.517681	69.848075	100.98	1990.2760	0.71	0.55	0.47	359.65	23.88	2.23	0.27
GA34	-71.623797	70.142990	100.38	1991.0470	0.16	0 18	0.16	211.88	23.93	5.14	1.00
GA30	-71.641152	68.469782	117.64	1991.0720	0.19	0.27	0.25	302.28	29.57	16.63	2.31
G282	-71.648194	68.987989	112.15	1991.0280	0.11	0.17	0.15	345.24	36.56	3.37	0.44
GA28	-71.654254	68.981055	111.08	1988.9660	3.03	3.69	2.83	-	-	-	-
GA31	-71.705691	69.549948	97.02	1991.0060	1.40	1.47	1.82	-	-	-	-
G31B	-71.705998	69.555313	100.53	1991.0520	0.09	0.05	0.15	360.31	34.85	2.17	0.40
GA35	-71.839398	68.433235	131.97	1991.0590	0.17	0.21	0.22	394.90	34.03	5.54	0.68
GA29	-71.916546	68.669469	119.14	1991.0220	0.13	0.17	0.17	382.04	35.87	3.58	0.44

5.1.2.5 Horizontal velocities

5.1.2.5.1 GPS-GPS comparison

In order to assess the precision of the estimated velocities, we compare the determined velocities of GPS sites located within two kilometres of each other. Over small regions the velocity of the ice shelf will vary little and hence this provides a first order check on the quality of the derived velocities. In all, ten station pairs satisfy this distance criterion. These station pairs are shown in Table 5-13. Unfortunately, the pairs are only from the later two campaigns, with only one site (C10) being determined from more than one season's data. Otherwise, the comparison is based on velocities obtained from data collected in only one season.

These comparisons will not, therefore, be representative of the velocities determined from the earlier data sets or for velocities determined using more than one season's data. The greatest inter-station velocity differences seen in Table 5-13 are at the G1 sites, although the differences are not as apparent once they are normalised.

In terms of the orientation differences, the sites appear to be well determined, with all of the sites agreeing with the neighbouring values to better than one degree, including those at G1.

From this intra-site comparison, we can conclude that these velocities are well estimated and are in good agreement with adjacent sites.

Site A	Site B	Inter-site distance (km)	Observation separation (yrs)	ΔV_{Mag} (myr^{-1})	% difference	ΔV_{Dir} (°)
G1E1	G1S1	0.07	0.0	21.3	2.6	0.4
G1E1	G1W1	0.09	0.0	11.4	1.3	0.0
G1S1	G1W1	0.06	0.0	10.0	1.1	-0.4
G2E1	G2W1	0.10	0.0	1.4	0.3	-0.8
C10_	A35_	1.12	2.3	3.5	0.1	0.9
A201	A130	1.66	0.0	3.1	0.9	0.3
A201	A129	1.58	0.0	2.8	0.8	0.1
CAMP	A130	1.73	0.0	2.2	0.6	-0.2
CAMP	A131	1.97	0.0	3.0	0.8	0.4
A130	A129	1.24	0.0	0.3	0.1	0.1
A130	A131	1.04	0.0	5.2	1.4	0.4
A129	A131	1.67	0.0	4.9	1.4	0.5

Table 5-13: Inter-site GPS-derived velocity comparison (SiteA - SiteB). Sites with an observation seperation of 0.0 years were observed on the same day.

5.1.2.5.2 Comparison with previous GPS solutions

As has been mentioned in Chapter 2, the 1988-91 data has previously been processed using the Wild Magnavox PoPS software (personal communication, I. Allison, 1998). A comparison of the differences between the PoPS and GAMIT/GLOBK solutions is shown in Table 5-14. Station latitude and longitude differences are negligible and unimportant in comparison to the determination of height and velocity, and hence the horizontal coordinates are not tabulated. Vertical velocities are not available for the PoPS data. It was not possible to determine an adequate velocity solution in GLOBK for the sites observed in the 1988-89 solution only. Therefore, it was not possible to produce a result for AIS sites G232 or GA28, although solutions were possible using PoPS. Figure 5-22, however, shows that the PoPS solution for GA28 appears incorrect given the velocity of nearby G282. Additionally, the direction of G232 appears to be quite different to that defined by the ice shelf flow lines. The PoPS velocity for GA32 is unusually high and hence it was removed from the comparison. For the sites where comparison is possible, the velocity differences range from -23 to +42myr^{-1}. When the change is expressed in terms of percentage of the velocity, differences of ±1-5% are common. This has significant implications for mass flux calculations. Significant differences are also seen in the velocity direction. In particular, there is a systematic difference between the two data sets with the GAMIT directions being 1.4° to the

north of the PoPs directions on average. From this comparison, it is not possible to tell which of the two data sets is the more accurate. An external assessment of the accuracy of these velocities is provided in Section 5.2 below.

Site	ΔV_{Mag} (myr^{-1})	% difference	ΔV_{Dir} (°)
Min	-23.7	-6.5	-7.5
Max	42.0	13.9	10.3
Mean	-0.1	0.3	1.4
RMS	12.8	4.2	3.5

Table 5-14: Differences between AIS station velocities derived from PoPS and GAMIT/GLOBK software.

In terms of the determined ellipsoidal heights, large differences of 1-10 metres are also seen (Table 5-15). In order to assess the quality of the different heights, a comparison is made with a Digital Elevation Model (DEM) derived from independent ERS-1/2 altimeter data (Fricker *et al.*, 2000). When compared against kinematic GPS ground tracks in the region of G3, the DEM was shown to have a mean error of 0.0m with a RMS of 1.7m. When compared to GPS data presented here, outliers in the DEM were apparent in regions of steeper slope. Radar altimeters are known to perform poorly in regions of steep slope. Other outliers were at sites close to locations where no DEM value existed due to a lack of altimeter signal in these areas (Phillips *et al.*, 1998). These outliers were removed from the comparison, leaving 31 sites to compare with the GPS.

In the case of the 1988-91 results, the mean difference between the DEM and PoPS is -9.7m with a RMS of 17.5m, while the GAMIT/GLOBK solutions have a mean difference of -2.3m and a RMS of 5.4m (Table 5-15). A further improvement is seen when the post-1991 data are included. This improvement in height justifies our choice of processing methodology and software. Furthermore, since GPS is a three-dimensional positioning system, a corresponding improvement in horizontal position and hence horizontal velocity may also be assumed.

We conclude, consequently, that the GAMIT/GLOBK solutions are more accurate than the estimates generated using PoPS and hence this new solution is a significant improvement over the previous analyses. The rigorous uncertainty analysis outlined is a further improvement over the previous uncertainty estimates.

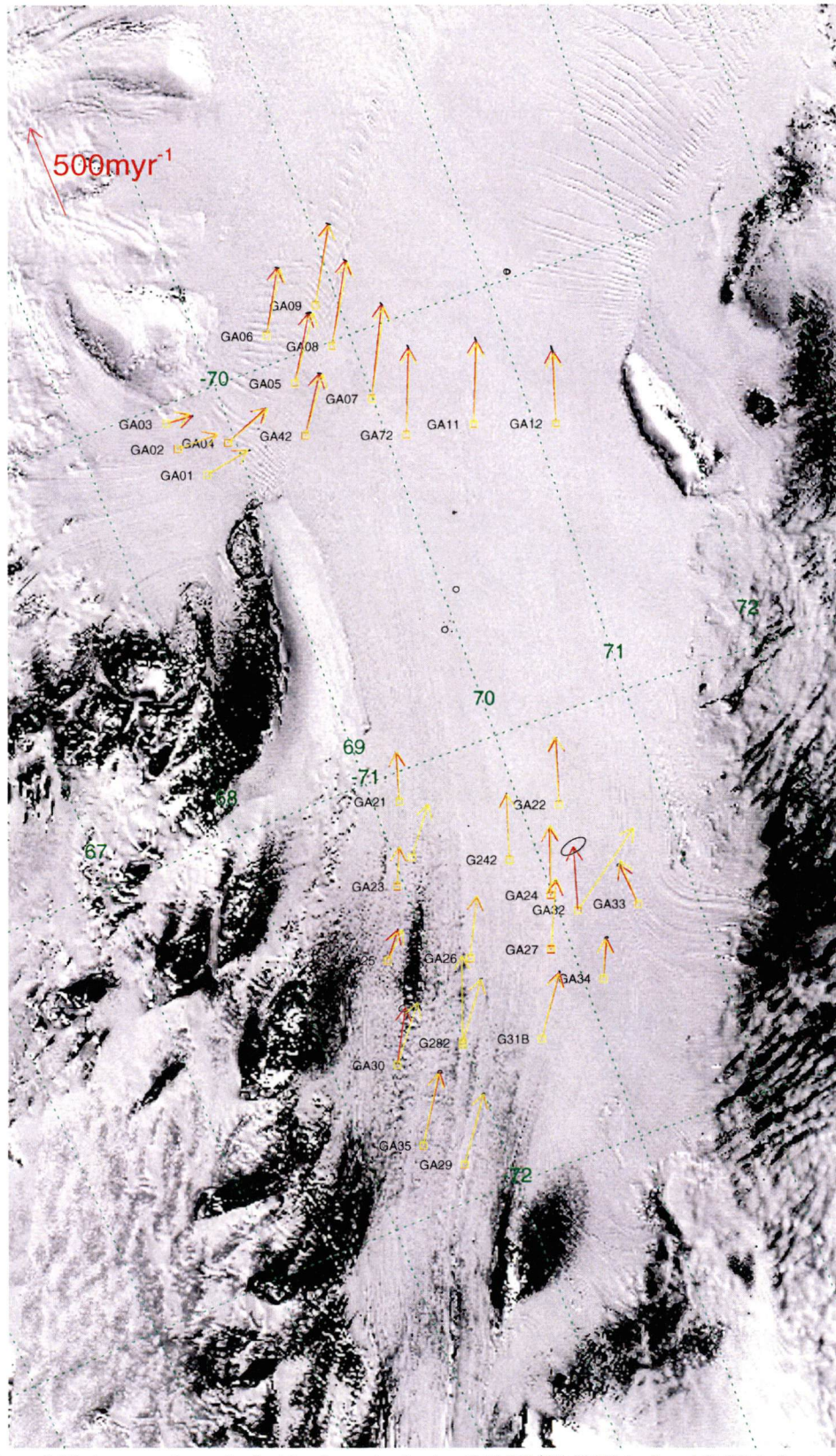

Figure 5-22: A comparison of velocities determined using GAMIT/GLOBK (red) and PoPS (yellow). Error ellipses at the 95% confidence interval are shown for the GAMIT/GLOBK results.

	DEM-GAMIT$_{88-99}$ (m)	DEM-GAMIT$_{88-91}$ (m)	DEM-PoPS (m)	GAMIT-PoPS (m)
Min	-14.2	-14.2	-48.1	-11.4
Max	20.2	4.8	9.3	0.7
Mean	-0.1	-2.3	-9.7	-2.2
RMS	4.7	5.4	17.5	3.1

Table 5-15: Differences between PoPS and GAMIT-derived heights and between an independent DEM and each of the GPS solutions.

5.1.2.5.3 GPS-terrestrial comparison

Many of the GPS sites are located in similar geographical locations to the position of the 'Corry poles' when they were originally surveyed. This provides an opportunity to test if the ice shelf velocity has changed at a particular geographical location during the intervening 30 years. It is expected that if the ice shelf were responding to climate change there would be some change in ice shelf strain and/or velocity. For example, the Larsen B ice shelf experienced an increase in velocity of 10-20% prior to its breakup (Rott *et al.*, 1998; Scambos *et al.*, 2000). A slight increase was also seen in the Larsen A ice shelf prior to its breakup (Rack *et al.*, 1999).

Figures 5-23 and 5-24 show a centreline velocity profile of the AIS as a function of distance from the geographical coordinates (at epoch 1969.5) of the southern-most terrestrial site, A406. The GPS sites (shown in blue) are not all on the exact line of the terrestrial survey, and hence there will be some expected variation. Overall, the centreline velocity magnitude (Figure 5-23) and direction (Figure 5-24) appear to have changed negligibly for the most part during the thirty-year period. There is some difference in the directions, and some of these are significant at the 3σ level.

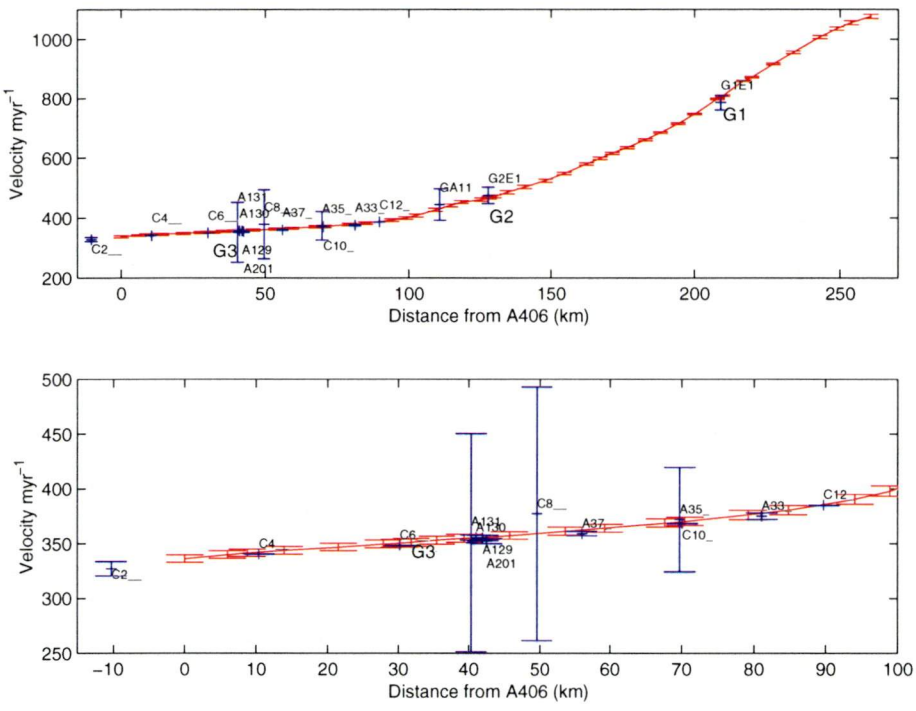

Figure 5-23: Centreline velocity magnitude profile of the AIS from terrestrial (red) and GPS (blue) as a function of distance from the geographical coordinates (epoch 1969.5) of the southern-most terrestrial site, A406. The lower panel is the same data shown at a different scale for the G3 region. The error bars are the formal errors from GLOBK (GPS) and FONDA (terrestrial) scaled to the 95% confidence interval.

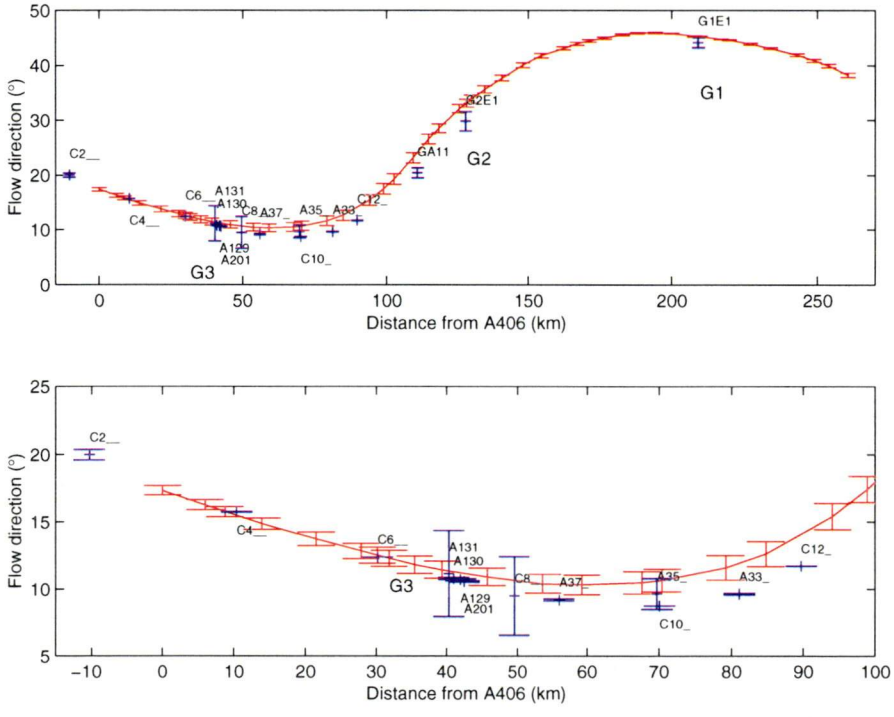

Figure 5-24: Centreline velocity direction profile of the AIS from terrestrial (red) and GPS (blue) as a function of distance from the southern-most terrestrial site, A406. The lower panel is the same data shown at a different scale

for the G3 region. The error bars are the formal errors from GLOBK (GPS) and FONDA (terrestrial) scaled to the 95% confidence interval.

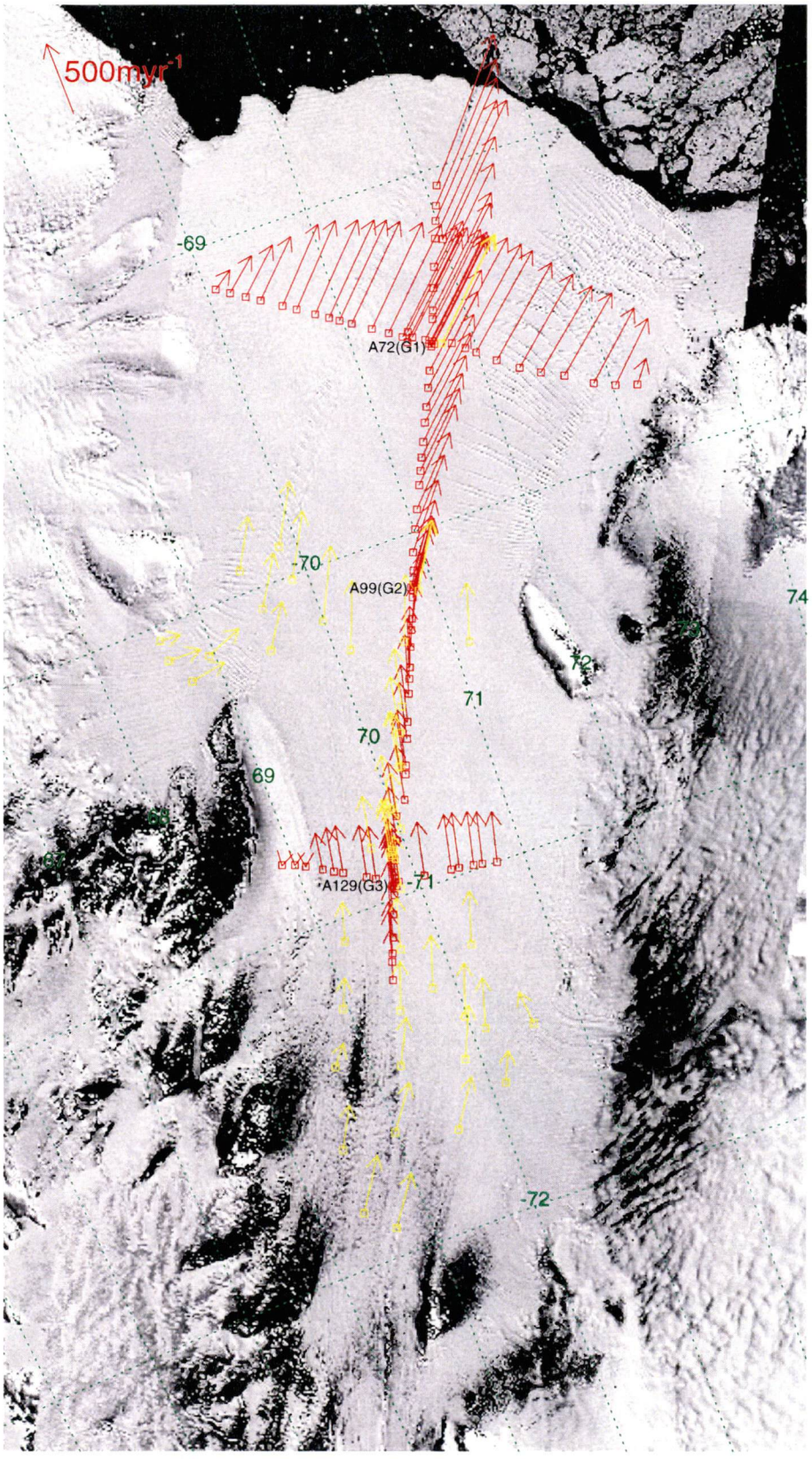

Figure 5-25: Velocities determined from GPS (yellow) and terrestrial (red) methods.

To test if the velocity of the ice shelf has changed between 1968-70 and 1988-99, a statistical congruency test was performed. Candidate pairs were chosen using the following three selection criteria: 1) That the GPS and terrestrial site are separated by no more than 5km; 2) if a site appeared more than once, take the pair with the lowest inter-station distance; and 3) there must be at least one GPS occupation after 1991 due to the poor data quality prior to this time. The candidate list is shown in Table 5-16, sorted south to north, with candidate pairs spanning the region from south of G3 to G1. Unfortunately, only nine pairs are available to test.

GPS site	Terrestrial site	Mean Lat. (°)	Mean Long. (°)	Inter-site distance (m)	ΔV_{Mag} (myr^{-1})	% difference	ΔV_{Dir} (°)
C4__	A404	-71.146	69.594	3163.2	-1.0	-0.3	0.00
C6__	A130	-70.971	69.815	1345.7	-2.8	-0.8	0.00
CAMP	A38_	-70.893	69.871	379.7	-1.0	-0.3	-0.01
A37_	A36_	-70.762	70.002	3018.0	-2.2	-0.6	-0.02
C10_	A33_	-70.640	70.226	1686.5	-1.8	-0.5	-0.03
A33_	A32_	-70.558	70.315	3103.2	-1.0	-0.3	-0.03
C12_	A30_	-70.461	70.437	4872.0	-5.0	-1.3	-0.06
G2W1	A101	-70.162	70.857	1557.0	5.3	1.1	-0.08
G1W1	A75_	-69.498	71.690	2399.9	-3.8	-0.5	-0.02

Table 5-16. Comparison of GPS and terrestrial horizontal velocities separated by 20-30 years in time. $\Delta V = V_{GPS} - V_{Terrestrial}$.

The congruency of the two data sets may be statistically tested as follows (Niemeier, 1987):

Hypothesis H_0 : The two data sets are equivalent. That is, there is no change during the period 1968-70 to 1988-1999.

Test Decision: $F_{test} < F_{r,r,1-\alpha} \Rightarrow$ Accept H_0.

where

$$F_{test} = \frac{\Delta \mathbf{x}^T \mathbf{Q}_{\Delta x}^{+} \Delta \mathbf{x}}{r.s_0^2}$$

$F_{r_1,r_2,1-\alpha}$ is the standard F probability distribution

$\Delta \mathbf{x} = \mathbf{x}_2 - \mathbf{x}_1$

$\mathbf{Q}_{\Delta x} = \mathbf{Q}_{x_1} + \mathbf{Q}_{x_2}$

$\mathbf{Q}_{x_1}$, $\mathbf{Q}_{x_2}$ are the coordinate covariance matrices for each of the two data sets

$1 - \alpha$ is the confidence interval

$r = r_1 = r_2 = u - d$ is the redundancy

u is the number of unknowns and d is the datum defect

$\mathbf{x}_2, \mathbf{x}_1$ are the velocity vectors from the two methods

$$s_0^2 = \frac{s_{01}^2 r_1 + s_{02}^2 r_2}{r_1 + r_2}$$

s_{01}^2 and s_{02}^2 are the χ^2 variance factors from the two data sets.

and the superscript + notation refers to the pseudo-inverse.

We perform two tests, one for each of velocity magnitude and direction. In our case the datum defect is zero, and hence the redundancy is equivalent to the number of unknowns. At the 95% confidence level, H_0 is rejected both for magnitude (1.73 > 0.31) and direction (18.38 > 0.31). This may be explained in a number of ways. There is some expected variation in horizontal velocity due to the different geographical locations of the sites and since this is not accounted for some bias will exist. The pair with the lowest inter-site distance agrees within their 1σ uncertainties. Secondly, the sample size is small and so the results may not be representative of the remainder of the ice shelf. Thirdly, the largest differences in both magnitude and direction occur in the region of G2 and this may point to some variation in ice flow in this region during the period 1968-1999. The ice flow in this region is heavily influenced by the inflow of ice from the Charybdis Glacier to the West. However, while the change in direction is similar in this region, the change in velocity is of opposite sign suggesting that this is not the cause of the variation. The G2 region is, however, close to the weakest point in the terrestrial traverse and hence there may be some undetected systematic errors, although changes of this magnitude, and of opposite sign, seem unlikely.

Finally, despite the rejection of the hypothesis for the tested data, the velocity magnitude variation over the 20-30 year period at these sites is less than approximately 1% in all cases, while the direction of flow agrees to less than 0.1°. Additionally, the change in velocity magnitude is not uniform. Consequently, without further data it is difficult to conclude if the velocity profile of the AIS has changed measurably during

the 20-30 year period of these data. If the state of balance of the AIS has changed during this period, it is not clearly exhibited in the GPS/terrestrial velocity profile.

5.1.2.6 Vertical velocities

The GPS-derived vertical velocities are generally poorly determined due to three reasons. Firstly, the sites observed during 1988-91 suffer from the poor data quality and lack of height measurements in some instances. Secondly, sites occupied in just one season do not have enough data to determine the vertical component of velocity. Furthermore, the actual velocities determined from the 1988-91 data are not the same as for the later data. This is because for many occupations in 1988-91, the height of the reference mark above the snow was not measured. Hence, the GPS measurements cannot be related to the reference mark, but only the snow surface. The later measurements are all relative to the reference mark. Therefore, velocities determined from the 1988-91 data only are snow surface velocities, whereas the velocities for the remainder of the marks are reference mark velocities. Thirdly, the local vertical component is the least well determined in GPS studies due to satellite geometry and tropospheric mismodelling.

Very few of the vertical velocities are well determined, since most have been either occupied during only one season or in 1988-91 only. A histogram of the 1988-91 GPS-derived vertical velocities is shown in the top panel of Figure 5-26. This shows that the determined velocities are generally randomly distributed, although with a slight bias toward -1myr^{-1}.

Those GPS-derived vertical velocities that are significantly different from zero at the 3σ level are shown in Table 5-17. The large upwards velocity at GA04 may be due to ice shelf ridging in the region where the ice flowing out of the Charydbis Glacier meets the main flow of the AIS, north of Beaver Lake. Alternatively, a large, positive ice shelf thickening rate will cause such a large positive vertical motion. The other sites near GA04 do not exhibit a uniform trend, although the location of GA04 does correspond with high freeze rates (0.5-1.0myr^{-1}) modelled by (Williams *et al.*, 2001). Further data are required to confirm this high vertical velocity.

The negative vertical velocities of GT05, GT82 and GT06 are expected due to their location on the grounded Charybdis Glacier and hence this is just the down-slope flow.

Four well-defined sites that were occupied in 1995-96 and 1998-99 (C4, C6, C10 and C12) are shown in the lower panel of Figure 5-26. The velocities at these sites are relative to the reference mark, rather than to the snow surface. They show a systematic trend and a weighted-linear regression performed on these sites reveals a slope in the vertical velocity of -0.003m/yr/km along the line of these sites. The inference of these vertical velocities is dependent on the pole motion being linear over the three year period. These velocities will almost certainly be contaminated by snow compaction and/or melting-in. The systematic trend shown in Figure 5-26 suggests that these effects are uniform across the sites or, alternatively, they are latitude dependent. These vertical velocities are used to derive basal melt-rates at these locations in Chapter 6.

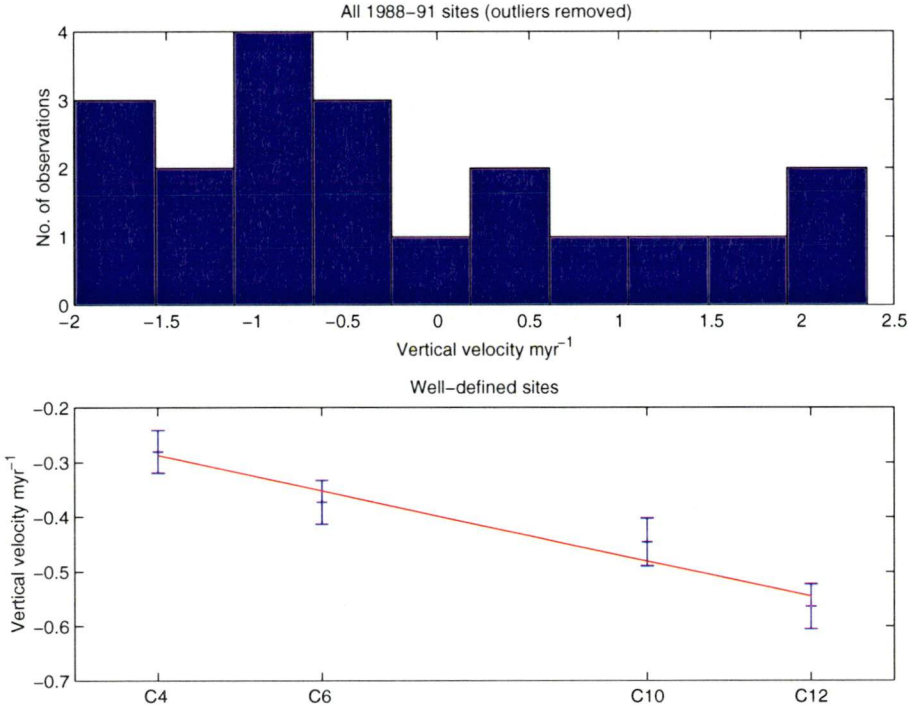

Figure 5-26: GPS-derived vertical velocities. The top panel is a histogram of all 1988-91 velocity determinations. Sites with velocities greater than 3myr^{-1} have been removed from the data. The lower panel is those well-defined sites with velocities that are significant at the 3σ level, spaced according to distance. The red line is the result of a weighted-linear regression.

Site	Velocity measured	Vertical velocity (myr^{-1})	1σ Error (myr^{-1})
C12__	Reference mark	-0.56	0.04
C10_	Reference mark	-0.45	0.04
C6__	Reference mark	-0.37	0.04
C4__	Reference mark	-0.28	0.04
GA04	Snow surface	+2.36	0.51
GT05	Snow surface	-2.10	0.46
GT82	Snow surface	-2.49	0.43
GT06	Snow surface	-1.85	0.43

Table 5-17. Vertical velocities of the reference mark at sites where the vertical velocities are significant at the 3σ level.

5.2 Comparison with satellite data

In an attempt to assess the quality of our determined GPS/terrestrial horizontal velocities, we have compared our results with those derived from remote sensing images (Young and Hyland, 2001, in press). The method used to determine the velocities is similar to that of Derauw (1999) and used maximum coherence of two Radarsat images (personal communication, N. Young, 2001). These Radarsat velocities are determined at the GPS and terrestrial locations through a nearest neighbour method. It was not possible to determine velocities at every location since the images were either not coherent in these regions or the sites were located away outside the images. The velocities derived from the satellite images are plotted with the terrestrial and GPS velocities in Figure 5-27 and Figure 5-28, respectively. The velocities from the *in situ* and satellite data are in general agreement, although the differences are not normally distributed as shown in Figure 5-29. The terrestrial data in particular has two peaks in each of the magnitude and direction differences. The velocity differences along the centreline profile of the terrestrial traverse are shown in Figure 5-30. These differences may be a result of changes in the state of the ice shelf between the time of the terrestrial traverse (1968-70) and the time of the satellite image acquisitions during September-October 1997.

However, this does not appear to be the case since the GPS velocities, determined from data observed during 1988-1999, exhibit a similar north-south trend to the

terrestrial data. That is, a systematic difference is apparent in the data, especially in the magnitude. For example, in Figure 5-27 the satellite velocities (yellow vectors) are less than the terrestrial velocities (red vectors) in the G3 region. North of this region there is a gradual change in this scenario, with the satellite velocities significantly greater than the terrestrial velocities north of the G2 region. A similar pattern is seen in Figure 5-28, with the southernmost satellite velocities smaller than the GPS velocities, while they are similar in magnitude in the G2 region.

In terms of the direction of the velocity vectors, the biases are evident in both the terrestrial and GPS comparisons (see Figure 5-29). The lower panel of Figure 5-30 shows the variation of the direction as a function of distance from the southernmost terrestrial site (A406).

Some biases remain in the satellite-derived velocities, including those from tidal signals, satellite orbits and the inverse barometer effect (personal communication, N. Young, 2001). Depending on the differential tidal cycle between satellite passes, errors greater than 20m may propagate into the horizontal coordinates since the technique deals with slant ranges. This error will not be uniform due to the amplification of the tidal signal towards the southern limits of the ice shelf. These errors will consequently form a significant part of any bias present in the satellite velocities. However, despite the presence of one or more systematic biases, the satellite velocities appear to be of a high precision as evidenced by the relative smoothness of the differences in Figure 5-30.

The GPS and terrestrial velocities have been shown to be in good agreement in Section 5.1.2.5.3, and so we conclude that the satellite velocities are contributing the majority of any systematic biases present in these comparisons.

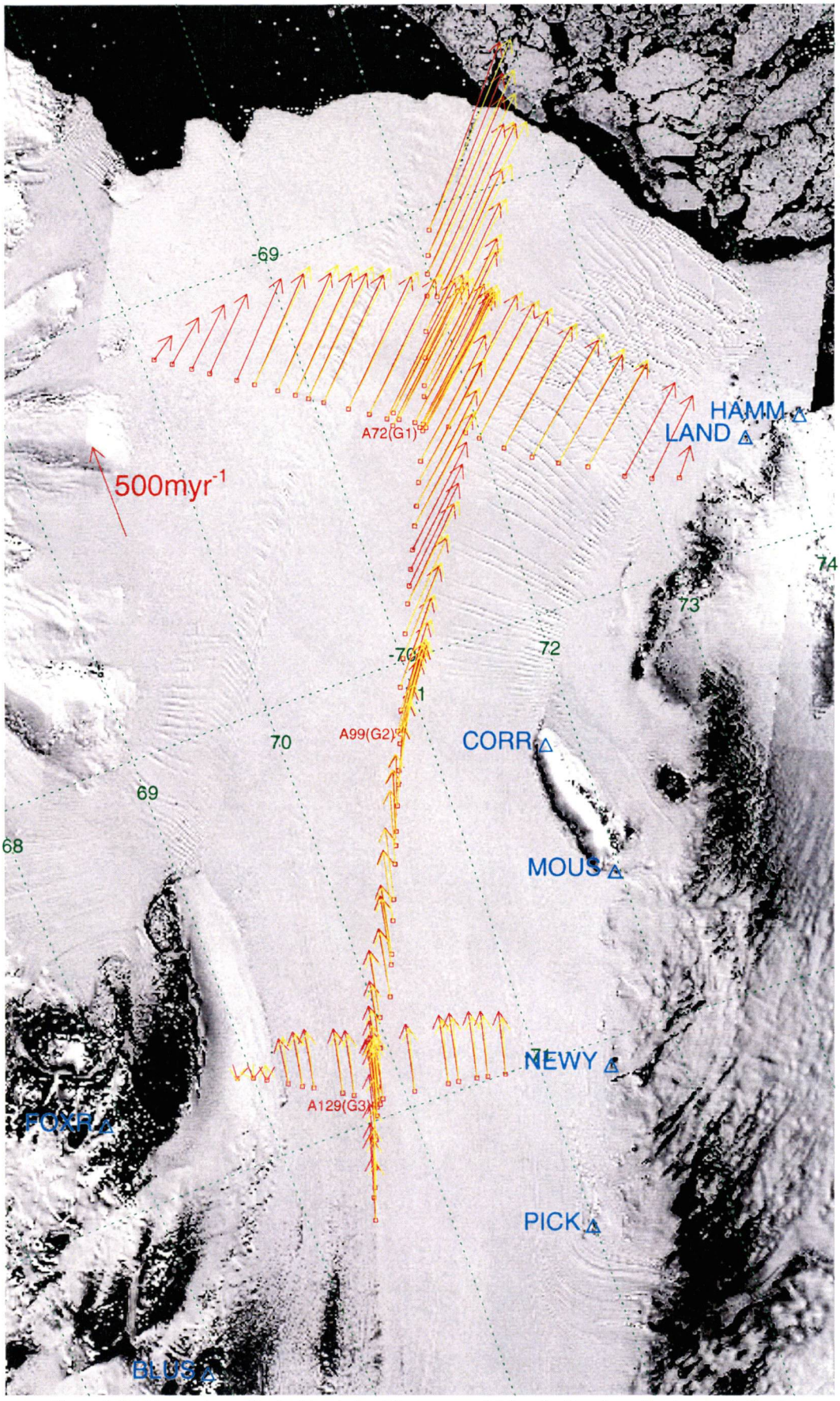

Figure 5-27: Comparison of velocities derived from terrestrial data (red) and satellite images (yellow).

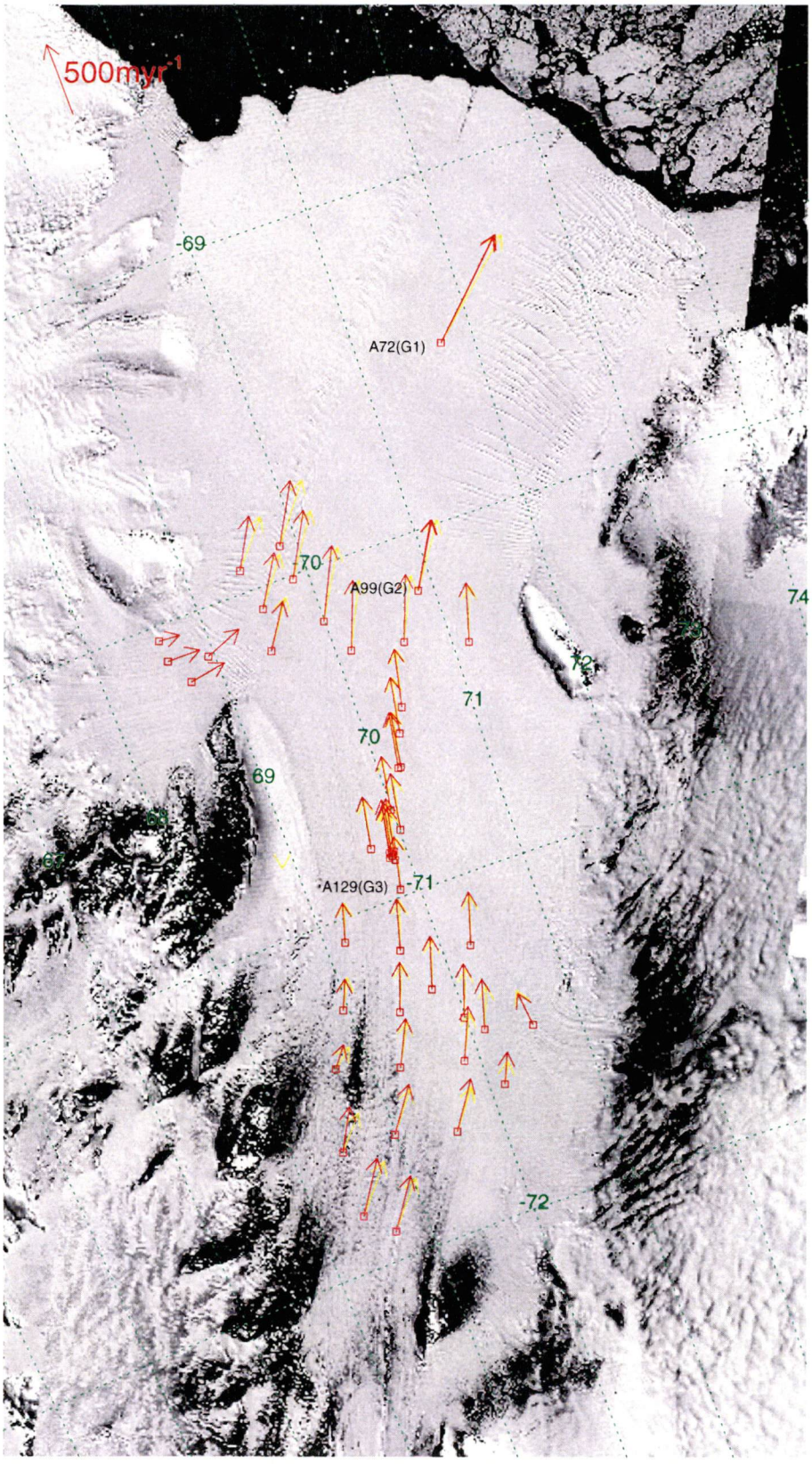

Figure 5-28: Comparison of velocities derived from GPS data (red) and satellite images (yellow).

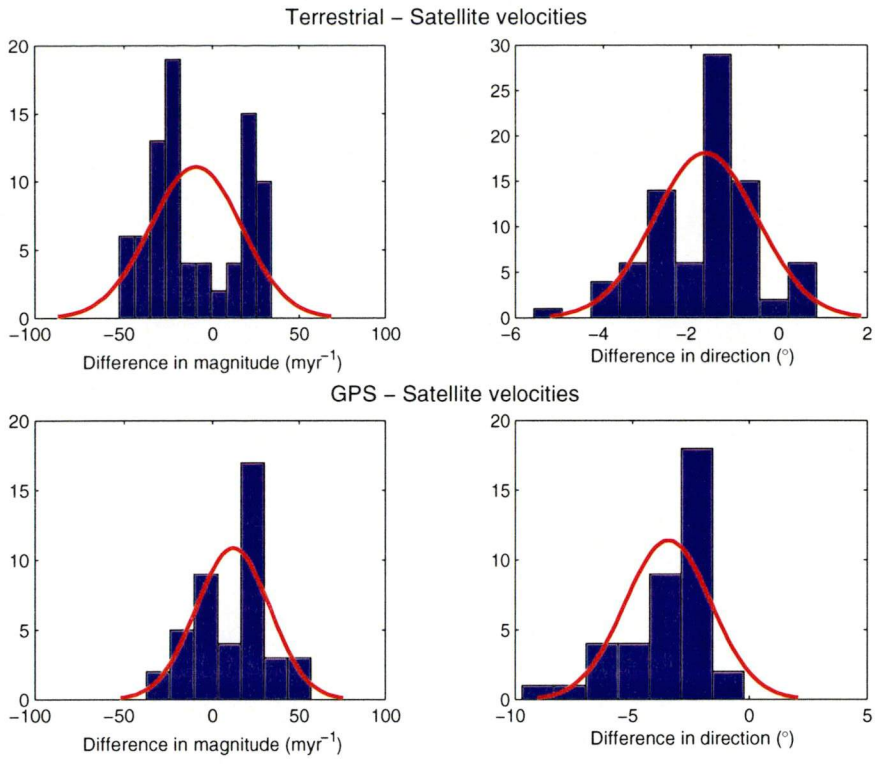

Figure 5-29: Histograms and normal distributions of the velocity magnitude and direction differences between the terrestrial and satellite data (top) and the GPS and satellite data (bottom).

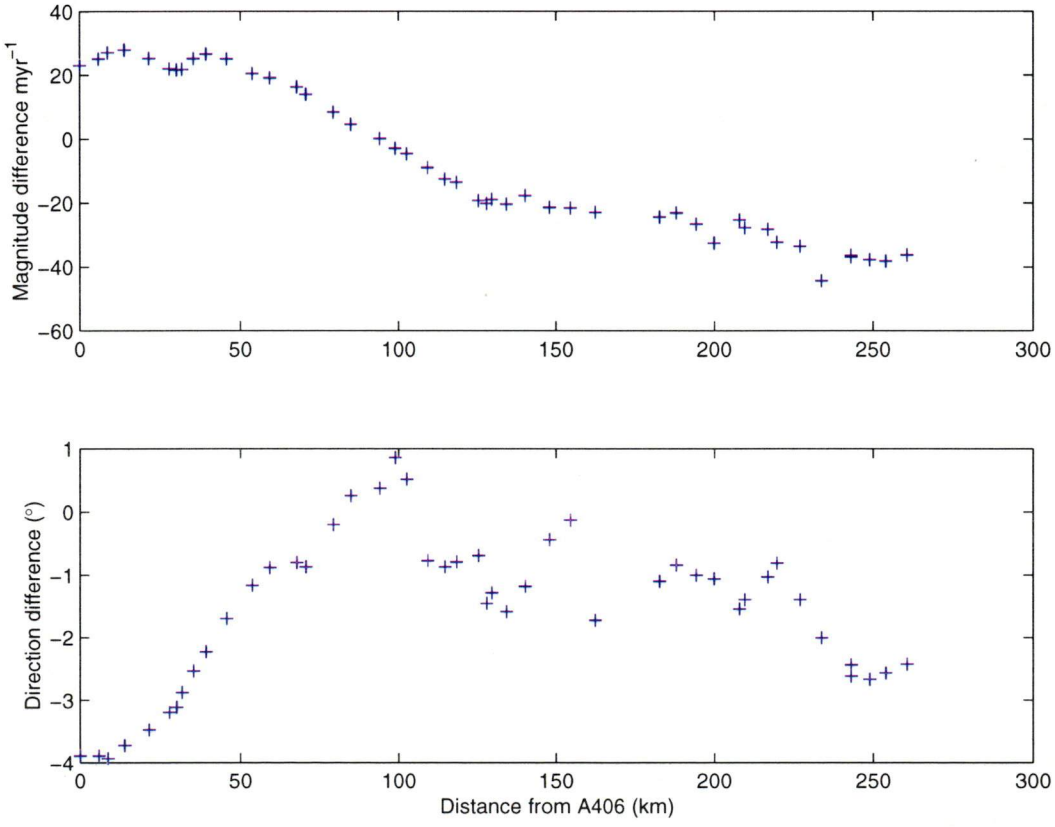

Figure 5-30: Centreline differences between the terrestrial and satellite velocity magnitude (top) and direction (bottom) differences as a function of distance from the southernmost terrestrial point A406.

5.3 Summary

The aim of this Chapter was to determine the velocity of the AIS from *in situ* survey data. The data are in the form of two terrestrial surveys (1968-1970) and six GPS (1988-1999) campaigns. The velocities presented in this Chapter represent the most complete set of velocities available for the AIS from *in situ* data. The importance of results being presented on a stable and accessible reference frame was emphasised in Chapter 2, and consequently the results in this Chapter are relative to the ITRF96 at 1969.5 (terrestrial) and ITRF97 at 1989.0205 (GPS). Differences between these frames are sub-cm and hence the two frames may be regarded as equivalent for these purposes. Of course, transformation parameters are available to transform the results from one system to another.

In terms of the terrestrial data, significant error was detected in an earlier reduction of the survey data. The major sources of the error were identified as two incorrectly entered angles, resulting in an angular misclose of approximately 43′. Further small errors (mainly in angles) were also detected. A large (ten month) timing error was also detected north of G1. These errors resulted in coordinate shift of up to 3-4km, mainly in the east-west component. Importantly, the understood position of the 1968 A1 borehole (the site of the only deep core on the AIS) changed by ~1km to the North and ~3km to the West. This has important implications for the oceanographic and glaciological interpretations of the ice core data.

By holding fixed the coordinates of stations at the southern end of the traverse, the misclose was computed using the corrected data and found to be ~2-4m and 15 arc-seconds. This misclose confirmed the high precision of the terrestrial survey. An increased amount of data were added to the analysis of the traverse, incorporating star observations for azimuths and complete strain grid observations. Mean coordinate precisions were 0.94m and 0.98m for latitude and longitude, respectively. Even at the weakest point of the traverse, coordinate uncertainty is only 3.5m and 2.4m for latitude and longitude, respectively.

Velocities were determined from the terrestrial data using the FONDA software and compared to values reproduced from the original erroneous observations. Differences were found to be as large as ~150myr^{-1} and ~38°, although median differences were

~5 myr^{-1} and 0.8°. Centreline and lateral profile values were compared to those values shown in Budd *et al.* (1982), the major publication from the 1968-1970 survey. The differences along the centreline profile reached a maximum at the northernmost point of the traverse, where the FONDA velocities taper-off slightly rather than continue to increase as in Budd *et al.* (1982). For the lateral profiles, the largest differences are seen at the northern profile, while the southern profile is largely unaffected by the traverse errors.

The daily GPS data were processed using GAMIT. The early (1988-91) GPS data were found to be heavily affected by the ionosphere due to single frequency measurements (1988-89), receiver multiplexing (1989-90 and 1990-91) and high ionospheric variability (1990-91). These early data also suffered from a lack of GPS satellites and permanently operating global receivers. Additional regional and global data (such as SCAR91 and GIG91) were included where available. Significant effort was required to achieve satisfactory results from these early GPS data, including manual data cleaning. The data collected after this period were of a good quality and the data cleaning process required little manual intervention. Where necessary, tidal and sub-daily horizontal motions were removed from the RINEX data prior to processing.

The daily solutions combined for each season were subsequently combined together using GLOBK, estimating velocities for the AIS sites when these were resolvable. Tidal motion at the 1988-91 sites was regarded as a constant during the period of measurement and removed at this stage. Further kinematic data processed in the Track software were also included at this stage. To produce the final velocity estimates, each season was combined together and then transformed to the ITRF97. The χ^2 per-degree-of-freedom value for the combination was 1.3, suggesting that the data fits together well.

The 1988-91 GPS velocities were compared against those from a previous analysis using early commercial software. Velocities from this study were found to be the more realistic when inter-compared with nearby sites and against ice shelf flow lines. Further evidence of their increased precision was obtained by comparing their heights against an independent DEM. The mean bias was reduced by 7.4m in this analysis.

A congruency test was performed on nearby terrestrial and GPS sites to test the hypothesis that the ice shelf velocity was constant over the period 1968-70 to 1988-1999. Nine station pairs were tested; the majority in the G3 region although one pair was near G2 and one near G1. The hypothesis that the ice shelf velocities were the same during the period 1968-1999 was rejected for both velocity magnitude and directions at the 95% confidence interval using the formal errors from GLOBK and FONDA. This suggests that the velocity profile of the AIS has changed at the 95% confidence level during the period 1968-70 to 1988-1999. Except for one site near G2, the pairs suggest a slowing and slight rotation of the ice shelf. Alternatively, the rejection of the hypothesis may be due to the small sample size unaccounted for errors in the GPS and terrestrial data. Consequently, we conclude that the Amery Ice Shelf may have slowed slightly during the period 1968-70 to 1988-1999 in the regions of the station pairs tested. Such a slowing may be a mass balance process resulting from increased ice mass loss from the ice shelf, such as from increased basal melting.

The terrestrial and GPS velocities were compared against independent velocities determined from repeat Radarsat images. The comparison revealed the presence of biases in the satellite velocities, presently at the 20-40myr^{-1} and 1-3° level. Some of these errors (10-20myr^{-1} and several degrees) may be explained by differential tidal motion between satellite passes. Otherwise, these satellite-derived velocities are of a high precision.

The results presented in this Chapter form the most precise, consistent and complete set of velocities determined for the AIS from *in situ* measurements. Significant improvements in precision have been demonstrated over previous analyses, while new data have also been presented. These results are significant for further (and past) ice shelf dynamics studies and, in comparisons against remote sensing measurements, they are a baseline against which velocities from future studies may be compared.

Chapter 6

STRAIN DETERMINATION USING A COMBINATION OF GPS AND TERRESTRIAL DATA

6.1 Introduction

A knowledge of strain at different locations on an ice shelf is of significant importance since it is a determining factor in ice dynamics, especially in initiating ice shelf break-up (Hughes, 1992). It is also an important parameter in determining the rate of ice shelf thickness change and basal melt rates (Budd *et al.*, 1982). Horizontal strain alone is of significant value since it can be used to infer the vertical strain and hence thinning of an ice shelf (see Section 6.2.6 for a description of this). In this Chapter we firstly review the theory of strain, showing the various strain parameters and their physical relationship to glacier / ice-shelf surfaces, along with a brief overview of basic strain computation surfaces. We then provide an overview of the different strain computation methodologies, distinguishing between two-dimensional and three-dimensional methods.

Most of the methods discussed below have their foundation in crustal strain, although there is no reason why these methods cannot be applied to the field of glaciology. This overview is provided with the aim of reducing the AIS survey data using the most efficient data reduction and strain computation methodology available. Deformation data is generally difficult and expensive to collect on a continuous basis, and this is nigh impossible to achieve in Antarctica. Therefore, it is important that we attempt to extract as much information as is possible from the small amounts of data we do have.

6.2 Overview of relevant strain theory

A substance is said to be *strained* when it "is distorted so that the relative configuration of a system of marked particles ... is changed in any way" (Jaeger, 1969, p.20). For distortion

to occur the particles need to move relative to one another, rather than in an absolute sense. If all of the particles are uniformly translated or rotated together, then no strain occurs.

When such a substance is strained, there are changes in either 1) the length of lines or 2) angles between intersecting lines, or both. These two changes are referred to as *longitudinal strain* ε and *shear strain* γ respectively.

6.2.1 Longitudinal strain

Longitudinal strain is defined in terms of an extension of a line. It is therefore a measure of change in one-dimension, as in Figure 6-1 and defined in equation (6.1). A positive value for ε means the line is expanded over time, while a negative value means contraction over time.

$$\varepsilon = \frac{l_1 - l_0}{l_0} = \frac{\delta l}{l_0} \tag{6.1}$$

where l_0 (PQ_0) and l_1 (PQ_1) are the original and deformed line lengths respectively.

Figure 6-1: Longitudinal strain along line PQ

6.2.2 Shear strain

Shear strain is defined in relation to the angular change (or *angular shear* ψ) between two perpendicular lines. It is therefore a measure of a two-dimensional change, as shown in Figure 6-2 and defined in equation (6.2). In the case shown in the figure, where an object is undergoing shear strain, a line parallel to OP would move a distance proportional to the shear strain in the direction of the line.

$$\gamma = \tan\psi \tag{6.2}$$

In terms of observed angular quantities, the angular shear may be expressed as the change of angle OPQ_0 to angle OPQ_1:

$$\psi = \langle OPQ_1 - \langle OPQ_0 \tag{6.3}$$

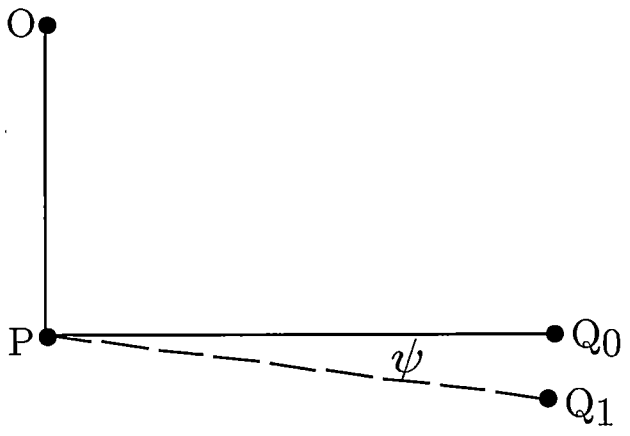

Figure 6-2: Shear strain on OPQ_0

6.2.3 Simplifications

The general theory of strain becomes extremely complicated when deformation of a non-homogenous medium or a long period of time is considered, since relationships may no longer be linear. To obtain a workable theory, two simplifying assumptions are often made: that the strain is infinitesimal and homogeneous.

6.2.3.1 Infinitesimal strain

The term *infinitesimal strain* refers to the fact that a finite amount of strain occurring over a period is actually the sum of small increments of infinitesimal strain. When a geodetic measurement of strain is taken it is infinitesimal strain, not finite strain, which is being measured. As pointed out by Jaeger (1969), these infinitesimal strains (ε) should be so small that their squares (ε^2) are negligible.

6.2.3.2 Homogenous strain

For strain in a substance to be homogenous, it must meet three criteria (Ramsay, 1967):

1. Straight lines must remain straight after deformation.

2. Parallel lines remain parallel after deformation, although their direction may be altered.

3. All lines in the same direction in the strained body have constant values of longitudinal and shear strain.

The implication here is that the strain must be uniform across the entire study area. Heterogeneous strain occurs where one or more of these criteria are not met.

6.2.4 Three-dimensional strain model

A strain occurring in a body will affect the body in all three-dimensions. However, in practice it is more difficult to determine the vertical component of strain since most motion occurs in the horizontal plane and using space geodetic methods the height measurements are the least precise. Most researchers have dealt with strain in a two-dimensional sense when using terrestrial geodetic data (see eg., Frank, 1966; Bibby, 1973; Prescott, 1976), ignoring the vertical component. This, however, may in fact distort the derived parameters (Brunner, 1979).

The components of infinitesimal strain are presented below in three-dimensions, although the two dimensional case is a trivial simplification.

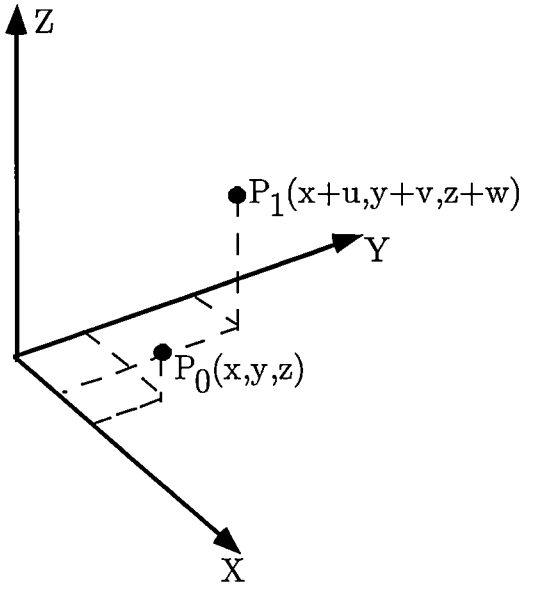

Figure 6-3. Three-dimensional deformation of point P from coordinates (x, y, z) to (x+u, y+v, z+w) in a left-handed coordinate system.

Constructing a three-dimensional reference frame, as in Figure 6-3, the following notation applies in regard to the fundamental components of strain (Jaeger, 1969). The extensions of lines in the directions of the axes are:

$$\varepsilon_x = \frac{\partial u}{\partial x}, \qquad \varepsilon_y = \frac{\partial v}{\partial y}, \qquad \varepsilon_z = \frac{\partial w}{\partial z} \tag{6.4}$$

The shear strains in each of the biaxial planes are:

$$\begin{aligned} \gamma_{yz} &= \gamma_{zy} = \frac{\partial w}{\partial y} + \frac{\partial v}{\partial z} \\ \gamma_{zx} &= \gamma_{xz} = \frac{\partial u}{\partial z} + \frac{\partial w}{\partial x} \\ \gamma_{xy} &= \gamma_{yx} = \frac{\partial v}{\partial x} + \frac{\partial u}{\partial y} \end{aligned} \tag{6.5}$$

The shear strains as defined here are often referred to as *engineering shear strains.* This definition of shear strain is more commonly used in the literature (as in, e.g., Ramsay, 1967; Jaeger, 1969) than tensor shear strain (as in, e.g., Paterson, 1994). Engineering shear strains are larger by a factor of two.

Rotations around each of the axes (the *components of rotation*) are:

$$\omega_x = \frac{1}{2}\left(\frac{\partial w}{\partial y} - \frac{\partial v}{\partial z}\right), \omega_y = \frac{1}{2}\left(\frac{\partial u}{\partial z} - \frac{\partial w}{\partial x}\right), \omega_z = \frac{1}{2}\left(\frac{\partial v}{\partial x} - \frac{\partial u}{\partial y}\right) \tag{6.6}$$

The ratio of the change in volume to the initial volume (the *dilation*) is:

$$\Delta = \varepsilon_x + \varepsilon_y + \varepsilon_z \tag{6.7}$$

Since *rate of change* is often more of interest than simply the level of change, strain rate values of each of these components may also be calculated. This is done by dividing each of these terms by the difference in time between observations (ΔT) to produce the strain ($\dot{\varepsilon}_x, \dot{\varepsilon}_x, \dot{\varepsilon}_x$), shear ($\dot{\gamma}_{yz}, \dot{\gamma}_{zx}, \dot{\gamma}_{xy}$), rotation ($\dot{\omega}_x, \dot{\omega}_y, \dot{\omega}_z$) and dilation ($\dot{\Delta}$) rates. Strain is a

unit-less quantity (although often referred to in terms of *μstrain*, analogous to a ppm). Strain rates are in units of $year^{-1}$.

From these fundamental components further parameters may be derived that are of significant value to the study of strain. Representing the above deformation process in matrix notation (Brunner, 1979):

$$\mathbf{x}_1 = (\mathbf{S} + \mathbf{R})\mathbf{x}_0 + \mathbf{t} \tag{6.8}$$

$\mathbf{x}_0$ and $\mathbf{x}_1$ represent the coordinate vectors of P_0 and P_1 at epochs t_0 and t_1 respectively (see Figure 6-3). In the case of homogenous strain, this is identical to an affine transformation (Love, 1952). $\mathbf{x}_1$ is the three-dimensional coordinate vector of a deformed point with initial coordinates of $\mathbf{x}_0$, while vector $\mathbf{t}$ contains the three-dimensional translation. The symmetric matrix $\mathbf{S}$ represents the strain tensor and $\mathbf{R}$ is the matrix of rigid body rotations, with the elements of both matrices shown below:

$$\mathbf{S} = \begin{bmatrix} \varepsilon_x & \frac{\gamma_{xy}}{2} & \frac{\gamma_{xz}}{2} \\ \frac{\gamma_{xy}}{2} & \varepsilon_y & \frac{\gamma_{yz}}{2} \\ \frac{\gamma_{xz}}{2} & \frac{\gamma_{yz}}{2} & \varepsilon_z \end{bmatrix} \tag{6.9}$$

$$\mathbf{R} = \begin{bmatrix} 1 & \omega_z & -\omega_y \\ -\omega_z & 1 & \omega_x \\ \omega_y & -\omega_x & 1 \end{bmatrix} \tag{6.10}$$

It is possible to transform the components of strain ($\mathbf{S}$) into a reference frame such that all shears are equal to zero ($\mathbf{S}_p$) (Grant, 1990).

$$\mathbf{S}_p = \begin{bmatrix} e_1 & 0 & 0 \\ 0 & e_2 & 0 \\ 0 & 0 & e_3 \end{bmatrix}$$

This provides the *principal strains* (e_1, e_2, and e_3) in their respective *principal directions.* These principal strains are found by finding the roots of the equation (Ramsay, 1967):

$$\begin{vmatrix} \varepsilon_x - e & \frac{1}{2}\gamma_{xy} & \frac{1}{2}\gamma_{zx} \\ \frac{1}{2}\gamma_{xy} & \varepsilon_y - e & \frac{1}{2}\gamma_{yz} \\ \frac{1}{2}\gamma_{zx} & \frac{1}{2}\gamma_{yz} & \varepsilon_z - e \end{vmatrix} = 0 \qquad (6.11)$$

6.2.5 Alternative strain models

The reference frame in which strain values are calculated for a given application may be chosen to best fit the particular application. Harvey (1985) has presented a series of models useful in determining strain in either three or two dimensions. Since most researchers are interested in deformations occurring near the surface of the Earth, those models which are defined in relation to the local gravity vector or local ellipsoidal normal are often the most useful. As has been mentioned above, in the context of geophysical surfaces the local vertical components of strain are often negligible given the present measurement techniques and time-scales of measurement. Consequently, the three-dimensional model of strain presented above is often reduced to the two-dimensional case.

Recognising that neglecting some or all of these vertical components of strain may mask the true character of the strain field, some researchers have adopted a full or simplified three-dimensional topocentric model (e.g., Harvey, 1985; Grant, 1990). A topocentric coordinate system (Figure 6-4) is tangent to an ellipsoid at some geodetic point with coordinates (ϕ, λ), where ϕ is the geodetic latitude and λ is longitude. The North axis is aligned toward the North Pole, the Vertical axis is normal to the ellipsoid at the origin, while the East axis completes the right-handed coordinate system. The three-dimensional topocentric (East, North, and Vertical) model is described below:

$$\mathbf{S} = \begin{bmatrix} \varepsilon_e & \frac{\gamma_{en}}{2} & \frac{\gamma_{ev}}{2} \\ \frac{\gamma_{en}}{2} & \varepsilon_n & \frac{\gamma_{nv}}{2} \\ \frac{\gamma_{ev}}{2} & \frac{\gamma_{nv}}{2} & \varepsilon_v \end{bmatrix} \tag{6.12}$$

$$\mathbf{R} = \begin{bmatrix} 1 & \omega_v & -\omega_n \\ -\omega_v & 1 & \omega_e \\ \omega_n & -\omega_e & 1 \end{bmatrix} \tag{6.13}$$

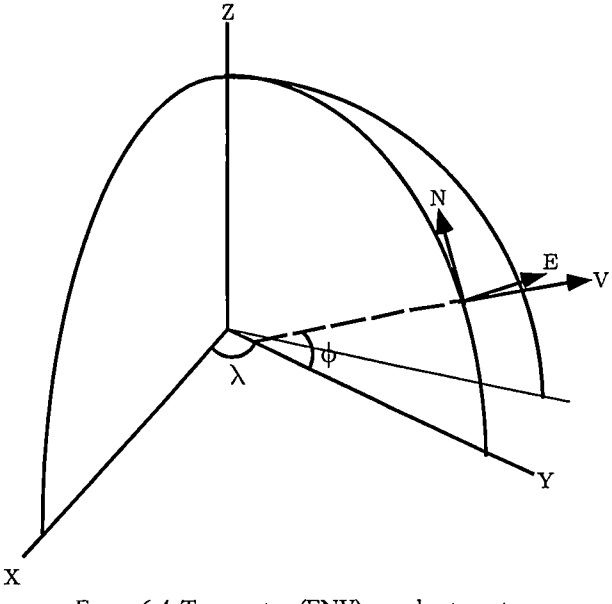

Figure 6-4: Topocentric (ENV) coordinate system

Neglecting the vertical components of strain (ε_v, γ_{ev} and γ_{nv}) altogether, allows for the following two-dimensional topocentric model:

$$\mathbf{S} = \begin{bmatrix} \varepsilon_e & \frac{\gamma_{en}}{2} \\ \frac{\gamma_{en}}{2} & \varepsilon_n \end{bmatrix} \tag{6.14}$$

$$\mathbf{R} = \begin{bmatrix} 1 & \omega_v \\ -\omega_v & 1 \end{bmatrix} \tag{6.15}$$

The following terms are commonly used to describe two-dimensional deformation (adopted from Welsch, 1983):

Pure Shear	$\gamma_1 = e_e - e_n$
Engineering Shear	$\gamma_2 = 2e_{en}$
Total Shear	$\gamma = \left(\gamma_1^2 + \gamma_2^2\right)^{\frac{1}{2}}$
Maximum principal strain	$e_1 = \frac{1}{2}\left(e_e + e_n + \gamma\right)$
Minimum principal strain	$e_2 = \frac{1}{2}\left(e_e + e_n - \gamma\right)$
Azimuth of e_1	$\theta = \frac{1}{2}\arctan\left(\frac{\gamma_2}{\gamma_1}\right)$
Azimuth of e_2	$\varphi = \theta \pm \frac{\pi}{2}$

Apart from the azimuths of principal strain, none of the above representations of strain are coordinate system specific.

Alternatively, the velocity gradient $\mathbf{L}$ may be expressed in terms of strain rate $\dot{\mathbf{E}}$ and rotation rate $\dot{\mathbf{W}}$ (Feigl *et al.*, 1990):

$$\mathbf{L} = \begin{bmatrix} \dot{E}_e & \dot{E}_{en} \\ \dot{E}_{en} & \dot{E}_n \end{bmatrix} + \begin{bmatrix} 0 & \dot{w} \\ -\dot{w} & 0 \end{bmatrix} \tag{6.16}$$

The strain rate $\dot{\mathbf{E}}$ can be represented in the coordinate system defined by the principal axes of strain by decomposing it into its eigenvalues $\dot{\varepsilon}_i$ and its eigenvectors $\hat{\mathbf{e}}_i$:

$$\dot{\mathbf{E}} = \sum_{i=1}^{2} \dot{\varepsilon}_i \hat{\mathbf{e}}_i \hat{\mathbf{e}}_i^T \tag{6.17}$$

By convention $\dot{\varepsilon}_1 > \dot{\varepsilon}_2$, and θ is the orientation of the maximum compressive strain rate $\dot{\varepsilon}_2$, measured clockwise from north to the principal axis $\hat{\mathbf{e}}_2$. As shown in Figure 6-5, the eigenvectors are:

$$\hat{\mathbf{e}}_1 = \begin{bmatrix} \cos\theta \\ \sin\theta \end{bmatrix} \quad \hat{\mathbf{e}}_2 = \begin{bmatrix} \sin\theta \\ \cos\theta \end{bmatrix} \tag{6.18}$$

Since the eigenvalues can be written as:

$$\hat{\varepsilon}_i = \hat{\mathbf{e}}_i^T \dot{\mathbf{E}} \hat{\mathbf{e}}_i \tag{6.19}$$

the magnitudes of the strain rates in the direction of the principal axes are:

$$\begin{aligned} \dot{\varepsilon}_1 &= \dot{E}_e \cos^2\theta + \dot{E}_n \sin^2\theta - 2\dot{E}_{en} \sin\theta \cos\theta \\ \dot{\varepsilon}_2 &= \dot{E}_e \sin^2\theta + \dot{E}_n \cos^2\theta - 2\dot{E}_{en} \sin\theta \cos\theta \end{aligned} \tag{6.20}$$

The four quantities ($\dot{\varepsilon}_1$, $\dot{\varepsilon}_2$, θ, $\dot{w}_v$) define the *eigenvalue parameterisation* of the two-dimensional velocity field (Feigl *et al.*, 1990). Furthermore, the angular shear strain rates are defined as:

$$\begin{aligned} \dot{\gamma}_1 &= \dot{E}_e - \dot{E}_n \\ \dot{\gamma}_2 &= 2\dot{E}_{en} \end{aligned} \tag{6.21}$$

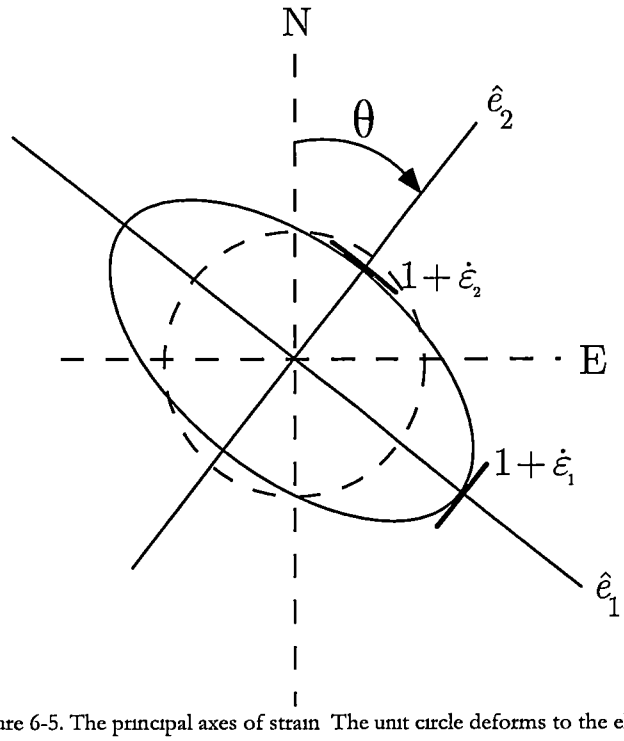

Figure 6-5. The principal axes of strain The unit circle deforms to the ellipse.

6.2.6 Strain in Ice

6.2.6.1 Infinitesimal and homogenous strain on an ice shelf

The question '*under what conditions does strain on an ice shelf fit the assumptions of infinitesimal and homogenous strain?*' is an important one to consider. If these assumptions are not appropriate on ice shelves then the more complex notation for finite and heterogeneous strain needs to be adopted. Fortunately this is not the case, since ice shelf strain is infinitesimal and homogenous within certain bounds. In terms of infinitesimal strain, strains on ice shelves may reach 10^{-2}, as is the case on the AIS (Budd, 1966a). Despite this, the squares of this value are still negligible and so the assumption of infinitesimal strain holds. Unfortunately, in the case of homogenous strain, the relevant conditions will not always be met over an entire ice shelf. In fact, given a large enough ice shelf, the conditions of homogeneity break down. However, by applying the condition to smaller areas, the homogenous strain condition will be met.

6.2.6.2 Incompressibility of ice

Since ice is incompressible (Paterson, 1994), it is held from equation (6.7) that:

$$\varepsilon_1 + \varepsilon_2 + \varepsilon_3 = 0 \tag{6.22}$$

and therefore:

$$\dot{\varepsilon}_1 + \dot{\varepsilon}_2 + \dot{\varepsilon}_3 = 0 \tag{6.23}$$

That is, the dilation and dilation rate is equal to zero. If only the horizontal components of strain ($\dot{\varepsilon}_1, \dot{\varepsilon}_2$) can be measured, then the vertical component ($\dot{\varepsilon}_3$) may be computed using equation (6.23). This relationship is used in Section 6.4.4 to determine ice shelf basal melt using, amongst other parameters, the sum of the horizontal strain rates to determine the vertical strain rate.

6.2.6.3 Local topocentric model

Rather than using a standard topocentric coordinate system (with the vertical axis normal to the ellipsoid), glaciologists tend to use a coordinate system with the axes along the flow direction and perpendicular to the surface (Nye, 1957). This is achieved by rotating the local topocentric coordinate system around one of the horizontal axes (Figure 6-6). 'Horizontal' strain values are then along the surface of the ice, rather than dipping into the ice surface. 'Vertical' strain is perpendicular to the horizontal surface, completing the orthogonal coordinate system. Since ice shelves, unlike glaciers, tend to have a small slope (only 1-2 degrees), the difference from the standard topocentric model is negligible for the computation of strain and the standard topocentric model is adopted.

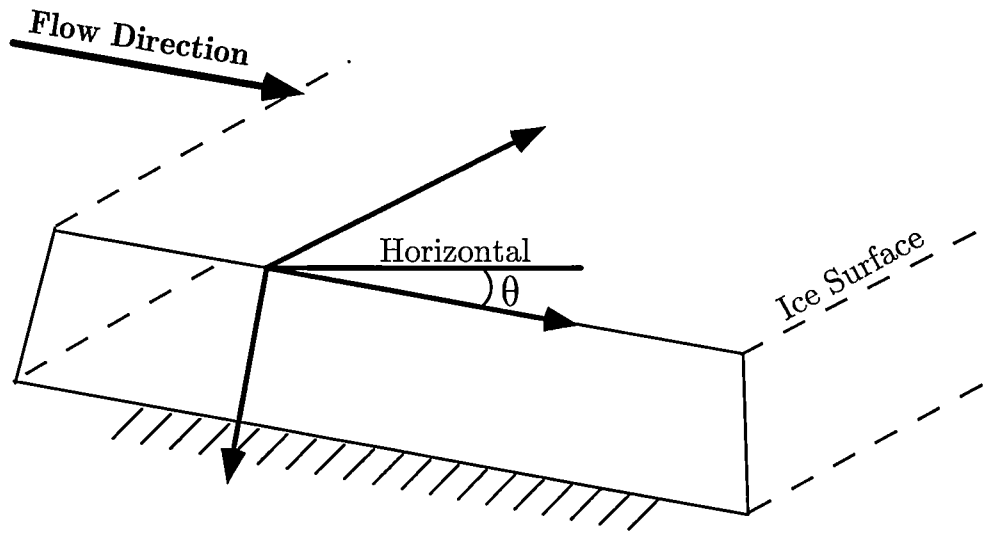

Figure 6-6: Coordinate system commonly used in the study of glaciers.

6.3 Strain computations

Conventional deformation surveys consider the measured network to be stationary during the epoch of measurement, as any deformation is well below the measurement noise during the time of the survey. With ice shelves / glaciers this is not the case. Any computation process will need to consider the systematic motion of ice when measurements to or from stations on moving ice are present.

Several methods have been suggested to account for this movement, of which the most widely used are:

1. *Time reduction of observations* – original observations are adjusted so as to refer to a particular reference epoch under the assumption that changes to both distances and angles are constant over time (Swithinbank, 1958).
2. *Time reductions of positions* – coordinates of points are corrected from their observation epoch to a chosen reference epoch by applying their observed displacement vector (Dorrer *et al.*, 1969).

The reader is referred to Dorrer *et al.* (1969) for a thorough description of the methods and formulae.

Thomas (1970) has shown that the assumptions on which the time reduction of observations method is based do not always hold true. This is because the rates of change of an angle will not always be constant, and proposed a "shuffle resection method" - an iterative least squares resection using moving control points. As with the time reduction of positions method, the proposed method relies on a constant rate of change of coordinates.

Motivated by a desire to overcome the reliance of the above methods on certain assumptions, Wager *et al.* (1980) proposed a method that relies only on the relative movement of the markers being "significantly greater than the survey accuracy". Standard least squares observation equations are extended to be time dependent and include velocity and acceleration parameters with results referred to the datum time. Wager *et al.* (1980) rightly point out that any gross or systematic errors in the network observations will be easily hidden within the velocity and acceleration solutions when these terms are parameterised.

During the period of the 1970s and 1980s, significant advances in conventional deformation computational techniques arose. These methods are reviewed with a view to their application in deformation computations involving moving and deforming ice shelves and glaciers.

6.3.1 Two Dimensional Methods

Initially, computations of Earth deformation involved only small areas, with most of the observations used of the conventional terrestrial geodetic type, beginning with angles, then progressively including distances, height differences and gravity observations (Frank, 1966; Bibby, 1975). As data increased in availability, quality and type, and as study areas were widened, computational methods were developed to extract as much deformation information as possible from the available data (e.g., Brunner *et al.*, 1981; Segall and Matthews, 1988).

Early surveys were initially limited to horizontal deformation measurements by the precision and nature of the available surveying equipment. The long time history of triangulation observations at some locations did, however, significantly increase the value

of even imprecise information collected in the late 1800s and early 1900s (see, for e.g., Bibby, 1975; Nyland, 1977; Pagarete *et al.*, 1998).

For the vertical component, levelling over long distances in rough terrain to collect accurate height information is both extremely difficult and time consuming compared with the relatively quick (horizontal) triangulation surveys. Therefore, the derivation of deformation information initially focussed only on the horizontal components of strain. While an extension of the devised methods would allow the vertical component to be considered, these methods were essentially two-dimensional (north and east system) with an optional up component based in the local topocentric system (see Figure 6-4).

6.3.1.1 Frank's Method

The classical method for determining small deformations used coordinate differences derived from repeat triangulation surveys from which displacement vectors were derived and strain inferred (see e.g., Whitten and Claire, 1960). This method suffers when the surveyed network is large in extent, as the measurement noise will often be greater than the deformation signal (Whitten and Claire, 1960). More generally, difficulties are involved in defining a fixed datum from one epoch to the next (as the datum stations are also most likely moving), with systematic error possibly being confused with genuine deformation (Brunner, 1979).

While analysing deformation along the San Andreas Fault in California, Whitten and Claire (1960) devised a method that sought to overcome some of the above-mentioned shortfalls. However a significant improvement from the previous model, this method has been criticised as having several shortcomings (Frank, 1966). Firstly, the method assumed that all displacements are parallel to a neighbouring fault, restricting its use in other locations. Secondly, the changes in angles as seen from only one station were used to define the strain, therefore depending on the uniformity of strain across the whole area. Thirdly, and perhaps most detrimentally, this method only produces strain at relatively few points, as few as half that produced using the method described by Frank (1966). Finally,

and somewhat curiously, the method is criticised for producing redundant measurements for which a least squares solution is required!

Pointing out that the components of local shear strain were directly derivable from every repetition of a survey on a single triangle, Frank (1966) deduced a method based on breaking a study area into a collection of triangles (see Figure 6-7 and Equation (6.24)). This allowed regions smaller than the entire area to be studied. If observation types were extended from solely triangulation measurements to include trilateration, the dilation component of the strain could be solved using conventional means. Likewise, using this method, network rotation must be derived relying on a trustworthy external reference direction. The simplicity of this method was its greatest weakness, since it was often impractical to observe identical networks at two different epochs using identical methods. The relative precisions of the observations were also not taken into account. A slight modification of this method by Savage and Burford (1970) based on quadrilaterals rather than triangles revealed strain significantly different to that derived for the same area by Whitten and Claire (1960).

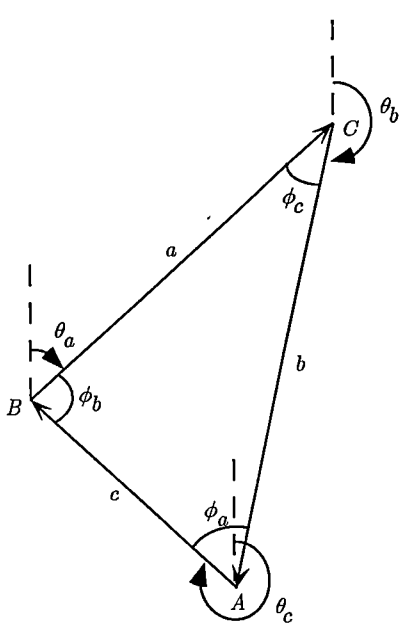

Figure 6-7: Notation for a survey triangle using Frank's method.

$$\gamma_1 = \frac{\sin(\theta_c + \theta_a)\cdot(\delta\phi_a / \sin\phi_a) - \sin(\theta_b + \theta_c)\cdot(\delta\phi_b / \sin\phi_b)}{\sin\phi_c}$$
$$\gamma_2 = \frac{\cos(\theta_c + \theta_a)\cdot(\delta\phi_a / \sin\phi_a) - \cos(\theta_b + \theta_c)\cdot(\delta\phi_b / \sin\phi_b)}{\sin\phi_c} \qquad (6.24)$$

where $\delta\phi$ signifies the difference in angle (ϕ) between one measurement epoch and the next, while θ is the azimuth of a line.

Noting that identical repeat surveys is often unrealistic in practice, Prescott (1976) extended Frank's method to allow any collection of angles to be included, with an arbitrary number of repeat surveys of each angle. To achieve this, the assumption is made that strain rate is uniform in both space (across the entire study area) and time (during the study period). Taking into account spherical excess, a least squares adjustment is performed on angles (reduced from the observed directions) to obtain a single value for shear strain rates.

6.3.1.2 Polynomial Methods

Earth motion in many areas of deformation (i.e., fault zones) is not simply uniform but also episodic. In order to allow for this non-linear motion, Bibby (1973) proposed a polynomial model of varying order as a model for strain over a region. An earlier but more simplistic technique allowed the coordinates of network stations to move in a polynomial fashion (Whitten, 1967). As with Frank's extended method, identical repeat surveys are not required with the Bibby (1973) method. This method has been used to determine strain in the Wairau Fault region of New Zealand where a rich time-history of observations exist, reaching back to 1880 (Bibby, 1975). A linear model was used in the adjustment as no earthquakes have been observed along the Wairau Fault since this time. Results were found to be in good agreement with geological estimates.

Snay *et al.* (1983) proposed a low-order polynomial model for determining strain in regions of complicated deformation. The model defines a station's movement as a combination of secular and episodic motion. The study region is divided into a mosaic of 'districts'. Deformation within each district is regarded as homogenous and occurring at a constant

rate with respect to time, while translation and rotation parameters define any inter-district movement. Martinez *et al.* (1998) used this method to successfully derive strain parameters from a combination of triangulation, trilateration and GPS measurements.

As large episodic events on a glacier or ice shelf are unusual, except perhaps near the grounding zone or ice front, and glaciological data are typically scarce (as is the case for the Amery Ice Shelf), there appears to be little advantage in using this method for glaciological applications.

6.3.1.3 Inner Coordinate Solutions

Brunner (1979) and Brunner *et al.* (1981) proposed a more complete and rigorous method that overcame the datum problem, allowing the inclusion of different observations types (with their associated weights) and varying network sizes. Furthermore, height information could be included in the adjustment, removing the possibility of the misrepresentation of the true three-dimensional strain by a two-dimensional strain field (Caputo, 1978). This method considers infinitesimal homogenous strain using an 'inner coordinate solution' (Meissl, 1969; Pelzer, 1971).

While this method is equivalent to the conventional approach using observation differences under certain conditions, there are "significant advantages gained in using the inner-coordinate approach", that is, the possibility of using heterogeneous data and non-repeat occupations or observations (Brunner *et al.*, 1981). The basis of this solution is to minimise the rotations of the stations around the centroid (centre of mass) of the network. Any constraints placed upon a network will potentially distort the network, thereby producing incorrect estimates of strain. The inner coordinate solution overcomes this, since it does not place tight constraints upon the network. The inner-coordinate solution is particularly useful where no prior deformation information exists for the study area.

Bibby (1982) later described a slightly different method where all observations from each of the measurement epochs are included in a single least squares adjustment. This 'simultaneous reduction' method models the combined network motions of translation and deformation as a similarity transformation between each epoch.

The datum defect of the solution is overcome using the inner coordinate solution, although any of the solutions summarised in Welsch (1979) may be used. It is important to note that the strain components and associated covariance matrices are not biased by the particular solutions of the free network.

A three dimensional extension of the simultaneous reduction method has been successfully used to analyse a combination of triangulation, trilateration and GPS data in New Zealand for strain rate and dilation (Pearson *et al.*, 1995).

Gu and Prescott (1986) have also used a similar approach, however they do not attempt to minimise the sum of the squares of all the displacements, as for the inner-coordinate method. Instead, they suggested that in some networks there may be a subset of stations for which this assumption is in fact reasonable (i.e., a subset of stations are regarded as being 'absolutely' stationary). Statistical tests are performed on the stations to determine their level of stability. The relative block motion between the stable block of stations and a moving block may then by calculated.

6.3.1.4 Outer Coordinate Solution

In using the inner-coordinate solution, the above methods specify a zero net rotation of all the stations around their centre of mass. However, deformation in some regions does not occur in a way compatible with this requirement, particularly in strike slip fault environments. Prescott (1981) has outlined a modification of the method by Brunner (1979) that finds a rotation of the network that minimises the components of the displacement that occur normal to the fault (i.e., deformation is constrained to occur largely parallel to the fault). This 'outer-coordinate' solution provided more realistic estimates than the inner-coordinate solution in the tested strike slip fault regions.

The possible application of this method to our present study of glacial / ice shelf motion is questionable. While the outer-coordinate method may apply well to glaciers moving in a reasonably constant direction, or on small sub-networks of larger glaciers, this method is ineffective in complex deformation zones. In the case of the most of the AIS, where movement generally occurs in a constant direction, this method may be suitable. However,

the precept of near-constant direction of movement is broken near the ice shelf grounding zones, and hence this method is not suitable in this region.

6.3.1.5 Model Coordinate Solution

With the application for both the outer and inner-coordinate solutions being limited by the nature of the study region, a further method was devised that minimised computed displacements with respect with those predicted by a geophysical model (Segall and Matthews, 1988). Studies conducted in complex regions of deformation may then include detailed *a priori* information as a way to overcome the datum defect.

Unlike many areas of deformation, glaciers and ice sheets generally provide an abundance of *a priori* information about the direction of its flow (e.g., through flow lines observed in photos or satellite images (Bindschadler, 1998)) even where no ground measurements have been made. However, while this information exists for the horizontal components, often little reliable prior information is available for the vertical component of movement. Although, it is possible to use the continuity condition to determine this value (Reeh *et al.*, 1999).

6.3.1.6 Remote Sensing Methods

The most recent methods for the detection of strain in glaciers and ice shelves involve remote sensing. Satellite image-to-image correlation (Scambos *et al.*, 1992; Fahnestock *et al.*, 1993) and interferometric synthetic aperture radar (InSAR) (Goldstein *et al.*, 1993; Rignot *et al.*, 1995; Joughin *et al.*, 1996) have both been applied to the problem of determining the velocity and strain of glaciers and ice shelves (see Bindschadler, 1998 for an overview of these techniques). Both of these methods have proven to provide a huge number of spatially distributed velocity vectors (or fringes in the case of InSAR) and hence detailed strain fields.

6.3.1.6.1 Image-to-image correlation

The image-to-image correlation technique used in the determination of ice sheet motion is closely based on the algorithm used to locate tie-points in two different images in order to co-register them (Scambos *et al.*, 1992). The correlation is performed on a reference

subsection (chip) from one image along with a test chip from the other image. This method depends on adequate surface features that may be matched in the two images. Based on the correlation between the images, a gridded set of velocities may be determined for the image. The calculation of the strain rate field comes from differencing velocities in adjacent gridded cells. Unfortunately, this method is a strictly two-dimensional method. Since the current SAR satellites only have two look directions, only the horizontal components may be computed directly, using an appropriate assumption or estimate of the vertical velocity (Reeh *et al.*, 1999).

6.3.1.6.2 InSAR

SAR interferometry involves the differencing of phases on a pixel-by-pixel basis between two SAR images separated by some distance or time. The difference between phases is referred to as an *interferogram*, which is an interference pattern of *fringes*. The fringes are caused by a combination of topography, orbital trajectory, atmospheric differences, phase variations within a pixel and ground movement (Massonnet and Feigl, 1998). It is, of course, the part of the interferogram contributed by the ground movement that needs to be extracted if strain is to be determined. The other fringe sources have no value for these purposes.

SAR interferograms may be calculated using one of two methods - two-pass or three-pass interferometry (Massonnet and Feigl, 1998). The methods differ around how biases introduced by topography are removed. Two-pass interferometry requires two radar images. Topographical information is removed using a suitable digital elevation model. Three-pass interferometry, on the other hand, does not require a pre-existing DEM since a third radar image is used to determine the topography for the region. This method is particularly useful for regions where the inadequate elevation information exists.

InSAR is complicated where tidal motions are present in the ice motion, as is the case with ice shelves. In this case, the tidal motion over the particular ice shelf study region must be known by some independent method[1] so that it may be removed from the processing.

Three satellite look directions are required if full three-dimensional velocities are to be determined. However, the current satellite systems have only two look directions and some further information or assumption is required to construct the three-dimensional velocity vector. This may be done by assuming surface-parallel flow (Mohr *et al.*, 1998) or using the equation of continuity (Reeh *et al.*, 1999).

Strain determination is inherent to the InSAR technique, producing the strain field in the satellite look direction prior to the phase 'unwrapping' procedure that results in the velocities.

6.3.2 Three Dimensional Methods

As seen above, the classical approach to the definition of regional geodetic datums is a two-dimensional (horizontal) datum together with an optional one-dimensional (vertical datum). The nature of the methods outlined above limited the usefulness of modern space-based data types, such as VLBI, SLR or GPS, which are inherently three dimensional (XYZ) in nature.

There are significant advantages in combining modern space-based observations with classical terrestrial observations. The time-history of available GPS observations (approximately one decade), the most widely used of these space-based techniques, is still short in terms of deformation measurements. Rather than wait for a longer time-history of observations, GPS data may be combined with older terrestrial data to determine regional strain fields immediately (Snay and Drew, 1988). It can be argued that any observation, properly weighted, is of value and should be included in geophysical studies (e.g., Bibby, 1975; Nyland, 1977). Using GPS with terrestrial observations also overcomes the inability of the terrestrial data to determine certain parameters of strain. Triangulation

1. Tidal motion may be determined using the InSAR method, although this method is presently limited since all of the current SAR satellites have orbital periods nearly identical to the period of semi-diurnal tidal motion (Rignot, 1996).

measurements alone cannot measure scale, network rotation or translation. Trilateration measurements alone cannot measure network rotation or translation (Frank, 1966). On a regional scale, GPS is unambiguous, and so the combination of GPS and terrestrial networks can significantly strengthen these historic observations (Dong, 1993). Consequently, more complete adjustment models were devised to allow the traditional measurements to be combined with global three dimensional data types in a consistent reference frame.

Hotine (1969) and Marussi (1985) are seen as the modern pioneers of three-dimensional geodesy. Their groundwork provided a path for several researchers to follow in attempting to integrate or compare three-dimensional data sets (e.g., Reilly, 1980; Hein, 1982b; Collier *et al.*, 1988; Cross, 1990; Welsch, 1993). The value of such a system is that heterogeneous data or networks may be combined in a very natural way. Cross (1990) strongly supported such a system in saying "classical two-dimensional and one-dimensional estimation procedures are no longer relevant and will soon be of little use except for highly localised surveying in very small regions."

In general, there are two different ways of integrating or comparing heterogeneous data, and a third hybrid model. Each of these is outlined below.

1. *Observation-level integration.* This is the approach adopted by Reilly (1980), Cross (1990) and Musyoka and Aduol (1997) amongst others. Reduced observations are all adjusted at the same time using observation equations suitable for a three-dimensional model. This allows for a single adjustment of the heterogeneous data, although systematic or gross errors in the various data types may go unnoticed when combining them at this level.

2. *Network-level integration.* In this approach, networks of reduced and adjusted homogeneous data are compared using a transformation of the network from their own independent coordinate system to one of the other systems, or alternatively, an entirely different system. Strain parameters are then determined using one of the methods outlined above (Section 6.3). Adjusting each of the data sets

independently may prevent smearing of errors across the entire combined network. Examples of implementations of this approach may be found in Wolfrum (1992) and Welsch (1993) amongst others.

3. *Quasi-observation integration.* This is a combination of the other two approaches, where each set of homogenous observations are reduced and adjusted independently, then quasi-observations of each network are combined to produce the final solution. A distinct advantage of this method is that it saves both computation time and data storage while still maintaining all the geodetic information. This is the approach adopted by Harvey (1985), Grant (1990) and Dong *et al.* (1998) amongst others.

The three-dimensional models described above are not of value to measurement of deformation until they can be extended to include time-dependant coordinates (i.e., station velocities). Based on the work by Hein (1982a), Collier *et al.* (1988) produced a theorem for the combination of three-dimensional networks in time, that is, a 'four-dimensional integrated geodesy' as they referred to it. They established such a model by extending the observation equations of Moritz (1978) and Hein (1982a), so that station coordinates may vary linearly with time. Their model included observation equations for astronomic latitude and longitude, absolute gravity, zenith distance, azimuth, terrestrial distance, potential difference and GPS baseline vectors.

Several other authors have since extended the four-dimensional approach of Collier *et al.* (1988) to allow the combination of heterogeneous data sets in three-dimensions over multiple epochs, in order to compute deformation parameters. Harvey (1985) adopted this approach to determine strain by combining both real and simulated terrestrial and VLBI data. Grant (1990) simulated the combination of GPS and terrestrial data in order to produce estimates of the quality of strain values in New Zealand. Both Snay and Drew (1988) and Shen *et al.* (1996) combined triangulation and trilateration observations with GPS data in studies of crustal deformation in California.

Station movement was modelled by Collier *et al.* (1988) as the combination of a systematic (trend) component and a random (stochastic) component. On the other hand, Dong *et al.* (1998) uses a Kalman filter to model the station motion described by the combination of quasi-observations from individual networks. Strain parameters are then determined from the station coordinates, velocities and their variance-covariance matrices. In this thesis we adopt the approach used by Dong *et al.* (1998), and describe the relevant methodology in more detail below.

The choice of a three-dimensional strain model is made since it best fits the data we have – namely three-dimensional heterogeneous data. The method by Dong *et al.* (1998) provides a rigorous, efficient and convenient way of combining the terrestrial and space-geodetic data described in Chapter 5. The terrestrial and GPS data are reduced separately, allowing for checks on gross and systematic errors, while maintaining all geodetic information at the combination level. GLOBK, used to combine daily and seasonal GPS solutions in Chapter 5 has the same theoretical basis as described here; that is, combination using quasi-observations.

6.3.2.1 Combination of heterogeneous data using the quasi-observation approach

The method outlined by Dong (1993) and Dong *et al.* (1998) involves a three-step procedure.

1. Obtain loosely constrained estimates of geodetic parameters from space-geodetic or terrestrial observations.
2. Combine these individual loosely constrained solutions into a single solution.
3. Impose general constraints upon position and velocity of a subset of sites to define a uniform reference frame.

The advantages of this method to general crustal deformation are outlined in Dong *et al.* (1998), but for our purposes the main advantages are the rigorous combination of regional and global observations including heterogeneous data. Software (**FONDA** – **FO**rward modelling and **N**etwork **D**eformation **A**nalysis) was written to perform steps two and

three (Dong, 1993). It also has the ability to produce coordinate estimates from terrestrial observations. FONDA has been used to determine horizontal crustal strain rates in several studies (e.g., Bawden *et al.*, 1997; Ferhat *et al.*, 1998; Cong and Feigl, 1999).

6.3.2.1.1 Combination Step 1:

Prior to this step it is expected that the raw observations be reduced (i.e., correction for first/second velocity correction for EDM or obtaining station coordinates along with their variance-covariance (VCV) matrix from GPS). These reduced observations are then adjusted using standard techniques in homogenous networks to estimate the relevant geodetic parameters (station coordinates, gravity or potential as appropriate), including their VCV matrices. At this stage each of the networks are required to be only loosely constrained to a particular reference frame (this is also important at the GPS processing stage). By not constraining the reference frame tightly at this stage, a consistent reference frame is able to be defined after combination. Some constraint is necessary since otherwise the normal matrices will become singular. This is consistent with the 'no-fiducial' approach applied in the processing of data from most regional or global GPS networks (Herring *et al.*, 1991; Heflin *et al.*, 1992).

These coordinates, along with their VCV matrices, are then passed to the next step in the form of quasi-observations. The quasi-observation method requires an order of magnitude less storage space and approximately two orders of magnitude less in terms of processing time, significant even in this day of large disks and fast processors (Dong *et al.*, 1998). The use of quasi-observations does not cause loss of information, since all the geodetic information is contained in the VCV matrices. However, if the original processing model requires modification, then quasi-observations are not sufficient.

Functional model

After omitting the time dependant disturbing potential, the functional model of a geodetic measurement $l(t)$ is expressed by Dong *et al.* (1998) as:

$$l(t) = F\left\{\mathbf{X}(\mathbf{a},t), U\left(\mathbf{X}(\mathbf{a},t)\right), \mathbf{h}(t)\right\}, \tag{6.25}$$

However, since the time dependant disturbing potential has been omitted, it is more correctly:

$$l(t) = F\{\mathbf{X}(\mathbf{a},t), U(\mathbf{X}(\mathbf{a})), \mathbf{h}(t)\} \tag{6.26}$$

where $\mathbf{X}(\mathbf{a},t)$ is the position vector, whose time-dependency is described by the parameter $\mathbf{a}$; $U(\mathbf{X}(\mathbf{a}))$ is the reference gravitational potential; $\mathbf{h}(t)$ are auxiliary parameters, representing propagation effects, satellite positions, etc.; and F denotes a nonlinear function which operates upon $\mathbf{X}$, U, and $\mathbf{h}$ to produce the scalar values of $l(t)$.

The generalised observation equations are (Dong *et al.*, 1998),

$$\delta l = A\Delta\mathbf{X}(\mathbf{a},t) + B\Delta U(\mathbf{X}_0) + C\Delta\mathbf{h}_0 + \varepsilon$$

where

$$A = \frac{\partial F}{\partial \mathbf{X}} + \frac{\partial F}{\partial U}\frac{\partial U}{\partial \mathbf{X}}; B = \frac{\partial F}{\partial U}; C = \frac{\partial F}{\partial \mathbf{h}}$$

δl represents the observed minus calculated (or model) term based on the *a priori* model; $\Delta\mathbf{X}(\mathbf{a},t)$ is the correction to the initial time-dependent position vector; $\Delta U(\mathbf{X}_0)$ is the correction to the reference potential at *a priori* position $\mathbf{X}_0$ (subscript '0' is used to denote the *a priori* values throughout this section); $\Delta\mathbf{h}_0$ is the correction to the *a priori* auxiliary parameter $\mathbf{h}_0$; and ε represents the errors in the observations.

Linearised observation equations

Linearised observation equations for terrestrial and GPS observations may be found in Dong (1993) and Collier *et al.* (1988), for example. In this thesis, we use those equations shown in Dong (1993) since these are in a right-handed coordinate system and are consistent with the rest of our work. Those relevant to our study of the Amery Ice Shelf are reproduced below.

Site displacement and velocity:

If the observables for site displacement ($\delta\mathbf{X}$) and velocity ($\delta\mathbf{V}$) are represented in a geocentric cartesian frame, the equations are (Dong, 1993):

$$\begin{aligned}\delta\mathbf{X} &= \mathbf{L}_x\begin{bmatrix}\delta\mathbf{X}_0\\ \delta\mathbf{V}_0\end{bmatrix} + \mathbf{L}_x\begin{bmatrix}\boldsymbol{\mu} & 0\\ 0 & \boldsymbol{\mu}\end{bmatrix}\begin{bmatrix}\boldsymbol{\omega}_x\\ \boldsymbol{\omega}_v\end{bmatrix} + \mathbf{L}_x\begin{bmatrix}\boldsymbol{\tau}_x\\ \boldsymbol{\tau}_v\end{bmatrix}\\ \delta\mathbf{V} &= \mathbf{L}_v\begin{bmatrix}\delta\mathbf{X}_0\\ \delta\mathbf{V}_0\end{bmatrix} + \mathbf{L}_v\begin{bmatrix}\boldsymbol{\mu} & 0\\ 0 & \boldsymbol{\mu}\end{bmatrix}\begin{bmatrix}\boldsymbol{\omega}_x\\ \boldsymbol{\omega}_v\end{bmatrix} + \mathbf{L}_v\begin{bmatrix}\boldsymbol{\tau}_x\\ \boldsymbol{\tau}_v\end{bmatrix}\end{aligned} \qquad (6.27)$$

The first term is the conventional parameter correction term, the second term is due to the frame rotation and the third term is due to frame translation, where

$$\mathbf{L}_x = \left[\mathbf{I}_3 + \frac{\partial\mathbf{V}_0}{\partial\mathbf{X}_0}(t-t_0) \quad \mathbf{I}_3(t-t_0)\right], \qquad \mathbf{L}_v = \left[\frac{\partial\mathbf{V}_0}{\partial\mathbf{X}_0} \quad \mathbf{I}_3\right]$$

$\mathbf{I}_3$ is the (3 x 3) identity matrix.

$\boldsymbol{\omega}_x$ is the vector of rotation angles around each of the axes and $\boldsymbol{\omega}_v$ is the vector of rotation angle rates.

$\boldsymbol{\tau}_x$ is the vector of translations along each axis and $\boldsymbol{\tau}_v$ is the vector of translation rates.

$\boldsymbol{\omega}_x$, $\boldsymbol{\omega}_v$, $\boldsymbol{\tau}_x$, $\boldsymbol{\tau}_v$ are common for all sites

$$\boldsymbol{\mu} = \begin{bmatrix} 0 & -z_0 & y_0 \\ z_0 & 0 & -x_0 \\ -y_0 & x_0 & 0 \end{bmatrix}$$ is the conventional rotation matrix (6.28)

x_0, y_0, z_0 are the *a priori* coordinates of the sites.

Horizontal and vertical angles and mark-to-mark distances:

Linearised observation equations for azimuth α, vertical angles β (relative to the local gravity vector) and mark-to-mark distances s from site **i** to site **j** are (Dong, 1993):

$$\begin{bmatrix}\delta\alpha\\ \delta\beta\\ \delta s\end{bmatrix}=\begin{bmatrix}\left(s_0\cos\beta_0\right)^{-1} & 0 & 0\\ 0 & s_0^{-1} & 0\\ 0 & 0 & 1\end{bmatrix}\left[\mathbf{S}^{\mathrm{T}}\mathbf{R}_0\mathbf{L}_{\mathrm{x}}\begin{bmatrix}\delta\mathbf{X}_{0\mathrm{j}}-\delta\mathbf{X}_{0\mathrm{i}}\\ \delta\mathbf{V}_{0\mathrm{j}}-\delta\mathbf{V}_{0\mathrm{i}}\end{bmatrix}-\frac{\mathbf{K}\mathbf{R}_0\mathbf{M}\mathbf{L}_{\mathrm{x}}}{g_0}\begin{bmatrix}\delta\mathbf{X}_{0\mathrm{i}}\\ \delta\mathbf{V}_{0\mathrm{i}}\end{bmatrix}\right] \quad (6.29)$$

where

$$\mathbf{S}=\begin{bmatrix}\cos\alpha_0 & -\sin\alpha_0\sin\beta_0 & \sin\alpha_0\cos\beta_0\\ -\sin\alpha_0 & -\cos\alpha_0\sin\beta_0 & \cos\alpha_0\cos\beta_0\\ 0 & \cos\beta_0 & \sin\beta_0\end{bmatrix}$$

$$\mathbf{R}_0=\begin{bmatrix}-\sin\Lambda_0 & \cos\Lambda_0 & 0\\ -\sin\Phi_0\cos\Lambda_0 & -\sin\Phi_0\sin\Lambda_0 & \cos\Phi_0\\ \cos\Phi_0\cos\Lambda_0 & \cos\Phi_0\cos\Lambda_0 & \sin\Phi_0\end{bmatrix}$$

$$\mathbf{K}=\begin{bmatrix}s_0\left(\tan\phi_0\cos\beta_0-\cos\alpha_0\sin\beta_0\right) & s_0\sin\alpha_0\sin\beta_0 & 0\\ s_0\sin\alpha_0 & s_0\cos\alpha_0 & 0\\ 0 & 0 & 0\end{bmatrix}$$

Φ_0 and Λ_0 are the *a priori* astronomic latitude and longitude at site *i*.

g_0 is the *a priori* gravity.

$\mathbf{M}=\left[\frac{\partial^2 U}{\partial\mathbf{X}^2}\right]$ is the Marussi tensor of second-order derivatives of U (Hein, 1986).

A superscript 'T' represents the transpose of a matrix or vector.

Linearised observation equations for horizontal directions are defined as for azimuth in (6.29), however an extra orientation parameter is solved for each "round" or "zero" of observations. This does not require a full VCV matrix, only the diagonal terms (Allman and Bennett, 1966). The linearised observation equations for quasi-observable rates are the same as equation (6.29), but with L_x replaced by L_v.

6.3.2.1.2 Combination Step 2:

The quasi-observations from the previous step are now combined. A Kalman filter is employed to produce a single estimate of position and velocity for each station. As mentioned above, and following Dong (1993), we treat the $\Delta\mathbf{X}(\mathbf{a},t)$ from individual subsets of data as quasi-observations to estimate station positions as a function of time, as shown in equation (6.30).

$$\begin{aligned}\Delta\mathbf{X}(\mathbf{a},t) = \Delta\mathbf{X}_0 + \lambda\mathbf{X}_0 + (t-t_0)\Delta\mathbf{V}_0 + \sum_k r_k(t,t_k)\delta\xi_k + \gamma(t) + \boldsymbol{\tau}_x \\ + (t-t_0)\boldsymbol{\tau}_v + \boldsymbol{\mu}\boldsymbol{\omega}_x + \boldsymbol{\mu}(t-t_0)\boldsymbol{\omega}_v\end{aligned} \tag{6.30}$$

where the parameter vector $\mathbf{a}$ consists of $\mathbf{V}$, ξ, γ, $\boldsymbol{\tau}_x$, $\boldsymbol{\tau}_v$, $\boldsymbol{\omega}_x$, $\boldsymbol{\omega}_v$ and λ which are defined below. $\Delta\mathbf{X}_0$, $\Delta\mathbf{V}_0$ are the adjustments to the *a priori* coordinates and velocities referred to a reference epoch; λ is the scale correction factor; $\delta\xi_k$ is the episodic station displacement from the k-th event, at time t_k, with

$$r_k(t,t_k) = \begin{cases} -1 \text{ if } (t < t_k < t_0) \\ 0 \text{ if } (t > t_k \text{ and } t_k < t_0) \text{ or } (t < t_k \text{ and } t_k > t_0) \\ 1 \text{ if } (t > t_k > t_0) \end{cases}$$

$\gamma(t)$ is a stochastic displacement due, for example, to some sort of short-term monument instability; $\boldsymbol{\tau}_x$ and $\boldsymbol{\tau}_v$ are the translation and translation rate of the network; $\boldsymbol{\omega}_x$ and $\boldsymbol{\omega}_v$ represent the rotation and rotation rate of the network or, in the case of global observations, the Earth rotation and rotation rate parameters. $\boldsymbol{\mu}$ is the same as defined in equation (6.28).

An episodic event on an ice shelf would only involve the breaking off of an iceberg from the ice shelf front, or a sudden surge. Since we do not expect such an event in our Amery Ice Shelf study region, we can simplify equation (6.30) by removing the episodic terms.

$$\begin{aligned}\Delta\mathbf{X}(\mathbf{a},t) = \Delta\mathbf{X}_0 + \lambda\mathbf{X}_0 + (t-t_0)\Delta\mathbf{V}_0 + \gamma(t) + \tau_x \\ + (t-t_0)\tau_v + \mu\omega_x + \mu(t-t_0)\omega_v\end{aligned} \tag{6.31}$$

Defining $\delta \mathbf{l}_k = \mathbf{l}_k - \mathbf{l}_{0k}$ as the vector of linearised quasi-observations at time t_k, where $\mathbf{l}_{0k}$ represents the *a priori* values and $\mathbf{l}_k$ the estimates of the quasi-observations from the analysis of the original observations.

At this combination stage, the linearised observation equation is represented as,

$$\delta \mathbf{l}_k = \mathbf{A}_k \delta \mathbf{x}_k + \varepsilon_k$$

in which $\mathbf{x}_k$ are the parameters to be estimated, $\mathbf{A}_k$ is the design matrix with standard Gauss-Markov conditions applying. In terms of the Kalman filter, the parameter state is represented by

$$\delta \mathbf{x}_{k+1} = \mathbf{S}_k \delta \mathbf{x}_k + \mathbf{q}_k$$

where $\mathbf{S}_k$ is the state-transition matrix and $\mathbf{q}_k$ is a Markov stochastic noise process with covariance matrix $\mathbf{Q}_k$ such that the Gauss-Markov condition applies, $E\left\{\mathbf{q}_k \varepsilon_k^T\right\} = 0$. The predictions equation from t_k to t_{k+1} (denoted by k|k+1) are (Dong *et al.*, 1998):

$$\delta \hat{\mathbf{x}}_{k+1|k} = \mathbf{S}_k \delta \hat{\mathbf{x}}_k$$

$$\mathbf{C}_{k+1|k} = \mathbf{S}_k \mathbf{C}_k \mathbf{S}_k^T + \mathbf{Q}_k$$

and the update equations are given as (Dong *et al.*, 1998):

$$\delta \hat{\mathbf{x}}_{k+1} = \delta \hat{\mathbf{x}}_{k+1|k} + \mathbf{K}_{k+1}\left(\delta \mathbf{l}_{k+1} - \mathbf{A}_{k+1} \delta \hat{\mathbf{x}}_{k+1|k}\right)$$

$$\mathbf{C}_{k+1} = \mathbf{C}_{k+1|k} - \mathbf{K}_{k+1} \mathbf{A}_{k+1} \mathbf{C}_{k+1|k}$$

where $\mathbf{K}_{k+1} = \mathbf{C}_{k+1|k} \mathbf{A}_{k+1}^T \left(\mathbf{P}_{k+1} + \mathbf{A}_{k+1} \mathbf{C}_{k+1|k} \mathbf{A}_{k+1}^T\right)^{-1}$ is the "Kalman gain" matrix.

In order to assess the level of compatibility of different data sets, the weighted sum of squared residuals (or χ^2) is often used. This value may then be used to rescale the *a posteriori* VCV matrix, detect gross errors or systematic differences between data sets. Segall and Matthews (1988), for example, used this statistic to test deformation data,

differentiating between the (mis-)fit of the data due to model insufficiencies and that due to "pure error" in the data. Feigl *et al.* (1993) use this value to rescale the *a posteriori* VCV matrix to produce more realistic estimates of confidence. Dong *et al.* (1998) defines the increment of χ^2 as data sets are added as,

$$\delta\chi^2_{k+1} = \chi^2_{k+1} - \chi^2_k = \Delta\hat{\mathbf{x}}^T_{k+1}\mathbf{C}^{-1}_{k+1|k}\Delta\hat{\mathbf{x}}_{k+1} + \left(\delta\mathbf{l}_{k+1} - \mathbf{A}_{k+1}\delta\hat{\mathbf{x}}_{k+1}\right)^T \mathbf{P}^{-1}_{k+1}\left(\delta\mathbf{l}_{k+1} - \mathbf{A}_{k+1}\delta\hat{\mathbf{x}}_{k+1}\right)$$

where $\Delta\hat{\mathbf{x}}_{k+1} = \delta\hat{\mathbf{x}}_{k+1} - \delta\hat{\mathbf{x}}_{k+1|k}$

After the removal of gross errors, a large $\delta\chi^2$ suggests that unmodelled systematic errors remain in the solution or that the *a priori* variances of the observations have been underestimated. In order to obtain realistic (although, not necessarily rigorous) uncertainties, the VCV matrix may be rescaled (Feigl *et al.*, 1993).

6.3.2.1.3 Combination Step 3:

The loosely constrained network is transformed to best fit a set or subset of well-known stations. Depending on the make-up of the network, there may be a twelfth-order rank defect – three translations, three rotations and their rates of change (scale and its rate are typically ignored). Traditional methods used to overcome the rank defect have been described already (e.g., Brunner, 1979; Prescott, 1981; Bibby, 1982; Segall and Matthews, 1988). However, these methods are suitable only for small areas where deformation is either uniform or generally in the same direction. As has been mentioned above, in the case of a combined terrestrial/space-geodetic network, the space-geodetic data is unambiguous over regional or smaller areas. By linking velocities of collocated stations, the combined data set may overcome the rank defect.

Expressing the constraints as observation equations leads to (Dong *et al.*, 1998):

$$\mathbf{l}_c = \mathbf{A}_c\delta\mathbf{x} + \varepsilon_c \text{ with covariance } \mathbf{C}_c$$

Following the imposition of constraints, the parameter adjustments ($\delta\hat{x}$) with their covariance ($\mathbf{C}_x$) and misfit (χ_x^2) become (Dong *et al.*, 1998):

$$\delta\hat{\mathbf{x}}_c = \delta\hat{\mathbf{x}} + \mathbf{C}_x\mathbf{A}_c^T\left(\mathbf{C}_c + \mathbf{A}_c\mathbf{C}_x\mathbf{A}_c^T\right)^{-1}\left(\mathbf{l}_c - \mathbf{A}_c\delta\hat{\mathbf{x}}\right)$$

$$\mathbf{C}_{x_c} = \mathbf{C}_x - \mathbf{C}_x\mathbf{A}_c^T\left(\mathbf{C}_c + \mathbf{A}_c\mathbf{C}_x\mathbf{A}_c^T\right)^{-1}\mathbf{A}_c\mathbf{C}_x$$

$$\chi_c^2 = \chi_x^2 + \left(\mathbf{l}_c - \mathbf{A}_c\delta\hat{\mathbf{x}}\right)^T\left(\mathbf{C}_c + \mathbf{A}_c\mathbf{C}_x\mathbf{A}_c^T\right)^{-1}\left(\mathbf{l}_c - \mathbf{A}_c\delta\hat{\mathbf{x}}\right)$$

The constrained solution is then analysed to check for systematic misfit (χ_c^2). Such a misfit will introduce incorrect parameter estimates, or result in the underestimation of uncertainties in the parameters, particularly position, velocity and strain in our case.

Types of Constraints

Various types of constraints are of practical use in the combination of terrestrial and space-geodetic data for the determination of velocity and strain parameters (Dong, 1993). The most useful constraints that may be applicable to our study are reproduced here:

1. Assign a specific value to station coordinates or velocities:

$$\delta\mathbf{x}_i = \mathbf{x}_{spec}, \qquad \delta\mathbf{v}_i = \mathbf{v}_{spec} \tag{6.32}$$

Setting ($\mathbf{C}_c = 0$) is known as a "hard" or "absolute" constraint (Vanicek and Krakiwsky, 1987), effectively fixing the coordinate or velocity at the specified value.

2. Tie the adjustments or values of the coordinates or velocities between points

$$\delta\mathbf{x}_i = \delta\mathbf{x}_j = \delta\mathbf{x}_k = \ldots, \qquad \delta\mathbf{v}_i = \delta\mathbf{v}_j = \delta\mathbf{v}_k = \ldots \tag{6.33}$$

This type of constraint is particularly useful where two or more sites are close together, and their velocity may be assumed identical.

3. Fix the centre of a sub-network or fix the motion of the sub-network centre:

$$\sum_{i=1}^{k}\delta\mathbf{x}_i = 0, \qquad \sum_{i=1}^{k}\left(\mathbf{v}_i + \delta\mathbf{v}_i\right) = 0 \tag{6.34}$$

4. Fix horizontal or vertical rotation of a sub-network to zero:

$$\begin{aligned}
&\sum_{i=1}^{k}\left(\mathrm{dx}_i\left(\mathbf{v}_i+\delta\mathbf{v}_i\right)-\mathrm{dy}_i\left(\mathbf{u}_i+\delta\mathbf{u}_i\right)\right)=0\\
&\sum_{i=1}^{k}\left(\mathrm{dy}_i\left(\mathbf{w}_i+\delta\mathbf{w}_i\right)-\mathrm{dz}_i\left(\mathbf{v}_i+\delta\mathbf{v}_i\right)\right)=0\\
&\sum_{i=1}^{k}\left(\mathrm{dz}_i\left(\mathbf{u}_i+\delta\mathbf{u}_i\right)-\mathrm{dx}_i\left(\mathbf{w}_i+\delta\mathbf{w}_i\right)\right)=0
\end{aligned} \tag{6.35}$$

Equations (6.34) and (6.35) differ from the inner and outer coordinate solution in one important aspect – rather than having equal weights assigned to each coordinate as in the case of the inner or outer solutions, parameter uncertainties affect these constrained solutions.

5. Link velocity gradients:

   After rotating the coordinate frame by a specified angle,

$$\frac{\mathbf{v}_j+\delta\mathbf{v}_j-\mathbf{v}_i-\delta\mathbf{v}_i}{\mathbf{x}_j-\mathbf{x}_i}=\frac{\mathbf{v}_k+\delta\mathbf{v}_k-\mathbf{v}_i-\delta\mathbf{v}_i}{\mathbf{x}_k-\mathbf{x}_i} \tag{6.36}$$

Formula (6.36) contains four independent constraints for horizontal velocities.

6. Inner, outer and model coordinate constraints for horizontal velocities, as discussed above and with details found in (Segall and Matthews, 1988).

6.3.2.1.4 Strain Determination

Strain rate values are derived from the coordinates and velocities and their covariance matrices. This may be done in a variety of ways, although in practice most authors have used the extended-Frank's method (Frank, 1966) as developed by Prescott (1976) since it is implemented in FONDA. Bawden *et al.* (1997) used this method to determine shear strain rates within triangles formed as sub-networks of the entire network. (Ferhat *et al.*, 1998) and Cong and Feigl (1999) also used this method.

FONDA also implements the method used by Shen *et al.* (1996) in estimating a uniform two-dimensional strain rate field. It is important to note that each of these studies were limited by their data to solving horizontal strain rates only.

6.4 AIS strain rates

6.4.1 Terrestrially-derived strain

Strain values may be derived from the terrestrial data presented in Chapter 5 using one of two networks. Firstly, the strain grids at each of G1, G2, G3 and A1 may be analysed. This analysis provides a rigorous determination of the various strain parameters. Secondly, the strain in the direction of the survey traverse may also be analysed. While not being as rigorous, this method provides valuable information on the strain regime of the AIS. These methods and their results are discussed below.

6.4.1.1 Strain grids

Using FONDA[2], the strain grid calculations were performed using a minimum constraint solution. The distances of the strain grids were originally measured by steel tape. However, these measurements are not available to us as the original records are missing. Instead, we used measured Tellurometer distances, although not as many measurements are available for every grid. The grids at G1, G2 and G3 are four station diamond-shaped grids with approximately 1.6km (1 mile) diagonals. The A1 grid is also diamond-shaped, but with diagonals approximately 3.2km (2 miles) in length. Two separate grids were formed at both G1 and G3 (see Figure 6-8). We refer to these is 'inner' and 'outer' grids. The outer grids are formed by taking advantage of the traverse junction points at these locations, allowing for longer grid diagonals (5-15km) and an additional station. This increases the degrees of freedom of the strain grid network to four for these grids. These grids are denoted as G3-outer and G1-outer in Table 6-1. The results are presented in Table 6-1 and Figure 6-9.

2. Several modifications were made to the FONDA code by the author to correct previous coding errors and to allow for the determination of large velocity and strain rates.

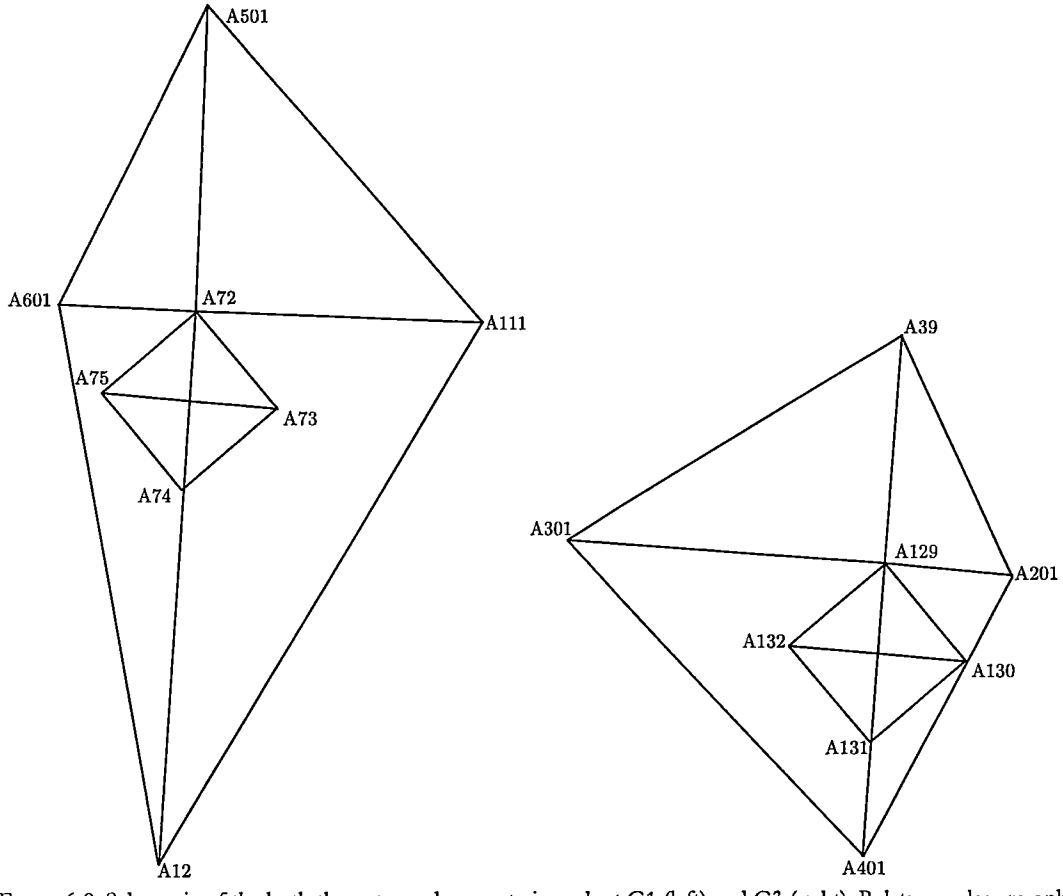

Figure 6-8: Schematic of the both the outer and inner strain grids at G1 (left) and G3 (right). Relative scales are only approximate. The G2 and A1 strain grids have similar dimensions to the inner strain grids shown here.

In terms of signal-to-noise ratios (SNR), the strain rate parameters are well determined. In most cases, the SNR is approximately 3-100, although this value increases further with grid size. Some differences exist in the strain parameters estimated from the two G3 grids. In terms of $\dot{\varepsilon}_2$ (maximum compressive strain rate) and θ (azimuth of $\dot{\varepsilon}_2$), the differences are within the 1σ errors. For $\dot{\varepsilon}_1$ (maximum extensive strain rate), however, the differences are not within the error margins. It is difficult to determine whether these differences are true indicators of the ice strain rates. The central coordinates for these grids, while being similar, are not the same. This may mean that the strain rate characteristics of the ice in each grid are not the same. Alternatively, this difference may be an indicator of a ~1m gross distance error ($1x10^{-4}$) in either season of the traverse campaign since the north-south traverse direction at G3 is approximately in the direction of the principal strain rate. Significant differences are also seen in the parameters derived from the two grids at G1.

The spatial separation of the grid centres are even less than at G3. This suggests that the strain rate may be very sensitive to location. To test the impact of the extra degree of freedom in the large grids, the central site from each of the two large grids was removed. Comparing the results to the unmodified grids showed that the number of degrees of freedom did not greatly impact the derived strain rates.

The large difference in the azimuth (θ) between the A1 and G1 grids seems unusual, given the short distance between the sites (~10km). Vertical strain rates may be computed from the determined horizontal strain rates through equation (6.23). These vertical rates are shown in Table 6-2 along with their precisions. The agreement between the vertical rates of the G1 – outer and A1 – inner strain grids is almost within the 1σ errors. This suggests that the determinations of the horizontal strain rates at these locations are indeed correct, and the different orientations of the grids are due to some real ice shelf effect.

Grid	Lat. (°)	Lon. (°)	$\dot{\varepsilon}_1$	σ_{ε_1}	$\dot{\varepsilon}$	σ_{ε_2}	θ (°)	σ_θ (°)	dof
			($\times 10^{-3}$ yr^{-1})		($\times 10^{-3}$ yr^{-1})				
G3 – inner	-70.9650	69.7809	0.41	0.04	-0.15	0.05	106.89	7.09	2
G3 – outer	-70.9521	69.7696	0.30	0.02	-0.13	0.02	102.29	1.87	4
G2 – inner	-70.1536	70.8308	2.40	0.06	-1.22	0.10	136.49	0.54	2
G1 – inner	-69.4934	71.6413	5.92	0.03	0.30	0.03	107.20	0.43	2
G1 – outer	-69.4929	71.6648	6.45	0.01	0.42	0.02	105.16	0.16	4
A1 – inner	-69.4526	71.4685	5.22	0.06	1.54	0.06	129.30	1.02	2

Table 6-1: Strain rate values determined from the terrestrial strain grids and the degrees of freedom (dof) for each grid.

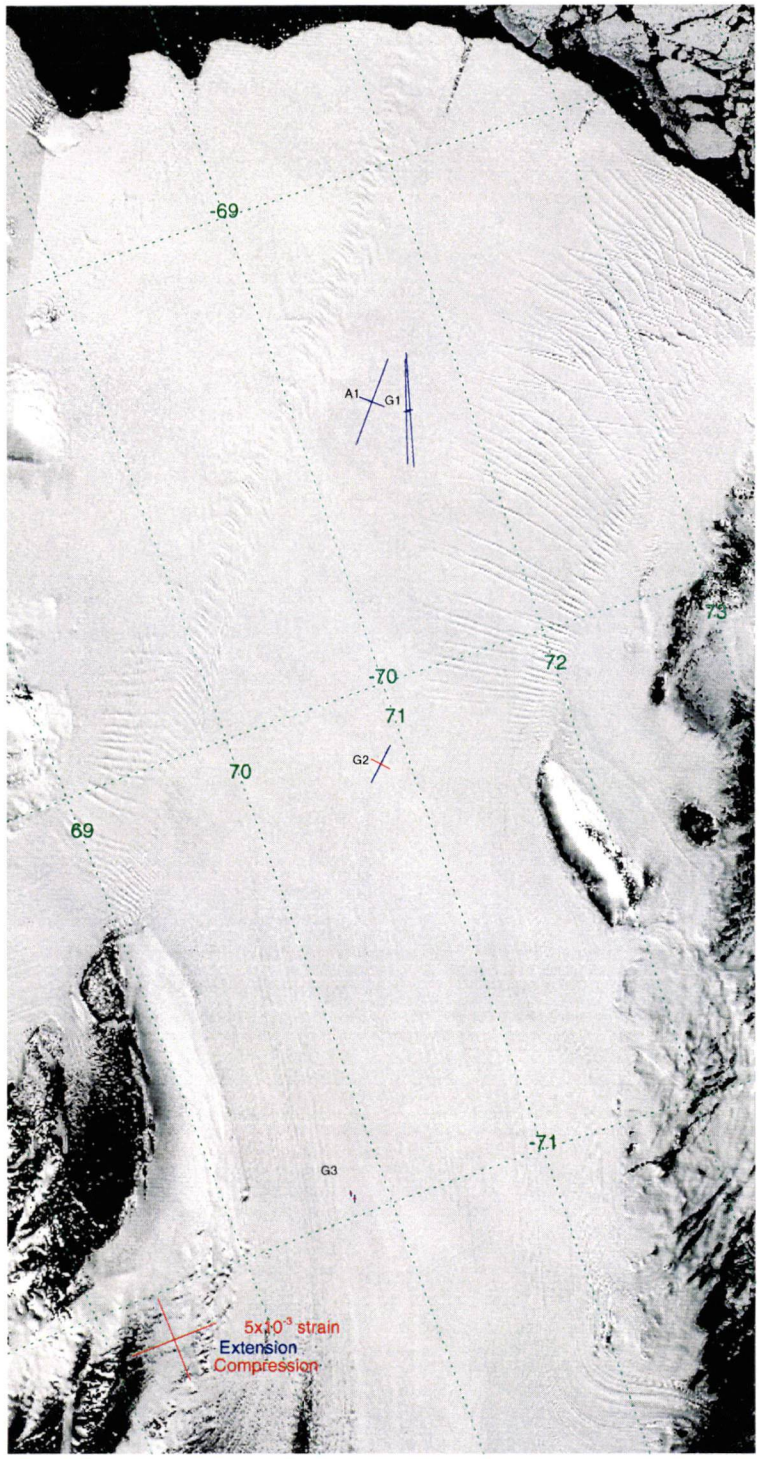

Figure 6-9: Strain rates determined from the 1968-70 terrestrial data at the A1, G1, G2 and G3 strain grids.

Grid	Lat. (°)	Lon. (°)	$\dot{\varepsilon}_3$	$\sigma_{\dot{\varepsilon}_3}$
			($x10^{-3}$ yr^{-1})	
G3 – inner	-70.9650	69.7809	-0.26	0.06
G3 – outer	-70.9521	69.7696	-0.17	0.03
G2 – inner	-70.1536	70.8308	-1.18	0.12
G1 – inner	-69.4934	71.6413	-6.22	0.04
G1 – outer	-69.4929	71.6648	-6.87	0.02
A1 – inner	-69 4526	71.4685	-6.76	0.08

Table 6-2. Vertical strain rates determined from the measured horizontal strains (equation (6.23)) at the 1968-70 strain grids.

The analysis of the 1968-70 traverses by Budd *et al.* (1982) did not include an analysis of the strain grids, and so the results presented above are first results based on these observations. A comparison is possible, however, with the strain values determined from the 1963-64 results presented in Budd (1966a). These results are reproduced in Table 6-3 along with the relevant values from the present analysis of the 1968-70 strain grids. The 1968-70 strain grids were installed within a few metres of the 1963-64 strain grids. Due to the movement of the ice during the intervening years, the geographic location of these grids had changed somewhat between the two surveys. This may result in some bias, although this will be well within the size of the estimated errors on the 1963-64 strain rates.

The 1963-64 strain rates are listed in terms of longitudinal and transverse components, with respect to the local ice flow direction. While these are not necessarily equivalent to the principal axes of strain, on the AIS they typically are (i.e., the principal axis of strain is typically aligned with the direction of flow). Given the very large errors in the 1963-64 results, we assume they are the same for the purpose of this comparison. The longitudinal strain rates agree at G1 and G3; however the G2 value is significantly higher using the later measurements. The transverse strain rates are quite different. Compression is seen at G3 and G2 in the later data, with especially high values at G2. In the case of G2, this is caused by the influx of ice from the Charybdis Glacier to the west of G2. The 1968-70 transverse

strain rate at G1 is less than half the value from the earlier data, although within the error margins.

Station	Budd (1966a)		Present study	
	Longitudinal strain ($\times 10^{-3}$ yr^{-1})	Transverse strain ($\times 10^{-3}$ yr^{-1})	$\dot{\varepsilon}_1$ ($\times 10^{-3}$ yr^{-1})	$\dot{\varepsilon}$ ($\times 10^{-3}$ yr^{-1})
G3	0.5 (0.5)	0.15 (0.5)	0.41 (0.04)	-0.15 (0.05)
G2	1.7 (0.5)	0.05 (0.5)	2.40 (0.06)	-1.22 (0.10)
G1	6.0 (0.5)	0.8 (0.5)	5.92 (0.03)	0.30(0.03)

Table 6-3: AIS strain rates values reproduced from Budd (1966a) determined from the 1963-64 surveys and those from the present analysis of the 1968-70 grids. The values in parentheses are estimated precisions of the strain rates.

6.4.1.2 Traverse strain

Further strain information may be derived from the remainder of the traverse, although the parameters are weakly determined, particularly the component perpendicular to the traverse. The formulae for the computation of these terms are (Jaeger, 1969):

$$\dot{\varepsilon}_r = \frac{\partial u}{\partial r}$$
$$\dot{\varepsilon}_\theta = \frac{1}{r}\left(u + \frac{\partial v}{\partial \theta}\right) \tag{6.37}$$

where

θ is the angle of divergence of two flow lines that are a distance d apart,

r is given by $d = r\theta$,

u and v are the forward (longitudinal) and transverse components of the velocity of the ice shelf,

and $\dot{\varepsilon}_r$ and $\dot{\varepsilon}_\theta$ are the rates of extension per unit length of a line in the direction of flow and perpendicular to the direction of flow, respectively.

Since $\frac{\partial v}{\partial \theta}$ is negligibly small compared to the other terms (Budd, 1966a),

$$\dot{\varepsilon}_\theta = \frac{u\theta}{d} \tag{6.38}$$

These values were determined from the terrestrial traverse along three traverse profiles – along the longitudinal (centreline) profile and along the two lateral profiles through G1 and G3 – and are shown in blue in Figure 6-10 and Figure 6-11, respectively. Since the ice shelf flow direction is not uniform, we defined this direction at each point to be a moving five point average along the traverse. This is valid since the ice shelf flow direction is slowly varying and the average is performed over distances less than approximately 15km from the point. To allow the computation of the five point moving averages at the extents of the profiles, we extrapolated the velocity values using a cubic Hermite function.

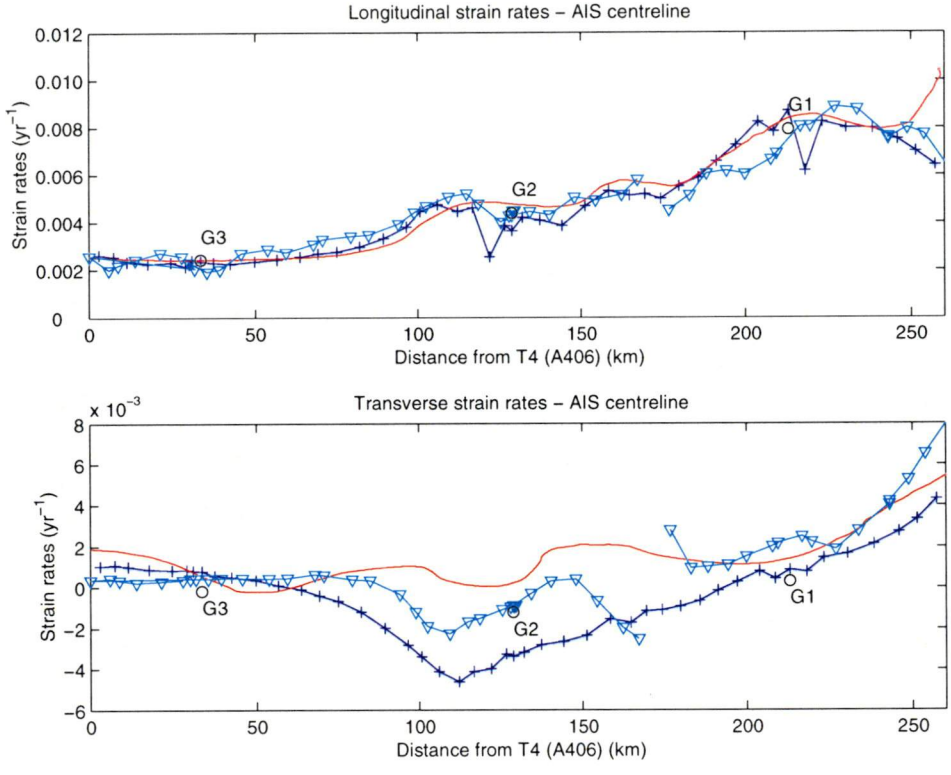

Figure 6-10: Forward (longitudinal) and transverse strain rate values determined from the centreline profile of the AIS traverses. The values determined from the present study are shown as a blue line and crosses and the results from Budd *et al.* (1982) are reproduced in red. Estimates from Radarsat images are shown as a cyan line and triangles. The black circles represent the strain rates determined using the strain grids in Section 6.4.1.1.

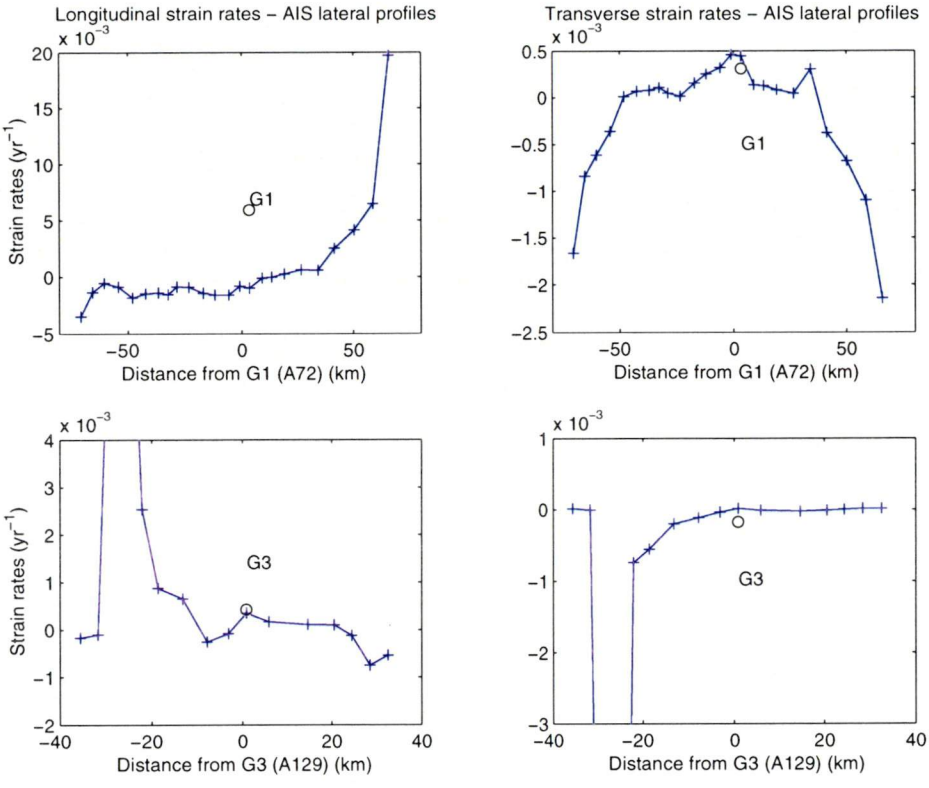

Figure 6-11: Forward (longitudinal) and transverse strain rate values determined from the lateral profiles of the AIS traverses through G1 (top) and G3 (bottom). The black circles represent the strain rates determined using the strain grids in Section 6.4.1.1. Distances are measured with east positive.

For each profile, the strain rates that are perpendicular to the line of the profile are poorly determined. That is, in Figure 6-10 the transverse strain rates will be poorly determined, while in Figure 6-11 the longitudinal strain rates will be poorly determined. Using the same traverse data as used here, Budd *et al.* (1982) also determined forward and transverse strains although only for the centreline profile. Their analysis of this centreline differed from ours as they extrapolated the traverse strain rate values to occur on a single central ice shelf flow band as shown in Figure 6-12. Our analysis does not include such an extrapolation. The Budd *et al.* (1982) values are reproduced in red in Figure 6-10, although it must be kept in mind that these values were determined using the erroneous traverse velocities discussed in Chapter 5.

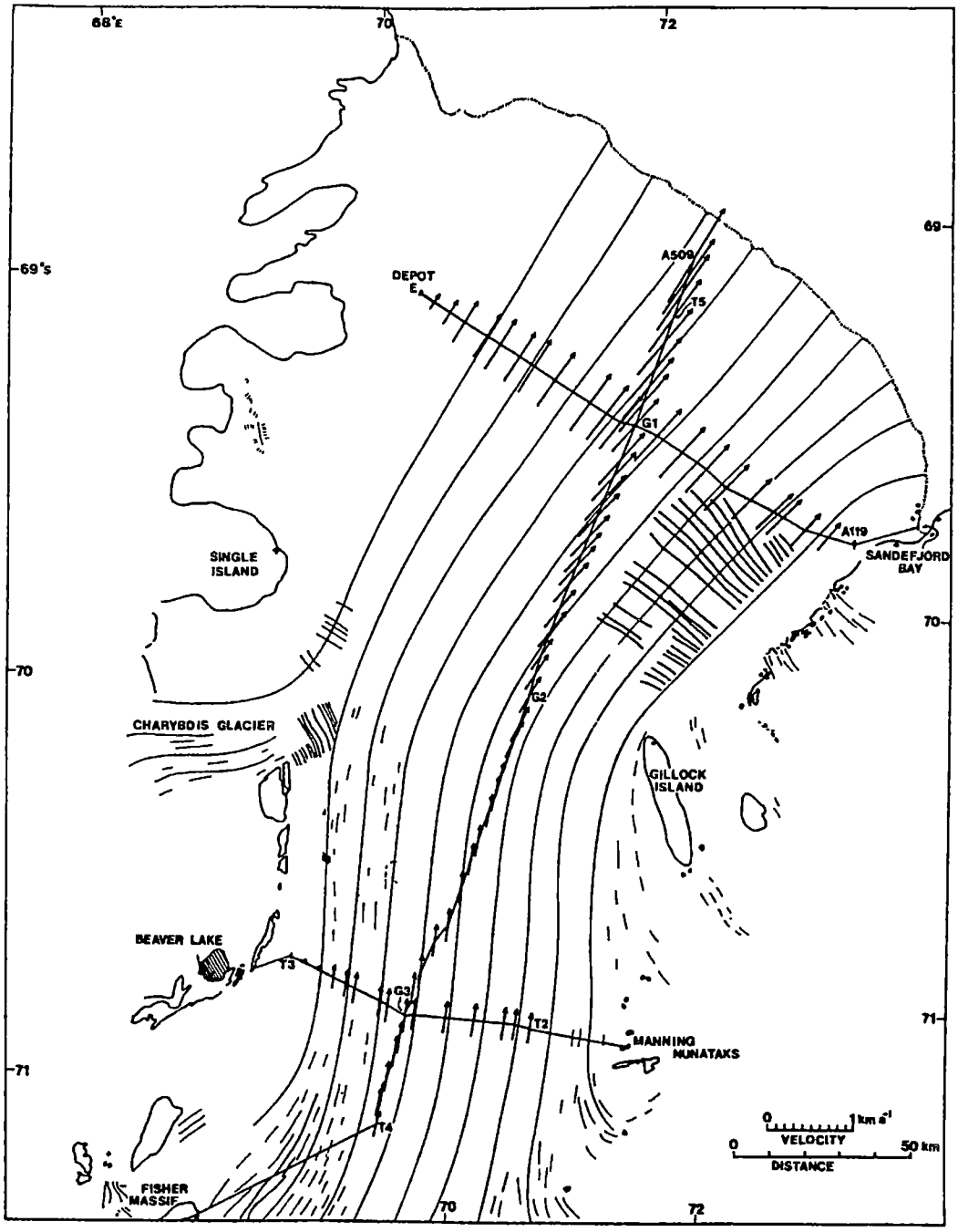

Figure 6-12: Reproduced from Budd *et al.* (1982) showing the terrestrial traverse and ice shelf flow lines. The centreline strain rates were extrapolated onto a central flow line.

In terms of the centreline profile, the longitudinal strain is extremely low in the G3 region, increasing rapidly south of G2, and again midway between G2 and G1, before dropping off at the ice shelf front. There is good agreement between the two analyses. The results of Budd *et al.* (1982) appear smooth compared to our results due to the extrapolation process

they applied. The main differences in longitudinal component occurs near G1 and G2 where there appear to be two outliers, and at the front of the ice shelf where the strain rates taper-off instead of continuing to increase. The difference at the front is due to errors in the Budd *et al.* (1982) velocity profile north of G1 discussed in Chapter 5. Other (smaller) differences are due mainly to the different velocity profiles in the two analyses.

Our analysis is confirmed by the close agreement with strain rates determined from coherence matching of Radarsat images (Young and Hyland, 2001, in press), averaged over 17km square cells (Figure 6-10). The large cells size will be the source of some of the differences between the present analysis and the Radarsat results. Due to a lack of image coherence, velocities were not able to be determined at all locations (e.g., 170-180km in Figure 6-10).

Larger differences are seen between the results from the present study and that of Budd *et al.* (1982) in the transverse component of the centreline profile. This is because Budd *et al.* (1982) extended the transverse strain rates to a central flow band, and this required extrapolations over large distances. The large dip in our results centred at 110km is due to the high compression experienced in this region due to the inflow of the Charybdis Glacier. As the ice moves away from this region, extensional transverse strain is re-established. The pattern of these values again agrees with the Radarsat measurements, although there are expected differences due to the greater ability of the Radarsat method to determine transverse strains along the centreline compared to the terrestrial data. As seen in Chapter 5, however, the Radarsat strain rates while providing the 'shape' of the strain rate, are contaminated with systematic biases.

The strain rates determined from the strain grids (Section 6.4.1.1) are shown as black circles in Figure 6-10. For purposes of comparison, $\dot{\varepsilon}_1$ and $\dot{\varepsilon}_2$ are regarded as being equivalent to the longitudinal and transverse components of strain rate. These values agree well with longitudinal strain rates, although as expected, there are significant differences in the poorly determined transverse component, especially at G2. The Radarsat values confirm the strain rates at G3 and G2 and the longitudinal component of G1. However, there is some difference in the transverse component at G1. This may be explained by the

large averaging area and the fact that the principal axis of strain rate at G1 was not exactly along the direction of flow.

For the two lateral profiles (through G1 and G3; Figure 6-11), there are no corresponding results in Budd *et al.* (1982). Again, the values in the direction of the profile (transverse strain rates) appear well determined when compared to the strain grid values. The longitudinal value at G3 is well determined, although it is poorly determined at G1. While the transverse strain rates are poorly determined, they do reveal the strain rate pattern along these profiles. The longitudinal strain profiles are generally consistent across the ice shelf at both G1 and G3. On the western end of the G3 profile and the eastern end of the G1 profile, these values increase dramatically. Figure 6-11 has been scaled to exclude these points. The values do not increase dramatically at the other ends since the traverse did not reach the grounding zones in these areas. For these lateral profiles, the longitudinal strain rates are analogous to shear strains.

For the transverse strain rates, the values shown here match the strain grid values well. The profile through G1 is generally parabolic in nature, although a significant peak occurs in the G1 region. The profile through G3 is significantly flatter, especially east of G3 due to the slow-moving ice in this region.

6.4.2 GPS-derived strain

We used GLOBK to combine the quasi-observations for the GPS surveys between 1988-1999 to estimate a consistent set of coordinates and velocities. We then used the resulting quasi-observations in FONDA to determine strain rates. The observations in this case are the GPS station coordinates and velocities and their variance-covariance matrices. For the purpose of the adjustment, only those sites in the AIS region were considered. The coordinates and velocities of IGS sites DAV1 and MAW1 were constrained tightly to their ITRF97 coordinates (10mm and 20mm for horizontal and vertical, respectively) and velocities (10mm and 30mm for horizontal and vertical, respectively). Numerical instabilities were encountered in the solution. The sources of these problems were traced to two AIS sites (GA42 and GA05) and these were removed from the adjustment. The reason for this instability is currently unknown, although both sites were observed only

twice and on identical days. The GPS data for these sites has gone through two combination stages (combination of daily then seasonal files in GLOBK) and the positions and velocities appear well-determined.

Strain rate parameters were estimated by forming Delaunay triangles[3] from the remaining AIS sites. Only those strain rates that were different from zero at the 2σ level were kept. This removed most of the triangles with a poorly determined GPS site, including the GPS sites observed in a single season. Further strain rates were removed where the Delaunay triangles were ill defined since they crossed regions of exposed rock or their sides were elongated. The final strain rate results are shown in Figure 6-13. The SNR for the strain rates are mostly in the range of 15-50, slightly lower than the terrestrially derived strain rates. This is due mainly to the relatively short occupation times of the GPS and, in the case of the 1988-91 campaigns, the poor data quality. The $\dot{\varepsilon}$ term (mean SNR of 27) is slightly better determined than $\dot{\varepsilon}_2$ (mean SNR of 20), due to the larger signal present in this component (i.e., the strain rates are better resolved along the flow lines rather than across the ice shelf).

The figure shows that the strain rates are highly variable, although systematic patterns exist. Firstly, the majority of the ice shelf region shown here experiences small strain rates away from the ice shelf edges. Strain rates in these mid-ice shelf regions are about 0.7-1.2x10^{-3}yr^{-1}. The highest strains are in those regions near where ice is grounded or where ice enters the main flow of the ice shelf. For example, strain rates are as high as 0.1x10^{-1}yr^{-1} where ice flows in from the west to the north of C12. High strain rates are also seen in the region of the dashed yellow line, which is still some distance from the grounded continental ice. This line marks a region that appears to be grounded, based on radar echo sounding and seismic measurements in the region (Ruddell, 2001). This is generally confirmed by the strain rates in this region, with high levels of compression south of the region and high levels of extension north of the region. However, since no strain rate estimates are available to the west of this region, it is difficult to be absolutely certain from this data.

3. Delaunay triangles are defined such that the circumcircle of each triangle does not contain any of the other points

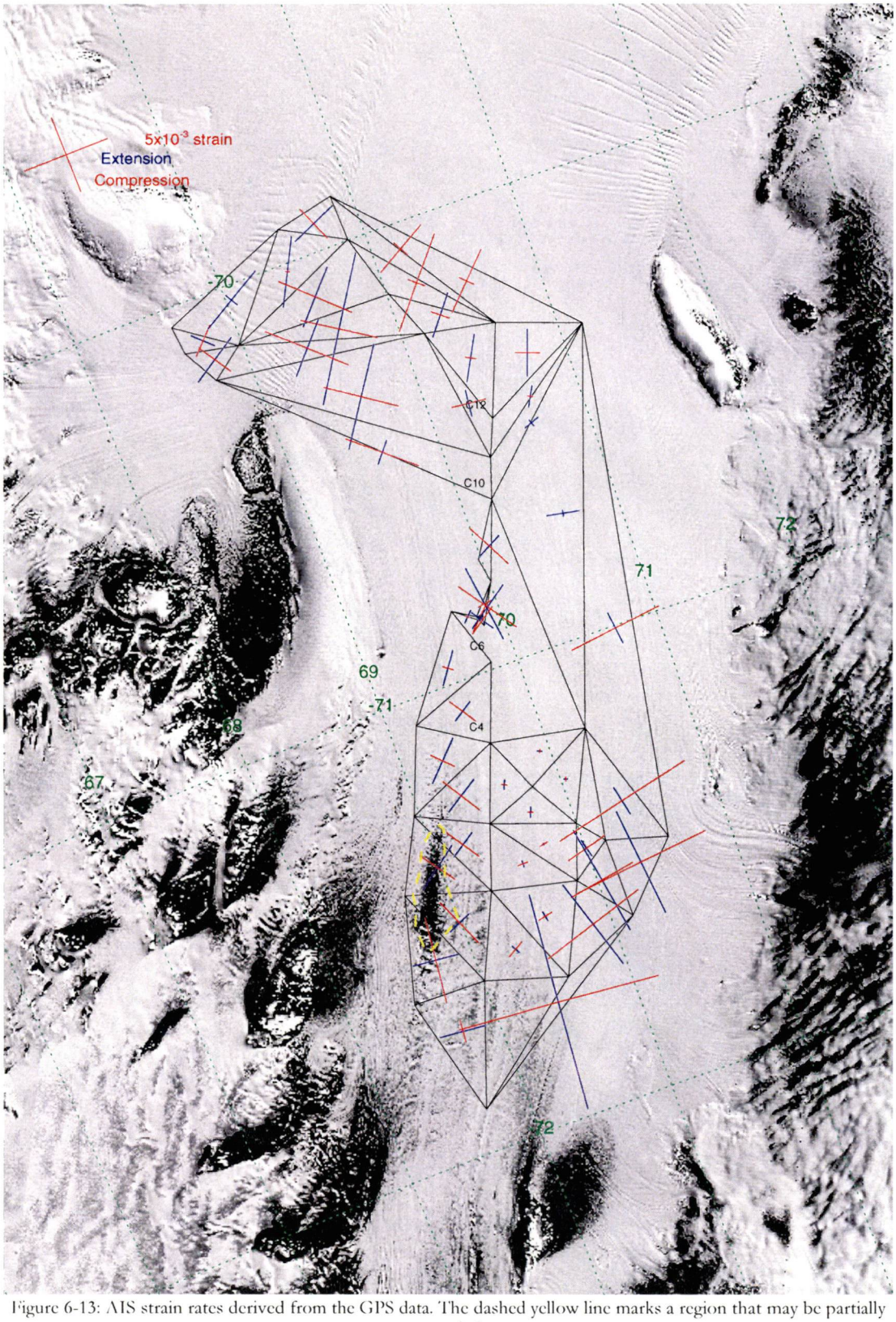

Figure 6-13: AIS strain rates derived from the GPS data. The dashed yellow line marks a region that may be partially grounded.

6.4.3 Combination of Terrestrial and GPS data

In Chapter 5 it was shown that the surface velocity profile of the AIS appears to be unchanged during the period 1968-1999. Consequently, these data may be combined so as to determine a more detailed strain grid for the AIS. The combination of the GPS and terrestrial data was limited to determinations of only site position and velocity by FONDA software limitations. Time-dependant velocities are not determined. When constraints (Section 6.3.2.1.3) are applied linking the velocities and coordinates of the terrestrial and GPS determinations of the same ice marker pole, the data is shown not to fit the functional model shown in equation (6.25). Values of $\delta\chi_c^2$ were in the order of 1200 per constraint. Conversely, when the same constraints are applied to rock sites with linear velocities, the values of $\delta\chi_c^2$ are significantly less than 1.0. This shows that the terrestrial and GPS networks are compatible and no significant systematic differences exist between the two.

Furthermore, if the software were able to determine the time-dependant variation of the velocity terms, the resulting sites would have been of little value for strain determinations since the strains would no longer have been homogeneous.

We therefore treat each of these site position and velocity determinations independently. Coordinates and velocities for MAW1 and DAV1 were tightly constrained to their ITRF97 values. Additionally, the coordinate and velocity estimates for BLUS, PICK, FOXR, NEWY, MOUS and LAND were constrained absolutely at their ITRF97 values determined by the GPS data. Only the velocities were constrained at HAMM since the ground mark occupied in the terrestrial survey could not be relocated in the GPS measurements. The χ^2 value for this combination was 72.6 and so is only slightly larger than the combination for the terrestrial-only measurements, showing that the data fits together well.

Strain rate values were determined from this combination using the method of Prescott (1976). Delaunay triangulation produced too many triangles and so the regions were defined manually to provide an even distribution of strain rates. The results are given in Table 6-4 and shown in Figure 6-14.

The additional velocity information provided through this combination significantly increases the number of degrees of freedom available in some of the triangles. This increases the likelihood of obtaining high quality strain estimates for these triangles. However, the majority of triangles have no such redundant measurements. The SNRs of $\dot{\varepsilon}$ are in the range ~2-860 with a median value of ~43. For $\dot{\varepsilon}_2$, the SNRs are in the range of ~2-230 with a median of ~23. Consequently, the $\dot{\varepsilon}$ values are slightly better determined than $\dot{\varepsilon}_2$ due to the larger signal in this component.

As can be seen by comparing Figures 6-13 and 6-14, the combined data provides the opportunity to estimate a significantly greater density of strain values across a much greater area of the ice shelf than from the GPS or terrestrial data only. In fact, the AIS region north of -72.0° is now well covered in terms of strain rates. The strain patterns in Figure 6-14, reveal that the ice shelf experiences low strain away from the ice shelf margins between approximately -70.5° and -71.5°. North of -70.5°, the longitudinal strain values increase linearly toward the ice shelf front. In regard to the transverse strain, the ice between -70.5° and -70.0° is affected by the inflow of ice from the west via the Charybdis Glacier. North of this region, the strain values are extensional in the centre of the ice shelf, with compression experienced away from the central flow lines. However, as seen in the G1 area, the transverse strain rates are highly variable.

The axis of principal strain is generally orientated along the direction of ice flow. The convergent strain values near G1 that were discussed in Section 6.4.1.1, remain in this analysis that uses larger strain grids and additional sites in these regions. This suggests that these values are real, although since they are determined from the terrestrial data only, they may be subject to errors remaining in the data.

These results represent the most complete set of strain values determined from *in situ* measurements of the AIS. They provide information on the horizontal strain values as recorded from data collected over a thirty year time period over which time the ice shelf is regarded as being unchanged in terms of its velocity and strain fields. These values may be used in further ice shelf dynamics studies and in comparisons with determinations from remote sensing methods such as InSAR and sequential image matching. In the next section an example of the use of the above strain rates is given with the computation of ice shelf basal melt rates.

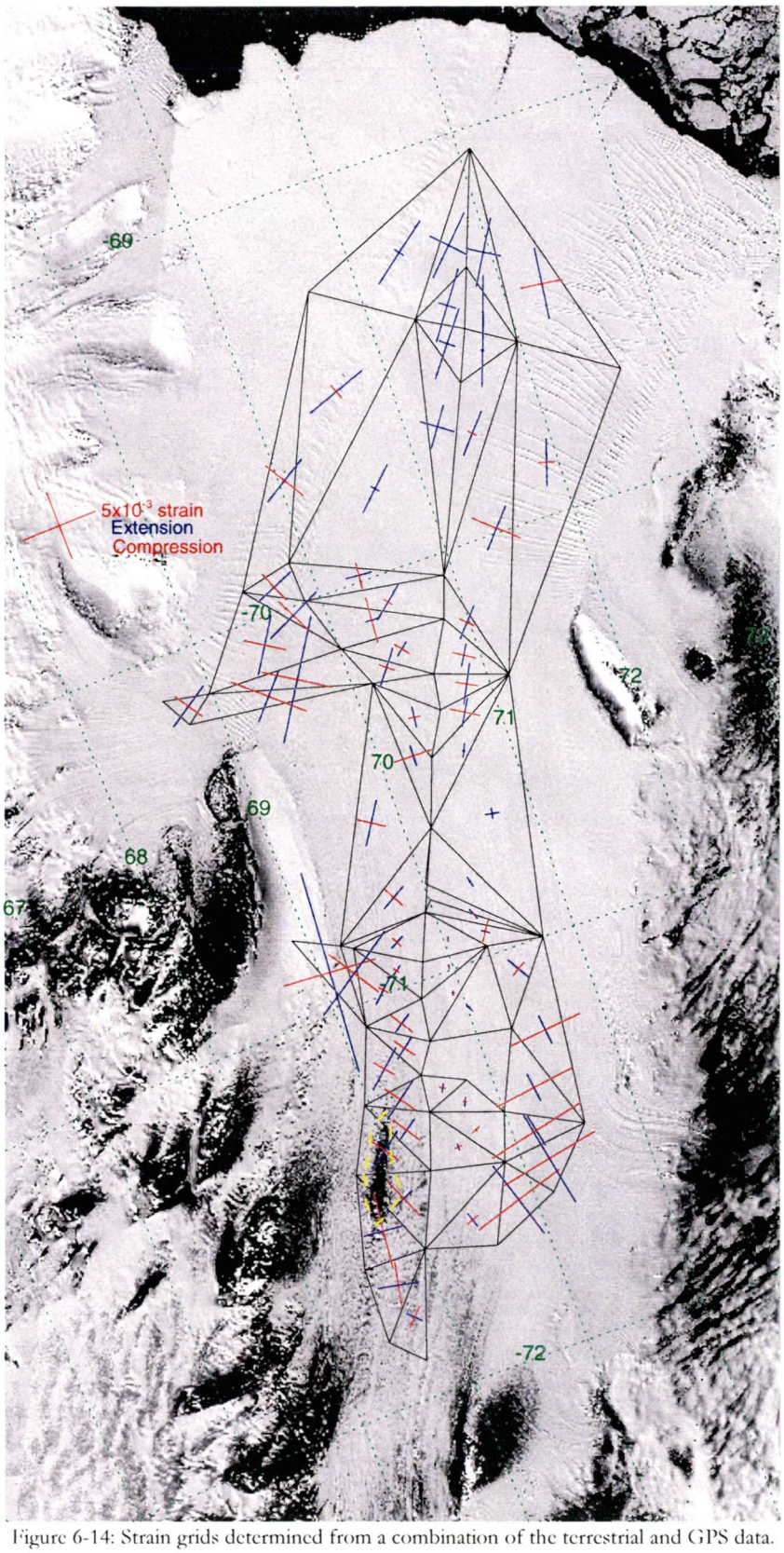

Figure 6-14: Strain grids determined from a combination of the terrestrial and GPS data.

Table 6-4 Amery Ice Shelf strain rates derived from a combination of terrestrial (1968-70) and GPS data (1988-1999). The number of sites and the degrees of freedom (dof) used in each triangle are also shown. The three sites listed in the right hand columns are only those that define the particular triangle

Lat. (°)	Lon. (°)	$\dot{\varepsilon}_1$	$\sigma_{\dot{\varepsilon}_1}$	$\dot{\varepsilon}_2$	$\sigma_{\dot{\varepsilon}_2}$	$\dot{w}$	$\sigma_{\dot{w}}$	θ (°)	σ_θ (°)	# sites	# dof	Triangles		
		(x10^{-3} yr^{-1})		(x10^{-3} yr^{-1})		(°yr^{-1})						SiteA	SiteB	SiteC
-71.6892	68.6747	3.06	0.38	-3.33	0.21	-2.01	0.20	12 0	1.7	3	0	$G282_{GPS}$	$GA35_{GPS}$	$GA30_{GPS}$
-71.7797	68.7474	1.23	0.36	-1.67	0.16	0.93	0.18	45.3	4.1	3	0	$GA29_{GPS}$	$GA35_{GPS}$	$G282_{GPS}$
-71.7362	69.1205	-0.16	0.14	-1.28	0.09	-0.53	0.11	0.8	5.3	3	0	$GA29_{GPS}$	$G282_{GPS}$	$G31B_{GPS}$
-71.5488	68.7497	2.93	0.33	-5.54	0.14	-1.60	0.15	6.6	1.0	3	0	$G282_{GPS}$	$GA25_{GPS}$	$GA30_{GPS}$
-71.4906	69.0128	1.70	0.09	-3.37	0.07	-5.22	0.07	-23.0	0.6	3	0	$GA25_{GPS}$	$GA26_{GPS}$	$G282_{GPS}$
-71.5231	69.4041	0.03	0.08	-0.95	0.10	-2.22	0.08	61.9	3.7	3	0	$G282_{GPS}$	$GA26_{GPS}$	$GA27_{GPS}$
-71.6021	69.5069	1.18	0.17	-1.00	0.12	-1.88	0.09	71 6	2.5	3	0	$G282_{GPS}$	$GA27_{GPS}$	$G31B_{GPS}$
-71.5958	69.8824	5.96	0.15	-7.15	0.20	3.55	0.13	72 9	0.6	3	0	$GA27_{GPS}$	$GA34_{GPS}$	$G31B_{GPS}$
-71.5246	70.2041	7.23	0.20	-7.45	0.18	1.97	0.16	78 8	0.6	3	0	$GA27_{GPS}$	$GA33_{GPS}$	$GA34_{GPS}$
-71.4411	70.1551	2.42	0.10	-7.37	0.18	2.22	0.11	77.5	0.6	4	2	$GA24_{GPS}$	$GA27_{GPS}$	$GA33_{GPS}$
-71.3601	68.9903	3.32	0.06	-2.57	0.05	-4.82	0.04	-35.8	0.5	3	0	$GA25_{GPS}$	$GA26_{GPS}$	$GA23_{GPS}$
-71.3308	69.2346	1.95	0.09	-2.46	0.06	-4.42	0.05	-33.6	0.7	3	0	$GA23_{GPS}$	$C2\_\_{GPS}$	$GA26_{GPS}$
-71.1419	69.2398	3.47	0.06	-1.74	0.09	-3.50	0.05	-40.3	0.6	3	0	$GA23_{GPS}$	$GA21_{GPS}$	$A406_{TER}$
-71.2279	69.3211	3.34	0.07	-2.72	0.09	-3.78	0.06	-35.7	0.5	3	0	$GA23_{GPS}$	$A406_{TER}$	$C2\_\_{GPS}$
-71.0955	69.5227	1.83	0.03	-1.79	0.05	-2.69	0.03	-36.6	0.3	5	4	$GA21_{GPS}$	$C4\_\_{GPS}$	$A406_{TER}$

Lat. (°)	Lon. (°)	$\dot{\varepsilon}$	σ_{ε}	$\dot{\varepsilon}_2$	$\sigma_{\dot{\varepsilon}_2}$	$\dot{w}$	$\sigma_{\dot{w}}$	θ (°)	σ_{θ} (°)	# sites	# dof	Triangles		
		($x10^{-3}$ yr^{-1})		($x10^{-3}$ yr^{-1})		(°yr^{-1})						SiteA	SiteB	SiteC
-71.4159	69.5395	0.45	0.07	-0.57	0.09	-1 97	0.04	89.4	2.2	3	0	C2__GPS	GA26GPS	GA27GPS
-71.3906	69.7785	0.18	0.07	-0.68	0.14	-1.74	0.08	71.1	4.3	3	0	C2__GPS	GA27GPS	GA24GPS
-71.2365	69.6025	0.68	0.07	-0.54	0.11	-1.11	0.06	119.1	2.6	3	0	A406TER	C2__GPS	G242GPS
-71.3142	69.7555	0.65	0.10	-0.36	0.07	-1.21	0.08	115.7	4.0	3	0	C2__GPS	G242GPS	GA24GPS
-71.2719	70.0374	0.19	0.12	-0.29	0.04	-0.51	0.07	15.3	6.5	3	0	G242GPS	GA22GPS	GA24GPS
-71.3412	70.2885	2.11	0.08	-6.03	0.17	3.28	0.08	82.1	0.5	3	0	GA24GPS	GA22GPS	GA33GPS
-71.1944	69.8836	0.04	0.08	-0.40	0.10	-0.43	0.07	-4 2	7.1	3	0	A406TER	GA22GPS	G242GPS
-71.1892	70.5543	2.18	0.07	-5.34	0.16	3.10	0.08	84.1	0.7	3	0	GA22GPS	A207TER	GA33GPS
-71.0405	69.5668	1.67	0.03	-2.00	0.04	-2.60	0.03	-33.2	0.3	4	2	GA21GPS	A402TER	C4__GPS
-70.9920	69.9220	0.35	0.04	-0.26	0.04	-0.65	0.03	107.8	3.2	3	0	A402TER	A203TER	C4__GPS
-71.0675	70.1014	0.74	0.09	0.16	0.03	-0.67	0.02	65.6	4.3	3	0	A203TER	C4__GPS	GA22GPS
-70.9434	70.5288	2.01	0.05	-1.17	0.03	0.03	0.03	58 8	0.4	6	6	GA22GPS	A203TER	A207TER
-71.1892	70.5543	2.18	0.07	-5.34	0.16	3.10	0.08	84.1	0.7	3	0	A207TER	GA33GPS	GA22GPS
-70.8391	69.0523	14.60	0.04	-6.76	0.03	-6.16	0.03	94.6	0.1	6	6	GA21GPS	A308GPS	A305TER
-70.8725	69.2696	7.43	0.04	-4.47	0.04	-6.94	0.03	-32.7	0.1	3	0	A305TER	A304TER	GA21GPS
-70.9301	69.4350	2.35	0.06	-0.83	0.02	-2.52	0.03	-42.5	0.6	3	0	GA21GPS	A304TER	A402TER
-70.8574	69.6875	0.98	0.02	-0.52	0.01	-2.71	0.02	-35.0	0.4	9	12	A304TER	A129TER	A402TER
-70.8989	69.9553	0.32	0.02	-0.10	0.01	-0.74	0.02	98 5	2.2	7	8	A129TER	A203TER	A402TER

Lat. (°)	Lon. (°)	$\dot{\varepsilon}$	$\sigma_{\dot{\varepsilon}}$	$\dot{\varepsilon}_2$	$\sigma_{\dot{\varepsilon}_2}$	$\dot{w}$	$\sigma_{\dot{w}}$	θ (°)	σ_θ (°)	# sites	# dof	Triangles		
		(x10^{-3} yr^{-1})		(x10^{-3} yr^{-1})		(°yr^{-1})						SiteA	SiteB	SiteC
-70.8384	69.8306	1.19	0.02	-0.92	0.02	-1.72	0.02	-27.3	0.2	9	12	A304$_{TER}$	A37$_{_TER}$	A129$_{TER}$
-70.8397	70.0070	0.32	0.01	-0.12	0.01	-0.67	0.02	105.9	2.0	7	8	A129$_{TER}$	A37$_{_TER}$	A203$_{TER}$
-70.8717	70.4786	0.66	0.02	-1.73	0.05	0.67	0.02	33.2	0.5	6	6	A37$_{_TER}$	A207$_{TER}$	A203$_{TER}$
-70.5511	69.8797	3.32	0.03	-2.19	0.04	-0.15	0.02	123 2	0.3	3	0	A305$_{TER}$	GA72$_{GPS}$	C10$_{_GPS}$
-70.7117	69.8811	2.10	0.02	-1.73	0.03	-2.45	0.02	-28.8	0.2	4	2	A305$_{TER}$	C10$_{_GPS}$	A37$_{_TER}$
-70.7878	70.2190	0.87	0.02	-0.15	0.02	0.06	0.02	67.1	0.6	4	2	A37$_{_TER}$	C8$_{__GPS}$	A207$_{TER}$
-70.6888	70.3055	0.84	0.02	0.15	0.02	0.11	0.02	74.6	0.8	5	4	A36$_{_TER}$	C10$_{_GPS}$	A207$_{TER}$
-70.6077	70.6211	1.05	0.03	0.76	0.04	0.37	0.03	10.6	4.8	4	2	C10$_{_GPS}$	GA12$_{GPS}$	A207$_{TER}$
-70.4909	70.2848	1.46	0.04	-2.86	0.05	2.14	0.05	91.4	0.7	6	6	C10$_{_GPS}$	GA72$_{GPS}$	C12$_{_GPS}$
-70.4665	70.5259	1.00	0.01	0.22	0.08	0.75	0.06	114.8	4.4	5	4	C12$_{_GPS}$	GA12$_{GPS}$	C10$_{_GPS}$
-70.3256	70.4126	1.50	0.04	-0.93	0.08	2.68	0.05	97.0	1.4	3	0	GA72$_{GPS}$	A28$_{_TER}$	C12$_{_GPS}$
-70.3449	70.6862	2.08	0.02	-2.28	0.11	2.02	0.08	120.8	0.9	5	4	A28$_{_TER}$	GA12$_{GPS}$	C12$_{_GPS}$
-70.2720	70.8094	2.93	0.02	-1.67	0.04	3.41	0.03	117.4	0.4	4	2	A28$_{_TER}$	GA11$_{GPS}$	GA12$_{GPS}$
-70.2590	70.4910	120.00	7.63	-2.97	0.75	18.70	2.39	109.4	1.4	3	0	GA72$_{GPS}$	GA11$_{GPS}$	A28$_{_TER}$
-70.0218	68.9295	5.72	0.12	0.33	0.18	-10.20	0.07	3.3	1.3	3	0	GA03$_{GPS}$	GA02$_{GPS}$	GA06$_{GPS}$
-70.1414	68.8150	3.57	0.23	-2.33	0.34	-4.95	0.27	-33.1	0.8	3	0	GA02$_{GPS}$	GA01$_{GPS}$	GA04$_{GPS}$
-70.0502	69.0531	4.18	0.03	0.01	0.08	-6.24	0.05	126.1	0.7	3	0	GA02$_{GPS}$	GA04$_{GPS}$	GA06$_{GPS}$
-70.1851	69.3176	3.85	0.18	-5.69	0.23	-2.81	0.25	131.7	1.1	3	0	GA01$_{GPS}$	GA04$_{GPS}$	GA72$_{GPS}$

Lat. (°)	Lon. (°)	$\dot{\varepsilon}$	$\sigma_{\dot{\varepsilon}}$	$\dot{\varepsilon}_2$	$\sigma_{\dot{\varepsilon}_2}$	$\dot{w}$	σ_w	θ (°)	σ_θ (°)	# sites	# dof	Triangles		
		($\times 10^{-3}$ yr^{-1})		($\times 10^{-3}$ yr^{-1})		(°yr^{-1})						SiteA	SiteB	SiteC
-70.1652	69.7353	9.15	0.07	-5.03	0.05	-2.58	0.07	122 4	0.3	3	0	$GA04_{GPS}$	$GA07_{GPS}$	$GA72_{GPS}$
-70.0566	69.5119	4.28	0.03	-3.03	0.06	-5.71	0.05	122.6	0.3	3	0	$GA04_{GPS}$	$GA06_{GPS}$	$GA07_{GPS}$
-69.9248	69.7652	3.20	0.07	-2 47	0.17	-2.64	0.10	-23.1	0.7	3	0	$GA06_{GPS}$	$GA09_{GPS}$	$GA08_{GPS}$
-70.0073	69.8131	4.60	0.16	-2.90	0.08	-1 81	0.13	-25 7	0.9	3	0	$GA06_{GPS}$	$GA08_{GPS}$	$GA07_{GPS}$
-70.2105	70 2789	2.85	0.10	-1.15	0.06	2.44	0.09	128.1	1.1	3	0	$GA07_{GPS}$	$GA72_{GPS}$	$GA11_{GPS}$
-70.1510	70.5630	1.22	0.06	-1.33	0.07	2.88	0.03	-39.6	1.4	3	0	$GA07_{GPS}$	$A99\_{TER}$	$GA11_{GPS}$
-70.0564	70.3210	0.98	0.05	-3.31	0.09	0.72	0.05	3.8	0.8	3	0	$GA08_{GPS}$	$GA07_{GPS}$	$A99\_{TER}$
-70.0150	70.8724	2.90	0.02	-0 71	0.05	1.94	0.02	-39.4	0.3	6	6	$GA08_{GPS}$	$A99\_{TER}$	$A22\_{TER}$
-69.9390	70.3204	1.91	0.05	-1.82	0.11	-0.28	0.09	4.8	1.5	3	0	$GA09_{GPS}$	$GA08_{GPS}$	$A22\_{TER}$
-70.1732	70.9235	1.64	0.01	-1.71	0.05	3.36	0.03	121.6	0.4	6	6	$A99\_{TER}$	$GA12_{GPS}$	$GA11_{GPS}$
-70.0733	71.0896	2.58	0.04	-1.26	0.08	2.44	0.06	132.7	0.7	6	6	$A22\_{TER}$	$GA12_{GPS}$	$A99\_{TER}$
-69.7028	70.9389	3.81	0.01	0.72	0.05	0.93	0.02	-43.1	0.4	3	0	$GA09_{GPS}$	$A602_{TER}$	$A22\_{TER}$
-69.6687	71.5633	3.12	0.01	2.53	0.03	2.14	0.02	124.9	1.7	11	16	$A602_{TER}$	$A13\_{TER}$	$A22\_{TER}$
-69.6823	71.6240	3.35	0.01	-0.76	0.04	1.26	0.02	131.3	0.2	11	16	$A112_{TER}$	$A13\_{TER}$	$A22\_{TER}$
-69.9021	71.5862	3.36	0.01	-3.70	0.10	1.23	0.05	130 5	0.4	3	0	$A112_{TER}$	$A22\_{TER}$	$GA12_{GPS}$
-69.3470	71.9346	5.25	0.01	1.23	0.01	0.18	0.02	127.5	0.2	9	12	$A602_{TER}$	$A72\_{TER}$	$A13\_{TER}$
-69.3902	72.1266	5.11	0.01	0.24	0.01	1.66	0.02	109.5	0.2	8	10	$A72\_{TER}$	$A112_{TER}$	$A13\_{TER}$
-69.2708	72.0575	5.43	0.01	1.33	0.01	0.03	0.02	125.2	0.2	7	8	$A602_{TER}$	$A503_{TER}$	$A72\_{TER}$

Lat. (°)	Lon. (°)	$\dot{\varepsilon}$	σ_{ε}	$\dot{\varepsilon}_2$	$\sigma_{\dot{\varepsilon}_2}$	$\dot{w}$	σ_w	θ (°)	σ_θ (°)	# sites	# dof	Triangles		
		($x10^{-3}$ yr^{-1})		($x10^{-3}$ yr^{-1})		(°yr^{-1})						SiteA	SiteB	SiteC
-69.3112	72.2366	5.23	0.01	0.12	0.02	1.36	0.02	108.4	0.2	7	8	$A503_{TER}$	$A72\_{TER}$	$A112_{TER}$
-69.2912	71.1813	4.74	0.02	-1.23	0.02	-1.21	0.02	-20.0	0.1	8	10	$GA09_{GPS}$	$A608_{TER}$	$A602_{TER}$
-69.6465	70.1347	3.78	0.04	-3.42	0.13	-1.41	0.05	-32.0	0.3	3	0	$GA09_{GPS}$	$GA06_{GPS}$	$A608_{TER}$
-69.1597	71.5138	5.38	0.01	0.81	0.01	-2.37	0 01	-38.2	0.1	8	10	$A509_{TER}$	$A608_{TER}$	$A602_{TER}$
-69.0269	72.3612	5.16	0.01	2.98	0.02	-1.08	0.02	134.3	0.3	8	10	$A509_{TER}$	$A503_{TER}$	$A602_{TER}$
-69.0452	72.4430	4.97	0.01	2.54	0.03	1.09	0.02	119.9	0.3	8	10	$A509_{TER}$	$A503_{TER}$	$A112_{TER}$
-69.3958	72.6653	5.11	0.01	-3.00	0.02	0.95	0.02	96.0	0.1	6	6	$A509_{TER}$	$A112_{TER}$	$A116_{TER}$
-69.6472	72.4395	3.34	0.03	-1.09	0.01	3.26	0.02	106.8	0.2	6	6	$GA12_{GPS}$	$A112_{TER}$	$A116_{TER}$

6.4.4 Determination of melt/freeze parameters

Ice shelf basal melt rates may be determined using several different techniques, including numerical ocean circulation models (e.g., Williams *et al.*, 2001) and remote sensing methods (personal communication, N. Young, 2001). While providing spatially dense data, these methods have some shortcomings. Numerical modelling relies on the quality of the input data, such as water-column thickness, bathymetry, salinity, temperature, etc. as well as the parameterisation of the forcing terms, especially friction. For most ice shelf regions, these input data values are often only available at the ice shelf front or are sparsely distributed in the sub-ice shelf regions. Alternatively, remote sensing measurements may be used although accumulation is not usually well known over large areas and hence this input term needs to be modelled. Perhaps more seriously, the change in ice shelf thickness with time needs to be assumed to be zero if melt rates are to be determined, since this value cannot presently be determined from remote sensing measurements.

We present here a method that determines the basal melt rate of an ice shelf without the need to assume ice shelf steady state. Such estimates of melt/freeze are a first attempt at using the GPS data to derive these parameters on the AIS. This method depends on the assumption that the melt, accumulation, ice density and strains are constant along the profile travelled by the reference mark between occupations. Since in our case these distances are only approximately one kilometre, these assumptions are reasonable.

Budd (1966a) provided the following relationship (illustrated in Figure 6-15) for the determination of change in ice shelf thickness with time using surface measurements at poles moving with the ice:

$$\frac{\partial Z}{\partial t} = A - M - \left(\dot{\varepsilon}_1 + \dot{\varepsilon}_2\right) Z + V \frac{\partial Z}{\partial x} - C \qquad (6.39)$$

where:

$\frac{\partial Z}{\partial t}$ is the rate of change of the ice shelf thickness at a location,

A is the measured surface accumulation rate in terms of its ice equivalent,

M is the basal melt rate (ice equivalent),

$(\dot{\varepsilon}_1 + \dot{\varepsilon}_2)$ is the total horizontal strain rate,

Z is the thickness of the ice shelf,

V is the horizontal velocity,

$\frac{\partial Z}{\partial x}$ is the longitudinal rate of change of ice shelf thickness at the position and

C accounts for errors due mainly to biases entering the accumulation measurements through snow/firn densification, melting-in of the measurement pole and other such transient surface effects.

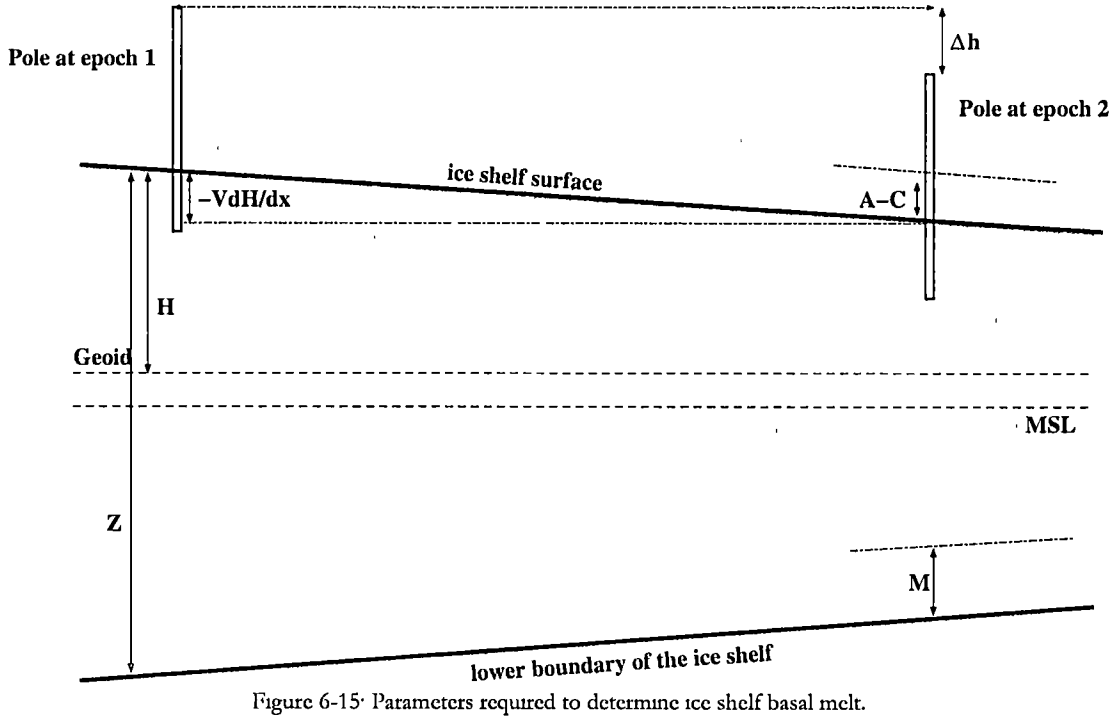

Figure 6-15: Parameters required to determine ice shelf basal melt.

In Figure 6-15, MSL is the Mean Sea Level, while the surface height of the ice shelf is related to the geoid. The Mean Sea Level does not likely coincide with the geoid and there will be some offset (of up to 1m) between these surfaces. Δh is the between epoch ellipsoidal height difference of the reference mark.

If the rate of thickness change is required at a single geographic location, the thickness gradient term ($\partial Z / \partial x$) is zero and equation (6.39) becomes:

$$\frac{\partial Z}{\partial t} = A - M - \left(\dot{\varepsilon}_1 + \dot{\varepsilon}_2\right) Z - C \tag{6.40}$$

Due to the buoyancy of the ice shelf, the ice shelf thickness Z and surface elevations H are related by the relationship (Fricker *et al.*, 2001b):

$$H = Z\left(\frac{\rho_w - \rho_i}{\rho_w}\right) \tag{6.41}$$

where ρ_w and ρ_i are the column averaged densities of water and ice, respectively. Differentiating with respect to time gives:

$$\frac{\partial H}{\partial t} = \left(\frac{\partial Z}{\partial t}\right)\left(\frac{\rho_w - \rho_i}{\rho_w}\right) \tag{6.42}$$

Substituting equation (6.40) into (6.42) and omitting C gives the rate of surface height change at a particular geographical location:

$$\frac{\partial H}{\partial t} = A\left(\frac{\rho_w - \rho_A}{\rho_w}\right) - M\left(\frac{\rho_w - \rho_M}{\rho_w}\right) - \left(\dot{\varepsilon}_1 + \dot{\varepsilon}_2\right) Z\left(\frac{\rho_w - \rho_i}{\rho_w}\right) \tag{6.43}$$

Where ρ_A and ρ_M are the densities of the accumulated snow and melted/frozen ice, respectively, and ρ is the column-averaged ice density.

Now, the GPS measurements of the vertical velocity of the reference pole ($\dot{h}_{GPS}$) corrected for the geoid gradient ($\partial N / \partial x$) and shifted to the snow surface via measurements from the reference mark to the snow surface (A_{meas}) are equal to the rate of surface height change plus the effects of down-slope motion, such that:

$$\dot{h}_{GPS} - (V\partial t)\frac{\partial N}{\partial x} + A_{meas} = \frac{\partial H}{\partial t} + (V\partial t)\frac{\partial H}{\partial x} \tag{6.44}$$

Any pole motions due to densification, melting-in, etc. are cancelled in this formula provided that the A_{meas} is the measurements made to the snow surface at the time of the GPS observations.

By rearranging:

$$\frac{\partial H}{\partial t} = \dot{h}_{GPS} - (V\partial t)\frac{\partial N}{\partial x} - (V\partial t)\frac{\partial H}{\partial x} + A_{meas} \tag{6.45}$$

Again, equations (6.44) and (6.45) refer to a particular geographical location. Combining equations (6.43) and (6.45) and rearranging to solve for melt rates:

$$M = -\left(\dot{h}_{GPS} - (V\partial t)\frac{\partial N}{\partial x} - (V\partial t)\frac{\partial H}{\partial x} + A_{meas}\right)\frac{\rho_w}{(\rho_w - \rho_M)} + \frac{A(\rho_w - \rho_A) - (\dot{\varepsilon}_1 + \dot{\varepsilon}_2)Z(\rho_w - \rho_i)}{(\rho_w - \rho_M)} \tag{6.46}$$

The vertical velocities from four sites (C4, C6, C8 and C12) are well determined as described in Chapter 5 and so we attempt to apply equation (6.46) at these sites. These sites were observed at two or three epochs over a period of 3.25 years, with observation periods greater than two hours. The tidal signals were removed from the GPS data prior to processing in GAMIT as described in Chapter 4. The formal errors from GLOBK are less than 70mmyr^{-1} at these sites. The horizontal velocities were determined from the GPS measurements (Chapter 5) and have errors below 50mmyr^{-1} at these locations, based on the GLOBK results.

The accumulation measurements were made at the same time as the GPS measurements (3.25 years apart). Where required, these terms were converted to ice equivalent values based on a snow density of 360kgm^{-3} and an ice density of 900kgm^{-3}. Unfortunately, the bases of these poles were placed only 0.5-1.0m below the snow surface and thus (unknown) snow/firn densification and thermal effects on the pole will bias the accumulation measurements. Errors in the accumulation measurements are taken to be 50mm at each measurement epoch due to uncertainty in measuring to the snow surface

and uncertainties in the snow/ice densities. Melting-in of the pole may bias these values and this is accounted for in the errors assigned to C. The error term (C) is unknown, and so it was given a value of 0.0.

The horizontal strain rates are well known from the GPS/terrestrial data within particular regions (Section 6.4.2). To estimate the strain values at each site we assume that the strain regime at each of these sites is unaffected by slow moving ice to the west of C4 and C6 and the ice entering from the west near C12 (see Figure 6-13). These assumptions are reasonable since the strain values to the east of C4 and C6 are unaffected by these slow moving sites, while C12 is just to the south of the region affected by the ice entering near there. Strain values near C10 are only available when computed over a wide area, although fortunately this region appears to be uniform in terms of its flow pattern. The ice thickness values were determined using two data sets of differing quality. The errors in the ice thickness values are 20m for C10 and C12 and 40m for C4 and C6 (personal communication, A. Ruddell, 2001).

The ice shelf surface profile was determined using a DEM of the ice shelf (Fricker *et al.*, 2000). It is important that local surface features do not bias the determination of this term and so a smoothed profile is required (filtered at about 30km length scales). To achieve this, a linear regression was applied to DEM points interpolated at 1km steps, 20km either side of the point in the line of the ice shelf flow. The errors in these values are difficult to assess and so they were assigned values of 10% of the gradient.

The column averaged water density is taken to be 1029kgm^{-3} based on *in situ* measurements made at the ice shelf front (Wong *et al.*, 1998), with an uncertainty of 0.2kgm^{-3} (personal communication, N. Bindoff, 2001). The column averaged ice densities and their errors (2kgm^{-3}) were interpolated from the non-linear density model described in (Fricker *et al.*, 2001b).

Equations (6.46) was used to estimate basal melt rates and their errors at the four locations and the results are shown at the bottom of Table 6-5. Two different solutions were computed: the first (*M1*) uses the data as described above, while the second (*M2*) replaces

the strain rates and slope described above with those used in a study using Radarsat data (personal communication, N. Young, 2001). The remote sensing technique used to determine these melt values does not include surface accumulation, and so the accumulation values measured at each of the poles was used to correct the estimates. The computation of the Radarsat strain rate values relies on the assumption that the ice shelf is in steady state – a reasonable assumption, given the velocity comparisons over 30 years shown in Chapter 5. Two estimates from the Radarsat data are shown – one solution averaging over 8x8km cells, the other averaging over 16x16km cells. The two Radarsat estimates are in good agreement, although a difference of $0.3myr^{-1}$ at C6 suggests that the melt rates may be highly variable in parts of the ice shelf and hence may be affected by averaging over large distances.

The results from this study are highly dependent and very sensitive to the terms in the second set of parentheses in equation (6:46) since they are scaled by a factor of approximately 10 due to the ratio of the density terms. Of the terms inside the second set of parenthesis, the accumulation measurements will be affected by mis-measurements to the snow surface. The GPS data could be biased by a mis-fit of the tide model used to remove the tidal signal. The determination of the surface slope term is sensitive to local variations and hence needs to be computed by filtering over a suitable distance. There may also be some systematic errors in the DEM. The horizontal velocities are well-known from GPS and can essentially be assumed error-free. The melt results are also affected by the terms outside the parentheses. The strain rate values from the GPS/terrestrial data are quite different to the values determined from the Radarsat data. This may be a result of the GPS/terrestrial strain rates being determined from too large a geographical area. The GPS/terrestrial strain rates were determined over triangular regions with side lengths approximately 20-30km, although some were much larger, while the Radarsat values are estimated on 8x8km and 16x16km grids. The unresolved systematic bias in the Radarsat velocities (Chapter 5) will also cause some error in their strain rate estimates. The error term (C) is largely unknown and also biases the results.

The *M1* and *M2* estimates from the GPS data compare poorly with the Radarsat values. The *M2* estimates are not significantly closer to the Radarsat estimates than the *M1* estimates. The *M1* estimates agree with the Radarsat 8x8km results within their errors at all of the sites except C4. The slope and strain rates for the C4 estimate may be dubious since they are both of opposite sign to the *M2* estimate.

Long-term measurements of accumulation at well-established poles are required to reduce the errors in our estimates. This will effectively cause the value of C to approach zero. Until the errors in the accumulation measurements can be reduced, the accuracies of these values are uncertain and are not likely to be of sufficient quality for quantitative studies. Observations of the 'coffee-can' style (Hamilton *et al.*, 1998) present an ideal way to increase the precision of these measurements. Furthermore, high precision slope measurements are required. In the future, ICESat measurements will contribute to our understanding of these parameters, although ICESat measurements require knowledge of the basal melt in order to determine accumulation.

Site		C4	C6	C10	C12
$(\dot{\varepsilon}_1 + \dot{\varepsilon}_2)_{M1}$ (x10^{-3}yr^{-1})		-0.10 (0.10)	0.98 (0.07)	1.62 (0.16)	1.01 (0.15)
$(\dot{\varepsilon}_1 + \dot{\varepsilon}_2)_{M2}$ (x10^{-3}yr^{-1})		0.2	0.3	2.1	1.8
$\frac{\partial H}{\partial x}_{M1}$ (x10^{-4})		0.2 (0.09)	-0.3 (0.02)	-0.3 (0.09)	-2.2 (0.18)
$\frac{\partial H}{\partial x}_{M2}$ (x10^{-4})		-0.2	-2.7	-2.0	-3.7
A (myr^{-1})		0.081 (0.016)	0.110 (0.016)	0.131 (0.016)	0.151 (0.016)
Z (m)		790 (40)	760 (40)	760 (20)	710 (20)
V (myr^{-1})		340.46 (0.01)	348.53 (0.01)	368.49 (0.01)	385.11 (0.05)
$\dot{h}_{GPS} - V\frac{\partial N}{\partial t}$ (myr^{-1})		-0.29 (0.04)	-0.38 (0.04)	-0.45 (0.05)	-0.56 (0.07)
ρ_w (kgm^{-3})		1029 (0.2)	1029 (0.2)	1029 (0.2)	1029 (0.2)
ρ_i (kgm^{-3})		915 (2)	911 (2)	907 (2)	903 (2)
This analysis	$M1$ (myr^{-1})	1.0	0.2	-0.0	0.3
	$M2$ (myr^{-1})	0.7	-0.1	-1.0	-0.8
Radarsat	M 8x8km (myr^{-1})	0.2	0.5	-0.6	0.4
	M 16x16km (myr^{-1})	0.1	0.8	-0.6	0.3

Table 6-5: Ice shelf parameters at the four GPS sites with well defined vertical velocities. Melt rates are positive (freeze is negative). The surface accumulation is for the ice equivalent of the actual snow accumulation. Estimated errors (1σ) are shown in parentheses. The errors associated with the *M2* estimates are unknown since the values come from the Radarsat measurements.

Williams *et al.* (2001) have estimated melt rates for the AIS using two different three-dimensional ocean circulation models. The two models differ in the boundary conditions applied at the ice shelf front. The first model (AIS1) allows barotropic exchange across the ice shelf front, while the second model (AIS2) does not. The melt rates from these two models are reproduced in Figure 6-16. The major effect, as is seen in the figure, is a shift in the magnitudes of the melt rates, while the broad-scale pattern remains largely the same.

The AIS1 model predicts melt rates at all sites in the range 0.1-1.0myr^{-1}, while the AIS2 model predicts less melt, with ranges of -0.1 to +0.5myr^{-1}. Both models show, however, a region of high freeze close to the locations of C10 and C12. The *M1* results are within the range of the AIS1 model, considering the *M1* errors. The *M2* estimate has high freeze rates at sites C10 and C12, suggesting that the large area of freeze near these sites in the models may encroach further to the east than suggested by the models. The Radarsat values in Table 6-5 also show freeze occurring at C10, although freeze is not shown occurring at C12. Averaging of melt rates over the Radarsat grid cells may be hiding the freeze rates in this region.

Given the low accuracy of the present results, it is not currently possible to assess the quality of these ocean circulation models shown in Williams *et al.* (2001), although the approximate magnitudes of the melt/freeze rates in the region of these sites is confirmed.

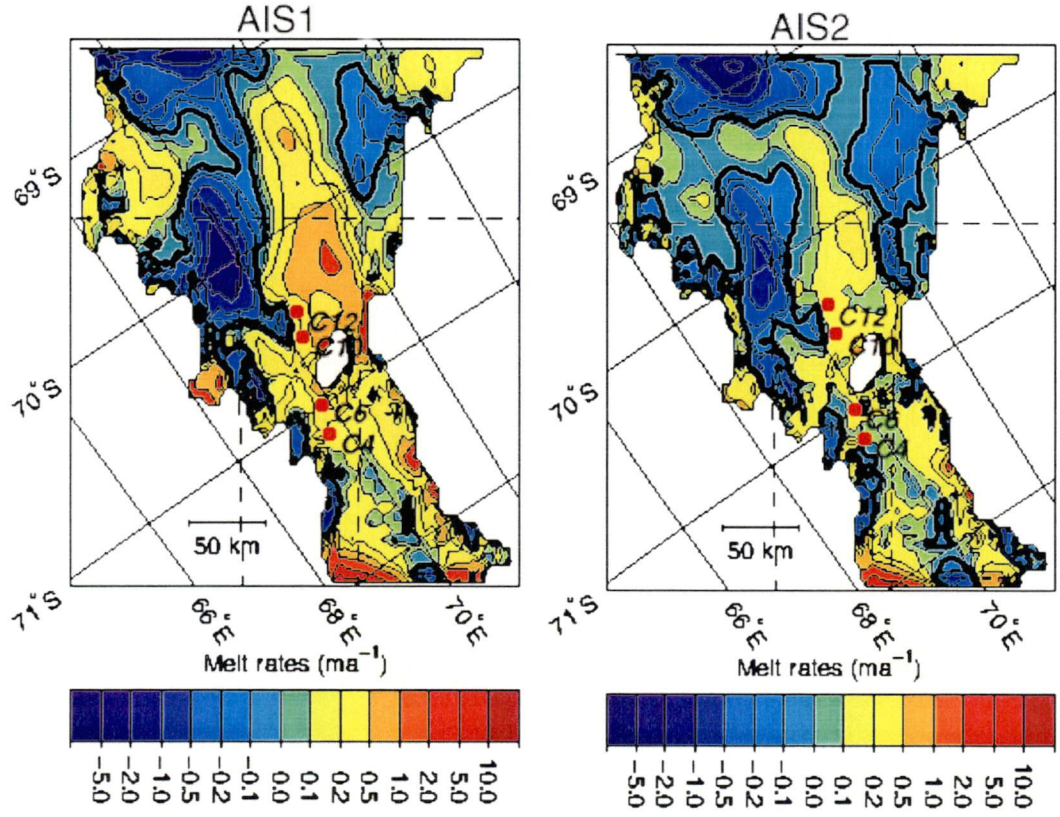

Figure 6-16: Melt rates reproduced from Williams *et al.* (2001), with the GPS locations over-plotted. Units are in metres per annum (year).

6.5 Summary

The focus of this Chapter has been the determination of strain rates on the AIS using a combination of terrestrial and GPS measurements. Firstly, the question as to how strain may be derived from geodetic observations was discussed. Both two-dimensional and three-dimensional methods were investigated. In terms of the available Amery Ice Shelf data, where both space-geodetic (GPS) and terrestrial observations (slope distances, horizontal angles, height differences and astronomical positions and azimuths) are available (Budd *et al.*, 1982), it is important that a method be adopted capable of handling the combination of these observations. Four-dimensional integrated geodesy is the most complete and consistent methodology for combining heterogeneous data that includes both space-geodetic and terrestrial observations. Consequently, a four-dimensional integrated geodesy technique has been adopted for this thesis, using the implementation of Dong (1993) and Dong *et al.* (1998).

Strain rates have been determined using both terrestrial and GPS data sets on the AIS. Apart from the imprecise measurements made in 1963-64, these data represent the entire set of AIS *in situ* survey measurements[4]. With regard to the terrestrial data, strain rates were determined using previously unpublished data from the 1968-70 measurements of strain grids at G1, G2, G3 and A1. Analysing pairs of traverse stations for their forward and transverse strain rates determined further strain rates. The strain profile of the front (of the ice shelf derived from the terrestrial data) was shown to differ significantly from that published in Budd *et al.* (1982), due to the errors identified in Chapter 5. The profile from the present study was confirmed by independent remote sensing estimates. However, further theoretical investigations are needed to understand the mechanics leading to the shape of the profile, particularly near the ice shelf front. This has implications for understanding calving events at the front of the ice shelf.

In terms of the GPS data, the strain rates were derived from all available data. The spatial distribution of the GPS data results in a significantly greater spatial density of strain rate

4 Excluding the 1997-98 data set, located ~150km south of the remaining data.

triangles than is provided by the terrestrial data. The combined results reveal a generally uniform strain pattern, although with interruptions due mainly to the inflow of ice, such as occurs near G2 as a consequence of ice flow from the Charybdis Glacier. The high compressive strain rates south-west of G3 confirm that this region is partially grounded, although further data is required to the west of this region to verify this.

Based on the assumption from Chapter 5 that the velocity profile of the AIS has not changed during the period 1968-1999, strain rates were determined using a combination of the terrestrial and GPS data. This combination resulted in a significantly greater distribution of strain rate values than could be obtained from just the GPS or terrestrial data alone, and represents the most spatially dense strain rate values obtained for the AIS from *in situ* data. The position and velocity of rock sites, with data from both measurement types, were constrained to be the same. These constraints resulted in only a minor increase in the χ^2 value compared to the unconstrained solution. The entire combination occurred within the context of ITRF97 as defined by tight constraints applied to two IGS stations. The determined strain rates were generally 1-2 orders of magnitude greater than their noise level, and are thus well determined.

The strain data was then used to determine basal melt parameters at four ice shelf sites. These were computed without the need to assume the ice shelf is in steady state during the period of the measurements, although the congruency test performed in Chapter 5 indicates that this is the case. The determined melt rates are in general agreement with those that have been determined from remote sensing measurements and ocean circulation models. The estimates are currently, however, dominated by errors in accumulation and unknown transient surface effects (thermal effects, densification etc.) and the difficulty in definitively determining the surface gradients. As further high precision vertical velocities are determined from GPS measurements and precise accumulation measurements are obtained, such as from 'coffee can' (Hamilton *et al.*, 1998) or ICESat observations, the spatial distribution of ice shelf basal melt information will increase significantly. Furthermore, provided highly stable GPS monumentation is available, the rate of thickness change of the ice shelf may be assessed using only a

knowledge of the horizontal and vertical velocity, surface slope, accumulation and ice and water density.

This Chapter has detailed the derivation of the most spatially dense strain rate fields from almost the entire set of *in situ* AIS survey measurements. These are of significant value for ice dynamic calculations and ground-truthing values determined from remote sensing techniques such as image cross-correlation (Scambos *et al.*, 1992) and InSAR (Bindschadler, 1998).

Chapter 7

GPS MEASUREMENTS OF ICE MOVEMENT (RECOMMENDATIONS)

Given the logistical effort that is required to collect ice movement information in Antarctica, it is prudent to carefully plan any measurement campaign. If the highest accuracy results are to be achieved, care needs to be taken in how these measurements are made. This is especially true of GPS measurements where it is not usually possible, or even preferable, to assess the quality of the observations in the field without the use of computers. Additionally, if high precision results are to be obtained from Antarctic GPS data, significant thought is required at the processing stage (Bouin and Vigny, 2000). Indeed, careful processing of the GPS data may provide significantly more information than may have been achieved otherwise (Manson, 1995; Dietrich *et al.*, 2001).

The Global Positioning System has been used in Antarctica to determine precise position since 1986 (Moller and Ritter, 1988), with widespread use from 1988 onwards (Tseng *et al.*, 1989; Murphy *et al.*, 1990). Today, GPS data is collected in continuous or campaign modes (WG-GGI, 2001). Consequently, a time-history of ice movement GPS measurements now exists spanning more than one decade. Through thorough planning (and perhaps some good fortune), terrestrial ice movement measurements conducted in the 1950s through to the 1970s are now providing valuable long-term ice movement information (e.g., Corry, 1996; Craven, 1996). If similar care is taken in the planning of current and future GPS measurement campaigns, these measurements will provide valuable information for many years to come (e.g., Tregoning *et al.*, 2000).

This chapter aims to provide a set of guidelines for the observation and use of GPS data in Antarctica. The recommendations have a particular emphasis on measurements of ice movement, although many of them are also highly applicable for GPS measurements made at rock sites. Recommendations for ice movement surveys have

been made previously (e.g., Seeber, 1993). These, however, are now out of date, and do not take advantage of the high precision solutions that are now possible with modern GPS receivers, a large global network of receivers, a full complement of GPS satellites or modern processing strategies.

The adoption of the recommendations bëlow will lead to the highest quality GPS results possible, given the logistical restrictions for the particular experiment. As with any set of recommendations there will be exceptions due to, for example, extreme environmental or site effects. Additionally, given the environmental and logistical considerations required for measurements in Antarctica, increased simplicity, robustness and redundancy in planning and equipment choice will always be of benefit. For example, while it may be possible to access a remote measurement location several days in a row, another visit to the site to retrieve equipment or download data may not be possible for 2-4 weeks or longer due to the weather. Many of the recommendations follow standard practice guidelines used by geodesists for GPS campaigns anywhere in the world. Other recommendations are more suited to Antarctica (polar environments) in particular. Regardless, in a field where glaciologists perform GPS measurements as frequently as geodesists, it is thought that these guidelines will be of benefit to the wider Antarctic science community.

A range of practical recommendations is made in the context of ice movement studies. Amongst them are antenna monumentation, observational procedures and processing methodologies. Suggestions are also made in relation to the suitability of secondary data (data other than GPS) that may complement GPS data. Furthermore, in an attempt to encourage further ice shelf tidal motion measurements, a description is provided of an autonomous GPS system capable of measuring ice shelf motion for a period of at least 8-10 weeks during the Antarctic summer. With a small number of modifications the system may be extended to observe for periods of ~12 months.

7.1 Data observation recommendations

7.1.1 GPS receivers

For observations further than 1-5km from a GPS reference station, dual frequency receivers must always be used if the highest precision measurements are to be achieved (Kluesberg, 1986). This distance is affected by the level of ionospheric activity during

the time of the observations (see Heroux and Kluesberg, 1989). Additionally, modern receivers capable of measuring full-wavelength L2 carrier signals are required. For decimetre-level precisions, single frequency measurements may be made at distances greater than 10-15km only in the case of a spatial and temporal network of dual frequency GPS receivers surrounding the antenna (Rocken *et al.*, 2000), which is unlikely to occur in Antarctica.

7.1.2 GPS antennas

The GPS antenna should ideally be a choke-ring style antenna in order to reduce multipath as much as possible. Pseudo-range multipath is reduced significantly with choke ring antennas. Carrier phase multipath is not reduced as significantly. GPS antennas with large ground-planes are significantly less effective at reducing multipath than choke ring antennas. In fact, antenna ground-planes have been shown to generate standing waves along the surface of the ground-plane (Weill, 1997), thereby biasing the GPS signals. In regard to the GPS antenna radome, Jaldehag *et al.* (1996) have shown that snow build-up on the radome can significantly retard GPS signals and increase signal scattering effects. Some GPS antenna radomes, such as those models with a conical shape (see lower left-hand image in Figure 7-1), have been shown to significantly affect the GPS signals (Johansson *et al.*, 1998). A non-conventional GPS radome (see upper right-hand image in Figure 7-1) installed at the South Pole between 1991 and 1999 has biased the GPS signals there, and hence have affected the determination of water vapour using GPS at this site (Manson, 2001, in preparation). The biases introduced by hemispherical shaped radomes (Figure 7-1, lower right), on the other hand, are significant only at the 1-2mm level (Johansson *et al.*, 1998) and are now the standard worldwide. It should be noted that the hemispherical dome installed at Davis (Figure 7-1, upper left) is installed incorrectly, as the base of the dome hemisphere has its centre at the antenna reference point (ARP), rather than at the antenna phase centre.

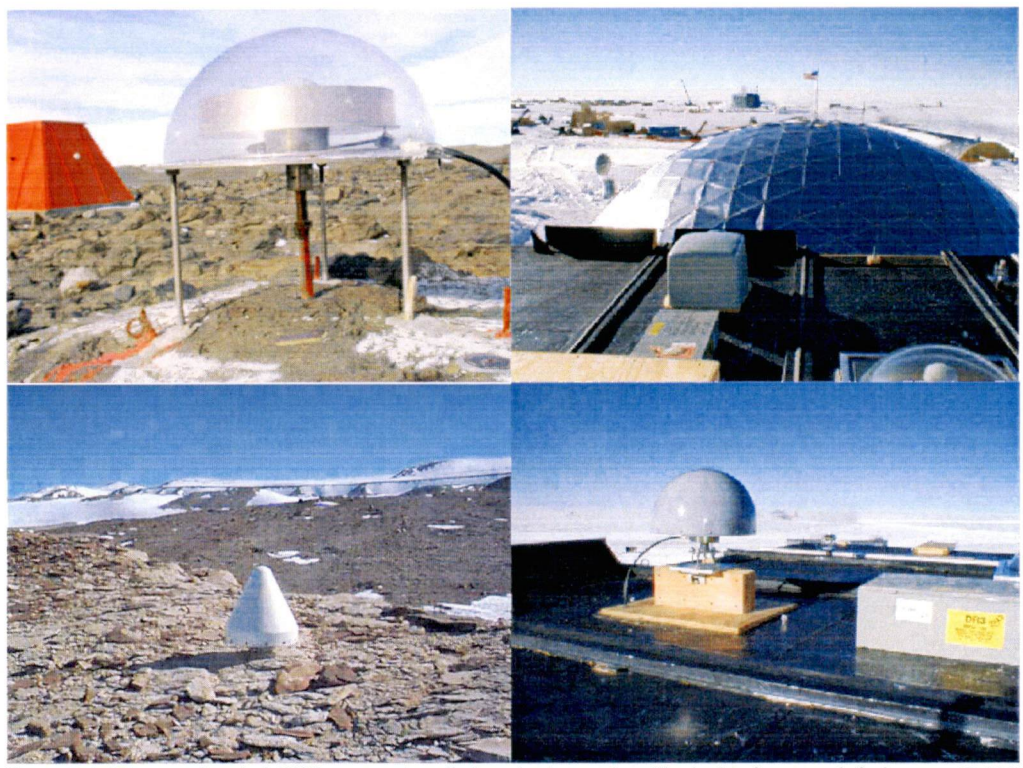

Figure 7-1: Photos of typical GPS antenna installations in Antarctica. Clockwise from top left they are: DAV1 IGS mark at Davis Station with hemispherical radome; AMUN mark at Amundsen-Scott base (South Pole) with cube-like Kearney-Powerglass lid radome installed between 1991 and 1999; AMUN mark with SCIGN[1] radome installed in 1999; BVLK mark operated by the Australian National University. The DAV1 photo was supplied by AUSLIG, AMUN photos were taken by Larry Hothem, USGS, and obtained from http://pasadena.wr.usgs.gov/scign/group/dome/album/AMUN and the BVLK photo was taken by Rachael Manson, UTas.

7.1.3 GPS Satellites

Due to the inclination of the GPS satellite orbits, the satellites are consistently lower in the sky at the Poles than any other place on Earth. In fact, at the South Pole the satellites do not pass higher than 45° above the horizon. Nearer the coast this value is ~70° (Figure 7-2). Consequently, the satellite signal propagation paths are more likely to pass through the thickest section of both the ionosphere and troposphere, and thus measurements are more severely affected than at other latitudes (Santerre, 1991). Furthermore, the observed satellite orbit arc lengths become increasingly shorter close to the Poles. One advantage is that all orbital planes may be viewed at once at the South Pole, increasing the number of satellites that may be tracked. Additionally, Morgan and Tiesler (1991) improved the precision of their GPS coordinates by taking advantage of the two daily passes of a single satellite. Since the satellite orbital along-track errors (the most difficult satellite motion to determine) are in opposite directions

1. Southern California Integrated GPS Network http://www.scign.org

in each of these passes, the error is cancelled. This was especially important when the satellite orbits were poorly determined although when using high precision modern IGS orbits, this should not be a problem.

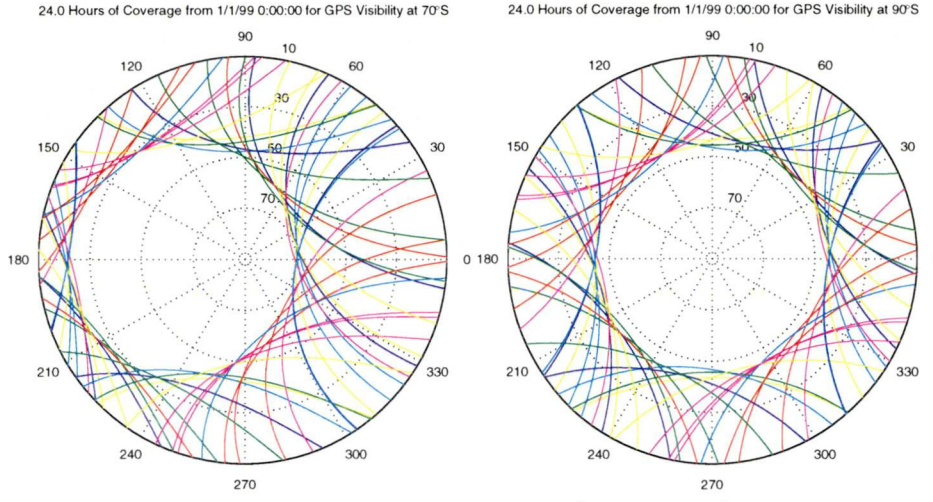

Figure 7-2: Sky plots for 24 hours of data at 70°S (left) and 90°S (right).

7.1.4 Observation procedure

7.1.4.1 Observation duration and re-observation times

Normally, ice movement measurements are conducted across two or more summer seasons. For some ice movement campaigns it may be advantageous to re-measure ice movement poles during the same summer season. This reduces field logistical costs (typical costs for one of our summer seasons is $A0.5-0.8M) and has the potential to produce research results in shorter time periods. The duration of GPS observations required to achieve a certain coordinate precision is mainly determined by the observation duration and the baseline lengths between the rover and reference stations. Due to the poorer satellite geometry and high ionospheric noise in Antarctica, these occupation times will be significantly longer than for similar precisions at mid-latitude sites. Observation duration has a significant effect on the ability to resolve carrier phase ambiguities. Measured velocity precisions are also related to the ice velocity and hence this needs to be considered when determining measurement re-observation times.

Manson *et al.* (2000) conducted a study on the observation duration required to achieve short-term horizontal velocity estimates within 1-3% of the long-term velocity estimates (direction and magnitude). The site velocities in the study ranged from 14-60 myr^{-1}. The short-term velocities were determined using a re-occupation interval of 6-7

weeks. They showed that for baselines up to 750km (the maximum distance tested), between two- and four-hour observation periods were required to achieve results with errors less than 3%. For some of the faster moving sites, as little as sixteen days occupation separation was required to achieve these results. This showed that it was possible to obtain high precision ice velocities over long baselines during a single Antarctic summer season.

In the case of much higher horizontal velocities, such as occur on an ice shelf (typical velocities of 200-2000m/yr), highly precise velocities may be able to be determined in a single occupation of several days, or less. Examples of this have been shown in Chapter 5.

For the vertical coordinate, Forsberg (2000) estimate that using up to a week of data produces height accuracies of approximately 100mm over 1000km baselines in Greenland. In contrast, Hulbe and Whillans (1994), citing a personal communication with P. Morgan, estimates height accuracies of 10mm over a 1300km baseline from McMurdo Station to the South Pole. It was further noted that if the ice velocity is large, the accuracy might be correspondingly degraded to about 50mm. Hamilton and Whillans (2000), citing a personal communication with J. Sonntag, estimates one sigma position precisions of ~10mm in both the vertical and horizontal coordinates using twelve hours or longer of data. Coordinate precisions are not given in Hamilton *et al.* (1998) although vertical velocity precisions of 43mmyr^{-1} and 18mmyr^{-1} are given using three 24 hour occupations over 3-4 years, suggesting vertical coordinate precisions for any given measurement of 50-100mm. Comparing vertical coordinates determined from segments of GPS data two hours in length with an independent tide model, Phillips *et al.* (1998) showed agreement in the order of 10-50mm over baselines 60-100km in length. Similar agreements have also been demonstrated in chapter 4 using segments of GPS data one hour in length.

7.1.4.2 Sampling rate

The most common GPS sampling rate for static GPS measurements is 30 seconds. This is the data rate employed at the majority of permanent IGS sites, including those in Antarctica. Higher sampling rates will be advantageous in the correction of carrier phase cycle slips due to loss of signal lock. The ability of the receiver to continuously

track satellites is not a function of sampling interval, however, but a function of the receiver's tracking loop integration time. Lower integration times are required for higher ionospheric activity, although this is normally set in the receiver hardware or firmware. The SCAR[2] Working Group on Geodesy and Geographic Information (SCAR WGGGI) recommend 15 second sampling intervals for their measurement campaigns. However, the 30 second data rate at the permanent IGS sites negates much of the usefulness of this higher data rate. There are few other reasons to have a higher sampling rate for static observations, as GPS data become more correlated as sampling frequency increases. However, higher observation frequencies should be employed in the case of kinematic processing. Typically, intervals for kinematic processing will be 5 seconds or less. If data storage is not a problem, one second intervals are recommended for kinematic data, since this may help overcome problems with frequent cycle slips.

7.1.4.3 GPS observables

The GPS observables that should always be standardly logged are L1, L2, C/A or P1 and P2. Additional measurements of the Doppler signals (D1 and D2) are only useful when computing kinematic baselines, and some proprietary software (e.g., Trimble) requires them. If these observables are available, and data storage space is not limited, it is prudent to log the Doppler signals for all kinematic campaigns.

There is ongoing research into the correlation of code and carrier signal-to-noise ratios (SNR) with data quality (Collins and Langley, 1999). The SNR values may also be useful for the modelling of signal multipath (Axelrad *et al.*, 1994)[3]. All geodetic quality GPS receivers store this information in their raw data format. These are then converted to the S1 and S2 observables in the RINEX format, although there are significant differences between the receiver manufacturers' algorithms (Collins and Langley, 1999). Until this is resolved, it is recommended that raw (binary) GPS measurements be archived along with their RINEX equivalent.

---

2. Scientific Committee for Antarctic Research http://www.scar-ggi.org.au/

3. Also see http://www-gpsg.mit.edu/~tah/snrprog/Example/

7.1.4.4 Elevation angle

The worldwide standard for satellite elevation cut-off angle has been 15° above the horizon. Ten and twenty degrees are also common. The 15° figure is seen as a good compromise between multipath mitigation and the precision of the height component. In Antarctica, where the majority of the satellites are at low elevations, considerably more data is obtained by logging lower than this value, for example ten or even five degrees. Figure 7-3 shows the number of observations made at McMurdo station (~S77.75°) and Hobart (~S42.5°) during one day in 1999. The difference in observation distribution between these sites is clearly visible with all of the McMurdo observations below 65°, while the Hobart observations are more evenly spread. Consequently the SCAR WGGGI recommend observations be made down to 5°, with 0° as a preference. These extra observations increase the number of double-differences available over long baselines. They might also be of value in the future for research into multipath mitigation, reflective characteristics of ice surfaces, tropospheric modelling, etc. However, most processing institutions do not process data from satellites below 10° (see e.g., Bouin and Vigny, 2000; Dietrich *et al.*, 2001), with these extra observations discarded. This is most likely due to the low precision of the various tropospheric mapping functions (e.g., Niell, 1996) at high latitudes for low elevation data (Mendes and Langley, 1994).

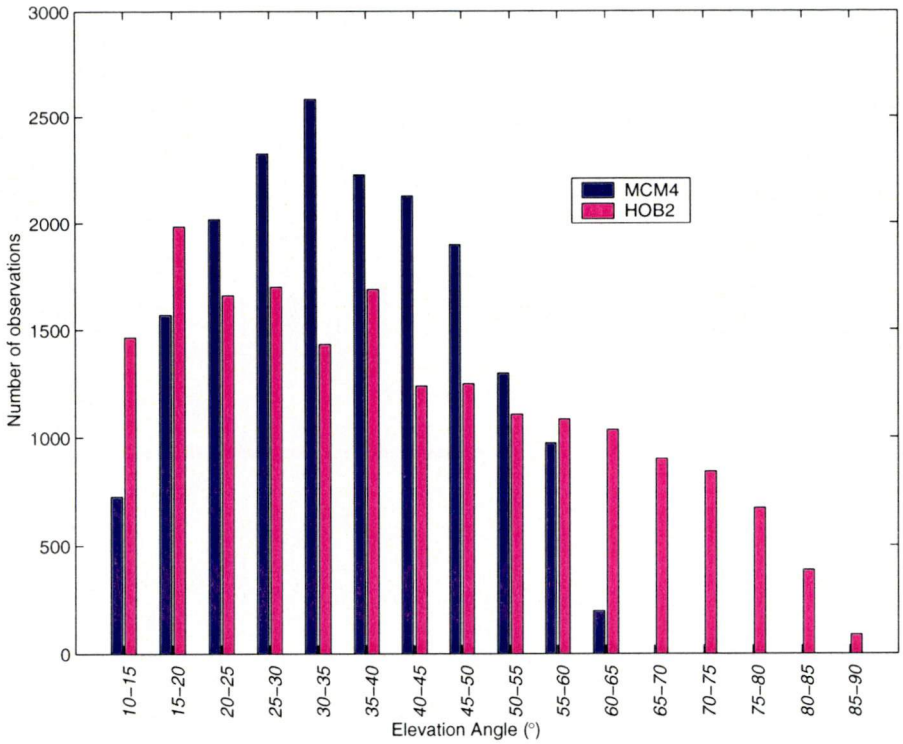

Figure 7-3: The number of observations made at McMurdo (MCM4, ~S77.75°) and Hobart (HOB2, ~S42.5°) on day 030, 1999 by satellite elevation angle. No observations were made below 10°. Note the high number of observations at low elevation and the low number at high elevation at MCM4.

Unless data storage space is limited, it is recommended that a satellite elevation cut-off angle of 0° be adopted for data collection. This value is also appropriate for kinematic surveys.

7.1.5 Reference marks

A variety of GPS antenna monuments has been used for ice movement measurements. While tripods or geodynamic marks can be used at the rock sites, the ice sites require a different style of monument since these are not stable on ice or snow surfaces. Since we are concerned here with both vertical and horizontal movement determinations, then we need a stable (horizontal and vertical) reference point. Traditionally, ice movement measurements have been made in relation to a ground mark, where the ground mark has taken the form of a bamboo cane. In this scenario, the GPS antenna is mounted on a tripod with the height of the GPS antenna measured in relation to the snow surface and/or some reference point on the ground mark. Horizontal and vertical connections are then made from the GPS antenna to the ground mark, normally using a pocket tape and compass (readings are later corrected for the

magnetic declination). This system, however, does not allow for a precise relocation of a GPS antenna, nor is a precise connection to the reference mark easy. Errors of several centimetres in both the horizontal and, more importantly, the vertical connection can occur. The tripod sinking into the snow under its weight or due to thermal effects is also a significant problem (Bondesan *et al.*, 1994).

More recently, systems have been devised that allow the antenna to be precisely relocated onto a steel or aluminium pole fixed in the snow surface (Hamilton *et al.*, 1998). If high precision GPS measurements are to be made then such a system is extremely important, especially if measurement re-observation periods are short. Precise antenna relocation is particularly important for the vertical coordinate, since vertical velocity is normally only 1-2% of the horizontal velocity in Antarctica.

The style of GPS antenna mounting that has been used successfully by glaciological and surveying expeditions within the Australian National Antarctic Research Expeditions (ANARE) since 1989 is shown in Figure 7-4. This has proved to be a stable and precise means of occupying and reoccupying survey marks on snow surfaces. The antenna is attached to an aluminium/stainless steel sleeve with a 5/8" Whitworth thread at the top. This sleeve is then joined to the pole via an internal wooden or fibreglass insert that is bolted into place with two bolts. Wing nuts are used in preference to standard nuts since they are easier to use in cold field conditions. It is worth mentioning the importance of adopting some means of systematically identifying individual marker poles. This is often done by stamping the pole with the station label.

The depth of the base of the pole is an important consideration. In most circumstances, a deep hole in which to place the pole is difficult to establish. However, the base of the pole needs to be below the level where solar warming of the pole will cause melting. If the pole moves vertically or begins to lean, then the results of the survey will be systematically biased. Forsberg *et al.* (2000) used a pole frozen with its base 80m(!) below the surface. However, this is not to prevent any thermal effects; rather, it is more a matter of convenience since the hole had been drilled previously. Hamilton *et al.* (1998) and Hamilton and Whillans (2000) used poles frozen into the ice some 5-20 metres below the snow surface. This depth was chosen so that the

measurements of snow accumulation and density are not biased by transient surface effects, rather than to prevent thermal effects (personal communication, G. Hamilton, 2001).

Further care needs to be taken in regard to compaction of snow. Such compaction will obviously bias the measurements of the vertical motion of the poles. To prevent this from happening, Hamilton *et al.* (1998) developed the 'coffee-can' system where the pressure applied by the pole is spread across the surface area of a coffee-can with the base of the pole set deeply enough to avoid high densification levels. More recent versions of this system (Hamilton and Whillans, 2000) use steel weights connected by wires to the surface.

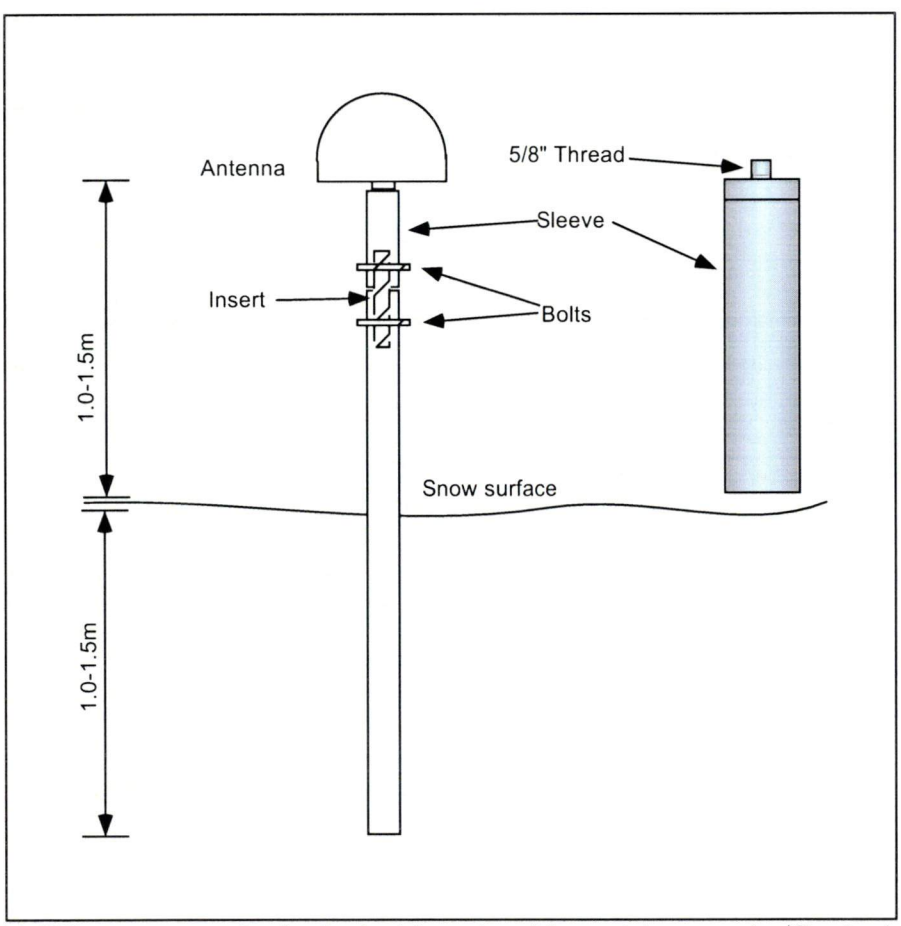

Figure 7-4: GPS antenna mount showing the aluminium pole, stainless steel sleeve, wooden/fibreglass insert and bolt positions.

7.1.6 Field notes

The importance of good field notes cannot be stressed enough. Despite significant amounts of time in planning and large amounts of resources required in conducting

Antarctic campaigns, the systematic making of field notes is frequently neglected. A simple error in reading an instrument height will seriously reduce the value of height measurements. Forgetting to clearly record the actual location measured can cause significant problems at the data processing stage, and also for site relocation and recovery.

Field notes are the historical records of what happened during the measurement campaign. In fact, the lack of adequate field notes may totally invalidate the measurements from use in future studies. Due to adverse field conditions, it is typically easy to enter the measurement information only into the GPS receiver while omitting to record it in a field book. If a mistake is made in the field, then there is no backup source of information.

Typical GPS surveying procedures may be found at http://www.anzlic.org.au/icsm/publications/sp1/sp1.htm. These are equally applicable in Antarctica. Some additional comments need to be made, however, for Antarctic measurements. These include the design or adaptation of appropriate field books. Books should be bound to prevent them blowing apart in high winds. Weatherproof paper is required along with a hard cover to protect the book. An A5 size is a more convenient size than A4 for fitting into clothing pockets. A sample of a field book designed for ice movement surveys is shown in Figure 7-5.

GPS Observation Log

Type Model S/No Receiver Operator . . .

Receiver .

Antenna .

Receiver Software and Version

Collection rate . (seconds)

Station Name . . . . . .

Location . .. .

Station Mark Inscription and Description . . . .

Antenna Setup : Distance(metres) vertical slant

Base of antenna . . . ☐ ☐

Top of ground plane ☐ ☐

Bottom of ground plane . ☐ ☐

Base of sleeve . ... ☐

Equipment Used
☐ Tribrach
☐ Tripod
☐ Pole

Eccentric Setup : ☐ Compass reading to Mark . . (degrees)

Magnetic Declination . (degrees)

Horizontal Distance . . . . (metres)

Timing Local Time Local date UTC Time UTC Date GPS Day

Actual Start Time . . . .

Actual End Time . .. .

Major Fault . ☐ started over with new Log

Receiver Navigation Position

UTC Time .

Latitude . . .

Longitude . . . . .

Height . . . . . metres

Download Information Date . / . /

1 .. .

2 . .

☐ Tapes ☐ Disks ☐ Backups made

Note Remember to measure a height at both the beginning and end of observations Done ☐

Site Plan Show antenna setup in relation to marker Show magnetic North and eccentric directions and distances where applicable.
Antenna Sketch Draw height of instrument on the antenna sketch Show accumulation measurements where applicable

Site Plan

Antenna Sketch

Cloud Temp Wind Pressure Humidity .
Accumulation Measurements Vertical Slope . Reference Point

Figure 7-5. Sample GPS log sheets suitable for use in ice movement surveys

7.1.7 Secondary data types

Recording additional data types (those other than GPS) may be of significant benefit to research outcomes. In some cases, they are vital. For example, atmospheric pressure measurements are required for the correction of the inverse barometer effect when measuring tidal motion of ice shelves. These measurements become increasingly valuable as campaign lengths become longer.

For ice thickness changes, ice density at the measurement site is vital, as is surface slope in the surrounding region (Hamilton *et al.*, 1998). Collocated gravity and GPS observations will provide information on the water column thickness below an ice shelf (if the ice thickness is also known). Tilt and strain measurements are especially helpful close to the grounding zone for grounding zone dynamic studies, since their measurement resolution is higher than GPS. Seismic measurements help define the bedrock topography, and combined with radio echo sounding (RES) measurements, provide the water column thickness.

For studying precipitable water vapour using GPS, both pressure and temperature measurements are required. Additionally, radiosonde and/or high altitude wind measurements will provide information on the flux of the precipitable water over the site (Manson, 2001, in preparation). Other valuable meteorological information may be gained by the addition of a small meteorological station, recording, for example, external temperature, pressure, wind speed and direction.

For system diagnostics, battery voltage, internal temperature, solar radiation levels and wind speed are important parameters (Zwartz *et al.*, 1999; Tregoning *et al.*, 2000).

Some of the above measurement types are both simple and inexpensive to include in the experiment. Others require significant expertise, time on site and expense. Most importantly, the potential for the inclusion of these additional measurements should be considered at the planning stage.

7.2 Data processing recommendations

To process GPS data, whether collected in static or kinematic mode, many similar issues need to be dealt with. These include dealing with atmospheric effects, ambiguity

resolution, satellite orbit computations, etc. Consequently, kinematic and static processing software uses, for the most part, similar methods. For example, forming the ionosphere free combination to remove the effect of the ionosphere, using the wide-lane combination for ambiguity resolution, or estimating the total tropospheric zenith delay. However, there are significant differences, such as the frequency at which zenith delay parameters are estimated or ambiguity resolution algorithms required for On-The-Fly resolution in kinematic solutions. This has led to distinct processing software to deal appropriately with each of these techniques. A thorough overview of the various aspects involved in the processing of GPS data is provided in Blewitt (1998). The following recommendations cover the processing of GPS data collected in polar regions.

7.2.1 Satellite orbits

As GPS observations move closer to the Pole, the maximum elevation of the GPS satellites is significantly reduced. For example, at the Pole satellites do not pass above 45°. Nearer to the Antarctic coast they do not pass above 65-75° (Santerre, 1991). This is a significant disadvantage for obtaining precise positions.

Processing GPS data from receivers located large distances from a known location were once a significant problem. As shown in Chapter 5, early GPS data needed to be processed in the context of a global network of receivers if the highest precision results were to be obtained. This is largely no longer the case. With the removal of Selective Availability on May 4, 2000, broadcast ephemerides are now of a high enough standard to not adversely affect results for baselines up to 80-200km[4]. Furthermore, the IGS routinely provide precise satellite orbits of a precision suitable for use in nearly every Antarctic GPS experiment. In general, perhaps only in geodynamic studies would the need arise for a computation of a global satellite ephemeris by the user. However, the IGS orbits are biased toward the Northern Hemisphere due to the low station density in Antarctica (Bouin and Vigny, 2000) and elsewhere in the Southern Hemisphere. Since additional regional data may become available following the IGS orbit determination, the user may wish to recompute precise orbits in this case. As it is convenient to obtain IGS precise ephemerides, and since it removes any reference

4. A comparison of the accuracies of the various satellite orbits is available at http://igscb.jpl.nasa.gov/components/prods.html

frame incompatibility, it is recommended that IGS orbits be employed wherever possible[5].

7.2.2 Antenna phase centre modelling

The electrical phase centre of an antenna varies with both elevation and azimuth, although most of the variation is in the elevation component. The IGS has produced elevation-dependent antenna phase centre models for the majority of antennas currently in use. The azimuthal variations are not yet taken into account. The use of such a model is vital if highest precision measurements are to be made, particularly in the height component and if different antennas are used in the same survey. Such models are not required in the case of identical antennas being used through the entire network. The IGS correction model is built into the majority of modern GPS processing software and it should be used at all times.

7.2.3 Elevation cutoff angle

The cutoff angle for processing is largely governed by two opposing factors: the level of multipath present in the solution and the desire for high precision heights. As mentioned in section 7.1.4.4, 10° or 15° are typical elevation cut-off angles for the collection of GPS data. Processing GPS data at this same elevation cut-off can result in edge effects at the data cleaning stage. One way of overcoming such difficulties is to clean the data at the elevation angle of the data (such as 10°) and then include only those data in the solution that are above a higher elevation angle (such as 15°). In the case of high multipath environments a higher cut-off angle may be required, although this will reduce the geometric sensitivity of the GPS results.

Consequently, some experimentation may be required at this stage to determine the best cut-off angle for a given data set. Additionally, due to elevation dependant effects present at many GPS sites[6], once an elevation cut-off angle has been determined this value should be maintained for all future measurement campaigns.

---

5. IGS precise ephemerides are available at ftp://igscb.jpl.nasa.gov/igscb/product/

6. For an example of this, see http://www-gpsg.mit.edu/~tah/snrprog/Example/

7.2.4 Atmospheric effects

7.2.4.1 Ionosphere

The ionosphere can have a dramatic effect on the quality of the GPS observations. In locations such as Antarctica where the ionosphere is particularly active, the effects of the ionosphere need to be taken into account over baselines as short as 1-5km. This is particularly true at times of high ionospheric scintillation when complete dropouts can occur. During 1998, many of dual frequency receivers experienced large numbers of cycle-slips and data loss due to an increasingly variable ionosphere as the ionospheric maximum approached (Springer, 1998). Observing with a measurement interval of one second (rather than the standard 30s) solved the problem until firmware or hardware upgrades were available. The highly variable ionosphere may result in difficulties in resolving ambiguities over long distances in both kinematic and static data since the ionosphere affects the wide-lane combination.

The first order ionosphere is most commonly dealt with by using the standard ionosphere-free linear combination of dual frequency observations. Currently, no software handles the higher order terms via modelling or other means. As described in Chapter 2, the epoch-by-epoch range errors may be as much as 40mm because of these terms remaining unaccounted for.

(Rocken *et al.*, 2000) has presented a method for the use of single frequency receivers at distances of greater than a few kilometres from a base station. This requires a network of dual frequency receivers surrounding the single frequency receiver. This method requires too many resources to be used widely in Antarctica.

GPS may also be used to measure the variation in the ionospheric TEC (Wilson *et al.*, 1995; Breed *et al.*, 1998). Absolute measurements are not possible due to the ambiguity in the carrier phase observables used in the solution. Ionospheric maps created using these measurements may be used in turn to aid long range kinematic GPS measurements (Colombo *et al.*, 2000).

Consequently, if high precision results are to be obtained from GPS observations in Antarctica, the effect of the ionosphere needs to be dealt with over baselines longer than 1-5km. Furthermore, the observation time required to resolve ambiguities for

static, rapid-static and kinematic applications will need to be revised upwards. The exact time increase required is difficult to determine since it depends on the ionospheric activity at the time of observation, although with some field testing conservative values may be obtained.

7.2.4.2 Troposphere

The method of dealing with the troposphere can vary significantly. Proprietary software most commonly applies theoretical or empirical tropospheric models (e.g., Saastamoinen, 1972; Niell, 1996) for both the wet and hydrostatic delay. While the hydrostatic delay can be modelled accurately using values of local barometric pressure, the wet delay can vary significantly from these models. In Antarctica this is still the case (Dach and Dietrich, 2000), although the troposphere is extremely dry. Processing software developed in a research environment allows the departure from such wet delay models to be modelled either stochastically or by a random walk process. Over short baselines (<5km), the tropospheric delay at the reference and receiver sites cancel, although some cancellation may occur at distances up to 50km. On longer baselines, the baseline error caused by not modelling or estimating the tropospheric delay is 1-2ppm, while with modelling this can be reduced to 0.1ppm (Janes *et al.*, 1991). This error almost exclusively effects the vertical coordinate. Consequently, if sub-cm vertical coordinates accuracies are to be achieved, tropospheric delays need to be estimated at distances greater than 5km. Furthermore, horizontal gradients are often evident in the troposphere (Chen and Herring, 1997; Bar-Sever *et al.*, 1998) and need to be modelled. Consequently, results from software that does not allow for such departures from the models will be of lower quality than those obtained from more sophisticated software.

The frequency of tropospheric delay parameter estimation depends on the stability of the troposphere at the time of observation. Thirteen tropospheric parameters per site per day (two-hourly) is a common figure for static applications. For some kinematic applications, however, it may be valuable to estimate a tropospheric parameter per site per measurement epoch as this may help identify undetected cycle slips. Parameters may also be estimated for azimuthal asymmetry in the troposphere, although these are not yet widely estimated (Chen and Herring, 1997). A recent study has shown that

these gradients are often short-lived with periods frequently less than fifteen minutes (Gradinarsky and Elgered, 2000). Walpersdorf *et al.* (2001), for example, estimated atmospheric gradients (north-south and east-west) at each site in their study region every thirty minutes. It is useful to remember that each extra parameter in the solution reduces the redundancy of the overall solution, although this reduction is largely insignificant in the context of the number of satellite observations in a 24-hour period.

GPS is a powerful tool in the study of the tropospheric water vapour content (Duan *et al.*, 1996). To date, little research has been conducted using GPS in Antarctica for this purpose. Exceptions are the studies by Dach and Dietrich (2000) and Manson (2001, in preparation). This is because the amount of water vapour present is often close to the accuracy limit of the method, particularly away from the Antarctic coast. As the GPS error budget is reduced, GPS will be an increasingly valuable resource for studying climate change (Yuan *et al.*, 1993).

For processing GPS data collected in Antarctica, the tropospheric delay will need to be estimated in most cases, given that distances are usually longer than 50-100km. The tropospheric models and mapping functions, used in most proprietary software, are somewhat less accurate in Antarctica than in other regions, especially at low elevation angles (Mendes and Langley, 1994) and so cannot always be relied upon to provide the most accurate results. Consequently, it is recommended that to achieve the highest precision results, only processing software that is capable of estimating the tropospheric zenith delay be used.

7.2.5 Ambiguity resolution

The correct determination of the unknown carrier phase ambiguities is required if the highest precision results are to be achieved from GPS data (Blewitt, 1989). This is particularly the case for short-occupation observations, such as with kinematic or rapid-static measurements. The most common method used to resolve these ambiguities uses the Melbourne-Wubbena wide-lane observable (Melbourne, 1985; Wubbena, 1985) as the first step. The ability to resolve the ambiguities successfully is largely dependent on the level of ionospheric activity and the number-of and proximity-to fixed stations. Site specific problems such as multipath also play a part. Unfortunately, the high level of ionospheric disturbance in Antarctica seriously affects

the wide-lane, so much so that it is found to be ineffective at distances longer than 50 kilometres (Vittuari, 1994). This makes ambiguity resolution difficult with baseline distances significantly longer than 50km. Some success has been achieved in resolving ambiguities on longer baselines than this by adopting a sequential processing methodology (Nguyen, 2000). Seeber (1993) has suggested that the L_{43} or L_{54} combinations may be useful for ambiguity resolution in the presence of an active ionosphere, since they are close to the ionosphere free combination while having a longer wavelength and maintaining integer ambiguities. Unfortunately, neither of these combinations is implemented in any known processing software (Vittuari, 1994).

Consequently, and as mentioned above, longer periods of observation are likely to be required for rapid-static and kinematic observations in Antarctica than would be required at mid-latitudes. In fact, for rapid-static observations a factor of 2-3 increase in observation duration will be required in most instances. A minimum of 15-30 minutes is required at each site to be confident of being able to resolve ambiguities even over short distances.

Using some *a priori* information on the state of the ionosphere may help deal with the ionosphere. For example, global ionospheric maps are now routinely produced from GPS data (Schaer *et al.*, 1996), although little work has been done to assess their precision in Antarctica. As the models are based on observations of the GPS carrier phase signal, the spatial density of observing stations plays a part in their precision. Due to the low spatial density of permanent sites in Antarctica, the entire region is not yet covered (Figure 7-6). Where measurements are available, they can be incorporated into processing software, assisting in long baseline ambiguity resolution.

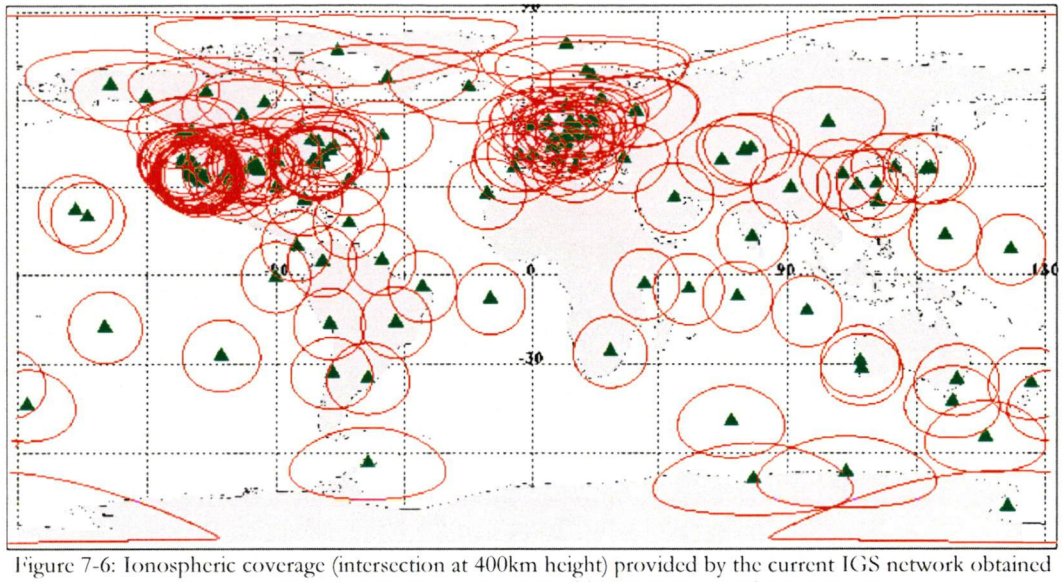

Figure 7-6: Ionospheric coverage (intersection at 400km height) provided by the current IGS network obtained from the Jet Propulsion Laboratory http://iono.jpl.nasa.gov/sitemap.html

For measurements on floating ice shelves, it has been shown that without the resolution of ambiguities, anomalous signals may appear in the horizontal components (personal communication, L. Nguyen, 2000). These signals are cyclic in nature and hence appear to be linked to the motion of the ice shelf. However, the removal of the tidal signal (see Chapter 4) or successful ambiguity resolution removes these signals. It is thought that it is these same corkscrew-like signals that have been observed in GPS data observed on the Ekstromisen ice shelf (Riedel *et al.*, 1999). This is one example of the care that needs to be taken at the ambiguity resolution stage.

If ambiguity resolution is not possible, the float solution will be acceptable for most static measurements. For kinematic measurements, the application of a smoothing algorithm such as a Kalman filter will provide the highest quality results.

7.2.6 Earth loading effects

Earth-body deformations need to be taken into account in the case of long baseline processing. In order of magnitude (and hence importance) they are solid Earth, Pole tides, ocean loading and atmospheric loading, with typical vertical magnitudes of 0.10-0.40m, 0.01-0.03m, 0.005-0.04m and 0.00-0.02m respectively (Bock, 1996; Yi *et al.*, 2000). The horizontal magnitudes are normally one-third of the vertical magnitudes. Each of these deformations also affects measurements taken on floating ice shelves. Atmospheric loading is typically correlated over 1000-2000 kilometres, and hence its

effect is negligible in most cases in Antarctica. For ice shelves, in particular, the effect of atmospheric loading can be regarded as constant since distances are rarely greater than these distances. Ocean loading is of importance to high precision surveys, even large distances from the coast. As has been shown in Chapter 4, most recent ocean tide models do not take into account the new definition of the AIS grounding zone. Some models also perform poorly in the sub-ice shelf regions. This will result in poor estimates of ocean loading parameters for this region. Solid Earth and Pole tides are well known and can be modelled precisely (Wahr, 1985; McCarthy, 1996). It is recommended, for baselines longer than 500 kilometres, that solid Earth, Pole and ocean tide loading be taken into account, except in the case of poorly modelled ocean tide parameters (Padman *et al.*, 2001) where the ocean tide models may in fact increase errors. Additionally, inverse barometer effects need to be considered for floating ice shelves.

7.2.7 Reference frames

As has been emphasised in Chapter 2, multi-epoch solutions can only be compared or combined if they are held in the same reference frame. Furthermore, an accurate reference frame is required since systematic distortions may otherwise be introduced. When compared to other parts of the Earth (e.g., North America and Europe), the density of permanent GPS stations in Antarctica is sparse. Furthermore, the observations of DORIS, SLR or VLBI data are even sparser. Consequently, the precision of ITRF solutions in Antarctic is not as good as in other places. This is especially true of early ITRF solutions. There is, however, a gradual increase in observation data type and stations, leading to significant improvements in the reference frame. The ITRF97 is the most recent global reference frame, and as such is the most accurate for Antarctica (Bouin and Vigny, 2000). Future versions of the frame (e.g., ITRF2000) will further improve the accuracy and increase station density. It is therefore recommended that the most recent ITRF be used for all GPS processing in Antarctica.

7.2.8 Data processing software

7.2.8.1 Static data processing software

Scientific software includes the GAMIT, Bernese and GIPSY packages. Each has been used for processing Antarctic GPS data (e.g., Manning *et al.*, 1992; Dietrich *et al.*, 1996;

Capra *et al.*, 1997; Ootaki and Fujiwara, 1998; Yamada *et al.*, 1998). Bernese and GAMIT both adopt a double difference approach to GPS solutions while GIPSY operates on the undifferenced data. Dietrich *et al.* (2001) compared results obtained from Antarctic data using each of GAMIT, Bernese, GIPSY and GEONAP packages[7], with agreements being 1cm and 2cm in horizontal and vertical components respectively. These values include the effects of applying different processing strategies, and so the actual difference between the various software will be less. Bondesan *et al.* (1994) has shown that some commercial software packages do not handle the situation where GPS measurements are highly disturbed by the ionosphere, and hence contain many cycle slips.

Recently three different methods have been developed that provides a further degree of flexibility. These are Precise Point Positioning (PPP) and Instantaneous Positioning. The GIPSY software offers the flexibility of performing precise point positioning (PPP). This method uses the IGS precise satellite orbits and clock values to allow precise coordinate determination using a single receiver (Zumberge *et al.*, 1997). The receiver clock and tropospheric parameters are estimated in the solution. The determined coordinates are of a similar precision as those determined in network solutions (Witchayangkoon and Segantine, 1999), although the PPP are more directly affected by reference frame and orbit errors. The disadvantage of this method is that the precision estimates from this method will not represent the true precision, since station correlations cannot be accounted for and orbits are assumed to be perfect (Zumberge *et al.*, 1997). The convenience of the PPP method is apparent in an Antarctic environment in the case of a base station receiver failing during a measurement campaign. The repeatability of a PPP solution of two hours of data is approximately 50mm and 170mm in the horizontal and vertical components respectively (Barnes and Cross, 1998).

Instantaneous positioning has been developed as a means of obtaining epoch-by-epoch positions using only the data from a single observation epoch (Bock *et al.*, 2000). The key to the method is being able to successfully resolve carrier phase ambiguities

7. Details of these packages may be found at http //bowie mit edu/ (GAMIT), http://www.aiub.unibe.ch/bernese html (Bernese), http://gipsy jpl nasa.gov/ (GIPSY) and http://www.geopp.com/ (GEONAP)

with just a single epoch of data. Site specific signals, such as multipath, are removed by applying a multi-day stacking procedure (Genrich and Bock, 1992). When dealing with only a single epoch, the notion of cycle-slip repair no longer exists. Data is instead rejected if it falls outside the central two quartiles of the data. The instantaneous positioning method has been shown to be valid over baselines as long as 37km. The achieved precisions were comparable to those obtained using batch-processing methods. It is thought that the present limit of this technique in terms of baseline length is around 50km (Bock *et al.*, 2000), although this will vary significantly with ionospheric activity. This method has been developed using the standard GAMIT modules as a base, but it is currently untested in equatorial or polar regions.

Nguyen (2000) has developed static sequential processing software capable of providing highly precise GPS solutions in Antarctica. While being static in methodology, the software is also capable of processing data where the antenna is slowly moving, as is the case for ice movement measurements. The software has been shown to be capable of resolving ambiguities over baselines longer than 30km in the Antarctic environment, and hence provides some significant benefits to the data analyst.

Apart from these differences, each of the above-mentioned software provides equally valuable options for the processing of Antarctic GPS data.

7.2.8.2 Kinematic data processing software

In contrast to static processing software, there is less distinction between commercial kinematic processing software and software developed at research organisations, particularly over short baseline lengths. While for such short baselines, commercial software such as GPSurvey[8] and GeoGenius[9] perform well, the major differences at the software level occur when baselines are longer than 30-50 kilometres. This requires special processing techniques to solve ambiguities and deal with the epoch-by-epoch estimation of tropospheric delay. A higher level of user control is required for successful processing over such lengths. Colombo *et al.* (2000) has shown that it is possible to resolve ambiguities over long baselines (400-1000km) during periods of

8. http://www.trimble.com

9. http://www.terrasat.com/geogen.htm

high geomagnetic activity. Some software (e.g, Track; Chen, 1998) is also able to simultaneously process multiple base/rover data, thus increasing the number of double differences in the solution (along with the required computer resources and the adjustment complexity). Coordinate and velocity constraints may also be placed on stations in Track, providing useful constraints on site motion and hence cycle slip detection. Examples of software capable of longer baseline kinematic processing include KARS (Mader, 1992), Track (Chen, 1998) and software written by Oscar Colombo (Colombo *et al.*, 2000).

The PPP technique can also be extended to solve for a coordinate at every measurement epoch (Zumberge *et al.*, 1998). This requires the computation, or alternatively the interpolation, of satellite clock and orbit terms to the required data rate. The precision is independent of distance from base station, with differences with static solutions at the 20mm level (Zumberge *et al.*, 1998).

Vittuari (1994) has tested the quality of kinematic solutions over short (2 and 5km), medium (50km) and long (>50km) baselines in Antarctica. They found that ambiguities were resolved satisfactorily using an L1-only solution over a 2km line. When the baseline was extended to 5km, the noise of the ionosphere was found to be greater than that caused by the introduction of the ionosphere free combination. Even over this short baseline the noise of the wide-lane solution was significantly higher than the ionosphere free solution, showing that the ionosphere free combination is required over baselines as short as 5km in Antarctica. For a 50km baseline the coordinate noise from the wide-lane solution was as high as 2m!

For optimum processing of kinematic data collected in Antarctica, it is advisable to process the data in more than one software package (due to the different data processing methodologies). High data rates are often important at this stage. If ambiguities cannot be resolved, a smoothed Kalman filter solution is the next best alternative. Furthermore it is suggested that kinematic data be processed in the field if possible, and observations repeated in the case of poor data quality.

7.3 Design of a GPS measurement system for ice shelf applications

Few long-term measurement time series of ice shelf motion have been recorded to date. As mentioned in Chapter 4, accurate in situ data is required for accurate modelling of sub-ice shelf tides (Padman *et al.*, 2001), which in turn is required for change detection of ice shelves from remote sensing methods. Provided here is a brief outline of an ice shelf GPS measurement system built at the Centre for Spatial Information Science, University of Tasmania. Six of these systems were concurrently operated at different locations on the AIS for the first time in the 2000-01 summer season. The system is designed to satisfy the following requirements:

- Capable of measuring and storing up to 12 weeks of GPS data and ancillary atmospheric pressure/temperature data
- Runs autonomously (i.e., power is maintained without user intervention)
- Short installation time
- Low cost/robust design

There will no doubt be improvements to this system with experience from the first field season, but this represents a starting point for future studies. The entire system can be built for approximately US$1000-1500 (per site, without labour costs), plus the cost of the receiver and antenna. It can be installed in less than ninety minutes in the field for typical snow surfaces, or slightly longer for ice surfaces.

7.3.1 System components

The system consists of five components:

- GPS receiver
- GPS antenna and mount
- Atmospheric pressure and temperature meter/logger
- Power supply, storage (batteries) and regulator
- Support frame and equipment storage 'warm box'.

Each of these components is explained below.

7.3.1.1 GPS receiver

The GPS receiver must be able to store up to 12 weeks of 30-second data on a storage device, such as an internal flash card. The amount of space consumed by this amount of data will vary with proprietary data formats and the number of satellites observed, although a 60Mb card is a typical size. In case of difficulty in retrieving the station due to weather conditions or other logistical factors, the receiver must be set up so that it does not overwrite data once the memory is full. Furthermore, the receiver must be capable of resuming logging following a power outage. The Leica CRS1000 receiver[10] we designed our system around draws 1.25A consistently at 12V (15W). Recently, new receiver designs have been released which draw a current as low as 0.7A, resulting in a significant reduction in power requirements, with obvious benefits to power requirements for such a system.

7.3.1.2 GPS antenna and mount

We mount our antennas on ~2.2m aluminium poles, with approximately 1m above the snow surface. This pole length is convenient for transportation within the Sikorsky S-76 helicopters frequently used in Australian Antarctic expeditions. In our experience, this places the base of the pole below the region of significant thermal effects and melt problems. It also prevents the pole from being blown over by strong winds. Deeper holes are required for basal melt rate studies or for long term tidal motion studies. Monumentation of the 'coffee-can' style is most suitable (Hamilton *et al.*, 1998). The mount we use is the one described in Section 7.1.5.

7.3.1.3 Atmospheric pressure meter

A pressure meter is required to log atmospheric pressure data for the period of the survey, with internal data storage capabilities. We choose to log pressure every one hour, providing a precise estimate of pressure change for the inverse barometer corrections. As with the case of the receiver, it is important that the pressure meter does not begin to overwrite data once its memory is full. In our system, we use the Microdaq PT-210[11] temperature and pressure meter. This meter is capable of storing ~85 days of hourly temperature and pressure readings (2048 recordings on two

10. Unfortunately the current version of the CRS1000 receiver firmware (version 8.03) does not provide a mechanism for stopping logging in the event of memory full.

11 http://www.microdaq.com

channels) with a precision of 0.5°C and <1hPa. It is capable of recording down to -40°C and runs off an efficient lithium battery. The pressure measurements are corrected for temperature dependence >0°C at the hardware level, while below this temperature correction terms need to be applied on an instrument-by-instrument basis. Since our system is designed to run above 0°C (by thermal insulation), this should not affect us (in the event of a temporary power outage the receiver may be recording for a short time while the storage box internal temperature is still below zero).

7.3.1.4 Power supply and storage

7.3.1.4.1 Choice of power supply method

The most difficult item of any remote system is the question of the choice of power source. How does one go about generating and storing power at air temperatures between -30°C and 0°C, while still making the system equipment as cost-effective as possible? In general, there are only two energy sources suitable for this type of experiment: wind and solar power. A third option, hydrogen fuel cells, is currently too expensive and still experimental in Antarctic conditions (Tregoning *et al.*, 2000).

Each of the examples has their advantages and disadvantages. Both systems have minimal operating costs. Solar power is available nearly 24 hours per day in summer months at high latitudes. Solar panels are actually most efficient at cold temperatures. However, the levels of solar energy received (kW/m^2) are not as high as elsewhere in the world since the sun spends more time at low elevation, with much energy absorbed by the thicker atmosphere. Figure 7-7 shows an estimate of the solar radiation assuming no cloud cover at two sites with latitudes 70°S and 45°S. The values were determined using the simple approximation (personal communication, G. Williams, 2001):

$$Radiation = \sin(SunElevation) * 1\mathrm{kWm}^{-2}$$

For all but the peak of summer, the northern site has significantly greater solar energy input. The summer-time difference is due to the sun being constantly above the horizon at this time at latitude 70°S. In reality, the actual radiation reaching a solar panel with a fixed inclination and azimuth will be less than these values, since they are determined based on the assumption that the panel is normal to the incoming

radiation. However, this simple model does provide realistic values when compared to our measured values.

A support frame needs to be constructed to hold the solar panels at the optimum sun angle, and be sufficiently rigid to withstand the solar panel acting as a sail in high winds. The frame installation should also not be time consuming to put together in the field. Furthermore, care needs to be taken so that the frame is designed to prevent snow buildup over the solar panels.

Since the predominant wind direction is often from the south in Antarctica, snow will tend to accumulate on the northern side of the solar panel. If, as is normal, the solar panels are orientated toward the north, then this build-up will often occur over the front of the solar panels.

Wind turbines, on the other hand, do not require a large support frame, and they deliver potentially large amounts of power. With high katabatic winds (50-120kmh^{-1}) frequenting the steeper parts of the Antarctic continent, the wind would seem a logical source of power (see Figure 7-8). Unfortunately, in Antarctic conditions wind turbines are currently not as reliable as solar panels for the supply of power. Firstly, it is difficult to manufacture wind generators that will operate reliably in cold temperatures and high winds, while still supplying power at low winds[12]. They also require some level of maintenance, as there are a number of moving parts and blades that may often need replacing. Perhaps the greatest difficulty for the AIS is that winds average less than 18kmh^{-1} (10 knots) near the centre of the ice shelf during summer periods, although peaking at greater than 90kmh^{-1} (50 knots) in blizzard conditions. An average wind speed of 18-27kmh^{-1} (10-15 knots) is required to continually maintain power to run an autonomous GPS station. Figure 7-8 shows, however, that average winds sufficient to operate a wind generator are present on the AIS during the non-summer periods.

12 At present, the Air 403 Industrial wind turbine (http://www.aapspower.com/airwintur30.html) is believed to be the model that most closely meets these requirements. These have been successfully operated near the front of the AIS (where winds are higher) for periods of 1-2 months during the 1999-2000 and 2000-2001 summer seasons by a team of glaciologists.

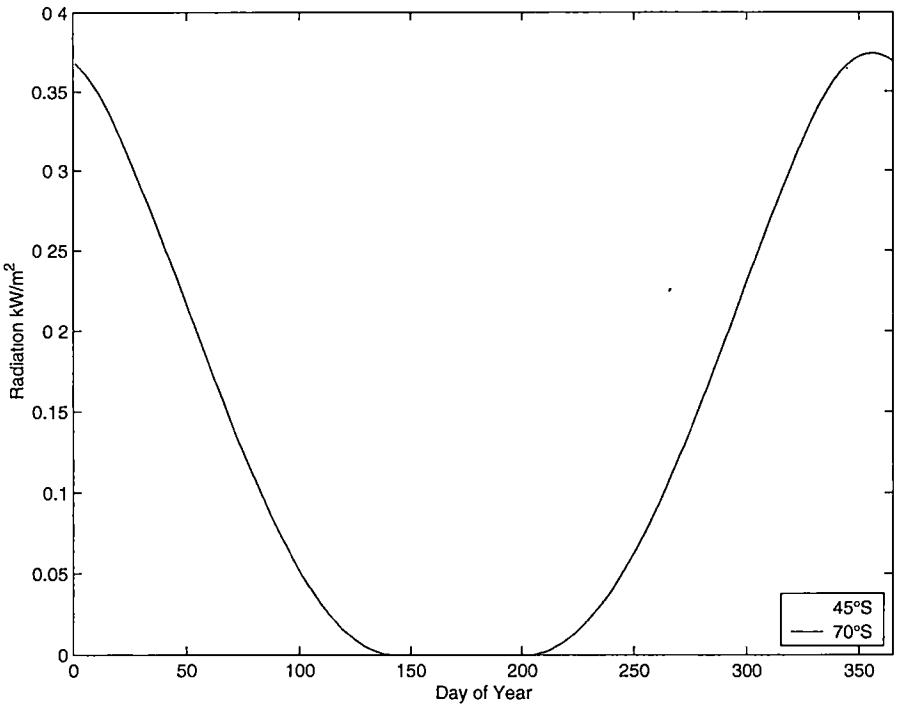

Figure 7-7: An approximation of mean daily solar radiation at 70°S and 45°S with no cloud cover.

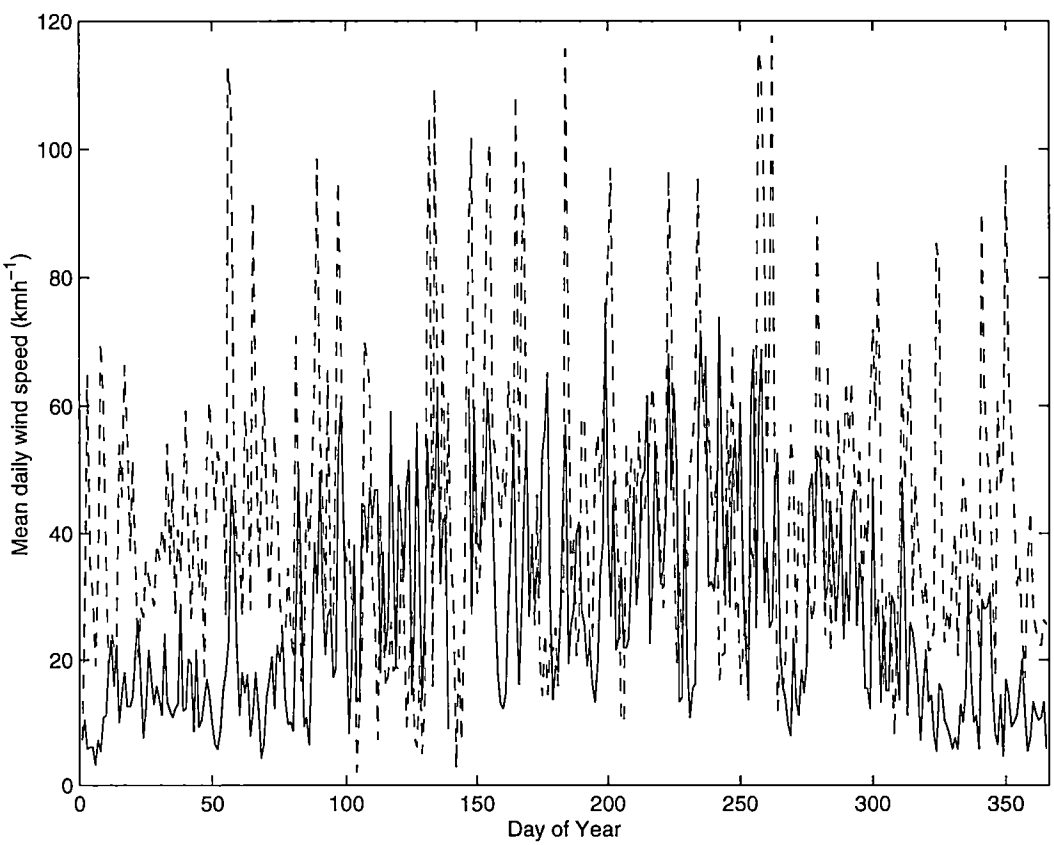

Figure 7-8: Average daily wind speeds at Mawson (dashed green) and near G3 (solid black). Data is from 1999, except for days 1-34 in the G3 data set since the Automatic Weather Station was not in operation until then. The values for the same period in 2000 have been substituted. The Bureau of Meteorology supplied the Mawson data and Ian Allison, Australian Antarctic Division, supplied the AIS data.

While wind turbines are suited to operation in the higher wind areas, such as nearer the grounding zone where katabatic winds are stronger, they are not suitable for all areas of the ice shelf for year-round operation. Conversely, the operation of solar panels is largely limited to the summer time. Ultimately, a wind/solar hybrid system would provide an optimum solution to this problem, and may provide the opportunity to operate such a system in Antarctica on a year-round basis. Such a system has two provisos: that the wind turbines be reliably manufactured and that the system cost and complexity be kept low. In terms of the later requirement, it is believed that year round operation would be possible with simple changes to power management, the addition of an external data storage device and the installation of a low power heater. Relatively small wind turbines as required here are yet to be widely tested across an Antarctic winter. Since we required a system suited for all locations during summer time we decided on solar panels as the only source of power. It is proposed to develop the system to suit year-round operations for future experiments.

7.3.1.4.2 What size solar panels and batteries?

Determining the size of solar panels requires an estimate or knowledge of the following parameters (Table 7-1):

Parameter	Value	How Determined
Efficiency of the solar panel	11.8%	Fixed
Efficiency of the batteries	80%	Fixed
Efficiency of the regulator	95%	Fixed
Average summer-time solar radiation at the site	0.263 kW/m^2	Measured at Davis
Capacity of the batteries	215Ah	Computed
Panel Area	0.52m^2	Computed

Table 7-1: Parameters for determining size of solar panels. The efficiency of the panels is based on an 80W Solarex SX80 panel. The average solar radiation is based on summer-time measurements at Davis.

Using advice and a simulation spreadsheet developed by Dr. Antoine Guichard (personal communication, August 21 2000) we computed our working parameters as shown in Table 7-1. By tuning the spreadsheet to these parameters, it was decided that one 80W solar panel in conjunction with 215Ah of deep-cycle storage capacity would be sufficient. This would deliver power continuously to our GPS receiver from mid-

December until mid-February, when the sun begins to set. Operation would continue, although interrupted, until approximately March/April.

The power generated by the solar panels will only reach its maximum when the panels are installed at the optimum angle for their latitude. This angle will also vary depending on the time of year the system has to operate. During December-January, the sun has a midday elevation of ~35-43 degrees at the latitudes covered by the AIS. The optimum solar panel angle for the entire AIS is therefore ~50-60° from the horizontal during the summer months. This includes only direct solar radiation – there will also be some additional radiation reflected from the snow surface.

7.3.1.5 Other equipment

Some additional equipment to those mentioned above is also required. An appropriate charge regulator is required which efficiently and intelligently directs the charge from the solar panels to the batteries. The CRS1000 GPS receivers currently have problems with the corruption of their flash memory in the event of a power failure during a 'write' operation. While this is rare, we included a voltage cut-off unit to cut the voltage instantly to the receiver at 11.1V and resupply when the batteries reach a charge of 12.5V.

In terms of the total receiver memory requirements, a typical daily data file recorded at 30s interval requires 0.4-0.7Mb per day. A twelve week campaign will therefore require ~35-60Mb of storage capacity. This must be stored either on the receiver's internal storage device or on an external storage device, perhaps driven by a PC card.

7.3.1.6 Storage equipment and support frame

For the equipment to operate continuously for up to 12 weeks on the AIS, the equipment needs to be kept warm. The batteries, in particular, begin to lose efficiency below +15-20°C. Our entire system depends on the equipment operating for the most part well above 0°C. To ensure this, we store the equipment (other than the antenna and solar panels) inside a ~0.3m^3 (~1.0x0.55x0.55m) black plastic box. The outside temperature may be as low as ~-25°C overnight and as high as ~0°C during the day. Consequently, we require sufficient insulation to allow a ~30-40°C temperature differential between the air and the contents of the box. In the current model, we use a

combination of Polystyrene and domestic fibreglass insulation batts, leaving less than 1% of the box volume as air. The heat source is the GPS receiver and to a lesser degree, the other electrical components. Solar heating of the box is minimal since the solar panels shade the box when the sun is at its hottest. The internal layout of the box is shown in Figure 7-9.

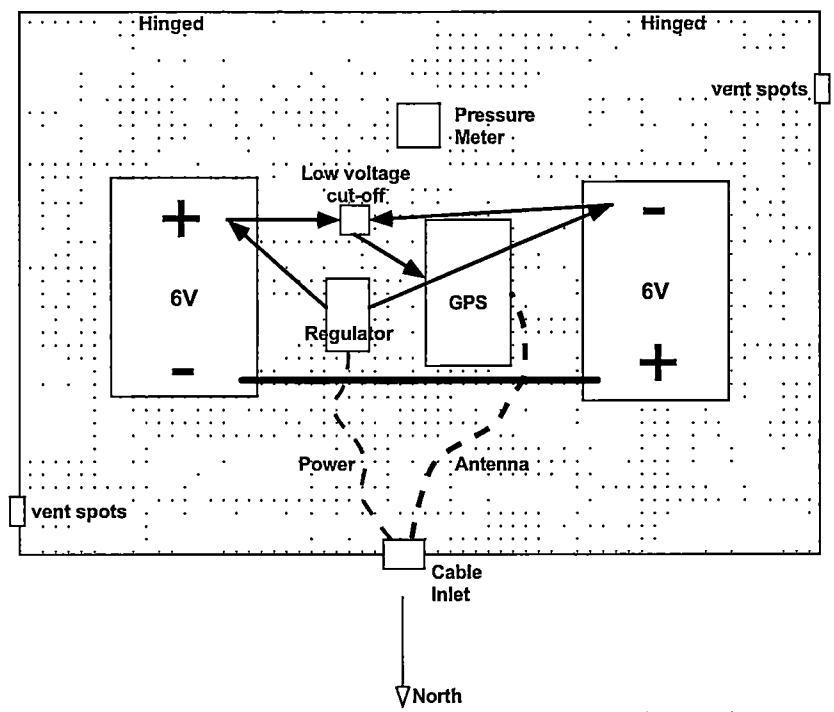

Figure 7-9: Internal layout of the system box showing electrical connections.

To ensure that the pressure meters were measuring actual outside air pressure, two small holes (~10mm diameter) were drilled in opposite corners of the box and covered with Teflon vent spots. These vent spots allow air to pass through while preventing snow from entering the box. The holes were drilled near the base of the box to reduce heat loss. Antenna and power cables pass through a cable gland that may be clamped down onto the cables. Rubber foam is wrapped around the cables to ensure that no snow passes through the gland.

The box and solar panels are supported by an aluminium frame designed by Dr Anthony Sprent at the Centre for Spatial Information Science, University of Tasmania (Figure 7-10). The frame consists of only ten pieces of aluminium (four legs, four horizontal sections and two solar panel arms), and is a lock-together design, with only twenty bolts in the entire frame. All but four of these are attached to the frame prior to

system installation. The horizontal sections are constructed of slightly smaller width aluminium than the legs. This allows two horizontal sections to fit firmly inside one leg. The frame gains further strength from the addition of a tie-down strap that is tightly clamped horizontally around the frame and box. The entire system is shown in plan view in Figure 7-11 and in elevation in Figure 7-12. The frame is designed so that snow may blow under the box, preventing a snow build-up in front of the solar panel. Once constructed, the entire frame is orientated with the solar panel facing True North. The frame is held in place by the four legs that are buried approximately 300mm into the snow. In the case of an ice surface the legs may be placed in holes drilled to ~100mm. There are also two tie-down points on the frame, used to attach ropes to four 'deadmen' snow anchors that are buried in the snow at approximately 45° to the frame (i.e., northeast, northwest, southeast and southwest).

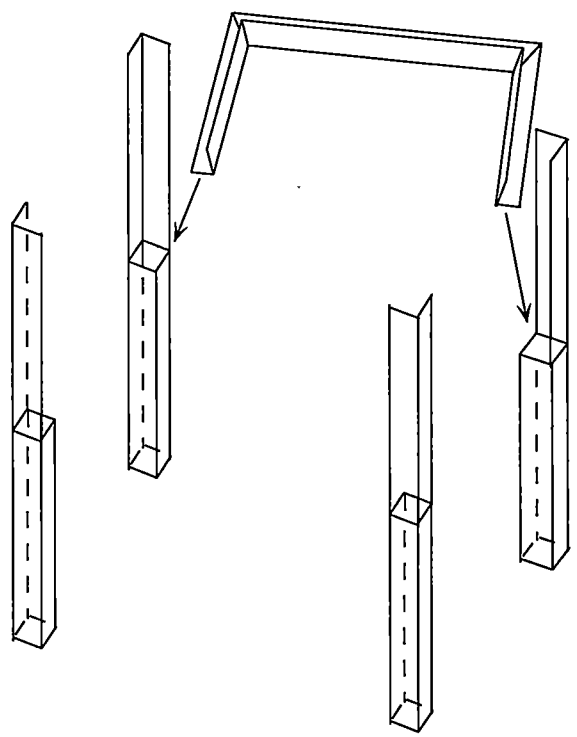

Figure 7-10. Aluminium frame components, showing frame legs and one horizontal section. The frame locks together as the horizontal sections are placed into the lower half of the legs.

In case of the observation location being on blue ice, holes will need to be drilled for both the antenna pole and legs of the frame. The feet of the frame also need to be moved up the frame legs so that they rest on the ice surface, reducing melt-in of the

frame. Additionally, the deadmen need to be replaced by ice screws. Figure 7-13 shows the system in operation on the AIS shortly after installation in January 2001.

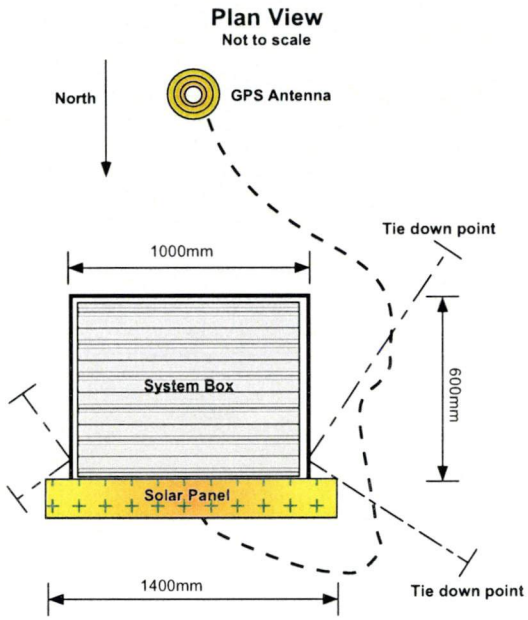

Figure 7-11: Plan view of the system.

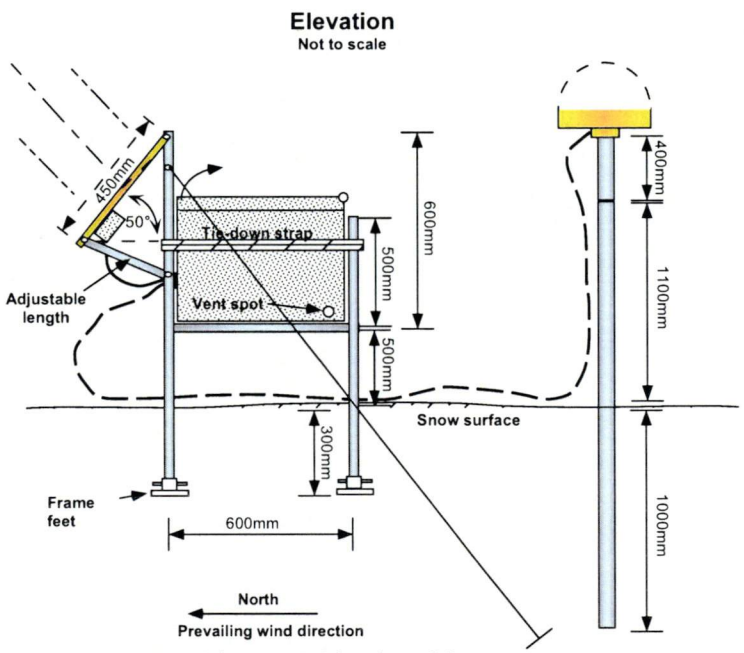

Figure 7-12: Elevation of the system.

Figure 7-13: The designed GPS system in operation at approximately 73.3°S on the Amery Ice Shelf during January 2001. Photo courtesy of Mike Moore.

7.3.1.7 Equipment listing and costing

Full equipment listing for the construction of one system is shown in Table 7-2. Each item has been priced in Australian Dollars, which at the time of purchase (June-September, 2000) was approximately A$1.00=US$0.60. The descriptions are provided only as a guide and individual items may be substituted for other types in most cases. The system weight mainly consists of the aluminium (30-50Kg) and batteries (30Kg each). Labour costs are not included as this was done by staff at the University of Tasmania. It is expected that labour costs, if incurred, may be as much as 30-40% of the cost of materials.

Component	Description	Cost (A$)
GPS system	Leica CRS1000 Receiver, choke ring antenna, dome and cables	~40,000
Pressure & Temp.	Able to record approximately hourly for greater than 12 weeks. Preferably onboard storage and power.	~500
Solar panel	80W	550
Solar panel frame	Aluminium	50
Charge Regulator	Temperature compensated	125
Voltage cut-off*	Cut-off ~11.1-11.2V, cut-in ~12.1-12.2V	30
Batteries	215Ah 6V (x2)	320
Storage Box	~0.3m^3; preferably with insulated wall structure	320
Insulation	Polystyrene, household insulation	20
Frame legs (north)	2 x 1.4m x 50mm x 4mm section aluminium; additional 0.8m required to weld onto lower half of leg to form a box	50

Component	Description	Cost (A$)
Frame legs (south)	2 x 1.3m x 50mm x 4mm section aluminium; additional 0.8m required to weld onto lower half of leg to form a box	50
Frame horizontals (N-S)	2 x 1.0m x 40mm x 4mm section aluminium. Exact lengths will depend on box size.	20
Frame horizontals (E-W)	2 x 0.6m x 40mm x 4mm section aluminium. Exact lengths will depend on box size.	20
Tie-down strap	All purpose high-strength ratchet compression strap	10
Frame feet	15mm plywood x 4 and aluminium off-cuts x 20	20
Nuts, wing-nuts, bolts and D-rings	Stainless steel; for solar panel construction, feet attachment to frame, sleeve attachment to pole and rope attachment to frame and deadmen	50
Aluminium pole	2.2m length; 39mm diameter (internal)	30
Sleeve	Aluminium/stainless steel; ~0.4m length; 39mm diameter	30
Rope	5m x 7mm (x4) nylon all purpose rope; for deadmen anchors	20
Deadmen anchors	4 x; galvanised iron 300mm x 300mm; bent into shape and holes drilled for rope to pass through	140
Miscellaneous (wiring)	Connecting batteries in series, voltage cut-off units, etc.	50
Miscellaneous (other)	Cable gland (For passing cables through inside/outside box; $10), Teflon vent spots (x 2; $5), wooden insert (for joining sleeve/pole; ~0.6m length; 38mm diameter - just smaller than internal pole diameter; $5), etc.	~40
Total (without GPS receiver)		~A$2500

Table 7-2 Complete system component listing and cost. Costs are only for materials and do not include the labour required for manufacture. * item may not be required, depending on the particular GPS receiver.

7.3.2 GPS System Summary

It is hoped that the information contained in this section will encourage others to conduct ice shelf (or sea ice) based studies in Antarctica. The extension of this system to run unattended year-round represents a significant challenge since either wind or fuel cells would be required for the winter months. As these technologies advance in reliability (and in the case of fuel cells, reduce in cost), permanent ice shelf sites may become possible. Furthermore, with advances in low-power receiver technology this challenge will be significantly reduced in the future. This, however, may come at the cost of less heat being generated by the receiver, and hence small heaters may be required inside the storage boxes to maintain efficient operating temperatures for the other equipment (i.e., batteries).

The system outlined above was installed at six AIS locations during the 2000/01 season (see Figure 8-1), with other sites to follow in 2001/02. Provided all goes to plan, 8-10 weeks of data should be collected at each location. Combined with the data in this thesis it will represent the most complete and consistent tidal data set available on a large Antarctic ice shelf.

7.4 Summary

For GPS measurements to provide the highest precision results possible, care needs to be taken at both the data collection and the data processing stages. This chapter has provided a series of practical recommendations in regard to these two aspects of using GPS data for ice movement studies. Many of these recommendations are a result of processing more than a decade of GPS data collected on the AIS from 1989 through to 2000 as presented in this thesis. Further personal experience in Antarctic environments also influences them. The additional collection of some secondary data may add another dimension to the information that is derivable from the data. It is hoped that these recommendations will prompt users of GPS in Antarctica to consider carefully the various aspects of GPS data collection and processing.

In an attempt to encourage others to conduct measurements of ice shelf tidal motion, an inexpensive GPS system has been described. The system is suitable for use on ice shelves during the Antarctic summer season, although its application is much wider than tidal motion studies. It is especially suited to the Antarctic environment as it can be installed on an ice shelf in approximately than ninety minutes. It is anticipated that the system described here will operate permanently for 8-12 weeks during the Antarctic summer (December-February). Further data will be collected outside of this period, although the receiver may experience intermittent power failures during this time. An increase in solar panel size would allow the system to operate permanently for 3-4 months. Such measurements help to determine the tidal constituents with periods less than 1-2 months. With future advances in alternative energy generation, such systems will operate throughout the year providing important information on the long-term tidal constituents under floating ice shelves.

Chapter 8

CONCLUSIONS

The aim of this thesis was to expand the knowledge of the dynamics of the Amery Ice Shelf from a combination of historical-terrestrial and space-geodetic measurements. The results may be separated into four categories:

I. Tidal dynamics of the AIS (Chapter 4);

II. AIS surface velocity from GPS and terrestrial data (Chapter 5);

III. AIS strain rates from GPS and terrestrial data (Chapter 6);

IV. Recommendations for the collection and processing of Antarctic GPS data (Chapter 7).

In this final chapter, the major findings of this thesis will be synthesised. The contribution made to the knowledge of the dynamics of the Amery Ice Shelf is summarised at the end of the chapter.

8.1 Tidal dynamics of the AIS

8.1.1 Tidal signals

All of the AIS GPS data collected after 1995 were processed in segments of one hour to resolve the vertical signal of the ice shelf, representing the most complete analyses of tidal data on the AIS. The data revealed vertical tidal signals at all locations, including sites as far south as 72.98°S, confirming that the southern-most AIS grounding zone was more than 200km south of the widely held grounding zone definition of Budd *et al.* (1982), and supports the work of Fricker *et al.* (2001a). This has direct implications for glaciological and oceanographic studies (e.g., mass balance calculations, freshwater production, etc.) in

the region, and for computations of ocean loading parameters for geophysical studies across Antarctica.

Each of the GPS time series was analysed to determine their tidal constituents. The harmonic and response methods were both tested, although the response method performed poorly over the shorter data sets. Using the harmonic method, data sets as short as 24 hours yielded useful information. The derived constituents showed a clear amplification approaching the southern-most grounding zone, due to reduced water column thickness in this region.

By assuming that the sub-ice shelf cavity behaves like a narrow channel, water column thicknesses were determined for each of the sites based on the water column thickness at G1 determined using a combination of ice thickness and seismic data. The K1 diurnal constituent agreed well with measured water column thicknesses where available. The M2 semidiurnal constituent did not agree well, presumably due to different frictional losses at this frequency. For the southern-most sites, where no water column thickness data is available, the estimates of 190m and 150m for V3 and V5 respectively are presently the only estimates of water column thickness in this region. These values seem plausible given the current state of knowledge of the ice shelf geometry.

The age of the tide – used to assess the level of tidal energy dissipation in a region – is about 51h in the AIS region, less than in the majority of ice shelf regions where ages of greater than 60h predominate (Doake, 1978). This suggests that the tidal energy dissipation in this region is less than in most other ice shelf regions in Antarctica.

8.1.2 Comparison of GPS-derived constituents with independent tide models

The GPS-derived tidal constituents were compared with three tidal models – the global FES99 model and the Antarctic regional CATS00.10 and CADA00.10 models. The comparison revealed that the FES99 model performs poorly south of the ice shelf front. Due to an incorrect bathymetry model and use of the incorrect grounding zone definition, the semidiurnal constituents are in error by as much as 70° in phase and 150-200mm in amplitude at the southern extent of the FES99 model. The CATS00.10 model is in

significantly better agreement with the GPS-derived constituents, although there are still significant differences, particularly in the semi-diurnal constituents. These models are very sensitive to the prescribed water column thickness and bathymetry (i.e., cavity geometry).

The CADA00.10 model provides the best agreement with the GPS-derived constituents due to the assimilation of tide gauge and other data into the model. These data include the GPS data from the AIS HWDT site. Both the CADA00.10 and CATS00.10 models also use a more accurate grounding zone location than the FES99 model.

With the inclusion of these new data, a predicted height from the CADA00.10 model may still differ from actual tidal motion by as much as 100-200mm, suggesting that significantly more *in situ* data, such as that provided by continuous GPS measurements, is required to constrain these models.

8.1.3 Removal of tidal signals from GPS data

A method for the removal of vertical tidal and horizontal velocity signals from GPS data was developed. Tests showed that the motions due to the tide and short-term horizontal motions are successfully removed, with the only errors introduced by the misfit of the tidal prediction/measurement and the velocity model. This method is important as it allows long-term integration and comparison of GPS data affected by tidal motion on a stable (tide-free) reference frame.

8.2 Surface velocities of the AIS

8.2.1 Identification of a large error in previous terrestrial analysis

A large misclose was identified in the previous analysis of the 1968-70 AIS traverse. The results from this erroneous analysis have been widely used and distributed. The coordinate misclose was in the order of 2km while the angular error was approximately 43′. Working from the available field notes, two large angular errors were located and corrected. Other, relatively small, angular, distance and timing errors were also identified. The resulting angular misclose of the corrected traverse was less than 15 arc-seconds, and positional errors were ~2-4m over a traverse of more than 500km in length. Importantly, these

corrections shifted the understood location of the 1968 A1 borehole by more than 3km, mainly to the west.

8.2.2 Production of AIS site positions and velocities

The positions of the ice shelf markers were determined using the available terrestrial and GPS data. They are held in the ITRF96 at 1969.5 (terrestrial) and the ITRF97 at 1989.0205 (GPS). The GPS coordinates have had the effects of tidal motion removed and hence are truly on a vertically stable reference frame. The terrestrial coordinate precisions are 0.94m and 0.98m for latitude and longitude on average. The GPS coordinate precisions are 0.31m, 0.35m and 0.35m for latitude, longitude and height, respectively. These new high precision position determinations form the basis for future long-term climate studies, InSAR/ICESat calibrations, etc.

Ice shelf velocities were determined using both the terrestrial and GPS data. The terrestrial data were processed using FONDA software relative to the ITRF96 at a reference epoch of 1969.5. Median errors (one sigma) of the velocities were approximately 1.5myr^{-1} in magnitude and 0.23° in orientation. The previous analysis of the terrestrial data did not include a formal error analysis and so this is the first time the 1968-70 surveys have had error bounds placed on them. While the velocity centreline and lateral profiles are similar in shape to those presented in Budd *et al.* (1982), the differences are significant, particularly north of G1 and on the northern lateral profile where differences greater than 100myr^{-1} in magnitude and 10° in direction are seen. These changes have important implications for mass flux calculations.

The GPS data used for the velocity determinations were collected between 1988 and 1999. The data were reduced using consistent techniques in the GAMIT software and combined together into the ITRF97. Median formal errors (one sigma) of the velocities from GAMIT were approximately 2.0myr^{-1} in magnitude and 0.41° in orientation.

To assess the precision of the 1988-91 GPS data, the AIS station height coordinates were compared to an independent DEM (Fricker *et al.*, 2000). Our analysis had a lower mean difference (-2.3m) than results from a previous analysis using early commercial software (-

9.7m). Velocity differences with this prior analysis had a mean of -0.1myr^{-1} and RMS of 12.8myr^{-1} for magnitude and a mean of 1.4° and RMS of 3.5° for orientation.

The positions and velocities determined from the terrestrial and GPS data form the complete set of AIS position and velocity information from *in situ* observations; their accuracy is unprecedented on the AIS.

8.2.3 Change in ice shelf dynamics

The velocities derived from the terrestrial and GPS data were compared to determine if the ice shelf velocity profile had changed during the thirty-one year period 1968-1999. Congruency tests were performed on both velocity direction and magnitude differences between GPS/terrestrial sites that were within 5km of each other. Just nine station pairs met the criteria, resulting in a small sample size. The tests on the velocity direction and magnitude both failed at the 95% confidence interval using the formal errors from FONDA and GAMIT. Except for one site near G2, the GPS velocities are uniformly slower than the terrestrial measurements. This suggests that the AIS may have slowed by 1-5myr^{-1} in the pole locations during the period of the measurements. This change in velocity may be a result of changes in the state of other balance forces, such as increased basal melt due to ocean temperature increases.

8.2.4 Comparison of GPS and terrestrial and satellite-derived velocities

The terrestrial and GPS data were compared with independent velocities derived from coherence matching of sequential Radarsat images. The differences between the *in situ* and satellite velocities were in the order of ±20-30myr^{-1} and 0-4°, with a strong systematic pattern. The majority of this bias was attributed to the satellite velocities, at least partly caused by tidal motion and satellite orbit errors. Otherwise, the satellite derived velocities are of a high precision. This comparison demonstrates the value of high precision velocities derived from *in situ* data.

8.3 Surface strain rates of the AIS

8.3.1 Production of AIS strain rates

Strain rates were produced from the terrestrial and GPS velocities, both separately and in a combined adjustment using the principles of four dimensional integrated geodesy. Strain rates were determined from the terrestrial data using two different techniques. Firstly, the strain grids at G3, G2, G1 and A1 were analysed. Strain rates at these grids were 1-2 orders of magnitude greater than their formal errors. In comparison to the strain rates shown in Budd (1966), these strain rates are well determined. Secondly, adjacent station pairs were used to determine the forward and transverse strain along the traverse centreline and the two lateral profiles. This revealed a significant tapering-off of the ice shelf longitudinal strain north of G1, in contrast to the earlier analysis of the same data (Budd *et al.*, 1982) which shows a further increase in strain at this location. The longitudinal strain reaches a maximum near G1 where strain rates of $6x10^{-3}yr^{-1}$ are experienced. The lateral profiles are parabolic in shape in terms of their transverse strain rates. The longitudinal strain rates from these profiles clearly show the delineation between the grounded continental ice and the ice shelf. The azimuth of the principal axis of strain is generally in the direction of the ice flow except near later grounding zones and where large inflows of ice join the ice shelf.

The strain rates determined from the GPS data were calculated in the form of Delaunay triangles. These results provided AIS strain rates between 70.0°S and 72.0°S. The signal-to-noise ratios of these results were in the range 20-30. The strain patterns are clearly seen, with relatively low strain rates near G3 increasing toward the ice shelf front. Lateral strain rates are increased close to the lateral grounding lines and due to the inflow of ice from the Charybdis Glacier. The suspected partial grounding of the ice shelf southwest of G3 (approximately 71.5°S, 69.0°E) appears to be confirmed by the high lateral strain rates in this region.

The combination of the terrestrial and GPS velocities provided the most widespread strain information available for the AIS derived from *in situ* measurements. The majority of the ice shelf region from 69.0°S to 72.0°S is covered by 77 Delaunay triangles, almost 50% of which have two or more redundancies. The signal-to-noise ratios of these strain rates have

median values of 44 ($\dot{\varepsilon}$) and 30 ($\dot{\varepsilon}_2$), although some values are as high as 600, suggesting that the strain rates are well determined.

8.3.2 Determination of AIS basal melt rates

Ice shelf basal melt rates were determined at four ice shelf locations where the marker pole vertical velocity was well known. A method was devised where the vertical velocity could be used to determine the rate of change of ice shelf thickness at a geographic location. Combining the vertical velocities together with horizontal velocities, horizontal strain rates, accumulation rates, ice thickness, ice shelf surface gradients and density profiles resulted in the determined melt rates. The melt rates were compared with modelled rates from an ocean circulation model (Williams *et al.*, 2001) and those estimated using remote sensing measurements. Unlike the remote sensing measurements, the melt rates determined using GPS measurements do not depend on any assumption of ice shelf steady state. In this regard they are the first such point measurements made for the AIS. Their current precision is low, however, due to high uncertainties in the accumulation rate and vertical velocities caused by the instability of the reference marks. As high precision accumulation rates become available, this method will provide realistic measurements against which ocean circulation models and remote sensing measurements may be compared.

8.4 Collecting and processing Antarctic GPS data

8.4.1 Recommendations

Recommendations were made as to procedures required for the collection and processing of Antarctic GPS data. Particular attention was paid to the collection of ice motion data, although most of the recommendations apply to a much wider region of study than Antarctica. We stressed that significant care is required at the planning stage if field time, measurements and research outcomes are to be optimised. In terms of processing GPS data, recommendations were given as to processing options for both static and kinematic data and algorithms were defined for correcting GPS data for tidal/horizontal motions. Up-to-date and detailed recommendations for the collection and processing of Antarctic GPS data are, at present, not widely available, and consequently these recommendations

will be of significant value to the wider geodetic and glaciological communities who are collecting and processing Antarctic GPS data.

8.4.2 Autonomous GPS system design

An inexpensive GPS system capable of operating autonomously for 8-12 weeks during an Antarctic summer was described in detail. This system has been operated successfully on the AIS during the 2000-01 summer at the sites shown in Figure 8-1. The entire system can be installed in the field in less than 2 hours and costs less than $A2500 ($US1500) plus the cost of the GPS receiver, antenna and radome and labour. The system could be extended to operate across an Antarctic winter through relatively simple modifications, such as the addition of a non-solar power source (wind generator or fuel cell), an further external storage device and heaters.

A system such as the one described in this thesis is required if long term ice movement measurements are to be made in the remote and hostile regions of Antarctica. In particular, long-term measurements are required for the determination of tidal constituents if remote sensing missions, such as ICESat, are to reach their accuracy potential over ice shelves such as the AIS (ICESat ground tracks (8-day calibration phase) over the AIS are shown in Figure 8-1).

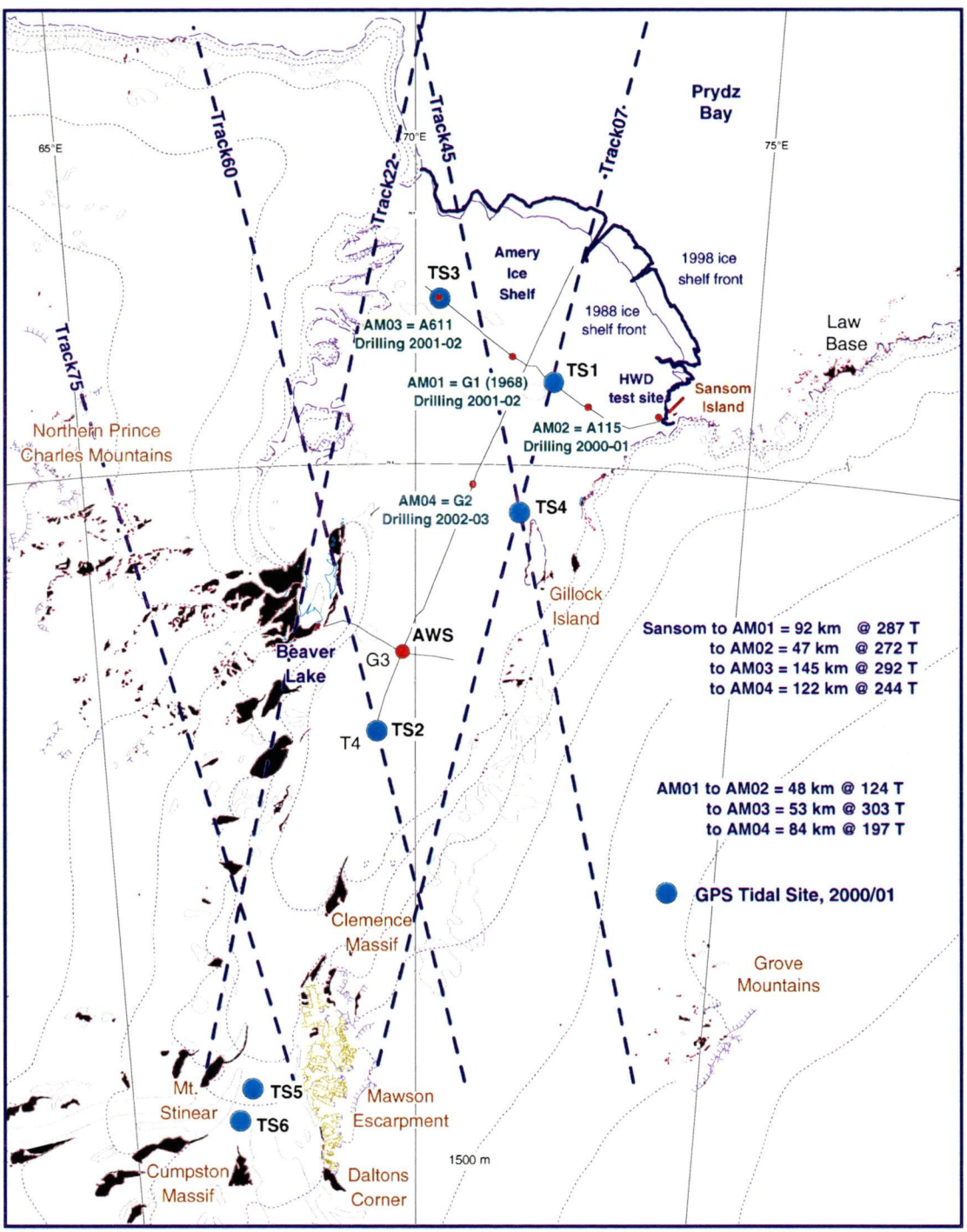

Figure 8-1: Logistics map of the AIS showing ICESat ground tracks and GPS tidal sites measured in the 2000-01 season. Figured produced by Mike Craven, Australian Antarctic Division.

8.5 Summary of research

This study has demonstrated the value of the *in situ* survey measurements made on the Amery Ice Shelf. We have shown that GPS and terrestrial data are capable of providing

valuable information on ice shelf dynamics. Additionally, the comparison and combination of these two data sets has provided more information than analysing the data sets separately. The results presented in this thesis largely agree with independent estimates from numerical models or remote sensing. Where disagreements occur, the results from this thesis were shown been to be superior in terms of accuracy in most instances.

Some of the variables presented here are important and sensitive indicators of climate change in ice shelf conditions and dynamics. Parameters that are susceptible to change are ice shelf velocity and strain and basal melt rate. Continued *in situ* measurements provide the most accurate point measurements of the dynamics of an ice shelf, and it is recommended that such measurements be continued on the AIS. In particular, due to the increased accuracies of remote sensing measurement techniques, GPS measurement of ice shelf tidal motion is of significant and increasing importance.

In summary, the major findings resulting from the application of GPS and terrestrial data to the Amery Ice Shelf in this thesis are as follows:

Determination of tidal constituents from GPS data (Chapter 4): The analysis of GPS time series longer than 20 hours in duration allowed tidal constituents to be determined for the floating AIS for the first time. A comparison between these results and numerical models showed that the models are yet to achieve the accuracies required by future satellite missions or for ocean loading models. Furthermore, the phase propagation in the constituents has provided information on the tidal current flow direction under the ice shelf. The age of the tide (51h) is lower than in most other ice shelf regions, suggesting that tidal energy dissipation is lower in the AIS region.

A method for the removal of tides and horizontal motions from GPS data (Chapter 4): A method was developed for the removal of tidal and horizontal motions from RINEX data at a pre-processing stage. This method allows the ice shelf data to be processed as a standard static site, with the only precision penalties due to misfit of the input tide and velocity models. Furthermore, this method allows multi-season data to be

compared on a consistent and stable (tide-free) reference frame for the purpose of long-term data comparison and integration.

Identification of large errors in the previous analysis of the 1968-70 terrestrial data (Chapter 5): A large error was detected and corrected in the 1968-70 terrestrial data. The effect of the error was to shift station coordinates by up to 3-4km(!), with the understood position of the 1968 borehole at A1 shifting by approximately 3km, mainly in a westerly direction. This has important implications for glaciological interpretation of the ice core and for comparisons with remote sensing and oceanographic measurements and numerical modelling. Other smaller errors in the traverse data were also found. The resulting station coordinate set is the most accurate, reliable and consistent data set that forms the basis for long-term studies of the AIS.

Surface velocity estimates (Chapter 5): Velocities were estimated from both terrestrial and GPS data. This provided unprecedented coverage of the AIS from *in situ* measurements. The formal errors (one sigma) of the velocities derived from the terrestrial data were 1.5myr^{-1} and 0.23° and from the GPS data 2.0myr^{-1} and 0.41°. Comparisons with velocities from an independent remote sensing method yielded differences of ±20-30myr^{-1} and 0-4°, suggesting the presence of large systematic biases in the remote sensing results.

Ice shelf velocity unchanged over period 1968-1999 (Chapter 5): A congruency test was applied to the terrestrial and GPS-derived velocities. This test failed at the 95% confidence interval for the velocity magnitude and direction. This suggests a slight reduction of the velocity of the AIS, and may be an indicator to increased basal melt due to increased oceanic temperatures.

Surface strain rate estimates (Chapter 6): Strain rate estimates were computed using both the terrestrial and GPS data individually and in a combined analysis. The combined analysis represents unprecedented coverage of the AIS from *in situ* measurements. The strain rates are well determined compared to their formal errors, with signal-to-noise ratios generally above 20-30. The strain rates appear to confirm the existence of a grounded or

partially grounded section of the AIS southwest of G3, although further data to the west of this region is required to substantiate this belief.

Basal melt rates (Chapter 6): Ice shelf basal melt rates were determined at four locations from a combination of the velocity (vertical and horizontal) and strain rates presented in this thesis with other ice shelf parameters. This method does not require that any assumptions be made about change in thickness of the ice shelf with time. The melt rates agree with the general melt/freeze pattern for the four locations as shown in ocean circulation models and satellite remote sensing measurements, although their current precision is limited by high uncertainties in the accumulation measurements and surface slopes. This method will prove itself to be a useful tool in determining rates of ice shelf basal melt and thickness change by adopting appropriate methods for stabilising the reference poles.

Autonomous GPS system (Chapter 7): A GPS system was described that is capable of operating autonomously during the summer periods in Antarctica. Such a system is required if long term ice movement data are required, such as for tidal studies. The system is particularly suited to use in the hostile Antarctic environment since it is quickly assembled in the field. It is hoped that the description of such a system will encourage others to make measurements of tidal motion on other ice shelves in Antarctica and Arctic regions.

Overall, this thesis has demonstrated a diverse range of glaciological and oceanographic applications of terrestrial and GPS data to the Amery Ice Shelf. The results of this thesis have provided invaluable information and insights into the dynamics of the Amery Ice Shelf and will serve as the benchmark for geodetic data and procedures for on-going, long-term studies in the region. These results allow for the full integration of results from remote sensing studies and provide unique calibration sites for such missions as ICESat/CryoSat. Furthermore, these data provide the best opportunity for regional tide model improvements due to their access to spatial and temporal coverage allowing possible estimation of non-linear terms.

Additional data sets are required to further advance our understanding of the AIS dynamics. Examples include: water column thickness information, particularly in the southern 200km of the ice shelf; better distributions of long-term GPS stations laterally across the ice shelf and across grounding zones; information on bending stresses at the ice shelf margins; ice berg calving rates; measurements across rifting and calving locations.

The addition of these data sets to those presented in this thesis will lead to an excellent understanding of the dynamics of Amery Ice Shelf in a changing climate.

REFERENCES

Agnew D. C. (1995). "Ocean-Load Tides at the South Pole - a Validation of Recent Ocean-Tide Models." *Geophysical Research Letters*, 22(22), 3063-3066.

Allan A. L., Hollwey J. R., and Maynes J. H. B. (1968). Practical Field Surveying and Computations, Heinemann, London, 689 pp.

Allison I. (1979). "The mass budget of the Lambert Glacier drainage basin, Antarctica." *Journal of glaciology*, 22(87), 223-235.

Allison I. (1991). "The Lambert Glacier/ Amery Ice Shelf Study: 1988-1991." *Aurora: ANARE Club Journal*, 10(4), 22-25.

Allman J. S., and Bennett G. G. (1966). "Angles and directions." *Survey Review*, 139, 219-228.

Andersen O. B., Woodworth P. L., and Flather R. A. (1995). "Intercomparison of Recent Ocean Tide Models." *Journal of Geophysical Research*, 100(C12), 25261-25282.

Andersen P. H., Hauge S., and Kristiansen O. (1993). "GPS relative positioning at a precision level of one part per billion." *Bulletin Géodésique*, 67, 91-106.

Aoki S., Ozawa T., Doi K., and Shibuya K. (2000). "GPS observation of the sea level variation in Lutzow-Holm Bay, Antarctica." *Geophysical Research Letters*, 27(15), 2285-2288.

Arias E. F., Charlot P., Feissel M., and Lestrade J. F. (1995). "The Extragalactic Reference System of the International Earth Rotation Service, ICRS." *Astronomy & Astrophysics*, 303(2), 604-608.

Ashjaee J., and Lorenz R. (1992)."Precision GPS surveying after Y-code." *ION GPS-92*, 657-659.

Axelrad P., Comp C., and MacDoran P. (1994)."Use of signal-to-noise ratio for multipath error correction in GPS differential phase measurements: Methodology and experimental results." *ION GPS 94*, Salt Lake City, Utah, September 20-23, 1994, 655-666.

Baarda W. (1973). "S-Transformations and Criterion Matrices." Publications on Geodesy *5(1)*, Netherlands Geodetic Commission, Delft.

Baker T. F. (1984). "Tidal deformations of the Earth." *Science Progress*, 69, 197-233.

Baker T. F., Curtis D. J., and Dodson A. H. (1995). "Ocean tide loading and GPS." *GPS World*, 6(3), 54-59.

Barkov N. I. (1985). Ice shelves of Antarctica, L. C. P. Datta, translator, A. A. Balkema, Rotterdam, 262 pp.

Barnes J. B., and Cross P. A. (1998). "Processing models for very high accuracy GPS positioning." *The Journal of Navigation*, 51(2), 180-193.

Bar-Sever Y. E., Kroger P. M., and Borjesson J. A. (1998). "Estimating horizontal gradients of tropospheric path delay with a single GPS receiver." *Journal of Geophysical Research*, 103(B3), 5019-5035.

Bassiri S., and Hajj G. A. (1993). "Higher-order ionospheric effects on the global positioning system observables and means of modeling them." *Manuscripta Geodaetica*, 18, 280-289.

Bawden G. W., Donnellan A., Kellogg L. H., Dong D. N., and Rundle J. B. (1997). "Geodetic measurements of horizontal strain near the White Wolf fault, Kern County, California, 1926-1993." *Journal of Geophysical Research*, 102(B3), 4957-4967.

Bennett G. G., and Freislich J. G. (1979). Field astronomy for surveyors, New South Wales University Press Limited, Kensington, Australia, 251 pp.

Beutler G., and Kouba J. (1998)."State of the IGS by the end of 1998." *IGS Network systems workshop*, Pasadena, California, November 2-5, 1998, 3-17.

Beutler G., Bauersima I., Botton S., Gurtner W., Rothacher M., and Schildknecht T. (1989). "Accuracy and biases in the geodetic application of the Global Positioning System." *Manuscripta Geodaetica*, 14, 28-35.

Bibby H. M. (1973). "The resection of geodetic survey data for the detection of earth deformation." Geophysics Division Report *84*, Department of Scientific and Industrial Research, Wellington.

Bibby H. M. (1975). "Crustal strain from triangulation in Marlborough, New Zealand." *Tectonophysics*, 29, 529-540.

Bibby H. M. (1982). "Unbiased estimate of strain from triangulation data using the method of simultaneous reduction." *Tectonophysics*, 82, 161-174.

Bindschadler R. A. (1998). "Monitoring ice sheet behaviour from space." *Reviews of Geophysics*, 36(1), 79-104.

Bindschadler R. A., Stephenson S. N., MacAyeal D. R., and Shabtaie S. (1987). "Ice dynamics at the mouth of ice stream B, Antarctica." *Journal of Geophysical Research*, 92(B9), 8885-8894.

Black A. N. (1951). "Laplace points in moderate and high latitudes." *Survey Review*, XI(82), 177-184.

Blewitt G. (1989). "Carrier phase ambiguity resolution for the Global Positioning System applied to geodetic baselines up to 2000 km." *Journal of Geophysical Research*, 98(B8), 10187-10203.

Blewitt G. (1998). "GPS data processing methodology: From theory to application." GPS for Geodesy, A. Kluesberg and P. J. G. Teunissen, eds., Springer, Berlin, 231-270.

Bock Y. (1996). "Reference Systems." GPS for geodesy, A. Kluesberg and P. J. G. Teunissen, eds., Springer-Verlag, Berlin, 3-36.

Bock Y. (1998). "Medium distance GPS measurements." GPS for Geodesy, A. Kluesberg and P. J. G. Teunissen, eds., Springer-Verlag, Berlin, 483-536.

Bock Y., Nikolaidis R. M., de Jonge P. J., and Bevis M. (2000). "Instantaneous geodetic positioning at medium distances with the Global Positioning System." *Journal of Geophysical Research-Solid Earth*, 105(B12), 28223-28253.

Bock Y., Wdowinski S., Fang P., Zhang J., Williams S., Johnson H., Behr J., Genrich J., Dean J., Vandomselaar M., *et al.* (1997). "Southern California Permanent GPS Geodetic Array: Continuous measurements of regional crustal deformation between the 1992 Landers and 1994 Northridge earthquakes." *Journal of Geophysical Research*, 102(B8), 18013-18033.

Bomford G. (1962). Geodesy, Oxford University Press, London, 561 pp.

Bondesan A., Capra A., Gubellini A., and Tison J. (1994). "On the use of static GPS measurements to record the tidal response of a small Antarctic ice shelf (Hells Gate Ice Shelf, Victoria Land)." *Geografia Fisica Dinamica Quaternaria*, 17, 123-129.

Born G. H. (1997). "Colorado Center for Astrodynamics Research Annual Report for 1997." Colorado Center for Astrodynamics Research, Colorado.

Bos M. S., Baker T. F., Lyard F. H., Zürn W. E., and Rydelek P. A. (2000). "Long-period lunar Earth tides at the geographic South Pole and recent models of ocean tides." *Geophysical Journal International*, 143, 490-494.

Boucher C., Altamimi Z., and Sillard P. (1999). "The 1997 International Terrestrial Reference Frame (ITRF97)." IERS Technical Note 27, Observatoire de Paris, Paris.

Boucher C., Altamimi Z., Feissel M., and Sillard P. (1996). "Results and analysis of the ITRF94." IERS Technical Note *20*, International Earth Rotation Service, Paris.

Boucher C., and Altamimi Z. (1989). "The initial IERS Terrestrial Reference Frame." IERS Technical Note *1*, International Earth Rotation Service, Paris.

Bouin M. N., and Vigny C. (2000). "New constraints on Antarctic plate motion and deformation from GPS data." *Journal of Geophysical Research-Solid Earth*, 105(B12), 28279-28293.

Breed A. M., Goodwin G. L., and Silby J. H. (1998). "Total electron content measurements in the southern hemisphere using GPS satellites, 1991 to 1995." *Radio Science*, 33(6), 1705-1726.

Brooks R. L., Campbell W. J., Ramseier R. O., Stanley H. R., and Zwally H. J. (1978). "Ice sheet topography by satellite altimetry." *Nature*, 274(5671), 539-543.

Brunner F. K. (1979). "On the analysis of geodetic networks for the determination of the incremental strain tensor." *Survey Review*, XXV(192), 56-67.

Brunner F. K., Chamberlain S. M., and Frei E. (1986). "Test measurements using the WM 101." *Sonderdruck aus der Osterreichischen Zeitschrift fur Vermessungswesen und Photogrammetrie*, 74, 141-154.

Brunner F. K., Coleman R., and Hirsch B. (1981). "A comparison of computations methods for crustal strains from geodetic measurements." *Tectonophysics*, 71, 281-298.

Budd W. (1966a). "The dynamics of the Amery Ice Shelf." *Journal of Glaciology*, 6(45), 335-357.

Budd W. (1966b). "Glaciology on the Amery Ice Shelf." *Aurora: ANARE Club Journal*, 14-19.

Budd W. F., Corry M. J., and Jacka T. H. (1982). "Results from the Amery Ice Shelf Project." *Annals of Glaciology*, 3, 36-41.

Capra A., F. R., and Vittuari L. (1997)."Italian geodetic network as reference frame for geodynamic purposes (Terra Nova Bay - Victoria Land - Antarctica)." *IAG Scientific Assembly*, Rio De Janeiro, Brazil, September 3-9, 498-503.

Capra A., Frezzotti M., Mancini F., F. R., and Vittuari L. (1997)."GPS for ice sheet movement monitoring and grounding line detection." *IAG Scientific Assembly*, Rio De Janeiro, Brazil, September 3-9, 486-491.

Capra A., Gandolfi S., Vittuari L., Lusetti C., and Stocchino C. (1999). "Kinematic GPS for the study of tidal undulation of floating ice tongue." *Bollettino di Geodesia e Scienze Affini*, LVIII(2), 151-173.

Caputo M. (1978)."Problems and advances in monitoring horizontal strain." *An International Symposium on the Applications of Geodesy to Geodynamics*, Columbus, Ohio, October 2-5, 1978, 103-109.

Cartwright D. E. (1993). "Theory of ocean tides with application to altimetry." Satellite altimetry in geodesy and oceanography, R. Rummel and F. Sando, eds., Springer-Verlag, Germany, 99-141.

Cartwright D. E., and Ray R. D. (1990). "Oceanic tides from Geosat altimetry." *Journal of Geophysical Research*, 95(C3), 3069-3090.

Caspary W. F. (1987). Concepts of network and deformation analysis, School of Surveying, University of New South Wales, Kensington, 183 pp.

Chang C. C. (1999). "Geophysical effects on site displacements for permanent GPS tracking stations in Taiwan." *Geomatics Research Australasia*, 71(December), 1-18.

Chelton D. B., Ries J. C., Haines B. J., Fu L.-L., and Callahan P. S. (2001). "Satellite Altimetry." Satellite Altimetry and Earth Sciences, L.-L. Fu and A. Cazenave, eds., Academic Press, San Diego, 1-131.

Chen G. (1998). "GPS Kinematic Positioning for the Airborne Laser Altimetry at Long Valley, California," PhD Thesis, Massachusetts Institute of Technology, Cambridge.

Chen G., and Herring T. A. (1997). "Effects of Atmospheric Azimuthal Asymmetry on the Analysis of Space Geodetic Data." *Journal of Geophysical Research*, 102(B9), 20489-20502.

Chen X., Bindschadler A., and Vornberger P. L. (1998). "Determination of velocity field and strain-rate field in West Antarctica using high precision GPS measurements." *Surveying and Land Information Systems*, 58(4), 247-255.

Clark D. (1963). Plane and geodetic surveying - Higher Surveying, Constable & Company, London, 685 pp.

Collier P. A., Eissfeller B., Hein G. W., and Landau H. (1988). "On a four-dimensional integrated geodesy." *Bulletin Geodesique*, 62, 71-91.

Collins J. P., and Langley R. B. (1999). "Possible weighting schemes for GPS carrier phase observations in the presence of multipath." for The United States Army Corps of Engineers Topographic Engineering Center, Geodetic Research Laboratory, Department of Geodesy and Geomatics Engineering, University of New Brunswick, Canada, Fredericton.

Colombo O., Hernandez-Pajares M., Juan J. M., and Sanz J. (2000)."Ionospheric tomography helps resolve GPS ambiguities on the fly at distances of hundreds of kilometres during increased geomagnetic activity." *IEEE PLANS 2000*, San Diego, California, March 2000.

Cong D. C., and Feigl K. L. (1999). "Geodetic measurement of horizontal strain across the Red River fault near Thac Ba, Vietnam, 1963-1994." *Journal of Geodesy*, 73, 298-310.

Corry M. (1987a). "Amery Ice Shelf Saga: Part 1 - pre 1968." ANARE News, 17-20.

Corry M. (1987b). "Amery Ice Shelf Saga: Part 2 - The Amery Ice Shelf Project 1968." ANARE News, 28-34.

Corry M. (1987c). "Amery Ice Shelf Saga: Part 3 - 1969-70." ANARE News, 25-29.

Corry M. (1996). "Those Amery Ice Shelf glaciological marker snowpoles." ANARE News, 18-20.

Craven M. (1996). "KAOS: Kinematic Amery Oversnow Survey." *Aurora: ANARE Club Journal*, 15(3), 15-17.

Craven M. (1996). "The Amery Ice Shelf Project - Kinematic GPS Survey." Unpublished Report, Cooperative Research Centre for the Antarctic and Southern Ocean environment, Hobart.

Craven M., Allison I., Kiernan R., and Higham M. (1995)."GPS application in Antarctic glaciology." *Satellite navigation technical conference*, Brisbane, Australia, June 1995.

Craven M., Brand R., Elcheikh A., and Jones N. (2000a). "Summer field report for Amery Ice Shelf HWD test season: AMISOR-1." Internal report, Cooperative Research Centre for the Antarctic and Southern Ocean environment, Hobart.

Craven M., Elcheikh A., Brand R., and Jones N. (2000b)."AMISOR: The Amery Ice Shelf hot water drill." *Ice Drilling Technology Workshop*, Japan.

Cross P. (1990)."Practical integration of GPS and classical geodetic control networks." *FIG XIX international congress*, Helsinki, Finland, 337-348.

Cunningham J. P., Swift E. R., and Mueller F. (1998)."Improvement of the NIMA precise orbit and clock estimates." *ION GPS-98*, Nashville, September 15-18, 1587-1596.

Dach R., and Dietrich R. (2000). "Influence of the ocean loading effect on GPS derived precipitable water vapor." *Geophysical Research Letters*, 27(18), 2953-2956.

Derauw D. (1999)."DInSAR and coherence tracking applied to glaciology: the example of Shirase Glacier." *FRINGE 99, European Space Agency's 2nd International Workshop on SAR Interferometry*, Liege, Belgium, 10-12 November, 1999.

Dietrich R., Dach R., Engelhardt G., Heck B., Kutterer H., Lindner K., Mayer M., Menge F., Mikolaiski H.-W., Niemeier W., *et al.* (1996). "The SCAR 95 GPS campaign: Objectives, data analysis and final solution." The Geodetic Antarctic Project GAP95 - German Contributions to the SCAR 95 Epoch Campaign, Deutsche Geodätische Kommission, München, 9-14.

Dietrich R., Dach R., Engelhardt G., Ihde J., Korth W., Kutterer H., Lindner K., Mayer M., Menge F., Miller H., *et al.* (2001). "ITRF coordinates and plate velocities from repeated GPS campaigns in Antarctica - an analysis based on different individual solutions." *Journal of Geodesy*, 74, 756-766.

Dixon, T.H. (1991). "An introduction to the Global Positioning System and some geological application." *Reviews of Geophysics*, 29(2), 249-276.

Doake C. S. M. (1978). "Dissipation of tidal energy by Antarctic ice shelves." *Nature*, 275, 304-305.

Doake C. S. M. (1992)."Gravimetric tidal measurements on Filchner Ronne Ice Shelf." *7th International Workshop of the Filchner-Ronne Ice Shelf Programme*, SchloB Senden, Germany, 24-26 June, 1992, 34-39.

Doake C. S. M., and Vaughan D. G. (1991). "Rapid disintegration of the Wordie Ice Shelf in response to atmospheric warming." *Nature*, 350, 328-330.

Dong D. (1993). "The horizontal velocity field in southern California from a combination of terrestrial and space-geodetic data." PhD Thesis, Massachusetts Institute of Technology, Cambridge.

Dong D., Herring T. A., and King R. W. (1998). "Estimating regional deformation from a combination of space and terrestrial geodetic data." *Journal of Geodesy*, 72(4), 200-214.

Donnellan A., and Luyendyk B. (2000). "GPS measurement of tectonic deformation and isostatic rebound in Marie Byrd Land, Antarctica." *EOS, Transactions, American Geophysical Union*, 81(48), F311.

Doodson. (1921). "The harmonic development of the tide-generating potential." *Proceedings of the Royal Society London A*, 100, 305-328.

Dorrer E., Hofmann W., and Seufert W. (1969). "Geodetic results of the Ross Ice Shelf Survey expeditions, 1962-63 and 1965-66." *Journal of Glaciology*, 8(52), 67-90.

Drewry D. J. (1983). "The bedrock surface of Antarctica." Antarctica: Glaciological and Geophysical Folio, D. J. Drewry, ed., Scott Polar Research Institute, Cambridge, UK.

Duan J. P., Bevis M., Fang P., Bock Y., Chiswell S., Businger S., Rocken C., Solheim F., Vanhove T., Ware R., *et al.* (1996). "GPS meteorology - direct estimation of the absolute value of precipitable water." *Journal of Applied Meteorology*, 35(6), 830-838.

Dunnell C. A., Ferriter P., Gebel G., Hopfield H. S., Schaefer M. M., and Yionoulis S. M. (1977). "National Geodetic Satellite Program." *Part I*, National Aeronautics and Space Administration, Washington.

Egbert G. D., Bennett A. F., and Foreman M. G. G. (1994). "TOPEX/POSEIDON Tides Estimated Using a Global Inverse Model." *Journal of Geophysical Research*, 99(C12), 24821-24852.

Ellis J. (1991). "Antarctica and global climatic change: review of prominent issues." Antarctica and global climatic change, C. Harris and B. Stonehouse, eds., Bellhaven Press, London, 11-20.

Estey L. H., and Meertens C. M. (1999). "TEQC: The multi-purpose toolkit for GPS/GLONASS data." *GPS Solutions*, 3(1), 42-49.

Fahnestock M., Bindschadler R., Kwok R., and Jezek K. (1993). "Greenland Ice Sheet Surface Properties and Ice Dynamics from ERS-1 SAR Imagery." *Science*, 262(5139), 1530-1534.

Feigl K. L., Agnew D. C., Bock Y., Dong D., Donnellan A., Hager B. H., Herring T. A., Jackson D. D., Jordan T. H., King R. W., *et al.* (1993). "Space geodetic measurement of crustal deformation in Central and Southern California, 1984-1992." *Journal of Geophysical Research*, 98(B12), 21677-21712.

Feigl K. L., Agnew D. C., Bock Y., Dong D., Donnellan A., Hager B. H., Herring T. A., Jackson D. D., Jordan T. H., King R. W., *et al.* (1993). "Space geodetic measurement of crustal deformation in Central and Southern California, 1984-1992." *Journal of Geophysical Research*, 98(B12), 21677-21712.

Feigl K. L., King R. W., and Jordan T. H. (1990). "Geodetic measurement of tectonic deformation in the Santa Maria fold and thrust belt, California." *Journal of Geophysical Research*, 95(B3), 2679-2699.

Ferhat G., Feigl K. L., Ritz J. F., and Souriau A. (1998). "Geodetic measurement of tectonic deformation in the Southern Alps and Provence, France, 1947-1994." *Earth & Planetary Science Letters*, 159(1-2), 35-46.

Forsberg R., Keller K., Nielsen C. S., Gundestrup N., Tscherning C. C., Madsen S. N., and Dall J. (2000). "Elevation change measurements of the Greenland Ice Sheet." *Earth Planets and Space*, 52, 1049-1053.

Frank F. C. (1966). "Deduction of earth strains from survey data." *Bulletin of the Seismological Society of America*, 56(1), 35-42.

Fricker H. A., Allison I., Craven M., Hyland G., Ruddell A., Young N., Coleman R., King M., Krebs K., and Popov S. (2001a). "Redefinition of the Amery Ice Shelf, East Antarctica, grounding zone." *Journal of Geophysical Research*, submitted.

Fricker H. A., Hyland G., Coleman R., and Young N. W. (2000). "Digital elevation models for the Lambert Glacier-Amery Ice Shelf system, East Antarctica, from ERS-1 satellite radar altimetry." *Journal of Glaciology*, 46(155), 553-560.

Fricker H. A., Popov S., Allison I., and Young N. W. (2001b). "Distribution of marine ice at the base of the Amery Ice Shelf." *Geophysical Research Letters*, in press.

Genrich J., and Bock Y. (1992). "Rapid resolution of crustal motion at short ranges with the Global Positioning System." *Journal of Geophysical Research*, 97(B3), 3261-3269.

Gill A. E. (1982). Atmosphere-ocean dynamics, Academic Press, New York, 662 pp.

Giovinetto M. B., and Bentley C. R. (1985). "Surface balance in ice drainage systems of Antarctica." *Antarctic Journal and the United States*, 20(4), 6-13.

Goldstein R. M., Engelhardt H., Kamb B., and Frolich R. M. (1993). "Satellite Radar Interferometry for Monitoring Ice Sheet Motion - Application to an Antarctic Ice Stream." *Science*, 262(5139), 1525-1530.

Gradinarsky L. P., and Elgered G. (2000). "Horizontal gradients in the wet path delay derived from four years of microwave radiometer data." *Geophysical Research Letters*, 27(16), 2521-2524.

Grant D. B. (1990). "Combination of terrestrial and GPS data for earth deformation studies." UNISURV Report *S-32*, School of Surveying, University of New South Wales, Kensington.

Groves G. W., and Reynolds R. W. (1975). "An orthogonalized Convolution Method of Tide Prediction." *Journal of Geophysical Research*, 80(30), 4131-4138.

Gu G., and Prescott W. H. (1986). "Discussion of displacement analysis: detection of crustal deformation." *Journal of Geophysical Research*, 91(B7), 7439-7446.

Gubellini A., and Postpischl D. (1991). "The Mount Melbourne (Antarctica) geodetic network." *Memorie di Scienze Geologiche*, 46, 595-610.

Hager B. H., King R. W., and Murray M. H. (1991). "Measurement of crustal deformation using the Global Positioning System." *Annual Review of Earth Planetary Sciences*, 19, 351-382.

Hamilton G. S., and Whillans I. M. (2000). "Point measurements of mass balance of the Greenland Ice Sheet using precision vertical Global Positioning System (GPS) surveys." *Journal of Geophysical Research*, 105(B7), 16295-16301.

Hamilton G. S., Whillans I. M., and Morgan P. J. (1998). "First point measurements of ice sheet thickness change in Antarctica." *Annals of Glaciology*, 27, 125-129.

Hamon B. V. (1966). "Continental shelf waves and the effects of atmospheric pressure and wind stress on sea level." *Journal of Geophysical Research*, 71(12), 2883-2893.

Han S., and Rizos C. (1995). "Selection and scaling of simultaneous baselines for GPS network adjustment, or correct procedures for processing trivial baselines." *Geomatics Research Australasia*, 63, 51-66.

Hansen A. J. (1998)."Real-time ionospheric tomography using terrestrial GPS sensors." *ION-GPS-98*, Nashville, September 14-17, 717-728.

Harvey B. R. (1985). "The combination of VLBI and ground data for geodesy and geophysics." UNISURV *S-27*, The University of New South Wales, Sydney, Australia.

Hatch R. R. (1996). "The promise of a third frequency." *GPS World*, 7(5), 55-58.

Hay C. (2000). "The GPS Accuracy Improvement Initiative." *GPS World*, 11(6), 56-61.

Heflin M., Bertiger W., Blewitt G., Freedman A., Hurst K., Lichten S., Lindqwister U., Vigue Y., Webb F., Yunck T., *et al.* (1992). "Global geodesy using GPS without fiducial sites." *Geophysical Research Letters*, 19(2), 131-134.

Hein G. W. (1982a)."A contribution to 3D-operational geodesy. Part 1: Principle and observational equations of terrestrial type." *International Symposium on Geodetic Networks and Computations of the International Associations of Geodesy*, Munich, August 31 - September 5, 1981, 31-64.

Hein G. W. (1982b)."A contribution to 3D-operational geodesy. Part 2: Concepts of solution." *International Symposium on Geodetic Networks and Computations of the International Associations of Geodesy*, Munich, August 31 - September 5, 1981, 65-85.

Hein G. W. (1986). "Integrated geodesy state-of-the art 1986 reference text." Mathematical and numerical techniques in physical geodesy, H. Sunkel, ed., Springer-Verlag, Berlin, 505-548.

Heiskanen W. A., and Moritz H. (1967). Physical Geodesy, W.H. Freeman and Company, San Francisco, 364 pp.

Heroux P., and Kluesberg A. (1989)."GPS precise relative positioning and ionosphere in auroral regions." *International Geodetic Symposium on Satellite Positioning*, Las Cruces, New Mexico, March 13-17, 475-486.

Herring T. (1997). "Global Kalman filter VLBI and GPS analysis program." Unpublished, Massachusetts Institute of Technology, Cambridge.

Herring T. A. (1996). "The Global Positioning System." *Scientific American*, February 1996, 32-38.

Herring T. A. (1999). "Geodetic applications of GPS." *Proceedings of the IEEE*, 87(1), 92-110.

Herring T. A., Davis J. L., and Shapiro I. I. (1990). "Geodesy by radio astronomy: the application of Kalman filtering to very long baseline interferometry." *Journal of Geophysical Research*, B95, 12561-12581.

Herring T. A., Dong D., and King R. W. (1991). "Sub-milliarcsecond determination of pole position using Global Positioning System data." *Geophysical Research Letters*, 18(10), 1893-1896.

Herring T. A., Dong D., and King R. W. (1991). "Sub-milliarcsecond determination of pole position using Global Positioning System data." *Geophysical Research Letters*, 18(10), 1893-1896.

Higham M., and Craven M. (1997). "Surface mass balance and snow surface properties from the Lambert Glacier basin traverses." Research report *9*, Cooperative Research Centre for the Antarctic and Southern Ocean environment, Hobart.

Hinze H., and Seeber G. (1988). "Ice-motion determination by means of satellite positioning systems." *Annals of Glaciology*, 11, 36-41.

Ho C. M., Wilson B. D., Mannucci A. J., Lindqwister U. J., and Yuan D. N. (1997). "A Comparative Study of Ionospheric Total Electron Content Measurements Using Global Ionospheric Maps of GPS, Topex Radar, and the Bent Model." *Radio Science*, 32(4), 1499-1512.

Hofmann W., Dorrer E., and Nottarp K. (1964). "The Ross Ice Shelf Survey (RISS) 1962-1963." Antarctic Snow and Ice Studies, M. Mellor, ed., American Geophysical Union, Washington, D.C., 83-117.

Hofmann-Wellenhof B., Lichtenegger H., and Collins J. (1992). GPS Theory and Practice, Springer-Verlag, Wien, 326 pp.

Holdsworth G. (1977). "Tidal interaction with ice shelves." *Annals of Geophysics*, 33(1), 133-146.

Hotine M. (1969). Mathematical geodesy, U.S. Government Printing Office, Washington, 416 pp.

Hughes T. (1992). "On the pulling power of ice streams." *Journal of Glaciology*, 38(128), 125-151.

Hulbe C. L., and Whillans I. M. (1993). "Stop-and-Go GPS in Antarctica." *Surveying and Land Information Systems*, 53(2), 151-158.

Hulbe C. L., and Whillans I. M. (1994). "A method for determining ice-thickness change at remote locations using GPS." *Annals of Glaciology*, 20, 263-268.

IPCC. (2001a). "Climate Change 2001: Impacts, Adaption and Vulnerability, Summary for Policy Makers." Working Group II of the Intergovernmental Panel on Climate Change, Geneva, Switzerland.

IPCC. (2001b). "Climate Change 2001: The Scientific Basis, Summary for Policy Makers." Assessment report *3*, Working Group I of the Intergovernmental Panel on Climate Change, Geneva, Switzerland.

Jacka T. H., and Budd W. F. (1998). "Detection of temperature and sea-ice-extent changes in the Antarctic and Southern Ocean, 1949-96." *Annals of Glaciology*, 27, 553-559.

Jacobs S. S., Helmer H. H., Doake C. S. M., Jenkins A., and Frolich R. M. (1992). "Melting of ice shelves and the mass balance of Antarctica." *Journal of Glaciology*, 38(130), 375-387.

Jaeger J. C. (1969). Elasticity, fracture and flow, Methuen & Co., London, 268 pp.

Jaldehag R. T. K., Johansson J. M., Davis J. L., and Elosegui P. (1996). "Geodesy using the Swedish Permanent GPS Network - effects of snow accumulation on estimates of site positions." *Geophysical Research Letters*, 23(13), 1601-1604.

Janes H. W., Langley R. B., and Newby S. P. (1991). "Analysis of tropospheric delay prediction models: comparisons with ray-tracing and implications for GPS relative positioning." *Bulletin Géodésique*, 65, 151-161.

Johansson J. M., Emardson T. R., Jarlemark P. O. J., Gradinarsky L. P., and Elgered G. (1998). "The atmospheric influence on the results from the Swedish GPS Network." *Physics & Chemistry of the Earth*, 23(1), 107-112.

Joughin I., Kwok R., and Fahnestock M. (1996). "Estimation of Ice-Sheet Motion Using Satellite Radar Interferometry - Method and Error Analysis with Application to Humboldt Glacier, Greenland." *Journal of Glaciology*, 42(142), 564-575.

Juan J. M., Rius A., Hernandez-Pajares M., and Sanz J. (1997). "A Two-Layer Model of the Ionosphere Using Global Positioning System Data." *Geophysical Research Letters*, 24(4), 393-396.

Kaplan E. D. (1996). Understanding GPS: principles and applications, Artech House, Norwood, 554 pp.

Kehle R. (1960). "Strain measurements in the deformation area." Deformation of the Ross Ice Shelf near the Bay of Whales, Antarctica, J. H. Zumberge, ed., American Geographical Society, New York, 53-90.

King H. L., Scott M. A., and Smith T. J. (1983). "Some remarks on the analysis of short tidal records." *Deutsche Hydrographische Zeitschrift*, 36(2), 45-59.

King M., Nguyen L. N., Coleman R., and Morgan P. (2000). "Strategies for High Precision Processing of GPS Measurements with Application to the Amery Ice Shelf, East Antarctica." *GPS Solutions*, 4(1), 2-12.

King R. W., and Bock Y. (1999). "Documentation for the GAMIT GPS analysis software (version 9.8)." Unpublished, Massachusetts Institute of Technology, Cambridge.

King R. W., Masters E. G., Rizos C., Stolz A., and Collins J. (1985). "Surveying with GPS." Monograph *9*, School of Surveying, University of New South Wales, Sydney.

Kirkby S. L. (1965). "Australian Antarctic Territory Mac Robertson Land - Kemp Land Tellurometer Traverse." Technical report *5*, Division of National Mapping, Canberra.

Klobuchar J. A. (1987). "Ionospheric time-delay algorithm for single-frequency GPS users." *IEEE Transactions on Aerospace and Electronic Systems*, 23(3), 325-331.

Klobuchar J. A. (1991). "Ionospheric effects of GPS." *GPS World*, 2(4), 48-51.

Kluesberg A. (1986). "Ionospheric propagation effects in geodetic relative GPS positioning." *Manuscripta Geodaetica*, 11, 256-261.

Lambeck K. (1988). Geophysical Geodesy, Oxford University Press, Oxford, 718 pp.

Langley R. B. (1996). "Propagation of the GPS signals." GPS for geodesy, A. Kluesberg and P. J. G. Teunissen, eds., Springer-Verlag, Berlin, 103-173.

Langley R. B. (1998). "A primer on GPS antennas." *GPS World*, 9(7), 50-54.

Larson K. M., Webb F. H., and Agnew D. C. (1991a). "Application of the Global Positioning System to crustal deformation measurement; 1, Precision and accuracy." *Journal of Geophysical Research*, 96(B10), 16,547-16,565.

Larson K. M., Webb F. H., and Agnew D. C. (1991b). "Application of the Global Positioning System to crustal deformation measurement; 2, The influence of errors in orbit determination networks." *Journal of Geophysical Research*, 96(B10), 16,567-16,584.

Le Provost C., Genco M. L., and Lyard F. (1995). "Modeling and predicting tides over the World Ocean." Quantitative Skill Assessment for Coastal Ocean Models, American Geophysical Union, 175-201.

Le Provost C., Genco M. L., Lyard F., Vincent P., and Canceil P. (1994). "Spectroscopy of the World Ocean Tides from a Finite Element Hydrodynamic Model." *Journal of Geophysical Research*, 99(C12), 24777-24797.

Lefevre F., Lyard F. H., and Le Provost C. (2000). "FES98: A new global tide finite element solution independent of altimetry." *Geophysical Research Letters*, 27(17), 2717-2720.

Lefevre F., Lyard F., Le Provost C., and Schrama E. J. O. (2001). "FES99: a tide finite element solution assimilating tide gauge and altimetric information." *Journal of Geophysical Research, submitted.*

Leick A. (1995). GPS Satellite Surveying, John Wiley & Sons, New York, 560 pp.

Lemoine F. G., Smith D. E., Kunz L., Smith R., Pavlis E. C., Pavlis N. K., Klosko S. M., Chinn D. S., Torrence M. H., Williamson R. G., *et al.* (1996)."The development of the NASA GSFC and NIMA Joint Geopotential Model." *International Symposium on Gravity, Geoid, and Marine Geodesy*, Tokyo, Japan, September 30-October 5, 1996, 461-469.

Lichten S. M. (1990). "Estimation and filtering for high-precision GPS positioning applications." *Manuscripta Geodaetica*, 15, 159-176.

Lichten S. M., and Border J. S. (1987). "Strategies for high precision Global Positioning System orbit determination." *Journal of Geophysical Research*, 92(B12), 12751-12762.

Lichten S. M., Marcus S. L., and Dickey J. O. (1992). "Sub-daily resolution of earth rotation variations with Global Positioning System measurements." *Geophysical Research Letters*, 19(6), 537-540.

Lisignoli C. A. (1964). "Movement of the Filchner Ice Shelf, Antarctica." *American Geophysical Union Transactions*, 45(2), 391-397.

Love A. E. H. (1952). A treatise on the mathematical theory of elasticity, University Press, Cambridge, 643 pp.

Lutjeharms J. R. E., and Stavropoulos C. C. (1985). "Tidal measurements along the Antarctic coastline." Oceanology of the Antarctic Continental Shelf, S. S. Jacobs, ed., American Geophysical Union, Washington, D.C., 273-289.

Ma C., Arias E. F., Eubanks T. M., Fey A. L., Gontier A. M., Jacobs C. S., Sovers O. J., Archinal B. A., and Charlot P. (1998). "The International Celestial Reference Frame as Realized by Very Long Baseline Interferometry." *Astronomical Journal*, 116(1), 516-546.

MacAyeal D. R. (1984). "Numerical simulations of the Ross Sea tides." *Journal of Geophysical Research*, 89(C1), 607-615.

Mader G. L. (1992). "Rapid Static and Kinematic Global Positioning System Solutions Using the Ambiguity Function Technique." *Journal of Geophysical Research*, 97(B3), 3271-3283.

Mader G. L. (1999). "GPS antenna calibration at the National Geodetic Survey." *GPS Solutions*, 3(1), 50-58.

Malys S., and Slater J. (1994)."Maintenance and enhancement of the World Geodetic System 1984." *ION GPS-94*, Salt Lake City, September 20-23, 17-24.

Manning J., Morgan P., and Murphy B. (1992). "Antarctica - Where is it, and where is it going?" *The Australian Surveyor*, 37(1), 5-12.

Manson R. (1995). "GPS processing strategies for Antarctic data," Honours Thesis, University of Tasmania, Hobart.

Manson R. (2001, in preparation). "Investigations of the Glaciology and Meteorology of the Lambert Glacier Basin Using High Precision GPS Techniques.", PhD Thesis, University of Tasmania, Hobart.

Manson R., Coleman R., Morgan P., and King M. (2000). "Ice velocities of the Lambert Glacier from static GPS observations." *Earth Planets and Space*, 52(11), 1031-1036.

Mao A. L., Harrison C. G. A., and Dixon T. H. (1999). "Noise in GPS coordinate time series." *Journal of Geophysical Research*, 104(B2), 2797-2816.

Martinez L. J., Meertens C. M., and Smith R. B. (1998). "Rapid deformation rates along the Wasatch Fault Zone, Utah, from first GPS measurements with implications for earthquake hazard." *Geophysical Research Letters*, 25(4), 567-570.

Marussi A. (1985). Intrinsic Geodesy, W. I. Reilly, translator, Springer-Verlag, Berlin, 219 pp.

Massonnet D., and Feigl K. L. (1998). "Radar interferometry and its application to changes in the earth's surface." *Reviews of Geophysics*, 36(4), 441-500.

Mazur B. A. (1982). "Technical and performance characteristics of GPS/NAVSTAR." Under contract to the European Space Agency *N82-32892*, Miller Communications Systems Ltd., Kanata, Canada.

McCarthy D. D. (1992). "IERS Standards (1992)." IERS Technical Note *13*, International Earth Rotation Service, Paris.

McCarthy D. D. (1996). "IERS Conventions (1996)." IERS Technical Note *21*, International Earth Rotation Service.

Medhurst T. G. (1985). "Dependence of satellite doppler measurements in Antarctica on ionospheric conditions." *The Australian Surveyor*, 32(7), 559-573.

Meertens C., Rocken C., Braun J., Stephens B., Alber C., Ware R., Exner M., and Kolesnikoff P. (1997). "Antenna Type, Mount, Height, Mixing, and Snow Effects in High-Accuracy GPS Observations." The Global Positioning System for the Geosciences: Summary and Proceedings of a Workshop on Improving the GPS Reference Station Infrastructure for Earth, Oceanic, and Atmospheric Science Applications, R. H. Ware, E. A. Bermann, T. A. Herring, R. E. Neilan, B. W. Remondi, R. J. Serafin, W. K. Stewart, D. A. Turner, G. M. Levin, and T. Morrison, eds., National Academy Press, Washington, D.C., 239.

Meier M. F. (1983). "Snow and ice in a changing hydrological world." *Hydrological Sciences Journal*, 28(1), 3-21.

Meier M. F. (1993). "Ice, climate, and sea level; do we know what is happening?" Ice in the Climate System, W. R. Peltier, ed., Springer-Verlag, Berlin, 141-160.

Meissl P. (1969). "Zusammenfassung und Ausbau der inneren Fehlertheorie eines Punkthaufens." Deutsche Geod. Komm., Reihe A.

Melbourne W. G. (1985)."The case for ranging in GPS-based geodetic systems." *First International Symposium on Precise Positioning with GPS*, Rockville, Maryland, 373-386.

Melbourne W. G., Fisher S. S., Neilan R. E., Yunck T. P., Engen B., Reigber C., and Tatevjan S. (1991)."The first GPS IERS and Geodynamics experiment - 1991." *Permanent satellite tracking networks for geodesy and geodynamics*, Vienna, Austria, August 11-24, 65-80.

Mendes V. B., and Langley R. B. (1994)."A comprehensive analysis of mapping functions used in modeling tropospheric propagation delay in space geodetic data." *KIS94, International Symposium on Kinematic Systems in Geodesy, Geomatics and Navigation*, Banff, Alberta, 30 August - 2 September 1994, 87-98.

Menge F. (1996). "Monitoring and Assessment of Ionospheric Disturbances during the Geodetic Antarctic Project." The Geodetic Antarctic Project GAP95 - German Contributions to the SCAR 95 Epoch Campaign, Deutsche Geodätische Kommission, München, 93-108.

Mercer J. H. (1978). "West Antarctic ice sheet and CO_2 greenhouse effect: a threat of disaster." *Nature*, 271, 321-325.

Merriman A. G. (1985). "Harmonic tidal analysis of short period observations, errors due to poor inference." *The Hydrographic Journal*, 38, 5-7.

Mohr J. J., Reeh N., and Madsen S. N. (1998). "Three-Dimensional Glacial Flow and Surface Elevation Measured with Radar Interferometry." *Nature*, 391(6664), 273-276.

Moller D., and Ritter B. (1988). "Glacial geodetic contributions to the mass balance and dynamics of ice shelves." *Annals of Glaciology*, 11, 89-94.

Morgan P. (1994)."The role of GPS in Antarctica." *FIG 1994 General Assembly*, Melbourne, Australia, March, 12 in total.

Morgan P., and Tiesler R. (1991). "First epoch GPS baselines between Australia and Antarctica January 1990." *Australian Journal of Geodesy, Photogrammetry, and Surveying*, 51, 55-66.

Morgan P., Tiesler R., Manning J., Murphy B., and Hendy M. (1992)."The Scientific Committee for Antarctica GPS project." *Australian National GPS Symposium*, University of New South Wales, Australia, June, 1992.

Morgan V. I., and Budd W. F. (1975). "Radio-echo sounding of the Lambert Glacier basin." *Journal of Glaciology*, 15(73), 103-111.

Moritz H. (1978). "The operational approach to physical geodesy." *277*, Department of Geodetic Science, Ohio State University.

Morris E. M. (1991). "Antarctic ice studies in global climatic change: a comment." Antarctica and global climatic change, C. Harris and B. Stonehouse, eds., Bellhaven Press, London, 51-62.

Mueller I. I. (1969). Spherical and Practical Astronomy as applied to Geodesy, F. Unger Publishing Co., Inc., New York, 615 pp.

Munk W. H., and Cartwright D. E. (1966). "Tidal spectroscopy and prediction." *Philosophical Proceedings of the Royal Society of London*, 259(A1105), 533-581.

Murphy B., Manning J., and Morrison T. (1990)."The transition to GPS : Australian experience in Antarctica with satellite positioning." *FIG XIX International Congress*, Helsinki, Finland, 296-311.

Musyoka S. M., and Aduol F. W. O. (1997). "A three-dimensional geodetic network model for the analysis of localised earth deformation." *Survey Review*, 34(263), 41-56.

Nguyen L. N. (2000). "Improving GPS results using continuous processing strategies," unpublished PhD Thesis, University of Tasmania, Hobart, Tasmania, Australia.

Nicholls K. W. (1997). "Predicted Reduction in Basal Melt Rates of an Antarctic Ice Shelf in a Warmer Climate." *Nature*, 388(6641), 460-462.

Niell A. E. (1996). "Global Mapping Functions for the Atmosphere Delay at Radio Wavelengths." *Journal of Geophysical Research*, 101(B2), 3227-3246.

Nielsen A. (1999). "Beaver Lake tidal analysis." Unpublished Internal Report, National Tidal Facility, Flinders University, Adelaide.

Niemeier W. (1987)."Course Notes." *Workshop on engineering networks and deformation analysis*, School of Surveying, University of New South Wales, Sydney, 14-18 September, 1987.

NIMA. (1997). "Department of Defense World Geodetic System 1984: Its definition and relationship to local geodetic datums." Technical Report *TR8350.2 Third Edition*, National Imaging and Mapping Agency, Bethesda, Maryland.

Nye J. F. (1957). "The distribution of stress and velocity in glaciers and ice-sheets." *Proceedings of the Royal Society of London*, 239(1216), 113-133.

Nye J. F. (1959). "A method of determining the strain-rate tensor at the surface of a glacier." *Journal of Glaciology*, 3(25), 409-418.

Nyland E. (1977). "Repeated geodetic surveys as experiments in geophysics." *The Canadian Surveyor*, 31(4), 347-360.

Oerlemans J., and van der Veen C. J. (1984). Ice sheets and climate, D. Reidel Publishing Company, Dordecht, Holland, 217 pp.

Oiu W., Lachapelle G., and Cannon M. E. (1995). "Ionospheric Effect Modelling for Single Frequency GPS Users." *Manuscripta Geodaetica*, 20(2), 96-109.

Ootaki O., and Fujiwara S. (1998). "Measurement of ice sheet movement at S16, East Antarctica using GPS." *Polar Geoscience*, 11, 9-13.

Oppenheimer M. (1998). "Global warming and the stability of the West Antarctic Ice Sheet." *Nature*, 393(6683), 325-332.

Padman L., and Kottmeier C. (2000). "High-frequency ice motion and divergence in the Weddell Sea." *Journal of Geophysical Research*, 105(C2), 3379-3400.

Padman L., Fricker H. A., Coleman R., Howard S., and Erofeeva S. (2001). "A new tide model for the Antarctic ice shelves and seas." *Annals of Glaciology, submitted.*

Pagarete J., Pinto J. T., Mendes V. B., Antunes C., and Ribeiro H. (1998). "The importance of classical geodetic observations for analyzing the geodynamic behaviour of the Acores archipelago." *Tectonophysics*, 294(3-4), 281-290.

Paterson W. S. B. (1994). The physics of glaciers, Elsevier Science Ltd., 480 pp.

Pearson C. F., Beavan J., Darby D. J., Blick G. H., and Walcott R. I. (1995). "Strain distribution across the Australian Pacific plate boundary in the central South Island, New Zealand, from 1992 GPS and earlier terrestrial observations." *Journal of Geophysical Research*, 100(B11), 22071-22081.

Pedley M., Paren J. G., and Potter J. R. (1986). "The tidal spectrum underneath Antarctic ice shelves." *Journal of Geophysical Research*, 91(C11), 13001-13009.

Peltier W. R. (1994). "Ice Age Paleotopography." *Science*, 265(5169), 195-201.

Pelzer H. (1971). "Zur Analyse geodätischer Deformationsmessungen." Deutsche Geod. Komm., Reihe C.

Phillips H. A. (1998). "Surface meltstreams on the Amery Ice Shelf, East Antarctica." *Annals of Glaciology*, 27, 177-181.

Phillips H. A. (1999). "Applications of ERS satellite radar altimetry in the Lambert Glacier - Amery Ice Shelf system, East Antarctica." PhD Thesis, University of Tasmania, Hobart.

Phillips H. A., Allison I., Coleman R., Hyland G., Morgan P., and Young N. W. (1998). "Comparison of ERS satellite radar altimeter heights with GPS-derived heights on the Amery Ice Shelf, East Antarctica." *Annals of Glaciology*, 27, 19-24.

Phillips H. A., Hyland G., Morgan P. J., Coleman R., and Young N. W. (1997)."Comparison of ERS altimeter and GPS heights on the Amery Ice Shelf, East Antarctica." *3rd ERS Symposium*, Florence, Italy, March 17-21, 1997, 899-904.

Piechocinska J., and Sjöberg L. E. (1989)."Some first experience with the WM102 GPS receiver." *Global Positioning System: An Overview*, Edniburgh, 106-111.

Potter J. R., Paren J. G., and Pedley M. (1985). "Tidal behaviour under an Antarctic ice shelf." *Brittish Antarctic Survey Bulletin*, 68, 1-18.

Prescott W. H. (1976). "An extension of Frank's method for obtaining crustal shear strains from survey data." *Bulletin of the Seismological Society of America*, 66(6), 1847-1853.

Prescott W. H. (1981). "The determination displacement fields from geodetic data along a strike slip fault." *Journal of Geophysical Research*, 86(B7), 6067-6072.

Pugh D. T. (1987). Tides, surges and mean sea-level: a handbook for engineers and scientists, John Wiley and Sons, Chichester, 472 pp.

Rack W., Rott H., Siegel A., and Skvarca P. (1999). "The motion field of northern Larsen Ice Shelf, Antarctic Peninsula, derived from satellite imagery." *Annals of Glaciology*, 29, 261-266.

Ramsay J. G. (1967). Folding and fracture of rocks, McGraw Hill, New York, 568 pp.

Rawer K., Bilitza D., and Ramakrishnan S. (1978). "Goals of status of the International Reference Ionosphere." *Reviews of Geophysics and Space Physics*, 16(2), 177-181.

Ray R. D., and Egbert G. D. (1997). "The Flux of Tidal Energy across Latitude 60°S." *Geophysical Research Letters*, 24(5), 543-546.

Reeh N., Madsen S. N., and Mohr J. J. (1999). "Combining SAR interferometry and the equation of continuity to estimate the three-dimensional glacier surface-velocity vector." *Journal of Glaciology*, 45(151), 533-538.

Reilly W. I. (1980). "Three-dimensional adjustment of geodetic networks with incorporation of gravity field data." Geophysics Division Report *160*, Department of Scientific and Industrial Research, Wellington.

Riedel B., Nixdorf U., Heinert M., Eckstaller A., and Mayer C. (1999). "The response of the Ekstromisen (Antarctica) grounding zone to tidal forcing." *Annals of Glaciology*, 29, 239-242.

Rignot E. (1996). "Tidal motion, ice velocity and melt rate of Petermann Gletscher, Greenland, measured from radar interferometry." *Journal of Glaciology*, 42(142), 476-485.

Rignot E., Jezek E. C., and Sohn H. G. (1995). "Ice Flow Dynamics of the Greenland Ice Sheet from SAR Interferometry." *Geophysical Research Letters*, 22(5), 575-578.

Rignot E., Padman L., MacAyeal D. R., and Schmeltz M. (2000). "Observation of ocean tides below the Filchner and Ronne Ice Shelves, Antarctica, using synthetic aperture radar interferometry: Comparison with tide model predictions." *Journal of Geophysical Research*, 105(C8), 19615-19630.

Rizos C. (1995). "Principles and practice of GPS surveying." Course Notes, School of Geomatic Engineering, University of New South Wales, Sydney.

Rizos C., Fu W. X., and Subsuantaeng S. (1990). "Antarctic GPS surveying with the WM101 receiver: relative positioning using pseudo-range data." *Australian Journal of Geodesy, Photogrammetry and Surveying*, 52, 57-82.

Robbins A. R. (1969). "Azimuth control in the Canadian latitudes." *The Canadian Surveyor*, XXIII(4), 389-398.

Robertson R. A., Padman L., and Egbert G. D. (1998). "Tides in the Weddell Sea." Ocean, Ice, and Atmosphere, Interactions at the Antarctic Continental Margin, S. S. Jacobs and R. F. Weiss, eds., AGU, Washington, 341-369.

Robin G. d. Q. (1966). "Mapping the Antarctic ice sheet by satellite altimetry." *Canadian Journal of Earth Sciences*, 3(6), 893-901.

Robin G. d. Q. (1979). "Formation, flow, and disintegration of ice shelves." *Journal of Glaciology*, 24(90), 259-271.

Rocken C., Johnson J. M., Braun J. J., Kawawa H., Hatanaka Y., and Imakiire T. (2000). "Improving GPS surveying with modeled ionospheric corrections." *Geophysical Research Letters*, 27(23), 3821-3824.

Rothacher M., and Mervart L. (1996). "Bernese GPS software version 4.0." Astronomical Institute, University of Berne.

Rothacher M., and Springer T. A. (1997)."Combination of Antenna Phase Center Variations." *IGS Analysis Center Workshop*, Pasadena, California, March 12-14.

Rott H., Rack W., Nagler T., and Skvarca P. (1998). "Climatically induced retreat and collapse of northern Larsen Ice Shelf, Antarctic Peninsula." *Annals of Glaciology*, 27, 86-92.

Rott H., Skvarca P., and Nagler T. (1996). "Rapid collapse of northern Larsen Ice Shelf, Antarctica." *Science*, 271(5250), 788-792.

Ruddell A. (2001). "Seismic survey (17-19 SAE): Map 1 - Bed elevation." Antarctic CRC, Hobart.

Saastamoinen J. (1972). "Atmospheric correction for the troposphere and stratosphere in radio ranging of satellites." Use of artificial satellites for geodesy, American Geophysical Union, Washington, D.C., 247-251.

Saastamoinen J. (1973). "Contribution to the theory of atmospheric refraction." *Bulletin Géodésique*, 107(1), 13-34.

Santerre R. (1991). "Impact of GPS satellite sky distribution." *Manuscripta Geodaetica*, 16, 28-53.

Savage J. C., and Burford R. O. (1970). "Accumulation of tectonic strain in California." *Bulletin of the Seismological Society of America*, 60(6), 1877-1896.

Scambos T., Dutkiewicz M. J., Wilson J. C., and Bindschadler R. A. (1992). "Application of image cross-correlation to the measurement of glacier velocity using satellite image data." *Remote Sensing of Environment*, 42, 177-186.

Scambos T., Hulbe C., Fahnestock M., and Bohlander J. (2000). "The link between climate warming and break-up of ice shelves in the Antarctic Peninsula." *Journal of Glaciology*, 46(154), 516-530.

SCAR WG-GGI. (2000). "A Unified Datum for the Antarctic Geodetic Infrastructure." SCAR WG-GGI.

Schaer S., Beutler G., Mervart L., and Rothacher M. (1995)."Global and regional ionosphere models using the GPS double difference phase observable." *1995 IGS Workshop*, Potsdam, Germany, May 15-17.

Schaer S., Beutler G., Rothacher M., and Springer T. A. (1996)."Daily Global Ionosphere Maps based on GPS carrier phase data routinely produced by the CODE Analysis Centre." *IGS Analysis Centre Workshop*, Silver Spring, USA, March 19-21.

Scherneck H. G., Johansson J. M., Mitrovica J. X., and Davis J. L. (1998). "The Bifrost Project - GPS Determined 3-D Displacement Rates in Fennoscandia from 800 Days of Continuous Observations in the Swepos Network." *Tectonophysics*, 294(3-4), 305-321.

Schmid H. (1977). "National Geodetic Satellite Program." *Part II*, National Aeronautics and Space Administration, Washington.

Schutz B. E. (1998). "Spaceborne laser altimetry: 2001 and beyond." Book of Extended Abstracts, WEGENER-98, H. P. Plag, ed., Norwegian Mapping Authority, Honefess, Norway.

Schwiderski E. W. (1980a). "Ocean Tides, Part I: Global Ocean Tidal Equations." *Marine Geodesy*, 3, 161-217.

Schwiderski E. W. (1980b). "Ocean Tides, Part II: A Hydrodynamical Interpolation Model." *Marine Geodesy*, 3, 219-255.

Schwiderski E. W. (1980c). "On charting global ocean tides." *Reviews of Geophysics and Space Physics*, 18(1), 243-268.

Schwiderski E. W. (1983). "Atlas of Ocean Tidal Charts and Maps, Part I: The Semidiurnal Principal Lunar Tide M_2." *Marine Geodesy*, 6(3-4), 219-265.

Seeber G. (1993). Satellite Geodesy, Walter de Gruyter, Berlin, 531 pp.

Segall P., and Davis J. L. (1997). "GPS applications for geodynamics and earthquake studies." *Annual Review of Earth Planet Science*, 25, 301-236.

Segall P., and Matthews V. (1988). "Displacement calculations from geodetic data and the testing of geophysical deformation models." *Journal of Geophysical Research*, 93(B12), 14954-14966.

Sharp R. P. (1956). "Objectives of Antarctic Glaciological Research." Antarctica in the International Geophysical Year, A. P. Crary, L. M. Gould, E. O. Hulbert, H. Odishaw, and W. E. Smith, eds., Waverly Press, Baltimore, 27-35.

Shen Z. K., Jackson D. D., and Ge B. X. (1996). "Crustal deformation across and beyond the Los Angeles basin from geodetic measurements." *Journal of Geophysical Research*, 101(B12), 27957-27980.

Shibuya K., Fukuda Y., and Michida Y. (1991). "Determination of geoid height at Breid Bay, East Antarctica." *Journal of Geophysical Research*, 96(B11), 18285-18294.

Shum C. K., Woodworth P. L., Andersen O. B., Egbert G. D., Francis O., King C., Klosko S. M., Leprovost C., Li X., Molines J. M., *et al.* (1997). "Accuracy Assessment of Recent Ocean Tide Models." *Journal of Geophysical Research*, 102(C11), 25173-25194.

Sillard P., Altamimi Z., and Boucher C. (1998). "The ITRF96 realization and its associated velocity field." *Geophysical Research Letters*, 25(17), 3223-3226.

Skvarca P. (1993). "Fast recession of the northern Larsen Ice Shelf monitored by space images." *Annals of Glaciology*, 17, 317-321.

Smith A. J. E., Ambrosius B. A. C., Wakker K. F., Woodworth P. L., and Vassie J. M. (1997). "Comparison between the Harmonic and Response Methods of Tidal Analysis Using Topex/Poseidon Altimetry." *Journal of Geodesy*, 71(11), 695-703.

Smith N. P. (1979). "Meteorological forcing of coastal waters by the inverse barometer effect." *Estuarine and Coastal Marine Science*, 8, 149-156.

Snay R. A., and Drew A. R. (1988)."Combining GPS and classical geodetic surveys for crustal deformation in the Imperial Valley, California." *High Precision Navigation*, Stuttgart and Altensteig, May 1988, 225-236.

Snay R. A., Cline M. W., and Timmerman E. L. (1983). "Regional deformation of the Earth Model for the San Diego region, California." *Journal of Geophysical Research*, 88(B6), 5009-5024.

Springer T. A. (1998). "Rogue Ionosphere Problem." IGS Mail 2071.

Stephenson S. N., Doake C. S. M., and Horsfall J. A. C. (1979). "Tidal flexure of ice shelves measured by tiltmeter." *Nature*, 282, 496-497.

Stewart M. P. (1988). "How accurate is the Australian National GPS Network as a framework for GPS heighting?" *Australian Surveyor*, 43(1), 53-61.

Swithinbank C. W. M. (1958). "The movement of the ice shelf at Maudheim." Scientific Results *Volume III*, Norweigian-British-Swedish Antarctic Expedition, 1949-52.

Tellurometer Limited. (1963). Operators' Manual for the operation and part I maintenance of the Tellurometer Micro-Distancer model MRA2, Rustica Press, Wynberg, South Africa, 130 pp.

Teunissen P. J. G., and Kluesberg A. (1996). "GPS observations and positioning concepts." GPS for geodesy, A. Kluesberg and P. J. G. Teunissen, eds., Springer-Verlag, Berlin, 175-217.

Thiel E., Crary A. P., Haubrich R. A., and Behrendt J. C. (1960). "Gravimetric determination of ocean tide, Weddell and Ross Seas, Antarctica." *Journal of Geophysical Research*, 65(2), 629-636.

Thomas R. H. (1970). "Survey on moving ice." *Survey Review*, XX(157), 322-338.

Toh H., and Shibuya K. (1992). "Thinning rate of ice sheet Mizuho Plateau, East Antarctica, determined by GPS differential method." Recent Progress in Antarctic Earth Science, Y. Yoshida, ed., Terra Scientific Publishing Company, Tokyo, 579-583.

Tralli D. M., and Lichten S. M. (1990). "Stochastic estimation of tropospheric path delays in Global Positioning System geodetic measurements." *Bulletin Géodésique*, 64, 127-159.

Tregoning P., Welsh A., McQueen H., and Lambeck K. (2000). "The search for postglacial rebound near the Lambert Glacier, Antarctica." *Earth Planets and Space*, 52(11), 1037-1041.

Tseng Y. H., I.M. W., and van der Veen C. J. (1989)."Ionospheric effects on GPS in central Antarctica." *Fifth International Geodetic Symposium on Satellite Positioning*, Las Cruces, New Mexico, March 13-17, 1114-1123.

van Dam T. M., and Herring T. A. (1994). "Detection of Atmospheric Pressure Loading Using Very Long Baseline Interferometry Measurements." *Journal of Geophysical Research*, 99(B3), 4505-4517.

van Dam T. M., Blewitt G., and Heflin M. B. (1994). "Atmospheric Pressure Loading Effects on Global Positioning System Coordinate Determinations." *Journal of Geophysical Research*, 99(B12), 23939-23950.

Vanicek P., and Krakiwsky E. (1987). Geodesy: the concepts, Elsevier Science Publishers B.V., Amsterdam, 697 pp.

Vaughan D. (1995). "Tidal flexure at ice shelf margins." *Journal of Geophysical Research*, 100(B4), 6213-6224.

Vaughan D. (1995). "Tidal flexure at ice shelf margins." *Journal of Geophysical Research*, 100(B4), 6213-6224.

Vaughan D. G. (1994). "Investigating tidal flexure on an ice shelf using kinematic GPS." *Annals of Glaciology*, 20, 372-376.

Vaughan D. G., and Doake C. S. M. (1996). "Recent atmospheric warming and retreat of ice shelves on the Antarctic peninsula." *Nature*, 379(6563), 328-331.

Vittuari L. (1994)."Advanced kinematic GPS in Antarctica." *4th Geodetic Meeting Poland-Italy*, Warsaw University of Technology, September 1994, 181-194.

Wager A. C., Doake C. S. M., Paren J. G., and Walton J. L. W. (1980). "Survey reduction for glacier movement studies." *Survey Review*, XXV(196), 251-263.

Wahr J. M. (1985). "Deformation induced by Polar Motion." *Journal of Geophysical Research*, 90(B11), 9363-9368.

Wahr J., Wingham D., and Bentley C. (2000). "A method of combining ICESat and GRACE satellite data to constrain Antarctic mass balance." *Journal of Geophysical Research*, 105(B7), 16279-16294.

Walpersdorf A., Calais E., Haase J., Eymard L., Desbois M., and Vedel H. (2001). "Atmospheric gradients estimated by GPS compared to a high resolution numerical weather prediction (NWP) model." *Physics & Chemistry of the Earth Part A-Solid Earth & Geodesy*, 26(3), 147-152.

Webb D. J. (1982). "Tides and tidal energy." *Contemporary Physics*, 23(5), 419-442.

Weill L. R. (1997). "Conquering multipath: The GPS accuracy battle." *GPS World*, 8(4), 59-66.

Wells D., Beck N., Delikaraoglou D., Kluesberg A., Krakiwsky E. J., Lachapelle G., Langley R. B., Nakiboglu M., Schwarz K., Tranquilla J. M., *et al.* (1986). Guide to GPS positioning, University of New Brunswick Graphic Services, Ottawapp.

Welsch W. (1979). "A review of the adjustment of free networks." *Survey Review*, XXV(194), 167-180.

Welsch W. (1983). "Finite element analysis of strain patterns from geodetic observations across plate margins." *Tectonophysics*, 97, 57-71.

Welsch W. M. (1993). "A general 7-parameter transformation for the combination, comparison and accuracy control of terrestrial and satellite network observations." *Manuscripta Geodaetica*, 18, 295-305.

WG-GGI (2001). "International database of SCAR Epoch GPS Campaigns." Institut für Planetare Geodäsie, Technische Universität Dresden.

Whillans I. M., van der Veen C. J., and Tseng Y. (1990). "Application of the Global Positioning System in Antarctica." *Antarctic Journal of the United States*, 25(2), 6-9.

Whitten C. A. (1967). "Geodetic networks versus time." *Bulletin Geodesique*, 84, 109-116.

Whitten C. A., and Claire C. N. (1960). "Analysis of geodetic measurements along the San Andreas Fault." *Bulletin of the Seismological Society of America*, 53, 404-415.

Wiederholt L. F., and Kaplan E. D. (1996). "GPS system segments." Understanding GPS: principles and applications, E. D. Kaplan, ed., Artech House, Norwood, 59-81.

Williams M. J. M., Grosfeld K., Warner R. C., Gerdes R., and Determann J. (2001). "Ocean circulation and ice-ocean interaction beneath the Amery Ice Shelf, Anarctica." *Journal of Geophysical Research*, in press.

Williams M. J. M., Warner R. C., and Budd W. F. (1998). "The effects of ocean warming and ocean circulation under the Amery Ice Shelf, East Antarctica." *Annals of Glaciology*, 27, 75-80.

Williams R. T., and Robinson E. S. (1979). "Ocean tide and waves beneath the Ross Ice Shelf, Antarctica." *Science*, 203.

Williams R. T., and Robinson E. S. (1981). "Flexural waves in the Ross Ice Shelf." *Journal of Geophysical Research*, 86(C7), 6643-6648.

Wilson B. D., Mannucci A. J., and Edwards C. D. (1995). "Subdaily Northern Hemisphere Ionospheric Maps Using an Extensive Network of GPS Receivers." *Radio Science*, 30(3), 639-648.

Witchayangkoon B., and Segantine P. C. L. (1999). "Testing JPL's PPP service." *GPS Solutions*, 3(1), 73-75.

Wolfrum O. (1992). "Merging terrestrial and satellite networks by a ten-parameter transformation model." *Manuscripta Geodaetica*, 17, 210-214.

Wong A. P. (1994). "Structure and dynamics of Prydz Bay, Antarctica, as inferred from a summer hydrographic data set." Masters Thesis, University of Tasmania, Hobart.

Wong A. P., Bindoff N., and Forbes A. (1998). "Ocean-ice shelf interaction and possible bottom water formation in Prydz Bay, Antarctica." Ocean, ice, and atmosphere: interactions at the Antarctic continental margin, S. S. Jacobs and R. F. Weiss, eds., American Geophysical Union, Washington, 173-187.

Wubbena G. (1985)."Software developments for geodetic positioning with GPS using TI4100 code and carrier measurements." *First International Symposium on Precise Positioning with GPS*, Rockville, Maryland, 403-412.

Yamada A., Maruyama K., Ootaki O., Itabashi A., Hatanaka Y., Miyazaki S., Negishi H., Higashi T., Nogi Y., Kanao M., *et al.* (1998). "Analysis of GPS data at Syowa station and IGS tracking stations." *Polar Geoscience*, 11, 1-8.

Yaskowich S. A. (1964). "Tellurometer ground swing on geodetic lines." *The Canadian Surveyor*, XVIII(1), 54-66.

Yi D., Minster J. B., and Bentley C. R. (2000). "The effect of ocean tidal loading on satellite altimetry over Antarctica." *Antarctic Science*, 12(1), 119-124.

Young N. W. (1979)."Application of Doppler satellite observations to the study of ice-flow in east Antarctica - problems peculiar to Doppler surveys in high latitudes." *Proceedings of the second International Geodetic Symposium on Satellite Doppler Positioning*, Austin, Texas, January 22-26, 1979, 373-391.

Young N., and Hyland G. (2001, in press)."Velocity and strain rates derived from InSAR analysis over the Lambert Glacier-Amery Ice Shelf system." *4th International Symposium on Remote Sensing in Glaciology*, Maryland, USA, 4-8 June 2001.

Yuan L. L., Anthes R. A., Ware R. H., Rocken C., Bonner W. D., Bevis M. G., and Businger S. (1993). "Sensing climate change using the Global Positioning System." *Journal of Geophysical Research-Atmospheres*, 98(D8), 14925-14937.

Yunck T. P. (1995). "GPS data, acquisition, environmental effects." *Reviews of Geophysics*, 33(Supplement), 349-352.

Zetler B., Cartwright D. E., and Berkman S. (1979). "Some comparisons of response and harmonic tide predictions." *International Hydrographic Review*, LVI(2), 105-115.

Zhang J., Bock Y., Johnson H., Fang P., Williams S., Genrich J., Wdowinski S., and Behr J. (1997). "Southern California Permanent GPS Geodetic Array - error analysis of daily position estimates and site velocities." *Journal of Geophysical Research*, 102(B8), 18035-18055.

Zumberge J. F., Heflin M. B., Jefferson D. C., Watkins M. M., and Webb F. H. (1997). "Precise point positioning for the efficient and robust analysis of GPS data from large networks." *Journal of Geophysical Research*, 102(B3), 5005-5017.

Zumberge J. F., Watkins M. M., and Webb F. H. (1998). "Characteristics and applications of precise GPS clock solutions every 30 seconds." *Navigation*, 44(4), 449-456.

Zumberge J. H. (1964). "Horizontal strain and absolute movement of the Ross Ice Shelf between Ross Island and Roosevelt Island, Antarctica, 1958-63." Antarctic Snow and Ice Studies, M. Mellor, ed., American Geophysical Union, Washington, D.C., 65-81.

Zwartz D., Tregoning P., Lambeck K., and Johnston P. (1999). "Estimates of present-day glacial rebound in the Lambert Glacier region, Antarctica." *Geophysical Research Letters*, 26(10), 1461-1464.

Appendix A – Mean Sea Level connection (1969)

As described in Chapter 3, the 1968-69 survey of the Amery Ice Shelf included an optical levelling run. If the heights from this levelling can be compared with modern estimates from GPS/remote sensing, an estimate may be made of the long-term ice shelf thickness changes. However, before these heights can be compared the levelling needs to be computed relative to the geoid and then corrected for the geoid-ellipsoid separation.

At the time of the survey, three connections were made to sea level. A connection made over the ice shelf front near A509, as reported in Budd (1982), did not actually occur (personal communication, M. Corry, 2001).

Firstly, a barometric connection was made to tidal Beaver Lake from Jetty Peninsula. Secondly, two measurements were made on different days to instantaneous sea level through a tide crack at Nickols Island (Wharf Island) near Landing Bluff. The barometric connection was accurate enough for it to be concluded that Beaver Lake was approximately at sea level, although the second and third connections through the tide crack were the more accurate of the two since sea level was actually levelled to.

Both of the levelled connections are recorded in a field book[1] from the 1968-69 campaign. Unfortunately, no date and time are given for the first tide crack connection, although an entry into a personal log by Max Corry shows the date to be December 30, 1968. The field book entry for the second tide crack connection shows an exact time of measurement of the connection between sea level and the benchmark of 1300 GMT[2] February 20, 1969. Unfortunately, at the time of the survey no local tide gauge measurements were made, and hence the instantaneous connection could not be corrected to Mean Sea Level.

1. field book 82 0038 (yellow, ~A5 in size)
2. 1900 MBT (Mawson Base Time)

Given the tidal range in this region, this could introduce an error of up to 1-1.5m into the heights of the ice shelf stations. Such an error is important if comparisons are to be made with more recent ice shelf profiles from GPS or remote sensing measurements.

Using the GPS data at HWDT[3], the tidal constituents that were determined in Chapter 4 allowing a prediction of sea level at the time of the second connection to be made. That is, using our GPS-determined tidal constituents, based on one months data, we predicted a tidal height at 1300 GMT February 20, 1969. Some error will be introduced by using a thirty day record to predict sea level thirty years earlier, however this will be significantly less than the present error in the height profile of the ice shelf. It is expected that this error would be approximately 5% of the tidal range at HWDT (~70-100mm; personal communication, J. Hunter, 2001). However, a much larger error may be introduced by local weather conditions. While atmospheric pressure is accounted for in the tidal analysis, no pressure values were recorded on the day of observation, and so the inverse barometer effect cannot be accounted for in the prediction.

Using the tidal constituents determined from the HWDT data, the predicted height of the instantaneous sea level above Mean Sea Level defined by the HWDT constituents is +0.322m. Consequently, the heights determined from the optical levelling of the AIS need to be increased by approximately 0.3m.

Currently, it is not possible to make an accurate comparison of the 1968-69 ice shelf heights with GPS/remote sensing measurements due to the low accuracy of global geopotential models in Antarctica. The low geoid accuracy is caused by the inclusion of very little local gravity data into the geopotential models, such as EGM96. It is expected that the accuracy of these models will improve significantly in Antarctica as more spatially dense gravity measurements are made, such as from the GRACE, GOCE and CHAMP satellite missions. Since the ice shelf is floating relative to the geoid, the difference between Mean Sea Level and the geoid, known as sea surface topography (SST), must also be accounted for (up to 1m). To a lesser extent, the unknown effects of post-glacial rebound since 1968-69 and local weather conditions at the time of the sea level connection also affect this comparison.

---

3. HWDT is within 10km of Nickols Island

Improvements in geoid model accuracy and knowledge of the SST will allow the ellipsoidal heights from GPS/remote sensing to be compared with the orthometric heights from the levelling. However, the relative height differences are unaffected by these biases. This will consequently reveal if any long term changes in the ice shelf thickness have occurred during the period since 1968-69.

Appendix B – GPS Site Occupation Details

Table B-1: AIS GPS site occupation list Each daily site occupation in one season is shown as a ✓; $^{\infty}$ denotes an L1-only solution; $^{\Pi}$ denotes observation during a kinematic campaign.

Year Site	Lat. (°)	Long. (°)	1988-89$^{\infty}$	1989-90	1990-91	1995-96	1998-99	Total number of days occupied	Time between first and last occupations (years)
A129	-70.867	69.846				✓$^{\Pi}$	✓✓	3	3
A130	-70.877	69.857				✓$^{\Pi}$	✓✓	3	3
A131	-70.881	69.831					✓✓	1	<1
B132	-70.871	69.815					✓	1	<1
A201	-70.867	69.889				✓$^{\Pi}$	✓	2	3
A202	-70.874	70.124					✓	1	<1
B207	-71.003	70.738			✓			1	<1
A301	-70.837	69.699				✓$^{\Pi}$	✓	2	3
A302	-70.823	69.625					✓	1	<1
A303	-70.794	69.433					✓	1	<1

Year Site	Lat. (°)	Long. (°)	1988-89[∝]	1989-90	1990-91	1995-96	1998-99	Total number of days occupied	Time between first and last occupations (years)
A304	-70.785	69.355					✓	1	<1
A305	-70.780	69.257					✓	1	<1
A306	-70.819	69 088					✓	1	<1
A307	-70.803	69.000					✓	1	<1
A308	-70.790	68.891					✓✓	2	<1
A401	-70.901	69.810					✓	1	<1
A403	-71.018	69.676					✓	1	<1
A404	-71.063	69 625					✓	1	<1
A405	-71.086	69.595					✓	1	<1
B406	-71.225	69.473			✓			1	<1
A32_	-70.482	70.384				✓[π]		1	<1
A33_	-70.546	70.295				✓[π]	✓	2	3
A34_	-70 580	70.260				✓[π]		1	<1
A35_	-70.641	70.178					✓✓	2	<1
B36	-70.774	70.030			✓			1	<1

Year Site	Lat. (°)	Long. (°)	1988-89[∝]	1989-90	1990-91	1995-96	1998-99	Total number of days occupied	Time between first and last occupations (years)
A37_	-70.749	69.988			✓		✓✓	3	8
A39_	-70.836	69.884					✓	1	<1
C12_	-70.476	70.389				✓✓✓	✓✓	5	3
C10_	-70.637	70 206				✓✓	✓	3	3
C8__	-70.814	70.011				✓✓✓		3	<1
C6__	-70.975	69 831				✓✓✓	✓	4	3
C4__	-71.143	69.637				✓✓✓	✓	4	3
C2__	-71.316	69.435				✓✓✓✓		4	<1
CAMP	-70.892	69.873					✓(12)	12	<1
G1E1	-69.501	71.722					✓✓	2	<1
G1N1	-69.501	71.722					✓	1	<1
G1S1	-69.502	71.721					✓✓	2	<1
G1W1	-69.501	71.720					✓✓	2	<1
G2E1	-70.169	70.864					✓✓✓	3	<1
G2S1	-70.169	70.862					✓	1	<1

Year Site	Lat. (°)	Long. (°)	1988-89[∝]	1989-90	1990-91	1995-96	1998-99	Total number of days occupied	Time between first and last occupations (years)
G2W1	-70.169	70.861					✓✓	2	<1
GA01	-70.189	68.733	✓✓✓		✓			4	2
GA02	-70.108	68.609	✓✓	✓	✓			4	2
GA03	-70.043	68.601	✓		✓			2	2
GA04	-70.137	68.946	✓✓	✓[∝]	✓			4	2
GA42	-70.186	69.472	✓✓		✓			3	2
GA05	-70.063	69.529	✓		✓			2	2
GA06	-69.935	69.458	✓✓		✓✓			4	2
GA07	-70 160	69.993	✓✓		✓			3	2
GA72	-70.268	70.134	✓✓		✓			3	2
GA08	-70.012	69.859	✓		✓✓			3	2
GA09	-69.908	69.848	✓✓		✓✓			4	2
GA11	-70.297	70.598	✓✓		✓			3	2
GA12	-70.360	71.145	✓✓		✓			3	2
GA21	-71.067	69.184	✓✓		✓			3	2

Year Site	Lat. (°)	Long. (°)	1988-89[∝]	1989-90	1990-91	1995-96	1998-99	Total number of days occupied	Time between first and last occupations (years)
GA22	-71.204	70.266	✓✓	✓	✓			4	2
GA23	-71.252	68.948	✓✓	✓[∝]	✓			4	2
G232	-71.200	69.125	✓✓					2	<1
GA24	-71.398	69.983	✓✓	✓	✓			4	2
G242	-71.287	69.789	✓✓	✓✓[∝]	✓			5	2
GA25	-71.404	68.688	✓✓	✓[∝]	✓			4	2
GA26	-71.469	69.260	✓✓	✓	✓			4	2
GA27	-71.518	69.848	✓✓	✓	✓[∝]			4	2
GA28	-71.654	68.981	✓✓					2	<1
G282	-71.648	68.988			✓✓			2	<1
GA29	-71.917	68.669			✓✓			2	<1
GA30	-71.641	68.470			✓[∝]✓			2	<1
GA31	-71.706	69.550			✓[∝]			2	<1
G31B	-71.706	69.555			✓✓			2	<1
GA32	-71.452	70.135			✓[∝]✓			2	<1

Year Site	Lat. (°)	Long. (°)	1988-89[∝]	1989-90	1990-91	1995-96	1998-99	Total number of days occupied	Time between first and last occupations (years)
GA33	-71.487	70.573			✓✓			2	<1
GA34	-71.624	70.143			✓✓			2	<1
GA35	-71.839	68.433			✓			1	<1
GT04	-70.252	66.527	✓✓	✓[∝]	✓			4	2
GT05	-70.502	66.463	✓✓	✓✓[∝]	✓			5	2
GT06	-70.350	65.598	✓✓	✓	✓			4	2
GT08	-70.638	65 587	✓	✓	✓			3	2
GT62	-70.314	66.167	✓✓	✓✓[∝]	✓			5	2
GT82	-70.532	66.075	✓	✓✓	✓			4	2

Appendix C – SCAR91 Results

The results from the SCAR91 have not been previously published (although the results from a previous analysis have been presented at a conference, personal communication, P. Morgan, 2001), and consequently site coordinates are shown here.

The station coordinates of the SCAR91 sites are shown in Table C-1 in ITRF97. Due to the shortness of the campaign, SCAR91 station velocities could not be determined, except at the Georg Neumayer site situated on the Ekström Ice Shelf. Each daily file for this site was split into two sections (12 hour segments). The tidal signal was not removed from this data set since suitable tide data was not available to us.

Table C-1 SCAR91 site coordinates in ITRF97

Site Name	Site Location	X	Y	Z	Solution Epoch	σX	σY	σZ
YAR1	Yaragadee, Australia	-2389025.3332	5043316.9650	-3078531.1029	1991.090	0.0080	0.0155	0.0097
TOWN	Townsville, Australia	-5041024.9045	3296980.4517	-2090553.5640	1991.133	0.0127	0.0147	0.0098
ORRO	Orroral, Australia	-4446478.8253	2678112.7501	-3696270.4324	1991.133	0.0166	0.0169	0.0132
DS40	Canberra, Australia	-4460987.9016	2682362.4394	-3674626.5947	1991.133	0.0126	0.0145	0.0100
TAS1	Hobart, Australia	-3950183.9588	2522364.6754	-4311588.6648	1991.078	0.0113	0.0139	0.0085
WELL	Wellington, New Zealand	-4780648.6815	436507.2801	-4185440.5197	1991.050	0.0127	0.0156	0.0101

Site Name	Site Location	X	Y	Z	Solution Epoch	σX	σY	σZ
WSAM	Western Samoa	-6134394.7946	-860418.4847	-1514829.6793	1991.133	0.0289	0.0282	0.0134
EIS1	Easter Island	-1884997.7801	-5357589.6551	-2892871.0760	1991.133	0.0278	0.0381	0.0204
SANG	Santiago, Chili	1769724.5648	-5044512.1734	-3468396.2868	1991.133	0.0266	0.0363	0.0186
HAR1	Hartebeestoek, South Africa	5084624.4989	2670367.7463	-2768494.5558	1991.133	0.1438	0.0843	0.0625
OHI1	O'Higgins, Antarctica	1525877.1119	-2432481.3865	-5676145.1959	1991.133	0.0305	0.0300	0.0387
WOMB	Mawson, Antarctica	1111246.9877	2169171.4110	-5874393.5181	1991.133	0.0169	0.0202	0.0212
DOVE	Dovers, Antarctica	885314.9173	1974378.6930	-5980928.4054	1991.133	0.0170	0.0200	0.0209
MCM0	McMurdo, Antarctica	-1310856.3477	310431.7741	-6213347.7173	1991.133	0.0467	0.0455	0.0920
NEUM	Georg von Neumayer, Antarctica	2102610.3243	-309037.7998	-5993558.8599	1991.133	0.1207	0.0997	0.1866
NEUN	Georg von Neumayer, Antarctica	2102610.6322	-309037.4961	-5993559.0798	1991.133	0.0970	0.0694	0.1128
NEUO	Georg von Neumayer, Antarctica	2102610.5460	-309037.5109	-5993558.7642	1991.133	0.0964	0.0595	0.2132
NEUP	Georg von Neumayer, Antarctica	2102611.2113	-309037.4788	-5993558.9697	1991.133	0.0461	0.0333	0.0590
NEUQ	Georg von Neumayer, Antarctica	2102610.9244	-309037.4145	-5993558.7045	1991.133	0.0730	0.0769	0.1781
NEUS	Georg von Neumayer, Antarctica	2102613.9434	-309037.7896	-5993557.5912	1991.133	9.1301	6.7379	4.9712
NEUT	Georg von Neumayer, Antarctica	2102611.8970	-309037.5668	-5993558.4495	1991.133	0.0938	0.0756	0.1610

Appendix D Raw terrestrial data availability (1968-1970)

Table D-1: Details of the directions found in the field books (sets of directions are represented here as angles for convenience) An asterix indicates that the direction was not used directly in the original reduction. Rather, it was used to compute another direction that was used in the original reduction. A ∞ indicates that a sizeable (>20″) error was found within computer output when compared with the correct reduction of the observation in the field notes Observations marked N/O were not observed

Site	Backsight	Foresight	1968-69			1969-70		
			Field-book (Original)	Field-book (Reduced)	Computer Output	Field-book (Original)	Field-book (Reduced)	Computer Output
BLUS	PICK/ FOXR	A406	✘	✘	✔	✘	✘	✔
A406	BLUS	A405	✘	✘	✔	✔	✔	✔∞
A405	A406	A404	✔	✘	✔	✔	✔	✔
A404	A405	A403	✔	✘	✔	✔	✔	✔
A403	A404	A402	✔	✘	✔∞	✔	✔	✔
A402	A403	A401	✔	✘	✔	✔	✔	✔
A401	A402	A129(G3)	✔	✘	✔	✔	✘	✔
A129(G3)	A39	A201	✔	✘	✔*		N/O	
A129(G3)	A39	A401	✔	✘	✔*		N/O	
A129(G3)	A39	A131	✔	✘	✔		N/O	
A129(G3)	A39	A301	✔	✘	✔*		N/O	
A129(G3)	A201	A131	✔	✘	✘		N/O	
A129(G3)	A131	A301		N/O		✔	✔	✔
A129(G3)	A131	A39		N/O		✔	✔	✔
A129(G3)	A131	A201		N/O		✔	✔	✔
A129(G3)	A131	A401		N/O		✔	✔	✔
A129(G3)	A201	A131	✔	✘	✔		N/O	
A202	A201	A203	✔	✘	✔	✔	✔	✔
A202	A201	A204	✔	✘	✘		N/O	
A203	A202	A204	✔	✘	✔	✔	✔	✔

Site	Backsight	Foresight	1968-69			1969-70		
			Field-book (Original)	Field-book (Reduced)	Computer Output	Field-book (Original)	Field-book (Reduced)	Computer Output
A204	A203	A205	✔	✘	✔	✔	✔	✔
A205	A204	A206	✔	✘	✔	✔	✔	✔
A206	A205	A207	✔	✘	✔	✔	✔	✔
A207	A206	NEWY	✘	✔	✔	✔	✔	✘
A207	A206	RUSS	✔	✘	✔	✔	✔	✘
NEWY	A207	MOUS	✘	✘	✔		N/O	
A301	A129(G3)	A302	✔	✘	✔	✔	✔	✔
A302	A301	A303	✔	✘	✔	✔	✔	✔
A303	A302	A304	✔	✘	✔	✔	✔	✔
A304	A303	A305	✔	✘	✔	✔	✔	✔
A305	A304	A306	✔	✘	✔	✔	✔	✔
A306	A305	A307	✔	✘	✔	✔	✔	✔
A307	A306	A308	✔	✘	✔	✔	✔	✔
A39	A38	A129	✔	✘	✔∞	✘	✔	✔∞
A38	A39	A37	✔	✘	✔	✘	✔	✔
A37	A38	A36	✔	✘	✔	✘	✔	✔
A36	A37	A35	✔	✘	✔	✘	✔	✔
A35	A36	A34	✔	✘	✔	✘	✔	✔
A34	A35	A33	✔	✘	✔	✘	✔	✔
A33	A34	A32	✔	✘	✔	✘	✔	✔
A32	A33	A31	✔	✘	✔	✘	✔	✔
A31	A32	A30	✔	✘	✔	✘	✔	✔
A30	A31	A29	✔	✘	✔	✘	✔	✔
A29	A30	A28	✔	✘	✔	✘	✔	✔
A28	A29	A27	✔	✘	✔	✘	✔	✔
A27	A28	A26	✔	✘	✔∞	✘	✔	✔∞
A26	A27	A25	✔	✘	✔∞	✘	✔	✔
A25	A26	A24	✔	✘	✔∞	✘	✔	✔

Site	Backsight	Foresight	1968-69			1969-70		
			Field-book (Original)	Field-book (Reduced)	Computer Output	Field-book (Original).	Field-book (Reduced)	Computer Output
A24	A25	A99(G2)	✔	✘	✔	✘	✔	✔
A99(G2)	A24	A98	✔	✘	✔	✘	✔	✔
A99(G2)	A24	CORR	✔	✘	✘		N/O	
A98	A99	A23	✔	✘	✔	✘	✔	✔∞
A23	A24	A22	✔	✘	✔	✘	✔	✔
A22	A23	A21	✔	✘	✔	✘	✔	✔
A21	A22	A20	✔	✘	✔	✘	✔	✔
A20	A21	A19	✔	✘	✔	✘	✔	✔
A19	A20	A18	✔	✘	✔	✘	✔	✔
A18	A19	A17	✔	✘	✔	✘	✔	✔
A17	A18	A16	✔	✘	✔	✘	✔	✔
A16	A17	A15	✔	✘	✔	✘	✔	✔
A15	A16	A14	✔	✘	✔	✘	✔	✔
A14	A15	A13	✔	✘	✔	✘	✔	✔
A13	A14	A12	✔	✘	✔	✘	✔	✔
A12	A13	A74	✔	✘	✔	✘	✔	✔
A74	A12	A72(G1)	✘	✘	✔∞	✘	✔	✔∞
A72(G1)	A74	A111	✔	✘	✔∞	✘	✔	✔
A111	A72(G1)	A110	✔	✘	✔	✘	✔	✔
A110	A111	A112	✔	✘	✔	✘	✔	✔
A112	A110	A113	✔	✘	✔	✘	✔	✔
A113	A112	A114	✔	✘	✔	✘	✔	✔
A114	A113	A115	✔	✘	✔	✘	✔	✔
A115	A114	A116	✔	✘	✔	✘	✔	✔
A116	A115	A117	✔	✘	✔	✘	✔	✔
A117	A116	A118	✔	✘	✔	✘	✔	✔
A118	A117	A119	✔	✘	✔	✘	✔	✔
A119	A118	LAND	✔	✘	✔	✘	✔	✔

Site	Backsight	Foresight	1968-69			1969-70		
			Field-book (Original)	Field-book (Reduced)	Computer Output	Field-book (Original)	Field-book (Reduced)	Computer Output
LAND	A119	HAMM	✔	✘	✔	✘	✔	✔
A72(G1)	A501	A601	✔	✘	✔*		N/O	
A72(G1)	A74	A501	✘	✘	✔*	✘	✔	✔
A72(G1)	A74	A601	✘	✘	✔*∞	✘	✔	✔
A601	A72(G1)	A602	✔	✘	✔	✘	✔	✔
A602	A601	A603	✔	✘	✔	✘	✔	✔
A603	A602	A604	✔	✘	✔	✘	✔	✔
A604	A603	A605	✔	✘	✔	✘	✔	✔
A605	A604	A606	✔	✘	✔	✘	✔	✔
A606	A605	A607	✔	✘	✔	✘	✔	✔
A607	A606	A608	✔	✘	✔	✘	✔	✔
A608	A607	A609	✔	✘	✔	✘	✔	✔
A609	A608	A610	✔	✘	✔	✘	✔	✔
A610	A609	A611	✔	✘	✔	✘	✔	✔
A611	A610	A612	✔	✘	✔	✘	✔	✔
A612	A611	A613	✔	✘	✔	✘	✔	✔
A501	A72(G1)	A502	✔	✘	✔	✘	✔	✔
A502	A501	A503	✔	✘	✔	✘	✔	✔
A503	A502	A504	✔	✘	✔	✘	✔	✔
A504	A503	A505	✔	✘	✔	✘	✔	✔
A505	A504	A506	✔	✘	✔	✘	✔	✔
A505	A504	A507	✘	✘	✔	✘	✔	✔
A507	A505	A508	✔	✘	✔	✘	✔	✔
A508	A507	A509	✔	✘	✔	✘	✔	✔

Table D-2: Details of the strain grid directions found in the field books (sets of directions represented here as angles for convenience). The strain grid directions were not used in the initial traverse reduction, and hence do not appear in the computer output. Measurements of the G1 strain grid were made twice (denoted by 2x) during 1968-69

Site	Dir1	Dir2	Dir3	1968-69		1969-70	
				Field-book (Original)	Field-book (Reduced)	Field-book (Original)	Field-book (Reduced)
A129(G3)	A130	A131	A132	✔	✘	✔	✘
A130	A131	A132	A129	✔	✘	✔	✘
A131	A132	A129	A130	✔	✘	✔	✘
A132	A129	A130	A131	✔	✘	✔	✘
A99(G2)	A100	A98	A101	✔	✘	✘	✘
A100	A98	A101	A99	✔	✔	✔	✘
A101	A99	A100	A98	✔	✔	✔	✘
A98	A101	A99	A100	✔	✔	✘	✘
A72(G1)	A75	A74	A73	✔x2	✘	✔	✘
A73	A72	A75	A74	✔x2	✘	✔	✘
A74	A73	A72	A75	✔x2	✘	✘	✘
A75	A74	A73	A72	✔x2	✘	✔	✘
A1	A2	A3	A11	✔	✘	✔	✘
A2	A3	A11	A1	✔	✘	✔	✘
A3	A11	A1	A2	✔	✘	✔	✘
A11	A1	A2	A3	✔	✘	✔	✘

Table D-3· Details of the Tellurometer distance information found in the field books

Site1	Site2	1968-69		1969-70	
		Field-book (Original)	Computer Output	Field-book (Original)	Computer Output
BLUS	A406	✘	✔	✘	✔
A406	A405	✔	✔	✔	✔
A405	A404	✔	✔	✔	✔
A404	A403	✔	✔	✔	✔
A403	A402	✔	✔	✔	✔
A402	A401	✔	✔	✔	✔
A401	A131	✘	✔	✘	✔
A129(G3)	A131	✘	✔	✔	✔
A129(G3)	A301	✔	✔	✔	✔
A129(G3)	A39	✔	✔	✘	✔
A129(G3)	A201	✔	✔	✔	✔
A129(G3)	A401	✔	✔	✔	✔
A201	A202	✔	✔	✔	✔
A202	A203	✔	✔	✔	✔
A203	A204	✔	✔	✔	✔
A204	A205	✔	✔	✔	✔
A205	A206	✔	✔	✔	✔
A206	A207	✔	✔	✔	✔
A207	NEWY	✘	✔	✘	✔
A301	A302	✔	✔	✔	✔
A302	A303	✔	✔	✔	✔
A303	A304	✔	✔	✔	✔
A304	A305	✔	✔	✔	✔
A305	A306	✔	✔	✔	✔
A306	A307	✔	✔	✔	✔
A307	A308	✔	✔	✔	✔
A39	A38	✔	✔	✘	✔

Site1	Site2	1968-69		1969-70	
		Field-book (Original)	Computer Output	Field-book (Original)	Computer Output
A38	A37	✔	✔	✘	✔
A37	A36	✔	✔	✘	✔
A36	A35	✔	✔	✘	✔
A35	A34	✔	✔	✘	✔
A34	A33	✔	✔	✘	✔
A33	A32	✔	✔	✘	✔
A32	A31	✔	✔	✘	✔
A31	A30	✔	✔	✘	✔
A30	A29	✔	✔	✘	✔
A29	A28	✔	✔	✘	✔
A28	A27	✔	✔	✔	✔
A27	A26	✔	✔	✔	✔
A26	A25	✔	✔	✔	✔
A25	A24	✔	✔	✔	✔
A24	A99(G2)	✔	✔	✔	✔
A99(G2)	A98	✔	✔	✔	✔
A98	A23	✔	✔	✔	✔
A23	A22	✔	✔	✔	✔
A22	A21	✔	✔	✔	✔
A21	A20	✔	✔	✔	✔
A20	A19	✔	✔	✔	✔
A19	A18	✔	✔	✔	✔
A18	A17	✔	✔	✔	✔
A17	A16	✔	✔	✔	✔
A16	A15	✔	✔	✔	✔
A15	A14	✔	✔	✔	✔
A14	A13	✔	✔	✔	✔
A13	A12	✔	✔	✔	✔
A12	A74	✔	✔	✔	✔

Site1	Site2	1968-69		1969-70	
		Field-book (Original)	Computer Output	Field-book (Original)	Computer Output
A74	A72(G1)	✔	✔	✔	✔
A72(G1)	A111	✔	✔	✔	✔
A111	A110	✔	✔	✔	✔
A110	A112	✔	✔	✔	✔
A112	A113	✔	✔	✔	✔
A113	A114	✔	✔	✔	✔
A114	A115	✔	✔	✔	✔
A115	A116	✔	✔	✔	✔
A116	A117	✔	✔	✔	✔
A117	A118	✔	✔	✔	✔
A118	A119	✔	✔	✔	✔
A119	LAND	✘	✔	✘	✔
A72(G1)	A601	✔	✔	✔	✔
A601	A1	✔	✔	✔	✔
A1	A602	✔	✔	✔	✔
A602	A603	✔	✔	✔	✔
A603	A604	✔	✔	✔	✔
A604	A605	✔	✔	✔	✔
A605	A606	✔	✔	✔	✔
A606	A607	✔	✔	✔	✔
A607	A608	✔	✔	✔	✔
A608	A609	✔	✔	✔	✔
A609	A610	✔	✔	✔	✔
A610	A611	✔	✔	✔	✔
A611	A612	✔	✔	✔	✘
A612	A613	✔	✔	✔	✔
A72(G1)	A501	✔	✔	✔	✔
A501	A502	✔	✔	✔	✔
A502	A503	✔	✔	✔	✔

Site1	Site2	1968-69		1969-70	
		Field-book (Original)	Computer Output	Field-book (Original)	Computer Output
A503	A504	✔	✔	✔	✔
A504	A505	✔	✔	✔	✔
A505	A506	✔	✔	✔	✔
A505	A507	✔	✔	✔	✔
A507	A508	✔	✔	✔	✔
A508	A509	✔	✔	✔	✔

Table D-4: Details of the Tellurometer measurements made of the strain grids found in the field books

Site1	Site2	1968-69		1969-70	
		Field-book (Original)	Computer Output	Field-book (Original)	Computer Output
A1	A3	✔	✘	✘	✘
A2	A11	✔	✘	✘	✘
A75	A73	✔	✘	✔	✘
A74	A72	✔	✔	✔	✔
A132	A130	✘	✘	✔	✘
A129	A131	✘	✘	✔	✔

Table D-5: Details of the azimuth information found in the field books for 1968-69. The 1969-70 observations are difficult to read and observations to only a few stars were made (for the observations found to date).

Site	Reference Object	Field-book (Original)	Field-book (Reduced)	Computer Output
A129(G3)	A131	✔	✘	✘
A99(G2)	A98	✔	✘	✘
A72(G1)	A74	✔	✘	✘
A1	A11	✔	✘	✘